

Control aspects of integrated design of wind turbines : a foundation

Mary C. M. Rogers

Industrial Control Centre,
Department of Electronic and Electrical Engineering,
University of Strathclyde,
50 George Street,
Glasgow G1 1QE

Thesis submitted to the
University of Strathclyde
for the degree of
Doctor of Philosophy
Sept. 1998

The copyright of this thesis belongs to the author under the terms of the United Kingdom Copyright Acts as qualified by University of Strathclyde Regulation 3.49. Due acknowledgement must always be made of the use of any material contained in, or derived from, this thesis.

Acknowledgements

First of all, I wish to express my sincere thanks to my supervisor, Bill Leithead, for his guidance and encouragement. I am also grateful for many helpful discussions with colleagues and friends in the Industrial Control Centre, particularly Jacqueline Wilkie, Barry Connor and Douglas Leith.

I have received valuable advice and encouragement from Peter Jamieson (Garrad Hassan and Partners), Colin Anderson and Tim Campbell (Edinburgh University), Ray Hunter (National Wind Turbine Centre, National Engineering Laboratory), Jack Noakes (Renewable Energy Systems Ltd), and Jan Pierek and Tim van Engelen (Netherlands Energy Research Foundation ECN).

I gratefully acknowledge the funding which has been provided for this work by the Engineering and Physical Sciences Research Council, the Engineering Technology Support Unit (ETSU) of the Department of Trade and Industry (formerly the Department of Energy) and Renewable Energy Systems Ltd.

Finally I must thank my family for their support and forbearance.

Abstract

The configuration of a wind turbine and its control system dictate the dynamics of the machine. Since the dynamics of each part of the wind turbine affect those of the others, the machine should be considered as an integrated unit. The objective of the research reported here is to lay the foundations for the control aspects of integrated design by determining the dependence of the power controller performance of medium- and large-scale, actively regulated, up-wind, horizontal-axis, grid-connected wind turbines on their configuration, that is, the dependence of the magnitude of the loads experienced by the drive train on the machine characteristics.

There is a tendency amongst manufacturers to move from conventional, heavy and stiff machines to ones with lighter and more flexible components which makes machines more dynamically active and hence makes the power control task more difficult. Simple thoroughly derived linear and non-linear models of the significant wind turbine dynamics for power control are used to obtain a greater understanding of how machine parameters effect the overall behaviour of the power train. The dependence of the power controller performance of different full-span and tip-regulated machines is discussed. Finally, explanation of the results is illustrated with regard to the design of a 1 MW wind turbine.

Contents

Acknowledgements	iii
Abstract	iv
Contents	v
1 Introduction	1
1.1 Synopsis	1
1.2 Original contributions	4
1.3 Publications	5
2 General Background	8
2.1 Basic characteristics of wind turbines	8
2.2 Normal operation of a wind turbine	9
2.3 Power regulation	11
2.4 Loads experienced by a wind turbine	13
2.4.1 Characteristics of wind speed	13
2.4.2 Aerodynamic loads	16
2.4.3 Drive-train loads	18
2.5 Active power control and controller design	18
3 Wind turbine dynamics	21
3.1 Dynamic models	21
3.1.1 Wind speed model	22
3.1.2 Aerodynamics	23
3.1.3 Modelling of spectral loads	24
3.1.4 Actuator dynamics	25
3.1.5 Power-train dynamics	27
3.2 Performance of the conventional power train	32
3.2.1 Simple performance indicators	32
3.2.1.1 Non-compliant mounted gearbox	32
3.2.1.2 Compliant mounted gearbox	37
3.2.2 Dynamic performance	39
3.3 Conclusions	42

4	Resonance Control	44
4.1	Drive train modification	45
4.1.1	Reduction of $n\Omega_o$ loads	49
4.1.2	Light rotor	51
4.1.3	Low generator slip	52
4.1.4	Discussion	53
4.2	Direct control of drive-train resonance	54
4.2.1	Controller synthesis	59
4.2.2	Performance evaluation	64
4.2.3	Discussion	65
4.3	Conclusions	66
5	Full-span pitch-regulated machines	67
5.1	Introduction	67
5.2	Different types of wind turbine configuration	67
5.3	Equivalent rotor designs for two- and three-bladed machines	70
5.4	Linear analysis	71
5.5	Performance assessment	72
5.6	Conclusions	85
6	Tip-regulated machines	87
6.1	Introduction	87
6.2	Different types of wind turbine configuration	87
6.3	Equivalent rotor designs for two- and three-bladed machines	88
6.4	Linear analysis	89
6.5	Performance assessment	90
6.6	Conclusions	102
7	Novel tip control devices	104
7.1	The FLEDGE	104
7.1.1	Effect of new rotor design on the drive-train dynamics	106
7.1.1.1	Reducing tip size	106
7.1.1.2	Replacing tip with fledge mechanism	109
7.1.2	Effect of fledges on actuator capability	108
7.1.3	Comparison of performance of fledges and conventional tips	109
7.1.4	Summary of fledge performance	111
7.2	Independent blade control	111

7.2.1	The compliant tip concept and aerodynamics	113
7.2.2	Estimation of the required tip angle	114
7.2.3	Comparison of compliance tip control with power control	117
7.2.4	Robustness of independent tip control	124
7.2.5	Assessment of independent tip control	124
7.2.6	Summary of independent tip control performance	126
7.3	Conclusions	126
8	Integrated Design	128
8.1	Summary of results	128
8.2	An illustrative example	130
9	Conclusions	139
10	Further Work	141
	References	145
	Appendix A Modelling of wind speed	A-1
A.1	Introduction	A-1
A.2	Modelling the spectrum of wind speed measured at a point	A-2
A.3	Modelling the wind speed experienced by the whole rotor	A-4
A.4	Separate wind speeds for the tip and the remainder of rotor	A-5
A.5	Modelling of loads on individual blades	A-7
	Appendix B Power-train dynamics	B-1
B.1	Introduction	B-1
B.2	Rotor	B-2
B.2.1	Equations of motion of rotor	B-2
B.2.2	Linearisation of rotor dynamics	B-5
B.2.3	Equations of motion of the hub	B-10
B.2.4	Aerodynamic/rotor interaction	B-13
B.3	Gearbox	B-16
B.3.1	Equations of motion of gearbox	B-16
B.3.2	Simplification of gearbox dynamics	B-18
B.4	Drive train	B-21
B.4.1	Equations of motion of generator rotor	B-21
B.4.2	Simplification of drive-train dynamics	B-22
B.4.3	Simple drive-train model	B-25
B.5	Summary	B-27

B.5.1	Full non-linear model	B-27
B.5.2	Full linear model	B-28
B.5.3	Simple linear model	B-30
B.5.4	Simple non-linear model	B-31
Appendix C	Control of wind turbines	C-1
C.1	Characteristics of a well designed controller	C-2
C.2	Parameteric study	C-9
C.2.1	Validation of linear analysis	C-13
C.3	Implementation of a dual mode controller	C-23
Appendix D	Induction generator dynamics	D-1
D.1	Dynamics	D-1
D.2	Reduced order dynamics	D-3
D.3	Simple linear models	D-5
Appendix E	Comparable machines	E-1
E.1	Equivalent rotor designs for two- and three-bladed machines	E-1
E.1.1	Equivalent rotors for the 300 kW machines	E-3
E.1.2	Equivalent rotors for the 1 MW machines	E-6
E.1.3	Discussion	E-8
E.2	The effects of power rating and rotor speed on machine parameters	E-10
E.2.1	Wind model	E-10
E.2.2	Spectral loads	E-10
E.2.3	Effect of size on machine parameters	E-11
Appendix F	Modelling of novel tip devices	F-1
F.1	The ball-joint fledge	F-2
F.1.1	The forces acting on the fledge plate	F-2
F.1.1.1	The aerodynamics of the fledge	F-3
F.1.2	The geometry of the fledge	F-4
F.1.3	The equations of motion of the fledge	F-5
F.1.4	The fledge dynamics	F-7
F.1.4.1	Behaviour required of the fledge to be an effective brake	F-7
F.1.4.2	The effect of geometry on braking	F-8
F.1.4.3	The effect of the masses of the fledge plate and the sliding mass on braking	F-8
F.1.4.4	The effect of external forces on braking	F-11

F.1.4.5	Cable control mechanism	F-12
F.1.5	The dynamics of the ball-joint fledge power-control device	F-15
F.2	Modelling issues for the compliant tip	F-16
F.2.1	The aerodynamics of the compliant tip	F-17
F.2.2	The compliant tip actuator	F-17
Appendix G	Aerodynamic torque tables	G-1
G.1	Full-span regulated machines	G-1
G.2	Tip-regulated machines	G-1
G.3	Fledge	G-1
G.4	Compliant tip	G-2
G.5	Full-span regulated machine	G-2
Appendix H	Machine performance	H-1

1 Introduction

Environmental concerns, such as those about global warming, necessitate a wider role for renewable energy resources. One of the most promising options is wind power.

Wind turbines can be built in a variety of configurations - up- or down-wind, vertical or horizontal-axis, one-, two- or three-bladed, variable or constant speed, grid-connected or stand-alone, - and can generate from tens to thousands of kilowatts.

The configuration of a wind turbine and its control system dictate the dynamics of the machine and hence the loads it experiences. Since the dynamics of each part of the wind turbine affect those of the others, the machine should be considered as an integrated unit. The necessity and utility of an integrated approach to the design of wind turbines is emphasised by Garrad (1998). The objective of the research reported here is to lay the foundations for the control aspects of integrated design by determining the dependence of the power controller performance of medium and large-scale, actively regulated, up-wind, horizontal-axis, grid-connected wind turbines on their configuration; that is, the dependence of the magnitude of the loads experienced by the drive train, on the machine characteristics, such as the number of blades, the drive-train configuration and the power regulation mechanism. Unlike other work on the control of wind turbines, (for reviews see de la Salle *et al.*, 1990, Dijkstra *et al.*, 1994) which assumes a fixed machine configuration and considers the application of controllers derived by a variety of techniques, the affect on the achievable performance for a variety of machine configurations with equivalent control is considered.

1.1 Synopsis

The objective of the research reported here is to lay the foundations for the control aspects of integrated design of wind turbines. To do so requires the following steps to be undertaken:

- (i) determine simple models of the wind turbine and the relationship of the model parameters to the physical parameters of the machine: determine the constraints on the achievable dynamic behaviour of the power train.
- (ii) determine the performance attainable for the various wind turbine configurations with conventional and unconventional aerodynamic control devices.

The manner in which they are achieved is summarised below. The research builds on that reported in Leithead *et al.* (1991a) in which the need to investigate the dependence of power control performance of a machine is identified.

A general introduction to power control of wind turbines and the motivation for this research is given in Chapter 2. A brief account of the economic context of wind power research and the basic characteristics of wind turbines is given. Power regulation is defined and the impact, that it has on the loads which cause fatigue of a machine, is discussed.

The wind turbine dynamics which are significant for power control are discussed in Chapter 3. A simple linear model useful for the parametric studies and control design is also derived. An analysis of the relationship between machine parameters and the dynamic characteristics of the drive-train is provided and verified in Section 3.2.

From the work described in Chapter 3 a better understanding is obtained of how machine parameters effect the overall behaviour of the power train. In attempting to reduce the costs of wind turbines, there is a tendency amongst manufacturers to move from conventional, heavy and stiff machines to ones with lighter and more flexible components (Simpson, 1994). This trend makes machines more dynamically active and hence makes the power control task more difficult. This difficulty is due to increased sensitivity to loads resulting from wind turbulence and/or to the quasi-periodic loads resulting from the blades sweeping the wind field. It is thought that increasing the slip of the generator, although making the machine less efficient, improves the drive-train dynamics by adding compliance to the drive train (Bossanyi and Jervis, 1988, Juggins and Holton, 1995). Various methods of adding compliance, *e.g.* fluid couplings (Hinrichsen and Nolen, 1982) and mounting the gearbox (Simpson *et al.*, 1993) have been attempted to improve machine dynamics. However, from the results of Chapter 3, it is clear that, other than increasing the slip of the generator and making the machine less efficient, it is not always possible to improve the damping of the first drive-train mode for light rotors by conventional means. Only non-conventional methods remain to be explored.

The feasibility of increasing the damping of the first drive-train mode by two non-conventional methods is investigated in Chapter 4. The first, a direct modification to the

drive train, *i.e.* compliantly mounting the generator, an idea of Leithead (Leithead and Rogers, 1995a, 1996) is considered in Section 4.1. The second, direct control of the drive-train resonance although not possible by pitch control, may be possible by torque control on variable speed machines. Direct control of the drive-train resonance on a lightweight, flexible variable speed machine is considered in Section 4.2.

The dependence of the power controller performance of different conventional full-span and tip-regulated machines (*e.g.* two- or three-bladed, medium- or large-scale), is discussed in Chapters 5 and 6, respectively.

Tip-regulated machines are known to have an advantage over full-span regulated machines in that they are lighter and hence are faster acting (Anderson 1990a). Two novel aerodynamic devices based on tip devices are ‘fledges’ (flying leading edge devices) designed by Jamieson and Agius (1989), and independently mobile (‘compliant’) tips designed by Anderson (Anderson *et al.*, 1990). A significant advantage of these devices over conventional tip control is that they are potentially fail-safe aerodynamic braking devices. Fledges have the additional advantage that they are lighter and hence are less expensive to build (NWTC, 1994). The use of the fledge and compliant tip, for power control devices is considered in Chapter 7.

In Chapter 8, the results relevant to the control aspects of integrated design of wind turbines are summarised. Their use is illustrated with respect to the design of a 1 MW wind turbine. The conclusions reached from the work reported in this thesis are drawn in Chapter 9.

Models of the aerodynamic torque and the wind speed sensed by a rotor (Leithead *et al.*, 1991a), a tip and the remaining part of the rotor (Leithead, 1992), which are suitable for the assessment of power control are described in Appendix A.

Wilkie *et al.* (1989) and Leithead *et al.* (1991a) used simple wind speed and wind turbine dynamic models which are suitable for assessing the performance of power control of grid-connected wind turbines. The linear and non-linear models were validated on the WEG MS3 (Bossanyi *et al.*, 1992), the Howden HWP330 (Wilkie and Leithead, 1988) and the Howden HWP1000 (Leithead *et al.*, 1991a). However, the model of the dynamics of the drive train was not rigorously derived in that several aspects of the dynamics were ignored. In Appendix B, a non-linear model accounting for all the significant dynamics together with a simplified non-linear model which is applicable to almost all wind turbines are rigorously derived. The corresponding linear models are determined.

A definition of what constitutes good power controller performance and how the performance of different machine configurations can be compared are reviewed in

Appendix C. The required ideal dynamic behaviour of a power controller is that described in Leithead *et al.* (1991a). The methodology of assessing good power performance is a development of that used by Leithead *et al.* (1991a). It is based on linear analysis methods and is described in Appendix C. Leithead *et al.* (1991a) considered a fixed wind turbine configuration but using different control design techniques to design a power controller.

The derivation of the model of the generator dynamics, used in the derivation of the power-train models in Appendix B, is described in Appendix D.

The manner in which different machine configurations are scaled to be equivalent while taking into account the number of blades, the change in size *etc.* is described in Appendix E.

Since the size and geometry of the fledges for power control are dictated by their braking ability an investigation of the feasibility of using the fledge as an aerodynamic brake is described in Appendix F. Also described are the modelling issues associated with fledges and the compliant tip. The model of the novel aerodynamic devices fledges is that of Jamieson (NWTC, 1994).

Tables of the aerodynamic coefficients and partial derivatives with respect to pitch angle and wind speed, of the related aerodynamic torque at rated power, for all the rotors and aerodynamic control devices are listed in Appendix G.

1.2 Original contributions

The original work presented in this work to which the author made a significant contribution are the following.

- Chapter 3 :** the derivation and validation, in Section 3.1, of the models of the drive-train dynamics discussed.
the analysis, in Section 3.2, of the relationship between the machine parameters and the dynamic characteristics of the drive train undertaken.
- Chapter 4 :** the investigation, in Section 4.1, of the feasibility of modifying the drive train to reduce specific loads or to enable the rotor inertia or generator slip to be reduced.
the investigation, in Section 4.2, of the feasibility of direct control of the drive-train resonance.
- Chapter 5 :** the parametric investigation of the influence of the machine parameters on the controller performance for full-span pitch wind turbines.

- Chapter 6 :** the parametric investigation of the influence of the machine parameters on the controller performance for part-span pitch wind turbines.
- Chapter 7 :** the comparative analysis, in Section 7.1, of the fledge as a control device.
the comparative analysis, in Section 7.2, of the compliant tip as a control device.
- Chapter 8 :** the control system design study, in Section 8.2, for a 1 MW commercial wind turbine.
- Chapter 9 :** the conclusions.
- Appendix C :** the validation of the parametric investigation.
- Appendix E :** the simple rotor designs.
the assumptions made to take account of the change in size of a machine.
- Appendix F :** the investigation into the feasibility of using the fledge as an aerodynamic brake.

In addition, the conclusions drawn in throughout this work are entirely those of the author.

1.3 Publications

Some of the work presented in this thesis has been previously published describes the work in greater detail.

- 1 Havard, M., 1990, *Feasibility study of an innovative control device for a HAWT*, Report ISC 1002 prepared for ETSU (DEn.), Industrial Systems and Control Ltd., Glasgow, UK.
- 2 Rogers, M. C. M., 1991, NWTC control system design study, report ISC/1019/91, prepared for National Engineering Laboratory, East Kilbride, Industrial Systems and Control Ltd, Glasgow, UK, included as part of *Innovative aerodynamic braking and control devices for horizontal axis wind turbines*, 1994, National Wind Turbine Centre report under contract E/5aqaA/6060/2495 W/42/00235/00/00 for AEA Technology Ltd., Ref. AET006.
- 3 Rogers, M. C. M., and Mckenna, P., 1991, NWTC control system design study, report ISC/1020/91, prepared for National Engineering Laboratory, East Kilbride, Industrial Systems and Control Ltd., Glasgow, UK included as part of *Innovative aerodynamic braking and control devices for horizontal axis wind turbines*, 1994, National Wind Turbine Centre report under contract E/5aqaA/6060/2495 W/42/00235/00/00 for AEA Technology Ltd., Ref. AET006.
- 4 Leithead, W. E., Rogers, M. C. M., Agius, P. R. D., 1992, *Dynamic analysis of the*

- compliant tip*, May 1992, Report prepared for DEn. (ETSU), University of Strathclyde, Glasgow, UK.
- 5 Leithead, W. E., Rogers, M. C. M., Agius, P. R. D., Reardon, D., 1992, *The simulation of the compliant tip*, May 1992, Report prepared for DEn. (ETSU), University of Strathclyde, Glasgow, UK.
 - 6 Leithead, W. E., Rogers, M. C. M., and Agius, P. R. D., 1993, *Clarification of drive-train design goals*, DTI Report No. ETSU W/42/00349/REP, University of Strathclyde, Glasgow, UK.
 - 7 Leithead, W. E., Rogers, M. C. M., Connor, B., van der Molen, G., Pierik, J. T. G., van Engelen, T. G., 1994, *Design and test of the controller for a variable speed wind turbine*, DTI report ETSU W/42/00242/REP, University of Strathclyde, Glasgow, UK.
 - 8 Rogers, M. C. M., and Leithead, W. E., 1994, *The dependence of control systems performance on the wind turbine configuration*, DTI Report ETSU W/42/00258/REP, University of Strathclyde, Glasgow, UK.
 - 9 Leithead, W. E., and Rogers, M. C. M., 1995, *Drive-train characteristics of constant speed HAWT's*, Report ICU/110 Industrial Control Centre, University of Strathclyde, Glasgow, UK.
 - 10 Rogers, M. C. M., and Leithead, W. E., 1996, *The dependence of control systems performance on the wind turbine configuration*, Report ICU/139 Industrial Control Centre, University of Strathclyde, Glasgow, UK.

Commercial reports

- 1 Rogers, M. C. M., and Leithead, W. E., 1994, *Review of wind turbine control strategies*, Report prepared for Renewable Energy Systems Ltd., Industrial Control Centre, University of Strathclyde, Glasgow, UK.
- 2 Rogers, M. C. M., and Leithead, W. E., 1994, *Development of control system for RES 1 MW machine*, Report prepared for Renewable Energy Systems Ltd., Industrial Control Centre, University of Strathclyde, Glasgow, UK.

Other publications stemming from the work.

- 1 Jamieson, P., Bowles, A., Derrick, A., Leithead, W., Rogers, M., 1992, *Innovative concepts for aerodynamic control of wind turbine rotors*, J. of Wind Engineering and Industrial Aerodynamics, 39, pp. 395-404, Elsevier Science Pub., B.V., Amsterdam.
- 2 Rogers, M. C. M., and Leithead, W. E., 1993, *Relationship of the controllability of power/torque fluctuations in the drive-train to the wind turbine configuration*, Proc. of

- the 15th British Wind Energy Association Conf., York, UK, pp. 213-219.
- 3 Leithead, W. E., and Rogers, M. C. M., 1993, *A comparison of the performance of constant speed HAWT's*, Renewable Energy - Clean Power 2001, London, IEE Conf. Publication No. 385, pp. 165-170.
 - 4 Leithead, W. E., Rogers, M. C. M., 1993, *An attempt to measure dynamic inflow phenomenon on a 1 MW wind turbine*, Proc. of 15th British Wind Energy Association Conf., York, UK pp. 305-311.
 - 5 Leithead, W. E., Rogers, M. C. M., Agius, P. R. D., 1993, *Independent Blade Control of HAWT's*, Proc. of the European Community Wind Energy Conf., Lübeck-Travemünde, Germany, pp. 522-525.
 - 6 Leithead, W. E., Rogers, M. C. M., Agius, P. R. D., 1994, *Dynamic characteristics of the drive-train: causes and effects*, Proc. of the 16th British Wind Energy Association Conf., Stirling, pp. 211-216.
 - 7 Leithead, W. E., Rogers, M. C. M., 1995, *Improving damping by a simple modification to the drive-train*, Proc. of 17th British Wind Energy Association Conf., Warwick, UK, pp. 273-278.
 - 8 Leithead, W. E., Rogers, M. C. M., Leith, D., J., Connor, B., 1995, *Design of wind turbine controllers*, Proc. of EURACO Workshop on recent results in robust and adaptive control, Florence, Italy, pp. 491-5132.
 - 9 Leithead, W. E., Rogers, M. C. M., Leith, D., J., Connor, B., 1995, *Progress in control of wind turbines*, Proc. of the European Control Conf., Roma, Italy, pp. 1562-1567.
 - 10 Leithead, W. E., Rogers, M. C. M., 1996, Drive-train characteristics of constant speed HAWT's: Part I-Representation by simple dynamic models, *Wind Engineering*, Vol. 20, No. 3, pp. 149-174.
 - 11 Leithead, W. E., Rogers, M. C. M., 1996, Drive-train characteristics of constant speed HAWT's: Part II-Simple characterisation of dynamics, *Wind Engineering*, Vol. 20, No. 3, pp. 175-201.
 - 12 Leithead, W. E., Rogers, M. C. M., 1996, *Options for drive-train design - a dynamic perspective*, Proc. of the European Community Wind Energy Conf., Goteborg, pp. 882-885.
 - 13 Leithead, W. E., Leith, D., J., Connor, B., Rogers, M. C. M., 1996, *Evaluation of the options for control design of constant speed wind turbines*, Proc. of the 18th British Wind Energy Association Conf., Exeter, UK, pp. 347-352.

2 General background

Wind turbine research began after World War I and received a fresh impetus after the 'oil crisis' of 1973-74. It is now world-wide, stimulated by national programmes particularly in Denmark, the Netherlands, Germany, the UK, Sweden and the USA, and by the EC research programmes THERMIE and JOULE. Until very recently, wind energy technology was in its infancy, as it was not competitive with conventional energy (gas, coal or nuclear). At present under 0.2% (BWEA, 1996) of the UK's electricity is generated from the wind. However, according to Milborrow (1993) wind energy can be less expensive than nuclear and coal depending on factors such as interest rates, and the site mean wind speed. In the Renewables Order Round 5 (NFF05) announced in September 1998 the bid-price for wind power was from 2.43p per unit (OFFER, 1998). However, the wind farm sites being developed have generally been chosen for their high mean wind speeds and short distance to the main electricity grid. There is a limited number of such 'cost-convenient' sites, so the average cost of wind power needs to decrease if it is to make a significant contribution. Therefore the main aim of wind turbine research is to reduce either directly or indirectly the price of the electricity produced. The major part of the cost of a wind energy scheme is the capital cost of the site, the turbines themselves and their foundations, the access roads and grid connections. One area where is scope for savings is that of machine costs, so the aim of much research is to design machines which offer improved value for money in terms of the trade-offs between initial costs, efficiency and life-span. In order to achieve the optimum combination of these factors an understanding of the dynamics of a machine as a whole, rather than just those of its constituent parts, is necessary.

2.1 Basic characteristics of wind turbines

The wind turbines considered in this thesis are all horizontal-axis, up-wind, grid-connected, medium- to large-scale (greater than 200 kW) machines, see Figure 2.1. All have variable pitch capability, *i.e.* the blades can change their orientations with respect to the wind. No stall-regulated machines are considered. The major components of such turbines

are the tower, the 'rotor' (consisting of the blades and hub), the 'drive train' (consisting of the low-speed shaft, gearbox, high-speed shaft and the rotor of the generator) and the power generation unit. The basic layout of a conventional 'power train' (drive train and generator) is shown in Figure 2.2. Commercial wind turbines of this type normally have two or three blades. Their components are made from a variety of materials, such that the drive-train components can be described as 'stiff' or 'soft', and the rotors as 'heavy' or 'light'. The wind turbines considered in this thesis have an induction generator and are known as constant speed machines, *i.e.* the generator is connected directly to the grid so that the rotational speed of the generator is locked subject to slip to the frequency of the grid. The only exception is the 'variable speed' machine considered in Chapter 4. In this case, the generator is decoupled from the grid by a DC/AC link and hence the rotational speed of the generator is free to vary.

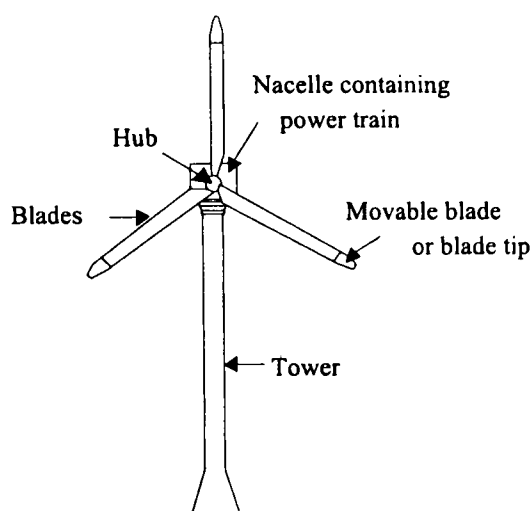


Figure 2.1 Horizontal axis wind turbine.

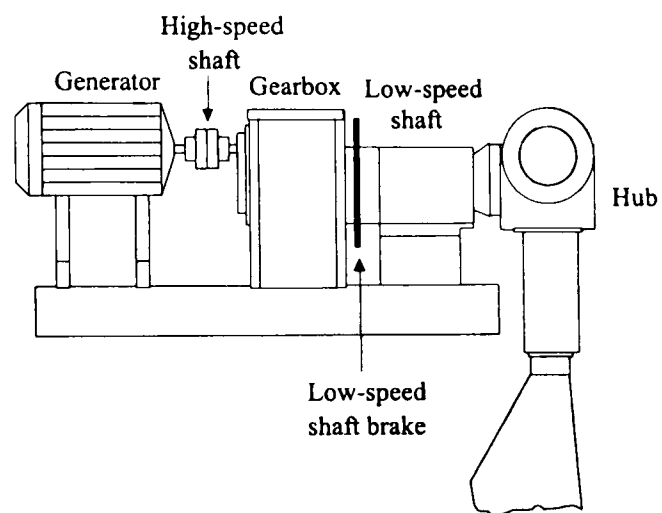


Figure 2.2 The power train.

2.2 Normal operation of a wind turbine

When a grid-connected wind turbine starts from rest the rotor is allowed to accelerate in a controlled manner ('speed control') until its rotational speed reflected to the high-speed shaft reaches the grid frequency ('synchronous speed'), at which point the machine is connected to the grid. Thereafter, on a constant-speed wind turbine, the speed of rotation is fixed by the grid frequency.

A well designed, fixed-geometry rotor, optimised in terms of its dimensions, profile and rotational speed to capture the greatest amount of energy over the most frequently occurring range of wind speed, will develop excessively large loads at high wind speeds. There is therefore a threshold wind speed above which it is more economical to reduce the loads than to build the machine to withstand the stresses and hence produce more power. The loads can be reduced by decreasing the aerodynamic torque on the rotor. The normal

methods of doing this are (i) to design the rotor such that it stalls at high wind speeds ('passive control'); or (ii) to vary the pitch of the whole ('full-span') or part ('tip') of the blades according to the amount of power generated ('power control'). In either case, above a predetermined wind speed ('rated wind speed') the power input to the wind turbine is kept constant ('rated power'). If the power is maintained at its rated value a wind speed limit is reached when the wind turbine is shut down. In very low wind speeds the amount of energy generated is so small that the turbine is stopped to reduce wear. The quality of power regulation which can be achieved will depend on the dynamics of the turbine, which in turn depend on the machine's configuration, *e.g.* the number of blades, the aerodynamics and the dynamics of individual components. Typical power curves for stall-regulated and pitch-regulated machines are shown in Figure 2.3.

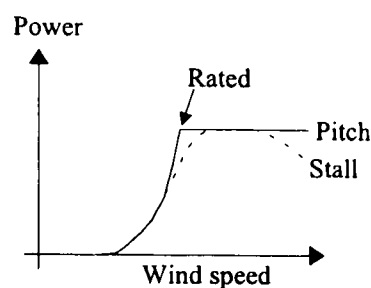


Figure 2.3 Typical steady-state power curves of stall and pitch regulated machines.

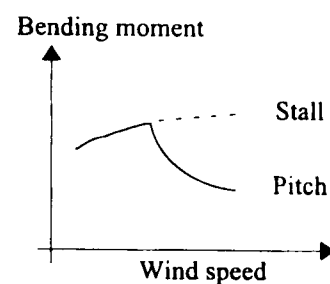


Figure 2.4 Typical flap-wise bending moment (Quarton, 1990b).

For a review of the types of commercial machine configurations available, see Madsen (1988) and Simpson (1994). Ideally, for simplicity of construction, cost and reliability, passive control is desirable. However, it does have disadvantages. A stall-regulated rotor is not as efficient as one which is actively controlled, particularly in the region just below rated wind speed, see Figure 2.3. It has no active control device to be used for speed control during start-up, and it requires for safety purposes an additional brake for emergency and routine shutdown. According to Quarton (1990a) there is a need for greater understanding of the aerodynamics of large-scale stall-regulated machines. Furthermore, using flexible blades on a large stall-regulated machine may cause structural problems from vibrations occurring when near the stall limit (Madsen and Frandsen, 1984).

Using active pitch control, on the other hand, whether full-span or tip-regulated, the aerodynamic loads are reduced as the blade is feathered or inclined. When the blades are inclined, *i.e.* moved out of the wind, the flow of air over them enters stall. This would be a simple method of power regulation, except that the aerodynamic theory of a blade while in stall is still in its infancy. However, the aerodynamics of feathered blades (where blade pitch angle is increased with increasing wind speed, *i.e.* the blade is tilted towards the wind

direction) are better understood. It is this form of pitch regulation which is more extensively used and is that investigated here.

The disadvantages of pitch regulation are increased fatigue, due to the flapping loads on the blades, and the expense of the regulation mechanism. The increased fatigue loading can be explained in simple terms by considering the curve of the steady-state flap-wise bending moments versus wind speed (Quarton, 1990b), see Figure 2.4. Flap-wise fatigue loads (those out of the plane of rotation) are proportional to the gradient of the curve of bending moment to wind speed. The effect of using pitch control to maintain rated power in above rated wind speeds is to cause a sharp decrease of the flap-wise bending moment with increasing wind speed. Therefore the fatigue loads reverse in sign and the cycles increase in magnitude. This explanation ignores the wind turbine dynamics and therefore may be an over-simplification of what occurs.

A disadvantage of constant speed wind turbines is the quantity of power flicker¹. The amount of flicker is greater at higher wind speeds (Gardner *et al.*, 1995). The quantity of power flicker depends mainly on the slope of the real power/reactive power characteristics of the induction generator. Hence machine performance improves with reduced flicker. The quantity of power flicker is reduced with good power control. Flicker is less of a problem for variable speed wind turbines. Reactive power flow can be a problem for constant speed machines but not need be for variable speed machines. However, variable speed wind turbines can have problems of high frequency voltage fluctuations, particularly on weak grids (Gardner *et al.*, 1995).

2.3 Power regulation

A discussion of the role and objectives of wind turbine control is given by Leithead *et al.* (1991a). Various objectives for power regulation are described in the literature. The most commonly cited are the following:

- i) to maximise energy capture;
- ii) to regulate and smooth the power output; and
- iii) to minimise the loads experienced by the rotor, drive train and tower.

¹ Power flicker (*i.e.* low frequency voltage fluctuation) is particularly important in rural areas where the grid is weak, as flicker may cause the grid and a wind turbine to desynchronise unless further adaptations of the grid such as capacitors are added to the network. Power flicker can be a particular problem on large machines.

Energy capture can be increased by increasing the efficiency of the rotor, reducing energy losses in the drive train and reducing the slip of the induction generator. An extensive discussion of rotor design is outwith the scope of this thesis. Energy losses in the power train are normally relatively small and are related to damping and the efficiency of the gearbox and generator. Reduction of generator slip by itself has the disadvantage that the dynamics of the power train deteriorate (see Section 3.2). This is particularly important for large machines since as machine rating increases the slip of the generator generally decreases and hence the machine can become more dynamically active. The later two objectives are distinctively linked. Some commercial machines are run at a lower than 'rated' power set-point in high wind speeds in order to limit machine loads (*e.g.* Botta *et al.*, 1994).

Unlike other electricity generators, a wind turbine, because it rotationally samples a turbulent wind field, does not have a smooth power output and does not experience steady loads. Much research has focused on smoothing power output in order to facilitate good grid connection. This is particularly important when the main electricity grid is weak. However, more recently it has been recognised that fatigue damage is a more important consequence of the transient loads on a wind turbine (Quarton, 1989, Barltrop *et al.*, 1993). In addition, in the case of a variable speed wind turbine smooth power output does not always imply smooth loads (Leithead, 1990). The quality of power can be improved and the loads acting on the machine reduced by varying the pitch of the blades, although fluctuations in loads cannot be completely removed. The rating of any turbine component, such as the gearbox or the generator, must be sufficient to withstand large transient loading.

Improvements in turbine design and regulation enable energy capture to be increased, or lower rated components, which are generally cheaper, lighter and hence require less support structure, to be used. Consequently, the penalty for a badly dynamically behaved wind turbine is greater cost.

One method of reducing the cost of energy production is to reduce the over-rating of components as much as possible without compromising their reliability. Typically the gearbox is a prime target and the tower, the blades and the generator are the next most important items to consider (Spruce, 1993). Another method of reducing the cost per kilowatt is to design a more efficient machine, whilst not reducing its life-span or reliability. To follow either approach it is necessary for the loads experienced by different machine configurations to be understood. Several configurations are investigated in the following chapters.

To understand the source of fatigue damage to the components of a wind turbine, it is necessary to consider the loads experienced by a machine at various different stages of operation, as outlined in the following section.

2.4 Loads experienced by a wind turbine

The loads experienced by a machine during each stage of operation are different. During start-up the torque fluctuations in the drive train are small compared to the very sharp transient which occurs on connection to the grid. Machines experience similar transient loads when mechanical brakes are applied. The components of a machine need to be designed to withstand these large torque fluctuations several times a day. More extreme loads are experienced during a grid failure when the machine starts to accelerate sharply until a mechanical or aerodynamic brake is applied. In any of these extreme situations the magnitude and the frequency of the load fluctuations depend on the dynamics of the power train which in turn depend on the machine's configuration, *i.e.* the inertia and stiffness of its components. These fluctuations dictate the maximum loads experienced, for example by the gearbox, but they occur infrequently. High loads which occur frequently are also a very significant source of fatigue. These include the loads experienced during power regulation, particularly at higher wind speeds (Madsen and Frandsen, 1984), and are of equal importance for fatigue as the extreme loads described above. It is these loads experienced during power regulation which are investigated here. To reduce these loads, it is necessary to understand the effects of rotationally sampling the wind field on the machine dynamics.

2.4.1 Characteristics of wind speed

The wind speed characteristics of significance to wind turbine dynamics are those from ground level to 100 m (Moores, 1988). Wind speed is stochastic. A convenient method of characterising the variability of the wind is to consider a typical time history of wind speed in the frequency domain. Figure 2.5 presents the power spectrum taken from van der Hoven (Moores, 1988) of horizontal wind speed near ground level ranging over several frequency decades. The spectrum has three energy peaks: one at a period of about four days, a second at about 1 day and a third at about a minute. These are caused respectively by migratory pressure systems, by daily variations of wind speed and by wind turbulence which is a complex and not completely understood phenomenon. Between the second and third peaks there is a broad spectral gap in the frequency range from ten minutes to an hour. Since the primary purpose of any power regulation is to provide load regulation in above rated

wind speeds, the long-term wind conditions are unimportant. The mean wind speed of the turbulence, typically over 10 minutes, can be thought of having a Rayleigh distribution² (Eggleston and Stoddard, 1987). Turbulence can be defined as variation in wind speed about a quasi-constant mean value. It can be visualised as a collection of spatially dispersed eddies travelling in the same direction and with the same velocity as the mean wind speed. The wind velocity within each eddy differs from the mean wind speed so that at a fixed point turbulent air flow is observed.

The mean wind speed experienced by a wind turbine also varies due to wind shear - the variation of wind speed with height within the boundary layer. At the surface of the earth the wind speed is approximately zero. Wind speed increases until a height of approximately 1 km is reached. The effect of wind shear is that the blades of the wind turbine experience different mean wind speeds at different heights, causing a periodic oscillation of rotor loads.

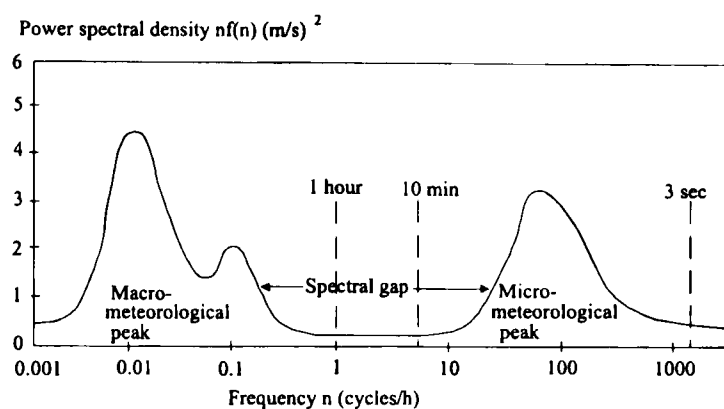


Figure 2.5 The van der Hoven spectrum (Moores, 1988).

The tower of a wind turbine provides some resistance to the flow past it and hence it will disturb the flow both upstream and downstream. As a blade approaches the tower the wind flow over the blade increases slightly and then is reduced. The resulting impulsive, but periodic loss in wind speed produces significant spectral peaks at the frequency of the rotor speed and its higher harmonics.

As result of the symmetry of the rotor, the effects of tower shadow and wind shear (Eggleston and Stoddard, 1987) are significant only to independent pitch regulation and to the comparison of wind turbines of different hub heights, as discussed in Chapters 3 and 7.

In estimating wind speed one is faced with the problems that a point measurement is unlikely to be representative of the average wind speed over the whole area swept by the blades (the rotor disc), and that the wind experienced by the rotor is significantly different

² Rayleigh distribution $Pr(V) = a V \exp(-0.5aV^2)$ where V is the hourly average wind speed, a is related to the very long time-scale wind speed.

when the rotor is rotating then when it is stationary. Power regulation is concerned with reducing the loads seen by the power train, and so the effect of the wind which is primarily of interest is that on the aerodynamic torque seen by the whole rotor. One approach to modelling the wind speed seen by the rotor is to represent the 'effective' wind speed which causes the net aerodynamic torque seen on the machine. For pitch regulation with the blades acting in unison, some of the loads experienced by an individual blade can be ignored because, as a result of symmetry of the blades, they are not seen in the net aerodynamic torque. However, individual blade loads are important when considering independent pitch actuation as discussed in Chapter 7.

Typical power spectra of wind turbulence at a point and loads on a blade are shown in Figure 2.6a. There is a depletion of power in the mid-frequency range as a result of disc averaging and there are peaks of power concentrated around the rated rotational frequency (Ω_o) and its higher harmonics. These peaks are called 'spectral peaks' and the majority are primarily stochastic. The peaks at $1\Omega_o$, $2\Omega_o$, $3\Omega_o$ are clearly seen in Figure 2.6a. The higher harmonics are suppressed because of the quality of the data. The peaks are mainly due to gravity, wind shear, tower shadow, yaw misalignment and rotational sampling of the turbulent wind field. The magnitude of the spectral peaks in the loads on a blade decreases with increasing frequency.

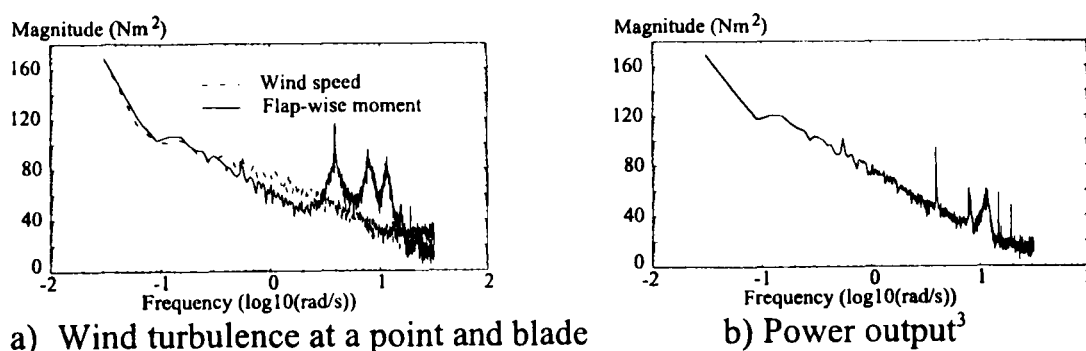


Figure 2.6 Typical power spectrum⁴ (data measured on a Howden 330 kW wind turbine).

An analogous power spectrum of the power output is shown in Figure 2.6b. Because of symmetry the intensity of several of the spectral peaks are reduced in comparison to the

³ The corresponding power spectrum of low-speed shaft showed that the strain gauge used to measure the low-speed shaft measurement was not properly aligned. The power spectrum of power is related to that of the hub torque by the square of the drive-train transfer function.

⁴ Power spectrum - plot of the square of the magnitude of a signal against frequency.

blade load spectra (in Figure 2.6a). The dominant peaks are now those at Ω_o and $n\Omega_o$, where n is the number of blades. The peak at Ω_o is mainly due to blade imbalance and is deterministic. The larger peak at $n\Omega_o$ on the other hand is stochastic. It is primarily the result of rotational sampling of the uneven wind field while the rotation frequency is varying slightly (Kristensen and Frandsen, 1982). On two-bladed machines the quantity of $2\Omega_o$ is enhanced if a teetered hub is used to reduce the hub flap-wise loads (van Grol *et al.*, 1990). The actual redistribution of energy is dependent on the amount of turbulence and the rotor size.

It is the turbulent component of the wind speed that dominates the rotor loads (Rasmussen and Madsen, 1990) and the fatigue loads (Quarton, 1990a) and hence is of most interest. The effect of turbulence on the net aerodynamic torque is to produce low and high frequency components. The wind turbulence alone is responsible for the low frequency loads with significant components situated below $1\Omega_o$. Wind shear and tower shadow and rotational sampling are responsible for the high frequency rotor loads, *i.e.* the spectral loads.

2.4.2 Aerodynamic loads

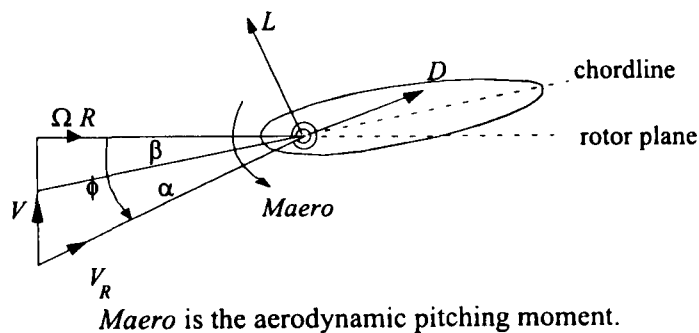


Figure 2.7 Velocity and force triangle of an element of a rotating blade.

The purpose of a wind turbine is to convert the kinetic energy of the wind into electrical energy. The wind creates lift and drag forces on the rotor blades which in turn produce a moment on the wind turbine hub. The forces and moments acting on an element of a blade in two dimensions are shown in Figure 2.7. The local relative wind speed, V_R , varies with the blade radius, R , and is composed of an axial component, V , and a rotational component, ΩR , arising from blade rotation. Ω is the rotational velocity. D is the drag force aligned to relative wind speed and L is the lift force perpendicular to the drag. The angle of the blade chord with respect to the blade rotation is denoted by β . The angle of attack of the aerofoil with respect to the local relative wind speed is denoted by α , and the angle of the local relative wind speed with respect to the rotor plane, the flow angle, by ϕ . The useful force in the direction of the blade rotation is $F_q = L \sin \phi - D \cos \phi$.

The interaction of the machine with the wind is complex but can be represented simply by modelling the effective wind speed, which is uniform across the rotor and produces a rotor torque which is statistically the same as that seen on a real wind turbine. This approach, described in Appendix A, has been validated against machine data (Leithead *et al.*, 1991a). The aerodynamics of the rotor can be described in two dimensions by strip theory, (Eggleston and Stoddard, 1987) which considers the forces acting on small radial aerofoil cross-sections. Strip theory is the used by the computer code (Anderson, 1990b) to generate two dimensional aerodynamic torque tables. The torque tables consist of steady state C_q values, which are parameterised with pitch angle and tip speed ratio, λ (where $\lambda = \Omega R / V$ and V is the horizontal wind speed sensed by the whole rotor). Figure 2.8 shows a typical example of a C_q against λ curve.

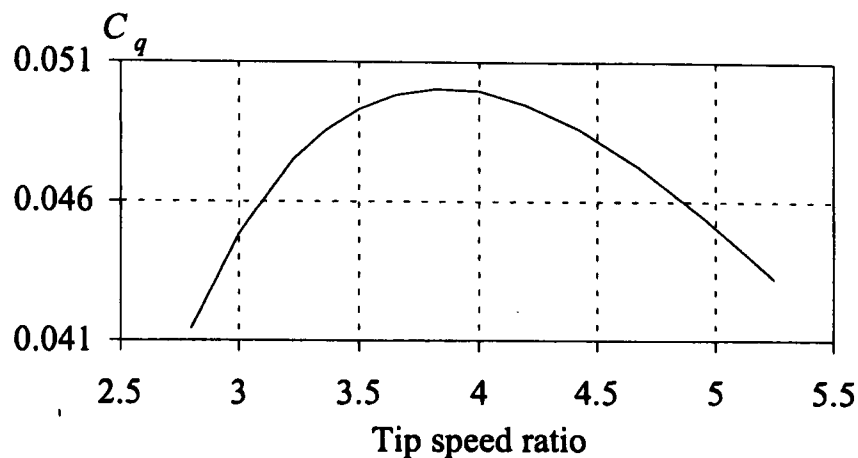


Figure 2.8 A typical example of a $C_q - \lambda$ curve.

The aerodynamic torque, T_a is calculated from

$$T_a = 0.5\rho\pi V^2 R^3 C_q \quad (2.1)$$

where ρ is the air density,

C_q is the torque coefficient which is a function of λ and β .

For constant speed machines, ΩR only varies very slightly and so tip speed ratio is a function of wind speed.

The wind speed spectrum is inherently stochastic and the aerodynamics are clearly strongly non-linear. The exact nature of the aerodynamic loads experienced by a wind turbine is dependent on the design of the rotor.

Dynamic inflow or induction lag (Stig Pyle, 1986) has been found to be unimportant for control design (Leith and Leithead, 1997). The dynamics of the induction lag are restricted to much lower frequency than the crossover frequency of the open-loop system when the gain is high. Hence, shaping the controller at these frequencies is unnecessary.

2.4.3 Drive-train loads

The net aerodynamic driving torque induced in the rotor is transmitted down the power train (the rotor, low-speed shaft, gearbox, high-speed shaft and generator) and affects all the components. The effect of the aerodynamic torque on power-train components depends on their dynamics. Since for constant-speed wind turbines, the rotor speed is locked to the grid frequency, the rotor cannot absorb the additional power due to wind fluctuations as changes in rotor speed. Instead it must be absorbed as changes in torque.

Both the high and low frequency components of the aerodynamic torque are transmitted to the drive train. Some protection against the low frequency loads is provided above rated wind speed by the power regulation. Care must be taken during control design not to enhance the loads at high frequency, particularly those at $n\Omega_o$ and at the frequency of the structural modes. Some protection against high frequency loads is provided by the compliance⁵ of the drive train. The degree of compliance of the power train is usefully characterised by the frequency of the first drive-train mode, *e.g.* if the first drive-train frequency is halved then the intensity of the $n\Omega_o$ loads is reduced by a factor of 4 (*cf.* Section 3.2.1). Hence this frequency is a key indicator of a turbine's dynamic performance. For many commercial wind turbines the frequency of the first drive-train mode is approximately $0.5n\Omega_o$.

A further key indicator of the dynamic performance of the drive train is the damping factor⁶ of the first drive-train mode. If the damping factor is too small, *i.e.* much less than 0.5, then the drive train becomes oscillatory and the wind turbulence induces greater torque transients in the drive train.

2.5 Active power control and controller design

A great deal of attention has been paid to the problem of power control of constant speed wind turbines in the 1980's. In recent years, however attention has moved to the power control of variable speed machines. Before and in the early 1980's the control design techniques applied to wind turbines were limited to PI (PID) control (*e.g.* Johnson and Smith, 1976, Wasynczuk *et al.*, 1981). A wide variety of control techniques have been

⁵ Compliance - the definition used here is the inverse of stiffness.

⁶ When dynamics can be described by a second order transfer function $\frac{\omega^2}{s^2 + 2\eta\omega s + \omega^2}$ the frequency of the mode is at ω and the damping factor is η .

proposed for the synthesis of the power controllers of constant-speed wind turbines, including classical loop shaping (Leithead *et al.*, 1991a), linear quadratic optimal state feedback (LQ) (Liebst, 1983, Connor *et al.*, 1994), H_∞ (Connor *et al.*, 1992, Dijkstra *et al.*, 1994) and adaptive Kalman filter (Bossanyi, (1989) to name a few. For thorough reviews of power control design strategies, see de la Salle *et al.* (1990) and Dijkstra *et al.* (1994). An extensive survey of the control of large wind turbines is given in Mattsson (1985). All the above papers assume a fixed machine configuration and considers the application of a particular control synthesis technique, unlike the work described in this thesis.

The control design problem for constant-speed wind turbines is SISO⁷ and the method of synthesis is considered in this thesis to be immaterial. However, it is important that the controller design is appropriate, see Appendix C.

There are three issues which dominate the literature on control of constant speed wind turbines (de la Salle *et al.*, 1990). The first is the excitation of the first drive-train mode (Wasynczuk *et al.*, 1981, Hinrichsen and Nolen, 1982), the second is enhancement of the $n\Omega_o$ loads (Leithead and Agius, 1992, Agius *et al.*, 1993) and the third is the choice of controller bandwidth⁸ or cross-over frequency⁹ (Rothman (1978), Kos (1978), Johnson and Smith (1976), Leithead and Agius, 1992). The excitation of the first drive-train mode by the interaction of the drive-train dynamics with wind turbulence can be reduced by selecting the drive-train components so that the first drive-train mode has high damping (*cf.* Section 3.2). The low-frequency loads experienced by a wind turbine can be reduced by careful power control design (*cf.* Appendix C). Extreme care must be taken to avoid amplification of disturbances, particularly those at $n\Omega_o$, and to avoid actuator saturation (see Section 3.1.4). A useful indicator of the speed of pitch control action is the cross-over frequency of the open-loop¹⁰ system. The cross-over frequency is constrained by the high-frequency loads transmitted to the actuator.

⁷ SISO - A system with one input and one output. In the case of a constant speed wind turbine the input is the demanded pitch angle and the output is the measured electrical power.

⁸ Bandwidth is the maximum frequency at which the output of a system will track an input sinusoid in a satisfactory manner, *i.e.* it is the frequency at which the frequency response of the closed-loop transfer function has a magnitude of -3 dB.

⁹ Cross-over frequency is the frequency where the open-loop transfer function crosses 0 dB.

¹⁰ Open-loop system - the system with all the dynamics present except for the feedback loop of the output compared to the reference input.

The power control achievable on a machine is influenced strongly by the aerodynamic characteristics of its rotor. The aerodynamics of the rotor depend on the number of blades and the type, shape and size of the aerodynamic device and the remaining part of the blade (if any). A review of the conventional power control devices is given by Madsen (1988). Various non-conventional devices have also been considered, *e.g.* compliant tips (Anderson and Campbell, 1992), fledges and sledges (Jamieson and Agius, 1989). A variety of people have analysed the use of such devices for braking and power control. The aerodynamic behaviour of the fledge and sledge has been investigated in wind tunnel tests by Jamieson and Agius (1989). The aerodynamic braking behaviour of the compliant tip has been investigated in a wind tunnel by Richon and Anderson (1993). The use of tips and fledges, sledges and other aerodynamic braking devices is discussed by Corbet and Brown (1992).

The aerodynamics of full-span and tip-regulated machines have been compared by Anderson (1990a). The design of equivalent rotors for different number of blades has been considered by Jamieson and Brown, (1992). The aerodynamics of the tip, the fledge and the sledge for power control have been discussed by Derrick (1992).

Dynamic models of a wind turbine are required for power control system design and validation. Unlike in fatigue studies, simple dynamic models can suffice (Wilkie *et al.*, 1989) to design a power controller and to investigate typical loads experienced in the power train. In addition, wind turbine components would ideally be designed taking into account the dynamics of the complete machine, as an integrated and complex design problem. In order to understand how each component affects the dynamics of the whole, simple yet accurate dynamic models of a machine are required. Such models can be used to evaluate the effects of different machine characteristics on the dynamics of the complete machine.

Suitable dynamic models for both these tasks are described in Chapter 3.

3 Wind turbine dynamics

To investigate how machine configuration influences performance, models of the wind turbine dynamics are required. It is convenient to use a very simple linear model both for parameteric studies and for control design, and then to validate the results using non-linear simulation. The simple linear model of the wind turbine dynamics used in this thesis has been thoroughly validated for several medium-scale commercial machines (Leithead and Agius, 1992, Wilkie *et al.*, 1989). However, the simple linear model of the aerodynamics and the power-train dynamics used by Leithead and Agius (1992) and Wilkie *et al.* (1989) were obtained without a detailed analysis of all the relevant aspects of the wind turbine dynamics; *e.g.* the interaction of the structural dynamics of the blades and the tower with those of the power train. The models of the power train and the aerodynamics are derived more rigorously in Appendices B and D and are shown to be valid for nearly all medium to large-scale full-span or tip-regulated machines not just those considered in Leithead and Agius (1992) and Wilkie *et al.* (1989).

Models suitable for linear analysis and non-linear simulation of wind turbulence, the aerodynamics, the actuator and the power train are described in Section 3.1. The role of the physical parameters of the power train in determining the overall dynamic behaviour of the wind turbine is discussed in Section 3.2.

3.1 Dynamic models

The dynamic behaviour of the wind turbine is dependent on the dynamics of the wind speed, the aerodynamics, the drive train and generator components and the control system (including its actuator), all of which can have significant components at less than 1 Hz, which is close to the rotational frequency of the rotor. The inter-relationships between each of these components are illustrated in Figure 3.1.

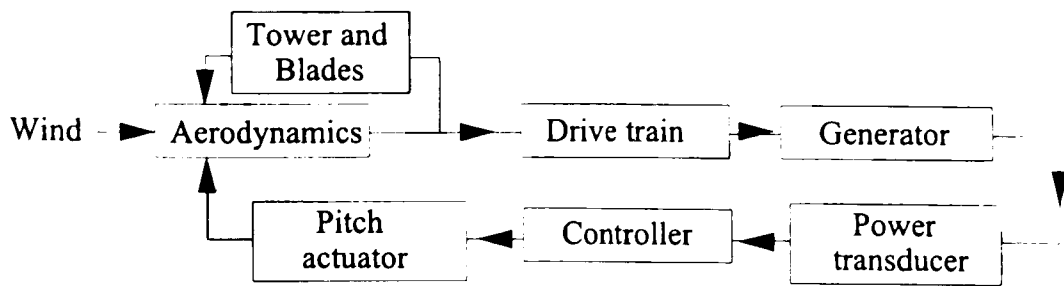


Figure 3.1 Block diagram for an actively regulated wind turbine.

3.1.1 Wind speed model

As discussed in Section 2.4.1, one source of rotor loads is wind turbulence. In this study, wind speed is modelled as a constant mean wind speed plus a turbulent component. A detailed description of the wind model is given in Appendix A.

Since the wind speed is stochastic, it is necessary for the wind model to reproduce the spectral density function for a particular torque or force, in particular the aerodynamic driving torque of the rotor. Hence, it is sufficient to model a point wind speed modified in the mid-frequencies to reflect a loss of power caused by averaging over the rotor disc (see Section 2.4.1).

The wind turbulence seen at a point is modelled by filtered white noise with the filter having the transfer function $b_f / (s + a_f)$, where s is the Laplace operand, (Leithead *et al.*, 1991a). The values of a_f and b_f are dependent on the mean wind speed, turbulence intensity, and the hub height (due to wind shear). Values for a_f and b_f for hub heights of 30 m and 50 m for 20% turbulence and a variety of mean wind speeds are given in Table A.1.

To represent the averaging over the rotor disc, the point wind speed is modified by a spatial filter which reduces the power intensity in the spectral density function in the middle frequency range. The filter has the following transfer function form (A.9):

$$G(s) = \frac{(1 + T_1 s)}{(1 + T_2 s)(1 + T_3 s)} \quad (3.1)$$

where

$$T_1 = K / \sqrt{2} \quad ; \quad T_2 = T_1 \sqrt{c_s} \quad ; \quad T_3 = K / \sqrt{c_s} \quad ; \quad c_s = 0.55 \quad ; \quad K = \gamma_s R / \bar{V}$$

A nominal value of γ_s , the decay factor over the disc, is 1.3 (Madsen and Frandsen, 1984). \bar{V} is a short term mean wind speed.

When independent tip control is being considered as in Chapter 7, the spatial filter must be modified to take account separately of rotational sampling over the tip and over the remaining part of the rotor. In this case, the effective wind speeds for the inner blade, V_r , and tip, V_o , can be expressed as (A.13) and (A.14), that is,

$$V_I = \frac{1.51\lambda_1 s(\lambda_1 s + 2.45)(\lambda_1 s + 2.79)(\lambda_1 s + 7.79)}{(\lambda_1 s + 0.707)(\lambda_1 s + 0.894)(\lambda_1 s + 3.464)(\lambda_1 s + 4.123)(\lambda_1 s + 10)} v_1 + \frac{10(\lambda_1 s + 2.45)}{(\lambda_1 s + 0.707)(\lambda_1 s + 3.646)(\lambda_1 s + 10)} v_3 \quad (3.2)$$

$$V_O = \frac{1.73\lambda_1 s(\lambda_1 s^2 + 2.064\lambda_1 s + 4.942)(\lambda_1 s + 9.14)}{(\lambda_1 s + 0.707)(\lambda_1 s + 0.775)(\lambda_1 s + 3.464)(\lambda_1 s + 7.071)(\lambda_1 s + 10)} v_2 + \frac{10(\lambda_1 s + 2.45)}{(\lambda_1 s + 0.707)(\lambda_1 s + 3.646)(\lambda_1 s + 10)} v_3 \quad (3.3)$$

where v_1 , v_2 and v_3 are independent point wind speeds and $\lambda_1 = \gamma R_1 / \bar{V}$, where R_1 is the distance of the tip joint from the hub.

The wind speeds (3.2) and (3.3) are used to generate hub torque and the tip pitching torque with the appropriate spectrum and cross-spectrum.

3.1.2 Aerodynamics

The aerodynamics are highly non-linear (Leith and Leithead, 1997). The steady state aerodynamic torque produced by the blades can be calculated theoretically as

$$T = 0.5\rho\pi R^3 V^2 C_q. \quad (3.4)$$

The simulation of blade dynamic equations are computationally intensive so the equations are approximated here by look-up tables of torque coefficients, C_q which are parameterised by the tip speed ratio and pitch angle. This approach has been validated by several studies by Leithead *et al.* (1988) and Leithead and Agius (1992). The aerodynamic tables used in this thesis are calculated using blade element theory and are listed in Appendix G.

The aerodynamic torque can be linearised as

$$\Delta T = \frac{\partial T}{\partial \beta} \Delta \beta + \frac{\partial T}{\partial V} \Delta V \quad (3.5)$$

The aerodynamics of a wind turbine vary strongly with some rotor characteristics, including whether full-span or tip regulated. Typical tip angle versa wind speed for rated power curves for full-span and tip-regulated machines are shown in Figure 3.2. It can be seen that the gradient of the curves of the tip-regulated machines decreases in high wind speeds while the gradient of the full-span pitch machines remains nearly constant.

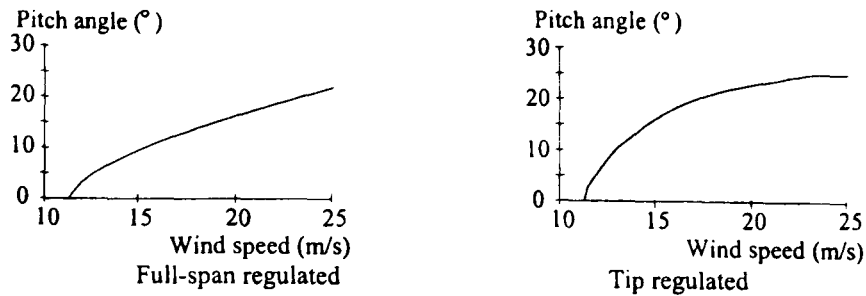


Figure 3.2 Typical pitch angle versus wind speed curves for rated power.

3.1.3 Modelling of spectral loads

The spectral peaks seen on the hub torque at $n\Omega_o$ are caused by the blades periodically sweeping through the wind field which changes relatively slowly as compared to the speed of rotation of the rotor. There are two cases. The first, and most common, is when the blades are acting in unison. The second is when the blades act independently. In the first case, the main peaks are those at $1\Omega_o$, which is deterministic and due to blade imbalance, and $n\Omega_o$ which is mainly stochastic and due to wind turbulence. The $1\Omega_o$ peak can be modelled by a simple sinusoid. The $n\Omega_o$ peak, can be modelled (Leithead *et al.*, 1991a) by the transfer function

$$wn\Omega = \frac{b_{nr}(s + \sqrt{a_{nr}^2 + (n\Omega)^2})}{(s^2 + 2a_{nr}s + a_{nr}^2 + (n\Omega)^2)} \quad (3.6)$$

driven by white noise. For higher harmonics of $n\Omega_o$ the spectral load model can be modified to add a tail to model the spectral loads for frequencies $2n\Omega_o$ and above. The model shown below is an approximate fit to the power spectrum of data collected from the Howden HWP330/33 330 kW machine.

$$\frac{3.692(s/n\Omega)^2((s/n\Omega)^2 + 0.242(s/n\Omega) + 0.919)}{((s/n\Omega)^4 + 2.382(s/n\Omega)^3 + 2.720(s/n\Omega)^2 + 2.157(s/n\Omega) + 0.822)} \quad (3.7)$$

The intensity of the spectral loads is usually higher on a two-bladed, teetered machine compared to a three-bladed, rigid-hub machine (*e.g.* see Figure 3.3).

In the second case, when the blades are acting independently there are high frequency components in the hub torque at every multiple of the rotational frequency as the cancellation of blade loads due to symmetry no longer occurs. The size of the peaks at $m\Omega_o$, $m = 1, 2, 3... \text{ etc.}$ reduces by $1/m$, see Figure 2.6a. In this case, the wind speed itself is modified, as those in Appendix F, to account for the periodic loads due to wind shear and tower shadow seen on the different blades.

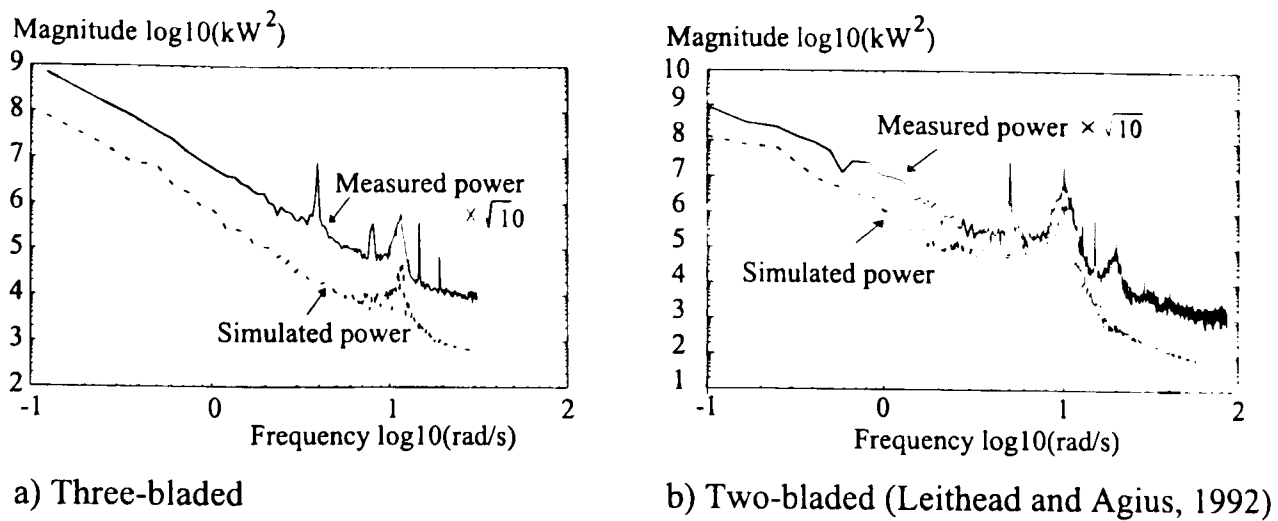


Figure 3.3 The power spectra of measured and simulated power on medium-scale commercial machines illustrating modelling of $n\Omega_o$ and tail for higher spectral peaks.

3.1.4 Actuator dynamics

The pitching mechanism of a wind turbine is normally either electro-mechanical or hydraulically driven. The capabilities of both mechanisms are restricted. In the case of the former, there is a maximum current that can drive the servo, which is equivalent to a maximum pitch acceleration, and a maximum voltage, which is equivalent to a maximum pitch velocity. In the case of the latter, when the circulation pump is running at its maximum rate, there is a maximum flow which can be equivalent to either a maximum pitch acceleration or a maximum pitch velocity. When either of these limitations is reached the pitching mechanism saturates. The limits normally can be easily reached, particularly if the pitching mechanism is prone to internal noise (Leithead and Agius, 1992). If the implementation of a control system does not take account of actuator saturation, limit cycling can occur in the output signal, as in the case of the power output in Figure 3.4. Near and in saturation the dynamics of the actuator are highly non-linear. Implementing the power controller as described by Leith and Leithead (1997) enables short intervals of actuator saturation without deteriorating the power output. In addition, the low actuator bandwidth on large-scale machines also has implications for the implementation of the controller (Leith and Leithead, 1997).

The saturation is caused by high-frequency components of the pitch demand spectrum, by measurement noise and by spectral peaks. Hence the actuator dynamics are extremely important and are usually the restricting factor to any control design. On medium-scale wind turbines conventional actuators can typically achieve a maximum acceleration (velocity) of up to $20^\circ/s^2$ ($10^\circ/s$). On large-scale wind turbines the actuators can achieve

considerably less due to the blade inertia increasing with R^{51} , while the force applied varies with area, *i.e.* R^{22} . A maximum of around 7°/s for actuator velocity is used by Rogers and Leithead (1994) for a 1 MW pitch regulated machine. No comparable figure could be determined for the maximum acceleration. One could also argue that the actuator capability would increase on tip regulated machines compared to full-span pitch regulated ones as the movable inertia is much less.

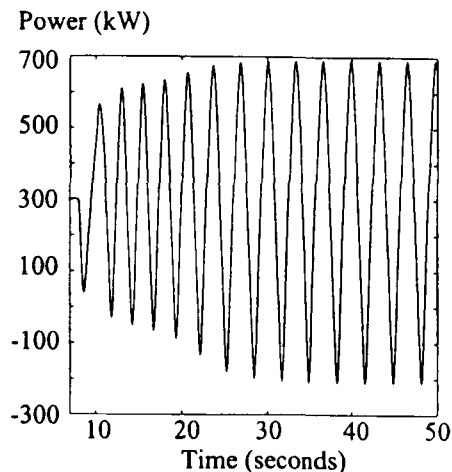


Figure 3.4 Limit cycling occurring in power output due to actuator saturation.

The non-linear model of the actuator used in the simulation model is shown in Figure 3.5, unless otherwise stated and the parameters used are shown in Table E.12 (Leithead *et al.*, 1991a). The non-linear actuator can be linearised when within the actuation limits to have the transfer functions from demanded pitch angle, β_d , to actual pitch angle, β_a as

$$A(s) = \begin{cases} \frac{3600(1 + 0.005s)}{0.0000175s^4 + 0.0085s^3 + 1.916364s^2 + 183.2727s + 3600} & \text{for 300 kW} \\ \frac{3600(1 + 0.05s)}{0.175s^4 + 8.5s^3 + 191.6364s^2 + 1832.727s + 3600} & \text{for 1 MW} \end{cases} \quad (3.8)$$

The low-frequency dynamics of (3.8) can be approximated by a first-order transfer function which is used for controller design and the linear co-variance analysis. For medium-scale machines a typical bandwidth is about 25 rad/s, while for a large-scale machine it is approximately 2.5 rad/s.

¹ Inertia is defined as the radius squared multiplied by the mass. Mass is proportional to volume, *i.e.* R^3 . Hence inertia is proportional to R^5 .

² On large-scale wind turbines the actuator is normally hydraulically driven. In which case the actuator force is proportional to area, *i.e.* R^2 .

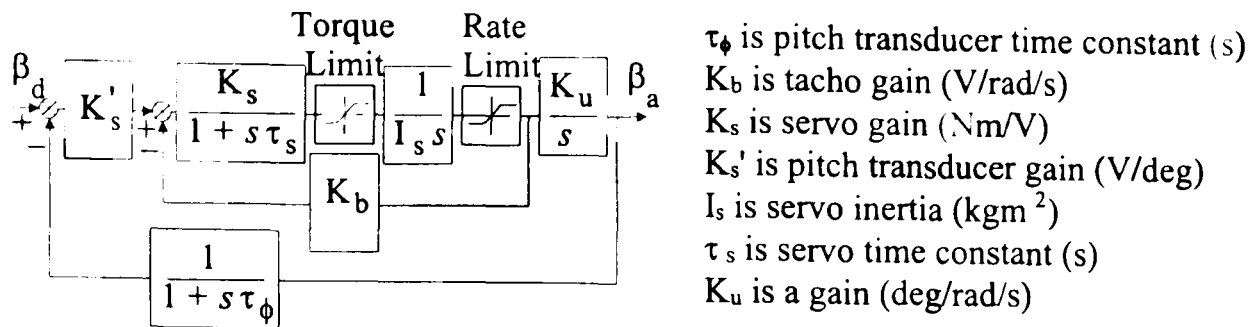


Figure 3.5 Block diagram of the actuator.

The parametric studies in Chapters 5 and 6, which are used to investigate full-span and tip-regulated machines, use the standard deviation of actuator acceleration and velocity to give an indication of actuator activity. Linear estimates of actuator activity can be obtained as shown in Section C.1. Since the amount of actuator acceleration is proportional to the closed-loop transfer function multiplied by s^2 , the amount of high frequency roll-off in the open-loop transfer function is important. This also implies that the internal signals of the actuator are sensitive to high-frequency disturbances, particularly those at $n\Omega_\infty$ and measurement noise (when the controller cross-over frequency is high). The actuator activity will also increase as the cross-over frequency of the closed loop increases, (see Chapters 5 and 6). To summarise, the controller is required to not have high actuator activity and hence is required not to have too high a cross-over frequency and to have a reasonable amount of high-frequency roll-off. Leithead *et al.* (1991a) suggested that the roll-off required in the controller at high frequency is $1/s^3$, see Section C.1. The effectiveness of the control system is dependent on the ratio of the sensitivity of aerodynamic torque to changes in pitch to the sensitivity of aerodynamic torque to changes in wind speed and actuator activity is very sensitive to wind speed. It can be seen in Figures 5.1 and 6.1, where wind speed is plotted against corresponding pitch angle for rated power, that the actuator activity will be greater at wind speeds just above rated, since the gradient of pitch angle to wind speed in this region is at its greatest. The change in the pitch angle required decreases as the wind speed rises.

3.1.5 Power-train dynamics

The power-train dynamics combine the dynamics of the drive train (rotor, low-speed shaft, gearbox, high-speed shaft and generator rotor) and the electrical generator to produce a low-frequency torsional mode, which on a badly designed wind turbine can dominate the low-frequency dynamics. For example the dynamic behaviour of a machine deteriorates when a medium/high-slip induction generator is replaced by a low-slip induction generator (Johnson and Smith, 1976, Hinrichsen, 1984).

A simple model of the drive-train dynamics (see Section B.5.3) with a compliant mounted gearbox is shown in Figure 3.6.

The dynamics of the generator are analysed and discussed in Appendix D. A simple model is adequate, in almost all cases, even for simulation-based investigations. The dynamics of the generator can be modelled by the first-order linear differential equation (D.32) that is,

$$\tau \dot{T}_R = -T_R + D_e(\theta_G - \theta_e / p) \quad (3.9)$$

where τ is the generator time constant, D_e is the slope of the torque/speed curve, p is the number of pole pairs, $\dot{\theta}_e$ is the frequency of the grid, and T_G is the generator torque.

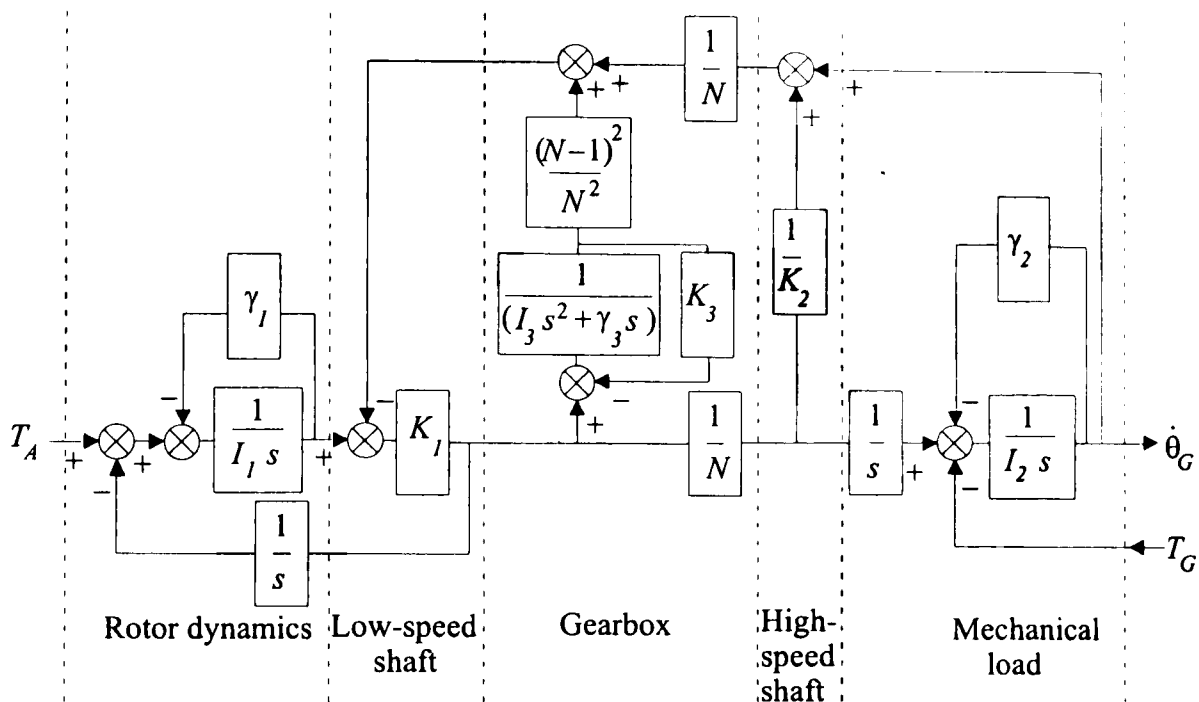


Figure 3.6 Drive-train dynamics.

Non-compliant gear-box mounting

Assuming that the gearbox is not compliantly mounted, the dynamics of the drive train then simplify further to those depicted in Figure 3.7. Combining Figure 3.7 and (3.9), the power-train dynamics relating T_G to the aerodynamic torque, T_A , for a wind turbine, can be represented by the transfer function

$$G(s) = \frac{b_o}{a_4 s^4 + a_3 s^3 + a_2 s^2 + a_1 s + a_0} \quad (3.10)$$

where

$$b_o = \kappa D_e / N$$

$$a_o = \kappa D_e + \kappa(\gamma_1 / N^2 + \gamma_2)$$

$$a_1 = \gamma_1 D_e + \tau \kappa(\gamma_1 / N^2 + \gamma_2) + \kappa(I_1 / N^2 + I_2) + \gamma_1 \gamma_2$$

$$a_2 = I_1 D_e + \tau \kappa(I_1 / N^2 + I_2) + \tau \gamma_1 \gamma_2 + (I_1 \gamma_2 + I_2 \gamma_1)$$

$$a_3 = \tau(I_1 \gamma_2 + I_2 \gamma_1) + I_1 I_2$$

$$a_4 = \tau I_1 I_2$$

$$\kappa = N^2 K_1 K_2 / (K_1 + N^2 K_2)$$

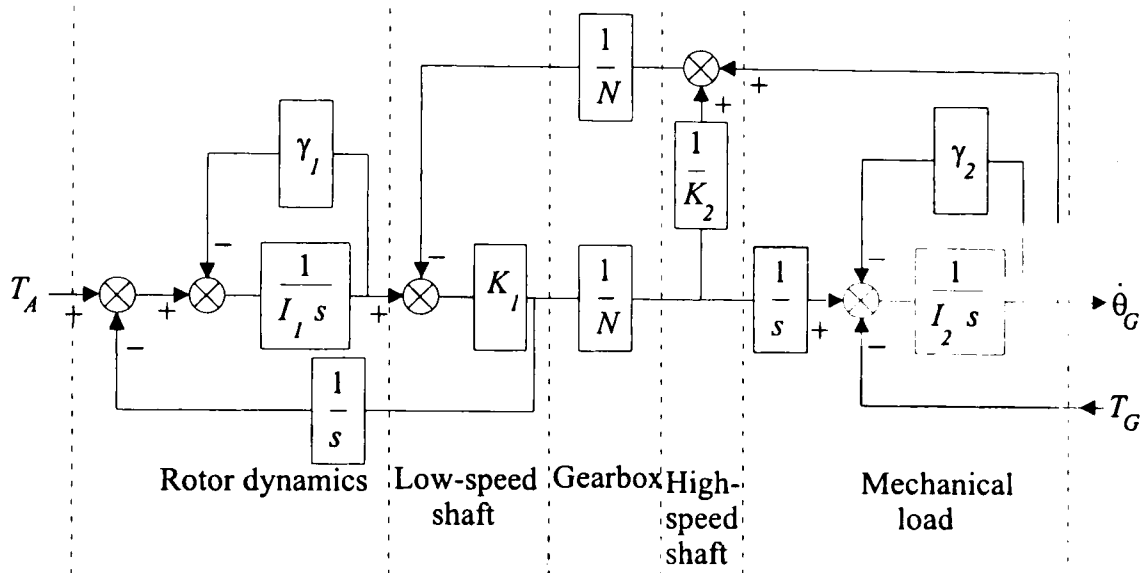


Figure 3.7 Drive-train dynamics for a wind turbine with no gearbox complaint mounting.

To indicate the extent to which this simple linear power-train model is equivalent to the more complete linear power-train model, obtained by combining the linear drive train of Section B.5.2 with (3.9), the Bode plots of the transfer function $G(s)$, which is fixed, together with its equivalent for the more complete linear model are depicted for a full-span pitch regulated large-scale machine in Figure 3.8. At low frequency, agreement in all wind speeds is good with only local discrepancies in the region of the frequencies of the tower natural modes and the blade flap-wise natural mode. At higher frequency, the simple model suffices since the details of the dynamics are submerged within the details of the spectrum of the wind disturbance inputs and since, in this context, the dynamics of frequencies greater than the dominant low frequency drive-train mode are not really of interest. As may be observed from Figure 3.8, the dynamics vary very little with wind speed. The measured frequency domain responses for the full non-linear model of Section B.5.1 are also depicted on Figure 3.8. In addition, the Bode plots of the fourth order model (B.48), for $T_w(s)$ and the fourth order model, (B.49), for $T_a(s)$ are depicted in Figures 3.9 and 3.10, respectively, together with their equivalents for the more complete linear model of Section B.5.2. Agreement, at all wind speeds, is again good with only local discrepancies in the region of

the frequencies of the tower natural modes. At low frequency, as anticipated, both $T_w(s)$ and $T_a(s)$ are essentially unity. At wind speeds close to rated, a rapid shift of 360° in the phase of the more complete linear model for $T_a(s)$ is evident, see Figure 3.10. It corresponds to a pair of non-minimum zeros induced by the tower dynamics. The measured frequency responses are also depicted in Figures 3.9 and 3.10. From the preceding, it is evident that the simple model, $G(s)$ as defined by (3.10), adequately represents the power-train dynamics of the large-scale wind turbine.

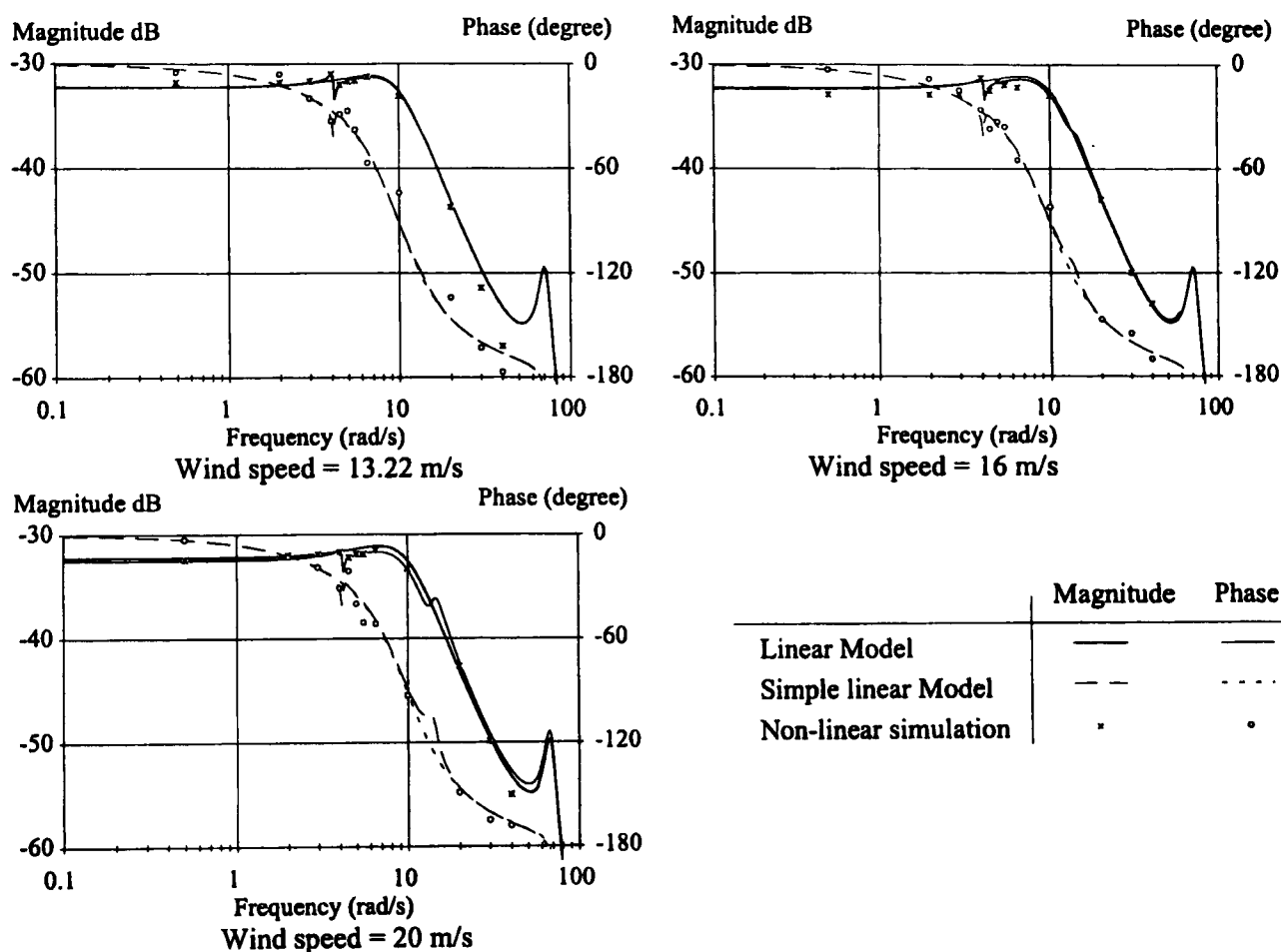


Figure 3.8 Bode plot of the transfer function, $G(s)$, for a commercial large scale machine.

To further support the adequacy of the simple linear model, the Bode plot of the transfer function for the simple linear model of a medium-scale wind turbine is compared in Figure 3.11 (Leithead and Agius, 1992) to the measured frequency domain response of the actual machine. As for the previously considered large-scale machine, the agreement is good, particularly in terms of phase which is less sensitive to the inevitable uncertainty concerning the prevailing wind conditions. (The discrepancy around 8 rad/s is probably due to the tower modes). Again, it is evident that the simple model adequately represents the drive-train dynamics.

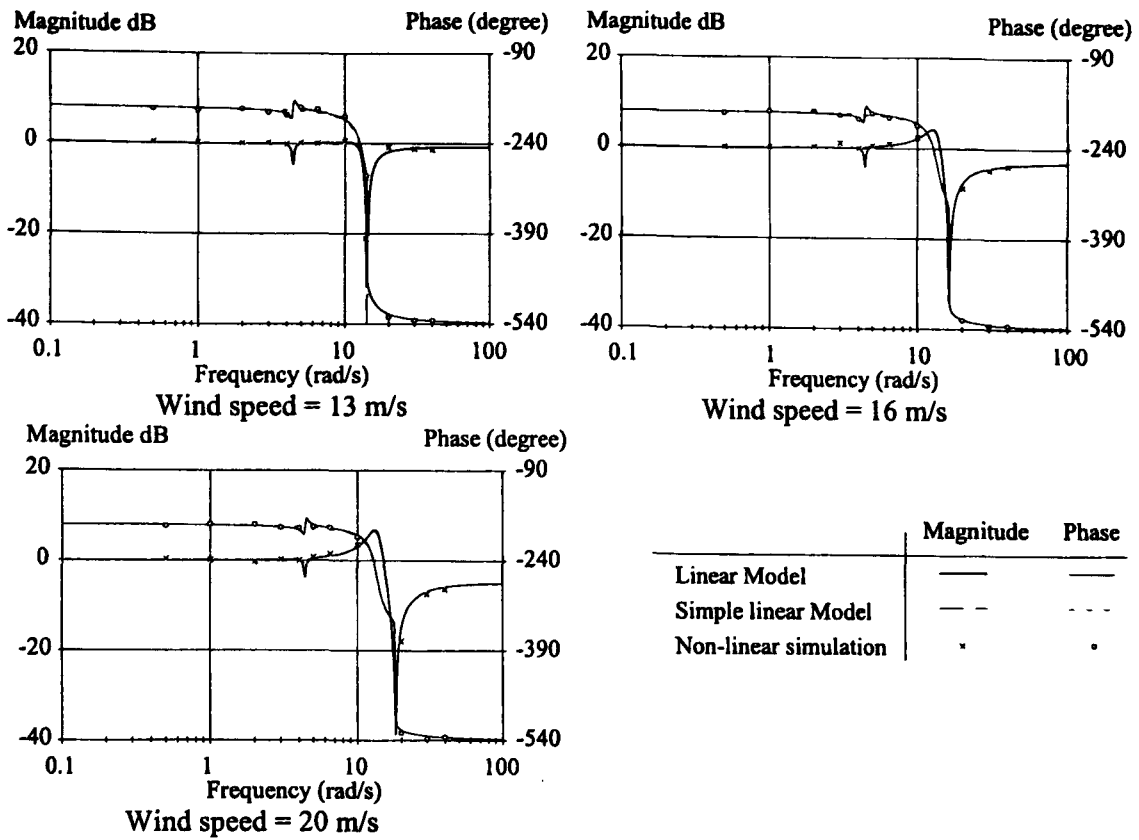


Figure 3.9 Bode plot of the transfer function $T_W(s)$.

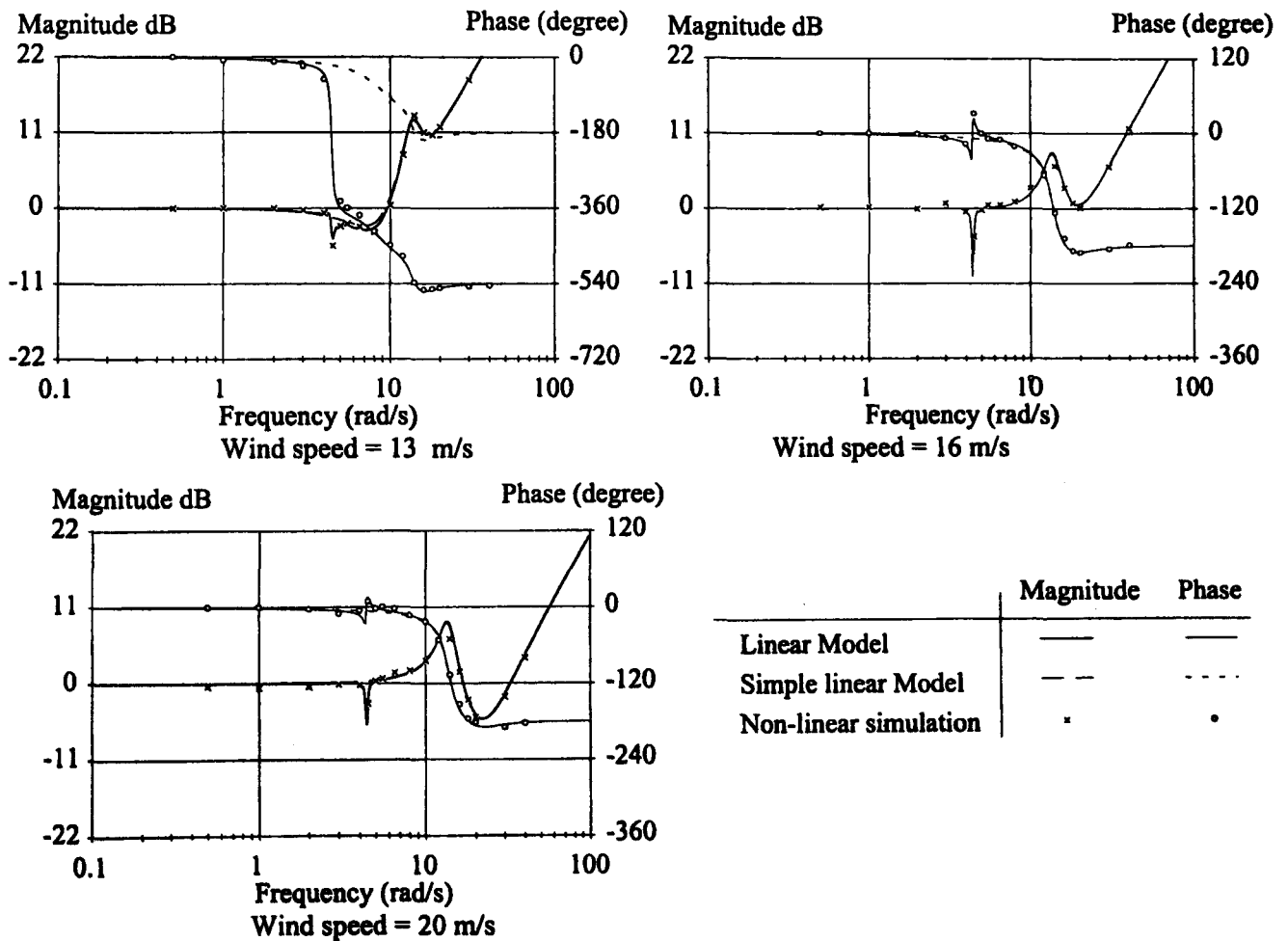


Figure 3.10 Bode plot of the transfer function $T_a(s)$.

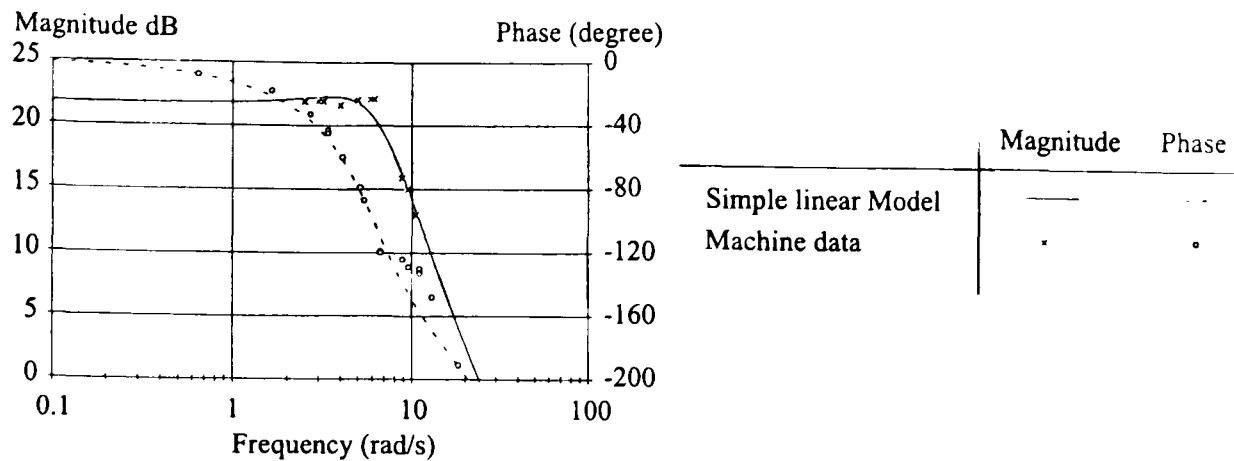


Figure 3.11 Bode plot of the transfer function, $G(s)$, for a commercial medium scale machine with site data.

Compliant gear-box mounting

The dynamics of a compliant gearbox mounting can be modelled by combining Figure 3.7 and (3.9) with the stiffness of the low-speed shaft is replaced by

$$\frac{1}{K_I} \rightarrow \frac{1}{K_I} + \frac{(N-1)^2}{N^2(I_3s^2 + \gamma_3s + K_3)} \quad (3.11)$$

3.2 Performance of the conventional power train

3.2.1 Simple performance indicators

3.2.1.1 Non-compliant mounted gearbox

In this section it is assumed that the gearbox is not compliantly mounted. (The dynamics of a compliantly mounted gearbox are considered in Section 3.2.1.2.)

The power-train dynamics are usually interpreted as consisting of the first drive-train mode at low frequency (ω_1 , say, with damping factor η_1) and a second drive-train mode at high frequency (ω_2 , say, with damping factor η_2). Both modes can be clearly seen in Figure 3.8. The first drive-train mode is mainly due to the rotor and low-speed shaft dynamics whilst the second drive-train mode is due to the generator and high-speed shaft dynamics. The position of the first drive-train frequency has primarily been considered in the literature to be important as a guide to the amount of $n\Omega_o$ as seen in the drive-train torques. To reduce the amount of $n\Omega_o$ fluctuations in the drive-train torque compliance has been added to the drive train to reduce the frequency of the first drive-train mode. Fluid couplings, spring mounted gearboxes and rubber mounted bedplates (Juggins and Holton, 1995) have all been used. Adequate damping of the first drive-train mode is also thought to

be important (Wasyncuk *et al.*, 1981 and Hinrichsen and Nolen, 1982), so that the low-frequency turbulence is not amplified.

Consider a three-bladed 330 kW wind turbine (with the parameter values in Table F.3 which has been modified for the British grid, *i.e.* D_e and N are replaced by 915.8 Nm/rad/s and 40.65, and τ is replaced by the more realistic value of 0.03s). Its drive-train transfer function, with the first and second drive-train modes explicitly shown, is

$$\frac{12771}{(s^2 + 6.72s + 52.9)(s^2 + 26.6s + 9822)}$$

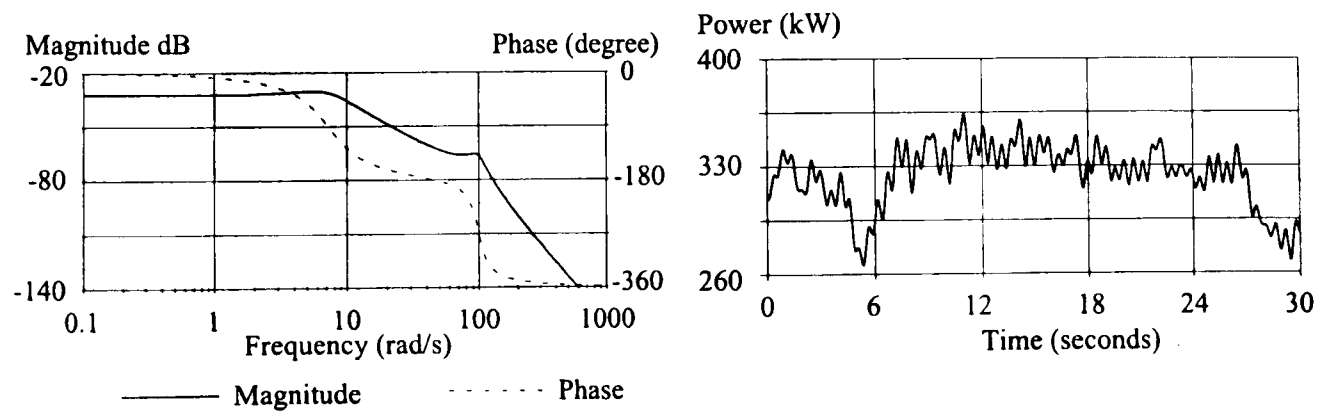
The first drive-train mode has characteristics $\omega_1 = 7.3$ rad/s and $\eta_1 = 0.46$ and the second drive-train mode has characteristics $\omega_2 = 99$ rad/s and $\eta_2 = 0.13$. The Bode plot for the drive-train transfer function is shown in Figure 3.12a. A typical section of generated power from a well validated simulation¹ of this machine is shown in Figure 3.12b. Although this turbine is dynamically benign with reasonably good damping, the power fluctuations can be seen clearly.

Since the dynamics of the power train are dominated by the first drive-train mode and since the high frequency dynamics are not important in this context, a simple spring-mass-damper model might suffice. Its dynamics would be modelled by the second order differential equation

$$I\ddot{y} + \gamma\dot{y} + Ky = x \quad (3.12)$$

where I is the mass, γ is the viscous damping coefficient and K is the spring stiffness. The equivalent transfer function representation is

$$G(s) = \frac{1}{Is^2 + \gamma s + K} = \frac{(K/I)/K}{s^2 + (\gamma/I)s + (K/I)} \quad (3.13)$$



a) Bode plot of power-train transfer function. b) Corresponding simulated power output.

Figure 3.12

¹ The simulation model consists of a PI controller $1.1908 \times 10^{-5} (1 + 10/s)$, with a controller cross-over frequency of 1 rad/s.

Since the canonical form for a second-order transfer function is $k / ((s / \omega_n)^2 + 2\eta s / \omega_n + 1)$, where ω_n is the natural frequency and η is the damping ratio, the following identifications can be made

$$2\eta\omega_n = \gamma/I \quad ; \quad \omega_n^2 = K/I \quad (3.14)$$

Hence, it follows that

$$\varepsilon = \eta/\omega_n = \gamma/(2K) \quad (3.15)$$

that is, as would be expected ε , the ratio of the damping factor to the natural frequency of the second order system, increases with increasing viscous damping coefficient but decreases with increasing stiffness.

Consider a wind turbine with infinite drive-train mechanical stiffness (Bossanyi and Jervis, 1988). The drive-train model reduces to that shown in Figure 3.13 where I is the rotor inertia. The power-train dynamics are represented by the transfer function

$$H(s) = \frac{ND_e}{I\tau s^2 + s(I + \gamma\tau) + (N^2 D_e + \gamma)} \approx \frac{ND_e / \tau}{Is^2 + sI / \tau + N^2 D_e / \tau} \quad (3.16)$$

assuming the mechanical damping, γ , is very light. The value of the generator time constant, τ , is similar for a broad range of generators with the same rating and the slope of the torque speed curve, D_e , is inversely proportional to the slip. By comparing (3.13) to (3.16) it might be concluded that the primary role in the power-train dynamics of the generator is to provide compliance. When a medium/high slip generator is replaced by a low-slip generator, degradation in dynamic behaviour occurs because the compliance of the drive train has been reduced.

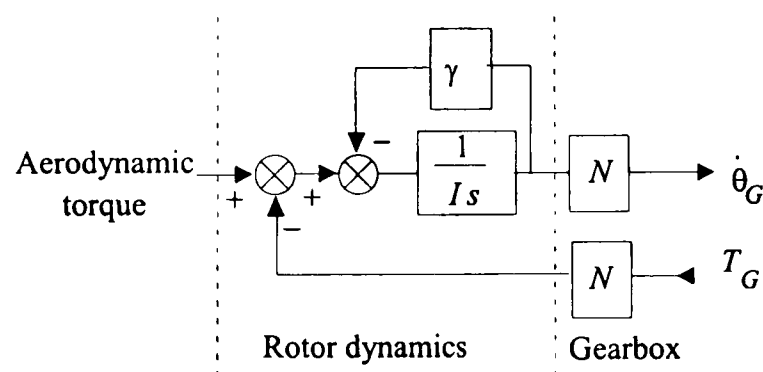


Figure 3.13 Block diagram a wind turbine with infinite drive-train mechanical stiffness.

However, the above analysis is misleading. A more appropriate characterisation of the power-train dynamics is as follows. The model of the power train (3.10) has the general formulation

$$\frac{\omega_1^2 \omega_2^2 / N}{(s^2 + 2\eta_1 \omega_1 s + \omega_1^2)(s^2 + 2\eta_2 \omega_2 s + \omega_2^2)} \quad (3.17)$$

Comparing (3.17) to (3.10), the following parameter identifications can be made.

$$\begin{aligned} b_o / a_4 &= \omega_1^2 \omega_2^2 / N \\ a_3 / a_4 &= 2\eta_2 \omega_2 + 2\eta_1 \omega_1 \\ a_2 / a_4 &= \omega_1^2 + \omega_2^2 + 4\eta_1 \eta_2 \omega_1 \omega_2 \\ a_1 / a_4 &= 2\eta_1 \omega_1 \omega_2^2 + 2\eta_2 \omega_1^2 \omega_2 \\ a_o / a_4 &= \omega_1^2 \omega_2^2 \end{aligned}$$

Perhaps the most significant relationship is

$$\begin{aligned} \frac{a_1}{a_o} &= 2 \left(\frac{\eta_1}{\omega_1} + \frac{\eta_2}{\omega_2} \right) \\ &= \frac{\gamma_1 D_e N^2 / \kappa + \tau(\gamma_1 + N^2 \gamma_2) + (I_1 + N^2 I_2) + \gamma_1 \gamma_2 N^2 / \kappa}{N^2 D_e + (\gamma_1 + N^2 \gamma_2)} \\ &\approx (I_1 + N^2 I_2) / (N^2 D_e) \end{aligned} \quad (3.18)$$

all the other terms being negligible. Since the second drive-train mode has a much higher frequency than the first drive-train mode, the relationship becomes

$$\varepsilon_1 = \eta_1 / \omega_1 \approx (I_1 + N^2 I_2) / (2N^2 D_e) \quad (3.19)$$

In other words, for a fixed first drive-train mode frequency the ratio of the damping factor to the frequency of the first drive-train mode depends only on the rotor inertia and the slope of the generator torque/speed curve, assuming the gearbox ratio is fixed; not on mechanical damping in the drive train or on any stiffness in the drive train. In comparison to the second-order system considered earlier (3.12) the behaviour of the fourth-order system as summarised by ε_1 is a little unexpected. For a fixed frequency of the first drive-train mode, no other parameters, including the mechanical damping, γ_1 and γ_2 , in the drive train, affect the damping factor.

When a medium/high-slip generator is replaced by a low-slip generator, there is little change in the frequency of the first drive-train mode. Degradation in dynamic behaviour occurs because the damping of the drive train has been reduced. A similar degradation is caused by replacing the rotor by one of lighter inertia.

A second relationship worthy of note is

$$\begin{aligned}
\frac{a_2}{a_o} &= \frac{1}{\omega_2^2} + \frac{1}{\omega_1^2} + 4 \frac{\eta_1 \eta_2}{\omega_1 \omega_2} \\
&= \frac{I_1 D_e + \tau \kappa (I_1 / N^2 + I_2) + \tau \gamma_1 \gamma_2 + (I_1 \gamma_2 + I_2 \gamma_1)}{\kappa D_e + \kappa (\gamma_1 / N^2 + \gamma_2)} \\
&\approx \frac{I_1 D_e + \tau \kappa (I_1 / N^2 + I_2)}{\kappa D_e}
\end{aligned} \tag{3.20}$$

all other terms being negligible. Since the second drive-train mode has a higher frequency than the first drive-train mode and both η_1 and η_2 are normally less than 1, this relationship becomes

$$\frac{1}{\omega_1^2} = \frac{I_1}{\kappa} + \frac{\tau (I_1 + N^2 I_2)}{N^2 D_e} \tag{3.21}$$

The frequency of the first drive-train mode is determined by a mechanical component, $N^2 \kappa / I_1$ and an electrical one, $N^2 D_e / \tau (I_1 + N^2 I_2)$. The mechanical component usually dominates and hence the frequency of the first drive-train mode is primarily determined by the drive-train compliance, $1/\kappa$. Hence, it is reasonably straightforward to design for a specified frequency of the first drive-train mode but from (3.19) it is problematic to design for a specified amount of damping. A reduction in the frequency of the first drive-train mode achieved solely by increasing the compliance is always accompanied by a reduction in the damping factor.

It should be noted that, for the 330 kW wind turbine whose drive-train transfer function described earlier in this section, the value of ε_1 , predicted by (3.19), is 0.065 and ω_1 , predicted by (3.21) is 7.2 rad/s which agrees well with the previously determined values of 0.064 and 7.3 rad/s respectively.

It follows that, rather than (3.12), the appropriate form for the spring-mass-damper model of the power train is obtained with the assignments

$$I = I_1 ; K = \omega_1^2 I_1 ; \gamma = 2\varepsilon_1 \omega_1^2 I_1 \tag{3.22}$$

in (3.12), where ε_1 and ω_1 are defined by (3.19) and (3.21). As is evident from (3.19) and (3.21), the generator dynamics have a minor influence on the dynamics of the first drive-train mode, *i.e.* the frequency and damping depend weakly on τ . In many cases, the electrical component of (3.21) is negligible, when the power-train dynamics can be represented by the second-order transfer function

$$H(s) = \frac{\kappa / N}{I_1 s^2 + \kappa (I_1 + N^2 I_2) / (N^2 D_e) \cdot s + \kappa} \tag{3.23}$$

The above analysis assumes that the stiffness of the gearbox is infinite. The influence on the dynamics of a compliant gearbox mounting is considered in the following sub-section.

3.2.1.2 Compliantly mounted gearbox

In this section, the influence on the dynamics of a compliant gearbox mounting is considered. The appropriate model of the power train is obtained by combining Figure 3.6 with (3.9). The model so derived is equivalent to the model (3.23) with the stiffness κ amended dynamically to $\bar{\kappa}$ such that

$$\begin{aligned} \frac{1}{\bar{\kappa}} &= \frac{1}{\kappa} + \frac{(N-1)^2}{N^2(I_3s^2 + \gamma_3s + K_3)} \\ &= \frac{1}{\kappa} \cdot \frac{[I_3s^2 + \gamma_3s + (K_3 + \kappa(N-1)^2 / N^2)]}{(I_3s^2 + \gamma_3s + K_3)} \end{aligned} \quad (3.24)$$

Since K_3 must sustain the rotor and I_3 is significantly less than the inertia of the rotor, the frequency $\sqrt{K_3 / I_3}$ is not low. Nevertheless, the poles and zeros of (3.24) can influence the low frequency dynamics of the power train. External damping to the gearbox may be introduced not only to reduce gearbox oscillations but also in an attempt to increase the damping of the first drive-train mode. In the latter case, the damping required is so great that the frequencies of the poles and zeros of (3.24) become distinct with one real pole and zero at low frequency and the other real pole and zero at high frequency.

When the external gearbox damping is heavy, the transfer function model (3.23) remains appropriate at low frequency and power-train dynamics can be represented by

$$\bar{H}(s) = \frac{\kappa[I_3s^2 + \gamma_3s + K_3] / N}{[I_1s^2(I_3s^2 + \gamma_3s + (K_3 + \kappa(N-1)^2 / N^2)) + (\kappa(I_1 + N^2I_2) / (N^2D_e).s + \kappa)(I_3s^2 + \gamma_3s + K_3)]} \quad (3.25)$$

The general dynamic characteristics of $\bar{H}(s)$ can be elucidated by simple root locus arguments.

The dependence of the zeros of $\bar{H}(s)$ on the damping coefficient, γ_3 , is clear. The dependence of the poles of $\bar{H}(s)$ on the damping coefficient, γ_3 , can be clarified by noting that they are the same as the zeros of

$$1 + \gamma_3 \frac{s[I_1s^2 + \kappa(I_1 + N^2I_2) / (N^2D_e).s + \kappa]}{[(I_1s^2 + \kappa(I_1 + N^2I_2) / (N^2D_e).s + \kappa)(I_3s^2 + K_3) + I_1s^2\kappa(N-1)^2 / N^2]} \quad (3.26)$$

The poles of (3.26) can be determined by simple root locus arguments to consist of two complex conjugate poles. The first pair has frequency greater than $\sqrt{K_3 / I_3}$ and are

marginally stable. When compared to the poles of the corresponding system with infinitely stiff gearbox mounting (3.23), the second pair of poles of (3.26) is similar but occurs at a lower frequency and has a smaller damping factor. It follows that the root locus, traced by the zeros of (3.26) as γ_3 varies, is as depicted in Figure 3.14. It can be seen that the pair of poles of $\bar{H}(s)$, which would normally be characterised as the first drive-train mode, migrate towards a pair of zeros which have the same frequency and damping factor as the poles of the corresponding system with infinitely stiff gearbox mounting, (3.23), but are slightly less damped for all values of γ_3 . The pair of poles due to the gearbox mounting migrate onto the real axis to become, as might be expected, distinct with one real pole at low frequency and the other real pole at high frequency.

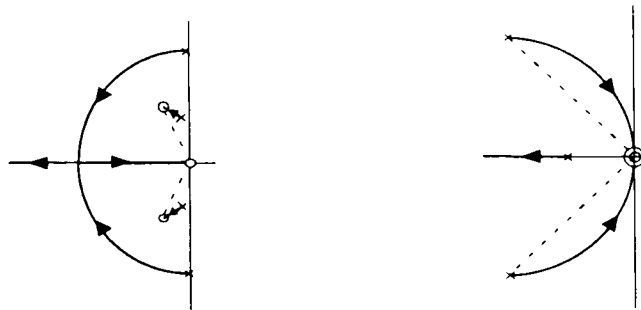


Figure 3.14 Root locus of zeros of (3.26). **Figure 3.15** Root locus of zeros of (3.29).

Since the damping of the pair of poles in Figure 3.14 which migrate towards the pair of zeros is not increased by the external gearbox damping, the only benefit that could accrue would be a reduction in the power-train transmittance caused by the low frequency real pole and zero, induced by heavy damping, in $\bar{H}(s)$. In these circumstances $1/\bar{\kappa}$ can, except at high frequencies, be approximated by

$$\frac{1}{\bar{\kappa}} \approx \frac{1}{\kappa} \cdot \frac{[\gamma_3 s + (K_3 + \kappa(N-1)^2 / N^2)]}{(\gamma_3 s + K_3)} \quad (3.27)$$

when $\bar{H}(s)$ becomes

$$\bar{H}(s) \approx \frac{\kappa(\gamma_3 s + K_3) / N}{[(I_1 s^2 (\gamma_3 s + (K_3 + \kappa(N-1)^2 / N^2))) + (\kappa(I_1 + N^2 I_2) / (N^2 D_e) \cdot s + \kappa)(\gamma_3 s + K_3)]} \quad (3.28)$$

The frequency of the low frequency real pole can be elucidated by noting that the poles of (3.28) are the same as the zeros of

$$1 + k \cdot \frac{s^2 I_1 \kappa (N-1)^2 / N^2}{(I_1 s^2 + \kappa(I_1 + N^2 I_2) / (N^2 D_e) \cdot s + \kappa)(\gamma_3 s + K_3)} \quad (3.29)$$

with k equal to one. The root locus, traced by the zeros of (3.29) as k varies, is as depicted in Figure 3.15. It can be seen that the frequency of the low frequency real zero of (3.29) is

greater than (K_3/γ_3) and so greater than the frequency of the low frequency real pole of (3.29). Hence, rather than reducing the power-train transmittance, the low frequency real pole and zero in $\bar{H}(s)$ effectively increase the power-train transmittance. Figure 3.15 also confirms that the pair of poles of $\bar{H}(s)$, which would normally be characterised as the first drive-train mode, are slightly less damped than those of the corresponding system with infinitely stiff gearbox mounting, (3.23).

In effect, the presence of heavy external gearbox damping reduces the compliance of the power train whilst slightly reducing the damping.

When the external gearbox damping is sufficiently light to reduce only gearbox oscillations, the damping factors for both the numerator and denominator of (3.25) are much less than one and (3.25) only exhibits phase shifts locally to the frequencies of its poles and zeros. Since these are not at low frequency, it follows that the simple dynamic model (3.10) remains appropriate but with the combined stiffness amended such that

$$\frac{1}{\kappa} = \frac{1}{K_1} + \frac{1}{N^2 K_2} + \frac{(N-1)^2}{N^2 K_3} \quad (3.30)$$

The effect of the compliance of the gearbox mounting is to reduce, as would be expected, the power-train stiffness and so the frequency of the first drive-train mode.

3.2.2 Dynamic performance

The restrictions on the achievable dynamic behaviour of the wind turbine from (3.19) are verified below.

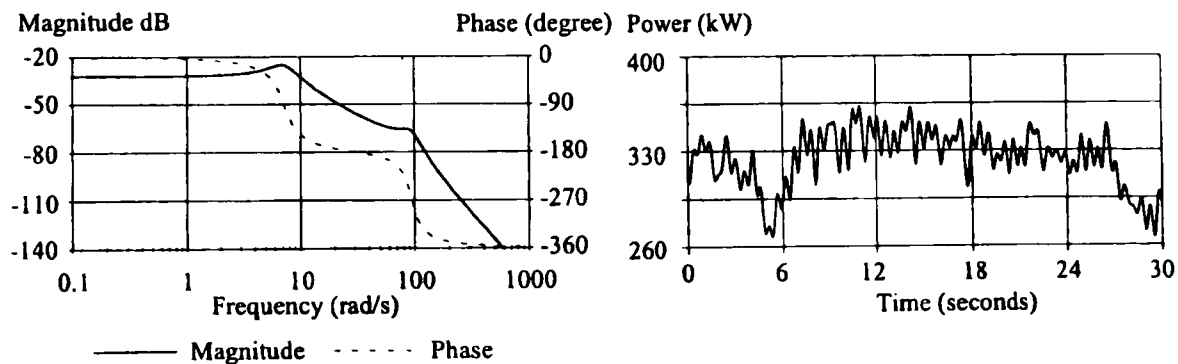


Figure 3.16 Bode plot of transfer function of power train with halved inertia and the corresponding simulated power output.

If the inertia I_1 is reduced to half its original value, but the compliance adjusted so that the frequency of the first drive-train mode remains at 7.3 rad/s then from (3.19) the value of ϵ_1 and also the damping is reduced to half. The Bode plot for the power-train transfer function and the corresponding generated power are shown in Figure 3.16. It can be

seen by comparison to Figure 3.12 that the effect of reducing the damping is to increase the fluctuations in the power. To recover the damping the slope of the torque/speed curve is halved so that ϵ_1 returns to its original value. The Bode plot for the power-train transfer function and the corresponding simulated generated power are shown in Figure 3.17. The response is very similar to the original system, see Figure 3.12.

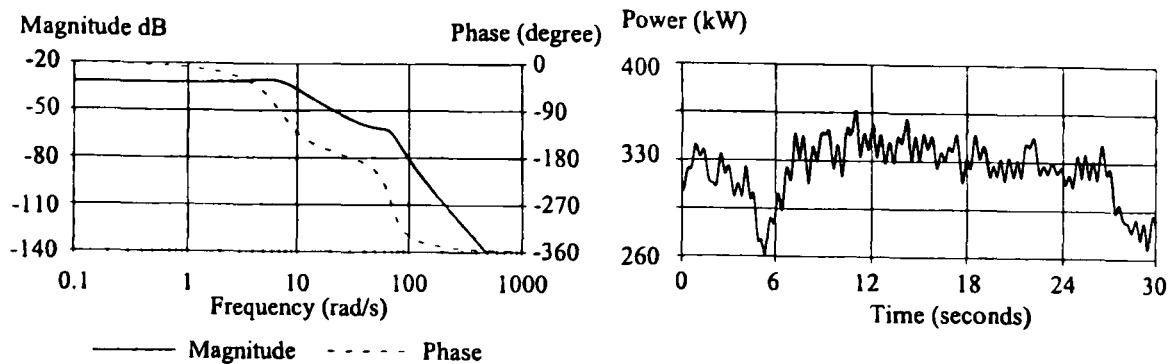


Figure 3.17 Bode plot of transfer function of power train with halved inertia and slope of torque/speed curve and the corresponding simulated power output.

If the inertia retains its original value and the stiffness of the low-speed shaft is adjusted to reduce the frequency of the first drive-train mode to half its previous value, then from (3.19) the value of ϵ_1 remains unchanged but the damping is reduced by half. Reducing the frequency of the first drive-train mode reduces the extent of the transients at high frequency by a factor of 4 but the transients at lower frequency increase with the reduced damping. The Bode plot for the power-train transfer function and the corresponding generated power are shown in Figure 3.18. The high frequency transients are no longer evident but there is no overall reduction in the fluctuations in power due to an increase in low-frequency transients, particularly at frequencies close to that of the first drive-train mode. To recover the damping the slope of the torque/speed curve is halved. The Bode plot for the power-train transfer function and the corresponding generated power are shown in Figure 3.19. The low-frequency fluctuations in power have been reduced without re-introducing the high-frequency fluctuations.

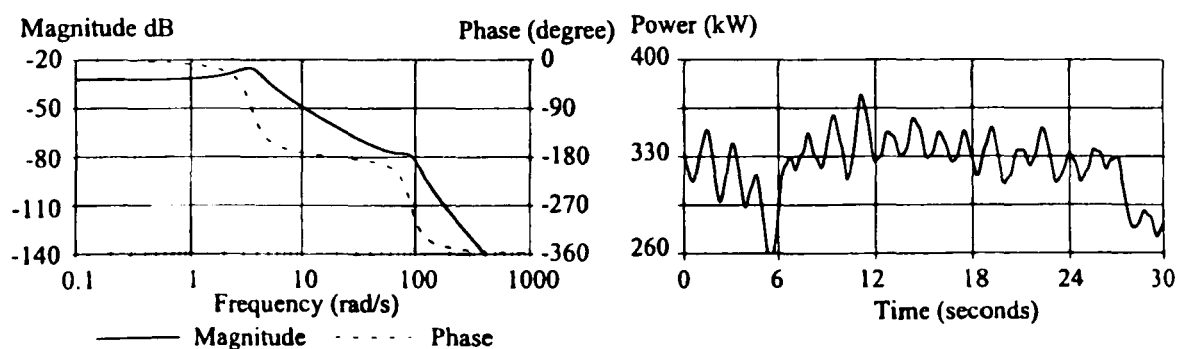


Figure 3.18 Bode plot of transfer function of power train with reduced stiffness, K_s , and the corresponding simulated power output.

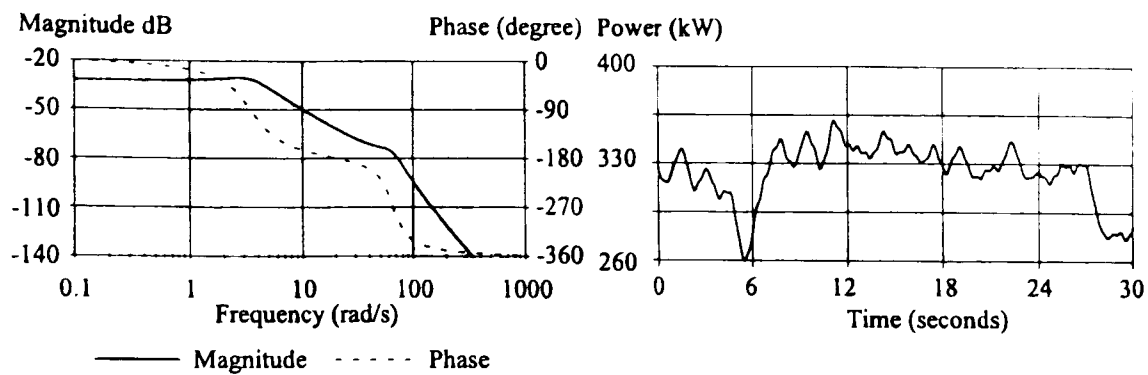


Figure 3.19 Bode plot of transfer function of power train with reduced stiffness, K_f , and half the slope of torque/speed curve and the corresponding simulated power output.

Simpson *et al.* (1993) describe a modification to the drive train whereby the gearbox and generator are mounted on a system of elastomeric mountings with very high flexibility about the rotational axis of the low-speed shaft on the WEG 400 prototype. They state that the advantages of this modification to the drive train are that the flexible mountings reduce the high-frequency drive-train loads, particularly those at $2\Omega_o$, and additional drive-train compliance is introduced, hence reducing the structural transmission noise. The dynamics of this gearbox mounting have been investigated by Juggins and Holton (1995) whose presented results support the analysis done in Section 3.2.1.2.

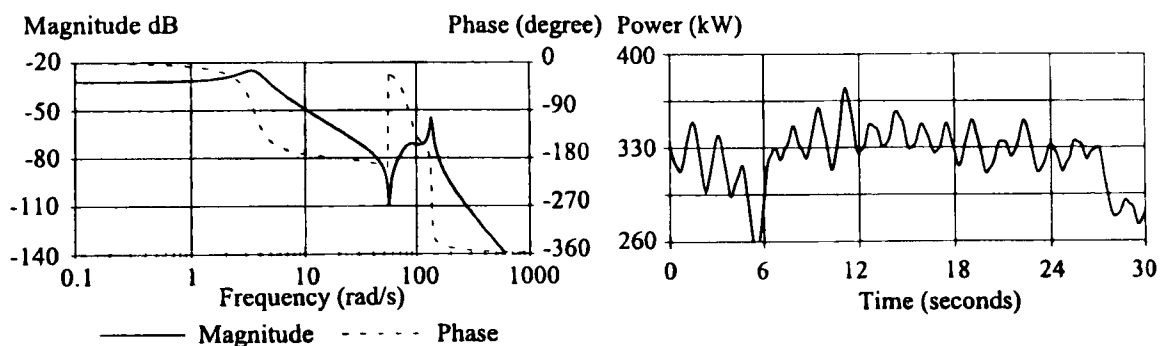


Figure 3.20 Bode plot of transfer function of drive train with a compliant gearbox mounting and the corresponding simulated power output, ($I_3 = 1000 \text{ kgm}^2$, $\gamma_3 = 100 \text{ Nm/rad/s}$ and $K_3 = 3 \times 10^6 \text{ Nm/rad}$).

Instead of reducing the stiffness of the low-speed shaft, the compliance of the gearbox mounting may be increased to reduce the frequency of the first drive-train mode (*cf.* Section 3.2.1.2). The outcome of the latter is the same as the former. With the original value of the slope of the torque/speed curve, the Bode plot for the drive-train transfer function and the corresponding generated power are shown in Figure 3.20. However, the reduction in stiffness in the drive train, which reduces the frequency of the first drive-train mode and hence the high-frequency loads, also reduces the ratio, η_f . The high frequency transients are reduced but the transients with frequency close to that of the first drive-train

mode are enhanced. A clear illustration of this effect is apparently evident on site data for a commercial machine in Simpson *et al.* (1993).

3.3 Conclusions

The first step towards attaining the objective to lay the foundation for the control aspects of integrated design has been achieved.

a) Simple models of the wind turbine are determined.

- The simple model, comprising the drive-train model, Figure 3.6, together with the generator model (3.9), adequately represents the dynamics of the power train. It is applicable to almost all wind turbines.
- The relationship of the lumped parameters of the simple model of the power train to the physical parameters of the wind turbine are summarised by (B.83) to (B.96).
- The simple power-train model together with the linear models of aerodynamic torque (3.5), actuator (3.8) and the power transducer (C.14) constitute a suitable plant model for control analysis and design. (This model is similar to that used by Leithead *et al.* (1991a) and Wilkie *et al.* (1989).)

b) The salient features of the power-train dynamics have been identified.

- The dynamics of the power train are characterised by the frequency of the first drive-train mode, ω_1 , and its damping factor, η_1 ;
- The relationship of ω_1 , and η_1 ; to the lumped parameters of the simple power-train model are determined to be (3.19) and (3.21), that is,

$$\eta_1 / \omega_1 \approx (I_1 + N^2 I_2) / (2N^2 D_e)$$

$$\frac{1}{\omega_1^2} = \frac{I_1}{\kappa} + \frac{\tau(I_1 + N^2 I_2)}{N^2 D_e}$$

- The validity of these relationships are verified by non-linear simulation.

c) The constraints on the achievable dynamic behaviour have been determined.

- Adding compliance (as suggested, amongst others, Simpson *et al.* (1993)) does not of itself improve the dynamic behaviour, since although the frequency of the first drive-train mode is decreased, thereby reducing the $n\Omega_o$ load, the damping factor is also decreased.

- The damping factor can only be increased by either increasing the slip of the generator or the inertia of the rotor and low-speed shaft; it does not depend on damping on either of the low- or high-speed shafts.
- It is reasonably straightforward to design for a specific frequency for the first drive-train mode by changing the compliance of the drive train. It is, however, not straightforward to design for a specific amount of damping factor.

It is clear from the above that the constraints on the achievable dynamic behaviour of the power train are quite strong, in particular, those affecting the damping factor of the first drive-train mode. For conventional drive trains, the damping of the power train can only be increased by methods which decrease the cost effectiveness of the machine and are inconsistent with the trend towards lighter and larger machines. It is worthwhile, therefore, to explore whether the restriction identified in c) can be circumvented by non-conventional means. In Chapter 4, the feasibility of increasing the damping of the drive train by non-conventional means is investigated.

4 Resonance control

In Chapter 3 it is observed that the frequency and the damping ratio of the first drive-train mode have considerable impact on the power controller performance. As discussed in Appendix C, the frequency of the first drive-train mode strongly influences the actuator activity due to the middle frequency spectral loads. The lower the frequency of the first drive-train mode the better the dynamic behaviour of the machine provided the damping ratio is maintained. One technique to lower the first drive-train mode is to add compliance to the drive train. However, this modification on its own makes, also makes the first drive-train mode increasingly resonant, due to the simple relationship (3.19) between the damping ratio of the first drive-train mode, η_1 , and the frequency of the mode, ω_1 , namely

$$\frac{\eta_1}{\omega_1} = \frac{(I_1 + N^2 I_2)}{2N^2 D_e} \quad (4.1)$$

where I_1, I_2 are the inertia of the rotor and the generator rotor

N is the gearbox ratio, D_e is the gradient of the generator torque speed curve.

From (4.1), it can be inferred that for a fixed frequency of the first drive-train mode, the damping ratio depends only on the inertias of the drive train and the slope of the generator torque/speed curve; it does not depend on mechanical damping nor compliance in the drive train. If the first drive-train mode is reduced by adding compliance and is not also accompanied by an increase of rotor inertia or an increase in generator slip then the drive train will become more resonant and hence more susceptible to low-frequency wind turbulence. However, neither of these solutions are particularly satisfactory as they make the machine more costly or less efficient. In addition to reducing costs, there is a trend for machines to become lighter, whereby the drive trains will become more dynamically active unless damping of the drive-train resonance is increased by some other means.

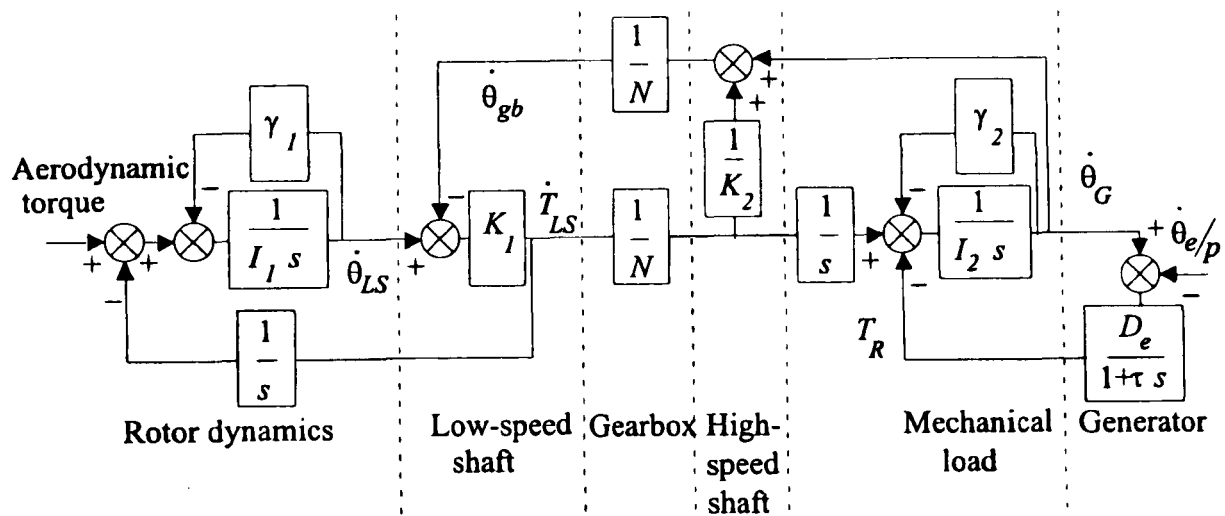
As observed in Chapter 3, drive-train damping cannot be increased by conventional means. Only non-conventional methods remain to be explored. This chapter investigates the feasibility of increasing the damping of the first drive-train mode. A direct modification to the drive train is considered in Section 4.1. The feasibility of using the modification of the drive train to reduce the $n\Omega_o$ loads or to accommodate a significant reduction in the rotor

inertia or generator slip is investigated. Direct control of the drive-train resonance is considered in Section 4.2. Since it is not possible by pitch control without excessive actuator activity (Fisher, 1997), torque control, which is only possible for variable-speed machines, must be used. Hence, in this sub-section unlike the rest of this thesis the wind turbine is a variable-speed machine.

On variable-speed machines, both the $n\Omega_o$ loads and the first drive-train resonance are normally not a problem, since the frequency of the first drive-train mode is comparatively high and the $n\Omega_o$ loads are absorbed by the inertia of the rotor. The first drive-train mode is highly resonant, since there is little damping in a variable speed drive, but it has little effect on the drive-train dynamics as the transfer function of the drive-train dynamics is well rolled-off before its frequency is reached. However, as variable speed rotors become lighter and more flexible as in the IRFLET project (Pierik *et al.*, 1993), the roll-off is reduced and the first drive-train mode can dominate the drive-train dynamics.

4.1 Drive train modification

The simple model of the power-train dynamics derived in Chapter 3 is depicted in Figure 4.1. The power-train dynamics relating the generator reaction torque to the aerodynamic torque for a wind turbine are represented by the fourth-order transfer function (3.10) and a typical Bode plot of the transfer function is shown in Figure 3.8.



where K_1, K_2 are the stiffnesses of the low- and high-speed shafts.
 γ_1, γ_2 are viscous damping of the low- and high-speed shafts.

Figure 4.1 Drive train and generator dynamics.

As discussed in Section 3.2 increasing the slip of the generator (*i.e.* decreasing D_e in (4.1)), while decreasing the efficiency of the generator does increase the damping ratio of the first drive-train mode. The modification considered here is to increase the slip only at specific frequencies by compliantly mounting the generator.

On a constant-speed wind turbine, the slip of the generator can vary only slightly, thereby preventing any change in aerodynamic torque from being absorbed as changes in rotor speed. If, however, the generator stator, *i.e.* the casing and the stator coils of the generator, is allowed to rotate slightly in an axial direction then the rotor speed need not be so strongly tied to the grid frequency. The feasibility of using this modification to improve the wind turbine's performance is discussed here.

The dynamics of an induction generator are approximated by the first-order differential equation (D.32), that is

$$\tau \dot{T}_G = -T_G + D_e(\dot{\theta}_G - \dot{\theta}_e / p) \quad (4.2)$$

where

T_G is the generator torque

$\dot{\theta}_G, \dot{\theta}_e$ are the generator rotor speed and the grid frequency

p, τ are the number of generator pole pairs and the generator time constant

D_e is the slope of the generator torque/speed curve

The speed of the generator rotor is related to the grid frequency through the slip of the generator, s_p , such that

$$s_p = p\dot{\theta}_G / \dot{\theta}_e - 1 \quad (4.3)$$

The slope of the torque speed curve, D_e is inversely proportional to slip as follows

$$D_e = \frac{T_G}{s_p \dot{\theta}_e / p} \quad (4.4)$$

Then the speed of the generator stator, $\dot{\theta}_{gs}$, can be thought of as modifying the speed of the high-speed shaft. Equation (4.2) becomes

$$\tau \dot{T}_G = -T_G + D_e(\dot{\theta}_G - \dot{\theta}_e / p - \dot{\theta}_{gs}) \quad (4.5)$$

Suppose the generator is mounted on a simple spring/damper system, so that the generator casing is allowed to 'rock' about the rotational direction of the high-speed shaft, then the dynamics of the generator mounting are modelled by

$$J_{gs} \ddot{\theta}_{gs} + B_{gs} \dot{\theta}_{gs} + K_{gs} \theta_{gs} = T_G \quad (4.6)$$

where J_{gs} is the inertia of generator stator

B_{gs} is the damping coefficient

K_{gs} is the spring coefficient

Combining (4.5) and (4.6), the dynamics relating changes in generator rotor speed, $\Delta\dot{\theta}_G$, to changes in generator torque, ΔT_G , are represented by the transfer function

$$\Delta T_G = D_e \left(1 - \frac{sD_e}{(J_{gs}s^2 + B_{gs}s + K_{gs})(1 + \tau s) + sD_e} \right) \frac{\Delta\dot{\theta}_G}{(1 + \tau s)} \quad (4.7)$$

Comparing (4.7) to (4.2), it can be seen that the effect of the spring/damper system can be interpreted as a frequency-dependent modification to the slope of the torque/speed curve, D_e . By choosing the damping coefficient, B_{gs} to be small, the generator mounting is resonant and the modification to the slope of the torque/speed curve is restricted to a small range of frequencies. The motion of the generator stator is thereby kept small.

The motion of the generator stator induces a notch at the frequency $\sqrt{(K_{gs} / J_{gs})}$ in the drive-train dynamics. The frequency of the notch is "tuned" by adjusting K_{gs} , and the width of the notch is decreased by increasing the inertia of the stator, J_{gs} . The depth of the notch is increased by decreasing the amount of damping, B_{gs} . The notch is accompanied by side lobes, enhancing adjacent disturbances, whose size increase with increasing depth and/or decreasing width of the notch. Therefore the size of the side lobes limits the magnitude of the notch. To be robust the notch is required to be wider than the resonance being controlled, *i.e.* J_{gs} is required to be as high as possible. The static stator displacement required to support the rated driving torque is $\theta_{gs} = T_G / K_{gs}$. Hence to minimise the stator motion, K_{gs} should also be as large as possible. There are, therefore, conflicting requirements for the design of the notch. (On a well designed machine the maximum value of the drive-train torque is considerably less than twice rated). The displacement at rated torque is limited here to be less than 25° on the 300 kW machine, or 15° on the 1 MW wind turbine which sets the minimum allowed value of K_{gs} and so the minimum frequency for the notch since there is a minimum stator inertia. The inertia of the stator chosen here is 100 kg/m² and 1100 kg/m² for a 300 kW and a 1 MW machine respectively.

There are two ways of exploiting the generator-mounting dynamics. The first is to reduce the most significant high-frequency drive-train load, *i.e.* the spectral peak at $n\Omega_o$. On two-bladed machines, in particular, the $2\Omega_o$ loads are large and hence severely restrict controller performance (see Section C.2.1). If the generator mounting could be used to reduce $2\Omega_o$ loads then the performance of the machine could be improved. The second is to increase the damping of the first drive-train mode. Light rotor inertias or low-slip generators may then be used without necessarily being accompanied by greater drive-train loads.

A well validated simulation was modified to model the generator modification on two machines. The first is a two-bladed, full-span regulated 300 kW machine¹ and has the drive-train transfer function

$$G(s) = \frac{2356.03}{(s^2 + 7.243s + 38.637)(s^2 + 24.028s + 1907.9)} \quad (4.8)$$

Its first drive-train mode has a frequency of 6.2 rad/s and a damping ratio of 0.58. The first and second drive-train modes can be clearly seen in the Bode plot of the transfer function in Figure 4.2a. Typical power output of this machine with a controller² is shown in Figure 4.2b for a mean wind speed of 20 m/s and 20% turbulence. The corresponding power spectrum is shown in Figure 4.4e. The power output has a standard deviation of 50 kW and a large percentage of the power fluctuations are concentrated at the frequency $2\Omega_o$ (*i.e.* 10.04 rad/s). This machine will be used when considering control of the spectral peak at $2\Omega_o$.

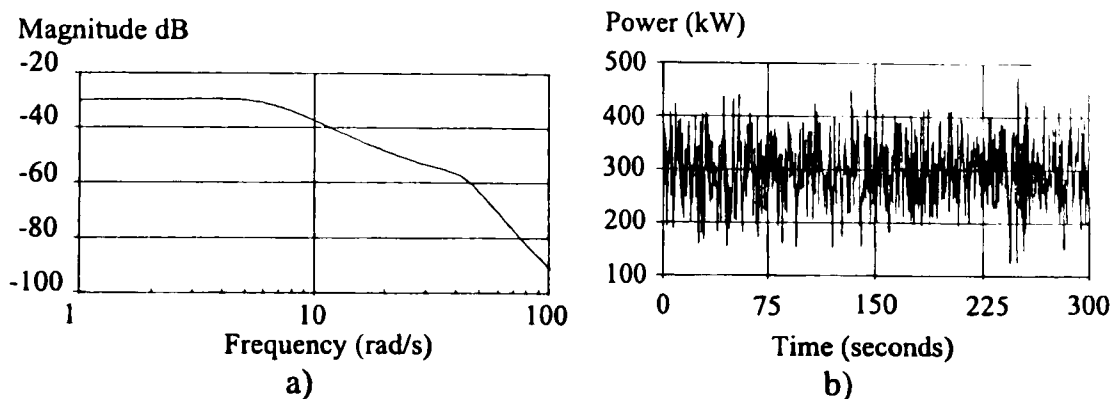


Figure 4.2 Bode plot of the drive-train transfer function and power output for the two-bladed, 300 kW wind turbine.

The second is a three-bladed, tip-regulated 1 MW machine³ and has the drive-train transfer function

$$G(s) = \frac{3019.02}{(s^2 + 2.966s + 35.55)(s^2 + 17.04s + 3992)} \quad (4.9)$$

Its first drive-train mode has a frequency of 6 rad/s and a damping ratio of 0.25 and its Bode plot is shown in Figure 4.3a. The frequency of the first drive-train mode is chosen to be fairly close to that of $3\Omega_o$, *i.e.* 6.7 rad/s, so that the side lobes associated with resonance

¹ The rotor of this machine is Configuration Ab, see Appendix C.

² The controller from Leith and Leithead (1995a) is

$$\frac{871.229(s + 1.6)^2 (s^2 + 7.243s + 38.637)(s^2 + 1.5s + 104.04)(s^2 + 6s + 416.16)}{s(s + 0.3)(s + 3.7)(s + 20)(s + 50)(s^2 + 11s + 104.04)(s^2 + 10s + 416.16)(s^2 + 65.8s + 2209)}$$

³ The rotor of this machine is Configuration Lb, see Appendix C.

control of the first drive-train mode does not enhance the loads at $3\Omega_o$. Typical simulated power output of this machine with a controller⁴ is shown in Figure 4.3b for mean wind speed of 20 m/s and 20% turbulence. The power output has a standard deviation of 36 kW and the machine is fairly well behaved. This machine will be used when considering providing additional damping to the first drive-train mode.

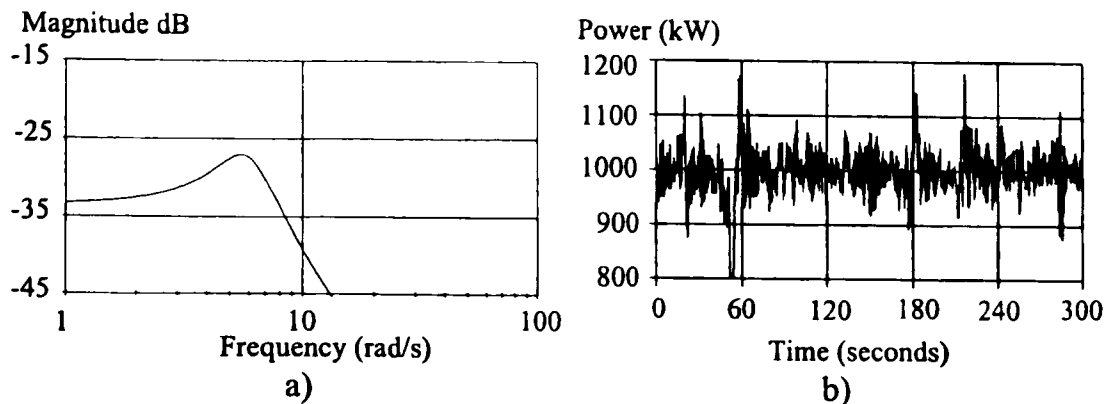


Figure 4.3 Bode plot of the drive-train transfer function and power output of a three-bladed, 1 MW wind turbine.

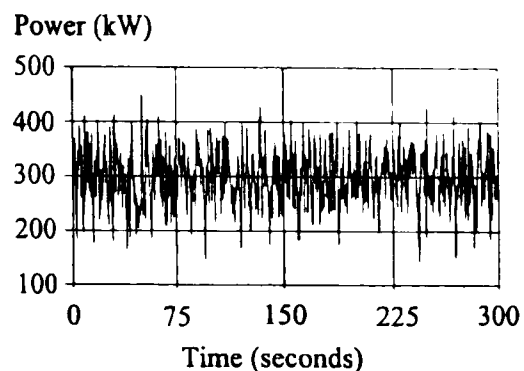
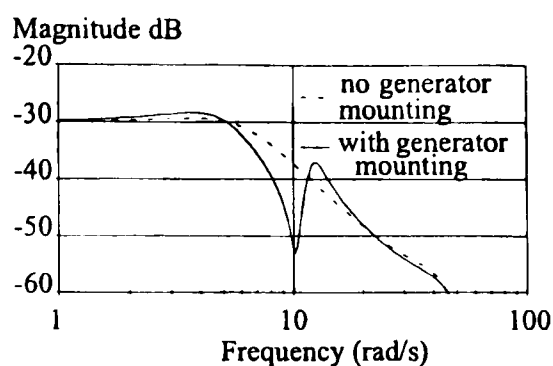
4.1.1 Reduction of $2\Omega_o$ loads

Bode plots of the drive-train transfer function of the 300 kW machine with and without the dynamic generator mounting predict that the magnitude of the spectral peak at $2\Omega_o$ should be reduced (see Figure 4.4a). Note that the notch has been designed so that the size of the side lobes of the notch have been kept relatively small, particularly so that the spectral peak at $4\Omega_o$ is not enhanced. Figure 4.4b depicts the simulated power output of the two-bladed machine with the generator modification. The original controller for the two-bladed machine is simply modified so that the open-loop transfer function for both is the same, hence maintaining similar actuator activity. The corresponding cumulative power spectrum is shown in Figure 4.4e. Comparing the original and modified cumulative spectra in Figure 4.4e it can be seen that, as predicted by the Bode plots, the magnitude of its torque at $2\Omega_o$ is almost eliminated while other frequencies are not particularly enhanced. The maximum power output is been reduce from 472 kW to 458 kW, and the time exceeding 400 kW is much reduced. In addition, the number of medium/large amplitude cycles is reduced. The standard deviation of the power output is reduced to 46 kW. The

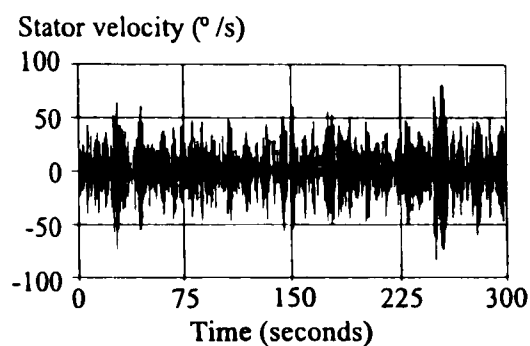
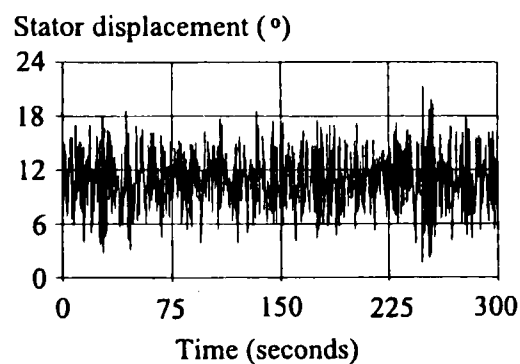
⁴ The controller is

$$\frac{14.253(s + 2.2)(s + 2.5)^2 (s^2 + 2.966s + 35.55)(s^2 + 0.66s + 45.56)(s + 50)}{s(s + 0.8)(s + 12)(s + 10)(s + 26)(s^2 + 1.85s + 45.56)(s^2 + 80s + 1763)(s^2 + 90s + 3600)}$$

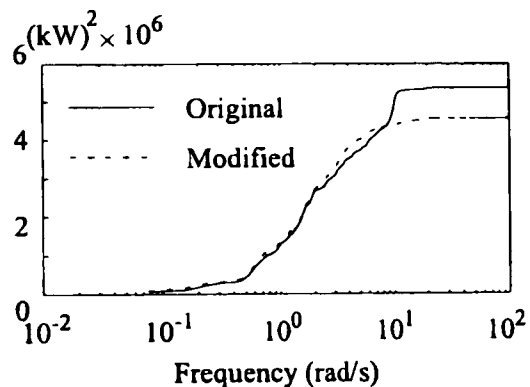
corresponding generator stator motion is shown in Figures 4.4c and 4.4d. The maximum amount of stator motion allowed is the main limitation in designing the notch.



a) Bode plot of the drive-train transfer function b) Power output



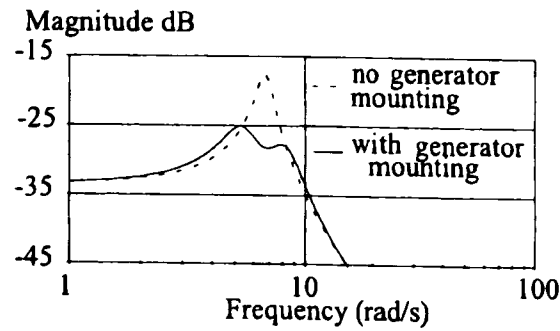
c) Generator displacement d) Generator stator velocity



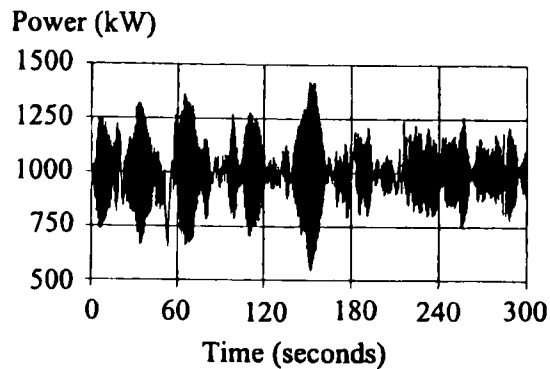
e) Cumulative plot of the power spectrum of power

Figure 4.4 Two-bladed machine with compliantly mounted generator with $J_{gs} = 100 \text{ kgm}^2$, $B_{gs} = 80$, $K_{gs} = 10404 \text{ Nm/rad}$.

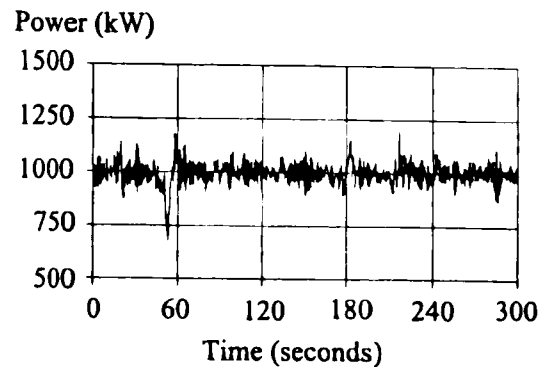
4.1.2 Light rotor



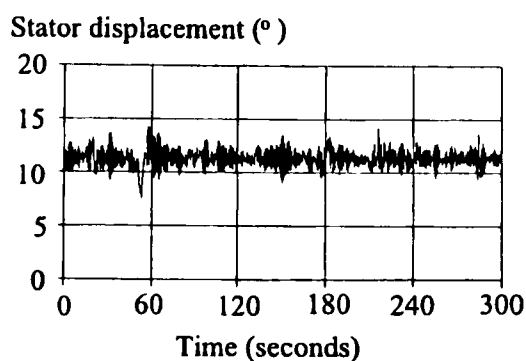
a) Bode plot of the drive-train transfer function with light rotor.



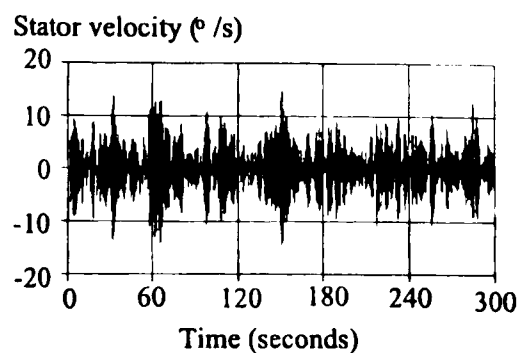
b) Power output without generator mounting.



c) Power output with generator mounting.



d) Stator displacement.



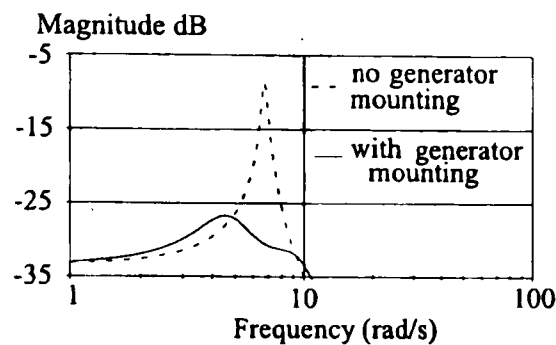
e) Stator velocity.

Figure 4.5 Three-bladed wind turbine a light rotor, without and with generator mounting, with $J_{gs} = 1100 \text{ kgm}^2$, $B_{gs} = 4000$, $K_{gs} = 50120 \text{ Nm/rad}$.

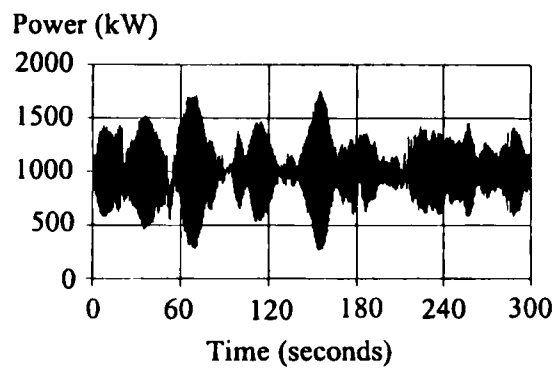
There is a tendency for blades to become lighter and more flexible and hence cheaper to make. If for example the blades of the three-bladed 1 MW wind turbine described above, which are assumed to be made of carbon epoxy, are replaced by carbon fibre blades, then the rotor inertia would reduce by a factor of approximately three. Reducing the stiffness of the drive train to retain the same first drive-train mode frequency, the damping of the mode is reduced to 0.08, *i.e.* the drive train becomes resonant. The resulting Bode plot of the drive-train transfer function in Figure 4.5a and the simulated power output in Figure 4.5b is totally unexceptionable and additional drive-train damping is required. Comparing the Bode plots of the drive-train transfer function with and without the dynamic generator mounting,

the drive-train resonance is predicted to be greatly reduced with the generator modification, see Figure 4.5a. The main limitation in designing the notch in this case is the size of the side lobes. The corresponding simulated power output, with the controller adapted so that the open-loop transfer function is the same as that used previously, is shown in Figure 4.5c. Comparing Figure 4.5c with Figure 4.5b, it can be seen that the drive-train resonance is greatly reduced as predicted. The standard deviation of the power output has been reduced from 123 kW to 58 kW. The corresponding generator stator motion is shown in Figures 4.5d and 4.5e.

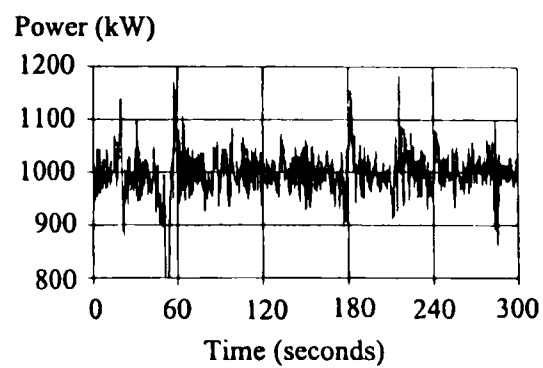
4.1.3 Low generator slip



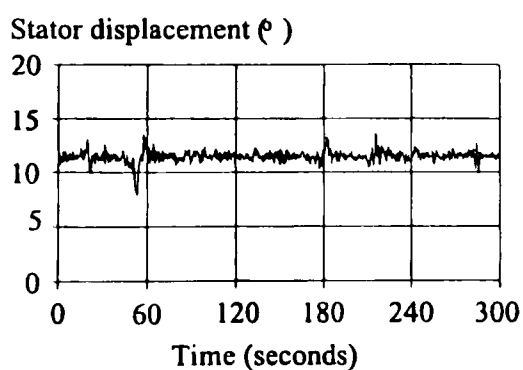
a) Bode plot of drive-train transfer function.



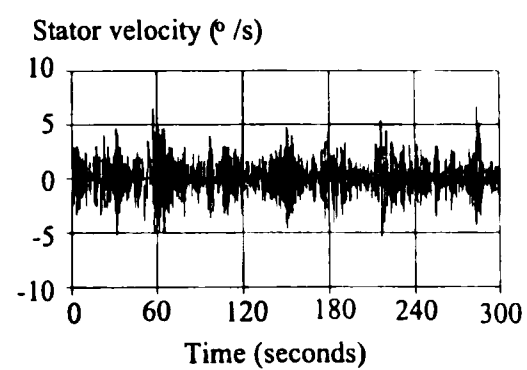
b) Power output without generator mounting.



c) Power output with generator mounting.



d) Stator displacement.



e) Stator velocity.

Figure 4.6 Three-bladed wind turbine with low slip, without and with generator modification, with $J_{gs} = 1100 \text{ kgm}^2$, $B_{gs} = 8000$, $K_{gs} = 50120 \text{ Nm/rad}$.

The drive train also becomes highly resonant if the slip of the generator is reduced, e.g. from 1% to 0.1%, at the same time as maintaining the same frequency of the first drive-train mode - see Figures 4.6a and 4.6b. Typical generated power output for this machine with the dynamically mounted generator is shown in Figure 4.6c. The standard deviation of power output has been reduced from 242 kW to 36 kW. The corresponding stator motion is shown in Figures 4.6d and 4.6e.

4.1.4 Discussion of results

In all the above cases, transients local to a particular frequency are reduced by the dynamically mounted generator. From any of the Bode plots shown in 4.4a, 4.5a, and 4.6a, it can be seen that the notch which is responsible for this reduction is not particularly narrow which implies that the generator modification is robust to frequency drift. The characteristics of the notch are easily tuned by adjusting the mass of the generator casing. The velocity of the stator, $\dot{\theta}_{gs}$, in all the above examples is very small, see Figures 4.4d, 4.5e, and 4.6e and the power loss due to the generator mounting (*i.e.* the amount of damping, B_{gs} , multiplied by the variance of the generator stator velocity, $\dot{\theta}_{gs}$) is very small (less than 0.022 kW in the examples shown above).

The results discussed here are only a sample of the wind turbine configurations investigated. Similar improvements can be obtained for any two- or three-bladed machine in the 300 kW to 1 MW range.

The dynamics of the drive train can be modified by dynamically mounting the generator to

- a) reduce high frequency torque transients, in particular those at $n\Omega_r$. The greatest improvement in performance is, of course, achieved for two-bladed machines.
- b) provide additional damping of the first drive-train mode without changing any other characteristics of the drive train. It is shown that light rotors or low-slip generators can then be used without a detrimental effect to the drive-train dynamics.

The mechanical modification to the power train described above has the advantage of being equally relevant to both pitch- and stall-regulated wind turbines. In the former case, it has a beneficial effect on the dynamics for both below and above rated operation. The effectiveness of the modification increases with the machine size and with the resonance of the drive train when employed to add damping.

4.2 Direct control of drive-train resonance

Variable speed operation of wind turbines is perceived to have several potential advantages over constant speed wind turbines of which two frequently mentioned ones are

- (i) additional energy capture below rated wind speed; and
- (ii) additional power-train compliance and associated load alleviation above rated wind speed.

In addition, the noise emitted by the wind turbine can be reduced in low wind speeds by reducing the rotor speed.

Pitch regulated variable speed machines require two controllers. One to control the speed and the another to control the power. The power controller and direct control of the first-drive-train resonance is described in this section for a very light-weight, flexible machine. Because the drive train is decoupled from the grid there is little damping and the drive train becomes very resonant. Normally, the resonance is at high frequency and the drive train is protected by rapid roll-off of the dynamics. As with constant speed machines there is a trend to design lighter and flexible variable speed machines to reduce costs. The drive train of such machines are not only highly resonant but the resonance occurs in the middle frequency range hence drastically reducing the protection of the drive train.

One such example is a machine developed by the Dutch Department of Energy under the research programme FLEXHAT. ECN in Holland have constructed a test-rig, IRFLET to investigate the problems arising from a resonant drive train. The test-rig for the IRFLET project is shown in Figure 4.7. It consists of a variable speed drive train, *i.e.* a flexible shaft, gearbox, synchronous generator and DC-link, together with a DC machine which mimics the aerodynamics of the rotor with the rotor inertia represented by a flywheel. It drives the variable speed drive train through a gearbox. The test-rig is rated at 30 kW and has a resonance at approximately 3 Hz with a damping ratio less than 0.005. For a complete description of the test-rig see Baltus (1991). The controller is required to control the generator reaction torque and reduce the drive-train resonance. Since the theoretical models of the power electronics were found to be inadequate, the dynamics of the test-rig were experimentally identified (Leithead *et al.*, 1994a) from data collected by ECN. A series of experiments were undertaken to identify the plant dynamics at one operating point with the firing angle, $\alpha = 0.47$ radians and the wind speed, $V = 12$ m/s. Shaft torque would not be measured in practice, hence measurements of current and rotor speed are used to estimate the shaft torque. The six transfer functions from V and α to current, I , rotor speed, N_g and shaft

torque, T_{sh} were determined from 160 seconds of PRBS¹ data, with a sampling rate of 100 Hz, using the MATLAB identification toolbox. No experiments were undertaken with the second possible control variable, the exciter field voltage (which is suitable for slow control) nor at other operating points. Hence the control algorithms are restricted to act on α alone and only at one operating point. They do demonstrate, however that the drive-train resonance can be controlled while maintaining rated power.

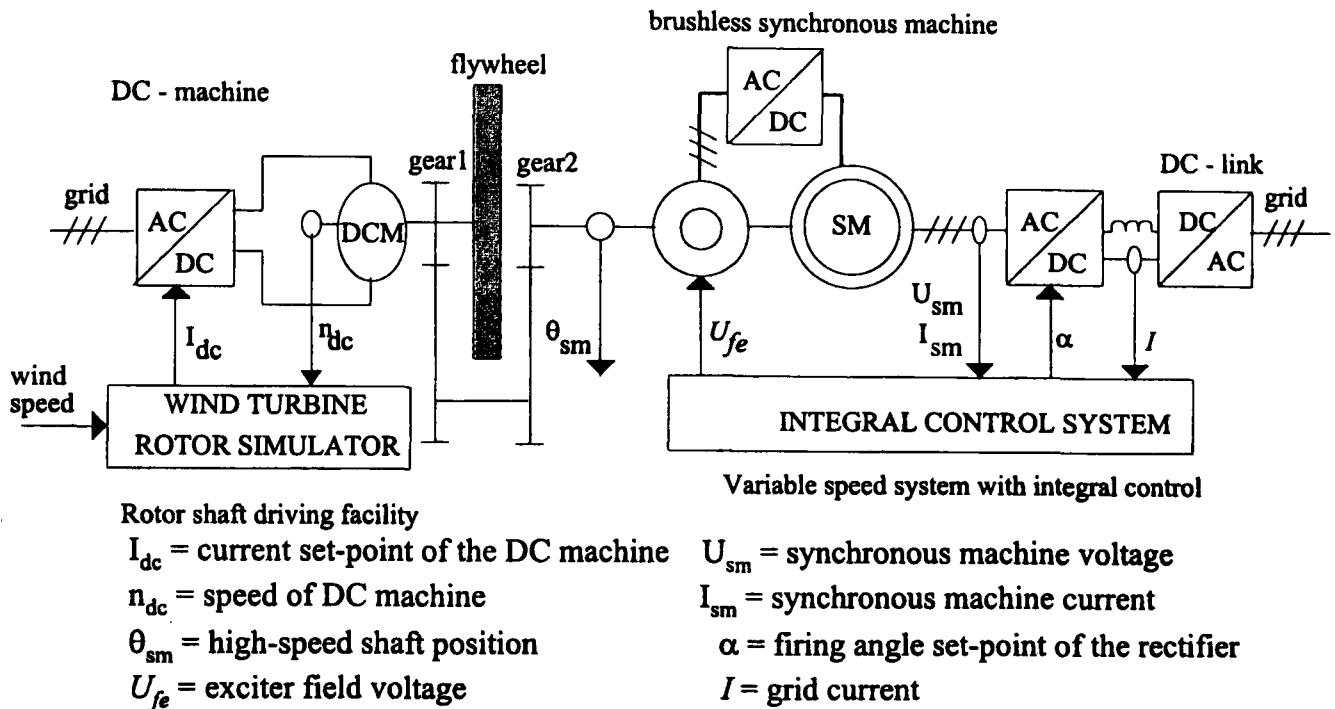


Figure 4.7 The test-rig for the IRFLET variable speed electrical system.

The transfer function between the firing angle and shaft torque is

$$\alpha \text{ to } T_{sh} = \frac{9.445(s^2 - 548s + 912543)(s^2 + 38s + 423191)(s^2 + 215s + 201760)}{(s - 200)(s^2 + 133s + 22163)(s^2 + 1.5s + 1656)(s^2 + 21s + 165)} \quad (4.10)$$

$$\frac{(s^2 + 109s + 579387)(s^2 + 433s + 97382)(s^2 + 420s + 44143)}{(s^2 + 392s + 38460)(s + 188)(s^2 + 29s + 2509)}$$

$$\frac{(s^2 + 29s + 2508)(s^2 + 1.83s + 355.6)}{(s^2 + 29s + 2508)(s^2 + 1.83s + 355.6)}$$

The transfer function between the firing angle and current is

$$\alpha \text{ to } I = \frac{-6.831 \times 10^{12} (s + 2.55)(s^2 + 19.2s + 181)(s^2 + 2.15s + 404)(s - 200)^2}{(s + 3.255)(s^2 + 3.15s + 354)(s^2 + 31.70s + 2260)(s + 200)^4 (s + 657)(s + 897)} \quad (4.11)$$

¹ PRBS Pseudo random binary signal is white noise with only two amplitudes.

The transfer function between the firing angle and shaft speed is

$$\alpha \text{to} N_g = \frac{-137.9(s+200)(s-200)(s+33.1)(s^2+3.89s+58.41)}{(s^2+115s+5850)(s^2+31s+2514)(s^2+1.9s+352)} \quad (4.12)$$

The transfer function between the wind speed and shaft torque is

$$V \text{to} T_{sh} = \frac{-8.638 \times 10^{-2} (s^2 + 20.35s + 1357)(s^2 + 81s + 1782) (s^2 + 25.8s + 6927)(s^2 + 10s + 14823)(s^2 - 217s + 28304) (s^2 - 37s + 30984)(s+200)^4 (s-200)^3 (s^2 - 105s + 61873) (s^2 - 8.8s + 139480)(s^2 - 215s + 3559000)(s^2 - 38s + 889000)}{(s+11.39)(s^2+0.14s+355.43)(s^2+7.6s+1519)(s^2+14.1s+3278) (s^2+18.7s+6758)(s^2+28.67s+12445)(s^2+30s+17872) (s^2+15s+29379)(s^2+28s+49037)(s^2+79s+109634) (s^2+287s+198721)(s^2+90s+246310) (s^2+193s+742324)(s^2+1173s+3288000)} \quad (4.13)$$

The transfer function between the wind speed and current is

$$V \text{to} I = \frac{-1.42 \times 10^{-4} (s+10.37)(s^2+13s+409.5)(s+23.13)(s^2-130s+8100) (s-90)^3 (s^2+30s+11000)(s^2-150s+24000)}{(s+0.507)(s^2+0.139s+355.43)(s^2+12.1s+2190) (s^2+130s+8100)(s+90)^3 (s^2+95s+11000)} \quad (4.14)$$

The transfer function between the wind speed and shaft current is

$$V \text{to} N_g = \frac{-8.39 \times 10^{-5} (s^2+13s+409.5)(s-90)^2 (s^2-130s+8100) (s^2+30s+11000)(s^2-150s+24000)(s-200)}{(s+0.507)(s^2+0.139s+355.43)(s+90)^2 (s^2+130s+8100)(s^2+95s+11000)(s+200)} \quad (4.15)$$

Further reduction of the order of these transfer functions is possible but was not required. The Bode plots for the above transfer functions are shown in Figure 4.8 together with the directly measured transmittances. Discrepancies between the transfer functions above 70 rad/s can be ignored as they occur at high frequency. The mismatch in the transfer from α to N_g ($\alpha \text{to} N_g$) at low frequency is unimportant since the measurement on N_g is not used to control the system at low frequency. Simulated responses of the test-rig using these transfer functions are compared to the measured responses in Figure 4.9. The agreement is good and the drive-train resonance can be clearly seen.

The two objectives for the controllers, namely power control and resonance control are treated separately by restricting the regulation of the wind turbine operating point to low frequency and restricting the regulation of the shaft torque to a small frequency interval in the region of the resonant frequency.

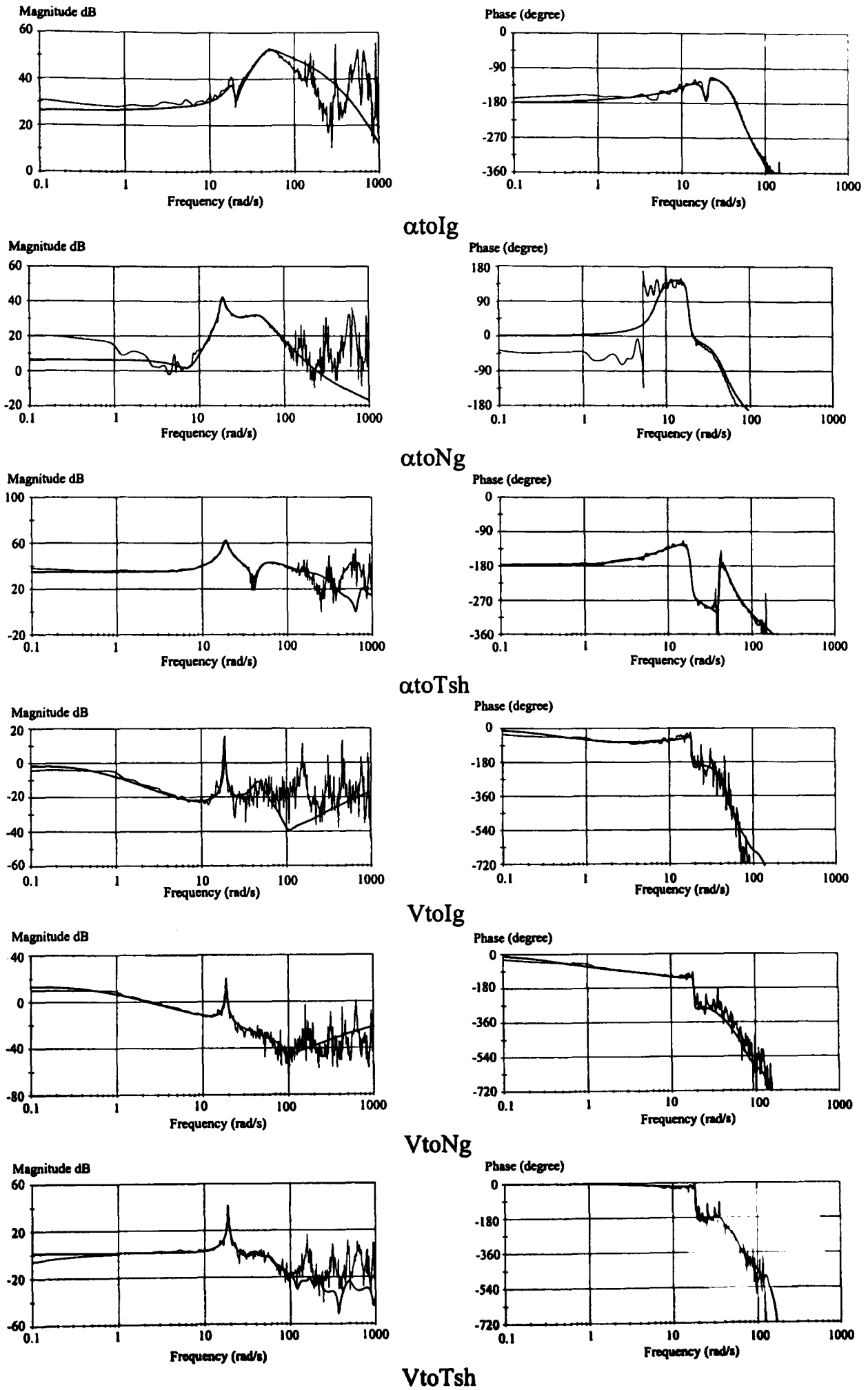


Figure 4.8 Bode plots of plant transmittances with identified transfer functions.

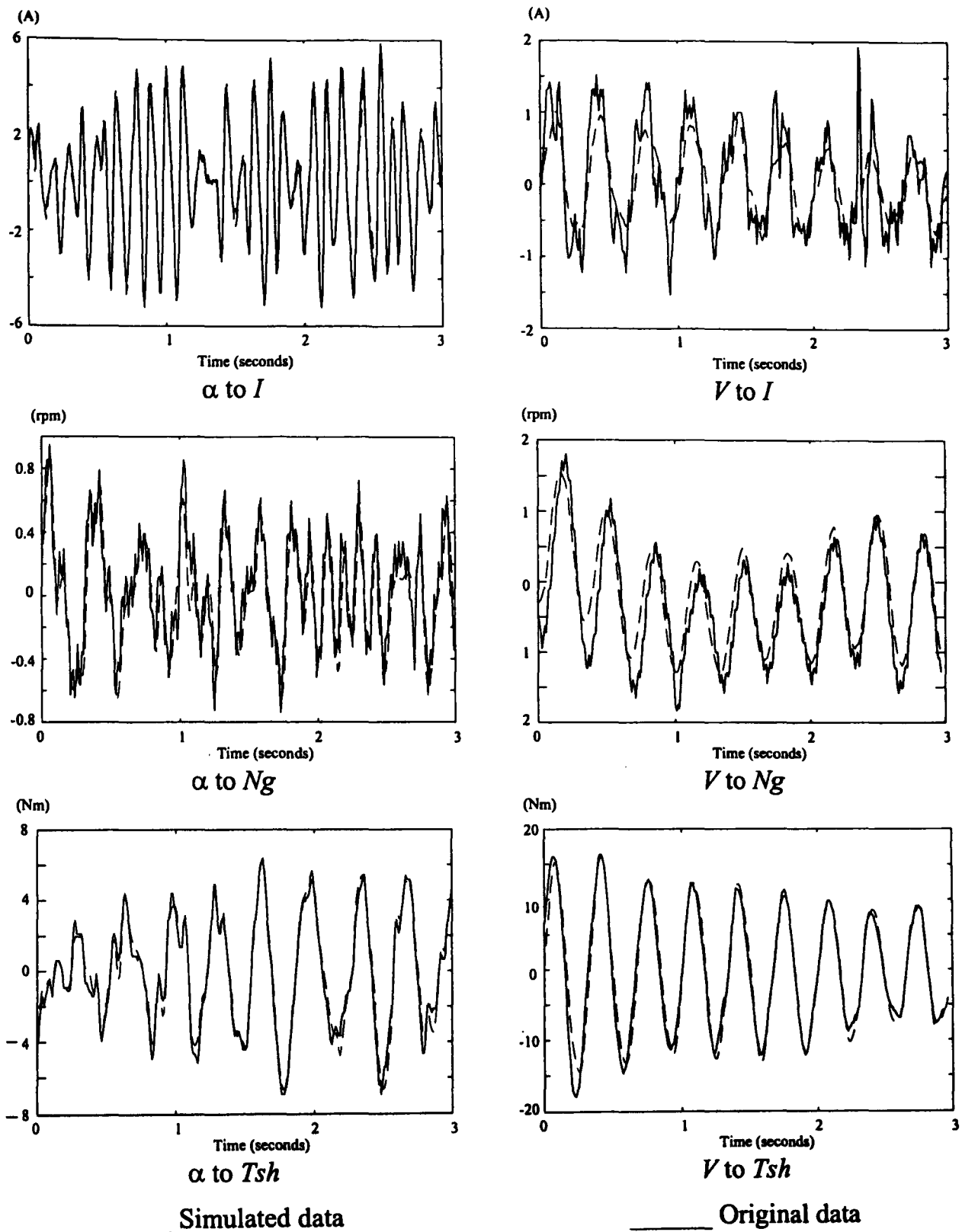
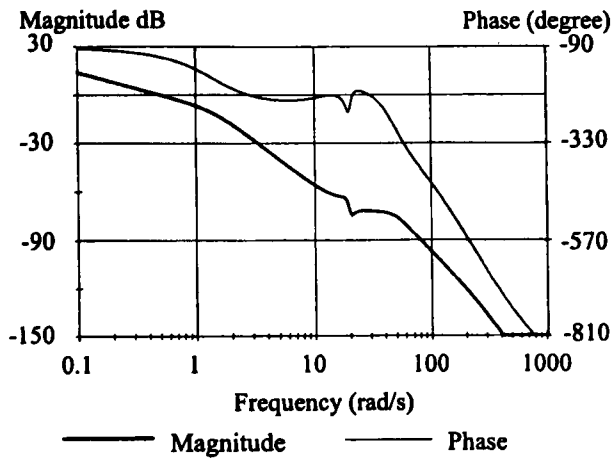


Figure 4.9 Time series of plant data with results from simulated data using the identified plant transfer functions.

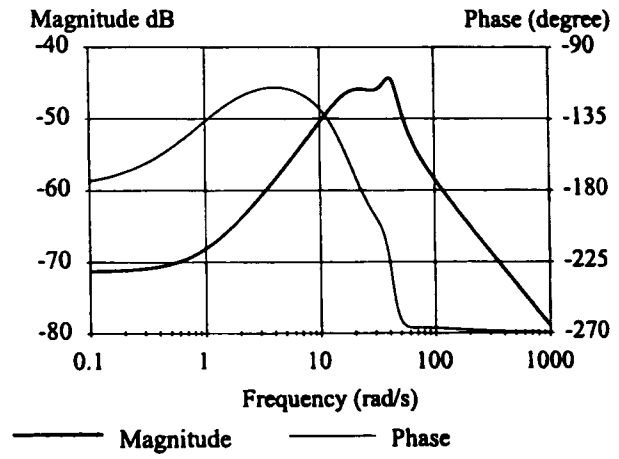
The power is controlled by controlling the current since the voltage is fixed with the controller acting on the firing angle. A suitable controller, for maintaining the most effective operating point for the test-rig, is $P(s)$ where

$$P(s) = \frac{-4.757 \times 10^{-2}}{s(s^2 + 2s + 2)} \quad (4.16)$$

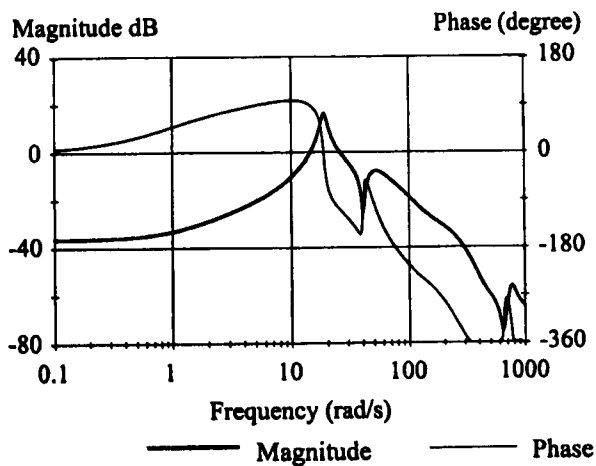
It is designed by classical Nyquist-Bode loop shaping on the basis of the transfer function relating the firing angle to current ($\alpha\omega I$). Integral action is required to reduce the steady-state errors. In addition rapid roll-off, which is supplied by the quadratic factor, is required to ensure the separation of the two control objectives. The controller cross-over frequency is approximately 0.5 rad/s as can be seen from the open-loop Bode plot depicted in Figure 4.10a together with its phase and gain margins.



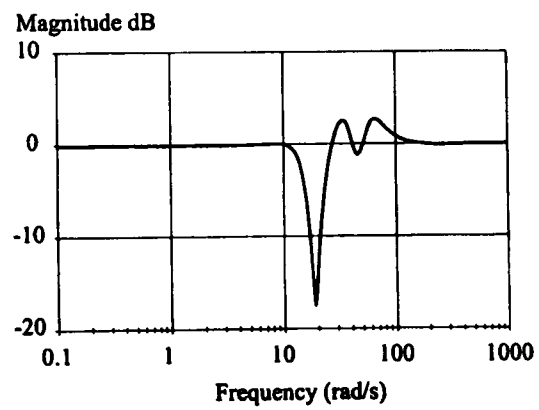
a) The Bode plot of the open loop $\alpha\omega I(s).P(s)$.



b) The Bode plot of the controller $C(s)$.



c) Open-loop Bode plot of $C(s).\alpha\omega Tsh(s)$.



d) Bode plot of the sensitivity function.

Figure 4.10

4.2.1 Controller synthesis

The first stage of the controller design is to determine a controller, acting on firing angle in response to a measurement of shaft torque were it available, to control the shaft torque. A suitable controller is

$$C(s) = \frac{-0.1128(s^2 + 30s + 1764)(s + 0.963)}{(s^2 + 24s + 400)(s^2 + 14s + 1764)} \quad (4.17)$$

This is designed for the transfer function relating the firing angle to shaft torque (α_{toTsh}). The controller Bode plot and the open-loop Bode plot are depicted in Figures 4.10b and 4.10c respectively, from which it can be observed to be effective about the region of 3 Hz as required. The inclusion of derivative action at low frequency ensures that regulation of the resonance does not interfere with the regulation of rated current (*i.e.* power). The phase and gain margins are indicated on Figure 4.10b. The controller reduces the intensity of the resonance by 17 dB as may be seen from the Bode plot of the sensitivity function, Figure 4.10d. The controller, $C(s)$ is designed so that the active gain in the region of 3 Hz is solely derived from the gain of the plant dynamics relating the firing angle to shaft torque, thereby making the design robust to any mis-identification or slight drift of the resonance frequency.

In practise, shaft torque is not normally measured, hence the shaft torque is estimated using measurements of current and shaft speed as shown in Figure 4.11a. The transfer functions $X(s)$ and $Y(s)$ are chosen such that the wind speed induced disturbances at $Tsh1^*$ and $Tsh2^*$ are the same as the wind speed disturbances on shaft torque; that is,

$$V_{toI}(s).X(s) = V_{toNg}(s).Y(s) = V_{toTsh}(s) \quad (4.18)$$

locally to 3 Hz. Since only those frequencies near 3 Hz are of interest, the transfer functions, $X(s)$ and $Y(s)$ match the phases at 3 Hz, and are

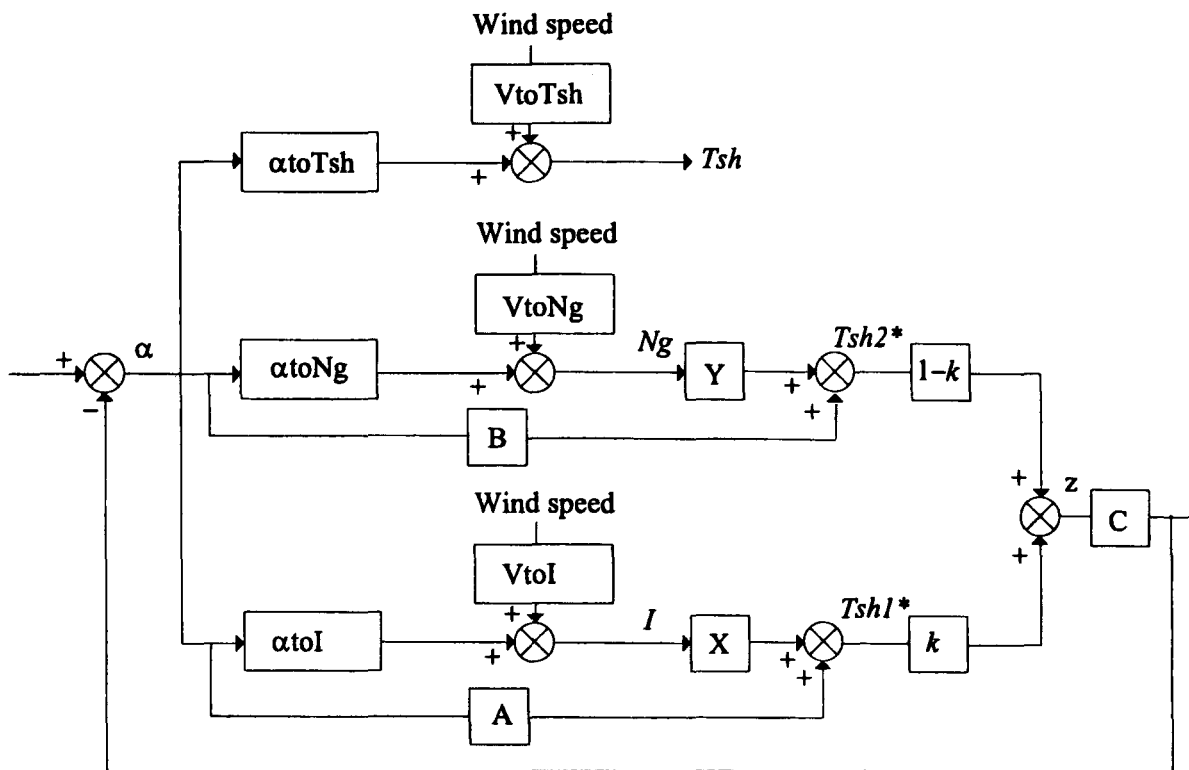
$$\begin{aligned} X(s) &= \frac{49.178(s + 15.86)(s + 25.084)(s^2 + 8.362s + 3709.1)}{(s + 22.52)(s^2 + 40s + 3709.1)(s + 61.544)} \\ Y(s) &= \frac{-18889(s + 15.86)(s^2 + 8.362s + 3709.1)}{(s + 9.918)(s + 22.52)(s^2 + 40s + 3709.1)(s + 61.544)} \end{aligned} \quad (4.19)$$

It can be observed in Figure 4.12 that both the transfer functions $V_{toI}.X$ and $V_{toNg}.Y$ are good approximations to V_{toTsh} in the region of 3 Hz. The additional shaping in X and Y at 60 rad/s is necessary to reduce the effect of disturbances near this frequency.

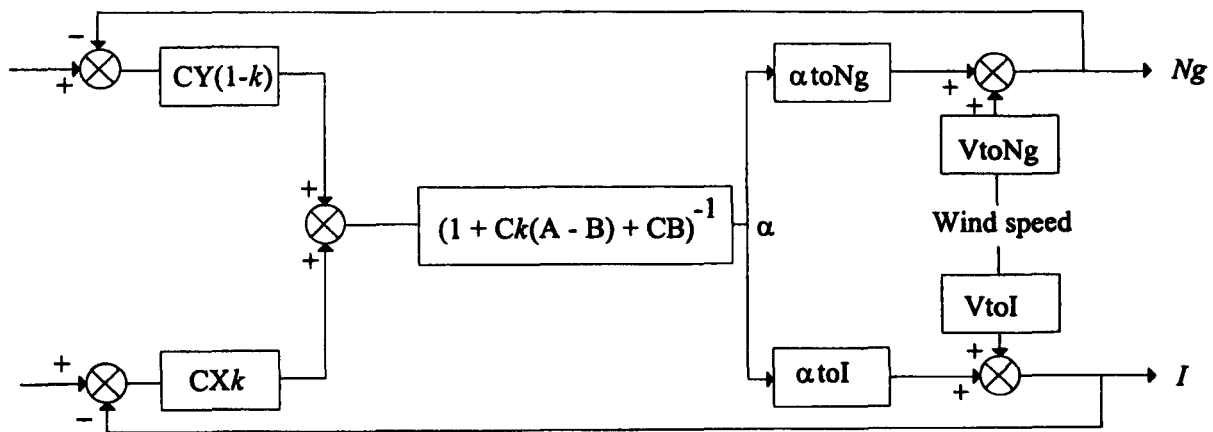
Similarly, the transfer functions, $A(s)$ and $B(s)$, are chosen such that the dynamic relationship of firing angle to $Tsh1^*$ and $Tsh2^*$ are the same, locally to 3 Hz, as the dynamic relationship of firing angle to shaft torque; that is,

$$\begin{aligned} A(s) &= \alpha_{toTsh}(s) - \alpha_{toI}(s).X(s); \\ B(s) &= \alpha_{toTsh}(s) - \alpha_{toNg}(s).Y(s) \end{aligned} \quad (4.20)$$

Hence, with the controller construction in Figure 4.11a the signals seen at $Tsh1^*$ and $Tsh2^*$ are essentially the shaft torque for all choices of $k(s)$. The controller, $C(s)$, can therefore be applied to z to regulate the drive-train resonance for all choices of $k(s)$.

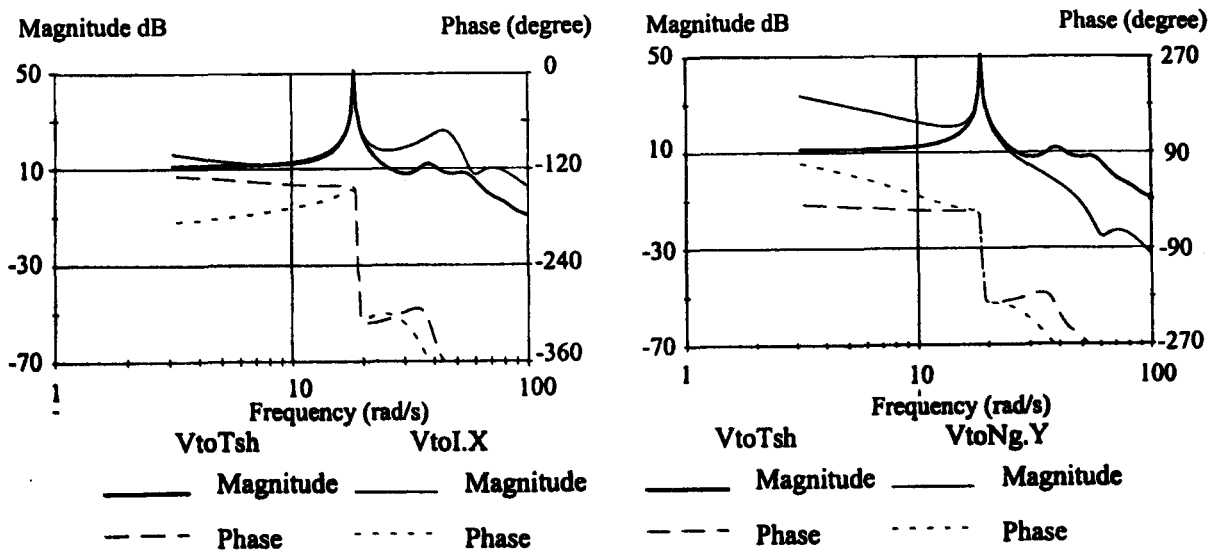


a) The controller configuration with explicit feed-forward.



b) Feedback controller.

Figure 4.11



a) Bode plots of $V_{toI.X}$ and V_{toTsh} .

b) Bode plots of $V_{toNg.Y}$ and V_{toTsh} .

Figure 4.12

k was selected so that the two control feed forward terms cancel; *i.e.* $k(s)A(s)$ and $(1 - k(s))B(s)$ cancel. The resulting controllers are $K_1(s)$ acting on Ng and $K_2(s)$ acting on I where

$$K_1(s) = (1 - k(s)) Y(s)C(s); K_2(s) = k(s)X(s)C(s) \quad (4.21)$$

The resultant controller transfer functions are

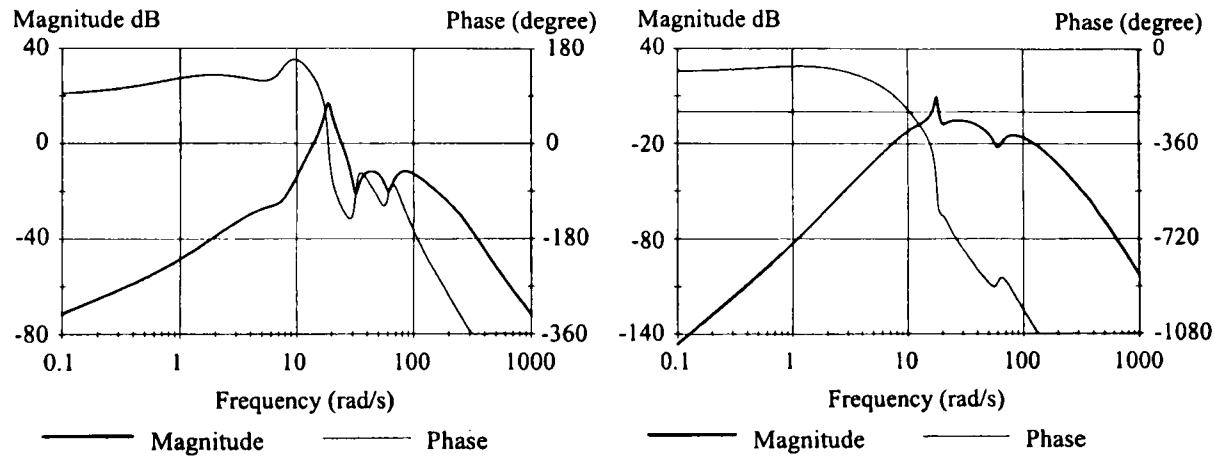
$$K_1(s) = \frac{1704.21s(s + 0.96)(s + 15.86)(s^2 + 3s + 1000)}{(s^2 + 24s + 2304)(s^2 + 8.36s + 3709)(s + 250)} \quad (4.22)$$

$$\frac{(s^2 + 19s + 98)(s^2 + 24s + 400)(s^2 + 40s + 3709)(s + 22.52)}{(s + 48)(s + 61.54)(s + 70.54)(s^2 + 250s + 62500)}$$

$$K_2(s) = \frac{39264.85(s^2 + 6.43s + 14.66)(s^2 + 1.45s + 18.23)}{(s^2 - 8s + 26.36)(s + 16.34)(s^2 - 5.87s + 338.90)} \quad (4.23)$$

$$\frac{(s^2 + 1.92s + 365)(s^2 + 24s + 2304)(s^2 + 8.35s + 3709)}{(s^2 + 7.302s + 96.544)(s + 11.05)(s^2 + 1.08s + 335.18)}$$

$$\frac{(s^2 + 3.44s + 389.27)(s^2 + 24s + 400)(s + 48)}{(s^2 + 40s + 3709)(s + 61.54)(s + 70.54)(s + 100)}$$



Gain margin at 107 rad/s = 13.7 dB
Phase margins at 14 rad/s = 55°, 24 rad/s = 58°
Gain margins at 7.7 rad/s = 19 dB,
18.2 rad/s = 19 dB, 55 rad/s = 17 dB
Phase margins at 16.5 rad/s = 153°, 18.9 rad/s = 73°
a) Open-loop Bode plot of $K_1(s) \cdot \alpha Ng(s)$. b) Open-loop Bode plot of $K_2(s) \cdot \alpha I(s)$.

Figure 4.13

The open-loop Bode plots, *i.e.* $K_1(s) \cdot \alpha Ng(s)$ and $K_2(s) \cdot \alpha I(s)$ are shown in Figures 4.13a and 4.13b. Since the Nyquist plot of the ratio of the two transmittances, *i.e.* $(K_1(s) \cdot \alpha Ng(s)) / (K_2(s) \cdot \alpha I(s))$, for a small frequency range local to 3 Hz indeed for any frequency does not go close to the point $(-1, 0)$, see Figure 4.14; that is, the two control actions do not compete with each other greatly. The open-loop Bode plot, *i.e.* $(K_1(s) \cdot \alpha Ng(s) + K_2(s) \cdot \alpha I(s))$, is shown in Figure 4.15a and the phase and gain margins indicated thereon ensure a reasonable degree of robustness since there is little cancellation

between the two control paths. The two controllers acting on I , namely $P(s)$ and $K_2(s)$, are combined as $K'_2(s)$ where

$$K'_2(s) = \frac{-1868(s^2 + 6.43s + 14.67)(s^2 + 1.45s + 18.23)(s^2 - 8s + 26.36)(s + 16.34)}{s(s^2 + 2s + 2)(s^2 + 7.3s + 96.54)(s + 11.05)(s^2 + 1.08s + 335.2)(s^2 + 3.44s + 389.3)(s^2 + 24s + 400)(s + 48)(s^2 + 40s + 3709)(s + 61.51)(s + 70.5)(s + 100)}$$

(4.24)

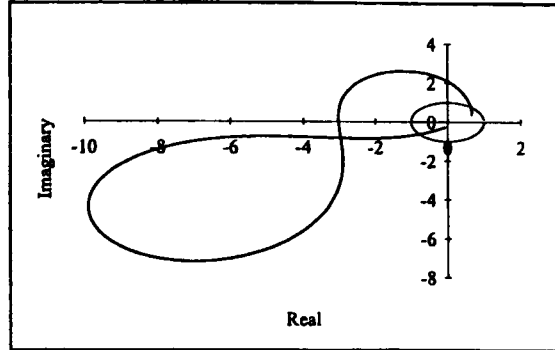
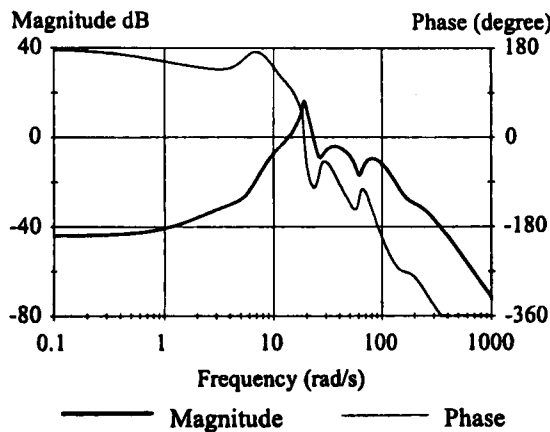


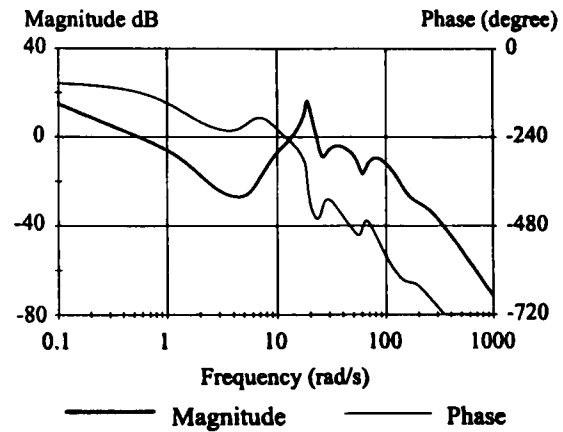
Figure 4.14 Nyquist plot of $(K_1(s) \cdot \alpha \cdot N_g(s)) / (K_2(s) \cdot \alpha \cdot I(s))$.



Gain margin at 91 rad/s = 10 dB
Phase margins at 13.7 rad/s = 76°, 23 rad/s = 79°

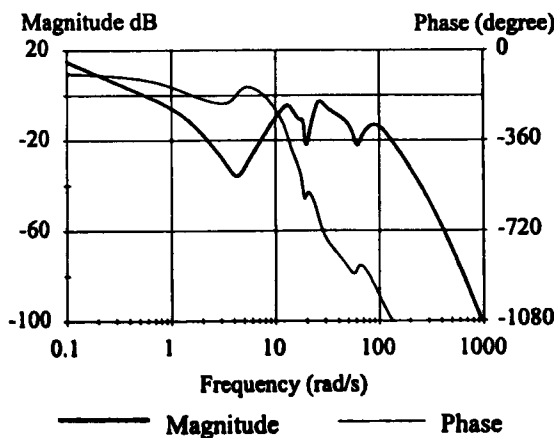
a) Open-loop Bode plot of

$$K_1(s) \cdot \alpha \cdot N_g(s) + K_2(s) \cdot \alpha \cdot I(s).$$



Gain Margins at 1.54 rad/s = 12 dB, 92 rad/s = 10.5 dB
Phase Margins at 0.55 rad/s = 61°, 13.7 rad/s = 76°,
23 rad/s = 79°

b) Bode plot of $K_1(s) \cdot \alpha \cdot N_g(s) + K'_2(s) \cdot \alpha \cdot I(s)$.



Gain margins at 1.56 rad/s = 13 dB, 4.2 rad/s, 36 dB,
7.7 rad/s = 18 dB, 18 rad/s = 10.7 dB, 80 rad/s = 14 dB
Phase margin at 0.56 rad/s = 60°

c) Bode plot of $K'_2(s) \cdot \alpha \cdot I(s) / (1 + K_1(s) \cdot \alpha \cdot N_g(s))$.

Figure 4.15

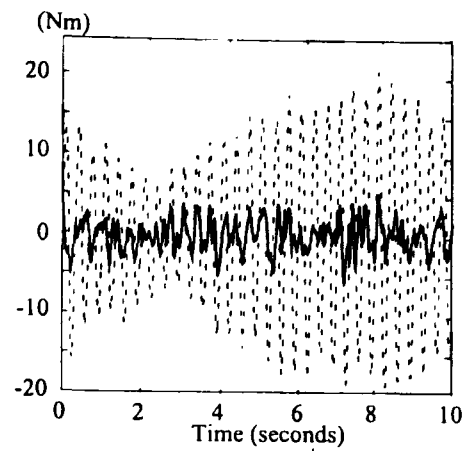
The open-loop Bode plot with the complete controller, *i.e.* $(K_1(s) \cdot \alpha \cdot N_g(s) + K_2'(s) \cdot \alpha \cdot I(s))$, is shown in Figure 4.15b with phase and gain margins indicated. The degree of robustness is confirmed from the Bode plot for $K_1(s) \cdot \alpha \cdot N_g(s)$, Figure 4.13a, and the Bode plot and the associated gain and phase margins for the system with feedback loop on N_g closed but with the feedback loop on I open, Figure 4.15c. In both cases the phase and gain margins are reasonable.

4.2.2 Performance evaluation

The dynamics of the test-rig as represented by the transfer functions (4.10) to (4.15) together with the controller transfer function for $K_1(s)$ and $K_2'(s)$, are used to simulate the response of the rig with the controller present to the same PRBS wind speed signal used in the identification experiment. The responses are shown in Figures 4.16a and b together with the cumulative spectra of the simulated shaft torque for both the controlled and uncontrolled cases. The standard deviation of shaft torque when controlled is reduced to 20 % of the standard deviation when uncontrolled. Since the background contribution has a standard deviation of 17 % of the total uncontrolled standard deviation, the performance is very close to the limits of what is possible.

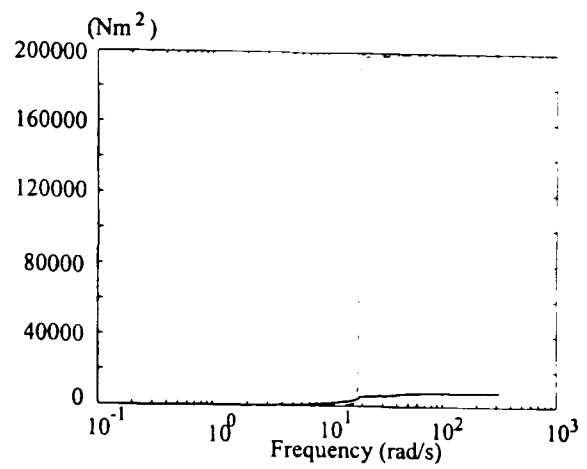
The controller was implemented on the test-rig and evaluation experiments undertaken by ECN. The measured response is shown in Figures 4.16c and d together with the cumulative spectra of the measured shaft torque for both the controlled and uncontrolled cases. The standard deviation of shaft torque is only reduced to 42% of the uncontrolled standard deviation by the controller. However, since the background contribution has a standard deviation of 35% of the total uncontrolled standard deviation, the controller performance, is deemed acceptable and the drive-train resonance is reduced.

(The reason for the difference between the predicted and actual performance is due to changes in the plant dynamics which occurred during the lengthy period of time which elapsed between the initial measurements taken for identification and the testing of the controller, *e.g.* there is a reduction in the variance of the resonance at 3 Hz by a factor of 5 which is apparent from a comparison of Figure 4.16b to Figure 4.16d. However, the robustness of the controller design enabled it to accommodate successfully the changes in the plant dynamics.)



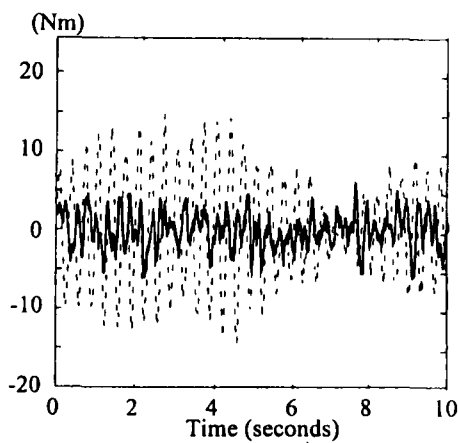
----- Uncontrolled _____ Controlled

a) Time series of the simulated response of shaft torque when controllers are used.



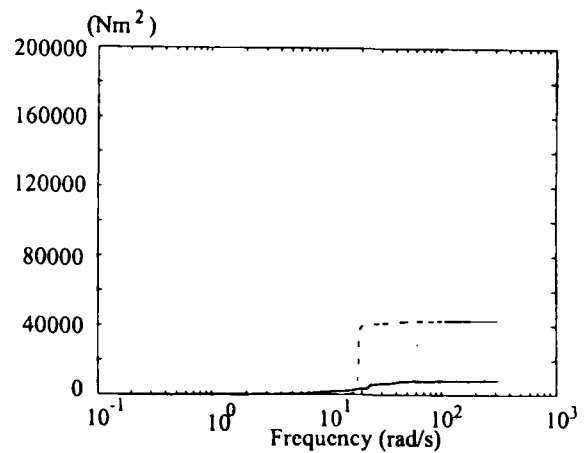
----- Uncontrolled _____ Controlled

b) Cumulative power spectrum of the predicted torque and the original uncontrolled torque.



----- Uncontrolled _____ Controlled

c) Time series of the measured shaft torque when controllers are used.



----- Uncontrolled _____ Controlled

d) Cumulative spectrum of measured shaft torque with and without control.

Figure 4.16

4.2.3 Discussion

The dynamics of a test-rig representing the drive train of a variable speed wind turbine were identified from experimental data. A controller to regulate both the turbine operating point and the drive-train resonance was designed using classical Nyquist-Bode loop shaping. The family of all possible controllers acting on speed and current were parameterised by means of control feed forward. The specific choice of controller was made to meet the requirement for robustness. On implementing the controller on the test-rig it performed reasonably well even though the dynamics of the plant had changed. The drive-train resonance of a lightweight flexible variable speed wind turbine can indeed be actively regulated by means generator reaction torque.

4.3 Conclusions

The dynamic characteristics achievable for the conventional design of power trains are subject to quite strong constraints. Non-conventional approaches has been investigated to determine whether these constraints can be circumvented.

Direct modification of the drive train is considered. The dynamics of the drive train can be modified to reduce high frequency torque transients at a particular frequency or provide additional damping to the power-train. However, the modification requires compliant mounting of the generator which continuously moves with small amplitude oscillations about its axis. Unfortunately, the latter motion may be unacceptable to manufacturers.

Direct control of the drive-train resonance is also considered. Since this is not possible using pitch regulation, torque control must be used. Although this approach is successful, it is only applicable to variable speed wind turbines and hence, is not appropriate for this context.

To conclude, the constraints on the damping factor of the first drive-train mode cannot be circumvented by non-conventional machine modifications considered here.

5 Full-span pitch-regulated machines

5.1 Introduction

As described in Chapter 2, the nature of the pitch regulation itself influences strongly the aerodynamics of a wind turbine (Figure 3.2) and hence the performance of a controller. The performance of conventional, full-span, pitch-regulated machines are discussed in this chapter while tip-regulated machines are discussed in Chapter 6. The purpose of this chapter and that which follows is to quantify the dependence on the configuration of the wind turbine of the performance of active pitch control in alleviating transient loads.

Appendix C describes a methodology using the simple models derived in Chapter 3 and Appendix B, whereby the performance for a specific configuration can be estimated. This approach was employed to determine the performance for an extensive range of configurations. Not only does this information permit the performance of different configurations of wind turbine to be compared, but it also supports the design process by providing insight into the influence of the rotor, drive train and control system on overall performance. The validation of the methodology by comparison with the results from non-linear simulation is described in Appendix C.

5.2 Different types of wind turbine configuration

This chapter deals both with medium (300 kW) and large-scale wind turbines (1 MW). The assumptions made about the effect of the size of a wind turbine on its machine parameters are considered in Appendix E. The machines are assumed to be typical of conventional, constant-speed commercial machines, comprising a rotor, gearbox and induction generator.

In addition to the type of pitch regulation, the aspects of the wind turbine configuration on which the effectiveness of the control system depends are (Leithead *et al.*, 1991a)

- the number of blades;
- the dynamic characteristics of the drive train;
- the dynamic characteristics of the controller;
- the intensity of the drive-train transient loads at $n\Omega_o$;
- the angular velocity of the rotor.

The machines investigated here have two or three blades, in common with the majority of conventional commercial machines. As discussed in Section 3.1, the dynamic characteristics of the drive train can be represented by the frequency of the first drive-train mode, ω_n , and its damping factor, η . (The design details of the drive train are immaterial and the performance will be the same, of all wind turbines having a specific first drive-train mode frequency and damping factor.) The frequency of the first drive-train mode can be easily and fairly cheaply varied by adding compliance (*e.g.* rubber) to the drive train, see Section 3.2. Adjusting the damping of the first drive-train mode, on the other hand, is more difficult and more expensive, see Section 3.2. Nevertheless, in this and the following chapter it is assumed that the damping of the first drive-train mode is ideal, 0.7¹. The dynamic characteristics of the controller are characterised by the cross-over frequency of the open-loop transfer function, ω_c (see Appendix C), and the phase and gain margins of the open-loop transfer function. The phase and gain margins are assumed to be 60° and 10 dB respectively unless otherwise stated (see Section C.1 for justification).

The configurations of wind turbines considered are listed in Table 5.1. For each configuration, the frequency of the first drive-train mode varies from 2 rad/s to 7 rad/s and the controller cross-over frequency varies from 1 rad/s to 6 rad/s in steps of 0.5 rad/s. Of course not all of these are appropriate or achievable for every configuration, but all are retained to facilitate performance comparison. The performance of each configuration has been investigated for mean wind speeds of 12 m/s, 16 m/s or 23 m/s and have 20% turbulence.

Both the two- and three-bladed machines were given nominal intensities of loads at $n\Omega_o$ based on the spectral components seen on the drive-train loads of commercial wind turbines (see Table C.1). The drive-train loads at $n\Omega_o$ are very much larger on a two-bladed machine compared with one with three blades of the same size, as two-bladed machines are normally teetered, and the spectral loads are normally at a lower frequency while the

¹ As the power-train dynamics can normally be approximated by the second-order transfer function (3.23) the ideal damping factor is 0.7. (This enables the transfer function to achieve rapid roll-off without being oscillatory).

rotational velocity of the rotor is normally higher. To investigate the sensitivity of the performance to the intensity of the transient loads at $n\Omega_o$, two intensity levels for each machine were studied. Since the intensity of the spectral peaks of the two-bladed machines are considerably larger than those on the three-bladed machine; the three-bladed wind turbine configurations may have either the nominal intensity of the drive-train loads at $3\Omega_o$ or twice the nominal intensity; whereas the two-bladed wind turbine configurations may have either the nominal intensity of the drive-train loads at $2\Omega_o$ or half the nominal intensity. To investigate the sensitivity of the performance to the angular velocity of the rotor, two three-bladed wind turbine configurations are considered with different angular velocities.

Configuration	No. of blades	Power rating (kW)	Rotor speed, Ω_o (rad/s)	Spectral loads
Aa	2	300	5.090	$1/2 \times \text{Nominal } 2\Omega_o$
Ab	2	300	5.090	Nominal $2\Omega_o$
B	3	300	5.201	Nominal $3\Omega_o$
Ca	3	300	4.125	Nominal $3\Omega_o$
Cb	3	300	4.125	$2 \times \text{Nominal } 3\Omega_o$
Da	2	1000	2.800	$1/2 \times \text{Nominal } 2\Omega_o$
Db	2	1000	2.800	Nominal $2\Omega_o$
E	3	1000	2.850	Nominal $3\Omega_o$
Fa	3	1000	2.250	Nominal $3\Omega_o$
Fb	3	1000	2.250	$2 \times \text{Nominal } 3\Omega_o$

Table 5.1 The full-span regulated wind turbine configurations investigated.

Since the velocities of the drive-train shafts are ‘locked’ to the grid frequency on a constant-speed machine (Leithead *et al.*, 1991a), the most important performance indicators for the drive train are the size of the transients of torque acting on the gearbox and generated power. Hence, above rated wind speed, the standard deviation of power is a good measure of performance. It should be noted that it is the extreme loads which are of concern but that these are much greater than three standard deviations above the mean (to perhaps as much as five standard deviations) (Leithead and Agius, 1992) since the distributions of the load transients are not Gaussian. However, extreme loads decrease as the standard deviation decreases.

The dynamic characteristics of the controller are characterised by the open-loop cross-over frequency which can be freely chosen as part of the controller design task. It is therefore independent of the main hardware aspects of the wind turbine configuration. For this reason, the performance indicators were calculated for various controller cross-over frequencies. As the controller cross-over frequency increases so, normally, does the actuator

activity. There are maximum and minimum limits to the actuator capability which fundamentally constrain its performance and thereby that of the control system. The measures of actuator activity used here are the standard deviation of the acceleration or velocity of the pitch angle of the blades (see Appendix C for justification).

Because there is a large number of configurations to be investigated, it is necessary to make simplifying assumptions to enable an analytical approach to performance assessment. Hence specific results must be interpreted with some caution. However, it is believed the trends exhibited by the results are correct as the performance of a subset of the configurations under consideration has been validated by non-linear simulation (see Appendix C).

5.3 Equivalent rotor designs for two- and three-bladed machines

Since the performances of different wind turbine configurations are to be compared, assumptions are required to design equivalent rotors for the various machines considered, as described in Appendix E. To obtain a set of unambiguously equivalent rotors presents some difficulty. Commercial practice does not exhibit any specific rules when it comes to the number of blades (see Table E.1), but in general three-bladed rotors have lower tip speeds than two-bladed rotors for the same power rating. However, to ensure a fair comparison each rotor of the same size should be subject to similar stresses and, for ease of comparison, the below rated performance should be similar.

Appendix E describes the design of two sets of equivalent rotors for 300 kW and 1 MW wind turbines using aerodynamic strip theory to have approximately the same size of rotor and either equal stress at the root tip or the same blade solidity. Curves of blade pitch angle versus wind speed for rated power, are depicted in Figure 5.1 for all six full-span pitch-regulated rotors. The blade pitch/wind speed curve for the 300 kW machine is very similar to that of the WEG MS3 (Leithead and Agius, 1992). (The radius of the 1 MW rotors, whose design is driven by the aerodynamic characteristics of the corresponding tip regulated-rotor, is rather large, see Appendix E. With better rotor design the radius would be smaller and therefore the gradient of the power curve would be less steep.) The gradients of all the curves increase at lower wind speeds and are approximately constant at higher wind speeds. The blade operates below stall at all times. The rotors have been designed such that the below-rated behaviour is the same.

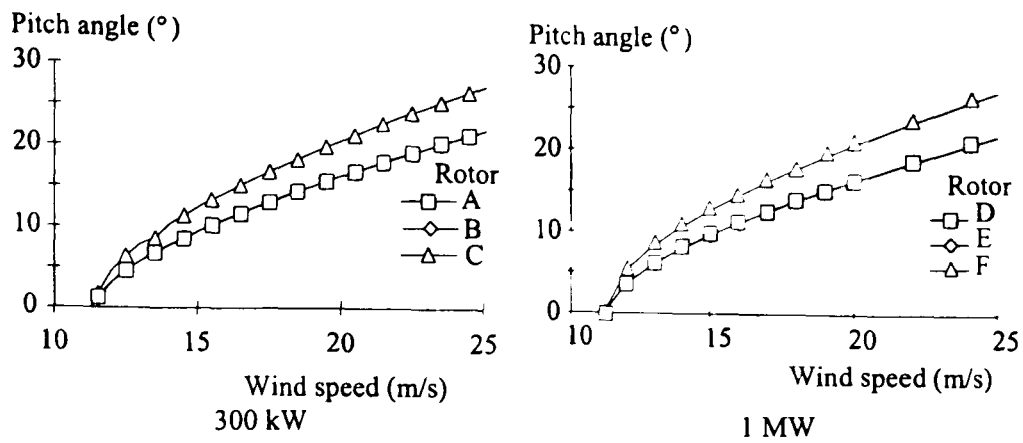


Figure 5.1 Blade pitch angle versus wind speed curves for rated power.

5.4 Linear analysis

The large number of configurations to be investigated necessitates the use of analytic methods rather than simulation models. Consequently performance is evaluated by linear covariance analysis (*cf.* Appendix C). The linear model of the wind turbine (Appendix C) is chosen in such a manner that the estimates of performance are in reasonable agreement with the performance determined by simulation.

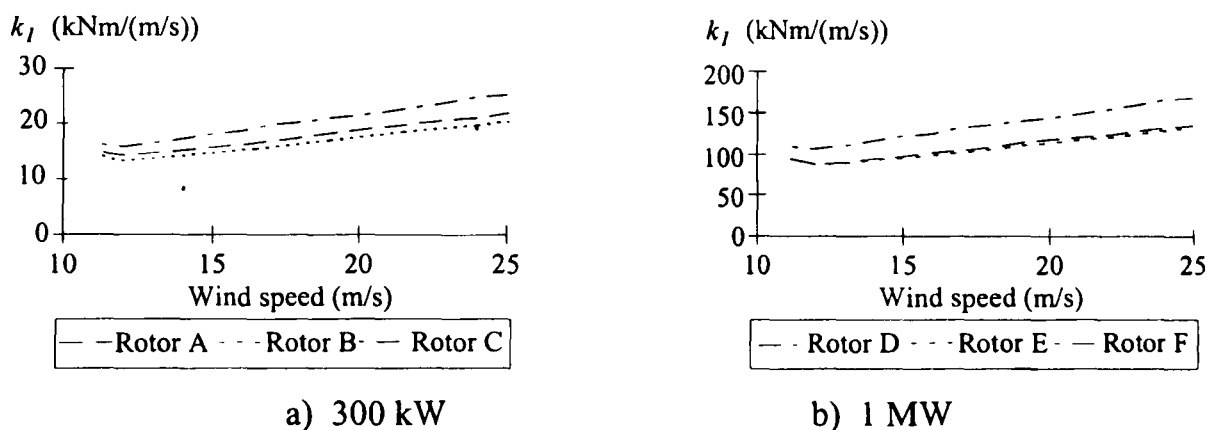


Figure 5.2 The value of k_1 for the range of wind speeds for each configuration.

The partial derivatives of aerodynamic torque with respect to wind speed, k_1 , and to pitch angle, k_2 , are determined from the aerodynamic torque coefficients (listed in Appendix G) for each rotor and are shown in Figures 5.2 and 5.3. For each configuration, k_1 appears to vary with tip-speed and machine size, but not with the number of blades, while k_2 is independent of tip-speed and the number of blades. Since for all the configurations the ratio k_2 / k_1 in Figure 5.4 is greatest at low wind speeds, the actuator activity would be predicted to be greater there than at higher wind speeds.

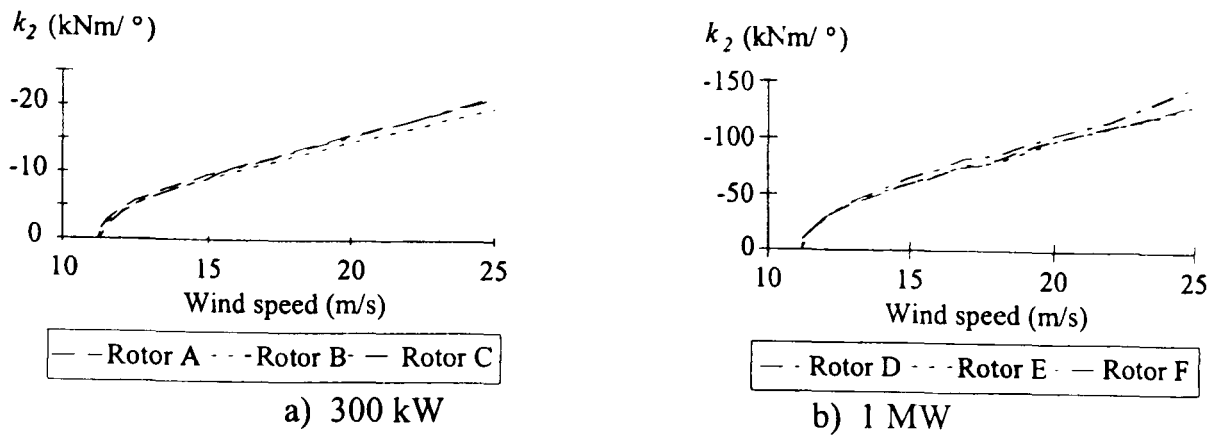


Figure 5.3 The value of k_2 for the range of wind speeds for each configuration.

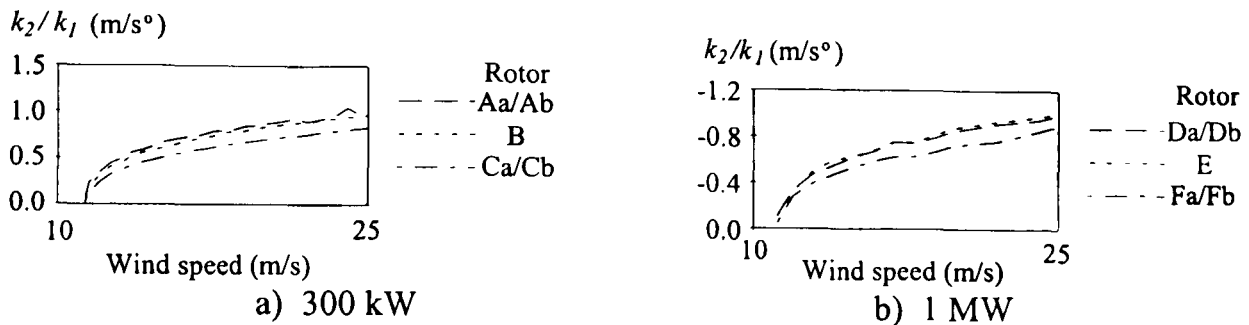


Figure 5.4 The value of k_2/k_1 for various wind speeds for each configuration.

5.5 Performance assessment

For each configuration the standard deviation of power is estimated for the ranges specified in Section 5.2 of controller cross-over frequencies, wind speeds, and frequencies of the first drive-train mode. Of course, whether a controller cross-over frequency can be achieved for a given configuration depends on the level of actuator activity. Accordingly the standard deviation of pitch angle acceleration and pitch angle velocity are also estimated in each case. In the discussion below it is assumed the controller is linear and is scheduled only with k_1 , unless otherwise stated.

The performances of configurations A to F are investigated separately. The performance of each is dependent on the first drive-train mode frequency, the controller cross-over frequency and wind speed. With the wind speed 16 m/s, the dependence is illustrated by Figure 5.5a which shows the standard deviation of power plotted against controller cross-over frequency for different first drive-train mode frequencies (the range is 2 rad/s to 7 rad/s in steps of 1 rad/s) and by Figures 5.5b and 5.5c which shows the standard deviation of pitch angle acceleration and velocity on log scales for the same parameter ranges. There is a very clear tendency for the standard deviation of power to decrease as controller cross-over frequency increases and the first drive-train mode frequency decreases. The greatest decrease in standard deviation of power occurs at the lower controller cross-over frequencies.

For some of the two-bladed machines the standard deviation of power does not decrease for controller cross-over frequencies greater than about 2 rad/s. In other words the performance is not always improved by upgrading the control system. For both the two-bladed wind turbines, the dependence of the standard deviation of power on the first drive-train frequency is more significant, particularly when the controller cross-over frequency is high. In comparison, the standard deviation of power for three-bladed machines is not sensitive to the first drive-train frequency. There is also a strong general tendency both for two- and three-bladed machines for the standard deviation of pitch angle acceleration or velocity to increase as the controller cross-over frequency increases and the first drive-train mode decreases. Hence an improvement in performance as measured by the standard deviation of power alone cannot be achieved without a concurrent increase in actuator activity. However, when the controller cross-over frequency is low, the standard deviation of pitch angle acceleration (or velocity) is not dependent on the first drive-train mode frequency.

Four typical but strongly contrasting configurations of wind turbines are compared to illustrate the wide range of performance possible. The first is a 300 kW, two-bladed configuration (Aa) with first drive-train mode frequency 6 rad/s; the second is a three-bladed, 300 kW machine (configuration Cb) with first drive-train mode frequency 7 rad/s; the third is a 1 MW, two-bladed machine (configuration Da) with first drive-train mode frequency 3 rad/s; and the fourth is a three-bladed, 1 MW machine (configuration Fb) with first drive-train mode frequency 4 rad/s.

Figure 5.6 shows the standard deviations of power plotted against controller cross-over frequency (in rad/s) for three different mean wind speeds (12 m/s, 16 m/s and 23 m/s) for each of the four configurations. It may be observed that the most testing conditions are usually in high wind speeds which are encountered rather infrequently. Except at high wind speeds, the standard deviation of power is only weakly related to the controller cross-over frequency. The benefit of increasing the controller cross-over frequency would only be perceived in high wind speeds, so there is little premium for so doing for a wind turbine situated on a low wind speed site. The standard deviation of power for a particular controller cross-over frequency is independent of the number of blades.

Also indicated on Figure 5.6 are the controller cross-over frequencies at which the standard deviation of pitch angle acceleration is 6, 18, 57 $^{\circ}/s^2$ for 300 kW machines (2, 6, 19 $^{\circ}/s^2$ for 1 MW machines), for a mean wind speed 12 m/s. (Since for all configurations the standard deviation of pitch angle acceleration increases with wind speed, the rating of the actuator is determined primarily by the conditions just above rated wind speed, namely

12 m/s.) The performance of the three-bladed wind turbines is better than the two-bladed wind turbine when the actuators have the same rating. Lack of detailed information about actuator capabilities for 1 MW wind turbines prevents direct comparisons to be made of medium- to large-scale machines. However, the conclusions described above appear to hold independent of power rating.

To enable a direct comparison of performance of the various configurations, the variance of generated power is plotted against actuator activity for all the configurations. Figures H.1a to H.5a show, for each of the wind turbine configurations investigated, the standard deviations of generated power for each wind speed against the standard deviations of the actuator acceleration for the worse case²; that is, the standard deviation of the actuator acceleration induced at 12 m/s by the controller cross-over frequency as it varies. Similarly, Figures H.1b to H.5b show for each of the wind turbine configurations investigated the standard deviations of generated power for each wind speed plotted against the standard deviations of the actuator velocity for 12 m/s. By comparing Figures 5.7a (5.8a) with 5.7b (5.8b), it can be seen that the performance is not sensitive to the rotor speed. Also, by comparing Figures 5.9a (5.10a) with 5.9b (5.10b) for the two-bladed machines and Figures 5.11a (5.12a) with 5.11b (5.12b) for the three-bladed machines, it can be seen that the difference in performance of two and three-bladed machines is not dominated by the relative intensities of the transient loads at $n\Omega_o$. The standard deviations of generated power do not vary in proportion to the intensities of the transient loads at $n\Omega_o$ and the performance is not strongly dependent on them.

The large improvement in performance as measured by the standard deviation of generated power accrues from increased control-system performance only below a standard deviation of actuator acceleration of 20 °/s² for 300 kW machines (10 °/s² for 1 MW machines) or actuator velocity of 8 °/s for 300 kW (4 °/s for 1 MW machines). In other words, to improve performance beyond this point requires a disproportionately large increase in the actuator capability. It should be noted that the performance does not always improve monotonically with an increase in drive-train compliance; *i.e.* a low first drive-train mode. The performance of the two-bladed machines improves as the first drive-train mode frequency decreases, whilst the performance of the three-bladed machines improves as the first drive-train mode frequency increases.

² For any of the mean wind speeds considered the wind speed may momentarily reach 12 m/s and the actuator activity is more sensitive to this instantaneous wind speed than long term wind speeds.

For all the configurations, the performance deteriorates with increasing wind speed. Except at high wind speeds, the standard deviation of power is only weakly related to the controller cross-over frequency. Figures H.6a to H.10a show, for each of the wind turbine configurations investigated, the standard deviation of generated power against the standard deviation of the actuator acceleration as it varies with cross-over frequency for each wind speed. Similarly, Figures H.6b to H.10b show the standard deviation of generated power against the standard deviation of the actuator velocity for each wind speed. Comparing these two sets of figures it can be seen that the performance of the two-bladed machines can be improved at high wind speeds by increasing the controller cross-over frequency compared to that used at low wind speeds (see Figures 5.13), as investigated by Leith and Leithead (1994-1996). The greatest improvement can be made on two-bladed machines. However, little improvement would be seen at low-wind speed site.

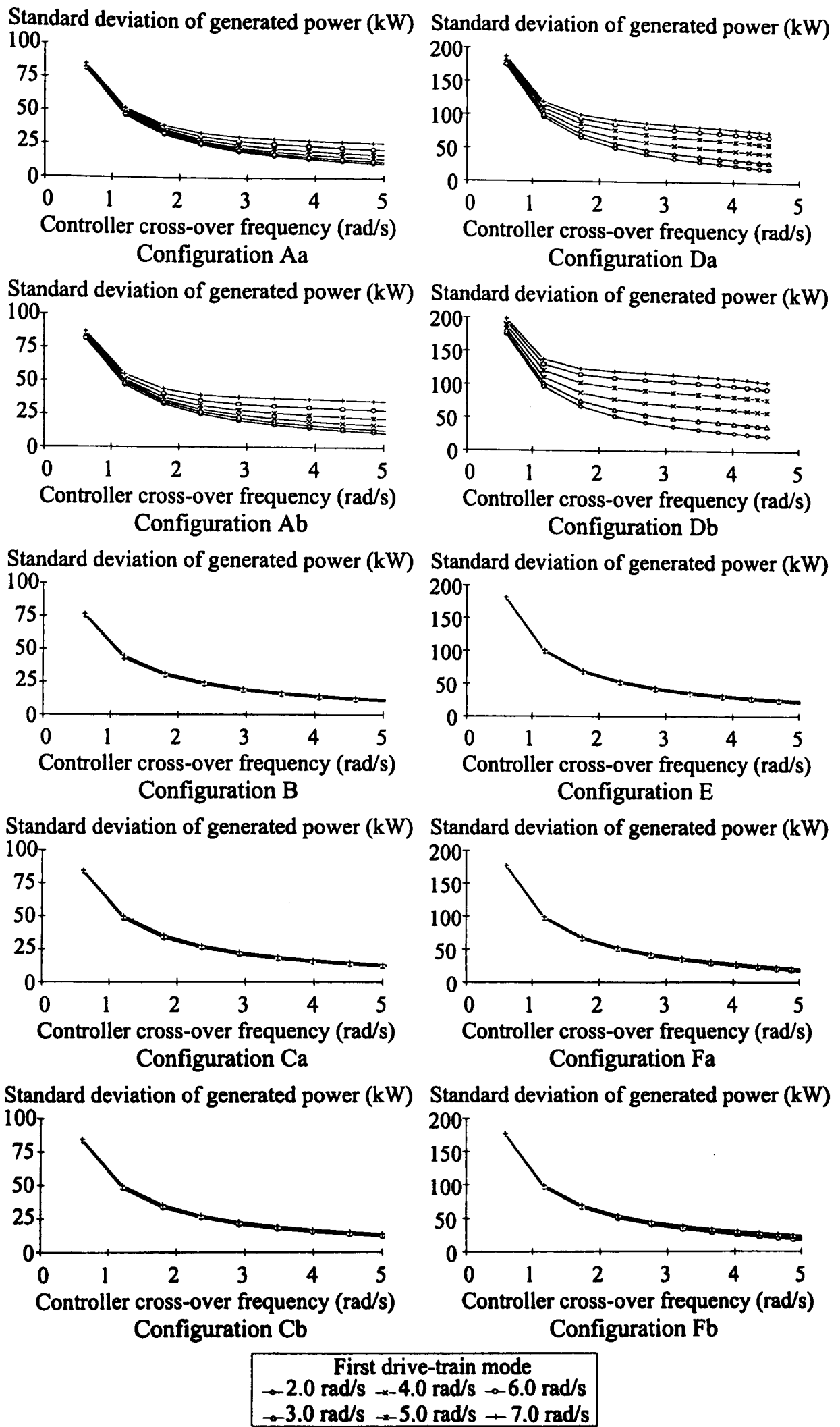


Figure 5.5a Standard deviation of generator power for 16 m/s wind speed.

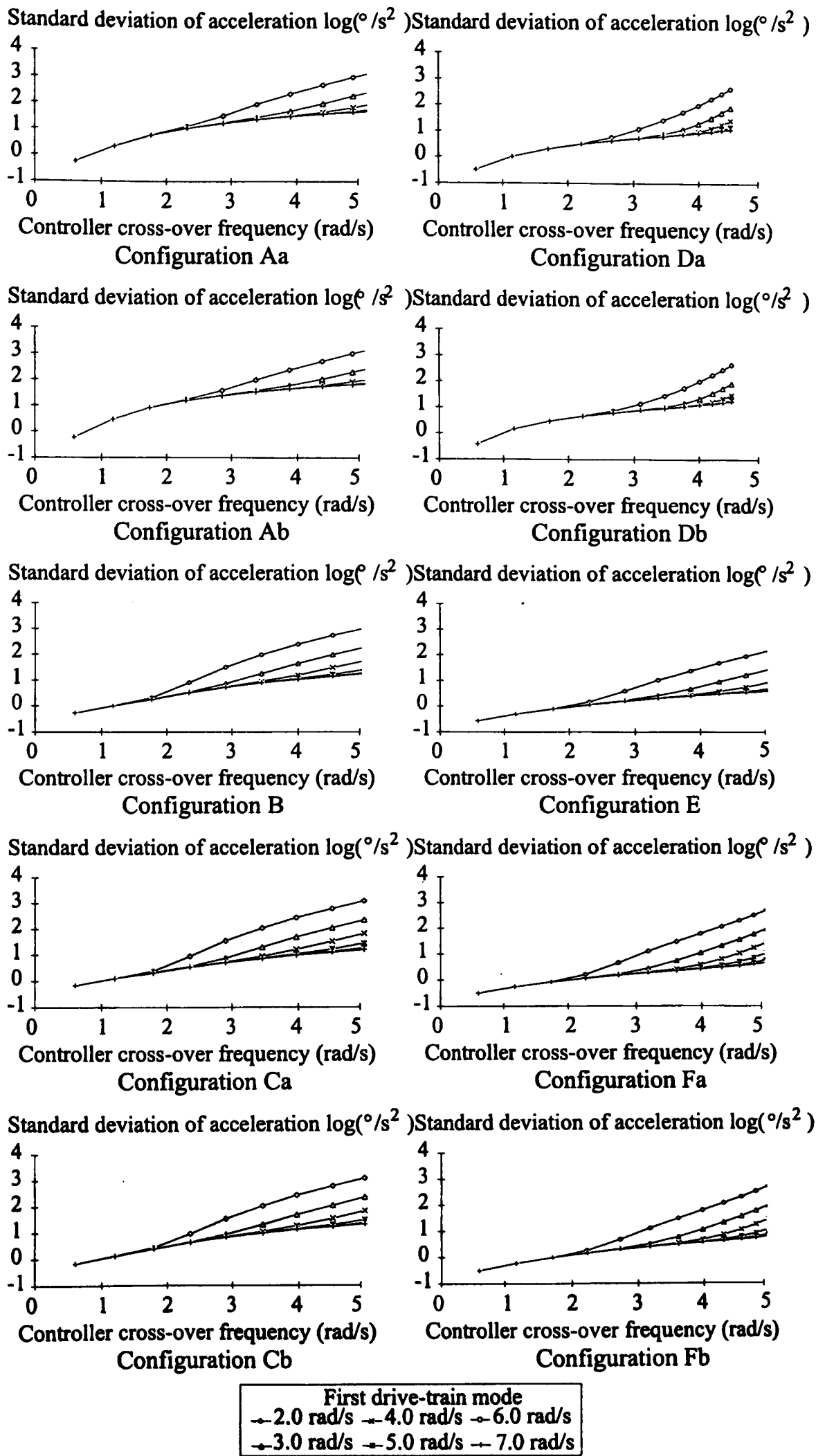
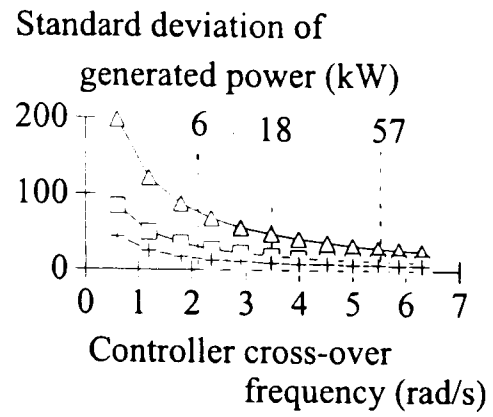
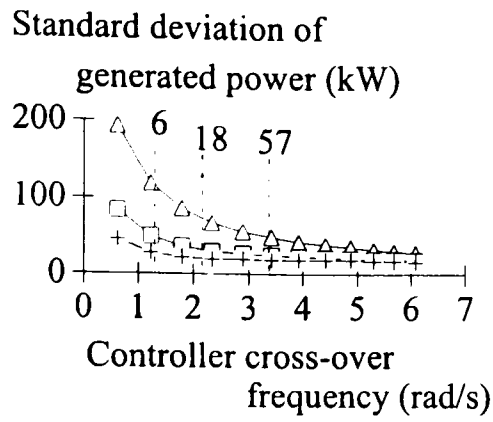
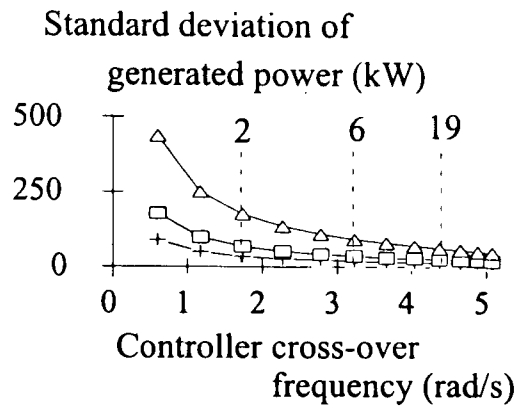
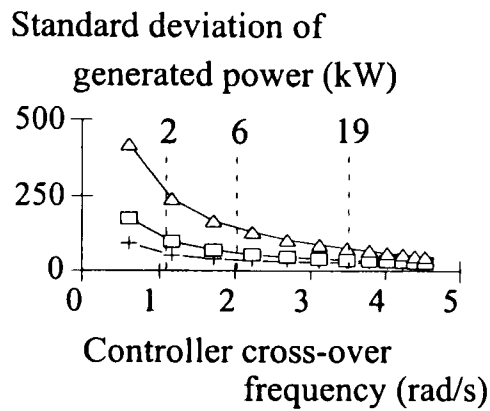


Figure 5.5b Standard deviation of actuator acceleration for 16 m/s wind speed.



Two blades, 300 kW, $1/2 \times \text{nominal } 2\Omega_o$ Three blades, 300 kW, $2 \times \text{nominal } 3\Omega_o$
 Aa, first drive-train mode 6 rad/s Cb, first drive-train mode 7 rad/s



Two blades, 1 MW, $1/2 \times \text{nominal } 2\Omega_o$ Three blades, 1 MW, $2 \times \text{nominal } 3\Omega_o$
 Da, first drive-train mode 3 rad/s Fb, first drive-train mode 4 rad/s

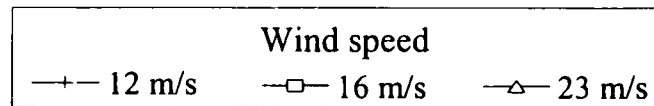


Figure 5.6 Power control performance for four different machine configurations

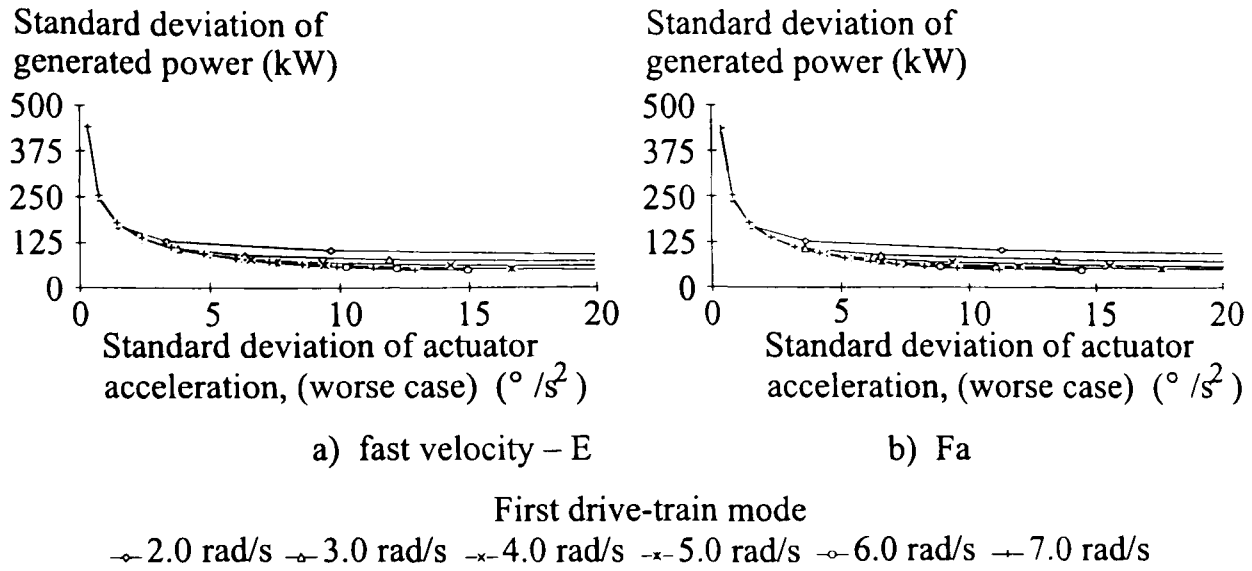


Figure 5.7 Worst case performance (actuator acceleration) of three-bladed 1 MW machines for 23 m/s.

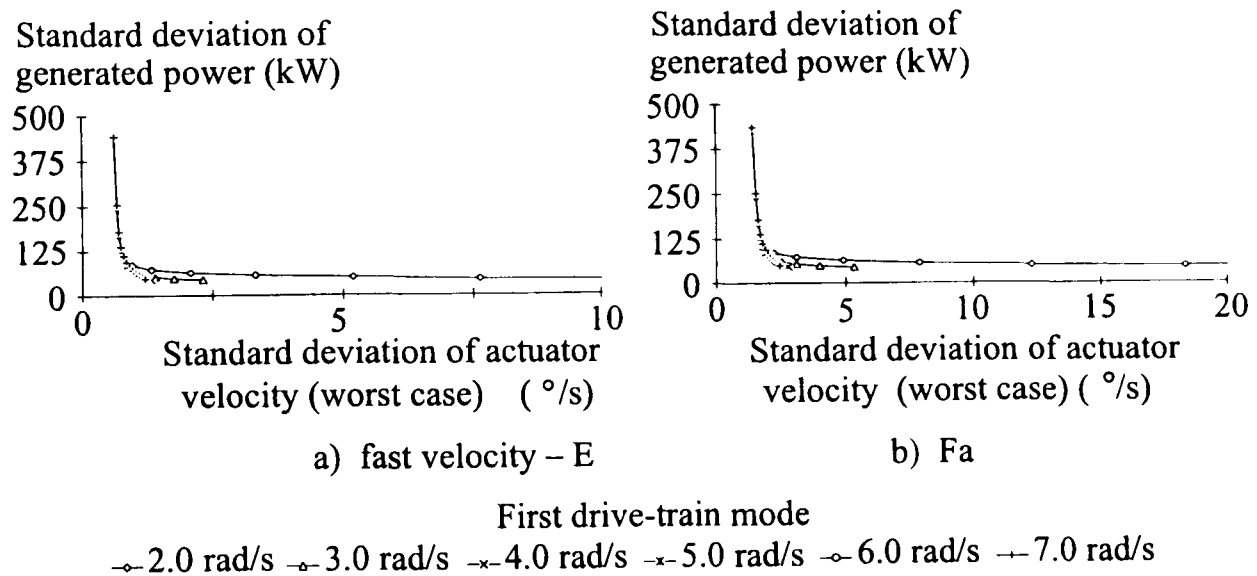
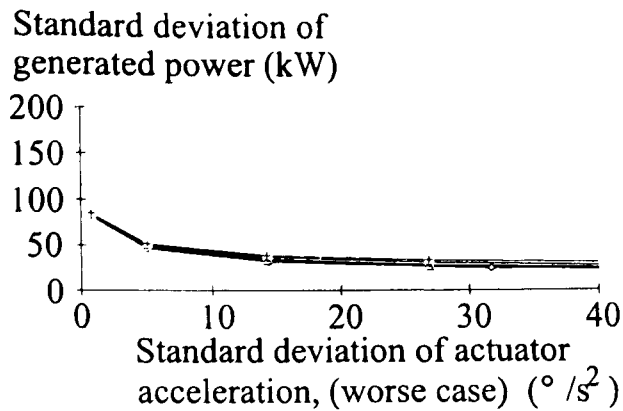
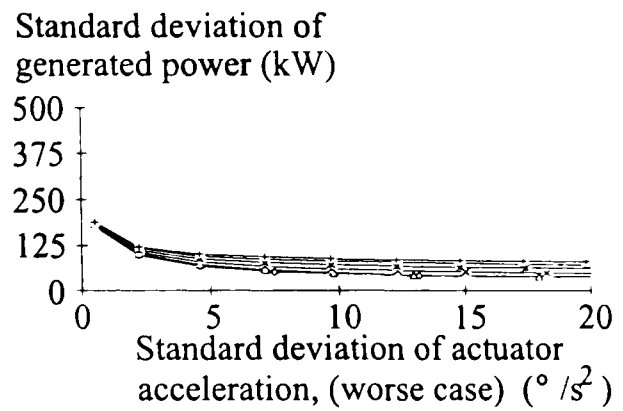


Figure 5.8 Worst case performance (actuator velocity) of three-bladed 1 MW machines for 23 m/s.

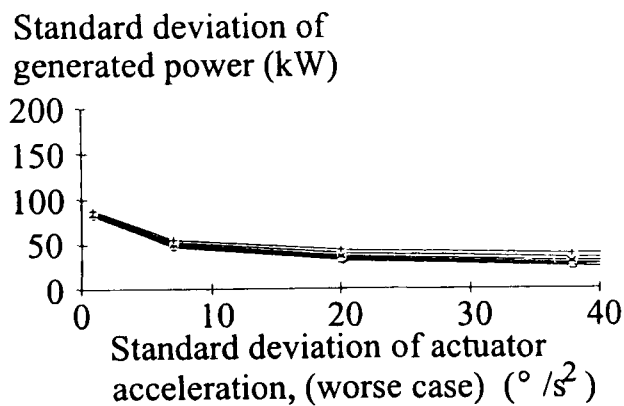


300 kW Aa

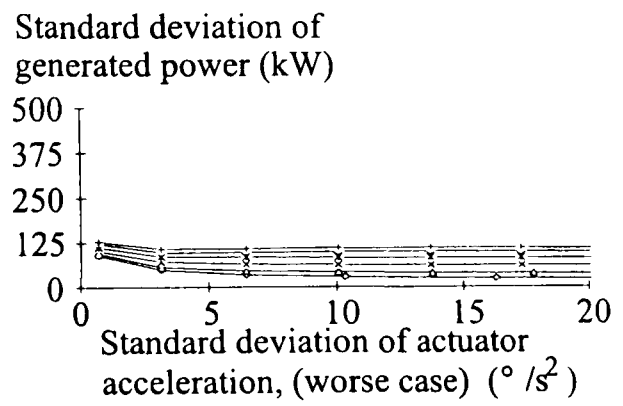


1 MW Da

a) $1/2$ nominal $2\Omega_0$



300 kW Ab



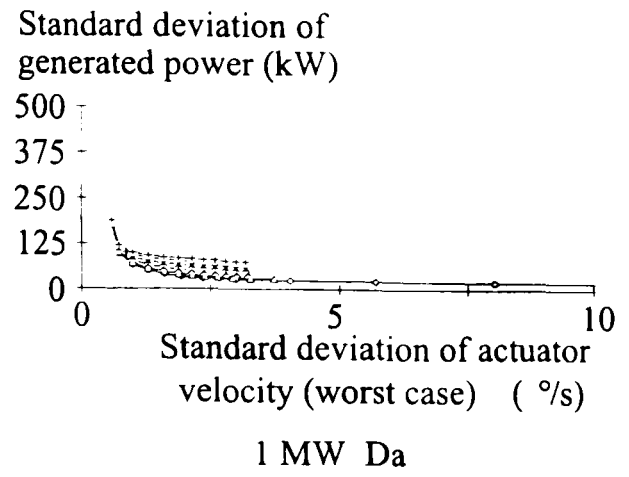
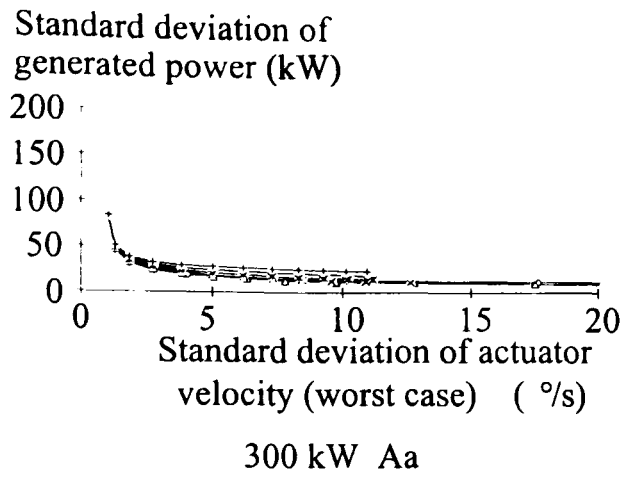
1 MW Db

b) nominal $2\Omega_0$

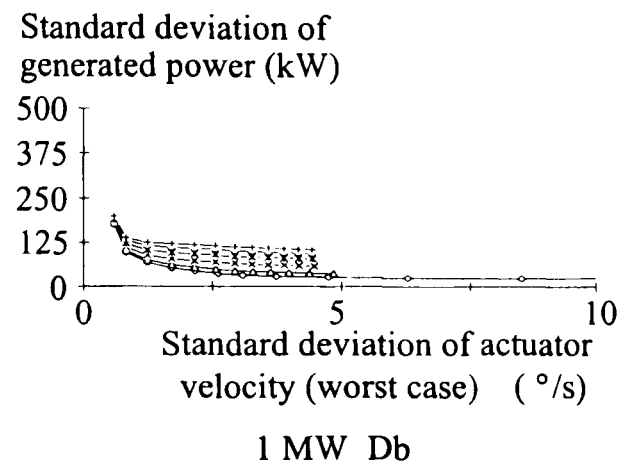
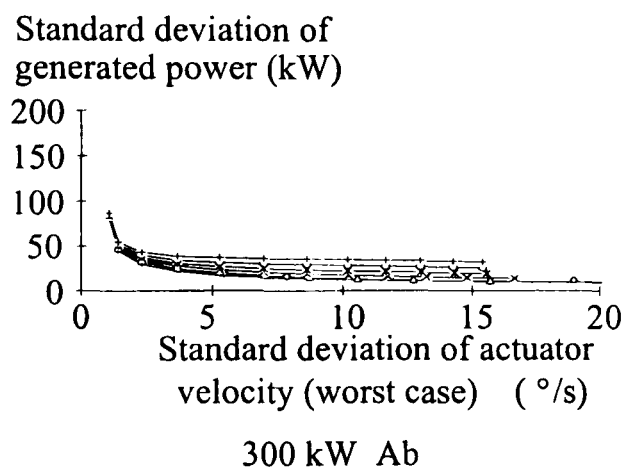
First drive-train mode

○ 2.0 rad/s ◻ 3.0 rad/s × 4.0 rad/s × 5.0 rad/s ◊ 6.0 rad/s — 7.0 rad/s

Figure 5.9 Worst case performance (actuator acceleration) of the two-bladed machines at 16 m/s



a) $1/2$ nominal $2\Omega_o$



b) nominal $2\Omega_o$

First drive-train mode

○ 2.0 rad/s ○ 3.0 rad/s × 4.0 rad/s × 5.0 rad/s ○ 6.0 rad/s → 7.0 rad/s

Figure 5.10 Worst case performance (actuator velocity) of the two-bladed machines at 16 m/s

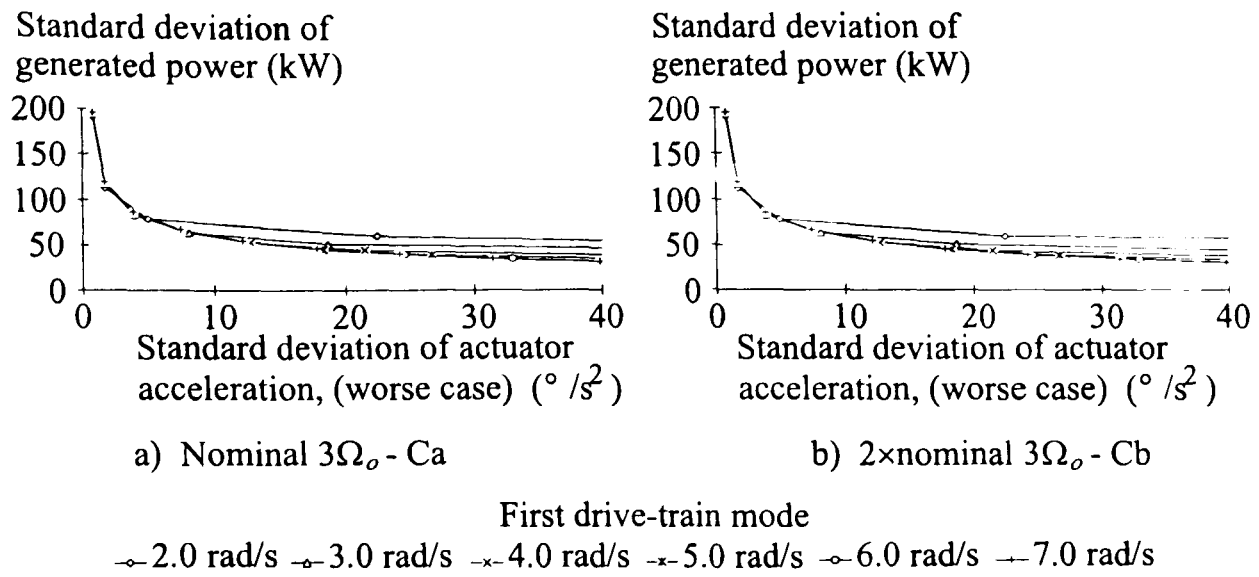


Figure 5.11 Worst case performance (actuator acceleration) of three-bladed machines for 23 m/s.

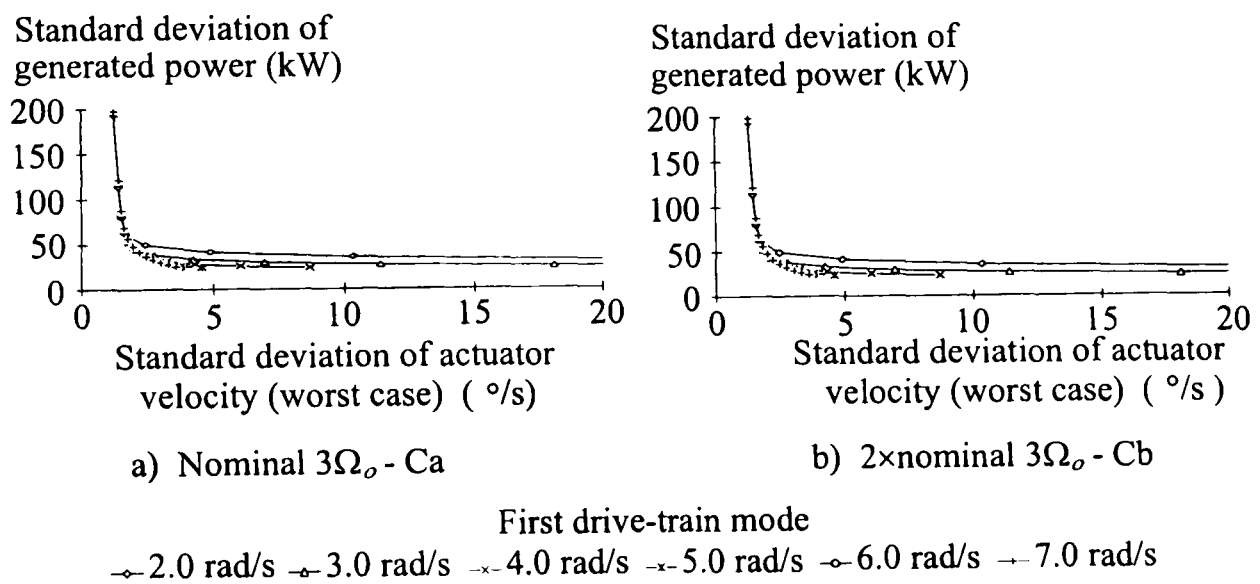
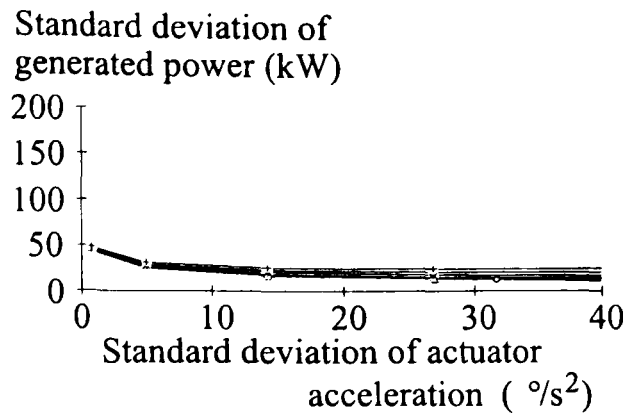
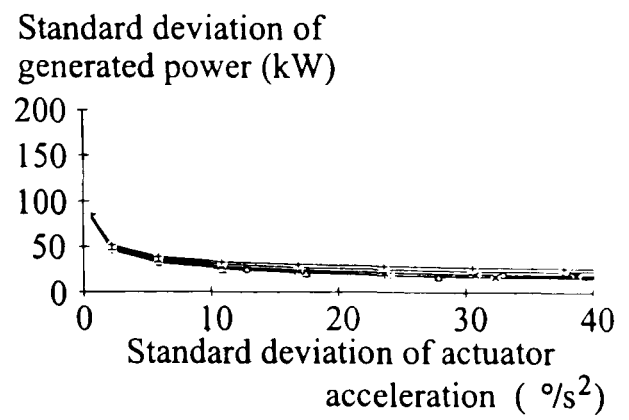


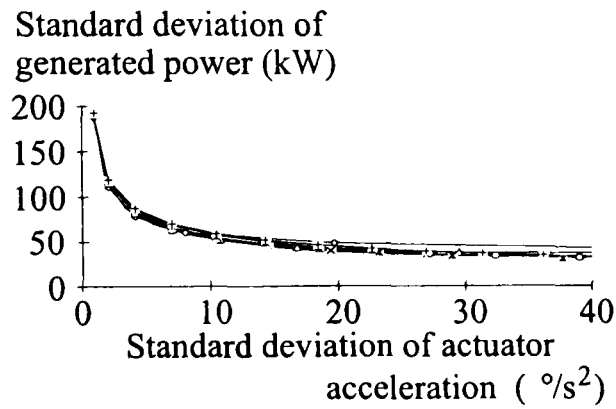
Figure 5.12 Worst case performance (actuator velocity) of three-bladed machines for 23 m/s.



Wind speed 12 m/s



Wind speed 16 m/s



Wind speed 23 m/s

First drive-train mode

○ 2.0 rad/s ◐ 3.0 rad/s × 4.0 rad/s -x- 5.0 rad/s ◑ 6.0 rad/s + 7.0 rad/s

Figure 5.12 Performance (actuator acceleration) of two-bladed ($1/2 \times$ nominal $2\Omega_0$) 300 kW machine Aa.

5.6 Conclusions

The second step to attaining the objective to lay the foundation for the control aspects of the integrated design of wind turbines has been achieved for full-span regulated wind turbines, as follows and with the following conclusions.

- a) The attainable performance of power control, which is surprisingly large, is determined for a range of configurations.
 - The performance of the three-bladed machines is significantly better (by an order of magnitude) than that of two-bladed machines for all but the lowest drive-train modes and controller cross-over frequencies.
 - The performance of two-bladed machines can be improved greatly by reducing the frequency of the first drive-train mode.
 - Three-bladed machines are insensitive to the first drive-train mode frequency.
 - Performance is weakly related to rotor angular velocity and the intensity of the transient loads at $n\Omega_r$.
 - As would be expected, performance is strongly related to controller activity for controllers with low cross-over frequencies.
 - Except at low frequencies, increasing the controller cross-over frequency requires a disproportionate increase in the rating of the actuator.
 - There is a limiting controller cross-over frequency, (roughly 2 rad/s) beyond which any improvement in performance is small.

The above conclusions hold for all the machines studied. Since many simplifying assumptions were made to allow linear analysis, a sample of the results has been validated by non-linear simulation, see Appendix C. Although ideal damping of the drive train is assumed, the methodology is readily adapted to configurations without ideal damping but many of the trends observed also apply to these configurations, see Chapter 8.

- b) The implications for controller design are also determined.
 - Increasing the controller cross-over frequency in high wind speeds can be advantageous. An improvement in performance can be achieved by increasing the controller cross-over frequency and hence the actuator activity at higher wind speeds. In contrast, the highest actuator activity for a particular controller cross-over frequency is required at the wind speeds just above rated wind speed. Therefore performance could be improved by increasing the controller cross-over frequency with wind speed, see Chapter 8.

- Attempting to improve performance by optimising the design of the controller can achieve little. (The gain in performance from increasing the cross-over frequency beyond 2 rad/s is marginal but requires an excessive increase in actuator capability.)

Any comparison between the performance of machines of different power rating should be treated with some caution due to the absence of detailed knowledge of actuators for 1 MW machines.

6 Tip-regulated machines

6.1 Introduction

The previous chapter describes an investigation of the dependence on configuration of the performance of active, full-span, pitch control in alleviating transient loads. The present chapter discusses the results of a parametric study where the full-span regulated rotors are replaced by tip-regulated rotors.

The methodology used to estimate the performance for a specific configuration is the same as that in Chapter 5, as is the set of configurations investigated. The only change is that regulation is done with part, not all of the blade. Since the movable part of the blade is lighter than on a full-span machine, the tip would be expected to be able to move faster for the same motive force. Although in below rated wind speeds the aerodynamics of a tip-regulated machine are identical to that of a full-span machine with the same rotor design, the above rated behaviour is very different. This chapter considers how the performance of tip-regulated machines is affected by the same machine characteristics considered in Chapter 5, namely

- the number of blades;
- the dynamic characteristics of the drive train;
- the dynamic characteristics of the controller;
- the intensity of the drive-train transient loads at $n\Omega_o$; and
- the angular velocity of the rotor.

6.2 Different types of wind turbine configuration

The wind turbine configurations considered are listed in Table 6.1. For each configuration, the intensity of $n\Omega_o$ is assumed to be identical to that of the corresponding full-span regulated machine. As before, the performance indicators considered are the standard deviations of generated power and the actuator acceleration and velocity. Similar

ranges of first drive-train frequencies, controller cross-over frequencies and wind speeds are considered to those in Chapter 5.

Again, because there are a large number of configurations to be investigated the simplifying assumptions described in Appendix C are required to enable an analytic approach to performance assessment. Hence, as in the previous chapter, specific results must be interpreted with some caution, but the trends exhibited by the results are validated by non-linear simulation (see Appendix C)

Configuration	No. of blades	Power rating (kW)	Rotor speed, Ω_o (rad/s)	Spectral loads
Ga	2	300	5.090	$1/2 \times \text{Nominal } 2\Omega_o$
Gb	2	300	5.090	Nominal $2\Omega_o$
H	3	300	5.201	Nominal $3\Omega_o$
Ia	3	300	4.125	Nominal $3\Omega_o$
Ib	3	300	4.125	$2 \times \text{Nominal } 3\Omega_o$
Ja	2	1000	2.800	$1/2 \times \text{Nominal } 2\Omega_o$
Jb	2	1000	2.800	Nominal $2\Omega_o$
K	3	1000	2.850	Nominal $3\Omega_o$
La	3	1000	2.250	Nominal $3\Omega_o$
Lb	3	1000	2.250	$2 \times \text{Nominal } 3\Omega_o$

Table 6.1 The different tip-regulated wind turbine configurations.

6.3 Equivalent rotor designs for two- and three-bladed machines

To ensure a fair comparison with the full-span regulated machines described in Chapter 5, the rotors of the tip-regulated machines considered here are identical to those of the full-span wind turbines, so that for each rotor of the same size similar stresses are experienced and the below rated performance is similar. The design of the equivalent rotors and the determination of the tip size are described in Appendix E. The resulting curves of tip angles versus wind speed for rated power are depicted in Figure 6.1. The tip angle/wind speed curve for the 300 kW machine is very similar to that of the Howden 330/33 wind turbine (Wilkie and Leithead, 1989), while the curve for the 1 MW machine is very similar to that of the Howden 1000/45 machine (Leithead *et al.*, 1991a). The gradients of all the curves decrease with increasing wind speed until at high wind speeds the gradient is nearly zero.

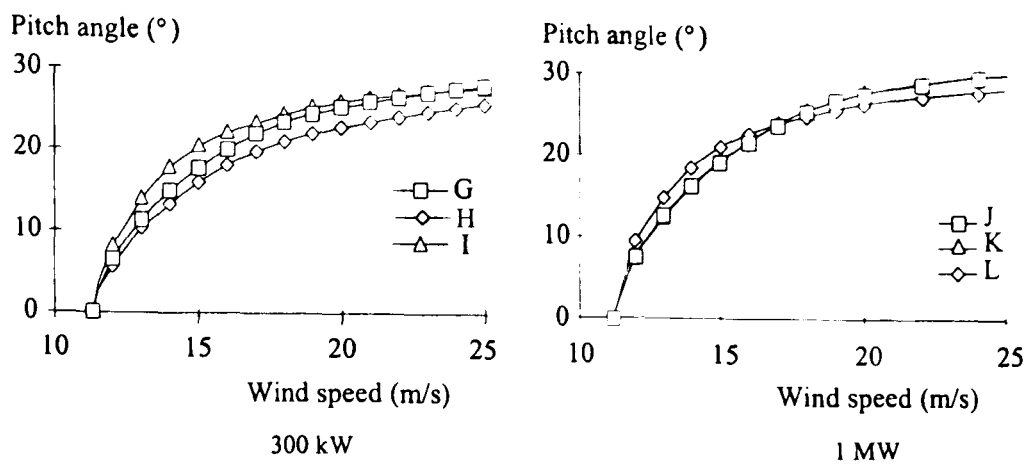


Figure 6.1 Tip angle versus wind speed for the tip-regulated rotors.

6.4 Linear analysis

As before, performance is evaluated by linear covariance analysis as described in Appendix C using the transfer functions (C.1) to (C.20). The three disturbances are assumed to be identical to those experienced by the full-span machines with the exception of the values of k_1 and k_2 .

The partial derivatives of aerodynamic torque with respect to wind speed, k_1 , and with respect to pitch angle, k_2 , are determined from the aerodynamic torque coefficients for each rotor (listed in Appendix G) and are shown in Figures 6.2 and 6.3. As with the full-span regulated machines, for all the configurations k_1 varies with tip speed and machine size, but not with the number of blades; and the ratio k_2 / k_1 in Figure 6.4 is greatest at the lower wind speeds. Hence the actuator activity would be predicted to be greater there than at higher wind speeds.

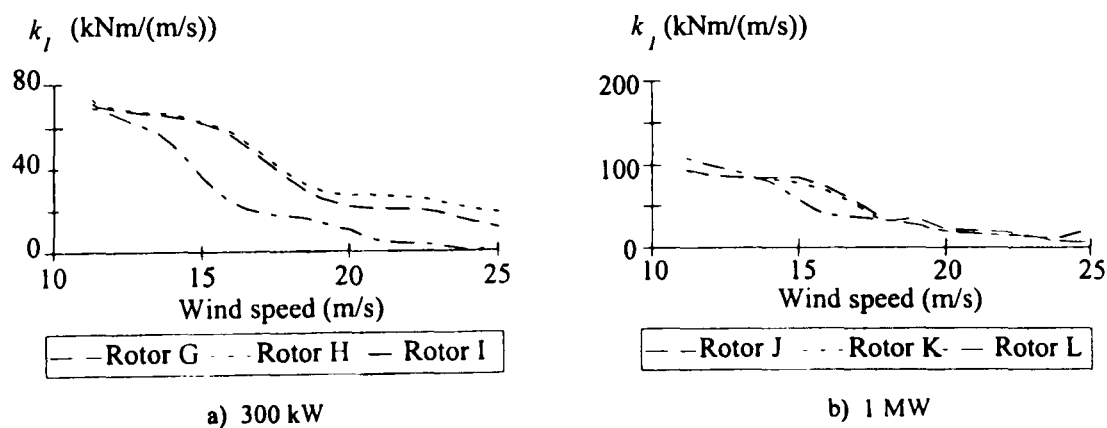


Figure 6.2 The value of k_1 for the range of wind speeds for each configuration.

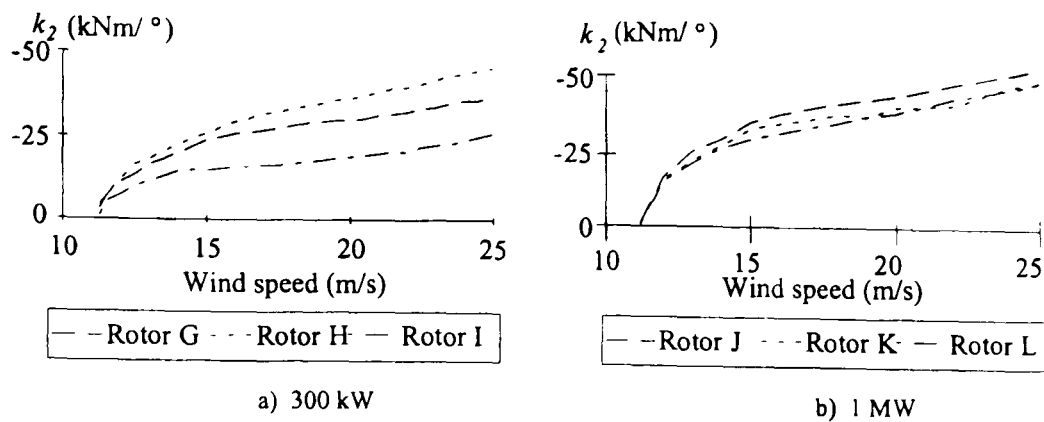


Figure 6.3 The value of k_2 for the range of wind speeds for each configuration.

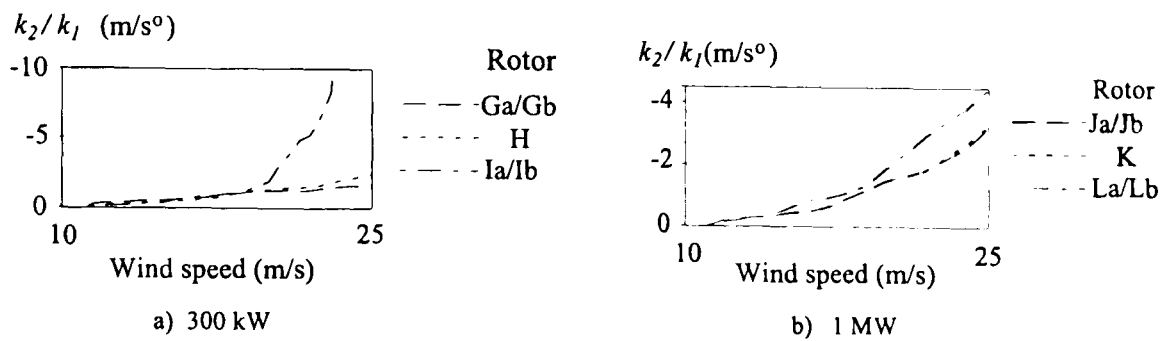


Figure 6.4 The value of k_2 / k_1 for various wind speeds for each configuration.

6.5 Performance assessment

The performances of configurations G to L are investigated separately in an identical manner to the configurations considered in Chapter 5. The performance of each is dependent on the first drive-train mode frequency, the controller cross-over frequency and wind speed. At a wind speed of 16 m/s, the dependence is illustrated by Figure 6.5a which shows the standard deviation of power plotted against controller cross-over frequency for different first drive-train modes and by Figures 6.5b and 6.5c which show the standard deviation of pitch-angle acceleration and velocity for the same parameter ranges. There is a general tendency for the standard deviations of power, acceleration and velocity to vary with controller cross-over frequency and first drive-train frequency in similar manners to the full-span regulated machines considered in Chapter 5.

Four typical but strongly contrasting configurations of wind turbines are compared to illustrate the wide range of performance possible. The first is a 300 kW, two-bladed configuration (Ga) with a first drive-train mode frequency of 6 rad/s; the second is a three-bladed, 300 kW machine (configuration Ib) with a first drive-train mode frequency of 7 rad/s; the third is a 1 MW, two-bladed machine (configuration Ja) with first drive-train mode frequency at 3 rad/s; and the fourth is a three-bladed, 1 MW machine (configuration Lb) with first drive-train mode frequency at 4 rad/s.

The standard deviations of power are plotted in Figure 6.6 against controller cross-over frequency for the three different mean wind speeds for each of the four configurations. Similar conclusions can be made to those from Figure 5.6. As in Figure 5.6, Figure 6.6 indicates the controller cross-over frequencies at which the standard deviation of pitch acceleration is 6, 18, 57 °/s² for 300 kW machines (2, 6, 19 °/s² for 1 MW machines) for a mean wind speed 12 m/s. The performance of the three-bladed wind turbines (as measured as the standard deviation of power) is better than that of the two-bladed wind turbine when the actuators have the same rating.

Once again, to enable a direct comparison of performance of the various configurations, the variance of generated power is plotted against actuator activity for all the configurations. Figures H.11a to H.15a show for each of the wind turbine configurations investigated the standard deviations of generated power for each wind speed against the standard deviations of the actuator acceleration for the worst case. Similarly Figures H.11b to H.15b show for each configuration the standard deviations of generated power for each wind speed against the standard deviations of the actuator velocity for 12 m/s.

By comparing Figures 6.7a (6.8a) with 6.7b (6.8b), it can be seen that performance is not sensitive to rotor speed. Also, by comparing Figures 6.9a (6.10a) with 6.9b (6.10b) for the two-bladed machines and Figures 6.11a (6.12a) with 6.11b (6.12b) for the three-bladed machines, it can be seen that the difference in performance of two and three-bladed machines is not dominated by the relative intensities of the transient loads at $n\Omega_o$. The standard deviations of generated power do not vary in proportion to the intensities of the transient loads at $n\Omega_o$ and the performance is not strongly dependent on them. As with the full-span pitch regulated machines, to improve performance beyond a certain point - *i.e.* beyond the standard deviation of generated power associated with a standard deviation of actuator acceleration of 10 °/s² for 300 kW machines (6 °/s² for 1 MW machines) or actuator velocity of 4 °/s for 300 kW machines (2 °/s for 1 MW machines) - requires a disproportionately large increase in the actuator capability. It should be noted that the performance does not always improve monotonically with an increase in drive-train compliance; *i.e.* a low first drive-train mode. Unlike previously, the performances of all the machines do not deteriorate with increasing wind speed. Little increase in the performance of each configuration can be achieved by increasing the controller cross-over frequency in high wind speeds compared to that used in low wind speeds (*e.g.* compare Figure 6.13) as investigated by Leith and Leithead (1995-1996).

Figures H.16a to H.25a show for each of the configurations investigated the standard deviations of generated power against the standard deviations of the actuator acceleration as

it varies with cross-over frequency for each wind speed. Similarly Figures H.16b to H.25b plot the standard deviations of generated power against the standard deviations of the actuator velocity for each wind speed.

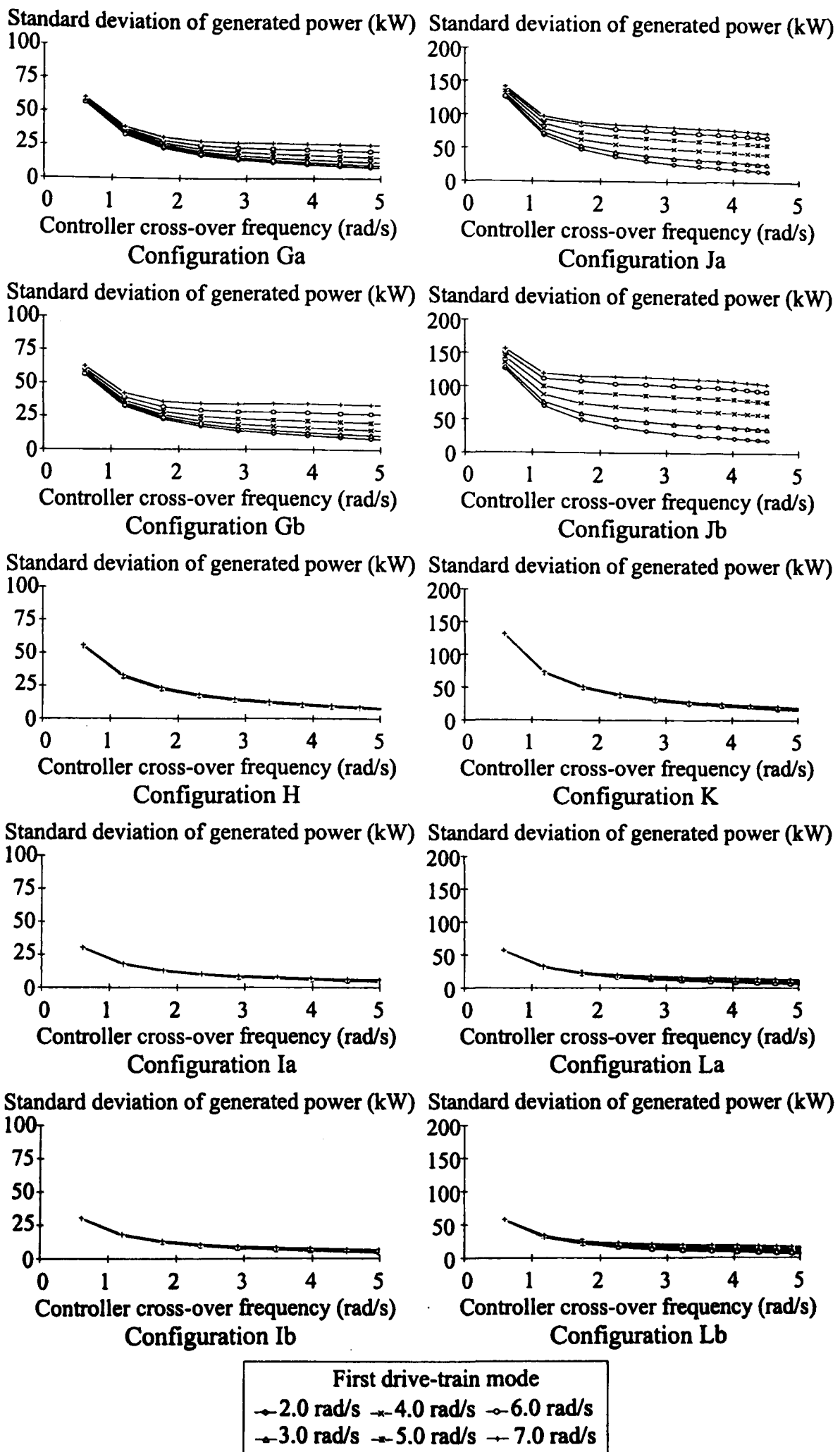


Figure 6.5a Standard deviation of generator power for 16 m/s wind speed.

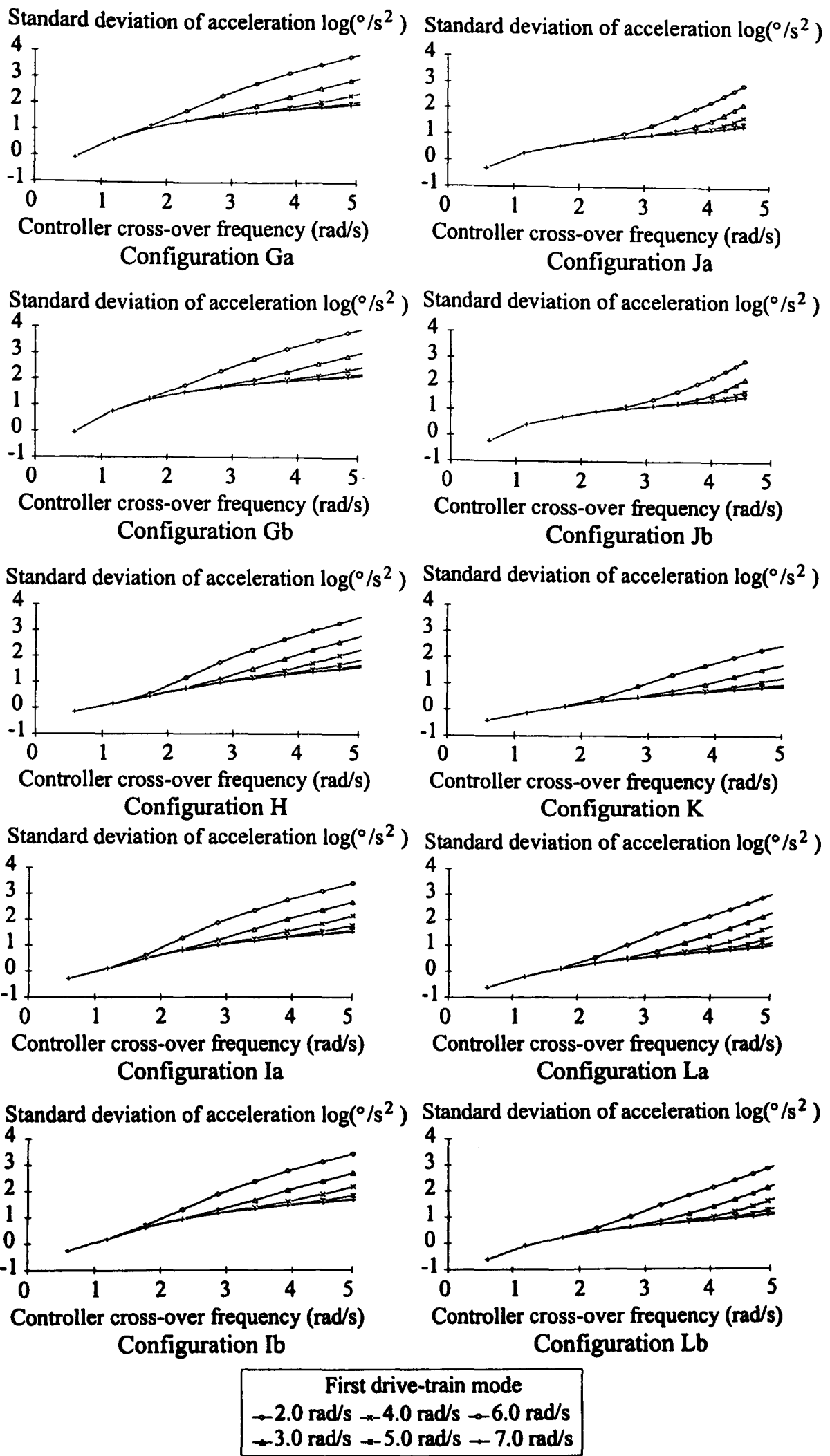


Figure 6.5b Standard deviation of actuator acceleration for 16 m/s wind speed.

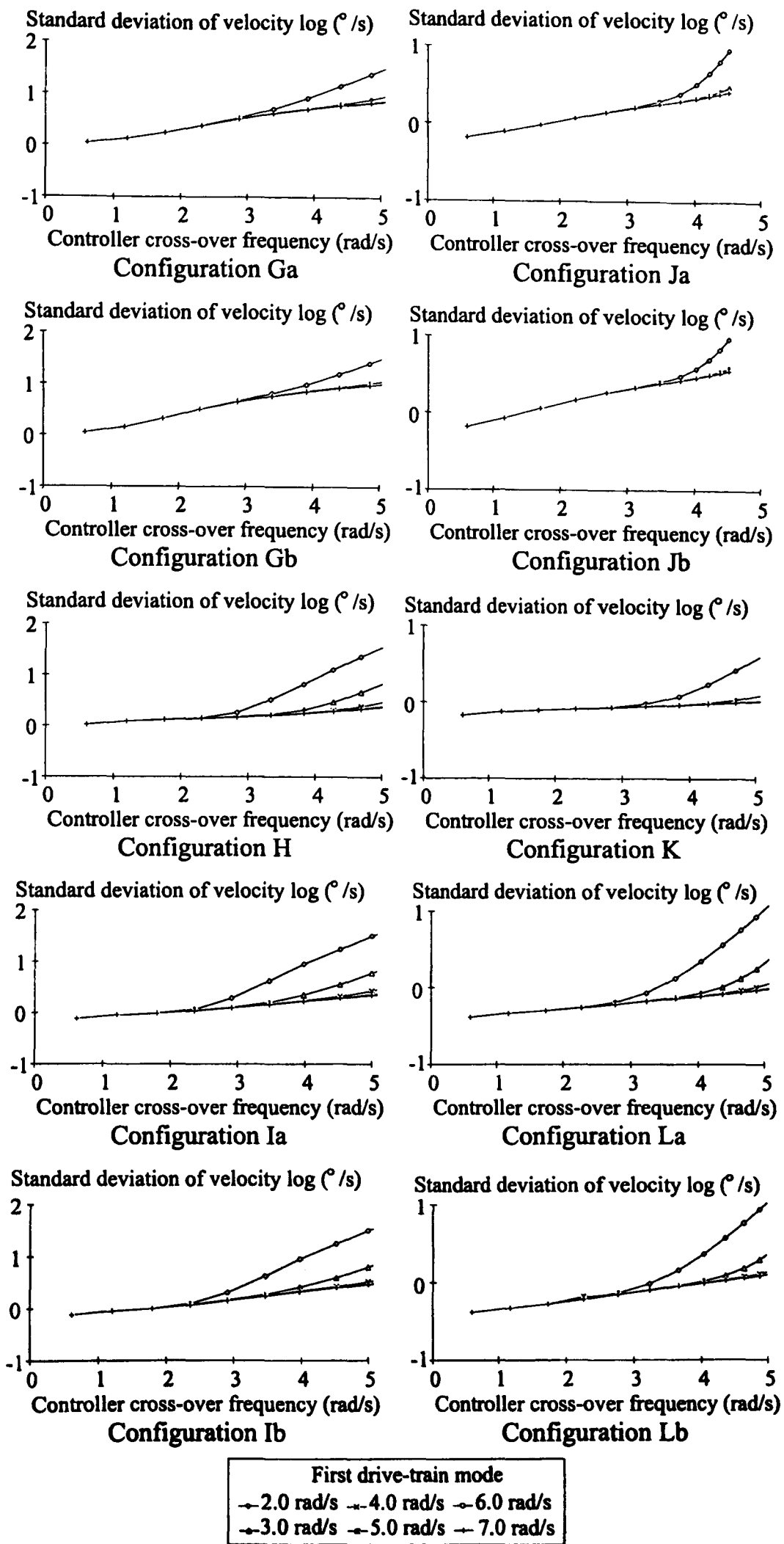
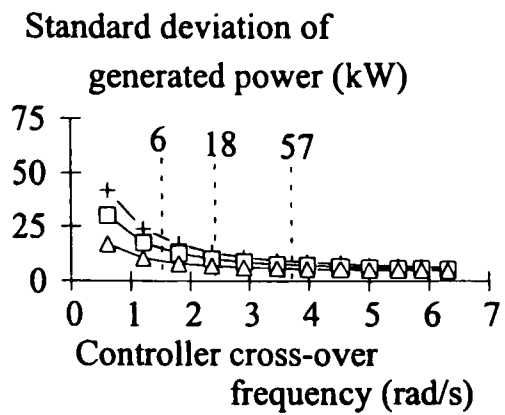
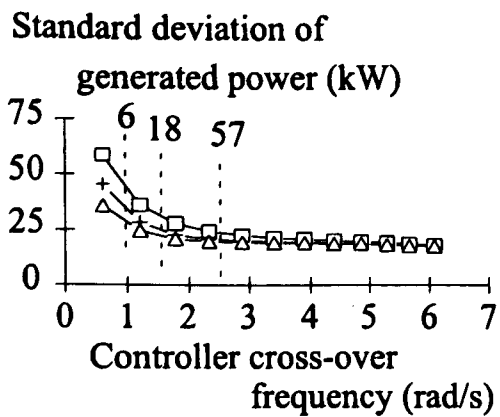


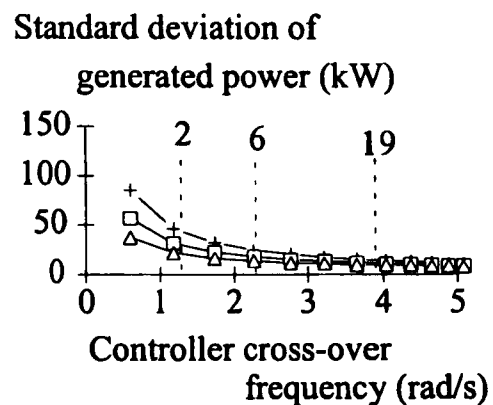
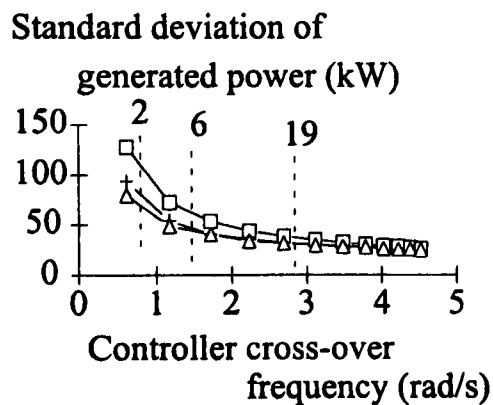
Figure 6.5c Standard deviation of actuator velocity for 16 m/s wind speed.



Two blades, 300 kW, $1/2 \times$ nominal $2\Omega_o$ Three blades, 300 kW, $2 \times$ nominal $3\Omega_o$

Ga, first drive-train mode 6 rad/s

Ib, first drive-train mode 7 rad/s



Two blades, 1 MW, $1/2 \times$ nominal $2\Omega_o$ Three blades, 1 MW, $2 \times$ nominal $3\Omega_o$

Ja, first drive-train mode 3 rad/s

Lb, first drive-train mode 4 rad/s

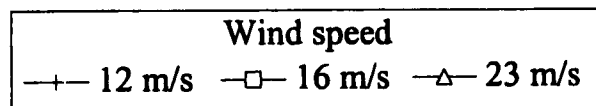
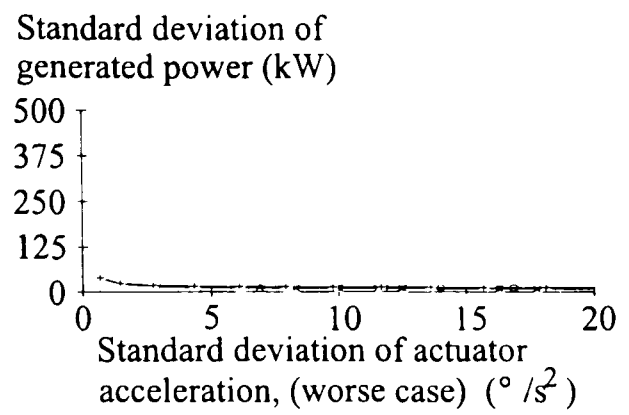
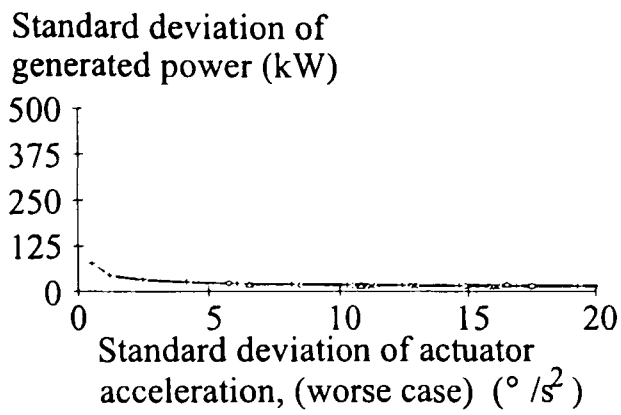


Figure 6.6



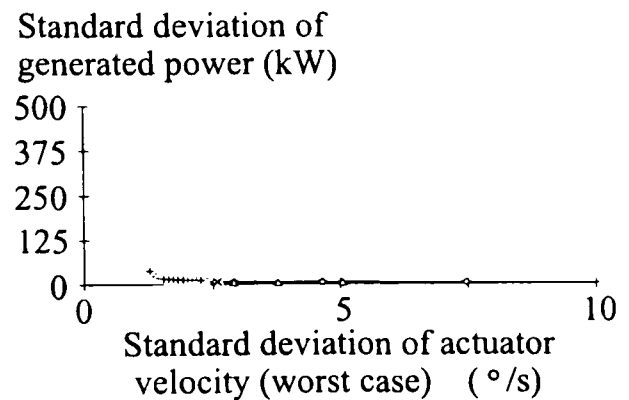
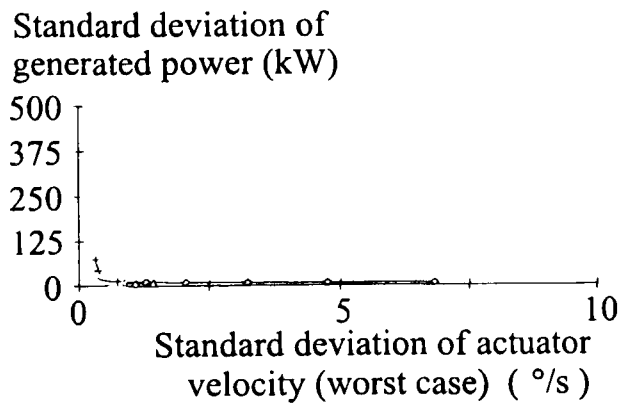
a) fast velocity – K

b) La

First drive-train mode

○ 2.0 rad/s ◓ 3.0 rad/s × 4.0 rad/s × 5.0 rad/s ◓ 6.0 rad/s × 7.0 rad/s

Figure 6.7 Worst case performance (actuator acceleration) of three-bladed 1 MW machines for 23 m/s.



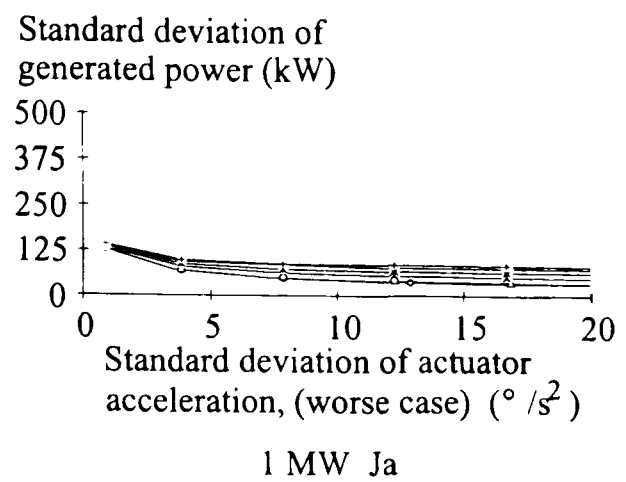
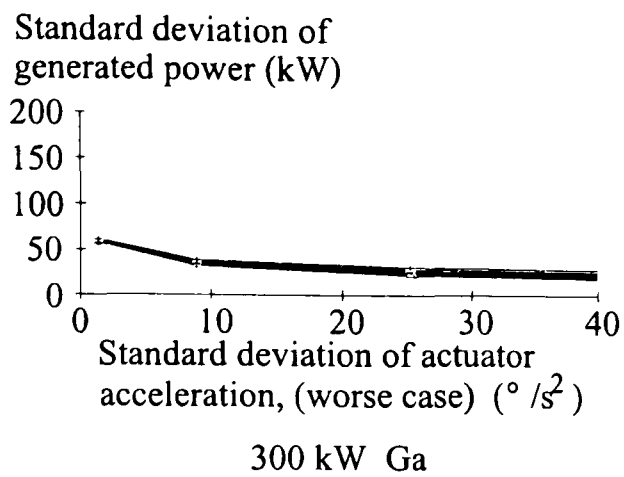
a) fast velocity – K

b) La

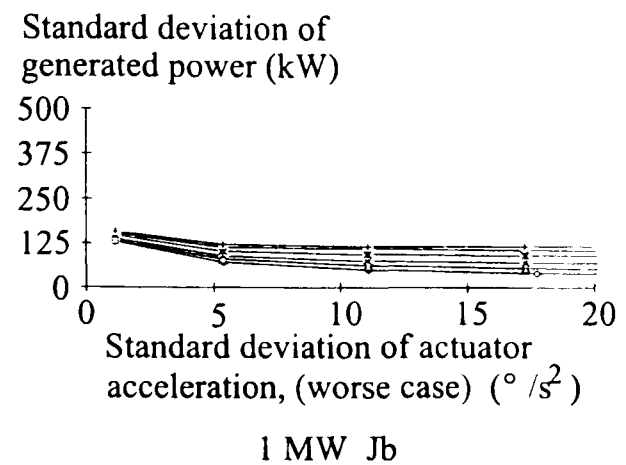
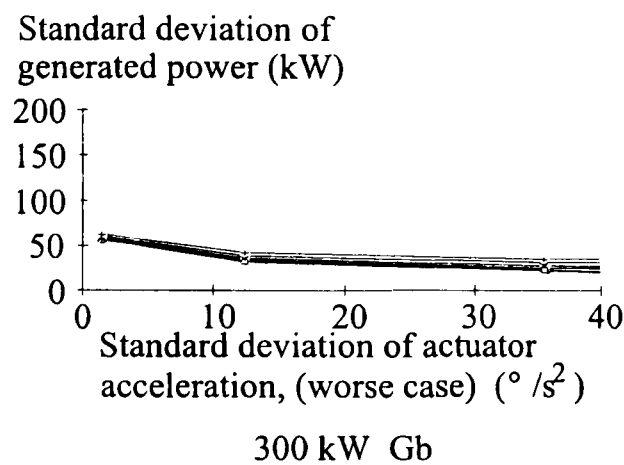
First drive-train mode

○ 2.0 rad/s ◓ 3.0 rad/s × 4.0 rad/s × 5.0 rad/s ◓ 6.0 rad/s × 7.0 rad/s

Figure 6.8 Worst case performance (actuator velocity) of three-bladed 1 MW machines for 23 m/s.



a) $1/2$ nominal $2\Omega_o$

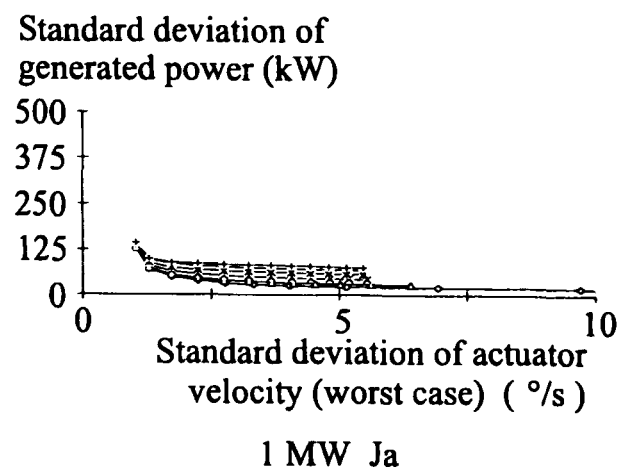
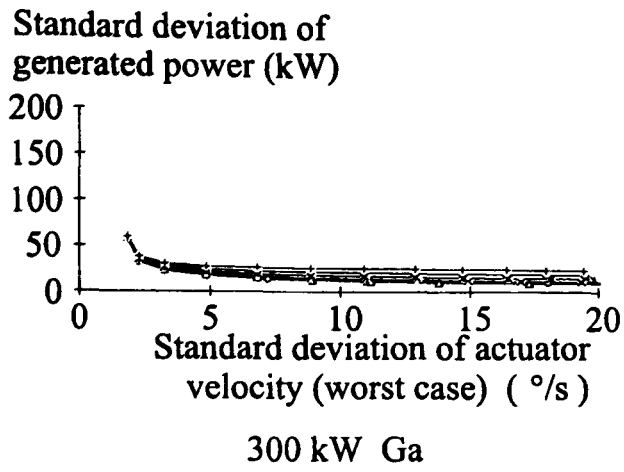


b) nominal $2\Omega_o$

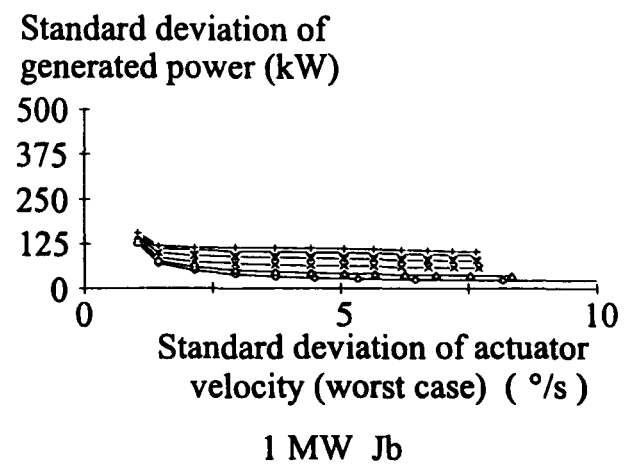
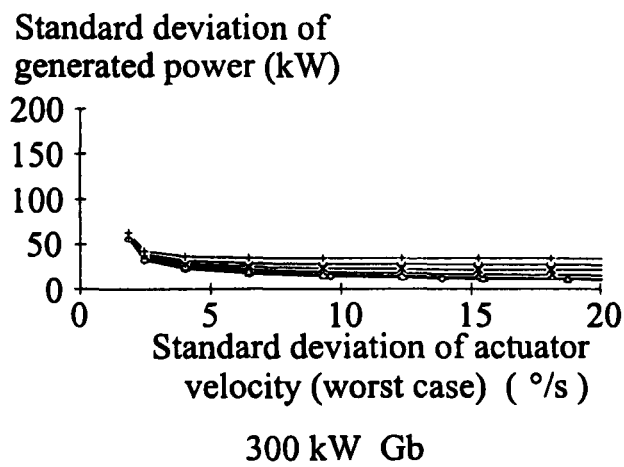
First drive-train mode

\diamond 2.0 rad/s
 \square 3.0 rad/s
 \times 4.0 rad/s
 \cdot 5.0 rad/s
 \circ 6.0 rad/s
 \leftarrow 7.0 rad/s

Figure 6.9 Worst case performance (actuator acceleration) of the two-bladed machines at 16 m/s



a) $1/2 \text{ nominal } 2\Omega_o$



b) nominal $2\Omega_o$

First drive-train mode
 -○- 2.0 rad/s -□- 3.0 rad/s -x- 4.0 rad/s -△- 5.0 rad/s -◇- 6.0 rad/s -▽- 7.0 rad/s

Figure 6.10 Worst case performance (actuator velocity) of the two-bladed machines at 16 m/s

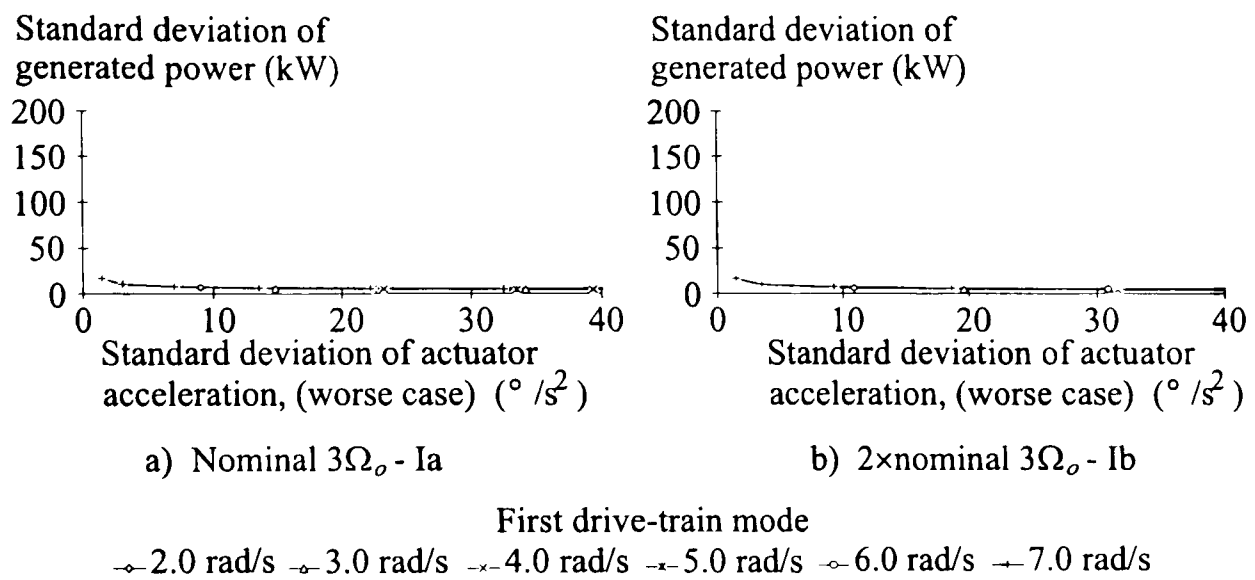


Figure 6.11 Worst case performance (actuator acceleration) of three-bladed machines for 23 m/s.

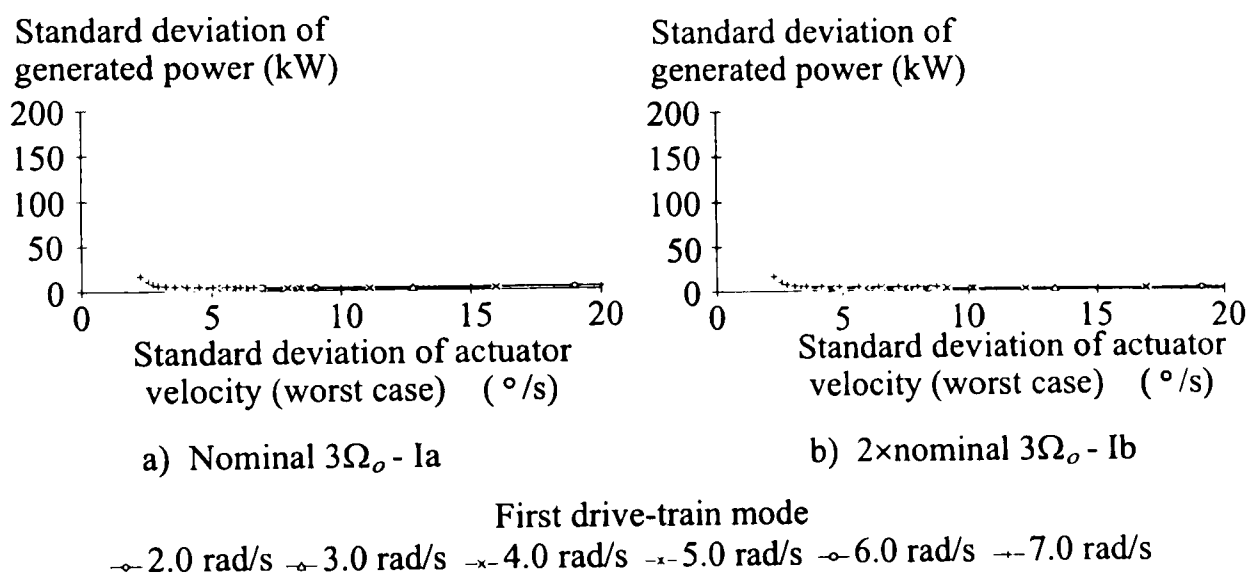
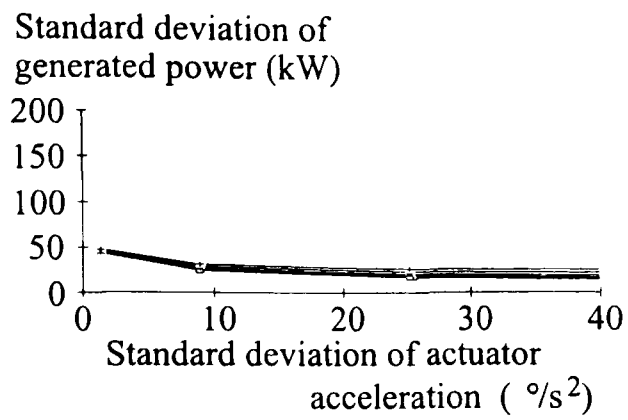
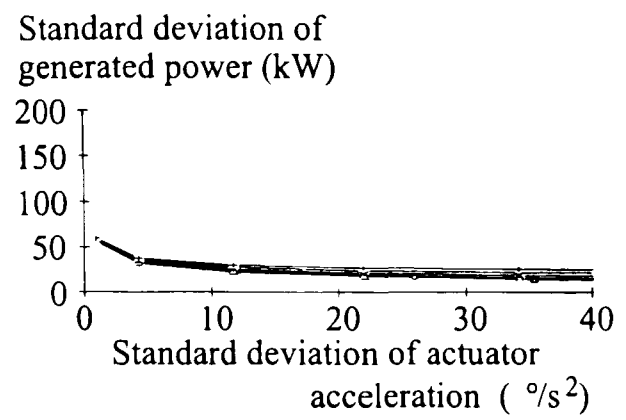


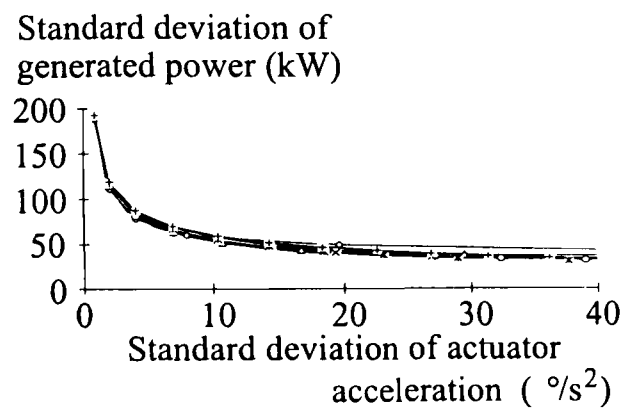
Figure 6.12 Worst case performance (actuator velocity) of three-bladed machines for 23 m/s.



Wind speed 12 m/s



Wind speed 16 m/s



Wind speed 23 m/s

First drive-train mode

○ 2.0 rad/s ◐ 3.0 rad/s × 4.0 rad/s × 5.0 rad/s ◐ 6.0 rad/s ··· 7.0 rad/s

Figure 6.13 Performance (actuator acceleration) of two-bladed ($1/2 \times$ nominal $2\Omega_n$) 300 kW machine Ga.

6.6 Conclusions

The second step to attaining the objective to lay the foundation for the control aspects of integrated design of wind turbines is achieved for part-span regulated wind turbines. The following conclusions are identical to those in Chapter 5.

- a) The attainable performance of power control, which is surprisingly large, is determined for the same machine configurations as considered in Chapter 5.
 - The performance of the three-bladed machines is significantly better (by an order of magnitude) than that of two-bladed machines.
 - The performance of two-bladed machines can be improved greatly by reducing the frequency of the first drive-train mode.
 - Three-bladed machines are insensitive to the first drive-train mode frequency.
 - Performance is weakly related to rotor angular velocity and the intensity of the transient loads at $n\Omega_o$.
 - As would be expected, performance is strongly related to controller activity for controllers with low cross-over frequencies.
 - Except at low frequencies, increasing controller the cross-over frequency requires a disproportionate increase in the rating of the actuator.
 - There is a limiting controller cross-over frequency, (roughly 2 rad/s) beyond which any improvement in performance is small.

The above conclusions hold for all the machines studied. Since many simplifying assumptions were made to allow linear analysis, a sample of the results has been validated by non-linear simulation, see Appendix C. Although ideal damping of the drive train is assumed, the methodology is readily adapted to configurations without ideal damping but many of the trends observed also apply to these configurations, see Chapter 8.

- b) The implications for controller design are also determined.
 - Attempting to improve performance by optimising the design of the controller can achieve little. (The gain in performance from increasing the cross-over frequency beyond 2 rad/s is marginal but requires an excessive increase in actuator capability).

In contrast to the results for full-span regulated machines set out in Chapter 5, the worst performance for tip-regulation does not occur at higher wind speeds. Therefore increasing the controller cross-over frequency in high wind speeds would not improve performance.

As in Chapter 5, any comparison between the performance of machines of different power rating should be treated with some caution due to the absence of detailed knowledge of actuators for 1 MW machines.

In this and the previous chapter consideration is restricted to conventional aerodynamic control devices. Whether any advantage accrues from non-conventional devices is investigated in Chapter 7.

7 Novel tip control devices

This chapter discusses the performance of some ‘novel’ tip control devices. One of the potential advantages of using a conventional tip control device over a full-span pitch-control device is the tip’s ability to be used as fast effective aerodynamic brakes and hence remove the necessity for one of the two compulsory emergency brakes. Tip length is dictated by the requirement for the tips to act in unison to brake the machine. The size of the remaining usually mechanical brake is dictated by the torque required to brake the rotor from the overspeed condition. If, however, the tips could work as independent brakes, the size and hence the cost of the mechanical brake could be reduced. In this case, the size of the brake is dictated by the maximum torque required to control the machine from the overspeed condition with one of the tips failing to deploy. Appendix F investigates the potential use of tips as independent aerodynamic brakes.

The performance of two novel tip devices for power control is considered in this chapter; firstly, the flying leading edge device (known as the FLEDGE) of Jamieson and Agius (1989); secondly independent blade control using the compliant tip device of Anderson *et al.* (1990). In each case, the concept of the control device is described and its ability as a fail-safe aerodynamic brake is discussed, and its performance as a power-control device is investigated.

7.1 The FLEDGE

The FLEDGE (flying leading edge) was conceived by Jamieson following wind-tunnel tests at Imperial College on a related tip device, the SLEDGE (sliding leading edge), (Jamieson and Agius, 1989). The steady-state aerodynamic performance of the fledge was compared to the conventional tip by Jamieson and Agius (1990). The fledge is similar to the Howden rotating tip (NWTC, 1994) except that its dynamics, the actuation system and the structural engineering are very different. An investigation of the design issues was undertaken by National Wind Turbine Centre at East Kilbride in a project funded by the Department of Environment (NWTC, 1994). The device was also tested under laboratory

conditions (Hunter *et al.*, 1993). NWTC (1994) investigated the sledge and two types of fledge, the off-set hinge fledge and the ball-joint fledge (see Figure 7.1), as braking devices and the ball-joint fledge as a power-control device. The sledge appears to be an effective brake (NWTC, 1994) and has the potential to be a control device (Havard, 1990). However, it suffers from severe blade loading at the tip joint (NWTC, 1994). The fledge with an offset hinge-line is a simple, low-cost air brake, but is not suited to control and so is not considered here. The most favourable braking and power control device of the three appears to be the ball-joint fledge. Its dynamics and braking behaviour are described in Appendix F. It is likely to cost a quarter of the equivalent tip system (NWTC, 1994).

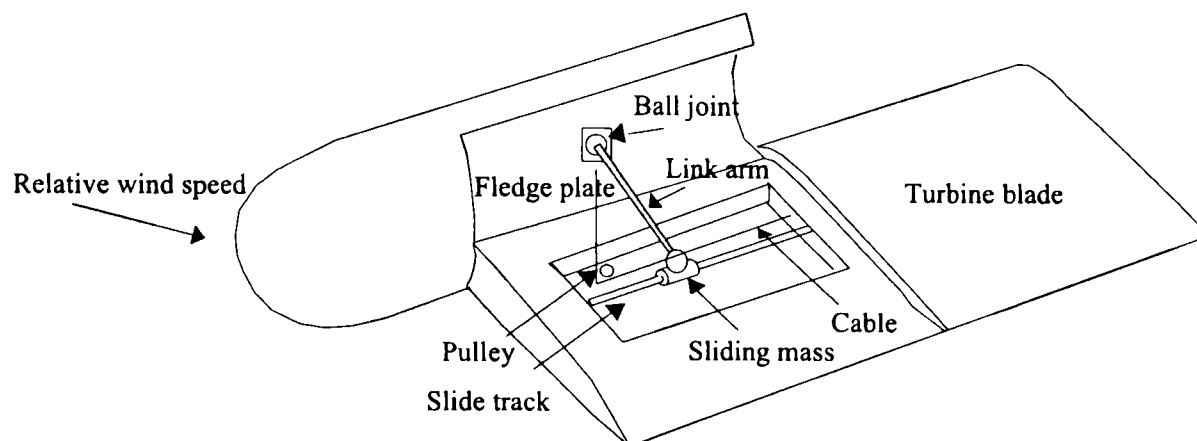


Figure 7.1 The ball joint fledge.

The ball-joint fledge consists of a portion of the upper blade surface (the fledge plate) at the tip of a blade, which rotates along the leading edge of the blade to present a high drag profile to the air flow. The fledge plate is attached by a rod to a mass on a slide track also situated locally at the tip as shown in Figure 7.1. The fledge plate is opened by inertial forces acting radially outwards on the actuating mass. To control the movement of the fledge, a cable is attached to the fledge plate as shown in Figure 7.1. The cable is passed around a pulley fed back to the hub to a hydraulic damper as described in Appendix F.

The dynamics of the fledge are described in Appendix F. Since the fledge must act as an effective brake, prior to investigating its use as a tip control device, a suitable geometry and dimensions for the fledge must be determined for that use.

This chapter uses the results of Appendix F to consider power-control performance of a wind turbine with fledges. The geometry and the masses used here are shown in Table 7.1.

Fledge plate	length	1.5 m
	chord	100 %
	mass, M	10 kg
Sliding mass, m		5 kg
Distance from hinge to sliding mass, r		0.3 m
Link rod length, R_o		15.25m
Height offset of hinge, h		0.04 m

Table 7.1 The geometry and the masses of the fledge mechanism.

7.1.1 Effect of new rotor design on the drive-train dynamics

The fledge device is smaller in length than the conventional tip. For this reason this sub-section first discusses the influence of reducing the size of conventional tips on control performance and then discusses the influence of using fledges instead of tips on the drive-train dynamics.

7.1.1.1 Reducing the tip size

One of the motivations for considering tips and other small power limiting devices on the NWTC project is their potential for reducing actuator loads. One method of reducing tip size is to design the rotor so that the operational curve is nearer stall in the higher wind speeds. The Howden HWP330/33 rotor is unusual as it does not stall regulate until the power output is above 800 kW. Hence NWTC (1994) designed a new 33 m diameter stall-regulated rotor (NWTCCON33) rated at 450 kW with a synchronous speed of 38 rev/min to investigate the aerodynamic behaviour of the fledge. The length of the tip for this new rotor is 1.5 m, which is here compared to the 2.5 m tip of the HWP330/33. The curves of tip angle versus wind speed for rated power for the HWP330/33 and NWTCCON33 rotors are compared in Figure 7.2 and the effect on the performance of the wind turbine is shown in Figure 7.3. (The standard deviations shown in Figure 7.3 are calculated by the same methodology as those in Chapters 5 and 6, using the partial derivatives in Table 7.2.) As would be expected with three bladed tip-regulated machines (see Section 6.5), the worst performance occurs at around rated wind speed. Since the tips of the NWTCCON33 rotor are considerably shorter, they have less inertia, and hence the achievable actuator accelerations and velocities would be expected to be greater than those for the HWP330/33 machine. Therefore, making direct comparisons between the two rotors is difficult. The predicted performance of the NWTCCON33 rotor is interpreted to be no worse than that of the Howden HWP330/33, see Figure 7.3.

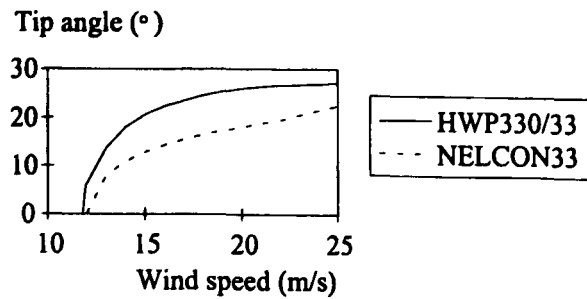


Figure 7.2 The curves of tip angle versus wind speed for rated power for the NWTCCON33 and Howden HWP330/33 rotors.

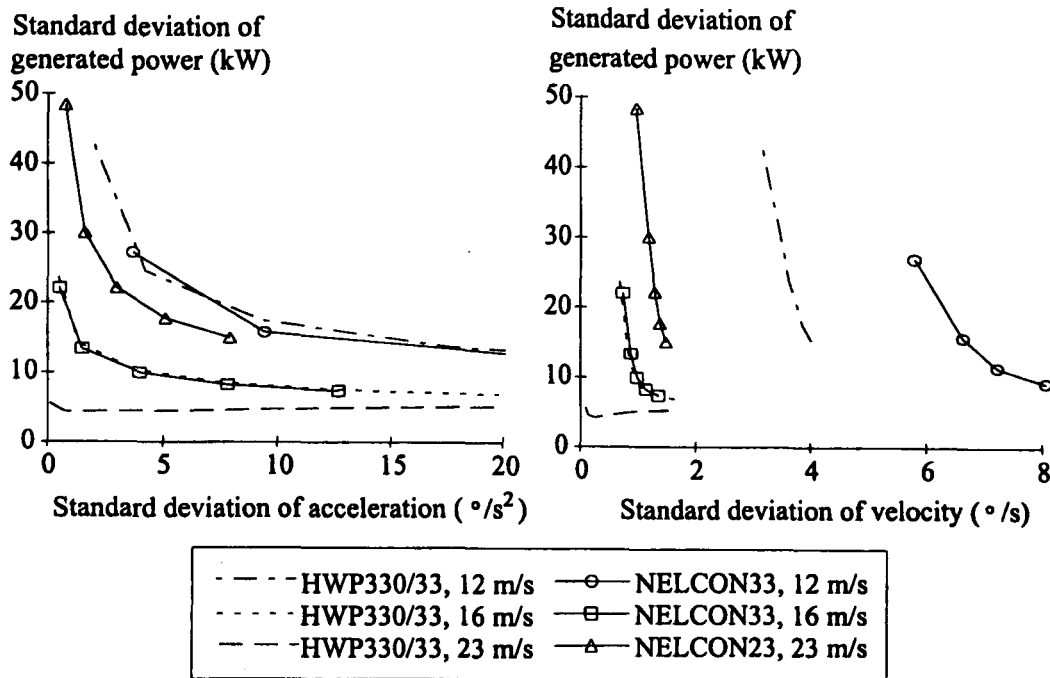


Figure 7.3 The performance of the NWTCCON33 and Howden HWP330/33 rotors.

7.1.1.2 Replacing tip with fledge mechanism

Since the use of the fledge mechanism obviates the need for hydraulic mechanism along the blade, it significantly reduces the inertia of the rotor. It is assumed here to be reduced to 10^5 kgm^2 if the NWTCCON33 blades are made of wood/epoxy composite. (The value 10^5 kgm^2 is rather low according to Mercer and Quarton (1992); who suggest $1.56 \times 10^5 \text{ kgm}^2$.) The effective rotor inertia now includes the inertia of the fledge devices and so from (F.15) it is adjusted to

$$I_1' = 3M(\tau^2 + r^2(1 - \cos\theta)^2) + 3m(R_o + s)^2 + I_1 \quad (7.1)$$

where $\tau = (R_o + R \cos \psi_o)$. (The variables are defined in Appendix F.)

Using (7.1), the rotor inertia when the fledge plate is closed becomes $1.109052 \times 10^5 \text{ kgm}^2$. As expected the reduction of the rotor inertia increases the frequency of the first drive-train mode, from 7.35 rad/s to 9.62 rad/s and decreases its damping ratio from 0.44 to 0.34. To avoid the problem of the first drive-train mode being too close to $3\Omega_o$ (11.94 rad/s), it is assumed that the stiffness of the low-speed shaft is also reduced to

6.702×10^6 Nm, so that the first drive-train mode is near its original value, 7.356 rad/s, safely between $1\Omega_o$ and $3\Omega_o$. The damping of the first drive-train mode is now further reduced to 0.257 and the drive-train transfer function is

$$G(s) = \frac{763}{(s^2 + 3.779s + 54.11)(s^2 + 29.55s + 6780)} \quad (7.2)$$

The aerodynamic gain, *i.e.* the rate of change of torque with respect to fledge angle is calculated from aerodynamic tables provided by NWTC for the mean wind speeds 16 m/s and 23 m/s. The aerodynamic tables are listed in Appendix G. However, the aerodynamic wind-tunnel test data on which the tables are based are executed at a higher Reynolds number when the fledge plate is closed, ($\theta = 0$) compared to the other fledge angles. This lack of aerodynamic information means that the aerodynamic behaviour of the fledge in wind speed just above rated is rather uncertain. As in the simulation work done by NWTC (1994) this mismatch at wind speeds just above rated is compensated for by using (7.3)¹ to calculate the partial derivatives for 12 m/s for the linear analysis. (The non-linear simulation used the torque tables provided by NWTC.)

$$\frac{\partial T}{\partial \theta_{\text{deg}}} = -(2 \times 104.3096(\theta_{\text{deg}} - 5) + 3178.926) / \Omega \quad (7.3)$$

The partial derivatives of aerodynamic torque with respect to fledge angle used to calculate performance are shown in Table 7.2 for mean wind speeds 12 m/s, 16 m/s and 23 m/s.

Wind speed (m/s)	HWP330/33 Tip			NWTC CON33 Tip			Fledge		
	Pitch angle (°)	$\partial T/\partial V$ (Ns)	$\partial T/\partial \beta$ (Nm/°)	Pitch angle (°)	$\partial T/\partial V$ (Ns)	$\partial T/\partial \beta$ (Nm/°)	Pitch angle (°)	$\partial T/\partial V$ (Ns)	$\partial T/\partial \beta$ (Nm/°)
12	6.07	18229	-1835	0.00	11553	-638	0.00	10854	-536
16	22.10	6062	-4606	14.22	5640	-4025	10.17	2563	-1692
23	26.65	596	-6501	20.50	6771	-6862	21.51	3432	-2256

Table 7.2 Aerodynamic torque partial derivatives.

7.1.2 Effect of fledges on actuator capability

Initially, it would be expected that the fledge mechanism has considerably greater actuator capability than the tip. Problems with space in the actuator design can be avoided by situating the fledge actuation system in the hub instead of at the tip as described in Appendix F. The fledge moving parts are considerably lighter and hence have less inertia

¹ This is calculated from a polynomial fit of the aerodynamic tables which is corrected for the mismatch in Reynolds number and then smoothed.

than a conventional tip. Hence, the actuator capabilities would be expected to increase. However, the modelling of the fledge described in Appendix F ignores flapping loads. The effect of blade flapping on the inertia loads and their potential to cause the cable actuator system to become slack has been investigated by McKenna (1992) and Mercer and Quarton (1992) for NWTC (1994). (Although they considered a slightly different fledge geometry and their machine is attached to the British grid, it is assumed that their result, that flapping loads can be ignored, would also hold for the type of fledge considered here.) McKenna (1992) found that only in very exceptional wind conditions would there be any risk of loss of cable tension as the predicted flapping loads were considerably smaller than the aerodynamic moment and the inertia forces. However, McKenna (1992) also found that there is an increase of noise in the tension in a cable which may effect the capability of the actuator. Since the actuator may be more susceptible to flapping loads it is assumed to have the same bandwidth as a conventional tip machine. Therefore the actuator dynamics are approximated by a first-order transfer function with a bandwidth of 23 rad/s. The extent to which the flapping loads affect the capability of the actuator is not clear, but it is thought that the achievable maximum actuator accelerations and velocities would be slightly greater for the fledge compared to the tip.

7.1.3 Comparison of performance of fledges and conventional tips

The fledge device is likely to cost a quarter of the equivalent tip system (NWTC, 1994). It has the advantage that it is predicted from steady-state calculations to suffer lower axial bending moments at the tip-joint than the tip during power regulation, see Figure 7.4 (NWTC, 1994). This is because the flying tip produces a sudden load reversal from positive to negative axial bending moment at the tip-joint around rated wind speed, whereas the axial bending moment for the fledge is almost constant. Hence, the fledge will induce less flapwise fatigue when used for power control. The fatigue damage problems associated with the flying tip are due to controlling the power by the rotating the tip to reduce the flow incidence which reduces the lift to slight negative values whilst maintaining constant low drag. The change in lift dominates the change in axial bending moments seen in Figure 7.4. The fledge, on the other hand, increases the drag to produce a braking torque whilst maintaining constant lift, effects the tangential bending moments instead of the axial ones.

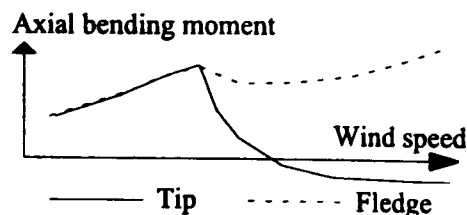
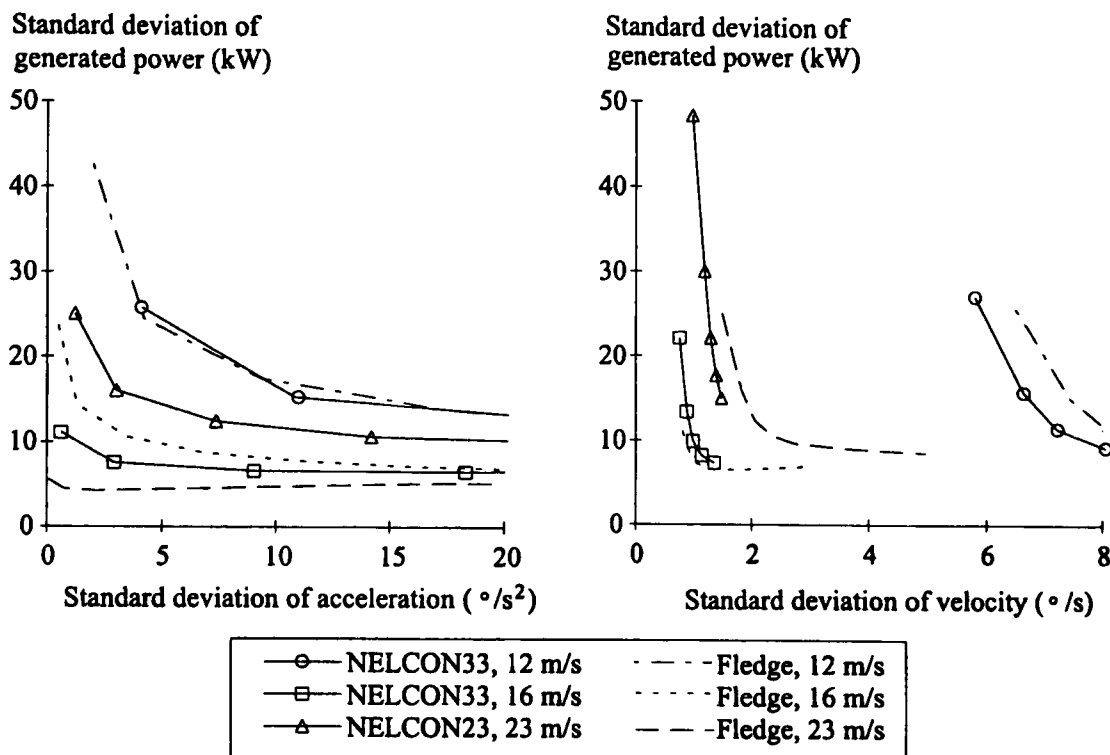


Figure 7.4 Axial bending moments at the tip joint for steady-state power regulation (NWTC, 1994).



(The standard deviations were calculated by the same methodology as described in Appendix C, using the partial derivatives shown in Table 7.2.)

Figure 7.5 The performance of the fledge compared to the tip.

The performance predicted by spectral analysis of a machine with fledges compared to conventional tips is shown in Figure 7.5. If the actuator capabilities and pitching linkages are the same then the performance of the fledges is slightly worse than conventional tips. It should be noted that the worst performance is at wind speeds just above rated, where the aerodynamic behaviour of the fledge is uncertain. However, taking into account the fledges' expected greater actuator capability it is considered that the performance of a fledge-controlled machine appears to be similar to that with conventional tips.

The ability of the fledge to be used as a power control device has been verified by non-linear simulation as part of the NWTC project (1994).

7.1.4 Summary of fledge performance

Benefits of the fledge

- The fledge is likely to cost less, perhaps a quarter of the equivalent tip system (NWTC, 1994).
- The fledge moving parts have a lower pitch inertia than the conventional tip device, and hence because of lower actuating force has the potential for higher actuator bandwidth and higher actuator velocities and accelerations. (However, the actuator capabilities may be restricted due to blade flapping.)
- There is less limitation on the size of the actuator as it is situated in the hub rather than in each blade.
- There appear to be fewer potential problems with ensuring the devices act in unison.
- The steady-state aerodynamic loading implies that the fatigue load cycling on a fledge is less severe (NWTC, 1994).

Disadvantages of the fledge

- The steady-state analysis implies that the blade root bending moment is higher on a fledge than on a tip (NWTC, 1994).
- The actuator may be more susceptible to flapping loads (McKenna, 1992).
- Large torsional bending moments are experienced around the tip joint when the fledge is fully deployed as a brake (NWTC, 1994).

The fledge is likely to be highly effective as an over-speed braking device and as a means of power regulation. The power control performance of a machine with fledges seems to be comparable with one with conventional tips, although this is very dependent on the aerodynamic behaviour of the fledge in just above rated wind speeds and on the expected extra capability of the actuator system. Fatigue damage due to variations in the axial bending moment during power control is predicted to be greatly reduced and the device is considered to be cheaper to build.

7.2 Independent blade control

The performance and design of conventional power control systems is thoroughly investigated in Chapters 5 and 6, and Appendix C. There the pitch of the blades is varied, with all the blades acting in unison, in response to the error between measured generated power and rated power.

Another approach to the control of wind turbines might be independent blade control. In this context, independent blade control refers to the situation when the control of each blade through its own independent actuator is driven by a feedback loop in response to a separate measurement made locally at its blade. The angle of pitch of each blade would be adjusted in response to the load it experiences and independently from the pitch of the other blades. Independent blade control has the following potential advantages.

- i) It reduces drive-train torque fluctuations induced by wind turbulence. The control response to drive-train loads due to wind turbulence is faster than conventional power control, since the control action is enacted directly on the rotor rather than of after the transients have propagated through the power train.
- ii) It regulates the torque transients experienced by a blade, such as the cyclic loads at $1\Omega_o$ which cannot be detected from generated power and so cannot be controlled by power control.

The load transients in both the above are induced by the interaction of the effective wind field with each blade, as explained in Chapter 2 and Appendix A.

In independent blade control a measurement local to the blade is required of its interaction with the wind field *i.e.* ideally an indirect measurement of the effective wind speed, w , is required. Independent blade control sets the actual pitch angle, β_a , to the required pitch angle, $G(w)$, at which power output would be rated, locally at each tip thereby smoothing out the transient loads induced on the blade and so the wind turbine. The controller acts on the error ($\beta_a - G(w)$) to provide a demanded pitch angle, β_d which is fed to the actuator.

One example of independent blade control which is discussed here is independent tip control, namely, compliant tip control. Using the tip has the advantage that the tip section of a blade operates at a high tip-speed ratio and remains nominally unstalled in all wind speeds.

The purpose of the latter part of this chapter is to compare the performance of independent tip control, both on its own and in combination with power control, to power control alone. The discussion is divided into two parts; in the first, the dynamics of the compliant tip are described and how they may be exploited for independent tip control; in the second, the dynamics of independent tip control are analysed with a view to optimise and assess its performance compared to conventional tip control. A simulation based on the Howden HWP330/33 wind turbine with the actuator replaced by the compliant tip actuator system, described in Appendix F, and the control system replaced by a continuously acting control system is used to verify the above analysis Leithead *et al.* (1992b), (Anderson and Campbell, 1992).

7.2.1 The compliant tip concept and aerodynamics

Pitch compliance is added to the tip by setting the pitch axis behind the aerodynamic centre² while maintaining the same angle of attack, see Figure 2.7. The tip is unstable and without any pitching moment the tip automatically fails to the braking position. (The fail-safe braking behaviour of the compliant tip has been validated in wind tunnel tests by Richon and Anderson (1993)).

Central to any independent blade control is a suitable measurement of the effective wind field affecting the blade. For compliant tips, one such measurement is the aerodynamic pitching moment on the blade, $Maero$ (Anderson and Campbell, 1992). As long as the tip speed ratio, $\Omega R/V$, is high, *i.e.*, ϕ is small, it follows from the wind triangle in Figure 2.7 that ϕ is approximated by

$$\frac{V}{V_R} \approx \alpha + \beta_a = \phi \quad (7.4)$$

Therefore a change in wind speed at the tip, V , is proportional to a change in the angle of attack and $Maero$ is a linear function of V as long as the lift is proportional to the angle of attack, *i.e.* the tip section remains unstalled (Anderson and Campbell, 1992).

An applied pitching moment from the actuator is used to compensate for changes in the aerodynamic moment so that the tip produces the correct amount of lift, and hence the aerodynamic pitching moment, $Maero$, to achieve rated power.

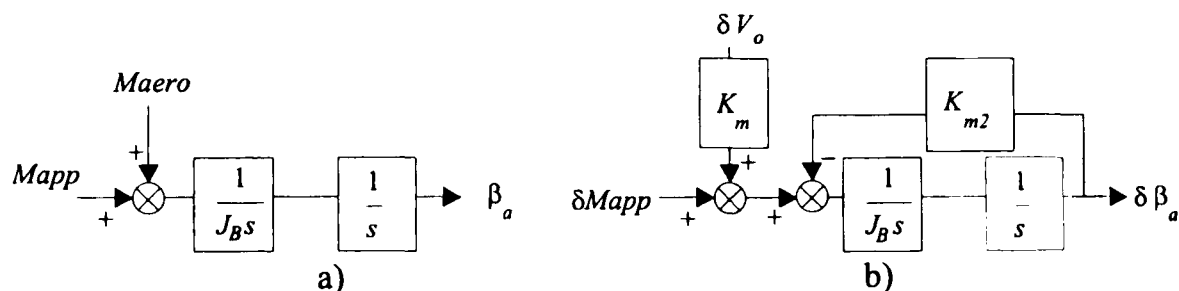


Figure 7.6 Linearising actuator interaction with aerodynamics.

Although, $Maero$ cannot be measured directly it can be estimated from measurements of the moment applied to the blade by the actuator, $Mapp$, and the pitch acceleration, $\ddot{\beta}_a$. The dynamics at the tip are

$$Maero = J_B \ddot{\beta}_a - Mapp \quad (7.5)$$

² The aerodynamic centre is the position at which the lift may be considered to act.

where J_B is the blade inertia. $Maero$ is a function of β_a and the wind speed seen by a tip, V_o . The relationship between $Maero$ and $Mapp$ is depicted in Figure 7.6a which may be linearised as in Figure 7.6b where

$$K_{m2} = -\frac{\partial Maero}{\partial \beta_a} \quad ; \quad K_m = \frac{\partial Maero}{\partial V_o}. \quad (7.6)$$

7.2.2 Estimation of the required tip angle

In this sub-section the estimation of the required tip angle for rated power for the current wind speed is investigated (*i.e.* “on-design” operating conditions). Two variables are available from the actuator, the tip angle and aerodynamic moment, $Maero$, calculated from measurements of the tip acceleration and the applied moment, $Mapp$, using (7.5). Hence, the estimate of the required tip angle for rated power for current wind speed is a function $L(\beta_a, Maero(V_o, \beta_a))$. Since L is the required tip angle for the current wind speed, it should change only in response to a change in wind speed and not in response to a change in tip angle, *i.e.*

$$\frac{dL(\beta_a, Maero)}{d\beta_a} = \frac{\partial L(\beta_a, Maero)}{\partial \beta_a} + \frac{\partial L(\beta_a, Maero)}{\partial Maero} \cdot \frac{\partial Maero(\beta_a, V_o)}{\partial \beta_a} = 0$$

Hence

$$\frac{\partial L(\beta_a, Maero)}{\partial \beta_a} = -\frac{\partial L(\beta_a, Maero)}{\partial Maero} \cdot \frac{\partial Maero(\beta_a, V_o)}{\partial \beta_a} \quad (7.7)$$

One implication of (7.7) is that in the neighbourhood of an on-design operating point, with β_a and $Maero$ belonging to a small interval enclosing that operating point

$$L(\beta_a, Maero) = N(Maero - f(\beta_a)) \quad (7.8)$$

where

$$\frac{df(\beta_a)}{d\beta_a} = \frac{\partial Maero(\beta_a, V_a)}{\partial \beta_a}$$

with V_a the on-design value of wind speed corresponding to β_a . Hence, when close to on-design operating conditions, there exists a function $f(\beta_a)$, for all β_a , such that the required tip angle, β_r , for rated power for the current wind speed is

$$\beta_r \approx N(Maero - f(\beta_a)) \quad (7.9)$$

along the on-design operating curve. It follows that

$$Maero(\beta_a, V_o) \approx N^{-1}(\beta_r) + f(\beta_a) \quad (7.10)$$

This relationship is investigated using the simulation of the compliant tip. The relationship between $Maero$ and the tip angle whilst on design, *i.e.* $\beta_a = \beta_r$, is plotted in Figure 7.7 and the tip angle varied with the wind speed kept constant so that curves of

constant wind speed intersect the on-design curve. (The data used to produce this figure is supplied in Table 7.3). The function $f(\beta_a)$ is found by smoothly joining the curves of constant wind speed and subsequently $N^{-1}(\beta_r)$, is determined from the on-design curve using (7.11).

$$N^{-1}(\beta_r) = Maero(\beta_r, V_o) - f(\beta_r) \quad (7.11)$$

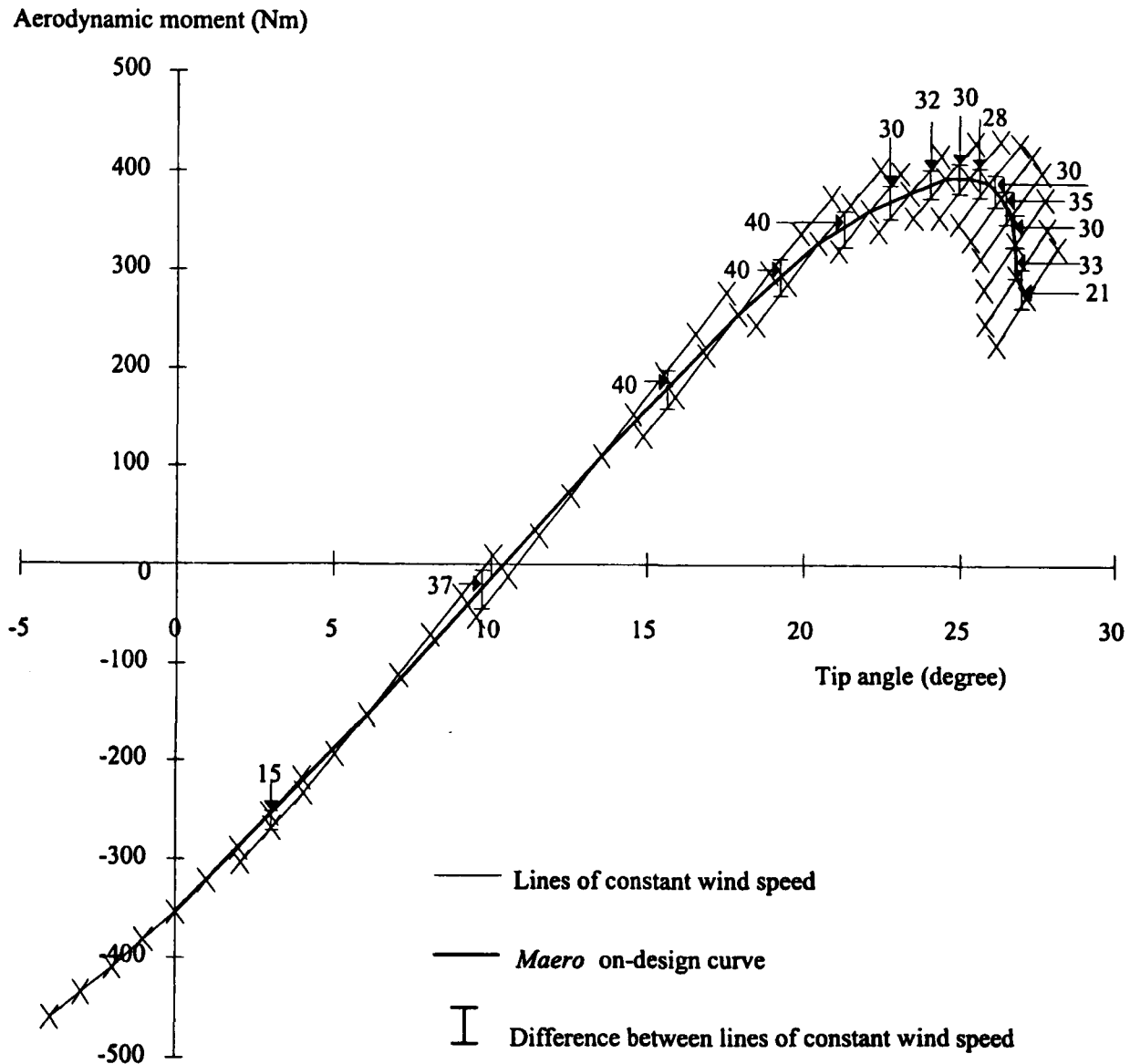


Figure 7.7 *Maero* and the tip angle for various constant wind speeds.

The function $f(\beta_a)$ is depicted in Figure 7.8 together with both on-design and off-design³ data and is a good representation for both. The function $N^{-1}(\beta_r)$ is also depicted in Figure 7.8. These functions can be adjusted so that the intersect of the β_a axis by $f(\beta_a)$ may be freely chosen.

³ Off-design - operating points that are in a small neighbourhood of the on-design points.

Wind speed, V (m/s)	Tip, β ($^\circ$)	$Maero$ ($V, \beta-4$)	$Maero$ ($V, \beta-3$)	$Maero$ ($V, \beta-2$)	$Maero$ ($V, \beta-1$)	$Maero$ (V, β)	$Maero$ ($V, \beta+1$)	$Maero$ ($V, \beta+2$)	$Maero$ ($V, \beta+3$)	$Maero$ ($V, \beta+4$)
11.6	0	-460.57	-434.98	-409.38	-381.52	-353.66	-321.68	-289.7	-253.81	-217.92
12	6.06	-304.06	-268.76	-233.18	-193.22	-153.2	-112.2	-71.26	-31.15	8.98
13	13.53	-52.97	-11.85	29.15	70.4	111.87	153.37	194.9	236.59	277.93
14	17.88	88.18	130.28	172.37	214.69	257.13	298.78	338.54	376.43	411.93
15	20.46	159.91	202.89	245.91	288.39	329.7	368.78	405.52	439.22	467.83
16	22.1	193.06	236.86	280.37	322.53	362.76	400.49	435.59	465.99	488.56
17	23.37	211.21	255.63	299.3	341.49	381.3	418.67	452.8	480.89	499.49
18	24.5	224.24	269.37	313.49	355.67	395.37	432.56	465.87	492.02	507.66
19	25.3	222.87	268.69	313.48	356.36	397.12	434.74	468.73	495.59	511.95
20	25.92	213.7	260.26	306.06	350.17	391.81	430.88	466.07	494.87	514.2
21	26.32	194.83	242.09	288.96	334.48	377.93	418.66	456.05	48.31	512.14
22	26.64	171.34	219.29	267.19	314.27	359.50	402.29	442.16	477.94	506.89
23	26.76	137.25	185.71	234.41	282.99	330.41	375.77	418.48	457.96	493.02
24	26.79	100.02	149.31	198.71	248.12	297.04	344.58	390.02	432.62	471.65
25	27.13	75.65	125.73	175.74	225.87	276.07	325.25	372.72	417.42	459.14

Table 7.3 The values of the aerodynamic moment, $Maero$ (Nm), varying with tip angle at constant wind speed.

The required tip angle resulting from a simulation, whilst using the estimate $N(Maero - f(\beta_a))$, is shown in Figure 7.9a. From Figure 7.8, it can be seen that the gradient of $f(\beta_a)$ is almost constant with a value of 2292 Nm/rad. Choosing $f(\beta_a)$ to be zero when β_a is zero, a new estimate for tip angle is $Q(Maero/2292 + \beta_a)$ and the simulated required tip angle using this new estimate is shown in Figure 7.9b. The estimates of the required tip angle in Figure 7.9 are reasonable.

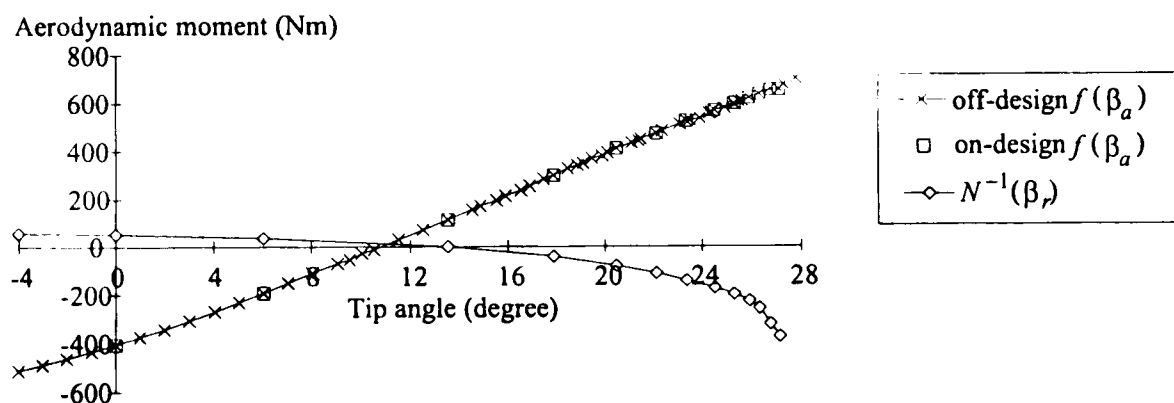


Figure 7.8 The functions $f(\beta_a)$ and $N^{-1}(\beta_r)$.

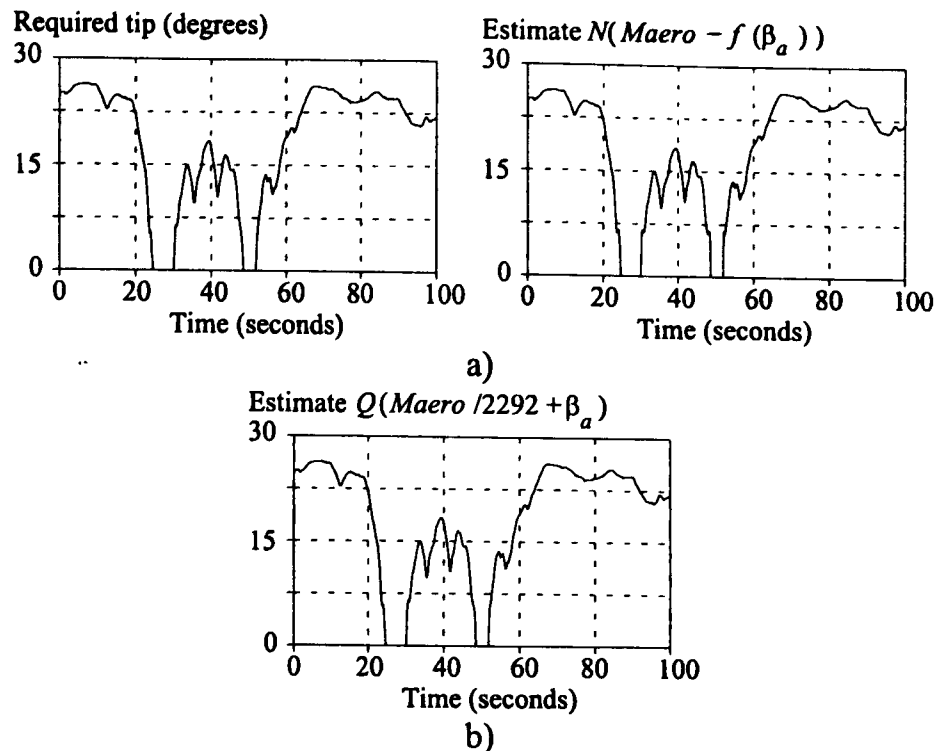


Figure 7.9 The required tip angle and estimates $N(Maero - f(\beta_a))$ and $Q(Maero/2292 + \beta_a)$.

7.2.3 Comparison of compliance tip control with power control

The performance of a wind turbine with independent tip control can only be compared with power control if similar tip accelerations and velocities are demanded of the actuator. The two types of control action are expressed in similar terms below, so that they can be compared and combined as required.

Both the control systems can be thought of as controlling drive-train torque fluctuations about rated torque. The two control systems each have their own method of measuring the fluctuations (see Figure 7.10). Power control measures the power output of the machine, P , and compares it with rated power, P_o , and the error is used for control action. With compliant tip control on the other hand, the applied moment, the blade pitch angle and acceleration are measured to estimate the required tip angle and $(\beta_a - L(\beta_a, Maero(V_o, \beta_a)))$ is used for the error for control action. In both cases the error is used to update the demanded tip angle, β_d , via a controller.

The two control systems are subject to different disturbances. The wind seen by the tip and that seen by the whole rotor are not identical, see Figure 2.6. At low frequencies the wind speeds do not correlate exactly while at higher frequencies the strengths of the spectral peaks differ. The limiting factor on the control system is the saturation of the actuator by high frequency disturbances, (see Appendix C). Hence, if the high frequency spectral peaks on $(\beta_a - L(\beta_a, Maero))$, in comparison to those on power error, are less prone to cause saturation of the actuator then there would be advantage in using compliant tip control.

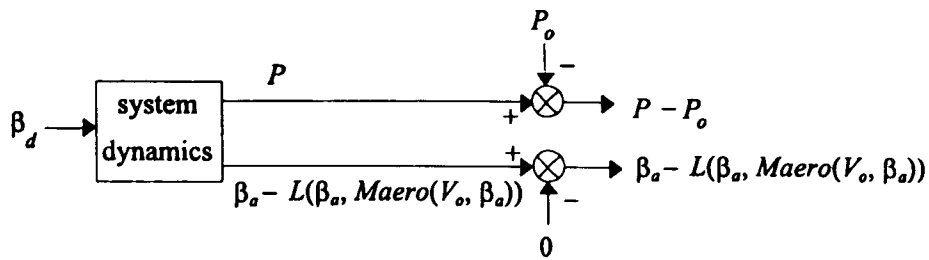


Figure 7.10 Two different types of control system.

a) *Power control*

The system for power control is shown in Figure 7.11. Linearising the system for power control about some operating point, as in Section C.1.1, it can be rearranged as in Figure 7.12, where D is the power-train transfer function incorporating $\partial T/\partial\beta_a$.

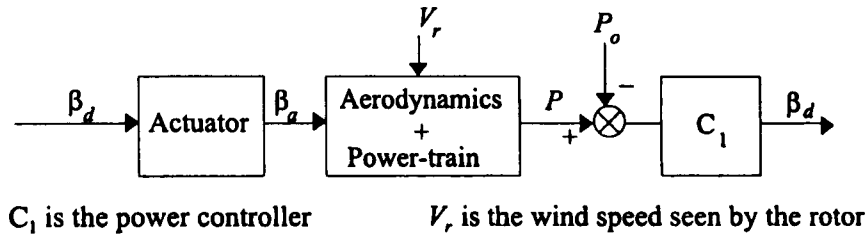


Figure 7.11 The system for power control.

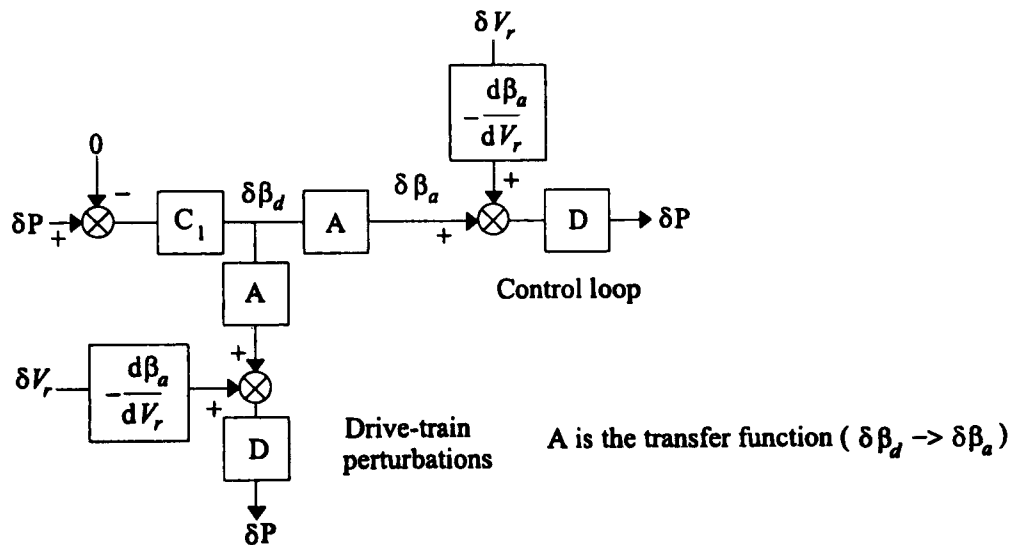


Figure 7.12 Linearised system with power control.

b) *Independent tip control*

The system for independent tip control is shown in Figure 7.13. Similarly to power control the system can be linearised as in Figure 7.14.

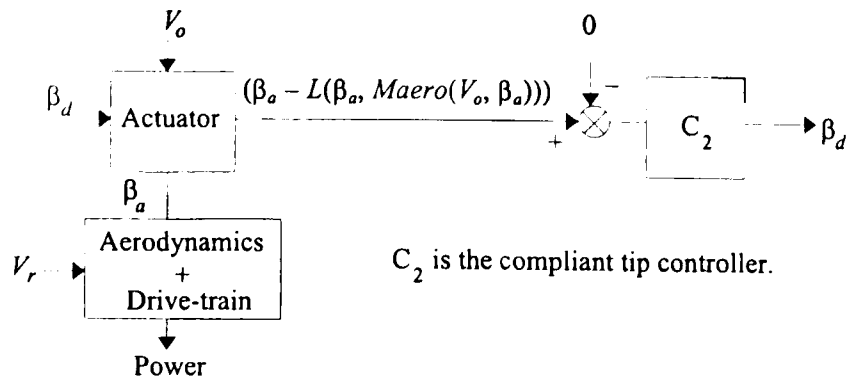


Figure 7.13 The system for independent tip control.

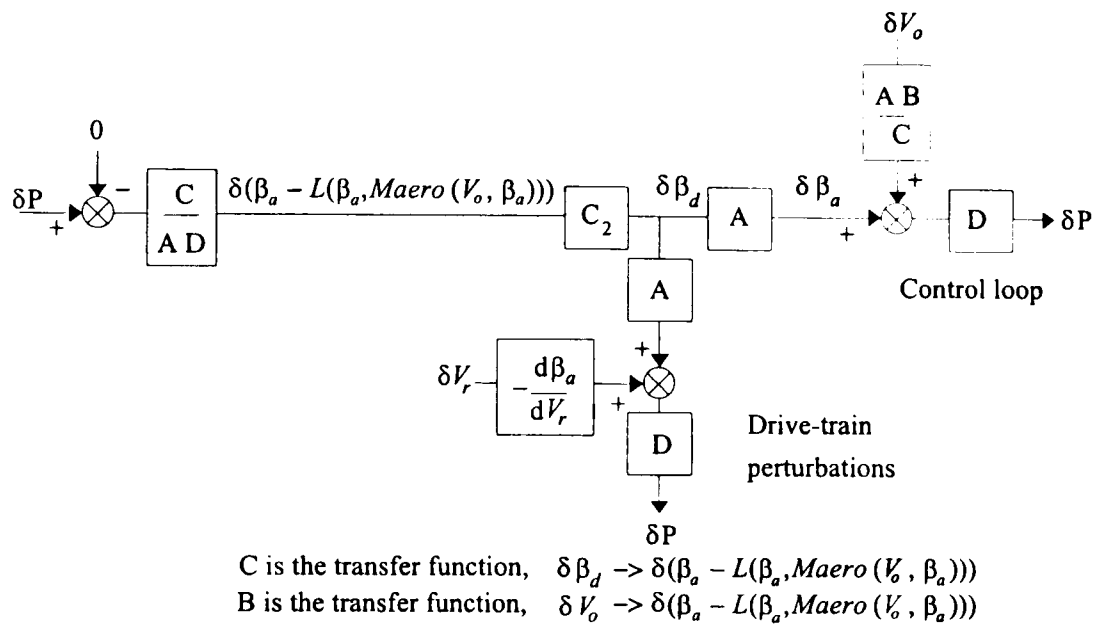


Figure 7.14 Linearised independent tip control system.

The two control loops, $\delta P \rightarrow \delta P$, are identical if the two controllers are related

$$\text{by } C_2 = \frac{AD}{C} C_1.$$

Since the wind speed V_o is not identical to V_r , independent tip control on its own cannot maintain rated power, but requires to be combined with a co-ordinating power control loop. Hence the power control loop is required to ensure the appropriate regulation of power particularly at low frequency. Therefore for independent tip control the dynamics of the control system are more complex as there are now two control actions, one acting locally at the blade and the other acting on the total response of the drive train, which must be co-ordinated. For a control system which combines both power control and independent tip control the error signals should be combined as in Figure 7.15.

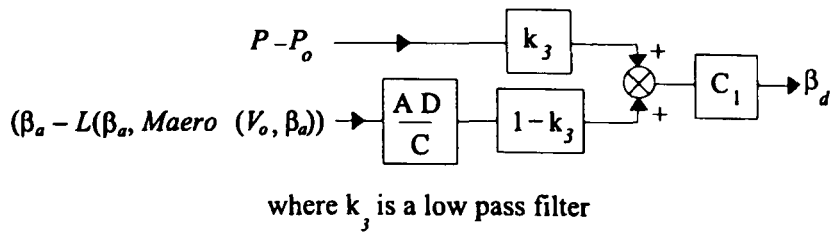


Figure 7.15 Combining power and independent tip control.

The low pass filter k_j allows the controller to maintain rated power by allowing $(P - P_o)$ control action at low frequencies where the wind speed seen by the tip is not the same as the wind speed seen by the rotor. The low pass filter also allows individual blade control to dominate at high frequency.

Whether independent tip control can be used to achieve better performance depends solely on the high frequency noise content of $\delta\beta_d$ and its effect on the actuator. The spectral peaks due to rotational sampling are the most dominant of the high-frequency disturbances affecting a wind turbine. Therefore, the main indicator of comparative performance is the transfer function $(A B)/C$ (which varies with wind speed).

To investigate the transfer function $(A B)/C$, first consider the transfer function C.

Since,

$$\delta(\beta_a - L(\beta_a, Maero)) = \delta\beta_a \left(1 - \frac{\partial L}{\partial \beta_a}\right) - \frac{\partial L}{\partial Maero} \delta Maero. \quad (7.12)$$

and using (7.5) it follows that

$$C = A \left(1 - \frac{\partial L}{\partial \beta_a}\right) - \frac{\partial L}{\partial Maero} (J_B T_{\beta_d \ddot{\beta}_a} - T_{\beta_d Mapp})$$

where $T_{\beta_d \ddot{\beta}_a}$ is the transfer function from $\delta\beta_d$ to $\delta\ddot{\beta}_a$ and $T_{\beta_d Mapp}$ is the transfer function from $\delta\beta_d$ to $\delta Mapp$. However, from Figure 7.16 with δV_o equal to zero it can be seen that

$$A = \frac{T_{\beta_d \ddot{\beta}_a}}{s^2} \quad \text{and} \quad A = \frac{T_{\beta_d Mapp}}{J_B s^2 + K_{m2}}$$

Hence

$$\begin{aligned} C &= A \left(1 - \frac{\partial L}{\partial \beta_a} - J_B s^2 \frac{\partial L}{\partial Maero} + (J_B s^2 + K_{m2}) \frac{\partial L}{\partial Maero}\right) \\ &= A \left(1 + \left(\frac{\partial Maero}{\partial \beta_a} + K_{m2}\right) \frac{\partial L}{\partial Maero}\right) \end{aligned}$$

and the transfer functions C and A are equal, using (7.6) and (7.7).

Now, consider the transfer function B. From (7.5) and (7.12)

$$B = \left(1 - \frac{\partial L}{\partial \beta_a}\right) T_{V_o \beta_a} - \frac{\partial L}{\partial Maero} (J_B T_{V_o \ddot{\beta}_a} - T_{V_o Mapp})$$

where $T_{V_o \beta_a}$ is the transfer function from δV_o to $\delta \beta_a$, $T_{V_o \ddot{\beta}_a}$ is the transfer function from δV_o to $\delta \ddot{\beta}_a$ and $T_{V_o Mapp}$ is the transfer function from δV_o to $\delta Mapp$. However, from Figure 7.6b it can be seen that $T_{V_o \beta_a} = (T_{V_o Mapp} + K_m) / (J_B s^2 + K_{m2})$ and $T_{V_o \ddot{\beta}_a} = T_{V_o \beta_a} / s^2$. It follows that

$$\begin{aligned} B &= T_{V_o \beta_a} \left[1 - \frac{\partial L}{\partial \beta_a} - J_B s^2 \frac{\partial L}{\partial Maero} + (J_B s^2 + K_{m2}) \frac{\partial L}{\partial Maero} \right] - K_m \frac{\partial L}{\partial Maero} \\ &= T_{V_o \beta_a} \left(1 + \left(\frac{\partial Maero}{\partial \beta_a} + K_{m2} \right) \frac{\partial L}{\partial Maero} \right) - K_m \frac{\partial L}{\partial Maero} \end{aligned}$$

using (7.7). Hence, using (7.6).

$$B = T_{V_o \beta_a} - K_m \frac{\partial L}{\partial Maero}$$

The actuator is usually designed to reject external disturbances, such as δV_o , i.e. the actuator has a high forward path gain so that the transfer function $T_{V_o \beta_a}$ has very low gain at low frequency. An illustration of this is shown in the Bode plot for $T_{V_o \beta_a}$ for the compliant tip actuator with the feedback loop acting on tip angle in Figure 7.16. Therefore, as s tends to zero, the transfer function B tends to the constant $-K_m \partial L / \partial Maero$.

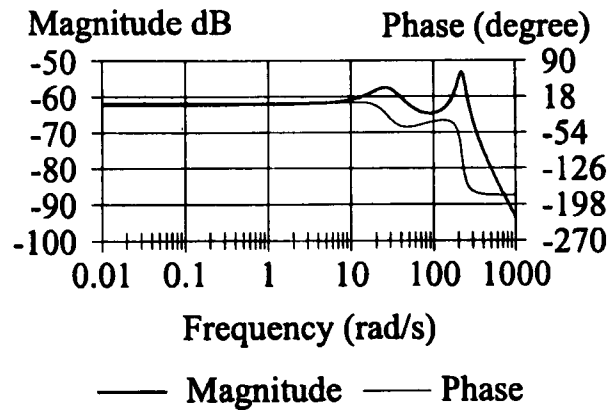


Figure 7.16 The Bode plot for $T_{V_o \beta_a}$.

It was demonstrated in sub-section 7.2.2 that when close to on-design operating conditions, the required tip angle

$$L(\beta_a, Maero) = N(Maero - f(\beta_a)) \equiv N(\psi)$$

and thus

$$\frac{\partial L}{\partial Maero} = \frac{dN(\psi)}{d\psi}$$

When on the on-design curve

$$\beta_a = N(Maero - f(\beta_a))$$

and differentiating with respect to β_a

$$1 = \frac{dN(\psi)}{d\psi} \left(\frac{dMaero}{d\beta_a} - \frac{df(\beta_a)}{d\beta_a} \right)$$

But

$$\frac{dMaero}{d\beta_a} = \frac{\partial Maero}{\partial \beta_a} + \frac{\partial Maero}{\partial V_o} \frac{dV_o}{d\beta_a}$$

and it follows that

$$\begin{aligned} \frac{dN(\psi)}{d\psi} &= 1 / \left(\frac{\partial Maero}{\partial \beta_a} + \frac{\partial Maero}{\partial V_o} \frac{dV_o}{d\beta_a} - \frac{df(\beta_a)}{d\beta_a} \right) \\ &= \frac{d\beta_a}{dV_o} / \frac{\partial Maero}{\partial V_o} \end{aligned}$$

Hence, using (7.8) and (7.6)

$$-K_m \frac{\partial L}{\partial Maero} = -K_m \frac{dN(\psi)}{d\psi} = -K_m \frac{d\beta_a}{dV_o} / \frac{\partial Maero}{\partial V_o} = -\frac{d\beta_a}{dV_o}$$

and $B = -\frac{d\beta_a}{dV_o} B^*$

with the gain of the transfer function B^* tending to 1 as s tends to zero.

To enable the direct comparison of power control to independent tip control Figure 7.14 can be amended to Figure 7.17 with C_2 substituted by $C_2 = A D/C$ $C_1 = DC_1$. The transfer function B^* is effectively 1 for the frequency range of interest.

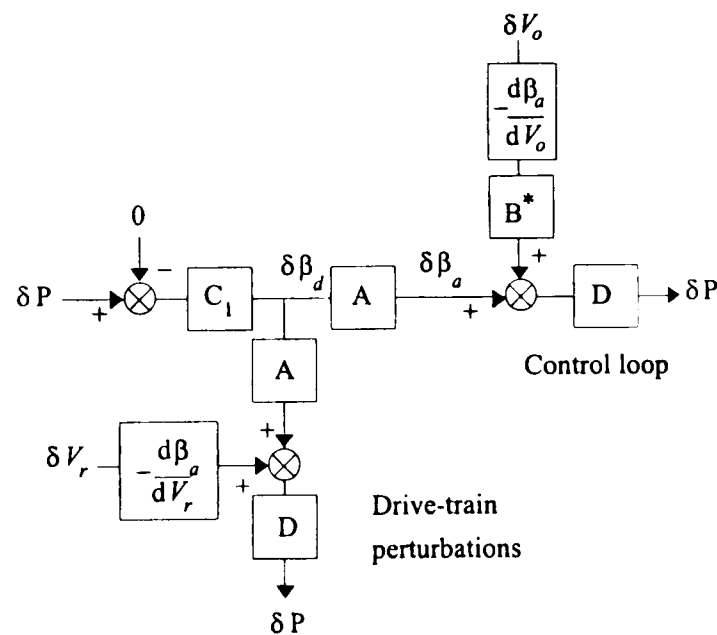


Figure 7.17

Hence independent tip control has an advantage over power control only, if the spectral density function⁴ of δV_o has a lower high-frequency content compared to the spectral density function of δV_r , and is therefore less likely to saturate the actuator. Figure 2.6a shows the power spectrum of the flapping moment seen by an individual tip on a Howden HWP330/33 machine and the power spectrum of the hub torque. (The flapping moment is directly proportional to the aerodynamic torque (Anderson *et al.*, 1992) while the blade is unstalled, and hence to V_o .) For independent tip control, the spectral density function for δV_o has rotationally induced spectral peaks at each integer multiple of Ω_o as sensed by one tip (Figure 2.6a). For power control, the spectral density function for δV_r has similar spectral peaks but sensed by the complete rotor. At low frequencies the contributions from each blade strongly correlate, with the result that only the spectral peaks at integer multiples of $n\Omega_o$ are present in the hub torque and so in power control. Although the magnitude of each remaining spectral peak is increased by a factor of n , the content of the spectral density function is much reduced at low frequency since the magnitudes of the individual blade contributions to the spectral peaks decrease rapidly as frequency increases. At higher frequency, the correlation across the wind field decreases and the concentration of the spectral density function for power control at every m^{th} peak (where $m = 1, 2, 3, \text{etc.}$) decreases with the intermediate frequencies becoming stronger. However, the magnitude of every m^{th} peak decreases m times to \sqrt{m} times that of the corresponding peaks of the spectral density function for a single blade. Hence, if no account is taken of spatial filtering, at very high frequencies the magnitude of the spectral density function for power control can be 5 dB greater for a three-bladed machine than the magnitude of the spectral density function for independent tip control. Nevertheless, it is unlikely to outweigh the weaker magnitude of the spectral density function for power control at the low and middle frequency ranges. However, even if the 5 dB advantage is assumed for all the spectral peaks the bandwidth of the controller can be made only slightly greater. Hence for the purpose of regulating drive-train transient loads independent tip control has no real advantage over power control. The control loops are subject to effectively the same level of middle- to high-frequency disturbances.

⁴ spectral density function - a measure of the frequency content of a function, uses of fast Fourier transform, $S(j\omega) \times S(-j\omega)$.

7.2.4 Robustness of independent tip control

At several points in the analysis in sub-section 7.2.3 $(\partial Maero / \partial \beta_a + K_{m2}) \partial L / \partial Maero$ is set to zero. However, $\partial Maero / \partial \beta_a$ is the partial derivative of the aerodynamic moment with respect to tip angle arising from the aerodynamic model used in designing the independent tip. In contrast, K_{m2} is the actual physical rate of change of the aerodynamic moment with respect to tip angle. The result that C and A are equal is robust if $(\partial Maero / \partial \beta_a \partial L / \partial Maero + K_{m2} \partial L / \partial Maero)$ is not the cancellation of two numbers large compared to one. Since $\partial L / \partial Maero = 1 / (dMaero / d\beta_a - df(\beta_a) / d\beta_a)$ and $\partial Maero / \partial \beta_a$ is equal to $df(\beta_a) / d\beta_a$, it follows that

$$(\partial Maero / \partial \beta_a \partial L / \partial Maero = df(\beta_a) / d\beta_a / (dMaero / d\beta_a - df(\beta_a) / d\beta_a)$$

Since for the compliant tip on the Howden 330 kW, $dMaero / d\beta_a$ from Figure 7.7 varies from 2005 to -11460, and $df(\beta_a) / d\beta_a$ from Figure 7.8, is for approximately 2292 Nm/rad it can be seen that at small tip angles $\partial Maero / \partial \beta_a \partial L / \partial Maero$ is approximately 8, *i.e.* large compared to 1. $(\partial Maero / \partial \beta_a \cdot \partial L / \partial Maero)$ is a function of tip angle (see Figure 7.18) and hence shows that at tip angles 0° to 20° the compliance tip performance is sensitive to uncertainty in K_{m2} . Hence, independent tip control performance may be sensitive to uncertainty in K_{m2} and may lack robustness.

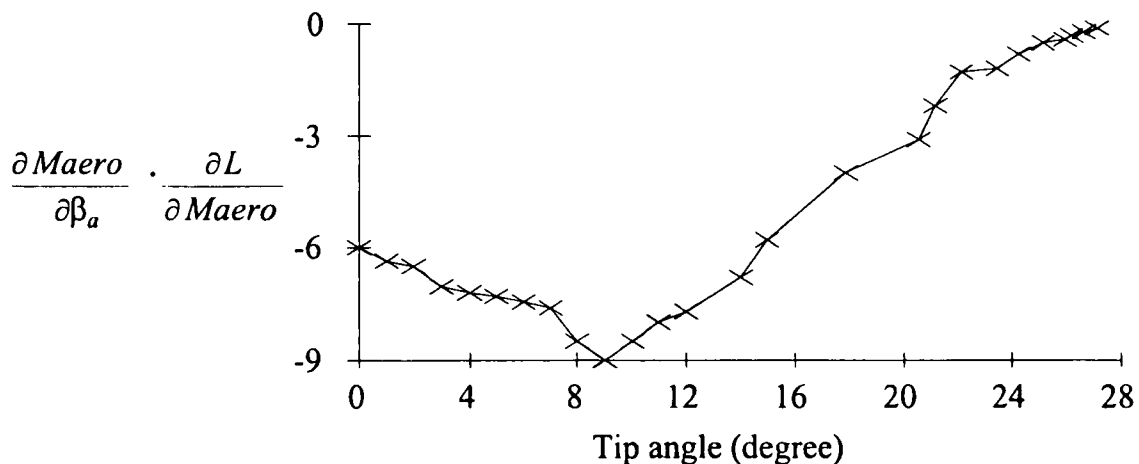


Figure 7.18 $(\partial Maero / \partial \beta_a \cdot \partial L / \partial Maero)$ as a function of tip angle for the compliant tip.

7.2.5 Assessment of independent tip control

It has been established that independent-tip-control and power-control loops are subject to disturbances of similar strengths. In addition, just as the power controller requires reasonable robustness margins to cater for the uncertainty in the description of the rotor aerodynamic torque, so the independent tip controller requires reasonable robustness margins

to cater for the uncertainty in the description of the tip aerodynamic moment (see Section 7.2.4). Hence, even when the wind speed sensed by the tip is identical to that sensed by the complete rotor, independent tip control can have no inherent advantage over power control. Any controller, C_2 , for independent tip control has a corresponding controller, C_1 , for power control which achieves the same performance.

Although independent tip control has no inherent advantages over power control for the regulation of fluctuations in drive-train torque, it might be used to actively control the $1\Omega_o$ loads on the blades. To actively regulate $1\Omega_o$ the gain and phase of the controller need to be considerably increased at Ω_o which is greater than the usual controller cross-over frequency (see Appendix C). Accordingly the gain of the controller must be raised considerably over the middle frequency range. Hence in wind speeds close to rated the actuator activity is increased over all frequencies except Ω_o at which the activity is decreased. Hence greater actuator activity would occur compared with regulating drive-train torque fluctuations. Since the wind speed sensed by the tips differs from that sensed by the rotor, independent tip control is not appropriate on its own but should be compared with power control. They should be combined as in Figure 7.15. The bandwidth of k_3 must significantly less than Ω_o , because only independent tip control senses the Ω_o disturbance. The performance of the control system in terms of controlling the drive-train torque fluctuations between the bandwidth of k_3 to Ω_o is degraded since it is not done solely in response to wind speed V_r , but a combination of V_r and V_o .

A more precise interpretation of the original compliant tip concept is now possible. The situation shown in Figure 7.19 is equivalent to power control and independent tip control combined as in Figure 7.15:

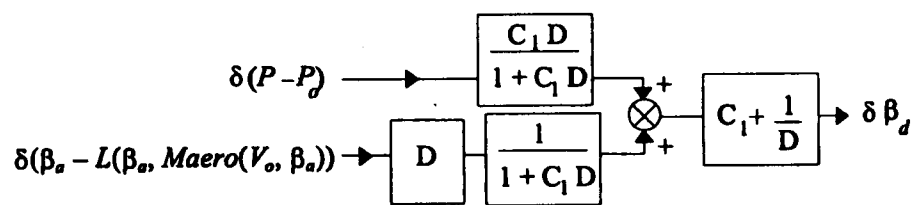


Figure 7.19 Combining power control and independent tip control.

It should be noted that the power control dominates as required at frequencies below the control cross-over frequency. The control action on the component of V_r independent of V_o is by the power-control loop with controller C_1 . The control action on the component of V_o independent of V_r is by the independent-tip control loop with unity controller. The control action for the component of V_o which correlates to V_r is equivalent to control action

on the power control loop alone with controller $(C_1 + 1/D)$. The nominal closed loop system has the sensitivity function

$$\frac{1}{(1 + (C_1 + 1/D)DA_o)} = \frac{1}{(1 + A_o)} \frac{1}{(1 + C_1DA)}$$

where A_o is the open-loop actuator transfer function. The sensitivity function for power control on its own, $(1 + C_1 D A)^{-1}$, is augmented by the sensitivity function for the actuator, $(1 + A_o)^{-1}$. Hence, the closed-loop system is dynamically well-behaved and stable. However, the inappropriateness of the controller $(C_1 + 1/D)$ is clear. The gain increases rapidly at high frequency and the actuator would experience an increased level of high frequency disturbances as compared to power control on its own. In addition, the system would lack robustness, due to the high controller gain, as both the power-control loop and the independent-tip control loop exhibit uncertainty. As for the design of controller on the power-control loop, it is evident from the preceding that it should be the same as for power control on its own.

7.2.6 Summary of independent tip control performance

The performance of independent tip control has been compared with that of power control or any combination of the two. The main conclusions are follows.

- i) *Independent-tip control without power control.* For the purpose of regulating drive-train transient loads independent-tip control has no real advantage over power control.
- ii) *Independent-tip control with power control.* Independent tip control has the potential of actively controlling the $1\Omega_o$ loads on the blades, but greater actuator activity is experienced than for power control. It is accompanied by a degradation in the regulation of drive-train transient loads between the cross-over frequency of k_3 and Ω_o .

7.3 Conclusions

Non-conventional aerodynamic control devices has been investigated to determine whether any advantage accrues in comparison to conventional devices.

Although the fledge may have several advantages, such as lower associated structural loads and high effectiveness as an overspeed brake, it does not in itself enable better drive-train load regulation to be achieved. Similarly, although the independent tip has the potential to regulate etc. the $1\Omega_o$ loads on the blades, the conclusions are similar.

To conclude, non-conventional aerodynamic control devices (at least those investigated) do not increase the range of dynamic behaviour in comparison to that observed for part-span regulation in Chapter 6.

8 Integrated Design

The previous work, in particular the results and methodology of Chapter 3, Chapter 5 and Chapter 6, lay the foundation for the control aspects of integrated design of wind turbines. In this chapter, these results are summarised and their usage illustrated with respect to a full-span regulated, 1 MW wind turbine.

8.1 Summary of results

A foundation for the control aspects of integrated design approach was developed in Chapter 3. The relevant results are summarised below.

- a) Simple models of the wind turbine are determined.
 - The simple model, comprising the drive-train model, Figure 3.6, together with the generator model (3.9), adequately represents the dynamics of the power train. It is applicable to almost all wind turbines.
 - The relationship of the lumped parameters of the simple model of the power train to the physical parameters of the wind turbine are summarised by (B.83) to (B.96).
 - The simple power-train model together with the linear models of aerodynamic torque (3.5), actuator (3.8) and the power transducer (C.14) constitute a suitable plant model for control analysis and design.
- b) The salient features of the power-train dynamics are identified.
 - The dynamics of the power train are characterised by the frequency of the first drive-train mode, ω_1 , and its damping factor, η_1 .
 - The relationship of ω_1 , and η_1 ; to the lumped parameters of the simple power-train model are determined to be (3.19) and (3.21), that is,

$$\varepsilon_1 = \eta_1 / \omega_1 \approx (I_1 + N^2 I_2) / (2N^2 D_e) \quad (8.1)$$

$$\frac{1}{\omega_1^2} = \frac{I_1}{\kappa} + \frac{\tau(I_1 + N^2 I_2)}{N^2 D_e} \quad (8.2)$$

c) The constraints on the achievable dynamic behaviour are determined.

- Adding compliance does not of itself improve the dynamic behaviour, since although the frequency of the first drive-train mode is decreased, thereby reducing the $n\Omega_o$ load, the damping factor is also decreased.
- The damping factor can only be increased by either increasing the slip of the generator or the inertia of the rotor and low-speed shaft; it does not depend on damping on either of the low- or high-speed shafts.
- It is reasonably straightforward to design for a specific frequency for the first drive-train mode by changing the compliance of the drive train; it is, however, not straightforward to design for a specific amount of damping factor.

It is clear from the above that the constraints on the achievable dynamic behaviour of the power train are quite strong, in particular, those affecting the damping factor of the first drive-train mode.

Using the above results, the dependence of the controller performance on the configuration of the wind turbine can be determined. This second step was completed for conventional full-span and part-span regulated wind turbines. The effectiveness of power control was determined for a variety of full-span and tip-regulated wind turbines and has been assessed for a range of wind speeds, first drive-train mode and controller cross-over frequencies in Chapters 5 and 6. The range of performance is surprisingly large. Although the damping of the first drive-train mode is assumed ideal, the methodology can be applied to configurations with different damping.

The relevant results from Chapter 5 and 6 are summarised below.

- Performance is strongly related to controller activity at low controller cross-over frequencies.
- Except for low frequency, increasing the controller cross-over frequency requires a disproportionate increase in the rating of the actuator.
- There is a limiting controller cross-over frequency, (roughly 2 rad/s) beyond which any improvement in performance is small.
- Performance is weakly related to rotor angular velocity and the intensity of the transient loads at $n\Omega_o$.
- The performance of the three-bladed full-span machines is significantly better (by an order of magnitude) than that of two-bladed full-span machines for all but the lowest drive-train modes and controller cross-over frequencies, see Chapter 5.
- The performance of the three-bladed tip-regulated machines is significantly better (by an order of magnitude) than that of two-bladed tip-regulated machines in a

high wind speed site, see Chapter 6. However, in low wind speed sites the performance of tip-regulated machines varies little with the number of blades.

- The performance of two-bladed machines can be improved greatly by reducing the frequency of the first drive-train mode.
- Three-bladed machines are insensitive to the first drive-train mode frequency.
- Tip-regulated, three-bladed machines perform better than two-bladed machines.
- The worst behaved machines are two-bladed with full-span control devices.
- The best behaved machines are three-bladed with tip control devices.

The above results hold quite generally.

8.2 An illustrative example

The previous work is now illustrated with respect to a full-span regulated, 1 MW wind turbine. The following characteristics have been selected

- three blades;
- blade edge-wise frequency of approximately $5\Omega_o$;
- stiff power-train dynamics with first drive-train mode frequency of approximately $4\Omega_o$;
- high slip generator with a slip of approximately 1.5%;
- dual mode control algorithm.

The reason for the selection is summarised below.

The pre-determined machine parameters are listed in Table 8.1. With these parameters, the ratio ε_l in (8.1) is approximately 0.03 (with a generator slip of 1%). Unfortunately this is very small and the ideal damping factor of 0.7 can only be achieved if the first drive-train frequency is very large, namely 23 rad/s. Assuming that a ratio of 0.05 could be achieved by increasing the slip of the generator to, say, 1.5%, a similar parametric study to that described in Appendix C is undertaken. Table 8.2 lists the partial derivatives of aerodynamic torque with respect to wind speed and pitch angle. The spectral peak at $n\Omega_o$ is modelled with $a_{3r} = 0.15$ and $b_{3r} = 4000$. The actuator is assumed have a bandwidth of 2.5 rad/s.

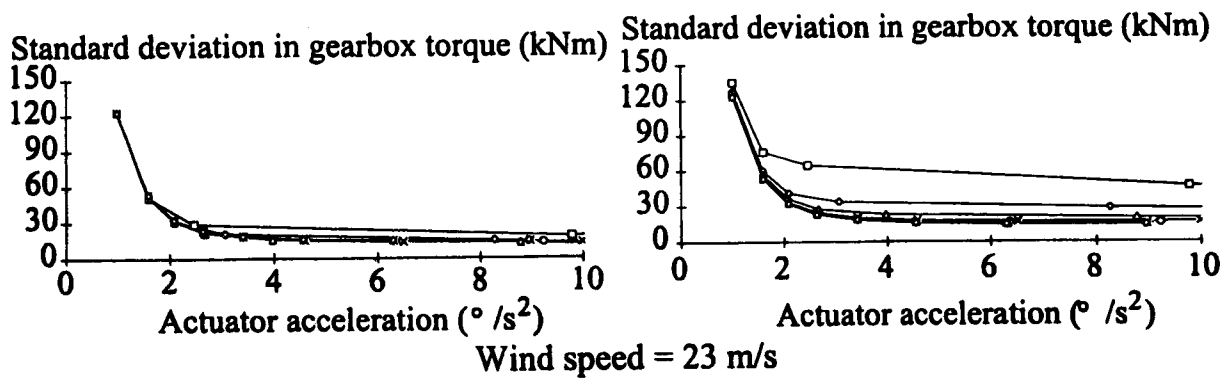
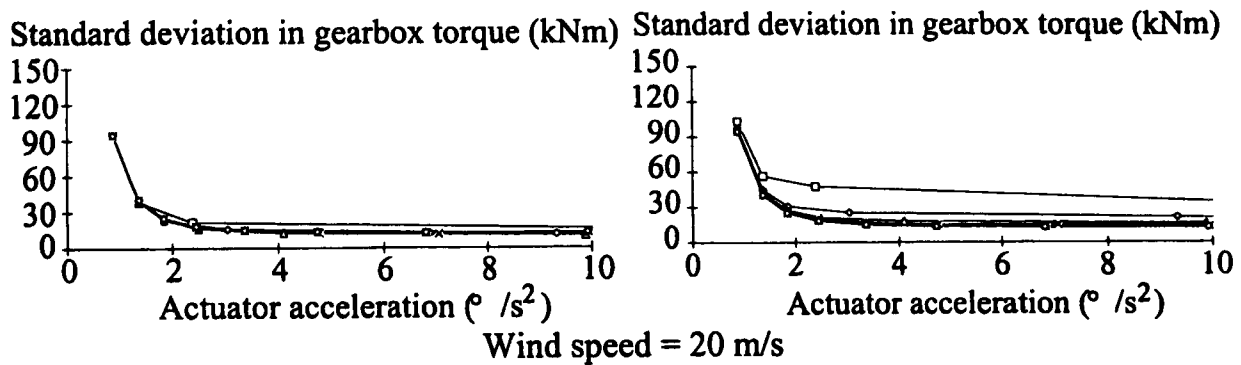
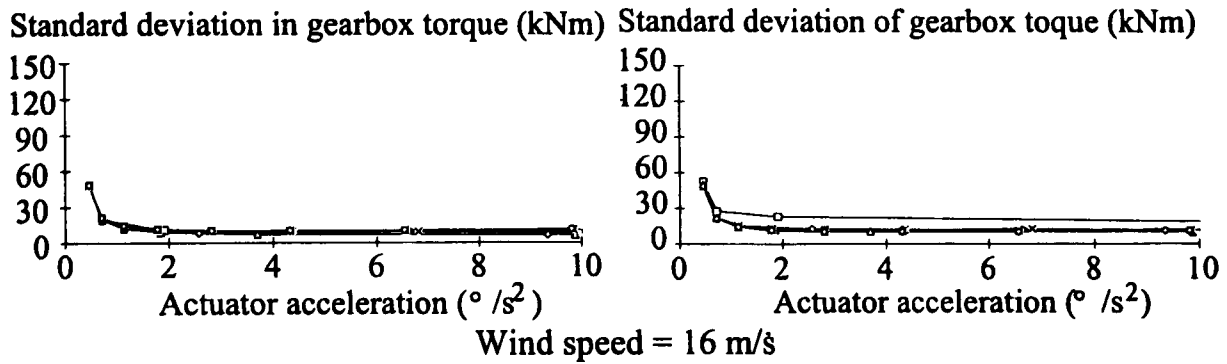
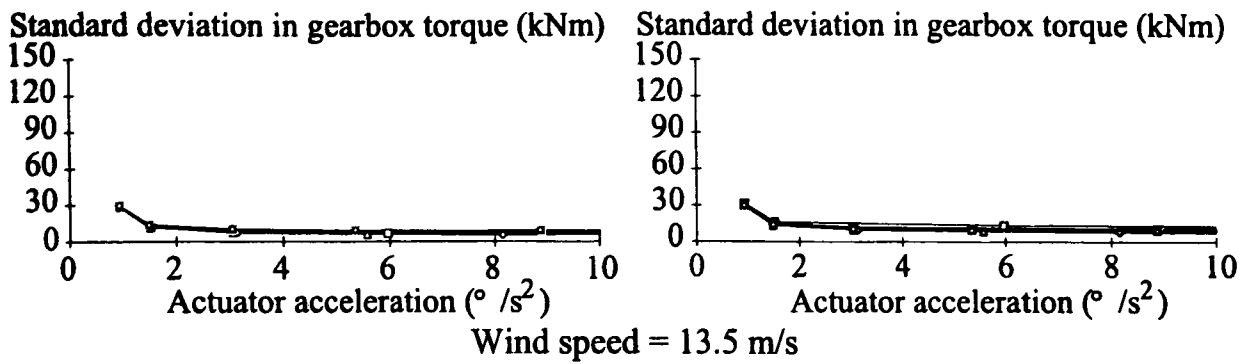
Machine parameter	
Gearbox ratio	40.91
Grid frequency	50 Hz
Rotor inertia	870000 kgm ²
Rotor radius	25 m
Rotor angular velocity	2.56 rad/s
Gearbox and generator efficiency	95%
Slip	0.6 % -> 1.5 %

Table 8.1 Machine parameters.

Wind speed (m/s)	Pitch angle (°)	k_1 kNm/(m/s)	k_2 kNm/(°)
13.5 m/s	4.47	61.1784	-13.7764
16	12.11	69.0644	-45.9266
20	19.77	82.5905	-54.3194
23	24.24	79.8829	-46.9918

Table 8.2 Aerodynamic derivatives.

The standard deviations of gearbox torque, actuator acceleration and velocity are calculated, with two drive-train dampings, (i) 0.7 and (ii) $0.05\omega_c$, for controller cross-over frequencies 0.5 to 4 rad/s and first drive-train modes $1\Omega_o$ to $5\Omega_o$. The standard deviation of the gearbox torque is plotted against actuator acceleration and velocity for each of the damping factors in Figures 8.1 and 8.2. As would be expected from the results of Chapter 5, the standard deviation of gearbox torque increases with wind speed and the actuator acceleration increases with controller cross-over frequency. The actuator velocity, on the other hand, decreases initially before increasing at high controller cross-over frequencies. The standard deviation of gearbox torque obtained with ideal drive-train damping is almost always lower than those for the machine being investigated. The difference decreases as the first drive-train mode and the controller cross-over frequency increases, see Tables C.6 and C.7. On a typical commercial machine, the first drive-train mode is approximately $1.5\Omega_o$ when a controller cross-over frequency of 1.5 to 2 rad/s can be obtained. In these circumstances and at high wind speeds, the standard deviation of torque fluctuations on the machine under investigation is considerably more than those with ideal damping. However, to increase the damping ratio to 0.7 would require either rotor inertia or generator slip to be increased by a factor of six - not a very practical solution.

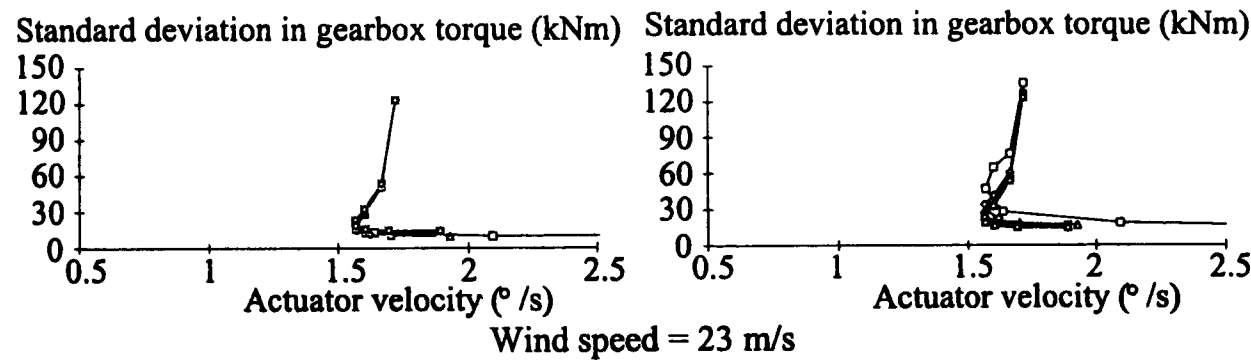
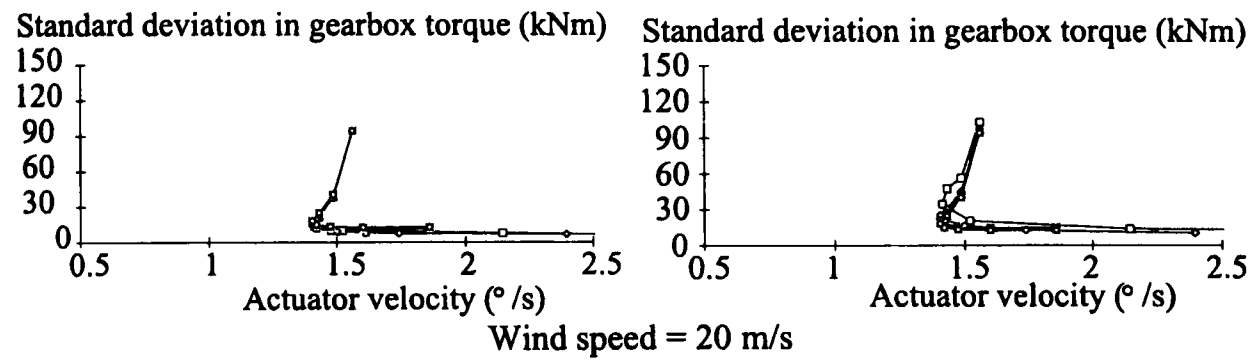
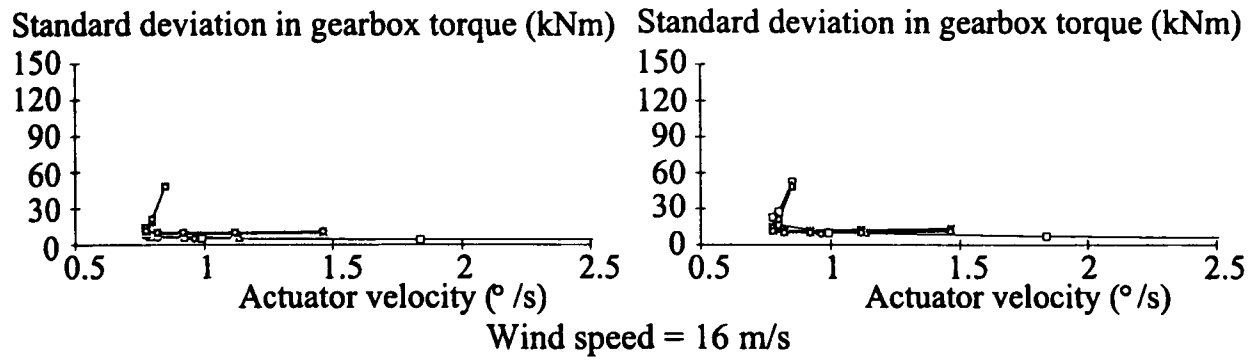
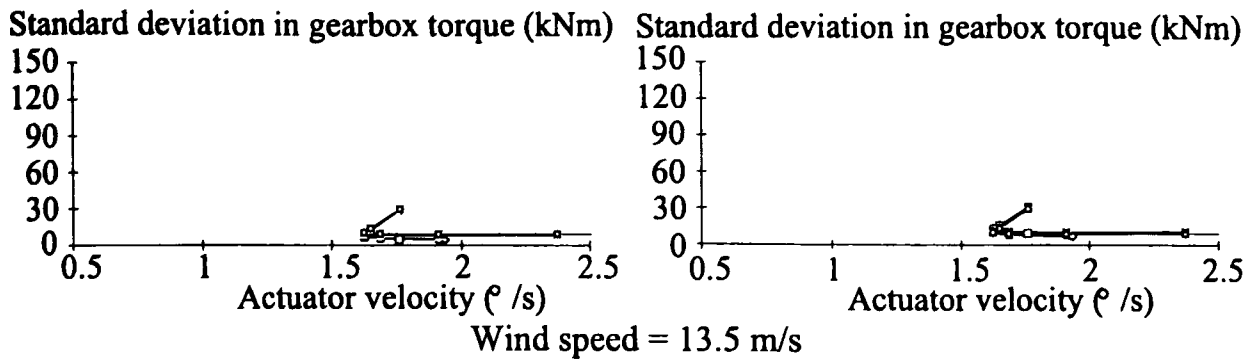


First drive-train mode		
□ 1Ω	× 3.5Ω	— 5Ω
○ 1.5Ω	◇ 4Ω	— 5.5Ω
△ 2Ω	+ 4.5Ω	

Ideal first drive-train mode

Constant ratio $\epsilon_f, \mu_f = 0.05 \times \omega_f$

Figure 8.1 The standard deviation of gearbox torque versa actuator acceleration.



First drive-train mode		
\square 1Ω	\times 3.5Ω	\cdots 5Ω
\circ 1.5Ω	\diamond 4Ω	\dashv 5.5Ω
\triangle 2Ω	\rightarrow 4.5Ω	

Ideal first drive-train mode

Constant ratio $\epsilon_1, \mu_1 = 0.05 \times \omega_1$

Figure 8.2 The standard deviation of gearbox torque versa actuator velocity.

It can be deduced that the controller cross-over frequency should be as high as possible and that a very high first drive-train mode is desirable, so that the demanded actuator activity is minimised. In other words, the machine is required to be as stiff as possible, for example by having no low-speed shaft, a very stiff high-speed shaft and the gearbox mounting must have little compliance. The generator must have high slip. To achieve a drive-train frequency of about $4\Omega_o$, the edge-wise frequency of the blades must at least $5\Omega_o$, or greater. The concept of having a very high first drive-train mode frequency exploits the low intensity of $3\Omega_o$ on a three-bladed machine as compared to that of $2\Omega_o$ on a two-bladed machine.

The actuator activity is at its highest at 13.5 m/s, see Tables C.8 and C.9. For a wind turbine with a high first drive-train mode frequency, a controller cross-over frequency of up to 2 rad/s could be obtained while maintaining a standard deviation limit of 5.7 %/s² for actuator acceleration and 2 %/s for actuator velocity. However, for wind speeds of 16 m/s and above, a higher cross-over frequency of between 3 to 3.5 rad/s is possible. Hence a 'dual mode' controller is required; that is, a controller with a low cross-over frequency at low wind speeds which switches to a higher cross-over frequency in wind speeds above, for example, 16 m/s.

Wind speed (m/s)	Drive-train transfer function
12.83	$\frac{5.176e9(s^2 + 0.125s + 17.283)(s^2 + 0.239s + 19.476)(s^2 + 3.127s + 177.156)}{(s^2 + 0.141s + 17.153)(s^2 + 0.235s + 19.470)(s^2 + 10.554s + 101.678)(s^2 + 3.078s + 175.654)(s^2 + 2.339s + 5374.208)(s^2 + 0.09619s + 406608)}$
20.1	$\frac{5.029e9(s^2 + 0.125s + 17.283)(s^2 + 0.221s + 19.469)(s^2 + 3.089s + 182.376)}{(s^2 + 0.143s + 17.164)(s^2 + 0.216s + 19.463)(s^2 + 10.574s + 99.560)(s^2 + 2.746s + 196.223)(s^2 + 2.454s + 5068.193)(s^2 + 0.09613s + 405399)}$
27.0	$\frac{4.830e9(s^2 + 0.125s + 17.283)(s^2 + 0.208s + 19.465)(s^2 + 3.038s + 189.969)}{(s^2 + 0.145s + 17.176)(s^2 + 0.200s + 19.458)(s^2 + 10.590s + 98.635)(s^2 + 2.562s + 221.027)(s^2 + 2.625s + 4715.028)(s^2 + 0.09607s + 404027)}$

Table 8.3 Drive-train transfer function for a variety of wind speeds.

Using the full linear model described in Section B.5.2, the transfer function of the drive-train dynamics for various wind speeds are listed in Table 8.3 and the corresponding Bode plots are shown in Figure 8.3. The drive-train transfer function varies little with the wind speed. The peak at frequencies near 12 rad/s is due to the flap-wise dynamics and the dip at approximately 4 rad/s is due to the tower dynamics. The second sharp peak at 70 rad/s is due to the generator and the third at 650 rad/s is due to the gear-train dynamics. The first

drive-train mode, clearly seen at 10 rad/s, is well damped (damping factor 0.52) as required. The corresponding transfer functions from pitch angle to load torque for various wind speeds are listed in Table 8.4 and the corresponding Bode plots are shown in Figure 8.4. In this case, the dependence of the transfer functions on wind speed is very strong at just above rated wind speeds with non-minimum phase behaviour due to the tower dynamics which causes a rapid loss of phase at about 4 rad/s. Fortunately, the non-minimum behaviour is absent at higher wind speeds and the tower dynamics become minimum phase for wind speeds above 16 m/s, thereby reducing the difficulty of the controller design task. The known actuator capability is such that a maximum pitch rate of only 7.1°/s, which would approximately correspond to a standard deviation of 1.4 °/s instead of the 2 °/s assumed earlier, can be achieved. Hence, the controller crossover frequency is further restricted in low wind speeds.

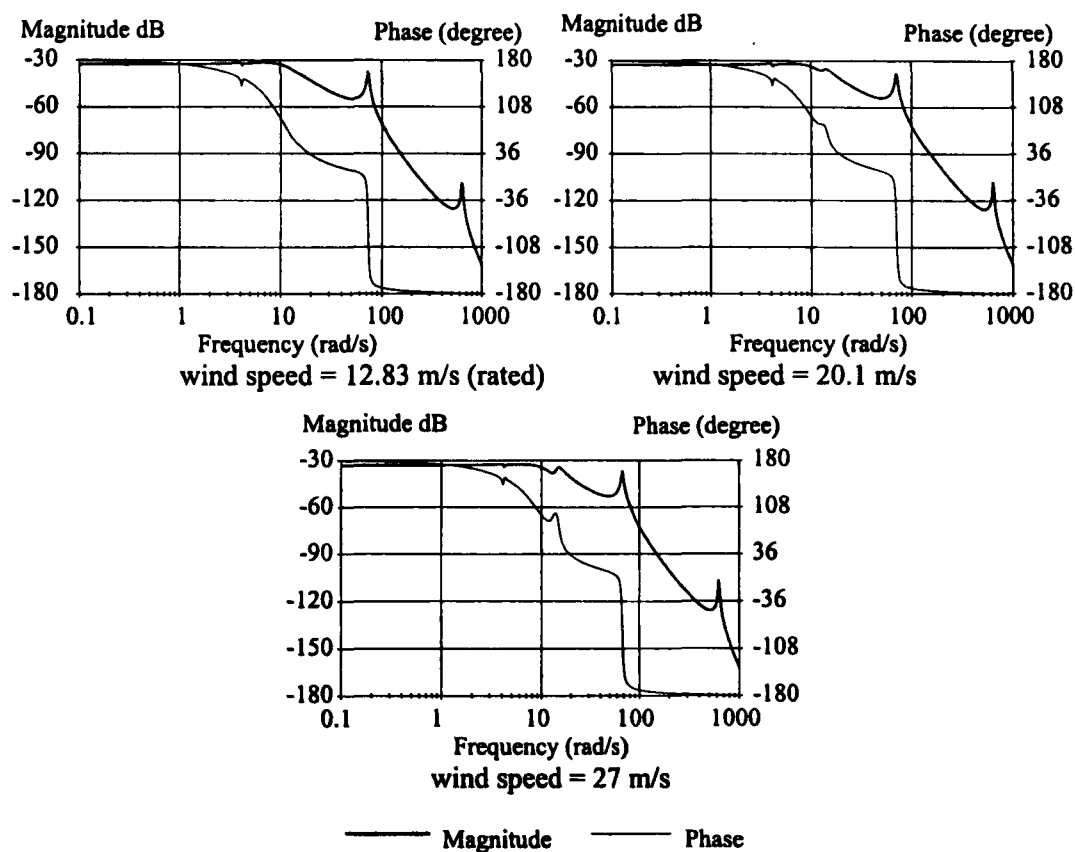


Figure 8.3 Bode plot of the drive-train transfer function for a variety of wind speeds.

A full design study was undertaken by the collaborating wind turbine manufacturer with the drive-train characteristics based on the above analysis. The proposed characteristics were shown to be feasible. Furthermore, the requirement of a stiff drive train somewhat simplified the design.

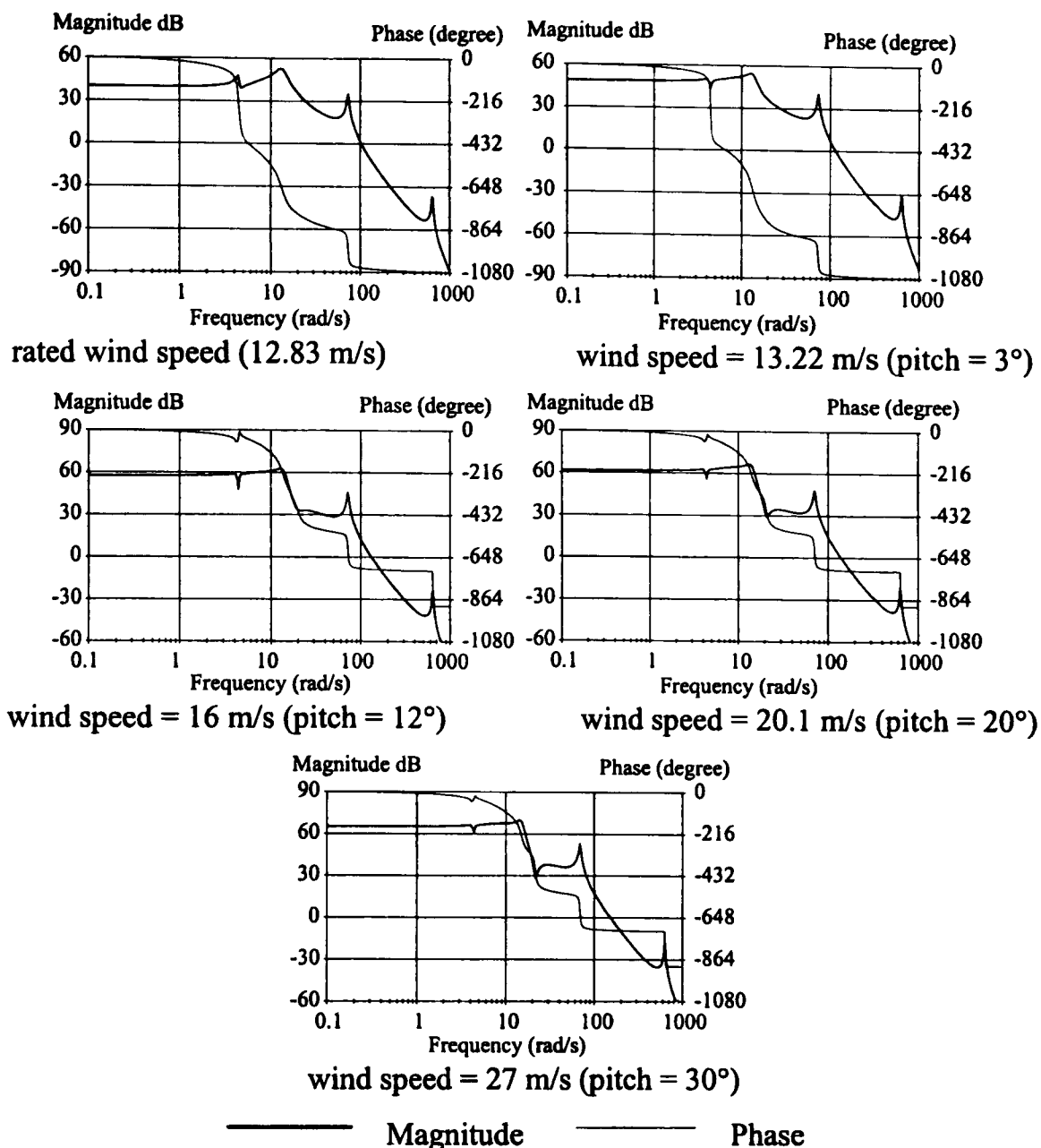


Figure 8.4 Bode plot of the transfer function from pitch angle ($^{\circ}$) to load torque (Nm).

A dual mode controller is designed to attain a controller cross-over frequency of 1 rad/s for wind speeds below 16 m/s and a controller cross-over frequency of 2 rad/s for wind speeds above 16 m/s. (The design and implementation of the dual mode controller is described in Appendix C). The performance of the wind turbine with and without a controller is investigated by using a non-linear simulation model based on the equations described in Chapter 3 (with an infinite low-speed shaft stiffness). An example of the behaviour of the machine with power control is shown in Figure 8.5 for a mean wind speed of 19 m/s. It can be seen from the time traces of actuator velocity that the actuator pitch rate limit is reached occasionally, but the performance of the controller does not markedly degrade. Statistics for above-rated operation of the wind turbine for a variety of wind speeds, in Table 8.5, indicate that the machine is very well behaved for its size and the limitations of its actuator capability. (In high wind speeds, where the performance is worst,

the wind turbulence levels would rarely reach 20 % in practise). Commercial full-span regulated 1 MW machines are known to have to be shutdown in high wind speeds, 20 m/s due to the power output reaching twice rated power.

Wind speed (m/s)	Transfer function from pitch angle (°) to load torque (Nm)
12.83	$\frac{2.140e13(s^2 + 0.125s + 17.283)(s^2 - 0.416s + 21.014)(s^2 - 21.267s + 164.190)}{(s^2 + 0.141s + 17.153)(s^2 + 0.235s + 19.470)(s^2 + 10.554s + 101.678)(s^2 + 3.078s + 175.654)(s^2 + 2.339s + 5374.208)(s^2 + 0.09619s + 406608)}$
13.22	$\frac{4.171e13(s^2 + 0.125s + 17.283)(s^2 - 0.103s + 19.658)(s^2 - 10.704s + 250.766)}{(s^2 + 0.141s + 17.154)(s^2 + 0.233s + 19.470)(s^2 + 10.582s + 101.441)(s^2 + 2.999s + 176.546)(s^2 + 2.337s + 5367.076)(s^2 + 0.09619s + 406580)}$
16.00	$\frac{8.093e13(s^2 + 0.125s + 17.283)(s^2 + 0.0690s + 19.463)(s^2 - 4.226s + 370.415)}{(s^2 + 0.142s + 17.158)(s^2 + 0.225s + 19.467)(s^2 + 10.598s + 100.533)(s^2 + 2.843s + 183.708)(s^2 + 2.373s + 5261.571)(s^2 + 0.09617s + 406161)}$
20.1	$\frac{1.128e14(s^2 + 0.125s + 17.283)(s^2 + 0.103s + 19.452)(s^2 - 2.285s + 430.859)}{(s^2 + 0.143s + 17.164)(s^2 + 0.216s + 19.463)(s^2 + 10.574s + 99.560)(s^2 + 2.746s + 196.223)(s^2 + 2.454s + 5068.193)(s^2 + 0.09613s + 405399)}$
27.0	$\frac{1.616e14(s^2 + 0.125s + 17.283)(s^2 + 0.115s + 19.450)(s^2 - 1.389s + 463.195)}{(s^2 + 0.145s + 17.176)(s^2 + 0.200s + 19.458)(s^2 + 10.590s + 98.635)(s^2 + 2.562s + 221.027)(s^2 + 2.625s + 4715.028)(s^2 + 0.09607s + 404027)}$

Table 8.4 Transfer function from pitch angle to load torque for a variety of wind speeds.

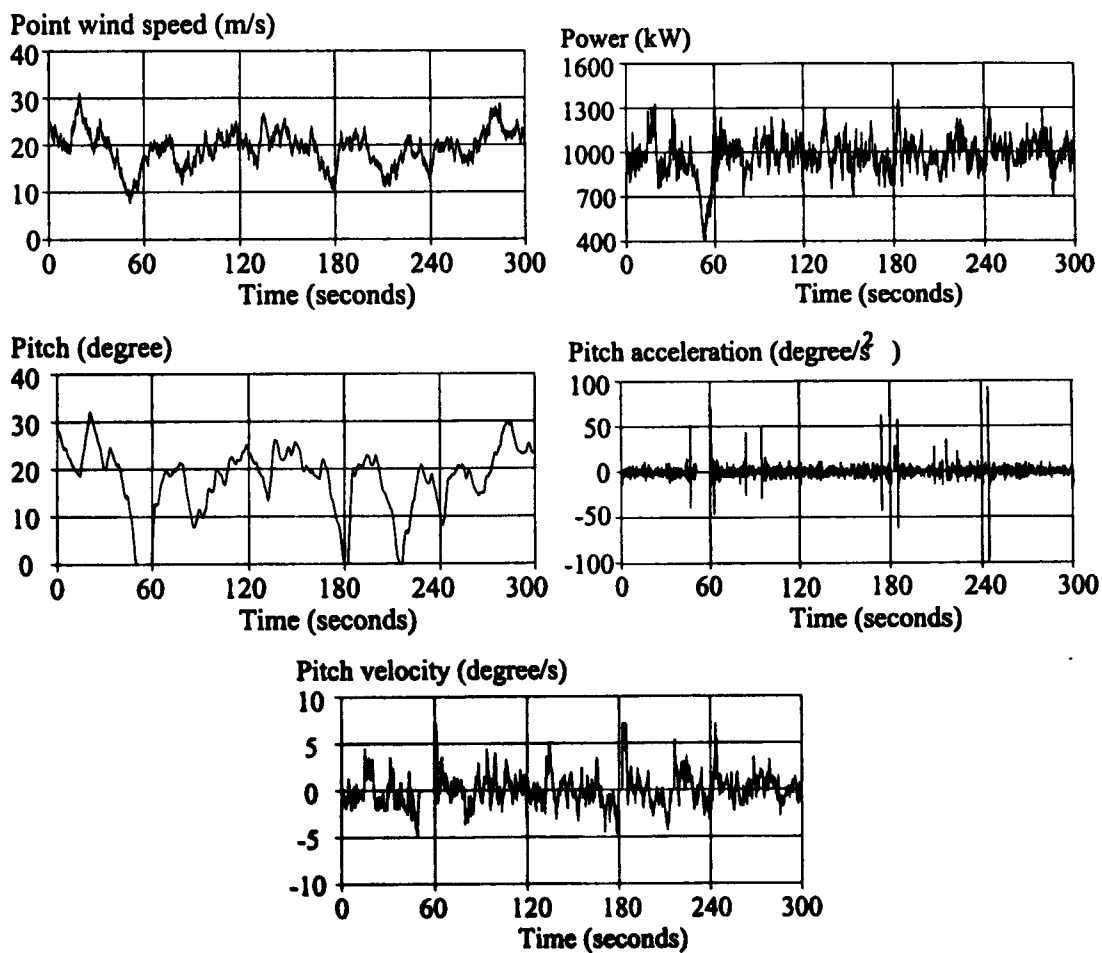


Figure 8.5 Machine performance in a mean wind speed of 19 m/s.

Power (kW)				
Mean wind speed, turbulence intensity	Mean	Standard deviation	Maximum	Minimum
13 m/s, 10 %	953.068	93.529	1142.877	588.195
16 m/s, 10 %	996.297	60.297	1204.183	789.434
19 m/s, 10 %	998.097	62.068	1197.010	800.838
22 m/s, 10 %	998.077	70.505	1234.626	772.883
25 m/s, 10 %	997.776	78.498	1256.054	742.677
13 m/s, 15 %	934.744	133.455	1193.384	427.060
16 m/s, 15 %	986.397	86.639	1251.863	480.224
19 m/s, 15 %	994.835	80.511	1267.354	732.916
22 m/s, 15 %	996.301	93.516	1307.319	719.318
25 m/s, 15 %	995.907	107.047	1367.019	666.897
13 m/s, 20 %	936.062	136.119	1229.679	388.309
16 m/s, 20 %	970.050	125.289	1288.714	229.065
19 m/s, 20 %	986.978	119.456	1484.602	373.785
22 m/s, 20 %	990.251	127.071	1445.275	567.004
25 m/s, 20 %	993.218	138.974	1488.705	570.889

Actuator velocity (m/s)				
Mean wind speed, turbulence intensity	Mean	Standard deviation	Maximum	Minimum
13 m/s, 10 %	-.0000365	.01715	.06621	-.06595
16 m/s, 10 %	-.0000556	.01139	.06491	-.04324
19 m/s, 10 %	-.0000753	.01108	.04432	-.04572
22 m/s, 10 %	-.0000928	.01001	.03278	-.03655
25 m/s, 10 %	-.0000991	.00913	.03019	-.03250
13 m/s, 15 %	-.0000519	.01084	.06437	-.04579
16 m/s, 15 %	-.0000875	.01368	.06962	-.05124
19 m/s, 15 %	-.000109	.01387	.06969	-.04895
22 m/s, 15 %	-.000143	.01373	.06455	-.04725
25 m/s, 15 %	-.000143	.01281	.04500	-.04238
13 m/s, 20 %	-.0000642	.01249	.06591	-.04979
16 m/s, 20 %	-.000113	.01602	.06963	-.05812
19 m/s, 20 %	-.000142	.01731	.06997	-.05920
22 m/s, 20 %	-.000183	.01792	.06993	-.05885
25 m/s, 20 %	-.000176	.01698	.06482	-.05216

(Actuator velocity maximum = +/-0.07 m/s which is equivalent to 7.1°.)

Table 8.5 Statistics for above rated operation of the wind turbine.

9 Conclusions

The foundations for the control aspects of integrated design, as summarised in Chapter 8, are now laid. Appropriate models of the dynamics are determined which represent all the important characteristics of the system. The relationship of the model parameters to the physical parameters of the wind turbine are derived. These models are used to determine the dependence of the controller performance on the wind turbine configuration; that is, on the number of blades (two or three), the type of active regulation (full-span or tip), the frequency of the first drive-train mode, and the controller cross-over frequency. The range of performance possible is surprisingly large but enough information is obtained to identify those configurations which enable the best controller performance to be achieved. These results and methodologies are illustrated by applying them to the design of a full-span regulated, 1 MW wind turbine. The controller performance for the resulting design is very acceptable.

Other results stemming from the work presented here, which are relevant to controller design, are the following

- the widely used simple two-mode model of the dynamics of the power train is rigorously derived.
- the power-train dynamics are characterised by the frequency and damping factor of the first drive-train mode.
- there is little potential benefit to be gained from optimising the design of the controller.
- controller performance for full-span regulated machines can be improved by increasing the controller cross-over frequency with wind speed.
- conventional modifications to the drive train cannot improve its damping.
- compliantly mounting the generator can improve the damping of the power train.
- the spectral loads at $n\Omega_o$ can be counteracted by compliantly mounting the generator.

- torque control of variable speed wind turbines can be improve the damping of the drive train.
- the best controller performance is attained by a three-bladed tip-regulated wind turbine because the ratio of the aerodynamic torque partial derivatives with respect to pitch angle and to wind speed is smaller than those of the other machine configurations and the size of the spectral loads is smaller on the three-bladed machines compared to two-bladed ones.
- the worst controller performance is attained by a two-bladed full-span regulated wind turbine because the ratio of the aerodynamic torque derivatives with respect to pitch angle and wind speed is larger than those of the other machine configurations and the size of the spectral loads is larger on the two-bladed machines compared to three-bladed ones.
- the controller performance of the fledge device appears to be similar to that of the conventional tip.
- the power performance of a tip-regulated machine is not improved by independent-tip regulation.

The above results apply to almost all configurations of wind turbine.

The first steps towards integrated design have been taken. Aspects other than power controller performance need to be explored.

10 Further work

This chapter describes some possible areas for further work.

- a) The control aspects of integrated design could be explored further in a variety of ways as follows.
 - i) The performance of medium- and large-scale machines could be compared. This would require typical actuator accelerations and velocities for both electromechanical and hydraulic actuators for both scales of machine.
 - ii) More comprehensive comparisons between the performance of full-span and tip-regulated wind turbines could be made if the increase in actuator capability for tip-regulated machines due to the lower movable inertia were taken into account.
 - iii) The same approach would allow a better comparison of the performance of the fledge device to that of the tip.
 - iv) A more comprehensive investigation of the performance of the fledge could be undertaken if aerodynamic behaviour in wind speeds just above rated were better understood and the design implications of such a device were tested in the field.
 - v) The motion of the compliantly mounted generator in Chapter 4 was assumed to be unacceptable. However, investigations into what is acceptable motion of the generator and whether the control system design could take account of that could be considered, while still maintaining the benefits of increasing the damping factor of the first drive-train mode or decreasing the quantity of $n\Omega_r$.

- b) Various other aspects of integrated design could also be investigated, as follows.
 - i) For the most part constant-speed machines have been considered here. The investigation could be expanded to include variable-speed machines. The use of torque control to increase the damping of the first drive-train mode on a very lightweight flexible variable-speed machine at one operating point was considered in Chapter 4. This work could be expanded to design a controller or

set of controllers suitable for controlling the drive-train resonance over the whole operating range.

- ii) It is known that good power control performance produces low levels of power flicker. The way in which power flicker varies with machine configuration could be investigated. Since power flicker only occurs at around one frequency, the modification to the generator mounting considered in Chapter 4 could be investigated to see if the amount of power flicker could be reduced, if it is a problem on a particular machine.
- iii) The fatigue aspects of integrated design could be considered, as could the way in which the configuration of a machine affects the fatigue of various components. Any limitations on machine configuration due to unacceptable fatigue could be taken into account in the control design.

References

- Agius, P.R.D., Anderson, C.G., Green, D.R.R., Smith, W.M.R., Urwin, N.J., *Machine for the nineties study for a cost effective HAWT*, Wind harvester Ltd., report for DTI under contract E/5A/6110/2874.
- Anderson, C.G., 1990a, *The merits of tip control for large horizontal-axis wind turbines*, Proc. of 12th British Wind Energy Assoc. Conf., Norwich, March 1990, pp. 195-204.
- Anderson, C.G., 1990b, *Wind turbine aerodynamic loading and performance code*, then of Fluid dynamics Unit, Dept. of Physics, University of Edinburgh, JCMB, Mayfield Rd. Edinburgh, EH9 3JZ.
- Anderson, C.G., 1991, Private communication, then of Fluid dynamics Unit, Dept. of Physics, University of Edinburgh, JCMB, Mayfield Rd. Edinburgh, EH9 3JZ..
- Anderson, C.G., Campbell, T.J., 1992, *'Front end' Aerodynamic control of horizontal axis wind turbines*, Sept. 1992, Final report produced by University of Edinburgh for D.En. under ETSU Contract No. E/5A/CON/6037/2259, (ref.: L300-186).
- Anderson, C.G., and Jamieson, P., 1988, *Mean load measurements on the Howden 33 m wind turbine*, Proc. of 10th British Wind Energy Assoc. Conf., March 1988, London, UK, pp. 63-74.
- Anderson, C.G., Richon, J-B., Campbell, T.J., 1990, *Fast-acting aerodynamic control of horizontal-axis wind turbines*, Proc. of European Community Wind Energy Conf., Madrid, Spain, pp. 521-526.
- Armstrong, J.R.C., 1995, *Wind turbine configurations*, Proc. of 17th British Wind Energy Assoc. Conf., July 1995, Warwick, UK, pp. 39-46.
- Baltus, C.W.A., *Opbouw Beproeving van de IRFLET - proefopstelling op de RAAF*, Technical Report DE-Memo-91-43, ECN, Petten, October 1991.
- Barltrop, N.D.P., Ward, I.P., Daw, D.J., 1993, *The implications of fatigue on the cost of HAWTs*, Proc. of 15th British Wind Energy Assoc. Conf., October 1993, York, UK, pp. 253-259.
- Bossanyi, E.A., 1985, *Adaptive pitch control for a 250 kW wind turbine*, Proc. 9th British Wind Energy Assoc. Conf., April 1985, UK, pp. 85-92.
- Bossanyi, E.A., 1989, *Adaptive pitch control of a 25m wind turbine generator*, TWC Library

Ref.: 014v/86/3143, WEG, December 1986.

- Bossanyi, E.A., Jervis, B., 1988, *Compliance in wind turbines with either synchronous or induction generators*, Proc. of 10th British Wind Energy Assoc. Conf., London, March 1988, pp. 23-25.
- Bossanyi, E.A., Smith, G. J., Leithead, W. E., Agius, P., 1992, *Design and testing of a classical controller for the MS-3 Wind Turbine*. DTI Report ETSU WN 6033, Energy Technology Support Unit, Harwell, UK.
- Botta, G., Castagna, R., Cavaliere, M., Lembo, E., Visco Gilardi, A., Proc. of 5th European Wind Energy Conf. and Exhibition, Vol. III, October 1994, Thessaloniki, Greece, pp. 207-214.
- British Wind Energy Assoc., 1996, *Wind Energy - Power for a sustainable future - Policy statement of the BWEA*.
- Campbell, T.J., 1990, *'Front end' Aerodynamic control of horizontal axis wind turbines, Progress Report 1, Hydraulic Tip Actuator*, July 1990, produced by The University of Edinburgh for D.En. under Contract No. 914 495 AR480.
- Connell, J.R., 1988, A primer of turbulence at the wind turbine rotor, *Solar Energy*, Vol. 41, No. 3, pp. 281-293.
- Connor, B., Iyer, S.N., Leithead, W.E., Grimble, M.J., 1992, *Control of a Horizontal axis wind turbine using H_∞ control*, 1992, Proc. 1st IEEE Conf. on Control Apps, Ohio, USA, Sept. 1992, pp. 117 -122.
- Connor, B., Leithead, W.E., Grimble, M.J., 1994, LQG of a constant speed horizontal axis wind turbine, Proc. 3rd IEEE Conf. on Control Apps, Glasgow, UK, August 1994, pp. 239-244.
- Corbet, D.C., and Brown, C.J., 1992, *Brakes for stall regulated wind turbines*, Proc. of 14th British Wind Energy Assoc. Conf., March 1992, Nottingham, UK, pp. 155-160.
- Derrick, A., 1992, *Aerodynamic characteristics of novel tip brakes and control devices for HAWTs*, Proc. of 14th British Wind Energy Assoc. Conf., March 1992, Nottingham, UK, pp. 73-78.
- Dijkstra, S.J., Bongers, P.M.M., van Baars, G.E., 1994, *Control of wind turbine system to reduce vibrations and fatigue loading*, Proc. of 5th European Wind Energy Conf. and Exhibition, Vol. I, October 1994, Thessaloniki, Greece, pp. 425-430.
- Dragt, 1984, *The spectra of wind speed fluctuations met by a rotating blade and resulting load fluctuations*, Proc. of European Wind Energy Conf., October 1984, Hamburg, Germany, pp. 453-458.
- Eggleston, D.M. and Stoddard, F.S., 1987, *Wind turbine Engineering Design*, Van Nostrand

Reinhold Co. New York, ISBN 0-442-22195-9.

- Engelen, T.G. van, Bongers, P.M.M., Pierik, J.T.G., Baars, G.E. van, 1993, *Integral control for damping of mechanical resonance and protection against grid failures: results in a full load operating condition*, Proc. European Community Wind Energy Conf., March 1993, Lübeck-Travemünde, Germany, pp. 545-550.
- Gardner, P., Jenkins, N., Allan, R.N., Saad-Saoud, Z., Castro F., Roman, J., Rodriguez, M., *Network connection of large wind turbine*, Proc. of 17th British Wind Energy Assoc. Conf., July 1995, Warwick, UK, pp. 161-166.
- Garrad, A., 1998, *Wind energy technology - a success story*, Proc. of 20th British Wind Energy Assoc. Conf., Sept. 1998, Swansea, UK.
- Fisher, A., 1995, *Active Control of drive-train resonance*, Exchange project report, Dept. of Electronic and Electrical Engineering, University of Strathclyde, April 1995.
- Frandsen S., 1988, *Flapwise Extreme Response of Wind Turbine Blades due to Turbulence Loading*, Proc. of 10th British Wind Energy Assoc. Conf., March 1988, London, UK, pp. 393-400.
- Frandsen S., Hauge Madsen P. and Hansen, J.C., 1984, *What is the difference between a large and a small wind turbine*, Proc. of European Wind Energy Conf., October 1984, Hamburg, Germany, pp. 287-294.
- van Grol, H.J., Snel, H., Schepers, J.G., 1990, *Wind turbine benchmark exercise on mechanical loads*, Proc. of European Community Wind Energy Conf., 1990, Madrid, Spain. pp. 389-394.
- Harrison, R., Jenkins, G., Macrae, A.N., 1990, *Study on the next generation of large wind turbines, Part 2. Manufacturing cost analysis*, Proc. of European Community Wind Energy Conf., 1990, Madrid, Spain. pp. 433-437.
- Havard, M., 1990, Feasibility study of an innovative control device for a HAWT, Feb. 1990, Report ISC 1002 prepared for ETSU (DEn.), Industrial Systems and Control Ltd.
- Hinrichsen, E.N., 1984, Controls for variable pitch wind turbine generators, IEEE Trans. Power Appar. and Syst., Vol. 103, pp. 886-892.
- Hinrichsen, E.N., and Nolen, P.J., 1982, Dynamics and Stability of wind turbine generators, IEEE Trans. Power Appar. and Syst., Vol. PAS-101, No. 8, August 1982, pp. 2640-2648.
- Hunter, R.S., Derrick, W.A., Robertson, N.I.D., Chapman, J.L., 1993, *Pre field test development of the 'FLEDGE' aerodynamic braking and control device*, Proc. of 15th British Wind Energy Assoc. Conf., June 1993, York, UK pp. 299-304.
- Jamieson, P., 1991, Private communication, Garrad and Hassan and Partners, Glasgow.

- Jamieson, P., 1993, *Further analysis of data from the Howden HWP330/33 wind turbine*, Garrad Hassan report prepared for DTI under contract E/5A/CON/6025/2212.
- Jamieson, P., and Agius, P., 1989, *SLEDGE - A novel braking device for HAWTs*. James Howden Group Technology, Report for DEn., under contract E/5A/CON/5119/1989, March 1989.
- Jamieson, P., and Agius, P., 1990, *A comparison of aerodynamic devices for control and overspeed protection of HAWTs.*, Proc. of 12th British Wind Energy Assoc. Conf., March 1990, Norwich, UK, pp. 205-213.
- Jamieson, P., and Brown, C.J., 1992, *The optimization of stall regulated rotor design*, Proc. of 14th British Wind Energy Assoc. Conf., March 1992, Nottingham, UK, pp. 79-84.
- Jamieson, P., Bowles, A., Derrick, A., Leithead, W., Rogers, M., 1992, *Innovative concepts for aerodynamic control of wind turbine rotors*, J. of Wind Engineering and Industrial Aerodynamics, **39**, pp. 395-404, Elsevier Science Pub., B.V., Amsterdam.
- Johnson, C.C., and Smith, R.T., 1976, *Dynamics of wind generators on electric utility networks*, IEEE trans. on Aerospace and Electronic Syst., Vol. **12**, No. **4**, July 1976, pp. 483-493.
- Juggins, P.T.W. and Holton, S.A., 1995, *An assessment of the effects of soft mounting systems on wind turbine dynamics*, report for DTI ETSU W/43/0346/REP.
- Kos, J.M., 1978, *On line control of a large horizontal axis wind energy conversion system and its performance in a turbulent wind environment*, Proc. 13th Intersoc. Energy Conv. Eng. Conf., August 1978, pp. 2064-2073.
- Krause, P.C., and Thomas, C.H., 1965, *Simulation of symmetrical induction machinery*, IEEE trans. on Power Appar. Syst., Vol **PAS-84**, No. **11**, No., 1965.
- Kristensen, L., and Frandsen, S., 1982, *Model for power spectra measured from the moving frame of reference of the blade of a wind turbine*, J. of Wind Engineering and Industrial Aerodynamics, Vol. **10**, pp. 249-262.
- Leith, D. J., and Leithead, W.E., 1994a, *Comparison of various control strategies for a two-bladed wind turbine*, Proc. of 16th British Wind Energy Assoc. Conf., June 1994, Stirling, UK, pp. 61-66.
- Leith, D.J., and Leithead, W.E., 1994b, *Benefits of optimising the controller with wind speed for a constant speed HAWT*. Proc. of 5th European Wind Energy Assoc. Conf. and Exhibition, Vol. I, Thessaloniki, Greece, October 1994, pp. 435-440.
- Leith, D.J., and Leithead, W.E., 1994c, *Application of nonlinear control to a HAWT*, Proc. of 3rd IEEE Conf. on Control Applications, 1994, Glasgow, UK, pp. 245-250.
- Leith, D.J., and Leithead, W.E., 1995a, *Directly responding to peak power excursions in*

- pitch regulated HAWTs*. Proc. of 17th British Wind Energy Assoc. Conf., July 1995, Warwick, UK., pp. 293-298.
- Leith, D.J., and Leithead, W.E., 1995b, *Strongly input constrained nonlinear control of a horizontal axis wind turbine*. Proc. of European Control Conf., 1995, pp. 1562-1567.
- Leith, D.J., and Leithead, W.E., 1995c, *An investigation of the benefits of nonlinear control for pitch-regulated wind turbines*. Report prepared under DTI contract No. ETSU W/42/00348/00/00, Industrial Control Centre, University of Strathclyde, Glasgow, UK
- Leith, D.J., and Leithead, W.E., 1996a, *Appropriate realization of gain-scheduled controllers with application to wind turbine regulation*. Int. J. of Control, Vol. 65, No. 2, pp. 223-248.
- Leith, D.J., and Leithead, W.E., 1996b, *Performance enhancement of wind turbine power regulation by switching linear control*, Int. J. Control, Vol 65, No. 4, pp. 555-572.
- Leith, D.J., and Leithead, W.E., 1997, *Implementation of wind turbine controllers*. Int. J. of Control, Vol. 66, pp. 349-380.
- Leithead, W.E., 1990, *Dependence of performance of variable speed wind turbines on the turbulence, dynamics and control*, Proc. of the Institution of Electrical Engineers, Vol. 137, PT. C., No. 6, November 1990, pp. 403-413.
- Leithead, W.E., 1992, *Effective wind speed models for simple wind turbine simulations*, Proc. of 14th British Wind Energy Assoc. Conf., March 1992, Nottingham, UK, pp. 321-326.
- Leithead, W.E., and Agius, P., 1992, *Design and testing of a classical controller for the MS-3 wind turbine*, Final report prepared for DTI under contract ETSU E/5A/CON/6033/2184, Industrial Control Centre, University of Strathclyde, Glasgow, UK.
- Leithead, W.E., Rogers, M.C.M., 1995a, *Improving damping by a simple modification to the drive-train*, Proc. of 17th British Wind Energy Assoc. Conf., July 1995, Warwick, UK, pp. 273-278.
- Leithead, W.E., and Rogers, M.C.M., 1995b, *Drive-train characteristics of constant speed HAWT's*, Report ICU/110 Industrial Control Centre, University of Strathclyde, Glasgow, UK.
- Leithead, W.E., Rogers, M.C.M., 1996, *Options for drive-train design - a dynamic perspective*, Proc. of European Community Wind Energy Conf., Goteborg, May 1996, pp. 882-885.
- Leithead, W.E., Salle, S.A. de la, Reardon, D., Grimble, M.J., 1988, *Wind turbine modelling*

- and control*, Report prepared for DEn. under contract no. E/5A/CON/s108/1851, University of Strathclyde, October 1988.
- Leithead, W. E., de la Salle, S.A., Reardon, D., Grimble, M.J., 1991a, *Wind turbine control systems modelling and design, Phase I + II*, Report No. ETSU WN 5108, Report prepared for DEn., University of Strathclyde.
- Leithead, W.E., de la Salle, S. A., Reardon, D., 1991b, Role and objectives of control for wind turbines, *Proc. of the Institution of Electrical Engineers*, Pt C, Vol. 138, No. 2, March 1991, pp. 135-148.
- Leithead, W.E., Rogers, M.C.M., Agius, P.R.D., 1992a, *Dynamic analysis of the compliant tip*, May 1992, Report prepared for DEn. (ETSU) under contract W/42/00349/00/00., University of Strathclyde, UK,
- Leithead, W.E., de la Salle, S.A., Reardon, D., 1992b, Classical control of active pitch regulation of constant speed HAWTs. *Int. J. of Control*, Vol. 55, pp. 845-876.
- Leithead, W.E., Rogers, M.C.M., Agius, P.R.D., Reardon, D., 1992c, *The simulation of the compliant tip*, May 1992, Report prepared for Edinburgh university, under DEn. contract W/42/00349/00/00.
- Leithead, W.E., Rogers, M.C.M., Connor, B., van der Molen, G., Pierik, J.T.G., van Engelen, T.G., 1994a, *Design and Test of the Controller for a Variable Speed Wind turbine*, report prepared for DTI, Report ETSU W/42/00242/REP, University of Strathclyde, Glasgow, UK.
- Liebst, 1983, Pitch control systems for large scale wind turbines, *J. Energy*, Vol. 7, Pt. 2, March-April 1983, pp. 182-192.
- Madsen, P.H., 1988, *Power regulation options for wind turbines*, Proc. of European Community Wind Energy Conf., Herning, Denmark, June 1988, pp. 1-7.
- Madsen, P.H., Frandsen, S., 1984, *Pitch angle control for power limitation*, Proc. of the European Wind Energy Conf., Hamburg, Germany, October 1984, pp. 612-619.
- Mattsson, S.E., 1985, *Modelling and control of horizontal axis wind turbines*, Ph.D. thesis, Lund University, Stockholm, Sweden..
- Mercer, A.S, Quarton, D.C, 1992, *An analysis of fledge dynamic loading*, Garrad Hassan Report No. 199/R/1 prepared for National Engineering Laboratory under contract NEL/F/845.
- Merit, H.E., 1967, *Hydraulic Control Systems*, John Wiley & Sons, Inc., New York.
- Milborrow, D.J., 1993, *Energy generation costs - now and for the year 2000*, Proc. of 15th British Wind Energy Assoc. Conf., York, UK, pp. 15-21.
- Moore, W.H., 1988, *Layman's' guide to wind The Geoff. Pontin Memorial Lecture*, Proc. of

- 10th British Wind Energy Assoc. Conf., March 1988, London, UK, pp. 81-88.
- National Wind Turbine Centre, 1994, *Innovative aerodynamic braking and control devices for horizontal axis wind turbines*, contract E/5A/6060/2495 W/42/00235/00/00 for AEA Technology Ltd., Ref. AET006.
- OFFER (Office of electricity regulation), 1998, Fifth renewables orders for England and Wales, Sept. 1988.
- Pierik, J.T.G., Bongers, P.M.M., Engelen, T.G. van, Baars, G.E. van, 1993, *Damping of mechanical resonance and protection against grid failure for variable speed wind turbines (IRFLET)*, ECN report ECN-C-93-004.
- Platts, M.J., 1990, *The design, development, and manufacture of large wood/composite wind turbine rotors*, Proc. of 12th British Wind Energy Assoc. Conf., March 1990, Norwich, UK, pp. 25-31.
- Quarton, D.C., 1989, *A theoretical investigation of the impact of control systems on fatigue of wind turbines*, report prepared for DEn. under contract E/5A/CON/6015/2116, October 1989.
- Quarton, D.C., 1990a, *The impact of pitch control on wind turbine fatigue*, Proc. of 12th British Wind Energy Assoc. Conf., March 1990, Norwich, UK, pp. 77-83.
- Rasmussen, F., Madsen, P.H., 1990, *Rotor loading - the influence of dynamics*, Proc. of European Community Wind Energy Conf., Madrid, Spain, pp. 306-311.
- Reardon, D.C., 1991, *Wind turbine control systems, objectives, modelling and design*, Ph.D. thesis, University of Strathclyde, Glasgow, UK.
- Richon, J-B., Anderson, C.G., 1993, *Wind tunnel testing of a blade tip actuator with aerodynamic moment feedback*, Proc. of European Community Wind Energy Conf., March 1993, Lübeck-Travemünde, Germany, pp. 551-554.
- Robb, D.M., and Leithead, W.E., 1998, Effective wind speed models for simple simulations of wind turbines with blade tips, *Wind Energy*, Vol. 2 - submitted for publication.
- Rogers, M.C.M., and Leithead, W.E., 1994, *Development of control system for RES 1 MW machine*, Report prepared for Renewable Energy Systems Ltd., Industrial Control Centre, University of Strathclyde, Glasgow, UK.
- Rothman, E.A., 1978, *The effects of control modes on rotor loads*, 2nd Int. Symp. Wind energy systems, Amsterdam, October 1978, pp. C7.107-C7.117.
- de la Salle, S.A., Reardon, D., Leithead, W.E., Grimble, M.J., 1990, A review of wind turbine control, *Int. J. of Control*, Vol. 52, No. 6, pp. 1295-1310.
- Simpson, P.B., 1994, *Development in wind turbine technology*, Proc. of 16th British Wind Energy Assoc. Conference, June 1994, Stirling, UK, pp. 29-40.

- Simpson, P.B., Haines, R.S., Sauven, R.H., 1993, *Development of an advanced two bladed HAWT*, Proc. of European Community Wind Energy Conf., March 1993, Lübeck-Travemünde, Germany, pp. 231-234.
- Snel, H., Schepers, J.G., 1993, *Investigation and modelling of dynamic inflow effects*, Proc. of the European Community Wind Energy Conf., March 1993, Lübeck-Travemünde, Germany, pp. 371-375.
- Spruce, C.J., 1993, *Simulation and control of windfarms*, D.Phil. thesis, University of Oxford, Dept. of Eng. Sci., Parks Rd., Oxford, OX1 3PJ.
- Stig-øye, 1986, *Unsteady wake effects caused by pitch-angle changes*, Report of Tech. Univ. of Denmark.
- Sullivan, J.P., 1982, *A review of resonances in large horizontal axis wind turbines*, *Solar Energy*, Vol. **29**, No. **5**, pp. 3777-3783.
- Wasynczuk, O., Man, D.T., Sullivan, J.P., 1981, *Dynamic behaviour of a class of wind turbine generators during random wind fluctuations*, *IEEE Trans. Power Appr. and Syst.* Vol. **PAS-100**, No. **6**, June 1981, pp 2837-2845.
- Wilkie, J., Leithead, W.E., 1988, *Dynamic modelling of wind turbine systems using ACSL*, Report prepared for DEN. by Industrial Systems and Control Ltd., Glasgow, UK.
- Wilkie, J., Leithead, W.E., Anderson, C.G., 1989, *Simulation of wind turbines by simple models*, Proc. of European Wind Energy Conf., 1989., Glasgow, UK, pp 336-340.

Appendix A Modelling of wind speed

A.1 Introduction

The objective of the models of wind speed adopted throughout this work, is to reshape the power spectrum of turbulence as seen from a fixed observation point (Frandsen, 1988) to represent either the effective wind speed averaged over the whole rotor disc or that experienced by an individual tip and the remaining part of the blade. The power spectrum of turbulence seen at a point can be modelled by the von Karman spectrum. There are major discrepancies between the power spectrum of turbulence seen at a point and the typical spectrum of hub torque seen on a wind turbine. There is a depletion of power in the mid-frequency range due to disc averaging and there are peaks of power concentrated around Ω_o and $n\Omega_o$. The peak at Ω_o is sharp and hence is primarily deterministic. It is primarily the result of blade mismatch. The peak at $n\Omega_o$ on the other hand is stochastic. It is primarily due to rotational sampling of the uneven wind field (Kristensen and Frandsen, 1982; Dragt, 1984). On a two-bladed machine with a teetered hub the $2\Omega_o$ is enhanced, (Grol *et al.*, 1990). The actual redistribution of energy depends on the amount of turbulence and the rotor size.

Since the turbulent nature of the wind is a source of fatigue (*c.f.* Section 2.4.1), appropriate modelling of the interaction of the wind speed and rotor is obviously needed for simulation and control design. The simulation model must represent all the wind and rotor characteristics relevant to the turbine dynamics. The model used in the parametric study and control design must be simple and represent only the dominant features in relation to power/load regulation. A summary of wind speed models described in the literature is given by Leithead *et al.* (1991a). Simple models of wind speed are required as they decrease the computational time required and increases clarity of analysis.

Two wind speed models are used in this thesis. The first model is for the wind speed experienced by the whole rotor. Reardon (1991) derived suitable parameters for a hub height of 30 m. This hub height corresponds to that of a medium-scale machine but not that of a large-scale machine. Hence suitable parameters for the same model and methodology are

derived for a hub height of 50 m. The second model is for the correlated wind speeds experienced by a tip and the remaining part of the blade (Leithead, 1992). Both models are driven by point wind speed¹, the modelling of which is described first.

A.2 Modelling the spectrum of wind speed measured at a point

This section reviews the derivation of an effective wind speed representing the averaging of the wind speed over the rotor disc. The effective wind model is intended to represent only the low-frequency turbulent component of the wind field. It is not intended to represent the deterministic components such as tower shadow and wind shear. Nor is it intended to represent the high-frequency spectral peaks due to rotational sampling of the wind field. The very low-frequency components may be considered to be uniform over the rotor disc. Hence they constitute a quasi-static mean wind speed which varies slowly over a time-scale of the order of a few minutes. The derivation of the effective wind speed model need cater only for the perturbations in the wind field about this quasi-static mean wind speed.

The standard deviation of the point wind speed, V , at height h is given by Madsen and Frandsen (1984) as

$$\sigma_V = \frac{V}{\ln(h/z_o)} \quad (\text{A.1})$$

where z_o is a measure of the roughness of the terrain. The effect of the roughness of the terrain on the turbulence intensity is suggested by Connell (1988) to be in the range 0.08 to 0.5 depending on the complexity of the terrain and a range of atmospheric conditions. Turbulence intensity is defined as

$$I = \sigma_V / V \quad (\text{A.2})$$

Reardon (1991) selected a turbulence intensity of 0.2 for a fictitious 300 kW wind turbine with hub height 30 m and a terrain surface roughness of 0.2. The resulting wind model is used for all the 300 kW machines investigated in this study. However, the large-scale machines have a more realistic hub height of 50 m. Therefore assuming that all the machines have the same terrain surface roughness, the low-frequency intensity of the wind speed would be less than that found on 300 kW machines.

¹ The wind speed sensed at a fixed (non-rotating) point, *e.g.* the wind speed measured by a small anemometer, is called a point wind speed.

There are numerous models for representing the power spectrum of turbulent wind speed relative to an average wind speed. Leithead *et al.* (1991a) selected the von Karman spectrum of the form (Frandsen, 1988)

$$S_v(\omega) = 0.475\sigma_v^2 \frac{(L\bar{V}^{-1})}{(1+(\omega L\bar{V}^{-1})^2)^{5/6}} \quad (\text{A.3})$$

The spectrum is centred on the average wind speed, \bar{V} , with a standard deviation of σ_v and a turbulent length scale, L . The turbulent length scale can be thought of as the size, or length, of typical eddies in the wind field. According to Frandsen (1988) measurements of L vary by a factor of at least 3 to 5, since the physics of turbulence is not understood. Madsen and Frandsen (1984) suggest that as an approximation the length scale may be taken as

$$L = 6.5h \quad (\text{A.4})$$

where h is the observation height of the spectrum. Madsen and Frandsen (1984) have also suggested that L may be as low as h . This would imply that the spectrum is broader compared to that for $L = 6.5h$. The point wind spectrum obtained from data obtained on the Howden HWP55/1000 machine (Leithead *et al.*, 1991a) and the Howden HWP33/330 (Wilkie and Leithead, 1989) verify that a multiple of 6.5 is reasonable.

Using $L = 6.5h$, (A.3) is approximated by a Dryden² spectrum as this is easily modelled by a first-order differential equation driven by white noise, (A.5).

$$\dot{v} = -av + b\omega_I, \quad \sigma_I^2 = 1 \quad (\text{A.5})$$

where v denotes the turbulent wind speed. The parameters a , and b , are selected to achieve the correct power spectrum characteristics for a range of wind speeds when σ_v is unity, and then scaled such that the turbulence is correct. The results for hub heights of 30 m and 50 m are presented in Table A.1. White noise filtered by the first-order transfer function

$$b/(s+a) \quad (\text{A.6})$$

approximates the turbulence at a point.

As shown in Figure 2.6, the resulting torque seen at low frequency by the rotor has the same spectrum as that at a point. However, since there is a discrepancy in the mid-frequency range a spatial filter is introduced to represent averaging over the rotor disc. When only the interaction with the wind speed of the complete rotor is required, for instance to model the total hub torque, a single spatial filter as described in the next section is adequate. When separate representation for the interaction of a main blade and a tip with the

² Dryden spectrum - $S_w(\omega) = \frac{K_v}{1+(\omega T_v)^2}$ where K_v and T_v are constants depending on the surface

roughness and the turbulence intensity.

wind speed is required, as in the case of the compliant tip (described in Chapter 7), separate spatial filters of the form described in sub-section A.4 are appropriate.

	Wind speed (m/s)	11	12	13	14	15	16	17	18	19	20	21	22	23
a_t	30	.063	.068	.074	.080	.086	.092	.097	.103	.108	.114	.119	.125	.131
b_t	30	.781	.885	1.00	1.12	1.24	1.37	1.50	1.63	1.77	1.91	2.05	2.2	2.35
a_t	50	.041	.045	.048	.052	.056	.060	.063	.067	.071	.075	.078	.081	.086
b_t	50	.570	.652	.729	.818	.909	1.004	1.093	1.193	1.297	1.403	1.502	1.604	1.728

Table A.1 Parameters for modelling a point wind speed by a first-order filter.

A.3 Modelling the wind speed experienced by the whole rotor

A spatial filter described by Madsen and Frandsen (1984) and used by Leithead *et al.* (1991a) in control analysis and simulation studies is used in this work to model the disc averaging effect on the total hub torque. The power spectrum of the hub torque (Madsen and Frandsen, 1984) is

$$S(\omega) \approx k^2 R^4 \pi^2 S_v(\omega) \Phi(x) \quad (\text{A.7})$$

where

$$\Phi(x) = \frac{2 + x^2}{(2 + c_s x^2)(1 + x^2 / c_s)} \quad (\text{A.8})$$

$S_v(\omega)$ is the power spectrum of wind speed measured at a point

c_s is a constant = 0.55

γ_s is the decay constant = 1.3

$$x = \gamma_s R / \bar{V} \cdot \omega$$

k is a normalising constant.

Equation (A.8) can be spectrally factorised to obtain a transfer function to represent the spatial filtering of the rotor as

$$G(s) = \frac{(1 + T_1 s)}{(1 + T_2 s)(1 + T_3 s)} \quad (\text{A.9})$$

where $T_1 = K / \sqrt{2}$; $T_2 = T_1 \sqrt{c_s}$; $T_3 = K / \sqrt{c_s}$; and $K = \gamma_s R / \bar{V}$

The spectral peaks seen on the rotor torque are modelled as additional torque components and are described in Section 3.1.3.

The validity of this approach to modelling the drop in the power in the mid-frequency range of the rotor torque by the spatial filter is obvious from Figure A.1 which

$$S_{IO} \approx S_v(\omega) \frac{(1 + x^2 / 6)}{(1 + x^2 / 0.5)(1 + x^2 / 12)(1 + x^2 / 100)} \quad (\text{A.10})$$

The spectrum for the effective wind speed over the inner swept disc is

$$S_{II} \approx S_v(\omega) \frac{(1 + x^2 / 6)}{(1 + x^2 / 0.8)(1 + x^2 / 17)} \quad (\text{A.11})$$

The spectrum for the effective wind speed over the outer annulus is

$$S_{OO} \approx S_v(\omega) \frac{(1 + x^2 / 10)}{(1 + x^2 / 0.6)(1 + x^2 / 50)} \quad (\text{A.12})$$

In all the above relationships, (A.10), (A.11) and (A.12), $x = \gamma R_I / \bar{V} \cdot \omega = \lambda_1 \omega$.

Using spectral factorisation the effective wind speeds for the inner blade and tip can be expressed respectively as

$$V_r = \frac{1.51\lambda_1 s(\lambda_1 s + 2.45)(\lambda_1 s + 2.79)(\lambda_1 s + 7.79)}{(\lambda_1 s + 0.707)(\lambda_1 s + 0.894)(\lambda_1 s + 3.464)(\lambda_1 s + 4.123)(\lambda_1 s + 10)} v_1 + \frac{10(\lambda_1 s + 2.45)}{(\lambda_1 s + 0.707)(\lambda_1 s + 3.464)(\lambda_1 s + 10)} v_3 \quad (\text{A.13})$$

$$V_o = \frac{1.73\lambda_1 s(\lambda_1 s^2 + 3.94\lambda_1 s + 4.942)(\lambda_1 s + 9.14)}{(\lambda_1 s + 0.707)(\lambda_1 s + 0.775)(\lambda_1 s + 3.464)(\lambda_1 s + 7.071)(\lambda_1 s + 10)} v_2 + \frac{10(\lambda_1 s + 2.45)}{(\lambda_1 s + 0.707)(\lambda_1 s + 3.464)(\lambda_1 s + 10)} v_3 \quad (\text{A.14})$$

where v_1 , v_2 and v_3 are independent point wind speeds. Although derived for torque, these effective wind speeds can be used to estimate the blade bending moments as those also vary with hub distance and the tip pitching moment since their dependence on hub distance for the tip forces is weak (Anderson, 1991). In addition, since the majority of the wind field spectrum is at a comparable or lower frequency than that of rotation, the same model may be used to estimate the effective torque for the complete rotor.

The effective wind speed model is depicted in Figure A.3. It is expected (Leithead, 1992) that the model should be a good approximation up to $1\Omega_\phi$. Robb and Leithead (1998) have validated similarly derived filters for large tip sizes which are good approximations beyond $1\Omega_\phi$. Time series for V_r and V_o are depicted in Figure A.3.

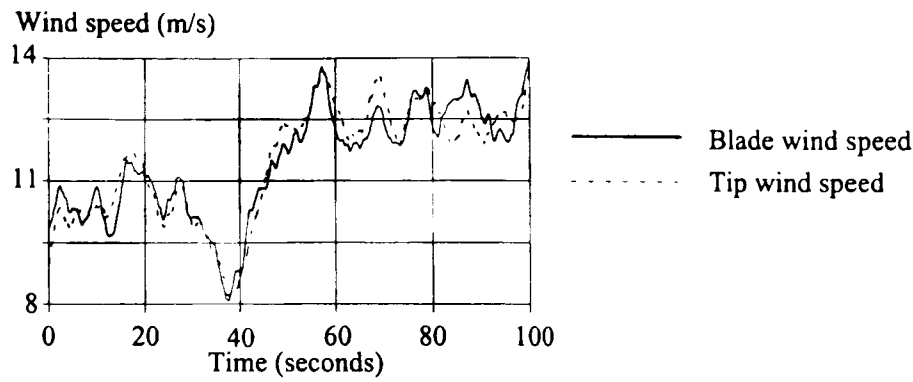


Figure A.3 Simulated wind speeds for the tip and inner rotor.

A.5 Modelling of loads on individual blades

The loads seen by an individual blade are different from those seen at the hub because of the cancellation of some of the blade loads due to symmetry. When considering independent tip control as in Chapter 7, the loads seen on an individual blade due to wind shear and tower shadow also require to be modelled. Anderson and Campbell (1992) provide the following models for the effects of wind shear and tower shadow which are seen in the wind sensed by the tip.

The wind shear factor, f_{shear} , can be expressed as

$$f_{shear} = (1 + r_t / h \cos(\theta_R))^c \quad (\text{A.15})$$

where

r_t is the radius of the mid point of the tip

h is the hub height

c is the wind shear exponent = 0.2

θ_R is angle of rotation of the blade.

The tower shadow factor, f_{tower} , is expressed as

$$f_{tower} = \begin{cases} 1.0 - \frac{r_{twr}^2}{(r_t^2 \sin^2 \theta_R + zz^2)} + \frac{2r_t^2 \sin^2 \theta_R r_{twr}^2}{(r_t^2 \sin^2 \theta_R + zz^2)^2} & ; \pi/2 < \theta_R < 3\pi/2 \\ 1.0 & ; \text{otherwise} \end{cases} \quad (\text{A.16})$$

where

zz is the distance from rotor plane to tower

r_{twr} is the radius of the tower.

Appendix B Power-train dynamics

The overall dynamic behaviour and hence the performance of a wind turbine is the result of a combination of the structural dynamics and those of the drive train, the generator and, when appropriate, the control system. A dynamically well-behaved machine requires the drive-train dynamics to complement in some sense the other wind turbine dynamics. In this appendix, equations of motion of the power train are derived for pitch-regulated machines as described in more detail by Leithead and Rogers (1995b). Although they are a composite of many dynamic modes of the tower, blades, hub, low-speed shaft, gearbox, gear-train, high-speed shaft and generator rotor, the power-train dynamics can be represented by a simple model.

B.1 Introduction

There are two separate aspects to the dynamics of a wind turbine. The first is the structural dynamics which are concerned with the motion of the blades, tower, *etc.* They influence the transient loads on the structure of the wind turbine and, thereby, its fatigue life. The second is the dynamics of the drive train, which influence the transient loads on the drive-train components, such as the gearbox, and the control system when the turbine is pitch regulated.

Poor drive-train dynamics and their consequences are well exemplified by the deterioration in dynamic behaviour which arises when a medium/high slip induction generator is replaced by a low-slip induction generator or even by a synchronous generator with no further modification of the drive train (Johnson and Smith, 1976, Hinrichsen, 1984). However, the relationship of the dynamic characteristics of the drive train to the dynamic attributes of the drive-train components, the generator and the rotor is obscured by the number of contributing factors.

Models of the drive-train dynamics are derived below which are well-suited to (i) the purpose of control system analysis and design, and (ii) the analysis of the relationship of the dynamic properties of the drive train to its physical parameters. (Clearly, in this context, the models need to be linear with the emphasis on the low frequency dynamics). For the former

case, exploiting the ability of the controller to accommodate any discrepancies, a simple model, applicable to particular configurations of wind turbine, is most appropriate. For the latter case, although a simple model is again the most appropriate, it must be derived with greater rigour and be applicable to all configurations of wind turbine under consideration since the drive-train dynamics can be affected by changes to the physical parameters, as investigated in Chapter 3.

Although, the drive-train dynamics of a wind turbine are a composite of many dynamic modes, they can be represented by a simple model which approximates very closely to the drive-train dynamics for almost all the wind turbine configurations under consideration. Firstly, in Section B.2, the equations of motion of the rotor blades, the hub and the low-speed shaft are determined together with their simplest possible representation. Secondly, in Section B.3, the equations of motion of the gearbox, including compliant coupling to the tower, are determined together with their simplest possible representation. Thirdly, in Section B.4, the equations of motion of the high-speed shaft and generator rotor are determined and the simplest possible representation of the combined drive-train dynamics is derived. The analysis presented is a sub-set of that of Leithead and Rogers (1995b).

B.2 Rotor

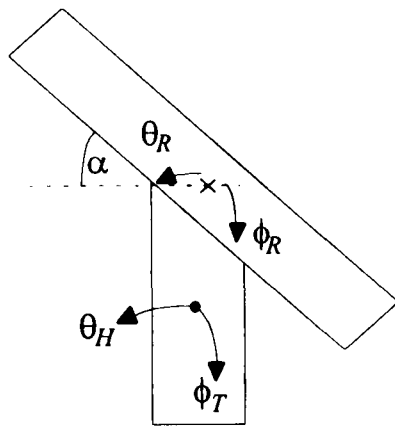
The analysis which follows of the rotor minus the hub assumes that the rotor has three blades. The analysis is, however, also applicable to a rotor with two blades.

B.2.1 Equations of motion of rotor

Each blade of the rotor has two dominant structural modes in the directions of the principal axes of the blade, one edge-wise and one flap-wise, which contribute to the low-frequency drive-train dynamics. The plane of the edge-wise mode is slightly skewed to the pitch plane of the blade and the plane of the flap-wise mode is perpendicular to the plane of the edge-wise mode. When all three blades are oscillating in phase at the same frequency the dominant edge-wise (flap-wise) mode is essentially the edge-wise (flap-wise) mode of an individual blade. Hence the rotor can be modelled by a single blade. For the edge-wise mode, the inertia of the single blade representation of the rotor may be approximated by the inertia, about the axis of the low-speed shaft, of the complete rotor. The stiffness is that required for the frequency to be the same as the edge-wise natural frequency of a blade in an inertial reference frame. The radius of gyration for the flap-wise mode of a blade is approximately the same as the radius of gyration for the edge-wise mode of a blade. Hence,

for the flap-wise mode, the inertia of the single blade representation of the rotor may again be approximated by the inertia of the complete rotor, and the stiffness is that required for the frequency to be the same as the flap-wise natural frequency of a blade in an inertial reference frame.

The net effect of the side-to-side motion of the tower on the rotor aerodynamic forces is negligible. The tip speed of the blades higher than the hub is increased (decreased) by the motion of the tower head, but the tip speed of the blades lower than the hub is decreased (increased) by a compensating amount. In addition, displacement in the plane of the rotor of the blades due to the dominant rotor normal mode does not induce motion, relative to the tower head, of the centre of mass of the rotor. Hence there is no need to include dynamics of the side-to-side motion of the tower in the analysis. In contrast, the fore-and-aft motion of the tower affects the rotor aerodynamics forces and induces motion, relative to the tower head, of the centre of mass of the rotor. Hence, the fore-and-aft motion of the tower couples directly to the rotor and so the analysis must include the dynamics of that motion.



- θ_R in-plane angular displacement of the centre of mass of the blade
- ϕ_R out-of-plane angular displacement of the centre of mass of the blade
- θ_H angular displacement of hub
- ϕ_T fore-and-aft angular displacement of the hub
- α angle of pitch of the blade

Figure B.1 Single blade and low-speed shaft viewed axially along blade.

The single blade model of the rotor is depicted in Figure B.1. The Lagrangian for the system is

$$\begin{aligned} \ell_R = & \frac{J\dot{\theta}_R^2}{2} + \frac{J\dot{\phi}_R^2}{2} + \frac{J_T\dot{\phi}_T^2}{2} + J_C\dot{\phi}_R\dot{\phi}_T - \frac{K_E}{2}[(\theta_R - \theta_H)\cos\beta - (\phi_R - \phi_T)\sin\beta]^2 \\ & - \frac{K_F}{2}[(\theta_R - \theta_H)\sin\beta + (\phi_R - \phi_T)\cos\beta]^2 - \frac{K_T\phi_T^2}{2} + D_T\phi_T + F_1\theta_R + F_2\phi_R \quad (\text{B.1}) \\ & - \frac{J\Omega_o^2}{2}(\theta_R - \theta_H)^2 - \frac{J\Omega_o^2}{2}(\phi_R - \phi_T)^2 \end{aligned}$$

where J is the inertia of the rotor, K_E and K_F are the edge-wise and flap-wise stiffnesses of the single blade, F_1 and F_2 are the in-plane and out-of-plane aerodynamic torques on the blade and Ω_o is the nominal angular velocity of the rotor. The last two terms in (B.1)

represent the centrifugal stiffening of the rotor. The dominant fore-and-aft structural mode of the tower is included in (B.1). J_T is the total moment of inertia of the complete wind turbine about its base with all components capable of independent motion treated as point masses. J_C is the tower/rotor cross-coupling inertia $J_C = MhR_C$, where M is the mass of the rotor, h is the hub height of the rotor and R_C is the horizontal distance from the hub to the centre of mass of a blade. K_T is the stiffness of the tower required for the frequency to be that of the fore-and-aft structural mode of the tower and D_T is the fore-and-aft damping force. D_T is a function of $\dot{\phi}_T$ with $D_T = -B_T \dot{\phi}_T$ and (F_1 / ν^2) and (F_2 / ν^2) are in general functions of the tip/speed ratio, λ , with

$$\lambda = R\Omega / \nu; \quad \nu = (w - h\dot{\phi}_T - L\dot{\phi}_R); \quad \Omega = \dot{\theta}_R$$

where R is the radius of the rotor, w is the wind speed and L is such that $L\dot{\phi}_R$ is the mean velocity of the blade relative to the wind speed. The angle β is that between the plane of the edge-wise mode of a blade and the plane of the rotor.

It follows from (B.1) that the equations of motion for the rotor are

$$J\ddot{\theta}_R = -(K_E + J\Omega_o^2)[(\theta_R - \theta_H) \cos\beta - (\phi_R - \phi_T) \sin\beta] \cos\beta - (K_F + J\Omega_o^2)[(\theta_R - \theta_H) \sin\beta + (\phi_R - \phi_T) \cos\beta] \sin\beta + F_1 \quad (\text{B.2})$$

$$\frac{(1 - J_C^2 / JJ_T)}{(1 + J_C / J_T)} J\ddot{\phi}_R = (K_E + J\Omega_o^2)[(\theta_R - \theta_H) \cos\beta - (\phi_R - \phi_T) \sin\beta] \sin\beta - (K_F + J\Omega_o^2)[(\theta_R - \theta_H) \sin\beta + (\phi_R - \phi_T) \cos\beta] \cos\beta + [F_2 - \frac{J_C}{J_T} D_T + \frac{J_C}{J_T} K_T \phi_T] / (1 + J_C / J_T) \quad (\text{B.3})$$

$$\frac{(1 - J_C^2 / JJ_T)}{(1 + J_C / J)} J_T \ddot{\phi}_T = -(K_E + J\Omega_o^2)[(\theta_R - \theta_H) \cos\beta - (\phi_R - \phi_T) \sin\beta] \sin\beta + (K_F + J\Omega_o^2)[(\theta_R - \theta_H) \sin\beta + (\phi_R - \phi_T) \cos\beta] \cos\beta + [D_T - K_T \phi_T - \frac{J_C}{J} F_2] / (1 + J_C / J) \quad (\text{B.4})$$

The torque transmitted to the hub, T_H , is

$$T_H = (K_E + J\Omega_o^2)[(\theta_R - \theta_H) \cos\beta - (\phi_R - \phi_T) \sin\beta] \cos\beta + (K_F + J\Omega_o^2)[(\theta_R - \theta_H) \sin\beta + (\phi_R - \phi_T) \cos\beta] \sin\beta \quad (\text{B.5})$$

Since the inertia of the rotor is very much less than the inertia of the complete turbine, the dynamics of the tower can be ignored and the dynamics of the rotor can be approximated by the equations

$$\begin{bmatrix} \ddot{\theta}_R \\ \ddot{\phi}_R \end{bmatrix} = A(\beta) \begin{bmatrix} (\theta_R - \theta_H) \\ \phi_R \end{bmatrix} + \begin{bmatrix} F_1 / J \\ F_2 / J \end{bmatrix} \quad (\text{B.6})$$

with

$$A(\beta) = - \begin{bmatrix} (\omega_E^2 \cos^2 \beta + \omega_F^2 \sin^2 \beta) & -(\omega_E^2 - \omega_F^2) \sin \beta \cos \beta \\ -(\omega_E^2 - \omega_F^2) \sin \beta \cos \beta & (\omega_E^2 \sin^2 \beta + \omega_F^2 \cos^2 \beta) \end{bmatrix} \quad (\text{B.7})$$

and

$$\lambda = R \Omega / v; \quad v = w - L \dot{\phi}_R; \quad \Omega = \dot{\theta}_R; \quad \omega_E^2 = (K_E + J \Omega_o^2) / J; \quad \omega_F^2 = (K_F + J \Omega_o^2) / J \quad (\text{B.8})$$

The hub torque, T_H , is approximated by

$$T_H = J \omega_E^2 [(\theta_R - \theta_H) \cos \beta - \phi_R \sin \beta] \cos \beta + J \omega_F^2 [(\theta_R - \theta_H) \sin \beta + \phi_R \cos \beta] \sin \beta \quad (\text{B.9})$$

B.2.2 Linearisation of rotor dynamics

The equations (B.6) to (B.9) can be linearised about an equilibrium point

$$\theta_R = \Omega_o t + \theta_{Ro}; \quad \theta_H = \Omega_o t; \quad \phi_R = \phi_{Ro}; \quad w = w_o$$

as follows

$$\begin{bmatrix} \theta_{Ro} \\ \phi_{Ro} \end{bmatrix} = - \frac{A^{-1}(\beta)}{J} \begin{bmatrix} F_1(\lambda_o, w_o) \\ F_2(\lambda_o, w_o) \end{bmatrix} = - \frac{A^{-1}(\beta)}{J} \begin{bmatrix} \frac{1}{2} w_o \frac{\partial F_1}{\partial w} + \frac{1}{2} \Omega_o \frac{\partial F_1}{\partial \Omega} \\ \frac{1}{2} w_o \frac{\partial F_2}{\partial w} + \frac{1}{2} \Omega_o \frac{\partial F_2}{\partial \Omega} \end{bmatrix} \quad (\text{B.10})$$

and

$$\lambda_o = \frac{R \Omega_o}{w_o}.$$

The two cases of tip and full-span regulation are considered separately.

Tip regulation

The angle β is equal to the coning angle, β_E , between the plane of the pitch of a blade and the plane of its edge-wise mode which is fixed and small, *i.e.* $\cos \beta \approx 1$ and $\sin \beta \approx 0$. The aerodynamic torques are dependent on the pitch angle, α , λ and v . On linearising (B.6) to (B.9) such that

$$\theta_R = \Omega_o t + \theta_{Ro} + \Delta \theta_R; \quad \theta_H = \Omega_o t + \Delta \theta_H; \quad \phi_R = \phi_{Ro} + \Delta \phi_R; \quad w = w_o + \Delta w; \quad \alpha = \alpha_o + \Delta \alpha \quad (\text{B.11})$$

the equations of motion become

$$\begin{bmatrix} (s^2 - s \frac{\partial F_1}{\partial \Omega} / J + \omega_E^2) & (sL \frac{\partial F_1}{\partial w} / J) \\ - (s \frac{\partial F_2}{\partial \Omega} / J) & (s^2 + sL \frac{\partial F_2}{\partial w} / J + \omega_F^2) \end{bmatrix} \begin{bmatrix} \Delta \theta_R \\ \Delta \phi_R \end{bmatrix} = \begin{bmatrix} \omega_E^2 & \frac{\partial F_1}{\partial w} / J & \frac{\partial F_1}{\partial \alpha} / J \\ 0 & \frac{\partial F_2}{\partial w} / J & \frac{\partial F_2}{\partial \alpha} / J \end{bmatrix} \begin{bmatrix} \Delta \theta_H \\ \Delta w \\ \Delta \alpha \end{bmatrix} \quad (\text{B.12})$$

It follows that the rotor dynamics can be represented by the model depicted in Figure B.2 where

$$K_R = J\omega_E^2 \quad (\text{B.13})$$

$$G_R(s) = \frac{\omega_E^2 (s^2 + s(L \frac{\partial F_2}{\partial w} / J) + \omega_F^2)}{(s^2 - s(\frac{\partial F_1}{\partial \Omega} / J) + \omega_E^2)(s^2 + s(L \frac{\partial F_2}{\partial w} / J) + \omega_F^2) + s^2(\frac{\partial F_2}{\partial \Omega} / J)(L \frac{\partial F_1}{\partial w} / J)} \quad (\text{B.14})$$

and

$$\Delta T_A = T_w(s) \frac{\partial F_1}{\partial w} \Delta w + T_\alpha(s) \frac{\partial F_1}{\partial \alpha} \Delta \alpha \quad (\text{B.15})$$

Both $T_w(s)$ and $T_\alpha(s)$ are discussed in Section B.2.4.

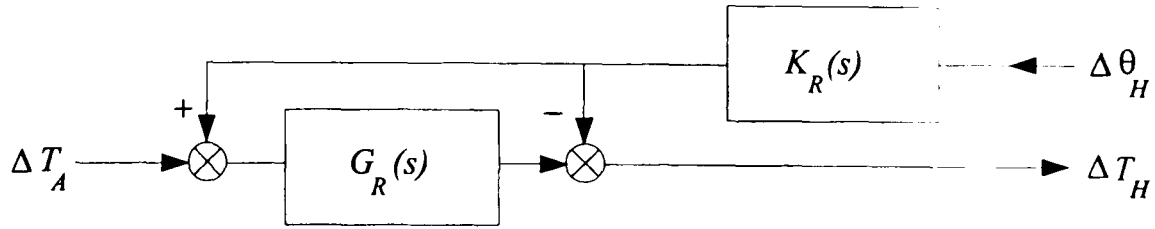


Figure B.2 Dynamics of rotor relating ΔT_H to ΔT_A

Since both the flap-wise and edge-wise modes are lightly damped, the term $-s^2(\frac{\partial F_1}{\partial \Omega} / J)(L \frac{\partial F_2}{\partial w} / J)$ in the denominator of (B.14) is small and so the transfer function, by which ΔT_H is related to ΔT_A , $G_R(s)$, can be approximated by

$$G_R(s) \approx \frac{\omega_E^2}{(s^2 - s(\frac{\partial F_1}{\partial \Omega} / J) + \omega_E^2)} \quad (\text{B.16})$$

In addition, the transfer function, by which ΔT_H is related to $K_R \Delta \theta_H$,

$$G_R(s) - 1 = \frac{-[(s^2 - s(\frac{\partial F_1}{\partial \Omega} / J))(s^2 + s(L \frac{\partial F_2}{\partial w} / J) + \omega_F^2) + s^2(\frac{\partial F_2}{\partial \Omega} / J)(L \frac{\partial F_1}{\partial w} / J)]}{(s^2 - s(\frac{\partial F_1}{\partial \Omega} / J) + \omega_E^2)(s^2 + s(L \frac{\partial F_2}{\partial w} / J) + \omega_F^2) + s^2(\frac{\partial F_2}{\partial \Omega} / J)(L \frac{\partial F_1}{\partial w} / J)} \quad (\text{B.17})$$

can be approximated by

$$G_R(s) - 1 \approx -\frac{(s^2 - s(\frac{\partial F_1}{\partial \Omega} / J))}{(s^2 - s(\frac{\partial F_1}{\partial \Omega} / J) + \omega_E^2)} \approx -G_R(s)(s^2 - s(\frac{\partial F_1}{\partial \Omega} / J)) / \omega_E^2 \quad (\text{B.18})$$

Hence the model of the rotor dynamics has the standard form of Figure B.3 with

$$J_R = J \quad (\text{B.19})$$

$$B_R = -\frac{\partial F_1}{\partial \Omega} \quad (\text{B.20})$$

and with K_R defined by (B.13).

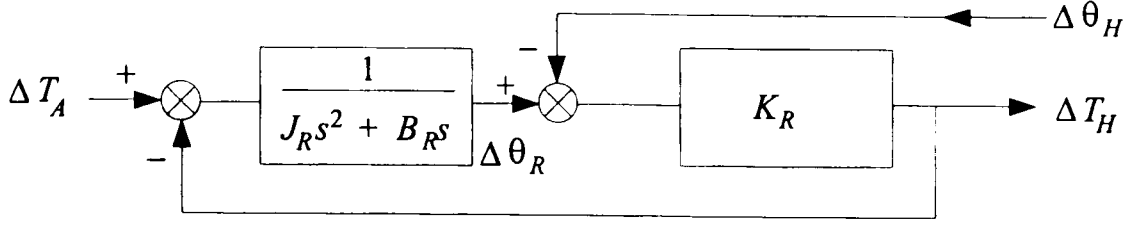


Figure B.3 Canonical form of dynamics of the rotor.

Full-span regulation

The angle β varies with pitch angle such that

$$\beta = \beta_E + \alpha \approx \alpha \quad (\text{B.21})$$

On linearising (B.6) to (B.9) with (B.21) and

$$\theta_R = \Omega_o t + \theta_{R0} + \Delta\theta_R; \theta_H = \Omega_o t + \Delta\theta_H; \phi_R = \phi_{R0} + \Delta\phi_R; w = w_o + \Delta w \quad (\text{B.22})$$

the equations of motion become

$$\begin{bmatrix} (s^2 - s \frac{\partial F_1}{\partial \Omega} / J + \omega_E^2 \cos^2 \alpha_o) & (sL \frac{\partial F_1}{\partial w} / J \\ & + \omega_F^2 \sin^2 \alpha_o) & -(\omega_E^2 - \omega_F^2) \sin \alpha_o \cos \alpha_o \\ (-s \frac{\partial F_2}{\partial \Omega} / J & (s^2 + sL \frac{\partial F_2}{\partial w} / J + \omega_E^2 \sin^2 \alpha_o) \\ -(\omega_E^2 - \omega_F^2) \sin \alpha_o \cos \alpha_o & & + \omega_F^2 \cos^2 \alpha_o) \end{bmatrix} \begin{bmatrix} \Delta\theta_R \\ \Delta\phi_R \end{bmatrix} = \begin{bmatrix} (\omega_E^2 \cos^2 \alpha_o + \omega_F^2 \sin^2 \alpha_o) & \frac{\partial F_1}{\partial w} / J & F_{1\alpha} / J \\ -(\omega_E^2 - \omega_F^2) \sin \alpha_o \cos \alpha_o & \frac{\partial F_2}{\partial w} / J & F_{2\alpha} / J \end{bmatrix} \begin{bmatrix} \Delta\theta_H \\ \Delta w \\ \Delta\alpha \end{bmatrix} \quad (\text{B.23})$$

where

$$F_{1\alpha} = \frac{\partial F_1}{\partial \alpha} + \frac{(\omega_E^2 - \omega_F^2)}{2\omega_E^2 \omega_F^2} [(\omega_E^2 + \omega_F^2) \sin \alpha_o \cos \alpha_o (w_o \frac{\partial F_1}{\partial w} + \Omega_o \frac{\partial F_1}{\partial \Omega}) + (\omega_E^2 \cos^2 \alpha_o - \omega_F^2 \sin^2 \alpha_o) (w_o \frac{\partial F_2}{\partial w} + \Omega_o \frac{\partial F_2}{\partial \Omega})] \quad (\text{B.24})$$

$$F_{2\alpha} = \frac{\partial F_2}{\partial \alpha} - \frac{(\omega_E^2 - \omega_F^2)}{2\omega_E^2 \omega_F^2} [(\omega_E^2 \sin^2 \alpha_o - \omega_F^2 \cos^2 \alpha_o) (w_o \frac{\partial F_1}{\partial w} + \Omega_o \frac{\partial F_1}{\partial \Omega}) + (\omega_E^2 + \omega_F^2) \sin \alpha_o \cos \alpha_o (w_o \frac{\partial F_2}{\partial w} + \Omega_o \frac{\partial F_2}{\partial \Omega})] \quad (\text{B.25})$$

The rotor dynamics can again be represented by the model depicted in Figure B.2 where

$$K_R = J(\omega_E^2 \cos^2 \alpha_o + \omega_F^2 \sin^2 \alpha_o) \quad (\text{B.26})$$

and

$$\begin{aligned}
& \left[s^2 (\omega_E^4 \cos^2 \alpha_o + \omega_F^4 \sin^2 \alpha_o) \right. \\
& \quad \left. + s \left(\begin{aligned} & L(\omega_E^2 \cos^2 \alpha_o + \omega_F^2 \sin^2 \alpha_o) \left\{ (\omega_E^2 \cos^2 \alpha_o + \omega_F^2 \sin^2 \alpha_o) \frac{\partial F_2}{\partial w} / J \right\} \right. \\ & + (\omega_E^2 - \omega_F^2) \sin \alpha_o \cos \alpha_o \frac{\partial F_1}{\partial w} / J \left. \right\} \\ & - (\omega_E^2 - \omega_F^2) \sin \alpha_o \cos \alpha_o \left\{ (\omega_E^2 \cos^2 \alpha_o + \omega_F^2 \sin^2 \alpha_o) \frac{\partial F_2}{\partial \Omega} / J \right. \\ & \quad \left. + (\omega_E^2 - \omega_F^2) \sin \alpha_o \cos \alpha_o \frac{\partial F_1}{\partial \Omega} / J \right\} \end{aligned} \right) \left. \right] \\
G_R(s) = & \frac{+ \omega_E^2 \omega_F^2 (\omega_E^2 \cos^2 \alpha_o + \omega_F^2 \sin^2 \alpha_o)}{[\{s^2 - s(\cos^2 \alpha_o \frac{\partial F_1}{\partial \Omega} / J + L \sin \alpha_o \cos \alpha_o \frac{\partial F_1}{\partial w} / J} \\
& \quad - L \sin^2 \alpha_o \frac{\partial F_2}{\partial w} / J - \sin \alpha_o \cos \alpha_o \frac{\partial F_2}{\partial \Omega} / J) + \omega_E^2 \}. \\
& \{s^2 - s(\sin^2 \alpha_o \frac{\partial F_1}{\partial \Omega} / J - L \sin \alpha_o \cos \alpha_o \frac{\partial F_1}{\partial w} / J} \\
& \quad - L \cos^2 \alpha_o \frac{\partial F_2}{\partial w} / J + \sin \alpha_o \cos \alpha_o \frac{\partial F_2}{\partial \Omega} / J) + \omega_F^2 \} \\
& - s^2 \{(\cos^2 \alpha_o \frac{\partial F_1}{\partial \Omega} / J + L \sin \alpha_o \cos \alpha_o \frac{\partial F_1}{\partial w} / J} \\
& \quad - L \sin^2 \alpha_o \frac{\partial F_2}{\partial w} / J - \sin \alpha_o \cos \alpha_o \frac{\partial F_2}{\partial \Omega} / J). \\
& \quad (\sin^2 \alpha_o \frac{\partial F_1}{\partial \Omega} / J - L \sin \alpha_o \cos \alpha_o \frac{\partial F_1}{\partial w} / J} \\
& \quad - L \cos^2 \alpha_o \frac{\partial F_2}{\partial w} / J + \sin \alpha_o \cos \alpha_o \frac{\partial F_2}{\partial \Omega} / J) \\
& \quad + L(\frac{\partial F_1}{\partial \Omega} / J \cdot \frac{\partial F_2}{\partial w} / J - \frac{\partial F_2}{\partial \Omega} / J \cdot \frac{\partial F_1}{\partial w} / J)\} \} \tag{B.27}
\end{aligned}$$

As before, $T_w(s)$ and $T_\alpha(s)$ are again discussed in Section B.2.4. As in the tip regulation case, the additional s^2 term in the denominator of (B.27) is small and can be neglected. Hence, the transfer function, by which ΔT_H is related to ΔT_A , G_R , can be approximated by

$$G_R(s) = \frac{\omega_E^2}{\{s^2 + s(-\cos^2 \alpha_o \frac{\partial F_1}{\partial \Omega} / J - L \sin \alpha_o \cos \alpha_o \frac{\partial F_1}{\partial w} / J} \\
+ L \sin^2 \alpha_o \frac{\partial F_2}{\partial w} / J + \sin \alpha_o \cos \alpha_o \frac{\partial F_2}{\partial \Omega} / J) + \omega_E^2 \} \tag{B.28}$$

with the discrepancy between (B.28) and (B.27) small and local to ω_F . In addition, the transfer function, by which ΔT_H is related to $K_R \Delta \theta_H$,

$$\begin{aligned}
G_R(s) - 1 = & \frac{-\left\{s^2 - s\left(\frac{\partial F_1}{\partial \Omega} / J\right)\right\} \left\{s^2 + s\left(L\frac{\partial F_2}{\partial w} / J\right) + \omega_E^2 \omega_F^2 / (\omega_E^2 \cos^2 \alpha_o + \omega_F^2 \sin^2 \alpha_o)\right\}}{[\{s^2 - s(\cos^2 \alpha_o \frac{\partial F_1}{\partial \Omega} / J + L \sin \alpha_o \cos \alpha_o \frac{\partial F_1}{\partial w} / J - L \sin^2 \alpha_o \frac{\partial F_2}{\partial w} / J - \sin \alpha_o \cos \alpha_o \frac{\partial F_2}{\partial \Omega} / J) + \omega_E^2\} \cdot \\
& \{s^2 - s(\sin^2 \alpha_o \frac{\partial F_1}{\partial \Omega} / J - L \sin \alpha_o \cos \alpha_o \frac{\partial F_1}{\partial w} / J - L \cos^2 \alpha_o \frac{\partial F_2}{\partial w} / J + \sin \alpha_o \cos \alpha_o \frac{\partial F_2}{\partial \Omega} / J) + \omega_F^2\} \\
& - s^2 \{(\cos^2 \alpha_o \frac{\partial F_1}{\partial \Omega} / J + L \sin \alpha_o \cos \alpha_o \frac{\partial F_1}{\partial w} / J - L \sin^2 \alpha_o \frac{\partial F_2}{\partial w} / J - \sin \alpha_o \cos \alpha_o \frac{\partial F_2}{\partial \Omega} / J) \cdot \\
& (\sin^2 \alpha_o \frac{\partial F_1}{\partial \Omega} / J - L \sin \alpha_o \cos \alpha_o \frac{\partial F_1}{\partial w} / J - L \cos^2 \alpha_o \frac{\partial F_2}{\partial w} / J + \sin \alpha_o \cos \alpha_o \frac{\partial F_2}{\partial \Omega} / J) \\
& + L(\frac{\partial F_1}{\partial \Omega} / J \cdot \frac{\partial F_2}{\partial w} / J - \frac{\partial F_2}{\partial \Omega} / J \cdot \frac{\partial F_1}{\partial w} / J)\}] \quad (B.29)
\end{aligned}$$

can be approximated by

$$\begin{aligned}
G_R(s) - 1 \approx & - \frac{[s^2 - s(\frac{\partial F_1}{\partial \Omega} / J)]}{[s^2 + s(-\cos^2 \alpha_o \frac{\partial F_1}{\partial \Omega} / J - L \sin \alpha_o \cos \alpha_o \frac{\partial F_1}{\partial w} / J + L \sin^2 \alpha_o \frac{\partial F_2}{\partial w} / J + \sin \alpha_o \cos \alpha_o \frac{\partial F_2}{\partial \Omega} / J) + \omega_E^2]} \quad (B.30) \\
\approx & - G_R(s)(s^2 - s(\frac{\partial F_1}{\partial \Omega} / J)) / \omega_E^2
\end{aligned}$$

Since both $(-\frac{\partial F_1}{\partial \Omega} / J) \ll \omega_E$ and $(-\cos^2 \alpha_o \frac{\partial F_1}{\partial \Omega} / J - L \sin \alpha_o \cos \alpha_o \frac{\partial F_1}{\partial w} / J + L \sin^2 \alpha_o \frac{\partial F_2}{\partial w} / J + \sin \alpha_o \cos \alpha_o \frac{\partial F_2}{\partial \Omega} / J) \ll \omega_E$, the rotor dynamics can be modelled by

the standard form of Figure B.3 with

$$J_R = J(\omega_E^2 \cos^2 \alpha_o + \omega_F^2 \sin^2 \alpha_o) / \omega_E^2 \quad (B.31)$$

Other than at very low frequencies, good agreement between the dynamics depicted in Figures B.2 and B.3 is obtained with

$$B_R = \left[-\cos^2 \alpha_o \frac{\partial F_1}{\partial \Omega} - L \sin \alpha_o \cos \alpha_o \frac{\partial F_1}{\partial w} + L \sin^2 \alpha_o \frac{\partial F_2}{\partial w} + \sin \alpha_o \cos \alpha_o \frac{\partial F_2}{\partial \Omega} \right] \cdot (\omega_E^2 \cos^2 \alpha_o + \omega_F^2 \sin^2 \alpha_o) / \omega_E^2 \quad (B.32)$$

since $G_R(s) - 1 \approx -G_R(s)s^2 / \omega_E^2$ and (B.32) is the appropriate damping factor for $G_R(s)$ when approximated by (B.28). At very low frequencies, good agreement is obtained with

$$B_R = -\frac{\partial F_I}{\partial \Omega} (\omega_E^2 \cos^2 \alpha_o + \omega_F^2 \sin^2 \alpha_o) / \omega_E^2 \quad (\text{B.33})$$

since $G_R(s) \approx 1$ and (B.33) is the appropriate damping factor for (B.30).

The contribution of the rotor to the drive-train dynamics is the relationship of $\Delta\theta_H$ to ΔT_H which, for all three types of regulation, may be modelled by Figure B.3; that is, an inertia with damping attached to the hub by a massless spring. Any discrepancy in comparison to the original model, (B.2) to (B.5), is local to the natural frequency of the tower, ω_T , and the edge-wise and flap-wise natural frequencies of the blade, ω_E and ω_F respectively.

This model of the rotor dynamics is linear. In addition, the dynamics of the low-speed shaft, hub and the remaining drive-train components are essentially linear. There is, therefore, no need to distinguish between variables and their increments. Hence, the dynamic variables themselves are employed in the remainder of this appendix except when otherwise indicated.

The simplified linear equations of motion for the rotor are

$$J_R \ddot{\theta}_R = -B_R \dot{\theta}_R + T_A - T_H ; \quad T_H = K_R (\theta_R - \theta_H) \quad (\text{B.34})$$

B.2.3 Equations of motion of the hub

The analysis of the rotor dynamics including the hub must also account for the low-speed shaft. Since the inertia of the low-speed shaft is very much less than the inertia of either the hub or the first stage of the gearbox, the low-speed shaft may be considered massless with appropriate fractions of its inertia allocated to the inertia of the hub and to the inertia of the first stage of the gearbox. When the low-speed shaft is uniform, the allocation to each is half the inertia of the low-speed shaft. The system is depicted in Figure B.4. The only significant damping is that of the rotor.

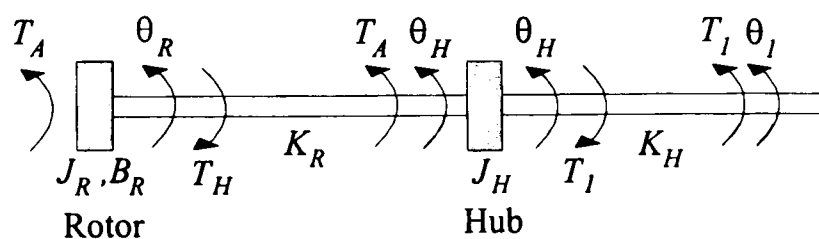


Figure B.4 The rotor, hub and low-speed shaft.

The equations of motion for the hub are

$$J_H \ddot{\theta}_H = T_H - T_I ; T_I = K_H(\theta_H - \theta_I) \quad (\text{B.35})$$

The block diagram representation of the rotor and hub dynamics is that shown in Figure B.5a which is equivalent to Figure B.5b where

$$G_I(s) = K_R K_H / D(s) \quad (\text{B.36})$$

and

$$G_2(s) = K_H [J_H J_R s^4 + J_H B_R s^3 + (J_H + J_R) K_R s^2 + B_R K_R s] / D(s) \quad (\text{B.37})$$

The denominator of (B.36) and (B.37), $D(s)$, is

$$D(s) = [J_H J_R s^4 + J_H B_R s^3 + ((K_R + K_H) J_R + K_R J_H) s^2 + (K_R + K_H) B_R s + K_R K_H]$$

which has the two dynamic mode form

$$D(s) = J_H J_R [s^2 + \alpha_1 s + \beta_1] [s^2 + \alpha_2 s + \beta_2] \quad (\text{B.38})$$

When determining β_1 and β_2 , it is permissible to set B_R to zero since the damping is much too small to noticeably shift the roots of (B.38). It follows that

$$\beta_1 = \frac{(K_R(J_R + J_H) + K_H J_R) - \mu \sqrt{1 + 4J_H^2 K_H K_R^3 / ((K_R + K_H)^2 \mu^2)}}{2J_R J_H}$$

where

$$\mu = \frac{[J_R(K_R + K_H)^2 + J_H K_R(K_R - K_H)]}{(K_R + K_H)}$$

Provided $K_R / K_H \ll 1$ or $K_H / K_R \ll 1$ or $J_H / J_R \ll 1$ then β_1 can be approximated as

$$\begin{aligned} \beta_1 &\approx \frac{\frac{K_R K_H}{J_R(K_R + K_H)}}{\left[1 + \frac{J_H K_R^2}{J_R (K_R + K_H)^2}\right]} \left[1 - \frac{(J_H / J_R)^2 K_R^3 K_H / (K_R + K_H)^4}{1 + (J_H / J_R) K_R (K_R - K_H) / (K_R + K_H)^2}\right] \\ &\approx \frac{K_R K_H}{J_R(K_R + K_H)} / \left[1 + \frac{J_H K_R^2}{J_R (K_R + K_H)^2}\right] \end{aligned}$$

This approximation is exact in the limits as K_R and/or K_H tend to infinity. Similarly,

$$\begin{aligned} \beta_2 &= \frac{(K_R(J_R + J_H) + K_H J_R) + \mu \sqrt{1 + 4J_H^2 K_H K_R^3 / ((K_R + K_H)^2 \mu^2)}}{2J_R J_H} \\ &\approx \frac{(K_R + K_H)}{J_H} \left[1 + \frac{J_H K_R^2}{J_R (K_R + K_H)^2}\right] \end{aligned}$$

The damping coefficients, α_1 and α_2 , are

$$\alpha_1 \approx \frac{B_R}{J_R} / \left[1 + \frac{J_H K_R^2}{J_R (K_R + K_H)^2}\right]$$

$$\alpha_2 \approx \frac{B_R}{J_R} \cdot \frac{J_H}{J_R} \frac{K_R^2}{(K_R + K_H)^2} / \left[1 + \frac{J_H}{J_R} \frac{K_R^2}{(K_R + K_H)^2} \right]$$

The damping ratio of the second factor in (B.38) is

$$\eta_2 = \alpha_2 / 2\sqrt{\beta_2} \approx \eta_R (J_H / J_R)^{3/2} (K_R / (K_R + K_H))^{5/2} \quad (\text{B.39})$$

where

$$\eta_R = B_R / 2\sqrt{K_R J_R}$$

is the damping factor of the rotor. It follows that η_2 is very much less than one and the second factor in (B.38) has an effect on the phase only local to the frequency $\beta_2^{1/2}$. Also the ratio of the squares of the two frequencies

$$\beta_1 / \beta_2 \approx \frac{J_H}{J_R} \frac{K_R K_H}{(K_R + K_H)^2} \quad (\text{B.40})$$

is small. Because of the significant separation between the two frequencies, as indicated by (B.40), and the low level of damping of the higher frequency, as indicated by (B.39), and because of the presence of further compliance in the drive train sufficient to roll-off the gain to less than 0 dB, the contribution of the second factor in $D(s)$ to the backward path drive-train dynamics relating T_l to θ_l , is not significant. However, because the rate of roll-off is partially determined by it, its contribution to the forward path relating T_l to T_A , remains significant. Hence, $D(s)$ may be approximated by

$$D(s) \approx J_H J_R [s^2 + \alpha_1 s + \beta_1] \beta_2 \quad (\text{B.41})$$

provided the factor $(s^2 + \alpha_2 s + \beta_2) / \beta_2$ is absorbed within $T_w(s)$ and $T_a(s)$. Hence,

$$G_2(s) \approx \frac{K_H s [s + B_R / (J_R + J_H)] [s^2 + \alpha_3 s + \beta_3]}{\beta_2 [s^2 + \alpha_1 s + \beta_1]} \quad (\text{B.42})$$

with

$$\alpha_3 \approx B_R J_H / J_R (J_R + J_H) ; \beta_3 \approx K_R (J_R + J_H) / J_H J_R \quad (\text{B.43})$$

The damping factor for the quadratic term in the numerator of (B.42) is

$$\eta_3 = \alpha_3 / 2\sqrt{\beta_3} \approx \eta_R (J_H / (J_H + J_R))^{3/2} \quad (\text{B.44})$$

Since the damping factor of the rotor, η_R , and so the damping term, B_R , are small, damping terms of the order of $(B_R J_H / J_R)$ may be considered negligible compared to other sources of damping in the drive train. It follows that an equivalent representation of the rotor and hub dynamics is that of Figure B.5c where

$$\begin{aligned}
 J_R^* &= J_R \left(1 + \frac{J_H}{J_R} \frac{K_R}{K_R + K_H} \right) ; J_H^* = J_H \frac{K_H}{K_R + K_H} \\
 B_R^* &= B_R ; K_I = \frac{K_R K_H}{(K_R + K_H)} \left(1 + \frac{K_R}{(K_R + K_H)^2} \frac{J_H}{J_R} \right)
 \end{aligned}
 \tag{B.45}$$

The conditions under which (B.45) is valid are the same as pertain to the factorisation (B.38).

Hence the rotor can be interpreted as a single compliant blade attached by a massless shaft to the hub which in turn is attached rigidly to the gearbox. The inertia of the hub, J_H^* , can thus be added to that of the first stage of the gearbox.

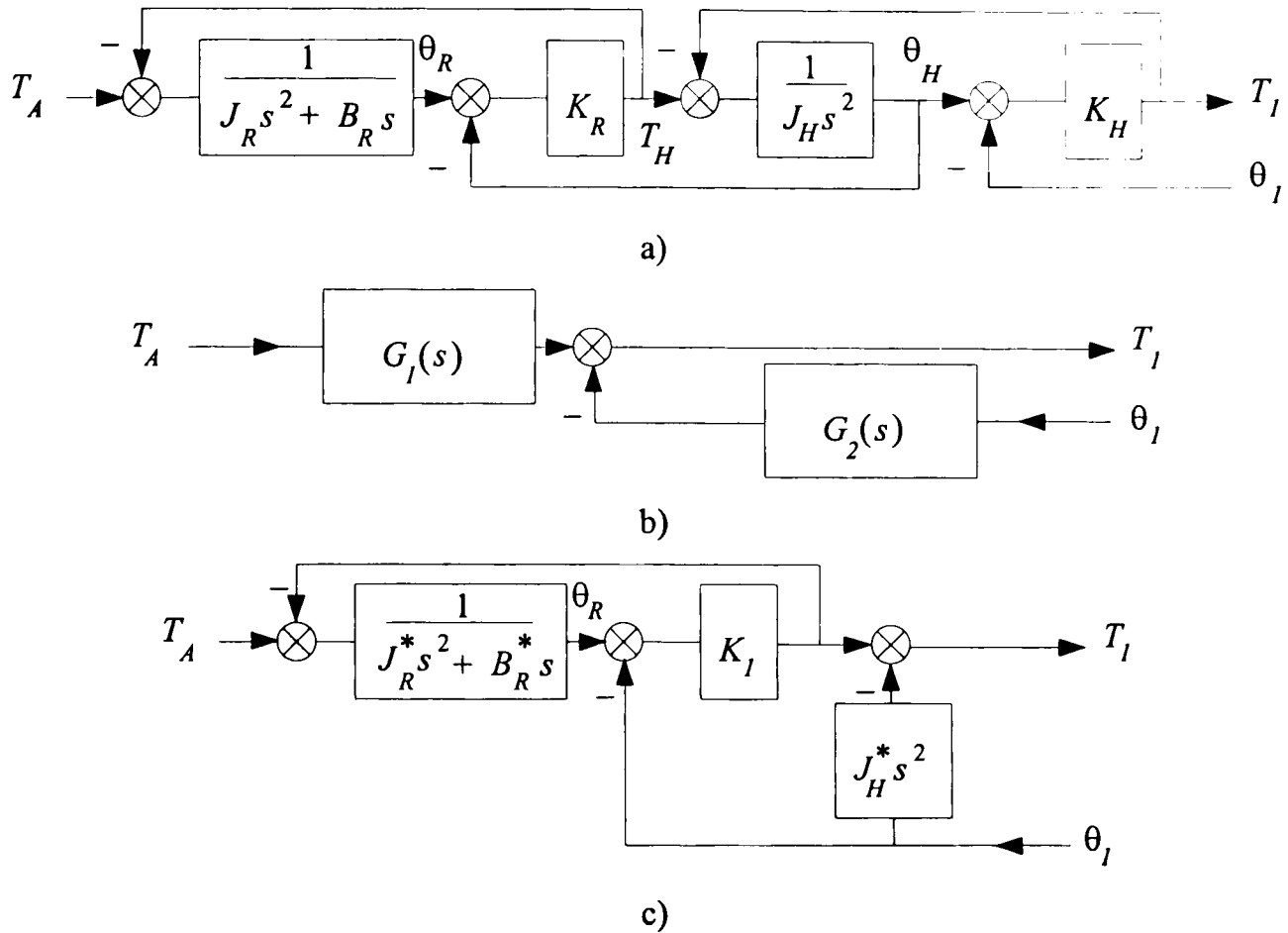


Figure B.5 The dynamics of the rotor, hub and low-speed shaft.

B.2.4 Aerodynamic/rotor interaction

Although the aerodynamic/rotor interaction, represented by (B.15), is external to the drive-train dynamics it is nevertheless required for control design and *e.g.* the parametric studies described in Chapters 5 and 6. The dynamics relating T_A to wind speed and pitch angle, modified by the inclusion of $\beta_2 / (s^2 + \alpha_2 s + \beta_2)$, are considered separately for tip and full-span regulation.

Tip regulation

The dynamics relating T_A to wind speed and α can be represented by (B.15) with

$$T_W(s) = \frac{(s^2 + \omega_F^2) \beta_2}{\{s^2 + s(L \frac{\partial F_2}{\partial w} / J) + \omega_F^2\} \{s^2 + \alpha_2 s + \beta_2\}} \quad (\text{B.46})$$

and

$$T_\alpha(s) = \frac{[s^2 \frac{\partial F_1}{\partial \alpha} + sL(\frac{\partial F_1}{\partial \alpha} \frac{\partial F_2}{\partial w} / J - \frac{\partial F_2}{\partial \alpha} \frac{\partial F_1}{\partial w} / J) + \omega_F^2 \frac{\partial F_1}{\partial \alpha}] \beta_2}{\{s^2 + s(L \frac{\partial F_2}{\partial w} / J) + \omega_F^2\} \{s^2 + \alpha_2 s + \beta_2\} \frac{\partial F_1}{\partial \alpha}} \quad (\text{B.47})$$

Full-span

The dynamics relating $T_A(s)$ to wind speed and pitch angle can be represented by (B.15) with

$$T_W(s) = \frac{\begin{aligned} & [s^2 \{(\omega_E^2 \cos^2 \alpha_o + \omega_F^2 \sin^2 \alpha_o) \frac{\partial F_1}{\partial w} \\ & \quad - (\omega_E^2 - \omega_F^2) \sin \alpha_o \cos \alpha_o \frac{\partial F_2}{\partial w}\} \\ & + s(\omega_E^2 - \omega_F^2) \sin \alpha_o \cos \alpha_o (\frac{\partial F_2}{\partial w} \frac{\partial F_1}{\partial \Omega} / J - \frac{\partial F_1}{\partial w} \frac{\partial F_2}{\partial \Omega} / J) + \omega_E^2 \omega_F^2 \frac{\partial F_1}{\partial w}] \cdot \\ & (\omega_E^2 \cos^2 \alpha_o + \omega_F^2 \sin^2 \alpha_o) / \frac{\partial F_1}{\partial w} \cdot \beta_2 \end{aligned}}{\begin{aligned} & [s^2 (\omega_E^4 \cos^2 \alpha_o + \omega_F^4 \sin^2 \alpha_o) \\ & + s \left(\begin{aligned} & L(\omega_E^2 \cos^2 \alpha_o + \omega_F^2 \sin^2 \alpha_o) \{(\omega_E^2 \cos^2 \alpha_o + \omega_F^2 \sin^2 \alpha_o) \frac{\partial F_2}{\partial w} / J \\ & \quad + (\omega_E^2 - \omega_F^2) \sin \alpha_o \cos \alpha_o \frac{\partial F_1}{\partial w} / J\} \\ & - (\omega_E^2 - \omega_F^2) \sin \alpha_o \cos \alpha_o \{(\omega_E^2 \cos^2 \alpha_o + \omega_F^2 \sin^2 \alpha_o) \frac{\partial F_2}{\partial \Omega} / J \\ & \quad + (\omega_E^2 - \omega_F^2) \sin \alpha_o \cos \alpha_o \frac{\partial F_1}{\partial \Omega} / J\} \end{aligned} \right) \\ & + \omega_E^2 \omega_F^2 (\omega_E^2 \cos^2 \alpha_o + \omega_F^2 \sin^2 \alpha_o)] \cdot (s^2 + \alpha_2 s + \beta_2) \end{aligned}} \quad (\text{B.48})$$

and

$$T_\alpha(s) = T_{\alpha A}(s) + T_{\alpha \lambda}(s) \quad (\text{B.49})$$

with

$$\begin{aligned}
& [s^2 \{(\omega_E^2 \cos^2 \alpha_o + \omega_F^2 \sin^2 \alpha_o) F_{1\alpha} - (\omega_E^2 - \omega_F^2) \sin \alpha_o \cos \alpha_o F_{2\alpha}\} \\
& + s \{L(\omega_E^2 \cos^2 \alpha_o + \omega_F^2 \sin^2 \alpha_o) (F_{1\alpha} \frac{\partial F_2}{\partial w} / J - F_{2\alpha} \frac{\partial F_1}{\partial w} / J) \\
& \quad - (\omega_E^2 - \omega_F^2) \sin \alpha_o \cos \alpha_o (F_{1\alpha} \frac{\partial F_2}{\partial \Omega} / J - F_{2\alpha} \frac{\partial F_1}{\partial \Omega} / J)\} \\
& + \omega_E^2 \omega_F^2 F_{1\alpha}] (\omega_E^2 \cos^2 \alpha_o + \omega_F^2 \sin^2 \alpha_o) / \frac{\partial F_1}{\partial \alpha} \cdot \beta_2 \\
T_{\alpha 1}(s) = & \frac{\quad}{[s^2 (\omega_E^4 \cos^2 \alpha_o + \omega_F^4 \sin^2 \alpha_o) \\
& + s \left(\begin{aligned}
& L(\omega_E^2 \cos^2 \alpha_o + \omega_F^2 \sin^2 \alpha_o) \{(\omega_E^2 \cos^2 \alpha_o + \omega_F^2 \sin^2 \alpha_o) \frac{\partial F_2}{\partial w} / J\} \\
& \quad + (\omega_E^2 - \omega_F^2) \sin \alpha_o \cos \alpha_o \frac{\partial F_1}{\partial w} / J\} \\
& - (\omega_E^2 - \omega_F^2) \sin \alpha_o \cos \alpha_o \{(\omega_E^2 \cos^2 \alpha_o + \omega_F^2 \sin^2 \alpha_o) \frac{\partial F_2}{\partial \Omega} / J\} \\
& \quad + (\omega_E^2 - \omega_F^2) \sin \alpha_o \cos \alpha_o \frac{\partial F_1}{\partial \Omega} / J\} \\
& + \omega_E^2 \omega_F^2 (\omega_E^2 \cos^2 \alpha_o + \omega_F^2 \sin^2 \alpha_o) \cdot (s^2 + \alpha_2 s + \beta_2)
\end{aligned} \right)} \quad (B.50)
\end{aligned}$$

$$T_{\alpha 2}(s) = \frac{\beta_2 (1 - F_{1\alpha} / \frac{\partial F_1}{\partial \alpha})}{(s^2 + \alpha_2 s + \beta_2) G_R(s)} \quad (B.51)$$

At low frequency the magnitudes of $T_\alpha(s)$ and $T_w(s)$ are one except locally around the tower frequency, ω_T , and the blade flap frequency, ω_F . However, the gain of $T_\alpha(s)$ increases rapidly between the blade edge frequency, ω_E , and the hub frequency, $\beta_2^{1/2}$, for full-span regulation. Nevertheless, this increase in gain is not significant. Although actuator position and so generated power is not directly affected to any great extent by medium- to high-frequency disturbances in the control signal, $1/s$ roll-off of the controller (see Appendix C) associated with pitch motion, provides insufficient actuator protection (Leithead *et al.*, 1991a, 1992b). To prevent degradation of power controller performance by actuator velocity or acceleration saturation, $1/s^3$ roll-off, which is also sufficient to counteract the increasing gain of $T_\alpha(s)$, is required (Leithead *et al.*, 1991a, 1992b). In addition, since it occurs at high frequency, the increase in gain of $T_\alpha(s)$ does not impact significantly on the controller design. Hence both $T_w(s)$ and $T_\alpha(s)$ can be assumed to be one, because the crossover frequency of the controller is considerably less than ω_T , ω_E and ω_F , and because the significant deviations occur at high frequency where in modelling the structural dynamics and aerodynamics considerable simplification has already been made; that is (B.15) becomes

$$T_A = \frac{\partial F_l}{\partial \alpha} \Delta \alpha + \frac{\partial F_l}{\partial w} \Delta w \quad (B.52)$$

B.3 Gearbox

This analysis of the gearbox assumes, without loss of generality, that it has three stages.

B.3.1 Equations of motion of gearbox

When the gearbox is rigidly mounted, the equations of motion are

$$J_S \ddot{\theta}_1 = T_1 + N T_2 ; \quad \theta_2 = N \theta_1 \quad (\text{B.53})$$

where J_S is the inertia of the gear-train reflected to the low-speed shaft. The gearbox ratio, N , is positive when the output shaft rotates in the same direction as the input shaft and negative when the opposite is the case. The block diagram representation of the dynamics is that shown in Figure B.6.

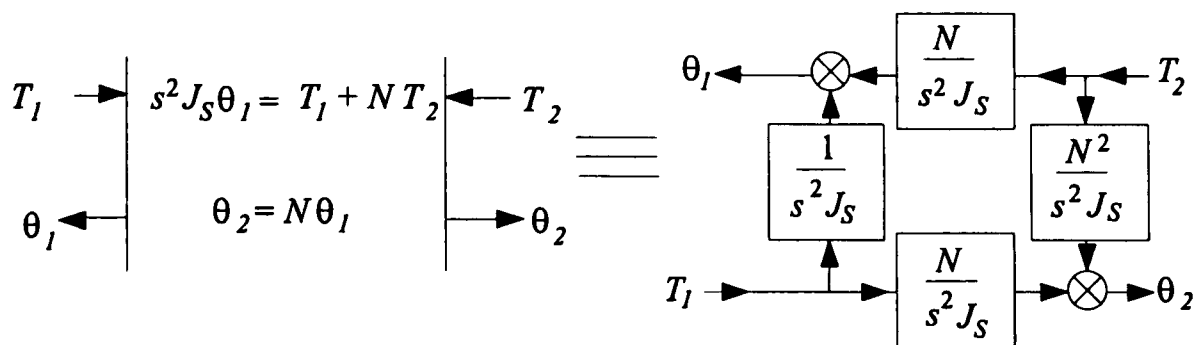
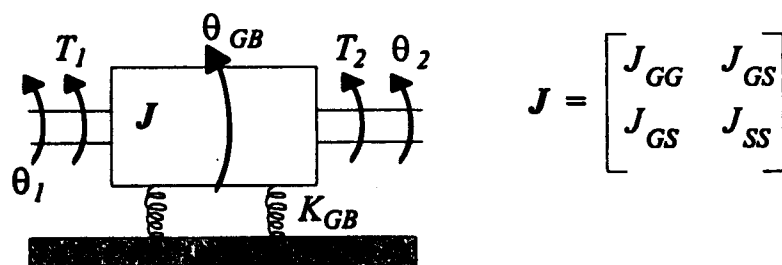


Figure B.6 Block diagram representation of rigidly mounted gearbox.

Now consider the case when the gearbox is mounted on a compliant suspension as depicted in Figure B.7. The side-to-side motion of the tower induces motion, relative to the tower head, of the centre of mass of the gearbox so the analysis must include the dynamics of that motion. Other than the angular displacement, θ_T , of the tower, the dynamics relate to three angular displacements, θ_1 , θ_2 and θ_{GB} . However, there are only two degree of freedom since

$$\theta_2 = N \theta_1 - (N - 1) \theta_{GB} \quad (\text{B.54})$$



Torques T_1 and T_2 are positive when acting on the gearbox

Figure B.7 Gearbox system.

The detailed arrangement of the gear-train is shown schematically in Figure B.8. The same sign convention as applies to the gearbox ratio, N , applies to the gearing ratios, N_1 , N_2 and N_3 and

$$N = N_1 N_2 N_3 \quad (\text{B.55})$$

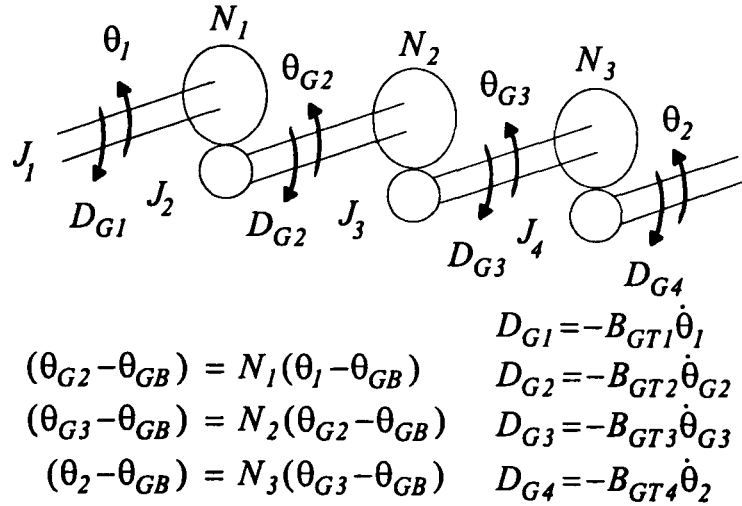


Figure B.8 Schematic arrangement of gear train.

The Lagrangian for the system is

$$\begin{aligned} \ell_{GB} = & \frac{1}{2} J_{GG} \dot{\theta}_{GB}^2 - J_{GS} \dot{\theta}_1 \dot{\theta}_{GB} + \frac{1}{2} J_{SS} \dot{\theta}_1^2 + \frac{1}{2} J_T \dot{\theta}_T^2 + J_X \dot{\theta}_T \dot{\theta}_{GB} \\ & - \frac{1}{2} K_{GB} (\theta_{GB} - \theta_T)^2 - \frac{1}{2} K_T \theta_T^2 + T_1 \theta_1 + T_2 (N \theta_1 - (N-1) \theta_{GB}) \quad (\text{B.56}) \\ & + D_T \theta_T + D_{GB} \theta_{GB} + D_{GT1} \theta_1 + D_{GT2} \theta_{GB} \end{aligned}$$

The inertia of the gear-train reflected to the low-speed shaft, J_S , is

$$J_S = J_1 + N_1^2 J_2 + N_1^2 N_2^2 J_3 + N_1^2 N_2^2 N_3^2 J_4$$

and the elements of the gearbox inertia matrix, J , are

$$\begin{aligned} J_{GG} &= J_{GB} + (N_1 - 1)^2 J_2 + (N_1 N_2 - 1)^2 J_3 + (N_1 N_2 N_3 - 1)^2 J_4 \\ J_{GS} &= N_1 (N_1 - 1) J_2 + N_1 N_2 (N_1 N_2 - 1) J_3 + N_1 N_2 N_3 (N_1 N_2 N_3 - 1) J_4 \quad (\text{B.57}) \\ J_{SS} &= J_S \end{aligned}$$

J_{GB} is the inertia of the complete gearbox with the components of the gear-train treated as point masses and J_X is the tower / gearbox cross-coupling inertia

$$J_X = M_{GB} h R_{GB}$$

where M_{GB} is the total mass of the gearbox and its attachments. R_{GB} is the distance from the axis of rotation of the gearbox to the centre of mass. Damping losses in the gear-train are represented by D_{GT1} and D_{GT2} with

$$D_{GT1} = -B_{G1} \dot{\theta}_1 - N B_{G2} \dot{\theta}_2$$

and

$$D_{GT2} = (N - 1) B_{G2} \dot{\theta}_2 - B_{G3} \dot{\theta}_{GB}$$

where

$$B_{G1} = B_{GT1} + \frac{N_1(N - N_1)}{(N - 1)} B_{GT2} + \frac{N_1 N_2 (N - N_1 N_2)}{(N - 1)} B_{GT3}$$

$$B_{G2} = \frac{N_1(N_1 - 1)}{N(N - 1)} B_{GT2} + \frac{N_1 N_2 (N_1 N_2 - 1)}{N(N - 1)} B_{GT3} + B_{GT4}$$

$$B_{G3} = -\frac{(N_1 - 1)(N - N_1)}{N} B_{GT2} - \frac{(N_1 N_2 - 1)(N - N_1 N_2)}{N} B_{GT3}$$

D_{GB} is the gearbox mounting damping force with

$$D_{GB} = -B_{GB} \dot{\theta}_{GB}$$

and D_T is the tower side-to-side damping force with

$$D_T = -B_T \dot{\theta}_T$$

The tower is assumed symmetrical such that the inertia, damping and stiffness are the same for fore-and-aft motion and side-to-side motion. However, the frequencies of the side-to-side and fore-and-aft natural modes of the tower are split by the differing cross-coupling to the rotor and drive train.

It follows from (B.56) that the equations of motion for the gearbox are

$$J_{SS} \ddot{\theta}_1 - J_{GS} \ddot{\theta}_{GB} = T_1 + N T_2 + D_{GT1} \quad (\text{B.58})$$

$$J_{GG} (1 - J_X^2 / J_T J_{GG}) \ddot{\theta}_{GB} - J_{GS} \ddot{\theta}_1 = -K_{GB} (1 + J_X / J_T) (\theta_{GB} - \theta_T) + K_T \frac{J_X}{J_T} \theta_T - (N - 1) T_2 + D_{GB} + D_{GT2} - J_X / J_T D_T \quad (\text{B.59})$$

$$J_T (1 - J_{GS}^2 / J_{GG} J_{SS} - J_X^2 / J_T J_{GG}) \ddot{\theta}_T = -K_{GB} (1 + J_X / J_{GG} - J_{GS}^2 / J_{GG} J_{SS}) (\theta_T - \theta_{GB}) - K_T (1 - J_{GS}^2 / J_{GG} J_{SS}) \theta_T + (N - 1) J_X / J_{GG} T_2 - J_X J_{GS} / J_{GG} J_{SS} (T_1 + N T_2) - J_X / J_{GG} (D_{GB} + D_{GT2}) + (1 - J_{GS}^2 / J_{GG} J_{SS}) D_T - J_X J_{GS} / J_{GG} J_{SS} D_{GT1} \quad (\text{B.60})$$

B.3.2 Simplification of gearbox dynamics

Ignoring the direct damping of the tower through D_T and indirect damping through D_{GB} , D_{GT1} and D_{GT2} , all of which are small,

$$\theta_T = \frac{-J_{GG} J_{GS} (s^2 J_X / J_{GB} - \omega_{GB}^2)}{(J_{GG} J_{SS} - J_{GS}^2) (s^2 + \omega_T^2 + \omega_{GB}^2 J_{GG} / J_T) (s^2 + \omega_{GB}^2 / (1 - J_{GS}^2 / J_{SS} J_{GG}))} (T_1 / J_T) + \frac{J_{GG} ((N - 1) J_{SS} - N J_{GS}) (s^2 J_X / J_{GB} - \omega_{GB}^2)}{(J_{GG} J_{SS} - J_{GS}^2) (s^2 + \omega_T^2 + \omega_{GB}^2 J_{GG} / J_T) (s^2 + \omega_{GB}^2 / (1 - J_{GS}^2 / J_{SS} J_{GG}))} (T_2 / J_T) \quad (\text{B.61})$$

where

$$\omega_T^2 = K_T/J_T ; \omega_{GB}^2 = K_{GB}/J_{GG}$$

Since the inertia of the gearbox is very much less than the inertia of the turbine as a whole, *i.e.* $J_{GG}/J_T \ll 1$ and $J_X/J_T \ll 1$, it follows that the contribution of T_1 and T_2 to (B.59) via θ_T is negligible. Hence the dynamics of the gearbox can be approximated by the equations

$$\begin{aligned} J_{SS}\ddot{\theta}_1 - J_{GS}\ddot{\theta}_{GB} &= T_1 + NT_2 + D_{GT1} \\ &= T_1 + NT_2 - B_{G1}\dot{\theta}_1 - NB_{G2}\dot{\theta}_2 \end{aligned} \quad (B.62)$$

$$\begin{aligned} J_{GG}\ddot{\theta}_{GB} - J_{GS}\ddot{\theta}_1 &= -K_{GB}\theta_{GB} - (N-1)T_2 + D_{GT2} + D_{GB} \\ &= -K_{GB}\theta_{GB} - (N-1)T_2 + (N-1)B_{G2}\dot{\theta}_2 - B_{G3}\dot{\theta}_{GB} - B_{GB}\dot{\theta}_{GB} \end{aligned} \quad (B.63)$$

The damping terms $B_{G1}\dot{\theta}_1$ and $B_{G2}\dot{\theta}_2$ can be interpreted as amendments to the input torques to the gearbox, T_1 and T_2 , respectively, and so need not be considered further here. The damping terms $B_{G1}\dot{\theta}_1$, $B_{G2}\dot{\theta}_2$ and $B_{G3}\dot{\theta}_{GB}$ are all small but the damping term $B_{GB}\dot{\theta}_{GB}$ may be large.

From (B.54), (B.62) and (B.63) the dynamic relationships of θ_1 and θ_2 to T_1 and T_2 are

$$\begin{aligned} \theta_1 &= \frac{(J_{GG}s^2 + (B_{G3} + B_{GB})s + K_{GB})}{s^2[(J_{SS}J_{GG} - J_{GS}^2)s^2 + J_{SS}(B_{G3} + B_{GB})s + J_{SS}K_{GB}]} T_1 \\ &+ \frac{[(NJ_{GG} - (N-1)J_{GS})s^2 + N(B_{G3} + B_{GB})s + NK_{GB}]}{s^2[(J_{SS}J_{GG} - J_{GS}^2)s^2 + J_{SS}(B_{G3} + B_{GB})s + J_{SS}K_{GB}]} T_2 \end{aligned} \quad (B.64)$$

$$\begin{aligned} \theta_2 &= \frac{((NJ_{GG} - (N-1)J_{GS})s^2 + N(B_{G3} + B_{GB})s + NK_{GB})}{s^2[(J_{SS}J_{GG} - J_{GS}^2)s^2 + J_{SS}(B_{G3} + B_{GB})s + J_{SS}K_{GB}]} T_1 \\ &+ \frac{[(N^2J_{GG} - 2N(N-1)J_{GS} + (N-1)^2J_{SS})s^2 + N^2(B_{G3} + B_{GB})s + N^2K_{GB}]}{s^2[(J_{SS}J_{GG} - J_{GS}^2)s^2 + J_{SS}(B_{G3} + B_{GB})s + J_{SS}K_{GB}]} T_2 \end{aligned} \quad (B.65)$$

Hence the gearbox dynamics can be represented by the model depicted in Figure B.9 where

$$J_{SS}^* = \frac{J_{SS}[(J_{GG} - J_{GS}^2/J_{SS})s^2 + (B_{G3} + B_{GB})s + K_{GB}]}{[(J_{GG} - (N-1)/NJ_{GS})s^2 + (B_{G3} + B_{GB})s + K_{GB}]} \quad (B.66)$$

$$1/K_{GB1} = \frac{(N-1)/NJ_{GS}}{[(J_{SS}J_{GG} - J_{GS}^2)s^2 + J_{SS}(B_{G3} + B_{GB})s + J_{SS}K_{GB}]} \quad (B.67)$$

$$1/K_{GB2} = \frac{[(N-1)^2J_{SS} - N(N-1)J_{GS}]}{[(J_{SS}J_{GG} - J_{GS}^2)s^2 + J_{SS}(B_{G3} + B_{GB})s + J_{SS}K_{GB}]} \quad (B.68)$$

It should be noted that

$$(N-1)^2J_{SS} - N(N-1)J_{GS} = (N-1) [(N_1N_2N_3-1)J_1 + N_1^2(N_2N_3-1)J_2 + N_1^2N_2^2(N_3-1)J_3]$$

which is clearly always positive. Comparing Figure B.9 to Figure B.6, the compliantly mounted gearbox is equivalent to a rigidly mounted gearbox with J_S replaced by J_{SS}^* and with additional input compliance, $1/K_{GB1}$, and additional output compliance, $1/K_{GB2}$.

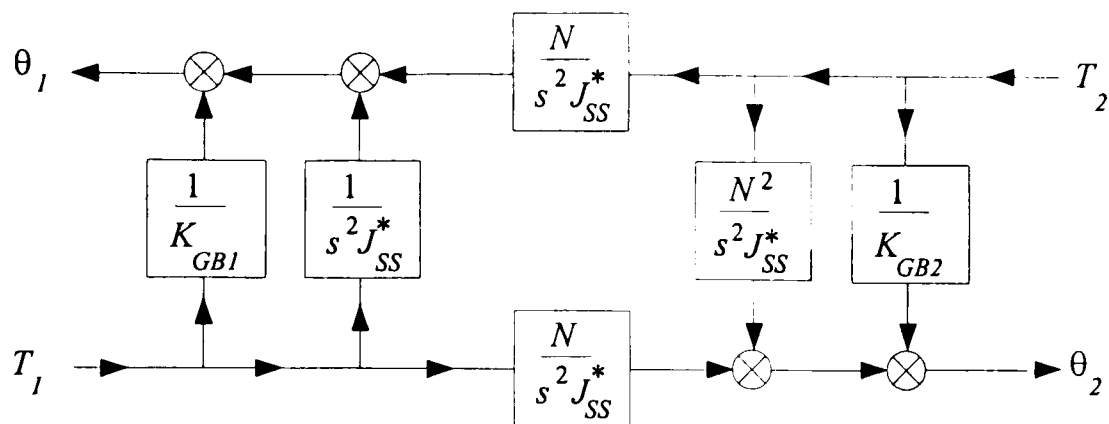


Figure B.9 Dynamics of compliantly mounted gearbox.

There are two cases of compliant gearbox mounting to be considered. In the first case, the rotor is supported by bearings independent of the gearbox when only the gearbox case and drive-train components contribute to J_{GB} . J_{GG} is much less than the inertia of the rotor. Since the gearbox stiffness, K_{GB} , must sustain the rotor, the gearbox frequency, ω_{GB} , is high and the poles and zeros of J_{SS}^* , which may be significantly different, are at high frequency. In the second case, the rotor is supported by bearings integral to the gearbox when the rotor contributes to J_{GB} . J_{GG} increases as the distance between the axis of rotation of the gearbox and that of the rotor increases. However, although it can be significantly greater than the previous case, J_{GG} is still significantly less than the inertia of the rotor since the rotor is treated as a point mass when included in J_{GG} . The frequencies of the poles and zeros reduce as the inertia J_{GG} increases, but they also become closer as both $(J_{GG} - J_{GS}^2 / J_{SS})$ and $(J_{GG} - (N-1)/N \cdot J_{GS})$ in (B.66) become increasingly dominated by J_{GG} . Hence in both cases J_{SS}^* is essentially equal to J_{SS} .

Since K_{GB} must sustain the rotor and J_{GG} is less than the inertia of the rotor, the frequency ω_{GB} is not low. Nevertheless the poles of $1/K_{GB1}$ and $1/K_{GB2}$ can influence the low-frequency dynamics. External damping to the gearbox, D_{GB1} , may be introduced not only to reduce gearbox oscillations but also in an attempt to increase the damping of the dominant dynamic modes of the drive train. In the latter case, the damping required is so great that the frequencies of the poles of $1/K_{GB1}$ and also $1/K_{GB2}$ become distinct with one at low frequency and the other at high frequency. Hence, the expressions (B.67) and (B.68) for $1/K_{GB1}$ and $1/K_{GB2}$ respectively cannot be simplified at this stage.

B.4 Drive train

The drive train consists of the rotor, hub, low-speed shaft, compliantly mounted gearbox, high-speed shaft and generator rotor. The simplified equations of motion, brought forward from Section B.2, for the rotor, hub and low-speed shaft are

$$J_R^* \ddot{\theta}_R = T_A - T_1 ; T_1 = K_1(\theta_R - \theta_1) \quad (\text{B.69})$$

Those for the gearbox, from Section B.3, are depicted in Figure B.9 with J_{SS}^* , K_{GB1} and K_{GB2} defined by (B.66), (B.67) and (B.68) respectively. The inertia of the hub, J_H^* , is included in J_{SS} and so in J_{SS}^* since, as inferred in Section B.2, the hub may be considered to be rigidly attached to the gearbox, *i.e.*

$$J_{SS} = J_S + J_H^* \quad (\text{B.70})$$

B.4.1 Equations of motion of generator rotor

Since the inertia of the high-speed shaft is very much less than that of either the generator rotor or the gear train reflected to the high-speed shaft, the high-speed shaft may be considered massless with appropriate fractions of its inertia allocated to those of the generator rotor and to the inertia of the final stage of the gearbox. When the high-speed shaft is uniform, the allocation to each is half the inertia of the high-speed shaft. The system is as depicted in Figure B.10. Damping has not been included explicitly in (B.69), but it may be considered to be present implicitly through the inertia terms. As noted in Section B.3, two of the gearbox damping terms, $B_{G1} \dot{\theta}_1$ and $B_{G2} \dot{\theta}_2$, can be interpreted as modifications to the torques T_1 and T_2 . Because the low-speed and high-speed shafts are relatively stiff and considered massless, the difference in angular velocity between the two ends of the shafts is small. It follows that, as these damping terms are light, they may be transferred to J_R^* and J_G , respectively. Any discrepancy occurs at high frequency and so can be ignored. Hence damping from the gearbox together with the rotor aerodynamic damping, $B_R^* \dot{\theta}_R$, and any losses from low-speed shaft bearings are incorporated within $J_R^* \ddot{\theta}_R$; damping from the gearbox and any losses from the high-speed shaft bearings are incorporated within $J_G \ddot{\theta}_G$; and the third gearbox damping term, $B_{G3} \dot{\theta}_{GB}$, and the gearbox mounting damping, $B_{GB} \dot{\theta}_{GB}$, are incorporated into $J_{GG} \ddot{\theta}_{GB}$.

The equations of motion for the generator rotor and high-speed shaft are

$$J_G \ddot{\theta}_G = T_G - T_2 ; T_2 = K_2(\theta_G - \theta_2) \quad (\text{B.71})$$

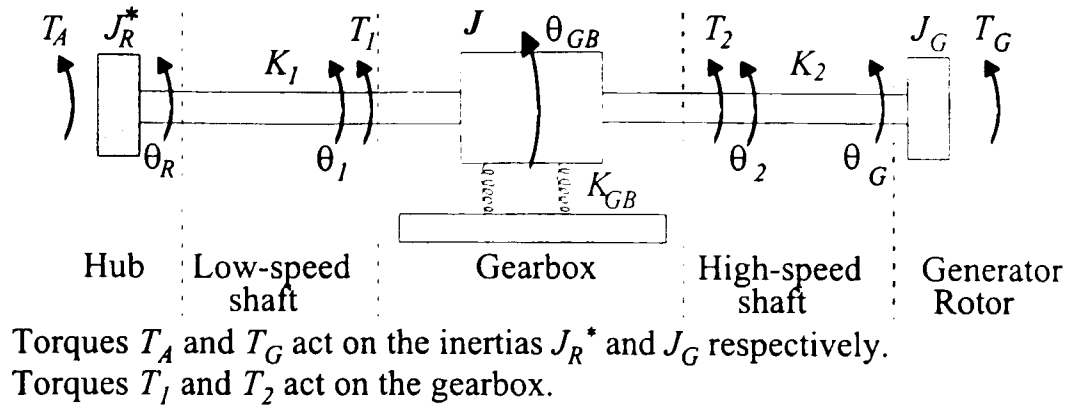


Figure B.10 General drive-train system.

B.4.2 Simplification of drive-train dynamics

Exploiting the equivalence of a compliantly mounted gearbox to a rigidly mounted gearbox (see Section B.3), the dynamics of the complete drive train in Figure B.10 can be represented as in Figure B.11a. The two stiffnesses of the low-speed shaft can be combined as can the two stiffnesses on the high-speed shaft. The dynamics simplify to those of Figure B.11b, with

$$\frac{1}{K_1^*} = \frac{1}{K_1} + \frac{1}{K_{GB1}} \quad ; \quad \frac{1}{K_2^*} = \frac{1}{K_2} + \frac{1}{K_{GB2}} \quad (\text{B.72})$$

As discussed in Leithead and Rogers (1995b), the dynamic model of the drive train in Figure B.11b can be reduced to that in Figure B.11c, with

$$L(s) = \frac{(K_1^* + N^2 K_2^*) / (J_{SS}^* s^2)}{1 + (K_1^* + N^2 K_2^*) / (J_{SS}^* s^2)} \quad (\text{B.73})$$

From (B.66), (B.67), (B.68) and (B.72),

$$\frac{(K_1^* + N^2 K_2^*)}{J_{SS}^*} = \frac{(K_1 + N^2 K_2)}{J_{SS}} \cdot \frac{[(J_{GG} - (N-1)/N \cdot J_{GS})s^2 + K_{GB}]}{[(J_{GG} - J_{GS}^2 / J_{SS})s^2 + (K_{GB} + (N-1)/N \cdot J_{GS} / J_{SS} \cdot K_1)]} \cdot \frac{[(J_{GG} - J_{GS}^2 / J_{SS})s^2 + (K_{GB} + (N-1)^2 / N^2 \cdot \kappa)]}{[(J_{GG} - J_{GS}^2 / J_{SS})s^2 + (K_{GB} + ((N-1)^2 / N^2 - (N-1)/N \cdot J_{GS} / J_{SS})N^2 \cdot K_2)]} \quad (\text{B.74})$$

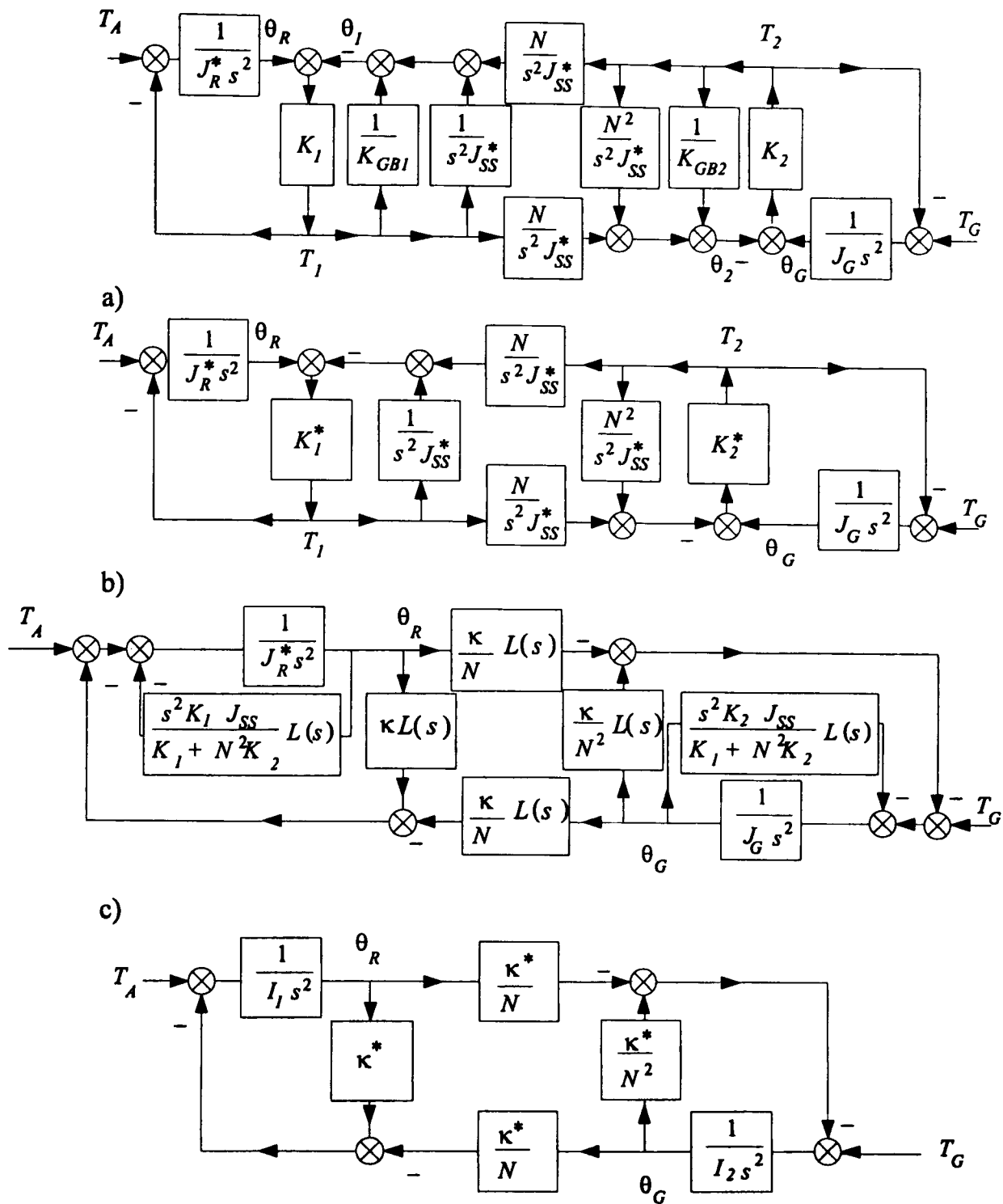


Figure B.11 Equivalent forms for the drive-train dynamics.

For all medium/large scale wind turbines, $L(s)$ is essentially one. First, note that the frequency $\sqrt{(K_1 + N^2 K_2) / J_{SS}}$ is not low, since both the shaft stiffness, K_1 and NK_2 , and indeed the gearbox stiffness, K_{GB} , must sustain the rotor and J_{SS} is much less than the rotor inertia. When the rotor is supported by bearings independently of the gearbox, the frequencies of the poles and zeros of $(K_1^* + N^2 K_2^*) / J_{SS}^*$ are very high. Hence in this case $(K_1^* + N^2 K_2^*) / J_{SS}^*$ is equal to $(K_1 + N^2 K_2) / J_{SS}$ at all but very high frequencies and $L(s)$ is essentially one. When the rotor bearings are incorporated into the gearbox, the frequencies

of poles and zeros of $(K_1^* + N^2 K_2^*) / J_{SS}^*$ are reduced. Though not at low frequency, the poles and zeros of $(K_1^* + N^2 K_2^*) / J_{SS}^*$ may no longer be at very high frequency. Nevertheless $L(s)$ is still essentially one, since $(K_1 + N^2 K_2) / J_{SS}$ is large and, by simple root locus arguments, the poles of $L(s)$, not at high frequency, migrate to be close to the zeros of $L(s)$, which are not at high frequency. The lower the frequencies, the closer the poles and zeros become. Perturbations of $L(s)$ due to small residual mismatches between these poles and zeros are kept small by the damping inevitably present in the drive train. It follows that the dynamics of the drive train can be modelled as in Figure B.11d with

$$I_1 = J_R^* + \frac{K_1^*}{K_1^* + N^2 K_2^*} J_{SS}^* \quad ; \quad I_2 = J_G + \frac{K_2^*}{K_1^* + N^2 K_2^*} J_{SS}^* \quad (\text{B.75})$$

and

$$\frac{N^2}{\kappa^*} = \frac{N^2}{K_1} + \frac{1}{K_2} + \frac{(N-1)^2 J_{SS}}{[(J_{SS} J_{GG} - J_{GS}^2) s^2 + J_{SS} K_{GB}]} \quad (\text{B.76})$$

As has already been noted in Section B.3, J_{SS}^* is essentially the same as J_{SS} . The ratio of stiffnesses

$$\frac{K_2^*}{(K_1^* + N^2 K_2^*)} = \frac{K_2}{(K_1 + N^2 K_2)} \cdot \frac{[(J_{SS} J_{GG} - J_{GS}^2) s^2 + J_{SS} K_{GB} + (N-1) / N \cdot J_{GS} K_1]}{[(J_{SS} J_{GG} - J_{GS}^2) s^2 + J_{SS} K_{GB} + (N-1)^2 / N^2 \cdot J_{SS} \kappa]} \quad (\text{B.77})$$

When the rotor is supported by bearings independent of the gearbox the poles and zeros of (B.76) are at high frequency and are not significant. When the bearings are incorporated into the gearbox, the frequencies of the poles and zeros are reduced. Depending on the values of the inertias and stiffnesses in (B.77), the poles and zeros might remain sufficiently different to induce significant dynamics at low frequency in $K_2^* / (K_1^* + N^2 K_2^*)$ and so in I_2 . However, these dynamics can be neglected as the drive train is coupled to an induction generator. The generator torque, T_G , is strongly related to the angular velocity of the generator rotor, $\dot{\theta}_G$, see Appendix D. I_2 is enclosed in a strong feedback loop and, by simple root locus arguments, the poles of I_2 migrate to be close to the zeros of I_2 . The lower the frequency, the closer the poles and zeros become. Hence,

$$I_2 \approx J_G + J_{SS} \frac{K_2}{(K_1 + N^2 K_2)} \cdot \frac{[J_{SS} K_{GB} + (N-1) / N \cdot J_{GS} K_1]}{[J_{SS} K_{GB} + (N-1)^2 / N^2 \cdot J_{SS} \kappa]} \quad (\text{B.78})$$

The ratio of stiffnesses is

$$\frac{K_1^*}{(K_1^* + N^2 K_2^*)} = \frac{K_1}{(K_1 + N^2 K_2)} \cdot \frac{[(J_{SS} J_{GG} - J_{GS}^2) s^2 + J_{SS} K_{GB} + ((N-1)^2 J_{SS} - N(N-1) J_{GS}) K_2]}{[(J_{SS} J_{GG} - J_{GS}^2) s^2 + J_{SS} K_{GB} + (N-1)^2 / N^2 \cdot J_{SS} \kappa]} \quad (\text{B.79})$$

As above, the poles and zeros in (B.79) might remain sufficiently different to induce significant dynamics at low frequency in $K_1^*/(K_1^* + N^2K_2^*)$ and so in I_1 . But again these can be discounted by a root locus argument. In this case the strong feedback is provided by the large inertia, J_R^* , of the rotor since, from (B.75),

$$(I_1 / J_R^*)^{-1} = G(s) / (1 + G(s)) \quad (\text{B.80})$$

where

$$G(s) = \frac{J_R^*}{J_{SS}^*} \cdot \left(\frac{K_1^*}{(K_1^* + N^2K_2^*)} \right)^{-1} \quad (\text{B.81})$$

Hence,

$$I_1 \approx J_R^* + J_{SS}^* \cdot \frac{K_1}{(K_1 + N^2K_2)} \cdot \frac{[J_{SS}K_{GB} + ((N-1)^2J_{SS} - N(N-1)J_{GS})K_2]}{[J_{SS}K_{GB} + (N-1)^2/N^2 \cdot J_{SS}\kappa]} \quad (\text{B.82})$$

B.4.3 Simple drive-train model

The total drive-train compliance, κ^* , as defined by (B.76), can be partitioned freely between the low- and high-speed shafts. The compliance

$$(N-1)^2 / N^2 J_{SS} / [(J_{SS} J_{GG} - J_{GS}^2)s^2 + J_{SS}K_{GB}]$$

is assigned to the low-speed shaft. The natural assignment is to assign the compliance $1/K_1$, to the low-speed shaft and the compliance $1/K_2$ to the high-speed shaft, but a possible alternative is to assign the combined compliance $1/\kappa$ to the low-speed shaft and no compliance to the high-speed shaft. It follows that the dynamics of the drive train in Figure B.11d can be modelled by the simple system depicted in Figure B.12.

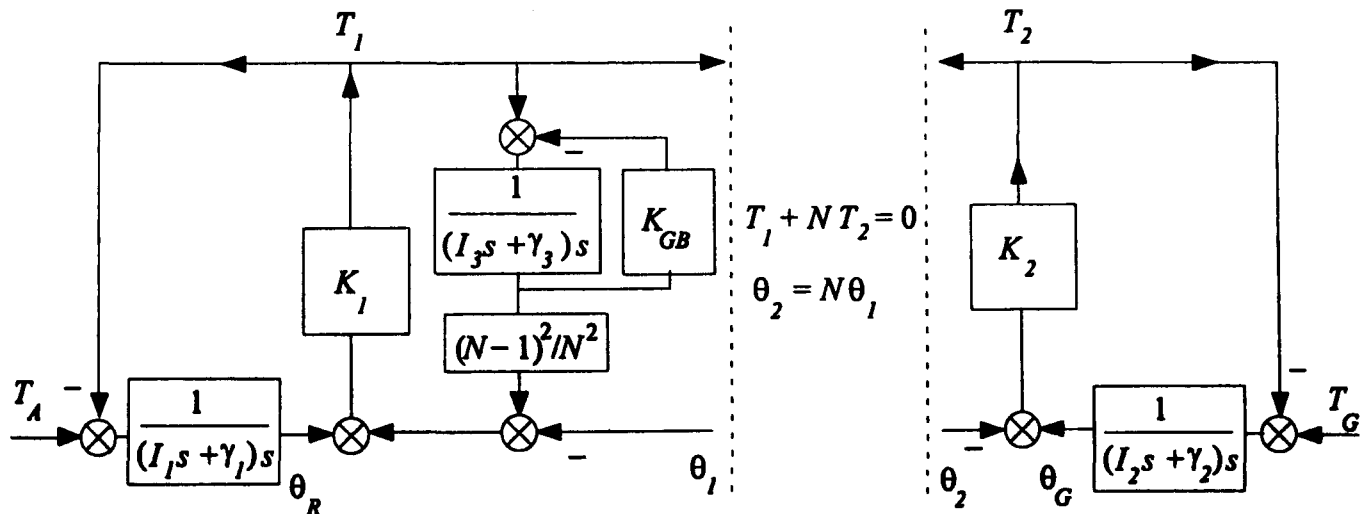


Figure B.12 Simplified representation of drive-train dynamics.

The lumped inertias I_1 , I_2 and I_3 , are related to the parameters of the drive-train components and the rotor such that

$$I_1 = J_R + J_H \frac{K_R}{(K_R + K_H)} + J_{SS} \cdot \frac{K_1}{(K_1 + N^2 K_2)} \cdot \frac{[J_{SS} K_{GB} + ((N-1)^2 J_{SS} - N(N-1) J_{GS}) K_2]}{[J_{SS} K_{GB} + (N-1)^2 / N^2 \cdot J_{SS} K]} \quad (\text{B.83})$$

$$I_2 = J_G + J_{SS} \cdot \frac{K_2}{(K_1 + N^2 K_2)} \cdot \frac{[J_{SS} K_{GB} + (N-1) / N \cdot J_{GS}] K_1}{[J_{SS} K_{GB} + (N-1)^2 / N^2 \cdot J_{GS} K]} \quad (\text{B.84})$$

$$I_3 = J_{GG} + J_{GS}^2 / J_{SS} \quad (\text{B.85})$$

It should be noted that $(I_1 + N^2 I_2)$ is the sum of all the inertias in the drive train reflected to the low-speed shaft, *i.e.*

$$I_1 + N^2 I_2 = J_R + J_H + J_S + N^2 J_G \quad (\text{B.86})$$

The inertias of the low-speed and high-speed shafts are not shown explicitly in (B.86) but are incorporated in J_R and J_H and J_S and J_G respectively. The lumped stiffnesses K_1 and K_3 , are related to the parameters of the drive-train components and the rotor such that

$$K_1 = \frac{K_R K_H}{(K_R + K_H)} \cdot \left(1 + \frac{K_R K_H}{(K_R + K_H)^2} \frac{J_H}{J_R}\right) \quad (\text{B.87})$$

$$K_3 = K_{GB} \quad (\text{B.88})$$

whilst the stiffness K_2 , remains the high-speed shaft stiffness. The lumped parameter damping coefficients, γ_1 , γ_2 and γ_3 , are

$$\gamma_1 = B_R^* + B_{G1} + B_S \quad (\text{B.89})$$

$$\gamma_2 = B_{G2} + B_H \quad (\text{B.90})$$

$$\gamma_3 = B_{G3} + B_{GB} \quad (\text{B.91})$$

where B_S and B_H represent the losses from the low- and high-speed shaft bearings respectively. For the tip-regulated case

$$J_R = J \quad ; \quad K_R = J \omega_E^2 \quad (\text{B.92})$$

and

$$B_R^* = -\frac{\partial F_1}{\partial \Omega} \quad (\text{B.93})$$

For the full-span regulated case

$$\begin{aligned} J_R &= J - J \sin^2 \alpha_o (\omega_E^2 - \omega_F^2) / \omega_E^2 \\ K_R &= J \omega_E^2 - J \sin^2 \alpha_o (\omega_E^2 - \omega_F^2) \end{aligned} \quad (\text{B.94})$$

and

$$\begin{aligned}
B_R^* = & -\frac{\partial F_1}{\partial \Omega} + \left(\sin^2 \alpha_o \frac{\partial F_1}{\partial \Omega} \right) \cdot (\omega_E^2 (1 + \cos^2 \alpha_o) - \omega_F^2 \cos^2 \alpha_o) / \omega_E^2 \\
& + \left(\left[-L \sin \alpha_o \cos \alpha_o \frac{\partial F_1}{\partial w} + L \sin^2 \alpha_o \frac{\partial F_2}{\partial w} + \sin \alpha_o \cos \alpha_o \frac{\partial F_2}{\partial \Omega} \right] \right) \\
& (\omega_E^2 \cos^2 \alpha_o + \omega_F^2 \sin^2 \alpha_o) / \omega_E^2
\end{aligned} \tag{B.95}$$

at other than low frequencies;

$$B_R^* = -\frac{\partial F_1}{\partial \Omega} + \frac{\partial F_1}{\partial \Omega} \sin^2 \alpha_o \cdot (\omega_E^2 - \omega_F^2) / \omega_E^2 \tag{B.96}$$

at low frequency, see discussion in Section B.2.2.

The terms by which (B.94) differ from (B.92) and by which (B.95) or (B.96) differ from (B.93), are typically small and can be neglected, particularly the terms in B_R^* , since other sources of damping in the drive train are generally much greater, for details see Leithead and Rogers (1995b). Indeed B_R^* can be omitted from (B.89) for the same reason making the difference between (B.95) and (B.96) immaterial. The resulting simple model of the drive train, Figure B.12, is no longer dependent on the equilibrium point at which it is linearised, but is fixed. Only the dynamics relating aerodynamic torque, T_A , to changes in pitch angle, α , and changes in wind speed, w , represented by (B.52), are dependent on the equilibrium point.

B.5 Summary

The drive-train dynamics of a wind turbine are a composite of many dynamic modes of the tower, blades, hub, low-speed shaft, gearbox, gear-train, high-speed shaft and generator rotor. However, the drive-train dynamics can be represented by a simple model which is adequate for analysing the relationship of the dynamic properties of the drive train to the physical parameters.

The full non-linear model, the full linearised model, the simple non-linear model and the simple linear model as given below.

B.5.1 Full non-linear model

Equations (B.2), (B.3), (B.4), (B.5), (B.35), (B.54), (B.58), (B.59), (B.60) and (B.71) together model all the significant dynamics of the drive train including coupling to the tower. Although these equations are suitable for simulation purposes, they are less well-suited for analytic purposes since they are both complex and non-linear.

The full non-linear model is described below.

The equations of motion of the rotor are (B.2) and (B.3), that is,

$$J\ddot{\theta}_R = - (K_E + J\Omega_o^2).[(\theta_R - \theta_H)\cos\beta - (\phi_R - \phi_T)\sin\beta]\cos\beta - (K_F + J\Omega_o^2).[(\theta_R - \theta_H)\sin\beta + (\phi_R - \phi_T)\cos\beta]\sin\beta + F_1 \quad (\text{B.97})$$

$$\frac{(1 - J_C^2 / J J_T)}{(1 + J_C / J_T)} J\ddot{\phi}_R = (K_E + J\Omega_o^2).[(\theta_R - \theta_H)\cos\beta - (\phi_R - \phi_T)\sin\beta]\sin\beta - (K_F + J\Omega_o^2).[(\theta_R - \theta_H)\sin\beta + (\phi_R - \phi_T)\cos\beta]\cos\beta + [F_2 + \frac{J_C}{J_T} B_T \dot{\phi}_T + \frac{J_C}{J_T} K_T \phi_T] / (1 + J_C / J_T) \quad (\text{B.98})$$

The equations of motion of the tower are (B.60) and (B.4), that is,

$$(1 - \frac{J_{GS}^2}{J_{GG} J_{SS}} - \frac{J_X^2}{J_T J_{GG}}) J_T \ddot{\theta}_T = - K_{GB} (1 + J_X / J_{GG} - J_{GS}^2 / J_{GG} J_{SS}) (\theta_T - \theta_{GB}) - K_T (1 - J_{GS}^2 / J_{GG} J_{SS}) \theta_T + (N - 1) J_X / J_{GG} \cdot T_2 - J_X J_{GS} / J_{GG} J_{SS} \cdot (T_1 + N T_2) - (1 - J_{GS}^2 / J_{GG} J_{SS}) B_T \dot{\theta}_T + J_X / J_{GG} \cdot ((N - 1) B_{G2} \dot{\theta}_2 + B_{G3} \dot{\theta}_{GB} + B_{GB} \dot{\theta}_{GB}) - J_X J_{GS} / J_{GG} J_{SS} \cdot (B_{G1} \dot{\theta}_1 + N B_{G2} \dot{\theta}_2) \quad (\text{B.99})$$

$$\frac{(1 - J_C^2 / J J_T)}{(1 + J_C / J)} J_T \ddot{\phi}_T = - (K_E + J\Omega_o^2).[(\theta_R - \theta_H)\cos\beta - (\phi_R - \phi_T)\sin\beta]\sin\beta + (K_F + J\Omega_o^2).[(\theta_R - \theta_H)\sin\beta + (\phi_R - \phi_T)\cos\beta]\cos\beta - [B_T \dot{\phi}_T + K_T \phi_T + \frac{J_C}{J} F_2] / (1 + J_C / J) \quad (\text{B.100})$$

The equations of motion of the hub and low-speed shaft are (B.35) and (B.5), that is,

$$J_H \ddot{\theta}_H = T_H - T_1 ; T_1 = K_H (\theta_H - \theta_1) \quad (\text{B.101})$$

$$T_H = (K_E + J\Omega_o^2).[(\theta_R - \theta_H)\cos\beta - (\phi_R - \phi_T)\sin\beta]\cos\beta + (K_F + J\Omega_o^2).[(\theta_R - \theta_H)\sin\beta + (\phi_R - \phi_T)\cos\beta]\sin\beta \quad (\text{B.102})$$

The equations of motion of the gearbox are (B.58) and (B.59), that is,

$$J_{SS} \ddot{\theta}_1 - J_{GS} \ddot{\theta}_{GB} = T_1 + N T_2 - B_{G1} \dot{\theta}_1 - N B_{G2} \dot{\theta}_2 \quad (\text{B.103})$$

$$J_{GG} (1 - J_X^2 / J_T J_{GG}) \ddot{\theta}_{GB} - J_{GS} \ddot{\theta}_1 = - K_{GB} (1 + J_X / J_T) \cdot (\theta_{GB} - \theta_T) + K_T J_X / J_T \cdot \theta_T - (N - 1) T_2 - (N - 1) B_{G2} \dot{\theta}_2 - B_{G3} \dot{\theta}_{GB} - B_{GB} \dot{\theta}_{GB} + J_X / J_T \cdot B_T \dot{\theta}_T \quad (\text{B.104})$$

The equations of motion of the generator rotor and high-speed shaft are (B.71) and (B.54), that is,

$$J_G \ddot{\theta}_G = T_G - T_2 ; T_2 = K_2 (\theta_G - \theta_2) \quad (\text{B.105})$$

$$\theta_2 = N \theta_1 - (N - 1) \theta_{GB} \quad (\text{B.106})$$

B.5.2 Full linear model

However, since the above model is non-linear, it is not particularly suitable for analysis purposes. The non-linear aspects of the drive-train dynamics can be linearised as discussed in Section B.2.2. (B.97) and (B.98) are replaced by

$$\begin{aligned}
 J\ddot{\theta}_R = & - (K_E + J\Omega_o^2) \cdot [(\theta_R - \theta_H) \cos \beta_o - (\phi_R - \phi_T) \sin \beta_o] \cos \beta_o \\
 & - (K_F + J\Omega_o^2) \cdot [(\theta_R - \theta_H) \sin \beta_o + (\phi_R - \phi_T) \cos \beta_o] \sin \beta_o \\
 & + \frac{\partial F_1}{\partial w} \Delta w + F_{1\alpha} \Delta \alpha + \frac{\partial F_1}{\partial \Omega} \dot{\theta}_R - L \frac{\partial F_1}{\partial w} \dot{\phi}_R - h \frac{\partial F_1}{\partial w} \dot{\phi}_T
 \end{aligned} \tag{B.107}$$

where

$$\begin{aligned}
 F_{1\alpha} = & \frac{\partial F_1}{\partial \alpha} + \frac{(\omega_E^2 - \omega_F^2)}{2\omega_E^2\omega_F^2} [(\omega_E^2 + \omega_F^2) \sin \alpha_o \cos \alpha_o (w_o \frac{\partial F_1}{\partial w} + \Omega_o \frac{\partial F_1}{\partial \Omega}) \\
 & + (\omega_E^2 \cos^2 \alpha_o - \omega_F^2 \sin^2 \alpha_o) (w_o \frac{\partial F_2}{\partial w} + \Omega_o \frac{\partial F_2}{\partial \Omega})]
 \end{aligned} \tag{B.108}$$

$$\omega_E^2 = \frac{(K_E + J\Omega_o^2)}{J} \quad ; \quad \omega_F^2 = \frac{(K_F + J\Omega_o^2)}{J}$$

and h is the hub height, L is such that $L\dot{\phi}_R$ is the mean wind speed seen by a blade.

$$\begin{aligned}
 \frac{(1 - J_C^2 / J J_T)}{(1 + J_C / J_T)} J\ddot{\phi}_R = & (K_E + J\Omega_o^2) \cdot [(\theta_R - \theta_H) \cos \beta_o - (\phi_R - \phi_T) \sin \beta_o] \sin \beta_o \\
 & - (K_F + J\Omega_o^2) \cdot [(\theta_R - \theta_H) \sin \beta_o + (\phi_R - \phi_T) \cos \beta_o] \cos \beta_o \\
 & + [\frac{\partial F_2}{\partial w} \Delta w + F_{2\alpha} \Delta \alpha + \frac{\partial F_2}{\partial \Omega} \dot{\theta}_R - L \frac{\partial F_2}{\partial w} \dot{\phi}_R \\
 & - h \frac{\partial F_2}{\partial w} \dot{\phi}_T + B_T \dot{\phi}_T + K_T \phi_T] / (1 + J_C / J_T)
 \end{aligned} \tag{B.109}$$

where

$$\begin{aligned}
 F_{2\alpha} = & \frac{\partial F_2}{\partial \alpha} - \frac{(\omega_E^2 - \omega_F^2)}{2\omega_E^2\omega_F^2} [(\omega_E^2 \sin^2 \alpha_o - \omega_F^2 \cos^2 \alpha_o) (w_o \frac{\partial F_1}{\partial w} + \Omega_o \frac{\partial F_1}{\partial \Omega}) \\
 & + (\omega_E^2 + \omega_F^2) \sin \alpha_o \cos \alpha_o (w_o \frac{\partial F_2}{\partial w} + \Omega_o \frac{\partial F_2}{\partial \Omega})]
 \end{aligned} \tag{B.110}$$

and Δw and $\Delta \alpha$ are the perturbations in wind speed and pitch angle, respectively, about some operating point and $\Omega = \dot{\theta}_R$ is the rotor speed. The angle β_o is the value of β corresponding to the choice of operating point. (B.100) is replaced by

$$\begin{aligned}
\frac{(1 - J_C^2 / J J_T)}{(1 + J_C / J)} J_T \ddot{\phi}_T = & - (K_E + J\Omega_o^2)[(\theta_R - \theta_H) \cos \beta_o - (\phi_R - \phi_T) \sin \beta_o] \sin \beta_o \\
& + (K_F + J\Omega_o^2)[(\theta_R - \theta_H) \sin \beta_o + (\phi_R - \phi_T) \cos \beta_o] \cos \beta_o \\
& - \left[\frac{J_C}{J} \frac{\partial F_2}{\partial w} \Delta w + \frac{J_C}{J} F_{2\alpha} \Delta \alpha + \frac{J_C}{J} \frac{\partial F_2}{\partial \Omega} \dot{\theta}_R - \frac{J_C}{J} L \frac{\partial F_2}{\partial w} \dot{\phi}_R \right. \\
& \left. - \frac{J_C}{J} h \frac{\partial F_2}{\partial w} \dot{\phi}_T + B_T \dot{\phi}_T + K_T \phi_T \right] / (1 + J_C / J)
\end{aligned} \tag{B.111}$$

and (B.102) is replaced by

$$\begin{aligned}
T_H = & (K_E + J\Omega_o^2)[(\theta_R - \theta_H) \cos \beta_o - (\phi_R - \phi_T) \sin \beta_o] \cos \beta_o \\
& + (K_F + J\Omega_o^2)[(\theta_R - \theta_H) \sin \beta_o + (\phi_R - \phi_T) \cos \beta_o] \sin \beta_o \\
& + \frac{\partial F_1}{\partial \alpha} - F_{1\alpha}
\end{aligned} \tag{B.112}$$

The remaining equations are unchanged.

B.5.3 Simple linear model

The lumped parameter model is depicted in Figure B.12. It should be noted that the simple model is linear - it does not vary with wind speed. It consists of the wind turbine rotor inertia, I_1 , connected by a massless shaft of stiffness, K_1 , connected to a rigidly mounted massless gearbox, with ratio N , which in turn is connected by a massless shaft of stiffness, K_2 , to the generator rotor inertia, I_2 . In addition, the compliance of the gearbox mount is incorporated into the low-speed shaft with inertia, I_3 , and stiffness, K_3 .

The lumped rotor inertia, I_1 , the low-speed shaft damping constant, γ_1 , and the low-speed shaft stiffness, K_1 are related to the actual drive-train parameters of Section B.2 (B.45, B.70, B.83) by

$$\begin{aligned}
I_1 = & J_R + J_H \cdot \frac{K_R}{(K_R + K_H)} \\
& + \frac{K_1 [(J_S + J_H K_H / (K_R + K_H)) \cdot (K_{GB} + (N-1)^2 K_2) - N(N-1) J_{GS} K_2]}{(K_1 + N^2 K_2) [K_{GB} + (N-1)^2 / N^2 \cdot \kappa]}
\end{aligned}$$

(B.113)

$$\gamma_1 = B_{GI} + B_S \tag{B.114}$$

$$K_1 = \frac{K_R K_H}{(K_R + K_H)} \left(1 + \frac{K_R K_H}{(K_R + K_H)^2} \cdot \frac{J_H}{J_R} \right) \tag{B.115}$$

where $\kappa = N^2 K_1 K_2 / (K_1 + N^2 K_2)$

The lumped generator rotor inertia, I_2 , and the high-speed shaft damping constant, γ_2 , are related to the actual drive-train parameters by

$$I_2 = J_G + \frac{K_2(J_S + J_H K_H / (K_R + K_H)) \cdot (K_{GB} + (N-1) / N \cdot J_{GS} K_I)}{(K_I + N^2 K_2) \cdot [K_{GB} + (N-1)^2 / N^2 \cdot \kappa]} \quad (\text{B.116})$$

$$\gamma_2 = B_{G2} + B_S \quad (\text{B.117})$$

The stiffness of the high-speed shaft remains K_2 . The lumped gearbox inertia, I_3 , the gearbox damping, γ_3 , and the stiffness of the gearbox mounting, K_3 , are related to the actual drive-train parameters by

$$I_3 = J_{GG} - \frac{J_{GS}^2}{J_S + J_H K_H / (K_R + K_H)} \quad (\text{B.118})$$

$$\gamma_3 = B_{G3} + B_{GB} \quad (\text{B.119})$$

$$K_3 = K_{GB} \quad (\text{B.120})$$

Simplification is possible because the tower head inertia, with respect to the base of the tower, is much greater than the inertia of the rotor which in turn is much greater than the inertias of the other drive-train components. The simple model is consistent with the control models of specific configurations of wind turbines employed in previous control design investigations (Leithead *et al.*, 1991a, Wilkie and Leithead, 1989, Bossanyi *et al.*, 1992).

B.5.4 Simple non-linear model

A simple global non-linear model of the drive-train dynamics can also be obtained as follows. In this case, B_R^* is not neglected. Instead, with B_R^* defined as in (B.93) and (B.52), it follows that the non-linear dynamics relating aerodynamic torque, T_A , to pitch angle, α , and wind speed, w , are adequately represented by

$$T_A = F_I(\alpha, w, \Omega) \quad (\text{B.121})$$

provided the term B_R^* is omitted from (B.89). It should be noted that the damping terms, (B.89) to (B.91), cannot be neglected in the non-linear model, since they account for significant internal drive-train mechanical losses. Hence Figure B.12, together with (B.121), constitutes an adequate non-linear model.

Appendix C Control of wind turbines

A typical wind turbine system, for which rated power is maintained using power feedback, is shown in Figure C.1. The system usually has one input, the power set-point, and one output, the electrical power (*i.e.* it is a SISO system). The system is subject to disturbances due to wind speed and power measurement, all of which are stochastic. The wind speed can be thought of as two external disturbance components, one at low frequency due to wind turbulence and the other at high frequency at multiples of $n\Omega_o$ due to rotational sampling. The size and the spectra of these disturbances vary with the wind turbine's configuration.

The role and design of power control of constant-speed wind turbines has been thoroughly investigated by Leithead *et al.* (1991b) and is well understood. The control design used here follows the methodology used by Leithead *et al.* (1991a). Since the power control of a constant speed wind turbine is a SISO system the control design technique is immaterial; the relationship between the input and the output (Leithead *et al.*, 1997) and how the control is implemented (Leith and Leithead, 1997) are the important issues.

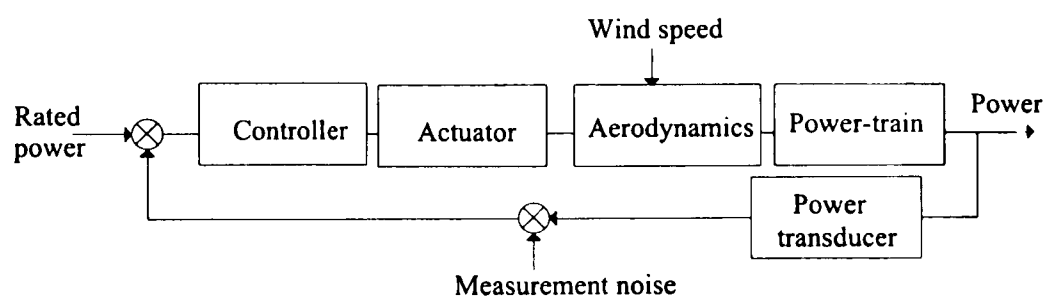


Figure C.1 The wind turbine system.

This appendix reviews what constitutes good power control performance and how the dynamic performance of different wind turbine configurations can be compared. It describes the ideal open loop transfer function and how this is used in the parametric studies in Chapters 5 and 6.

The main aim of a power controller is to minimise the loads on the drive train while not increasing the structural loads. The power controller performance of a particular wind turbine configuration can be investigated by simple models of the power-train dynamics,

described in Chapter 3. In Chapters 5 and 6 the simple linear models derived in Chapter 3 are used in a parametric study to investigate the effects of changing the characteristics of conventional machines. The resulting trends are validated using non-linear models described in Chapter 3 in an ACSL simulation. In order to compare the power controller performance of any two configurations the ideal dynamic behaviour of the machine is required. In addition, some indicator of the power controller performance is necessary so that any two configurations can be compared.

C.1 Characteristics of a well designed controller

In above rated wind speeds a wind turbine would ideally produce power at the rated value of the machine. In practise, however, this is not possible since the wind is stochastic with low and high frequency components. The introduction of a power controller can reduce the low-frequency disturbances but can do little to reduce those at medium or high frequencies as this would demand excess actuator capability. Since a wind turbine should produce as small as possible power (torque) fluctuations about a mean of rated power, the influence of the wind and measurement disturbances on the power output of the machine are required to be minimised. On a constant-speed wind turbine, the power output is directly proportional to the torques seen throughout the drive train since the speed of the low-speed shaft varies only very slightly.

To make fair comparisons between machine performance, each controller is required to have similar stability margins and operate within the same actuator restrictions. In addition, to avoid bias towards a particular configuration, consistent actuator capabilities are required. All the controllers are designed to have a gain margin of approximately 10 dB and a phase margin of approximately 60° and their performance is compared for equivalent actuator capability. The measure of actuator activity is the force or torque within the actuator since, for all actuators these have a maximum and minimum limit. However, to eliminate bias due to differences in the nature of the actuator and in the geometry of the linkages and gearing arrangements between the actuator and the rotor blades, pitch acceleration, being directly related to the force or torque within the actuator, is used instead as a measure of actuator activity. Its standard deviation reflects the activity over the medium and long term. Another measure of actuator activity is the standard deviation of its velocity since most actuators have maximum and minimum rates of deployment. Again, to eliminate bias pitch velocity is used. In defining these measures, the dynamics of the linkages and pitch gearing arrangements are ignored.

To investigate the effects of the disturbances on the power output and the internal actuator signals, the dynamics of the wind turbine together with the control system need to be considered. The control system structure, shown in Figure C.2, is based on that developed by Leithead *et al.* (1991a) to assess the effects of the controller on a wind turbine's dynamic performance. The controller is designed for a nominal wind speed of 16 m/s. To accommodate the effect of changes of wind speed on the wind turbine dynamics an aerodynamic gain K_a is included. The aerodynamic gain is the ratio of the partial derivative of aerodynamic torque with respect to pitch angle for 16 m/s wind speed to the partial derivative for the current wind speed. Since the wind speed cannot be measured, K_a is parameterised by the current pitch angle. This implementation of the non-linear aerodynamic gain is thoroughly justified by Leith and Leithead (1997). The simulations in Chapter 5 and Chapter 6 are constructed by combining a model of the control system equivalent to Figure C.2 with the wind turbine models described in Chapter 3.

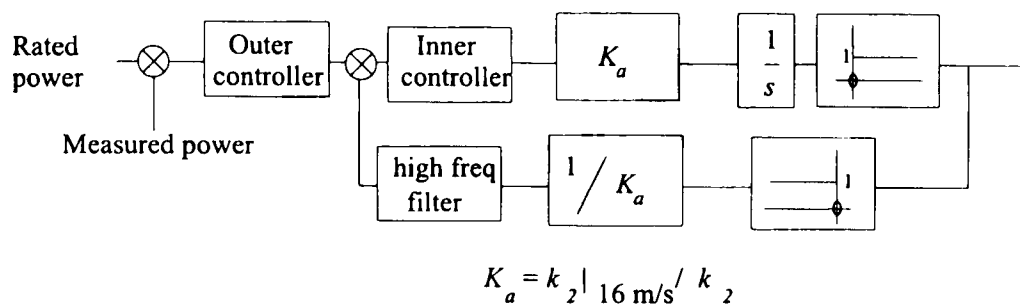
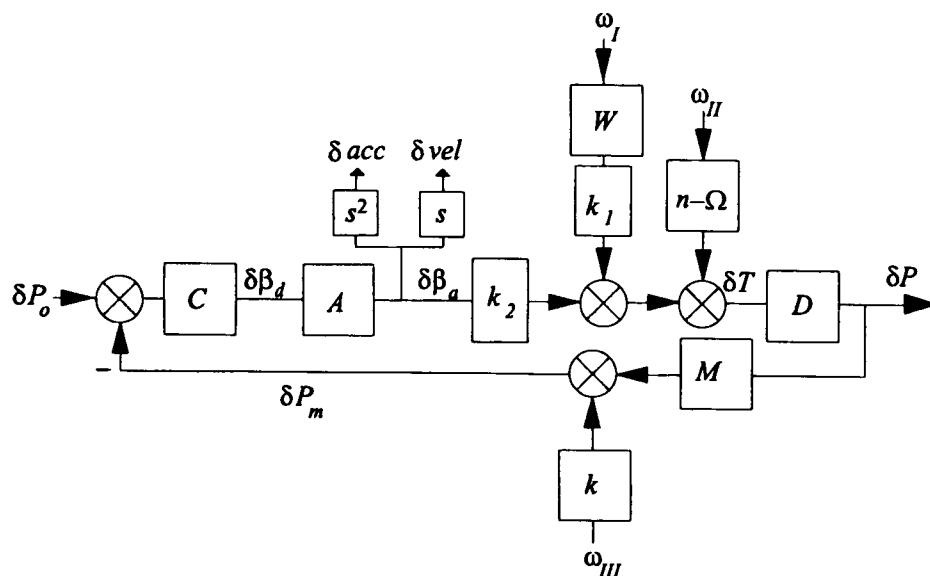


Figure C.2 Block diagram of a wind turbine controller.

For a particular actuator capability the power controller performance is dictated by the physical parameters of the machine; *e.g.* the number of blades and whether it is tip or full-span regulated, as described in Sections 5.3 and 6.3. The inertias and stiffness of the drive-train components influence the dynamics of the drive-train as described in Section 3.1. Many aspects of wind turbine dynamics are non-linear, particularly the aerodynamics. As described in Section 2.4.1, the effect of wind speed on aerodynamic torque can be divided into two time-scales corresponding to slow mean wind-speed changes and rapid turbulent wind-speed variations. Changes in mean wind speed cause the mean pitch angle of the blades to alter to maintain the mean power output at its rated value. Every wind speed above rated has a related blade-pitch angle which, if the wind speed were constant, would produce rated aerodynamic torque and rated power. These blade positions can be treated as quasi-static operating points when viewed from the fast turbulence time scale. In a control context

the mean wind speed changes may be interpreted as a slow disturbance, which the control system having integral action¹ rejects, and need not be further considered.

Using the linearised models from Chapter 3, the linear control model for the wind turbine is as shown in Figure C.3.

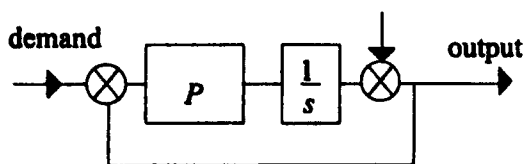


- where
- ω_I, ω_{II} and ω_{III} are zero-mean white noise with intensity one,
 - β_d is the demanded pitch angle, β_a is the actual pitch angle
 - T is the aerodynamic torque
 - P is the electrical power, P_m is the measured electrical power
 - C is the controller, M is the power transducer
 - A is the actuator
 - D is the power-train
 - W is the wind filter
 - k is the measurement noise filter
 - k_2 is the partial derivative of aerodynamic torque with respect to pitch angle
 - k_1 is the partial derivative of aerodynamic torque with respect to wind speed
 - acc, vel are the actuator acceleration and velocity

Figure C.3 Block diagram of linearised wind turbine model.

Figure C.3 can be reorganised as in Figure C.4.

¹ Integral action - the inclusion of integral action in a feedback loop drives the steady state error in reference to a step input to zero. In addition, any constant disturbance input is driven to zero.



transfer function from demand to output $\frac{P / s}{1 + P / s} \rightarrow 1$ as $s \rightarrow 0$

transfer function from disturbance to output $\frac{W}{1 + P / s} \rightarrow 0$ as $s \rightarrow 0$

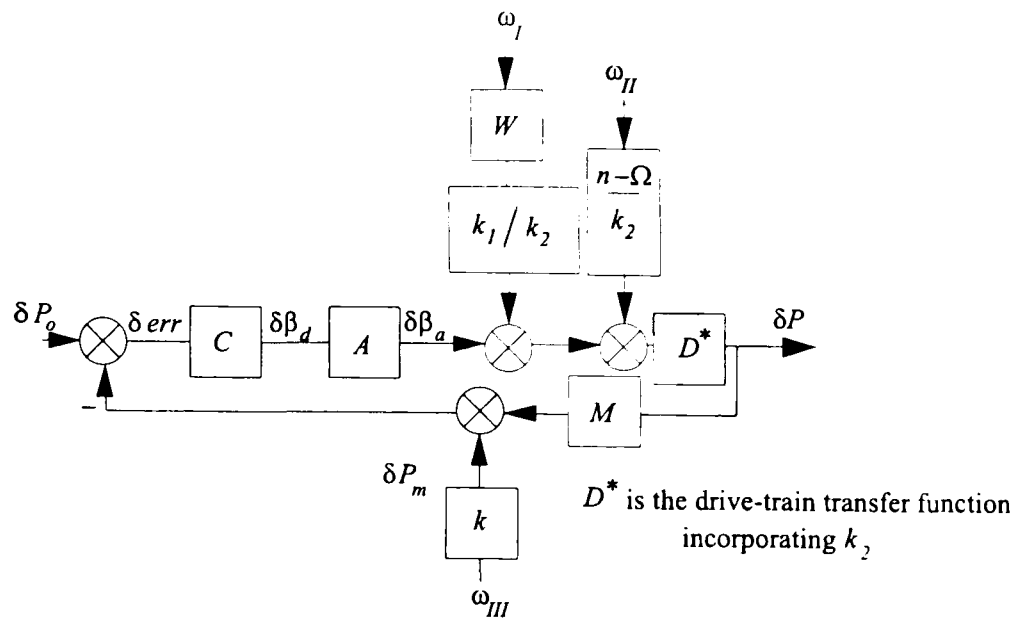


Figure C.4

Assume that the controller can be designed so that there is an ideal open-loop transfer function, O , between δerr and δP_m , i.e.

$$O = CAD^*M \quad (C.1)$$

(for further details see Leithead *et al.* (1992)). The effects of each of the disturbances on the power output can then be described by the following transfer functions:

$$\text{the transfer function from } \omega_I \text{ to electrical power, } T_{\omega_I P} = W k_1 / k_2 \cdot T_{TP}; \quad (C.2)$$

$$\text{the transfer function from } \omega_{II} \text{ to electrical power } T_{\omega_{II} P} = n\Omega / k_2 \cdot T_{TP}; \quad (C.3)$$

$$\text{the transfer function from } \omega_{III} \text{ to electrical power } T_{\omega_{III} P} = kO / (MD^*) \cdot T_{TP}; \quad (C.4)$$

where T_{TP} is the transfer function from aerodynamic torque to electrical power, specifically

$$T_{TP} = D^* / (1 + O). \quad (C.5)$$

From (C.5) it can be seen that to reject the wind disturbances requires the following features:

- i) the frequency of the sensitivity function $(1 + O)^{-1}$ when it crosses 0 dB should be as high as possible to reject low-frequency disturbances due to wind turbulence;
- ii) the power-train, D^* , should have high damping and high compliance (*i.e.* low first drive-train mode frequency and high damping factor);
- iii) the machine should respond to changes in mean wind speed and ramps in wind speed, *i.e.* the controller should contain integral action and an additional low-frequency pole;
- iv) it should not saturate the actuator, except for very short periods (Leith and Leithead, 1996);
- v) it should protect the actuator from measurement noise and the high-frequency components due to rotational sampling;

- vi) to make the system robust to uncertainty in aerodynamics, the open-loop transfer function of the system (plant with the controller) must have sufficiently high phase and gain margins and have adequate roll-off; and
- vii) the controller must cope with non-linearities, *i.e.* it must operate over range of wind speeds and cope with the transition between below and above rated wind speed and actuator saturation.

The transfer functions relating the variable under consideration to the appropriate input noise are required to evaluate the power controller performance attained by a machine. First consider the performance of the system driven by low-frequency wind speed turbulence, *i.e.* the transfer function relating the input, ω_t , to electrical power, (C.2). This low frequency disturbance must be minimised to achieve low drive-train loads. Hence the controller is designed to shape the open-loop transfer function as depicted in Figure C.5. The cross-over frequency is kept as high as possible. In addition to the integral action, a low-frequency pole is included to reduce offsets in power, due to ramps in wind speed, by increasing the velocity error constant. This low-frequency shaping has the further advantage of matching the shape of the wind disturbance intensity which is represented in W by a roll-off initially of $1/s$ but increasing to $1/s^2$.

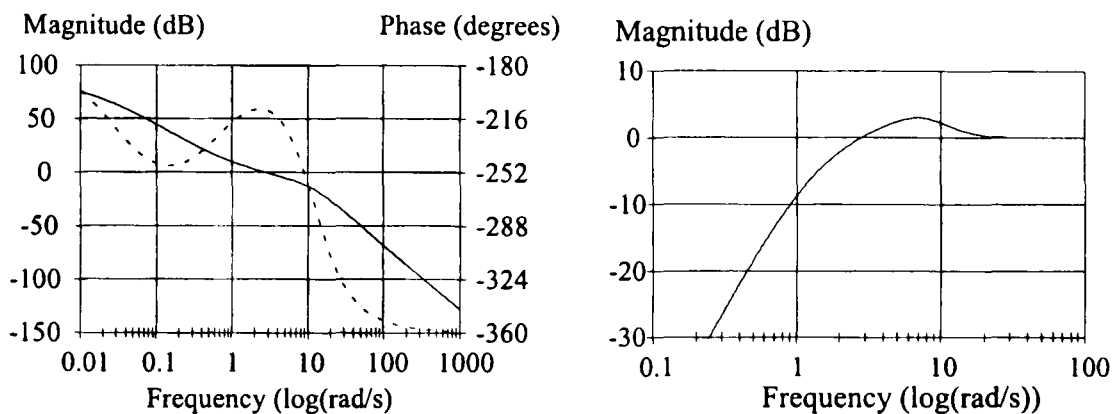


Figure C.5 Bode plot of the ideal open-loop and sensitivity transfer functions.

From (C.5), another factor affecting the results of wind turbulence on the drive-train loads is the dynamic behaviour of the drive train. The relationship between aerodynamic torque and electrical power can be approximated by the fourth-order transfer function (see (3.10), Section 3.1.5)

$$D(s) = \frac{b_o}{s^4 + a_3s^3 + a_2s^2 + a_1s + a_o} = \frac{NEffy\Omega_o\omega_1^2\omega_2^2}{(s^2 + 2\zeta_1\omega_1 + \omega_1^2)(s^2 + 2\zeta_2\omega_2 + \omega_2^2)} \quad (C.6)$$

As shown in Section 3.2, the dynamics of the drive train at low frequency are characterised by the dynamics of the first mode. The size of the power fluctuations caused by the low-frequency wind turbulence is related to the damping factor of the first drive-train mode,

whilst the size of the torque fluctuations caused by the spectral peaks is related to the frequency of the first drive-train mode. (In the parametric study in Chapters 5 and 6 the damping factor of the first drive-train mode is assumed to be ideal, and the effect of varying the frequency of the first drive-train mode only is investigated.)

There is maximum achievable cross-over frequency of the open-loop transfer function which is due to the internal operation of the actuator. The effects of each of the disturbances on the actuator acceleration are described by the following transfer functions:

$$\text{the transfer function from } \omega_I \text{ to actuator acceleration, } T_{w_I \ddot{\beta}_a} = Wk_1 / k_2 \cdot s^2 T_{closed}; \quad (\text{C.7})$$

$$\text{the transfer function from } \omega_{II} \text{ to actuator acceleration, } T_{w_{II} \ddot{\beta}_a} = n\Omega / k_2 \cdot s^2 T_{closed}; \quad (\text{C.8})$$

$$\text{the transfer function from } \omega_{III} \text{ to actuator acceleration, } T_{w_{III} \ddot{\beta}_a} = k(D^*)^{-1} s^2 T_{closed}; \quad (\text{C.9})$$

$$\text{where } T_{closed} \text{ is the closed-loop transfer function, i.e. } T_{closed} = O / (M(1 + O)). \quad (\text{C.10})$$

Similarly, the effects of each of the disturbances on the actuator velocity are described by the following transfer functions:

$$\text{the transfer function from } \omega_I \text{ to actuator velocity, } T_{w_I \dot{\beta}_a} = Wk_1 / k_2 \cdot s T_{closed}; \quad (\text{C.11})$$

$$\text{the transfer function from } \omega_{II} \text{ to actuator velocity, } T_{w_{II} \dot{\beta}_a} = n\Omega / k_2 \cdot s T_{closed}; \quad (\text{C.12})$$

$$\text{the transfer function from } \omega_{III} \text{ to actuator velocity, } T_{w_{III} \dot{\beta}_a} = k(D^*)^{-1} s T_{closed}. \quad (\text{C.13})$$

A Bode plot of the typical transfer function from pitch angle to actuator acceleration and velocity is shown in Figure C.6. In Figure C.6, the frequencies in the range 10 rad/s to 100 rad/s are greatly enhanced due to the s^2 in the relationship between the actual pitch and the pitch acceleration. Therefore the actuator is very sensitive to frequencies in the middle frequency range, particularly the spectral peaks, and to measurement noise (when the controller cross-over frequency is high), and the controller transfer function is required to roll-off like $1/s^3$ (Leithead *et al.*, 1991a) to protect the actuator from saturation from internal noise (Bossanyi *et al.*, 1992). Typically the frequency of roll-off starts at approximately 10 times the open-loop bandwidth (Leithead and Agius, 1992). The actuator activity also increases as the controller cross-over frequency increases and it is very sensitive to wind speed since the relationship actuator acceleration/velocity to wind turbulence is proportional to k_1/k_2 . For most configurations the partial derivative of aerodynamic torque with respect to pitch angle increases rapidly with wind speed while the partial derivative to wind speed

does not, see Figures 5.4 and 6.4. Hence, the actuator is not required to work as hard at high wind speeds. Leith and Leithead (1996) have exploited this unused actuator capability in high speeds to develop some non-linear controllers which greatly improve power controller performance. The ratio k_1 / k_2 varies with the machine aerodynamics and so the actuator activity varies with the number of blades and the type of power regulation for a particular controller cross-over frequency.

In addition to disturbance rejection properties, the system must be robust to uncertainty in the modelling of the wind turbine. For the closed-loop system to cope with the considerable uncertainty, particularly from the modelling of the aerodynamics, Leithead *et al.* (1991a) found that the open-loop transfer function gain and phase margins should be approximately 10 dB² and 60°³ respectively. Since the phase and gain of any transfer function are strongly related, there is a trade-off between the amount of disturbance rejection at low frequency and the amount of the high frequency roll-off. From Figure C.5, it can be seen that the rejection of low frequency disturbance is accompanied by an enhancement at the middle frequencies. The enhancement although unavoidable should be shaped and positioned to be least damaging - Leithead *et al.* (1991a) suggest between $1\Omega_o$ and $n\Omega_o$. In addition, a notch at $n\Omega_o$ may be required (Bossanyi *et al.*, 1992) to reduce the impact of the spectral peak on the actuator and reduce its chances of saturating. The introduction of a notch does, however, reduce the phase margin and so there are limits to its possible depth and width of the notch. The notch used in the parametric study is based on that used in Leithead and Agius (1991). The Bode plot of an 'ideal' open-loop transfer function, O , satisfying all the conditions required of the wind turbine system described above, is shown in Figure C.5, together with the corresponding sensitivity transfer function.

² The gain margin is an indication of the extra gain which can be introduced into a system before it becomes unstable. It is the amount the magnitude of the transfer function is less than 1 when the phase of the transfer function reaches -180°. It is usually measured in decibels, *i.e.* $20 \log_{10}(\text{magnitude})$.

³ The phase margin is a measure of the amount of extra phase shift which a system can tolerate and still remain stable. It is the amount of phase at which the magnitude of the transfer function crosses 1, (or 0 dB) is short of the -180° needed for instability. A figure of 45° is often quoted as a suitable margin for many systems. Leithead *et al.* (1991a) found that 60° was more suitable for wind turbines. With a phase margin of 60° the open-loop transfer function bandwidth frequency is equal to the frequency the sensitivity transfer function crosses 0 dB.

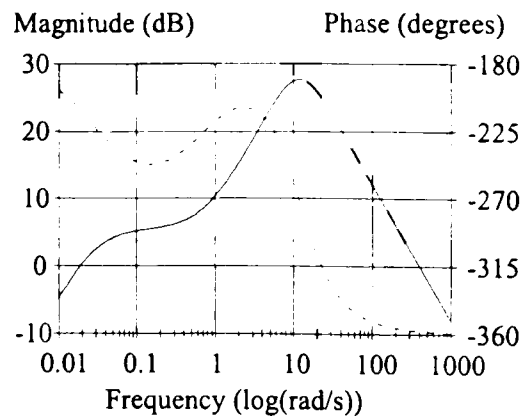


Figure C.6 Bode plot of a typical transfer function from pitch angle to pitch acceleration.

C.2 The parametric study

The parametric study, whose results are discussed in Chapters 5 and 6, investigates the influence of machine configuration on the achievable power regulation. Various machine configurations are considered. Turbines can have two or three blades, and be full-span or tip-regulated, and medium or large in size. They can have a first drive-train frequency from 2 to 7 rad/s, and the open-loop transfer function can have a cross-over frequency of 0.5 to 6 rad/s. The transfer functions used in this context are described here, together with any assumptions made.

The large number of configurations to be investigated necessitates the use of analytic methods rather than simulation methods. Consequently power controller performance is evaluated by linear analysis. The linear model of the wind turbine is chosen in such a manner that the estimates of performance are in reasonable agreement with those determined by simulation. The wind turbine system is depicted in Figure C.1 and the linear model in Figure C.3. The construction of the linear model is strongly influenced by experience gained on previous investigations of wind turbine control (Leithead and Agius, 1992, Wilkie and Leithead, 1988, Leithead *et al.*, 1991a).

The transfer function relationships from each disturbance to generated power and from each disturbance to pitch angle acceleration (velocity) are (C.2) to (C.5), and ;

(C.7)

((C.11)) to (C.10) ((C.13)), respectively.

Three separate transfer functions are required, namely $M(s)$, $D(s)$ and $O(s)$, the transfer functions for the power transducer, the drive-train and the open-loop transfer function respectively. The transfer function, $M(s)$, describing the dynamics of the power transducer can be represented by a simple lag (Leithead *et al.*, 1991a) such that

$$M(s) = 50/(s + 50) \quad (C.14)$$

The transfer function, $D(s)$, describing the dynamic relationship of generator power to aerodynamic torque has the general form

$$D(s) = \frac{100\Omega_n / Effy}{\left(\left(\frac{s}{\omega_n}\right)^2 + 2\zeta\left(\frac{s}{\omega_n}\right) + 1\right)\left(\left(\frac{s}{\omega_n}\right)^2 + 2.2\left(\frac{s}{\omega_n}\right) + 100\right)} \quad (C.15)$$

where $Effy$ is the combined efficiency of the gearbox and generator. In practice, the efficiency of the gearbox and generator increases as a machine increases in size. Therefore typical commercial values were used; the 300 kW machines were assumed to have an efficiency of 91% and the 1 MW machines 95%. The frequency of the first drive-train mode, ω_n , is varied to represent the range of drive-train dynamics from 2 rad/s to 7 rad/s and the damping factor of the first drive-train mode is assumed to be ideal, *i.e.* $\zeta = 0.7$. The ratio of the frequencies of the two modes, is assumed to be 10 which is typical for commercial machines (*e.g.* see Bossanyi *et al.*, 1992). The same basic drive-train shape was also observed when investigating the drive-train dynamics of the Howden HWP330/33 (Wilkie and Leithead, 1988) and HWP1000/45 (Leithead *et al.*, 1991a) machines. Normally the damping factor of the second drive-train mode is fairly small. It was chosen to be 0.11. This damping factor is not so critical as it occurs at high frequency, by which point the drive-train transfer function is well rolled-off.

In order to ensure that the transfer functions (C.2), (C.3), (C.4) are proper in the parametric study the transfer function, $D(s)$, describing in (C.15) is at times unsuitable. It is necessary to approximate the drive-train transfer function further to have the form

$$D'(s) = \frac{\Omega_n / Effy}{\left(\left(\frac{s}{\omega_n}\right)^2 + 2\zeta\left(\frac{s}{\omega_n}\right) + 1\right)} \quad (C.16)$$

This transfer function does not model the high frequency dynamics properly. The additional phase loss in the middle frequency range due to the simplifications causes the peak of the sensitivity function, see Figure C.5, to be higher and narrower.

The transfer function, $O(s)$, for an open-loop system with cross-over frequency 2 rad/s is depicted in Figure C.7. It represents an attempt to include all the important features of the 'ideal' open-loop transfer function described in Section C.1.1 and represents the dynamics of a typical pitch regulated commercial wind turbine. (Note that the low frequency shaping is omitted for simplicity but its inclusion would not markedly change the results.) It may be interpreted to consist of two components, $O_o(s)$ and $N(s)$, where

$$O(s) = O_o(s)N(s)$$

$$O_o(s) = \frac{4.37 \times 10^{12} (s^2 + 3s + 1.33)}{s(s^2 + 73.3s + 1344)(s^2 + 86.7s + 1111)(s^2 + 46.7s + 88.9)(s^2 + 53.3s + 1333)(s^2 + 3.8s + 1.556)} \quad (\text{C.17})$$

The transfer function, $N(s)$, is the notch filter incorporated into the controller to protect the actuator from the transient loads at $n\Omega_o$. As the notch is dependent on the rotor speed of the wind turbine it is considered separately from the remaining part of the open-loop transfer function. Unfortunately the notch cannot be made sufficiently deep to completely remove the transient loads since the associated phase and gain loss in the open loop would be too great. The depth and width of the notch for each machine configuration are based on those achieved on the WEG MS3 (Leithead and Agius, 1992) and scaled with rotor speed as follows

$$N(s) = \frac{(s / (n\Omega_o))^2 + 0.098\varepsilon(s / (n\Omega_o)) + 1}{(s / (n\Omega_o))^2 + 0.274\varepsilon(s / (n\Omega_o)) + 1} \quad (\text{C.18})$$

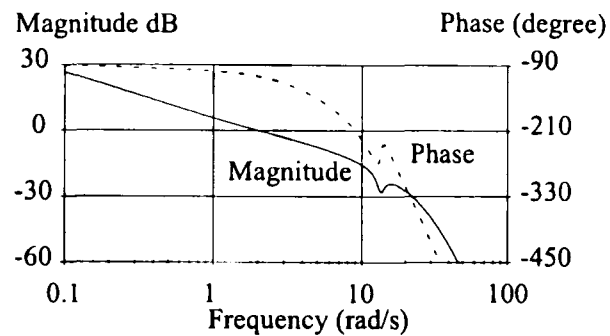


Figure C.7 Bode plot of the open-loop transfer function, $O(s)$, with $\omega_c = 2$ rad/s.

The open-loop transfer function, $O(s)$, appropriate to a specific controller cross-over frequency is derived in two steps. First, the transfer function, $O_o(s)$, is scaled by the substitution $s \rightarrow 2s/\omega_c$. Second, the value of ε in $N(s)$ is adjusted to obtain an open-loop transfer function gain margin of 10 dB and a phase margin of approximately 45° ; that is, the phase margin for $O(s) = O_o(2s/\omega_c)N(s)$ is 45° . This phase margin was chosen to compensate for the underestimation of phase loss in the middle frequency range due to simplifying the drive-train transfer function. The peak in the corresponding sensitivity function is sharper and narrower than would be obtained with a phase margin of 60° . In the non-linear simulation the fourth order drive-train transfer function is used and so, in this case, a phase margin of 60° is chosen. The maximum possible filtering for any specific controller cross-over frequency is then ensured.

The effects of wind turbulence on the aerodynamic torque can be modelled as ω_l coloured by the transfer function, $W(s)$, where $W(s)$ is

$$W(s) = \frac{b_T}{s + a_T} \frac{(1 + T_1 s)}{(1 + T_2 s)(1 + T_3 s)} \quad (\text{C.19})$$

where $T_1 = K/\sqrt{2}$, $T_2 = T_1 \sqrt{c_s}$, $T_3 = K/\sqrt{c_s}$ $K = \gamma_s R/V$, $R = \text{radius}$,

$V = \text{mean wind speed}$, $\gamma_s = 1.3$, $c_s = 0.55$.

The values of a_T and b_T vary with wind speed, the values used correspond to 20% turbulence and are shown in Table A.1.

To model the transient loads at $n\Omega_o$, Gaussian⁴ white noise, ω_{II} , is filtered by the transfer functions (3.6) and (3.7), see Section 3.1.3. The intensity of the load transients at $n\Omega_o$ are chosen for the two- and three-bladed configurations such that the standard deviation of the corresponding spectral peaks on the generated power are, respectively, 24 kW and 6 kW for 300 kW machines, and 34 kW and 5 kW for 1 MW machines, when the frequencies of the first drive-train mode are approximately $\frac{1}{2} n\Omega_o$. The nominal intensities for the two-bladed and three-bladed wind turbines are similar to those which have been observed on commercial wind turbines (Bossanyi *et al.*, 1992, Wilkie and Leithead, 1988, Leithead *et al.*, 1991a) and whose parameters are listed in Table C.1.

Configuration	Aa, Ga	Ab, Gb	B, H	Ca, Ia	Cb, Ib	Da, Ja	Db, Jb	E, K	Fa, La	Fb, Lb
a_{nr}	0.4	0.4	1.99	1.58	1.58	0.04	0.04	0.19	0.15	0.15
b_{nr}	7495	10600	4691	2954	4178	7901	11173	3417	3036	4294

Table C.1 Spectral load model parameters for each configuration.

To model the measurement noise, Gaussian white noise, ω_{III} , is simply scaled by the constant k where

$$k = 0.2 \times \text{Gearbox ratio} \times \Omega_o \quad (\text{C.20})$$

The values of the gearbox ratio and the rotor speed, used to scale the measurement noise, are tabulated in Table C.2. These values assume that the generators for all the 300 kW machines have 1.5 % slip and those for all the 1 MW machines have 1 % slip. This intensity of measurement noise corresponds to power being measured to an accuracy of 200 W at a sampling time of 80 ms.

⁴ A random variable, x , with a Gaussian distribution has the probability density function

$$p(\xi) = \frac{1}{\sigma_x \sqrt{2\pi}} \exp\left[-\frac{(\xi - \varepsilon(x))^2}{2\sigma_x^2}\right] \text{ where } \varepsilon(x) \text{ is the mean and } \sigma(x) \text{ is the standard deviation.}$$

Configuration	Aa/Ab, Ga/Gb	B, H	Ca/Cb, Ia/Ib	Da/Db, Ja/Jb	E, K	Fa/Fb, La/Lb
Rotor speed (rad/s)	5.090	5.201	4.125	2.800	2.850	2.250
Gearbox ratio	30.86	30.65	38.65	37.77	37.11	47.01

Table C.2 Rotor speed and gearbox ratio for each configuration.

The partial derivatives of aerodynamic torque with respect to wind speed, k_1 , and with respect to pitch angle, k_2 , are determined from the aerodynamic torque coefficients for each rotor and are shown in Figures 5.2, 5.3, 6.2 and 6.3 for each rotor.

Power controller performance is evaluated by determining the standard deviation of the power output, the actuator acceleration and the velocity due to the three disturbances. Since these variables are modelled by a transfer function, $H(s)$, driven by Gaussian white noise, the standard deviation can be calculated as

$$sd = \left(\frac{1}{2\pi} \int_{-\infty}^{\infty} |H(j\omega)|^2 d\omega \right)^{1/2} \quad (C.21)$$

with the integral evaluated by the Calculus of Residues. Hence the transfer functions (C.1) to (C.13) can be directly used to estimate the power controller performance of a wind turbine.

C.2.1 Validation of linear analysis

The estimation of power controller performance using the linear models described in Section 5.4 is validated by comparison with the results from a simulation of the wind turbine for various configurations. The results from both the linear analysis and the simulation analysis are tabulated in Table C.3. The standard deviations of power, actuator acceleration and actuator velocity are given in each case. The results from the linear analysis are shown in brackets. There is reasonable agreement between the two sets of results although the estimates of actuator accelerations obtained by simulation are sometimes rather higher. The reason for the discrepancy is the occurrence of spikes in the actuator acceleration associated with transitions between below-rated and above-rated operation (Figure C.8). (These spikes may not be significant in practice.) Hence the simulated standard deviation of actuator acceleration is greater than the estimate by linear analysis, particularly in wind speeds with a mean close to 12 m/s. For example, the standard deviation of actuator acceleration for configuration Ca is estimated by simulation to be 9.9 °/s². However, when the statistics are collected for accelerations less than 50 °/s² to exclude the spikes, the estimate is reduced to 7 °/s².

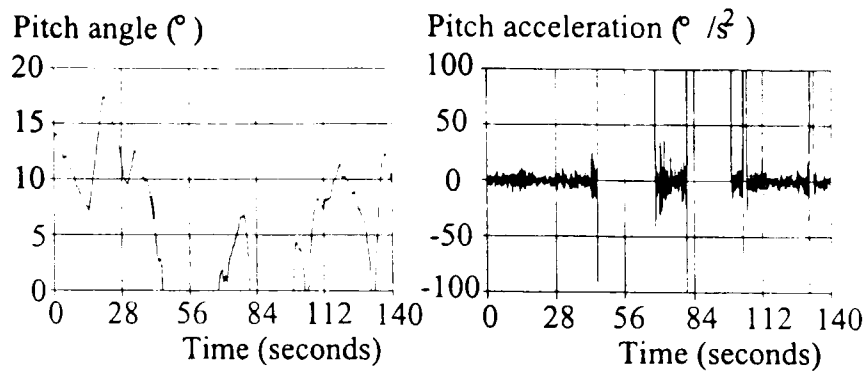


Figure C.8 Simulated pitch acceleration and power output for configuration Ca, first drive-train mode 6 rad/s and controller cross-over frequency 2.38 rad/s.

Configuration Aa		Controller cross-over frequency (rad/s)				
Wind speed (m/s)	First drive-train mode (rad/s)	Standard deviation	1.20	2.32	3.40	4.40
13.4 (12)	5	power (kW)	30.6 (26.8)	19.0 (17.7)	16.3 (15.6)	15.4 (14.7)
		acceleration ($^{\circ}/s^2$)	5.37 (5.00)	26.0 (26.8)	58.0 (58.6)	85.2 (96.4)
		velocity ($^{\circ}/s$)	1.10 (1.29)	2.28 (2.72)	4.34 (4.99)	5.72 (7.26)
	6	power (kW)	-	-	20.6 (19.8)	-
		acceleration ($^{\circ}/s^2$)	-	-	45.4 (58.5)	-
		velocity ($^{\circ}/s$)	-	-	3.48 (4.99)	-
16.4(16)	5	power (kW)	-	38.3 (26.7)	-	20.4 (18.7)
		acceleration ($^{\circ}/s^2$)	-	14.6 (10.8)	-	49.5 (38.7)
		velocity ($^{\circ}/s$)	-	1.95 (1.40)	-	3.62 (3.05)
20 (23)	6	power (kW)	-	-	43.0 (48.8)	-
		acceleration ($^{\circ}/s^2$)	-	-	16.8 (14.2)	-
		velocity ($^{\circ}/s$)	-	-	1.89 (1.93)	-

Table C.3a) Configuration Aa - Two blades, $\frac{1}{2}$ nominal $2\Omega_{\infty}$, 300 kW, full-span regulated.

Configuration Ca		Controller cross-over frequency (rad/s)				
Wind speed (m/s)	First drive-train mode (rad/s)	Standard deviation	1.21	2.36	3.47	4.52
12	5	power (kW) acceleration ($^{\circ}/s^2$) velocity ($^{\circ}/s$)	27.5 (24.4) 5.68 (1.70) 1.41 (1.44)	-	10.3 (8.94) 20.2 (18.3) 1.90 (1.98)	-
	6	power (kW) acceleration ($^{\circ}/s^2$) velocity ($^{\circ}/s$)	27.5 (19.6) 5.30 (1.70) 1.40 (1.44)	15.9 (13.2) 9.87 (7.40) 1.55 (1.63)	10.5 (9.13) 20.7 (17.9) 1.91 (1.98)	8.09 (7.08) 36.6 (33.0) 2.36 (2.48)
	7	power (kW) acceleration ($^{\circ}/s^2$) velocity ($^{\circ}/s$)	37.5 (24.5) 2.90 (1.70) 1.48 (1.44)	15.3 (13.3) 10.4 (7.40) 1.58 (1.63)	10.7 (9.35) 20.4 (17.8) 1.90 (1.97)	-
16	6	power (kW) acceleration ($^{\circ}/s^2$) velocity ($^{\circ}/s$)	52.5 (49.4) 5.05 (1.20) 1.44 (1.08)	29.3 (27.0) 6.70 (3.20) 1.58 (1.20)	20.1 (18.5) 11.5 (7.00) 1.70 (1.31)	15.4 (14.1) 18.6 (12.5) 1.88 (1.44)
23 (20)	5	power (kW) acceleration ($^{\circ}/s^2$) velocity ($^{\circ}/s$)	87.2 (120.3) 2.63 (1.90) 1.49 (1.51)	49.4 (67.4) 4.73 (3.50) 1.66 (1.72)	34.1 (46.4) 7.79 (5.50) 1.77 (1.81)	-
	6	power (kW) acceleration ($^{\circ}/s^2$) velocity ($^{\circ}/s$)	87.4 (120.6) 2.53 (1.90) 1.49 (1.51)	49.8 (67.9) 4.57 (3.50) 1.66 (1.72)	36.2 (47.0) 7.44 (5.50) 1.74 (1.81)	26.3 (35.8) 12.8 (8.40) 1.88 (1.88)
	7	power (kW) acceleration ($^{\circ}/s^2$) velocity ($^{\circ}/s$)	106 (121) 2.60 (1.90) 1.46 (1.51)	50.0 (68.2) 4.55 (3.50) 1.66 (1.72)	34.7 (47.3) 7.87 (5.50) 1.78 (1.81)	-

Table C.3b) Configuration Ca - Three blades, nominal $3\Omega_{\infty}$, 300 kW, full-span regulated.

Configuration Db		Controller cross-over frequency (rad/s)		
Wind speed (m/s)	First drive-train mode (rad/s)	Standard deviation	1	2
13.4 (12)	2	power (kW) acceleration ($^{\circ}/s^2$) velocity ($^{\circ}/s$)	43.5 (50.1) 2.59 (3.10) 0.77 (0.82)	46.7 (29.4) 7.66 (10.3) 1.34 (1.71)
	4	power (kW) acceleration ($^{\circ}/s^2$) velocity ($^{\circ}/s$)	66.7 (71.3) 2.57 (3.10) 0.77 (0.82)	67.0 (63.7) 7.48 (10.0) 1.34 (1.71)
	5	power (kW) acceleration ($^{\circ}/s^2$) velocity ($^{\circ}/s$)	78.8 (86.4) 2.57 (3.10) 0.77 (0.82)	81.4 (84.0) 7.50 (10.0) 1.34 (1.71)
	6	power (kW) acceleration ($^{\circ}/s^2$) velocity ($^{\circ}/s$)	89.8 (99.1) 2.57 (3.10) 0.77 (0.82)	93.2 (100) 7.45 (10.0) 1.33 (1.71)
	8	power (kW) acceleration ($^{\circ}/s^2$) velocity ($^{\circ}/s$)	101 (114) 2.57 (3.10) 0.77 (0.82)	105.9 (118) 7.43 (10.0) 1.33 (1.71)
16.4 (16)	2	power (kW) acceleration ($^{\circ}/s^2$) velocity ($^{\circ}/s$)	94.2 (96.4) 1.95 (1.39) 0.83 (0.59)	47.5 (51.6) 5.25 (4.45) 1.12 (0.89)
	4	power (kW) acceleration ($^{\circ}/s^2$) velocity ($^{\circ}/s$)	107 (110) 1.93 (1.39) 0.83 (0.59)	72.0 (77.6) 5.12 (4.34) 1.11 (0.89)
	5	power (kW) acceleration ($^{\circ}/s^2$) velocity ($^{\circ}/s$)	115 (121) 1.94 (1.39) 0.83 (0.59)	87.2 (95.1) 5.15 (4.34) 1.11 (0.89)
	6	power (kW) acceleration ($^{\circ}/s^2$) velocity ($^{\circ}/s$)	125 (130) 1.92 (1.39) 0.83 (0.59)	100 (110) 5.08 (4.34) 1.11 (0.89)
	8	power (kW) acceleration ($^{\circ}/s^2$) velocity ($^{\circ}/s$)	134 (142) 1.92 (1.39) 0.83 (0.59)	113 (126) 5.06 (4.34) 1.11 (0.89)
20 (23)	2	power (kW) acceleration ($^{\circ}/s^2$) velocity ($^{\circ}/s$)	168 (234) 1.41 (1.08) 0.89 (0.80)	81.9 (123) 3.76 (2.84) 1.04 (0.94)
	4	power (kW) acceleration ($^{\circ}/s^2$) velocity ($^{\circ}/s$)	179.3 (247) 1.39 (1.08) 0.89 (0.80)	101 (142) 3.66 (2.78) 1.04 (0.94)
	5	power (kW) acceleration ($^{\circ}/s^2$) velocity ($^{\circ}/s$)	181 (252) 1.39 (1.08) 0.89 (0.80)	111 (153) 3.67 (2.78) 1.03 (0.94)
	6	power (kW) acceleration ($^{\circ}/s^2$) velocity ($^{\circ}/s$)	190 (257) 1.39 (1.08) 0.89 (0.80)	122 (163) 3.61 (2.78) 1.04 (0.94)
	8	power (kW) acceleration ($^{\circ}/s^2$) velocity ($^{\circ}/s$)	-	133 (175) 3.59 (2.78) 1.03 (0.94)

Table C.3c) Configuration Db - Two blades, nominal $2\Omega_{\infty}$ 1 MW, full-span regulated.

Configuration Fa		Controller cross-over frequency (rad/s)			
Wind speed (m/s)	First drive-train mode (rad/s)	Standard deviation	1	2	3
13.4 (12)	5	power (kW)	59.9 (64.7)	31.4 (29.7)	21.7 (19.8)
		acceleration ($^{\circ}/s^2$)	0.90 (0.63)	2.21 (1.85)	3.89 (3.69)
		velocity ($^{\circ}/s$)	0.80 (0.74)	0.86 (0.82)	0.93 (0.91)
	7	power (kW)	60.3 (62.8)	32.4 (30.9)	25.2 (21.7)
		acceleration ($^{\circ}/s^2$)	0.90 (0.63)	2.21 (1.85)	3.44 (3.66)
		velocity ($^{\circ}/s$)	0.80 (0.74)	0.86 (0.82)	0.91 (0.91)
9	power (kW)	61.0 (63.1)	33.1 (31.7)	26.1 (23.0)	
	acceleration ($^{\circ}/s^2$)	0.89 (0.63)	2.20 (1.85)	3.44 (3.66)	
	velocity ($^{\circ}/s$)	0.80 (0.74)	0.86 (0.82)	0.91 (0.91)	
16.4 (16)	5	power (kW)	113 (125)	59.6 (60.4)	40.6 (38.9)
		acceleration ($^{\circ}/s^2$)	0.76 (0.47)	1.57 (1.00)	2.52 (1.70)
		velocity ($^{\circ}/s$)	0.83 (0.60)	0.89 (0.67)	0.93 (0.70)
	7	power (kW)	114 (125)	60.4 (60.9)	45.8 (40.1)
		acceleration ($^{\circ}/s^2$)	0.76 (0.47)	1.57 (1.00)	2.24 (1.70)
		velocity ($^{\circ}/s$)	0.83 (0.60)	0.89 (0.67)	0.91 (0.70)
9	power (kW)	115 (125.7)	60.9 (61.3)	46.5 (40.9)	
	acceleration ($^{\circ}/s^2$)	0.75 (0.47)	1.56 (1.00)	2.21 (1.70)	
	velocity ($^{\circ}/s$)	0.83 (0.60)	0.89 (0.67)	0.91 (0.70)	
20 (23)	5	power (kW)	195 (315)	103.9 (156)	70.8 (101)
		acceleration ($^{\circ}/s^2$)	0.78 (0.76)	1.42 (1.33)	2.13 (1.85)
		velocity ($^{\circ}/s$)	0.91 (0.83)	0.98 (0.99)	1.01 (1.02)
	7	power (kW)	195 (326)	104.8 (157)	79.0 (102)
		acceleration ($^{\circ}/s^2$)	0.78 (0.76)	1.42 (1.33)	1.89 (1.84)
		velocity ($^{\circ}/s$)	0.91 (0.83)	0.98 (0.99)	1.00 (1.02)
9	power (kW)	196 (315)	105.3 (158)	79.7 (103)	
	acceleration ($^{\circ}/s^2$)	0.77 (0.76)	1.42 (1.33)	1.86 (1.84)	
	velocity ($^{\circ}/s$)	0.91 (0.83)	0.98 (0.99)	1.00 (1.02)	

Table C.3d) Configuration Fa - Three blades, nominal $3\Omega_{\infty}$, 1 MW, full-span regulated.

Configuration Ga		Controller cross-over frequency (rad/s)				
Wind speed (m/s)	First drive-train mode (rad/s)	Standard deviation	1.20	2.32	3.40	4.40
13.4 (12)	5	power (kW) acceleration ($^{\circ}/s^2$) velocity ($^{\circ}/s$)	-	-	15.8 (15.6) 123 (104) 8.39 (8.86)	15.0 (14.7) 181 (171) 10.9 (12.9)
	6	power (kW) acceleration ($^{\circ}/s^2$) velocity ($^{\circ}/s$)	-	21.9 (20.7) 47.5 (47.6) 3.95 (4.82)	19.9 (19.7) 97.4 (104) 6.67 (8.86)	19.1 (19.2) 156 (167) 9.41 (12.89)
16.4 (16)	5	power (kW) acceleration ($^{\circ}/s^2$) velocity ($^{\circ}/s$)	-	-	18.0 (17.8) 62.4 (47.8) 4.94 (4.19)	16.5 (16.0) 104 (78.6) 7.12 (6.01)
	6	power (kW) acceleration ($^{\circ}/s^2$) velocity ($^{\circ}/s$)	-	-	-	20.9 (20.3) 87.8 (76.9) 5.98 (6.00)
20 (23)	5	power (kW) acceleration ($^{\circ}/s^2$) velocity ($^{\circ}/s$)	-	-	17.9 (15.0) 44.3 (36.4) 3.85 (3.07)	-
	6	power (kW) acceleration ($^{\circ}/s^2$) velocity ($^{\circ}/s$)	-	26.5 (19.6) 18.7 (16.7) 2.11 (1.64)	22.3 (19.2) 53.2 (36.4) 4.23 (3.07)	20.8 (18.9) 59.9 (58.5) 4.65 (4.49)

Table C.3e) Configuration Ga - Two blades, $\frac{1}{2}$ nominal $2\Omega_{\infty}$, 300 kW, tip regulated.

Configuration Ia		Controller cross-over frequency (rad/s)				
Wind speed (m/s)	First drive-train mode (rad/s)	Standard deviation	1.20	2.32	3.40	4.40
13.4 (12)	5	power (kW) acceleration ($^{\circ}/s^2$) velocity ($^{\circ}/s$)	-	10.65 (12.75) 27.77 (13.5) 2.83 (2.90)	7.312 (9.03) 55.78 (33.4) 3.49 (3.52)	5.63 (6.66) 88.24 (75.2) 4.57 (4.51)
	6	power (kW) acceleration ($^{\circ}/s^2$) velocity ($^{\circ}/s$)	19.56 (23.85) 18.56 (3.0) 2.46 (2.55)	11.32 (12.93) 28.62 (13.5) 2.77 (2.91)	7.92 (8.92) 53.42 (32.7) 3.44 (3.53)	6.22 (6.94) 87.34 (60.2) 4.45 (4.44)
16.4 (16)	5	power (kW) acceleration ($^{\circ}/s^2$) velocity ($^{\circ}/s$)	22.04 (17.59) 14.86 (1.3) 2.03 (0.89)	11.92 (9.68) 17.46 (6.3) 2.21 (1.08)	8.17 (6.76) 26.3 (15.7) 2.51 (1.41)	6.27 (5.22) 43.76 (35.1) 3.00 (1.88)
	6	power (kW) acceleration ($^{\circ}/s^2$) velocity ($^{\circ}/s$)	22.15 (17.66) 15.12 (1.3) 2.03 (0.89)	12.66 (9.82) 17.63 (6.3) 2.20 (1.08)	-	6.62 (5.54) 42.64 (27.5) 3.01 (1.88)

Table C.3f) Configuration Ia - Three blades, nominal $3\Omega_{\infty}$, 300 kW, tip-regulated.

Configuration Jb		First drive-train mode (rad/s)		
Wind speed (m/s)	Controller crossover freq. (rad/s)	Standard deviation	1	2
13.4 (12)	2	power acceleration velocity	43.1 (50.8) 5.77 (5.35) 1.49 (1.43)	44.9 (29.7) 15.3 (17.7) 2.60 (2.95)
	4	power acceleration velocity	62.5 (71.8) 5.76 (5.35) 1.49 (1.43)	66.2 (63.9) 15.0 (17.2) 2.58 (2.95)
	5	power acceleration velocity	75.9 (86.8) 5.76 (5.35) 1.49 (1.43)	81.4 (84.1) 14.9 (17.2) 2.58 (2.95)
	6	power acceleration velocity	86.6 (99.4) 5.74 (5.35) 1.49 (1.43)	93.2 (100) 14.9 (17.2) 2.58 (2.95)
	8	power acceleration velocity	98.4 (114) 5.72 (5.35) 1.49 (1.43)	106 (118) 14.9 (17.2) 2.58 (2.95)
16	2	power acceleration velocity	55.7 (69.8) 3.94 (2.55) 1.33 (0.84)	31.0 (38.7) 10.4 (8.33) 2.01 (1.49)
		power acceleration velocity	74.0 (87.0) 3.94 (2.55) 1.33 (0.84)	61.6 (69.2) 10.2 (8.12) 2.00 (1.49)
	4	power acceleration velocity	87.2 (99.8) 3.93 (2.55) 1.33 (0.84)	80.1 (88.1) 10.2 (8.12) 2.00 (1.49)
		power acceleration velocity	97.8 (111) 3.93 (2.55) 1.33 (0.84)	94.0 (103) 10.2 (8.12) 2.00 (1.49)
	8	power acceleration velocity	110 (124) 3.92 (2.55) 1.33 (0.84)	109 (121) 10.2 (8.12) 2.00 (1.49)
20 (23)	2	power acceleration velocity	51.1 (45.1) 2.50 (1.95) 0.83 (0.49)	28.3 (27.7) 7.43 (6.28) 1.41 (1.06)
	4	power acceleration velocity	71.2 (68.2) 2.50 (1.95) 0.83 (0.49)	61.9 (63.1) 7.30 (6.28) 1.42 (1.06)
	5	power acceleration velocity	85.3 (83.8) 2.51 (1.95) 0.83 (0.49)	81.6 (83.5) 7.31 (6.28) 1.42 (1.06)
	6	power acceleration velocity	96.6 (96.9) 2.51 (1.95) 0.83 (0.49)	96.4 (99.7) 7.31 (6.28) 1.42 (1.06)
	8	power acceleration velocity	109 (112) 2.51 (1.95) 0.83 (0.49)	112 (118) 7.32 (6.28) 1.42 (1.06)

Table C.3g) Configuration Ja - Two blades, nominal $2\Omega_{\infty}$, 1 MW, tip-regulated.

Configuration La		Controller cross-over frequency (rad/s)			
Wind speed (m/s)	First drive-train mode (rad/s)	Standard deviation	1	2	3
13.4 (12)	5	power acceleration velocity	44.4 (59.3) 1.91 (1.17) 1.37 (1.34)	23.6 (28.5) 4.62 (3.50) 1.50 (1.50)	16.8 (19.1) 8.14 (6.99) 1.68 (1.67)
	7	power acceleration velocity	45.0 (59.7) 1.91 (1.17) 1.37 (1.34)	24.9 (29.7) 4.60 (3.50) 1.50 (1.50)	20.1 (21.0) 7.18 (6.95) 1.62 (1.66)
	9	power acceleration velocity	45.4 (60.1) 1.90 (1.17) 1.37 (1.34)	25.8 (28.5) 4.60 (3.50) 1.50 (1.50)	21.2 (22.3) 7.19 (6.93) 1.61 (1.66)
16.4 (16)	1	power acceleration velocity	51.3 (40.0) 1.26 (0.50) 1.13 (0.44)	27.1 (20.2) 2.91 (1.67) 1.22 (0.53)	19.2 (14.3) 5.05 (3.40) 1.34 (0.63)
	2	power acceleration velocity	51.9 (40.7) 1.26 (0.50) 1.13 (0.44)	28.4 (21.1) 2.90 (1.67) 1.22 (0.53)	22.8 (16.7) 4.43 (3.42) 1.30 (0.63)
	3	power acceleration velocity	52.2 (41.2) 1.26 (0.50) 1.13 (0.44)	29.3 (22.9) 2.90 (1.67) 1.22 (0.53)	23.9 (18.3) 4.37 (3.42) 1.29 (0.63)
20 (23)	1	power acceleration velocity	45.1 (27.0) 0.76 (0.32) 0.74 (0.21)	24.5 (14.9) 1.98 (1.14) 0.82 (0.27)	17.7 (11.3) 3.58 (2.49) 0.91 (0.36)
	2	power acceleration velocity	45.7 (27.5) 0.76 (0.32) 0.74 (0.21)	25.9 (16.9) 1.98 (1.14) 0.82 (0.27)	21.2 (14.2) 3.15 (2.33) 0.88 (0.36)
	3	power acceleration velocity	46.1 (28.7) 0.76 (0.32) 0.74 (0.21)	26.9 (18.7) 1.98 (1.14) 0.82 (0.27)	22.5 (15.5) 3.10 (2.33) 0.87 (0.36)

Table C.3h) Configuration La - Three blades, nominal $3\Omega_\infty$, 1 MW, tip-regulated.

The breakdown of the contribution of the three disturbances, ω_I , ω_{II} and ω_{III} to the total power, acceleration and velocity estimates are given for four cases in Table C.4. The agreement between the three sets of estimates can be seen to be good, except for the contribution of the wind disturbance for Configuration La. The reason for the disagreement is due to this configuration being most sensitive to the non-linear behaviour of the aerodynamics, in particular the stalling aerodynamic behaviour of the three-bladed tip-regulated rotor. The controllers incorporated in the simulations are derived directly from the open-loop transfer functions, *i.e.*

$$C(s) = \frac{O(s)}{k_2 A(s) M(s) D(s)} \quad (\text{C.22})$$

The transfer function $A(s)$ (Leithead *et al.*, 1991a) is a linear model of actuator dynamics included in the simulation. For the medium scale wind turbines it is (3.8). The bandwidth of the actuator would be expected to be considerably lower on a large-scale machine compared to a medium-scale machine. Following discussions with manufacturers, the bandwidth is

chosen to be approximately 2.5 rad/s and (3.8) scaled accordingly to obtain the actuator transfer function for the large-scale machines, (3.9). Of course, a controller derived by this method may not be entirely satisfactory. To confirm that no undue errors arise from using these controllers in the above simulations, estimates of performance are obtained from eight further simulations using properly designed controllers, one for each of the two-bladed machines and one for each of the three-bladed machines with the lower rotor velocity. The properties of the configurations and the performance estimates are shown in Table C.5. It may be observed that there is no major discrepancy between the results of Table C.4 and the corresponding results of Table C.5.

Configuration Aa	Simulation (Linear analysis)		
Wind speed 12 m/s Controller cross-over frequency 4.4 rad/s First drive-train mode 6 rad/s	Generated Power (kW)	Actuator Acceleration ($^{\circ}/s^2$)	Actuator Velocity ($^{\circ}/s$)
Wind	8.11 (6.75)	3.77 (4.32)	2.07 (2.33)
$2\Omega_o$	18.2 (18.0)	155.0 (166.4)	9.3 (12.69)
Meas. noise	0.042 (0.048)	17.9 (18.2)	0.32 (0.342)
Total	19.13 (19.19)	156.0 (167.5)	9.41 (12.89)
Configuration Ca	Simulation (Linear analysis)		
Wind speed 12 m/s Controller cross-over frequency 2.36 rad/s First drive-train mode 6 rad/s	Generated Power (kW)	Actuator Acceleration ($^{\circ}/s^2$)	Actuator Velocity ($^{\circ}/s$)
Wind	15.05 (13.04)	6.72 (2.11)	1.52 (1.55)
$3\Omega_o$	2.25 (2.08)	7.46 (7.06)	0.56 (0.53)
Meas. noise	0.036 (0.035)	1.010 (0.712)	0.037 (0.042)
Total	15.9 (13.2)	9.87 (7.40)	1.55 (1.63)
Configuration Db	Simulation (Linear analysis)		
Wind speed 16.4 m/s Controller cross-over frequency 1 rad/s First drive-train mode 2.8 rad/s	Generated Power (kW)	Actuator Acceleration ($^{\circ}/s^2$)	Actuator Velocity ($^{\circ}/s$)
Wind	109.9 (96.1)	0.512 (0.435)	0.679 (0.536)
$2\Omega_o$	26.3 (28.8)	1.098 (1.349)	0.204 (0.232)
Meas. noise	0.396 (0.17)	0.013 (0.015)	0.001 (0.001)
Total	112.5 (100.3)	1.507 (1.322)	0.724 (0.650)
Configuration Lb	Simulation (Linear analysis)		
Wind speed 16 m/s Controller cross-over frequency 1 rad/s First drive-train mode 5 rad/s	Generated Power (kW)	Actuator Acceleration ($^{\circ}/s^2$)	Actuator Velocity ($^{\circ}/s$)
Wind	51.0 (31.0)	1.06 (0.38)	1.125 (0.46)
$3\Omega_o$	6.15 (6.37)	0.50 (0.52)	0.072 (0.074)
Meas. noise	0.33 (0.17)	0.011 (0.012)	0.001 (0.001)
Total	51.3 (31.6)	1.26 (0.64)	1.13 (0.46)

Table C.4 Breakdown of standard deviations.

Configuration Aa	Simulation (Linear analysis)		
Wind speed 13.4 (12)m/s Controller cross-over frequency 3.65 (3.9) rad/s First drive-train mode 6 rad/s	Generated Power (kW)	Actuator Acceleration (°/s ²)	Actuator Velocity (°/s)
Wind	7.24 (7.70)	7.49 (7.29)	4.28 (4.16)
2Ω _o	18.89 (17.9)	66.3 (75.9)	5.58 (6.01)
Meas. noise	0.027 (0.045)	13.78 (5.09)	0.16 (0.13)
Total	19.75 (19.49)	68.19 (76.09)	5.99 (6.15)

Configuration Ca	Simulation (Linear analysis)		
Wind speed 13.4 (12)m/s Controller cross-over frequency 2.0 (1.8) rad/s First drive-train mode 6 rad/s	Generated Power (kW)	Actuator Acceleration (°/s ²)	Actuator Velocity (°/s)
Wind	15.46 (17.03)	3.16 (1.77)	1.68 (1.51)
3Ω _o	2.18 (1.92)	5.12 (3.38)	0.36 (0.28)
Meas. noise	0.038 (0.030)	1.34 (0.23)	0.038 (0.013)
Total	15.58 (17.12)	5.26 (3.82)	1.70 (1.53)

Configuration Db	Simulation (Linear analysis)		
Wind speed 16.4 (16.0)m/s Controller cross-over frequency 1 rad/s First drive-train mode 2.8 rad/s	Generated Power (kW)	Actuator Acceleration (°/s ²)	Actuator Velocity (°/s)
Wind	93.4 (81.9)	0.77 (0.60)	0.62 (0.45)
2Ω _o	27.4 (29.75)	0.26 (0.30)	1.43 (1.85)
Meas. noise	0.025 (0.018)	0.002 (0.002)	0.031 (0.040)
Total	96.6 (87.1)	0.83 (0.67)	1.95 (1.91)

Configuration La	Simulation (Linear analysis)		
Wind speed 16.5 (16.0) m/s Controller cross-over frequency 1 rad/s First drive-train mode 5 rad/s	Generated Power (kW)	Actuator Acceleration (°/s ²)	Actuator Velocity (°/s)
Wind	52.2 (39.65)	1.21 (0.482)	1.16 (0.581)
3Ω _o	6.108 (6.527)	0.271 (0.558)	0.043 (0.078)
Meas. noise	0.490 (0.016)	0.005 (0.022)	0.0006 (0.0013)
Total	52.6 (40.18)	1.270 (0.737)	1.17 (0.586)

$$\text{Aa controller} = \frac{91.65(s^2 + 3.2s + 2.56)(s^2 + 8.35s + 36.44)(s^2 + s + 103.6)}{s(s + 0.3)(s + 3.7)(s + 50)(s^2 + 280s + 40000)(s^2 + 2.795s + 103.6)}$$

$$\text{Ca controller} = \frac{0.455(s^2 + 1.5s + 1)(s^2 + 8.68s + 38.48)(s + 25.9)(s^2 + 3.39s + 153)}{s(s + 0.95)(s + 2.15)(s + 3)(s^2 + 56s + 1600)(s^2 + 3.39s + 153)}$$

$$\text{Db controller} = \frac{0.2(s + 0.5)(s + 1.23)(s + 2.5)(s + 50)(s^2 + 3.95s + 7.97)(s^2 + 0.55s + 31.36)}{s(s + 0.1)(s + 1.67)(s + 50)(s^2 + 20s + 200)(s^2 + 23s + 216)(s^2 + 1.53s + 31.36)}$$

$$\text{La controller} = \frac{0.1206(s + 0.27)(s + 1.23)(s + 2.5)(s^2 + 6.97s + 24.94)(s + 50)(s^2 + 0.66s + 45.56)}{s(s + 0.23)(s + 1.67)(s + 7.82)(s + 23.33s + 222)(s + 18.2)(s + 18.5)(s + 35.5)(s^2 + 1.85s + 45.56)}$$

Table C.5 Breakdown of standard deviations for simulations with designed controllers.

The results of the parametric study are presented in Chapters 5 and 6. The same methodology is used in Chapter 7 to analyse the power controller performance of the fledge.

The methodology is also used in Chapter 8 to analyse the power controller performance of a full-span regulated, 1 MW machine and the results are shown in Tables C.6 to C.9. It should be noted that this wind turbine does not have ideal damping. The machine parameters for the machine investigated in Chapter 8 are listed in Table C.10 and the aerodynamic torque coefficients for this machine is listed in Table G.9.

C.3 Implementation of a dual mode controller

A dual mode structure for the controller, *i.e.* a crossover frequency of 1 rad/s in low wind speeds and a crossover frequency of 2 rad/s in high wind speeds is adopted for the wind turbine considered in Chapter 8. The digital implementation of such a dual mode controller (Leith and Leithead, 1996) is described in this sub-section.

The actuator pitch rate limits are restrictive. Unlike the controllers described in Section C.1, to avoid excessive actuator saturation there is no shaping at low frequency to cater for ramps in wind speed. Therefore, exceptional peak power transients can occur. A modest improvement in the actuator capability would accordingly improve performance markedly in response to ramps in the wind speed. Also, the loss of phase due to the tower dynamics restricts the effectiveness of the notch filter which protects the actuator from the spectral peak at $3\Omega_o$.

The controller is implemented digitally with a sampling frequency of 25 Hz and the overall controller structure (very similar to that in Figure C.2) with the required additional filters is shown in Figure C.9. (The analogue pre-filter $80/(s + 80)$ is required to reduce the high frequency noise components in the analogue signal (anti-aliasing) and so to prevent noise from being transferred to a lower frequency by the sampling process. To protect the actuator from additional high frequency disturbances due to digitalisation, an analogue filter after the D/A converter is required, *i.e.*, $3600/(s^2 + 40s + 3600)$). To account for the delays due to digitalisation, the continuous controller in the simulation and in the control models include an additional delay for the A/D and D/A conversion, namely $(1 - s/80)/(1 + s/80)$.

measured pitch angle goes above or below a pitch angle limit *i.e.* 12° (which is equivalent to a wind speed of 16 m/s).

Drive-train freq. (rad/s)	Controller cross-over frequency (rad/s)							
	0.5	1.0	1.5	2.0	2.5	3.0	3.5	4.0
1.0Ω	28793.9	11543.0	6620.6	4462.0	3343.9	2746.0	2430.4	2247.9
1.5Ω	28910.9	11913.6	7214.0	5180.5	4151.4	3666.5	3499.4	3527.3
2.0Ω	29023.0	12217.2	7742.3	5938.5	5135.6	4869.3	4917.2	5201.5
3.5Ω	29468.0	13284.6	9417.8	8134.7	7774.1	7895.4	8317.1	9064.0
4.0Ω	29571.0	13519.1	9761.2	8556.0	8253.1	8421.6	8887.9	9690.5
4.5Ω	29644.1	13683.5	9998.1	8842.6	8575.7	8773.2	9266.7	10102.7
5.0Ω	29695.2	13797.3	10160.4	9037.2	8793.2	9008.9	9519.1	10385.6
5.5Ω	29731.2	13877.0	10273.1	9171.4	8942.4	9169.8	9690.5	10559.7

Wind speed 13.5 m/s

Drive-train freq. (rad/s)	Controller cross-over frequency (rad/s)							
	0.5	1.0	1.5	2.0	2.5	3.0	3.5	4.0
1.0Ω	47762.4	19214.8	10863.6	7164.0	5217.2	4136.3	3517.5	3090.2
1.5Ω	47916.4	19737.7	11684.3	8079.8	6122.3	5044.8	4491.7	4223.1
2.0Ω	47997.2	19985.5	12139.4	8748.2	6998.4	6124.5	5781.0	5778.5
3.5Ω	48270.1	20682.0	13328.6	10450.1	9213.4	8828.3	8949.2	9487.9
4.0Ω	48332.7	20834.4	13576.6	10786.3	9627.8	9309.7	9490.4	10096.5
4.5Ω	48377.2	20941.9	13749.4	11017.8	9909.4	9633.3	9850.7	10497.6
5.0Ω	48408.2	21016.6	13868.7	11176.0	10100.3	9851.0	10091.3	10763.4
5.5Ω	48430.0	21069.0	13951.9	11285.7	10231.6	9999.8	10254.9	10942.8

Wind speed 16 m/s

Drive-train freq. (rad/s)	Controller cross-over frequency (rad/s)							
	0.5	1.0	1.5	2.0	2.5	3.0	3.5	4.0
1.0Ω	93556.6	38317.8	21414.2	13854.9	9862.6	7621.6	6298.6	5323.8
1.5Ω	93847.8	39339.7	23003.7	15540.2	11350.0	8874.2	7407.4	6415.5
2.0Ω	93923.5	39625.3	23556.3	16340.2	12337.9	9993.6	8645.1	7840.3
3.5Ω	94071.0	40051.2	24350.9	17567.2	14052.3	12222.8	11395.4	11216.6
4.0Ω	94102.4	40132.9	24496.0	17784.7	14350.3	12604.4	11858.8	11772.5
4.5Ω	94124.5	40189.9	24596.6	17934.4	14553.3	12861.6	12168.3	12139.4
5.0Ω	94139.8	40229.4	24726.8	18036.8	14691.2	13035.1	12375.3	12382.7
5.5Ω	94150.4	40256.9	24714.0	18107.7	14786.3	13153.9	12516.2	12547.0

Wind speed 20 m/s

Drive-train freq. (rad/s)	Controller cross-over frequency (rad/s)							
	0.5	1.0	1.5	2.0	2.5	3.0	3.5	4.0
1.0Ω	122023.5	50955.7	28362.0	18182.2	12811.7	9805.3	8031.5	6722.0
1.5Ω	122427.3	52369.8	30566.3	20509.5	14829.6	11437.8	9386.6	7946.7
2.0Ω	122515.8	52721.8	31256.8	21503.0	16027.0	12737.6	10747.4	9426.8
3.5Ω	122636.9	53102.9	31998.5	22674.8	17684.0	14903.5	13424.7	12726.7
4.0Ω	122660.5	53166.9	32116.5	22857.5	17942.5	15245.6	13853.1	13256.0
4.5Ω	122677.0	53211.1	32197.2	22981.5	18116.8	15474.5	14137.6	13604.3
5.0Ω	122688.2	53241.3	32252.2	23065.7	18234.5	15628.1	14327.4	13834.9
5.5Ω	122696.0	53262.1	32290.2	23123.7	18315.2	15733.0	14456.3	13990.4

Wind speed 23 m/s

Table C.6 Standard deviation of gearbox torque (Nm) for first drive-train mode with ideal damping

Drive-train freq.(rad/s)	Controller cross-over frequency (rad/s)							
	0.5	1.0	1.5	2.0	2.5	3.0	3.5	4.0
1.0Ω	31385.7	16235.2	13492.0	9870.2	6117.4	4302.8	3457.2	2986.0
1.5Ω	29910.8	13478.2	9383.7	7944.7	7154.5	6270.0	5600.7	5327.9
2.0Ω	29808.3	13608.5	9701.0	8428.6	8175.6	8493.2	9081.0	9856.1
3.5Ω	30299.2	14993.1	11759.8	10894.7	10851.7	11261.7	11988.9	13145.5
4.0Ω	30081.1	14573.0	11209.8	10263.5	10154.6	10496.3	11142.9	12183.8
4.5Ω	29919.6	14254.1	10784.6	9770.6	9608.9	9899.5	10488.6	11450.1
5.0Ω	29806.1	14027.2	10477.9	9412.1	9210.7	9463.7	10012.1	10918.2
5.5Ω	29724.9	13864.0	10255.1	9150.1	8918.7	9144.0	9662.7	10529.0

Wind speed 13.5 m/s

Drive-train freq. (rad/s)	Controller cross-over frequency (rad/s)							
	0.5	1.0	1.5	2.0	2.5	3.0	3.5	4.0
1.0Ω	52324.8	27521.3	23001.5	16741.9	10174.0	6936.5	5361.7	4397.4
1.5Ω	49600.8	22347.4	15284.9	12627.4	10904.2	8899.9	7301.8	6383.7
2.0Ω	49005.9	21599.7	14348.7	11564.7	10444.5	10159.2	10262.6	10623.3
3.5Ω	48891.9	21954.1	15212.0	12845.6	12041.3	12036.9	12525.2	13518.1
4.0Ω	48712.5	21614.4	14735.2	12262.5	11369.9	11282.8	11682.4	12555.0
4.5Ω	48582.6	21363.6	14376.8	11818.0	10854.2	10702.8	11037.2	11825.1
5.0Ω	48491.1	21186.5	14121.6	11498.9	10481.6	10282.5	10569.6	11297.7
5.5Ω	48425.3	21059.4	13937.6	11267.4	10210.1	9975.4	10227.9	10912.6

Wind speed 16 m/s

Drive-train freq. (rad/s)	Controller cross-over frequency (rad/s)							
	0.5	1.0	1.5	2.0	2.5	3.0	3.5	4.0
1.0Ω	103262.3	56174.4	47430.6	34451.5	20651.5	13792.1	10399.5	8245.7
1.5Ω	97357.1	44830.9	30575.7	25063.6	21214.1	16533.1	12600.6	9962.5
2.0Ω	95744.5	42355.0	27136.0	20796.1	17650.3	15899.1	14675.0	13720.3
3.5Ω	94663.1	41086.0	25839.4	19519.1	16480.7	15124.7	14761.3	15132.4
4.0Ω	94460.6	40759.6	25398.6	18970.0	15826.5	14368.9	13903.7	15132.4
4.5Ω	94319.0	40528.9	25083.8	18573.7	15349.4	13813.0	13270.1	14145.4
5.0Ω	94218.8	40366.5	24862.3	18294.3	15011.6	13417.8	12818.3	13416.2
5.5Ω	94145.9	40249.1	24702.9	18093.2	14768.2	13132.3	12491.2	12518.1

Wind speed 20 m/s

Drive-train freq. (rad/s)	Controller cross-over frequency (rad/s)							
	0.5	1.0	1.5	2.0	2.5	3.0	3.5	4.0
1.0Ω	135417.6	75822.6	64537.5	46874.2	27943.8	18522.2	13857.9	10892.2
1.5Ω	127241.9	60007.7	41114.5	33763.3	28527.2	22033.6	16504.2	12695.2
2.0Ω	124955.2	56384.3	36026.4	27402.1	22997.9	20352.7	18280.2	16412.1
3.5Ω	123308.2	54195.8	33501.7	24604.0	20070.3	17764.2	16764.1	16643.8
4.0Ω	123065.1	53824.9	33020.7	24017.9	19378.6	16968.4	15865.2	15614.7
4.5Ω	122897.9	53567.1	32684.7	23605.9	18888.6	16399.8	15217.9	14869.8
5.0Ω	122777.9	53385.6	32449.1	23317.2	18544.8	15999.8	14761.0	14342.4
5.5Ω	122690.9	53253.9	32279.0	23109.5	18297.7	15712.0	14431.8	13961.8

Wind speed 23 m/s

Table C.7 Standard deviation of gearbox torque (Nm).

Drive-train freq. (rad/s)	Controller cross-over frequency (rad/s)							
	0.5	1.0	1.5	2.0	2.5	3.0	3.5	4.0
1.0Ω	0.93	1.52	5.96	37.52	168.30	570.24	1594.52	3918.71
1.5Ω	0.93	1.50	3.13	8.15	31.00	105.31	298.81	743.00
2.0Ω	0.93	1.49	3.05	5.57	11.95	32.74	89.71	223.54
3.5Ω	0.93	1.49	3.04	5.36	8.90	14.17	22.42	36.86
4.0Ω	0.93	1.49	3.04	5.36	8.89	14.07	21.74	33.65
4.5Ω	0.93	1.49	3.04	5.36	8.88	14.05	21.58	32.79
5.0Ω	0.93	1.49	3.04	5.35	8.87	14.04	21.53	32.54
5.5Ω	0.93	1.49	3.04	5.35	8.87	14.03	21.51	32.46

Wind speed 13.5 m/s

Drive-train freq. (rad/s)	Controller cross-over frequency (rad/s)							
	0.5	1.0	1.5	2.0	2.5	3.0	3.5	4.0
1.0Ω	0.46	0.71	1.91	11.29	50.52	171.15	478.57	1176.12
1.5Ω	0.46	0.71	1.16	2.57	9.35	31.62	89.69	223.00
2.0Ω	0.46	0.71	1.14	1.85	3.70	9.88	26.95	67.10
3.5Ω	0.46	0.71	1.14	1.79	2.81	4.37	6.81	11.12
4.0Ω	0.46	0.71	1.14	1.79	2.81	4.34	6.61	10.17
4.5Ω	0.46	0.71	1.13	1.79	2.81	4.33	6.56	9.91
5.0Ω	0.46	0.71	1.13	1.79	2.81	4.33	6.55	9.84
5.5Ω	0.46	0.71	1.13	1.79	2.81	4.32	6.54	9.81

Wind speed 16 m/s

Drive-train freq. (rad/s)	Controller cross-over frequency (rad/s)							
	0.5	1.0	1.5	2.0	2.5	3.0	3.5	4.0
1.0Ω	0.88	1.37	2.38	11.16	49.38	167.19	467.45	1148.80
1.5Ω	0.88	1.37	1.86	3.04	9.33	30.96	87.64	217.83
2.0Ω	0.88	1.37	1.84	2.49	4.10	9.88	26.43	65.59
3.5Ω	0.88	1.37	1.84	2.45	3.36	4.77	7.06	11.16
4.0Ω	0.88	1.37	1.84	2.44	3.36	4.75	6.87	10.26
4.5Ω	0.88	1.37	1.84	2.44	3.36	4.74	6.83	10.01
5.0Ω	0.88	1.37	1.84	2.44	3.36	4.74	6.81	9.94
5.5Ω	0.88	1.37	1.84	2.44	3.36	4.74	6.81	9.92

Wind speed 20 m/s

Drive-train freq. (rad/s)	Controller cross-over frequency (rad/s)							
	0.5	1.0	1.5	2.0	2.5	3.0	3.5	4.0
1.0Ω	1.00	1.60	2.46	9.78	42.76	144.65	404.40	993.84
1.5Ω	1.00	1.60	2.10	3.06	8.27	26.86	75.85	188.47
2.0Ω	1.00	1.60	2.09	2.66	3.97	8.78	22.97	56.80
3.5Ω	1.00	1.60	2.09	2.64	3.41	4.59	6.50	9.99
4.0Ω	1.00	1.60	2.09	2.63	3.41	4.57	6.35	9.23
4.5Ω	1.00	1.60	2.09	2.63	3.41	4.56	6.32	9.03
5.0Ω	1.00	1.60	2.09	2.63	3.41	4.56	6.30	8.97
5.5Ω	1.00	1.60	2.09	2.63	3.41	4.56	6.30	8.95

Wind speed 23 m/s

Table C.8 Standard deviation of actuator acceleration ($^{\circ}/s^2$).

Drive-train freq. (rad/s)	Controller cross-over frequency (rad/s)							
	0.5	1.0	1.5	2.0	2.5	3.0	3.5	4.0
1.0Ω	1.76	1.65	1.63	1.76	2.67	5.81	13.18	27.98
1.5Ω	1.76	1.65	1.62	1.69	1.94	2.55	3.94	6.81
2.0Ω	1.76	1.65	1.62	1.69	1.91	2.38	3.24	4.70
3.5Ω	1.76	1.65	1.62	1.69	1.91	2.37	3.17	4.46
4.0Ω	1.76	1.65	1.62	1.69	1.91	2.37	3.17	4.46
4.5Ω	1.76	1.65	1.62	1.69	1.91	2.37	3.17	4.46
5.0Ω	1.76	1.65	1.62	1.69	1.91	2.37	3.17	4.46
5.5Ω	1.76	1.65	1.62	1.69	1.91	2.37	3.17	4.46

Wind speed 13.5 m/s

Drive-train freq. (rad/s)	Controller cross-over frequency (rad/s)							
	0.5	1.0	1.5	2.0	2.5	3.0	3.5	4.0
1.0Ω	0.85	0.80	0.77	0.79	0.99	1.84	4.00	8.42
1.5Ω	0.85	0.80	0.77	0.78	0.82	0.96	1.32	2.13
2.0Ω	0.85	0.80	0.77	0.78	0.82	0.92	1.13	1.53
3.5Ω	0.85	0.80	0.77	0.78	0.82	0.92	1.12	1.46
4.0Ω	0.85	0.80	0.77	0.78	0.82	0.92	1.12	1.46
4.5Ω	0.85	0.80	0.77	0.78	0.82	0.92	1.12	1.46
5.0Ω	0.85	0.80	0.77	0.78	0.82	0.92	1.12	1.46
5.5Ω	0.85	0.80	0.77	0.78	0.82	0.92	1.12	1.46

Wind speed 16 m/s

Drive-train freq. (rad/s)	Controller cross-over frequency (rad/s)							
	0.5	1.0	1.5	2.0	2.5	3.0	3.5	4.0
1.0Ω	1.56	1.49	1.43	1.41	1.52	2.14	4.08	8.31
1.5Ω	1.56	1.49	1.43	1.41	1.42	1.50	1.74	2.40
2.0Ω	1.56	1.49	1.43	1.41	1.42	1.48	1.61	1.91
3.5Ω	1.56	1.49	1.43	1.41	1.42	1.48	1.60	1.86
4.0Ω	1.56	1.49	1.43	1.41	1.42	1.48	1.60	1.86
4.5Ω	1.56	1.49	1.43	1.41	1.42	1.48	1.60	1.86
5.0Ω	1.56	1.49	1.43	1.41	1.42	1.48	1.60	1.86
5.5Ω	1.56	1.49	1.43	1.41	1.42	1.48	1.60	1.86

Wind speed 20 m/s

Drive-train freq. (rad/s)	Controller cross-over frequency (rad/s)							
	0.5	1.0	1.5	2.0	2.5	3.0	3.5	4.0
1.0Ω	1.72	1.67	1.60	1.57	1.64	2.09	3.66	7.26
1.5Ω	1.72	1.67	1.60	1.56	1.57	1.62	1.79	2.30
2.0Ω	1.72	1.67	1.60	1.56	1.57	1.61	1.70	1.93
3.5Ω	1.72	1.67	1.60	1.56	1.57	1.60	1.69	1.89
4.0Ω	1.72	1.67	1.60	1.56	1.57	1.60	1.69	1.89
4.5Ω	1.72	1.67	1.60	1.56	1.57	1.60	1.69	1.89
5.0Ω	1.72	1.67	1.60	1.56	1.57	1.60	1.69	1.89
5.5Ω	1.72	1.67	1.60	1.56	1.57	1.60	1.69	1.89

Wind speed 23 m/s

Table C.9 Standard deviation of actuator velocity (°/s).

Machine parameter		Machine parameter	
I_1	1.0337e6 kgm ²	$slip$	1.5%
I_{12}	55 kgm ²	$Effy$	0.929
K_1	1.131e8 Nm/rad	τ_{el}	0.05s
K_2	4.85e6 Nm/rad	p	3
N	40.9	$\dot{\theta}_G$	50 Hz
Ω_o	2.599 rad/s		

Table C.10 Machine parameters

$X \frac{(s-80)(s^2 + 0.312s + 60.79321)}{(s^2 + 24s + 400)(s + 2.5)(s + 50)}$ $\frac{s(s^2 + 1.5594s + 60.79321)(s^2 + 50s + 2500)}{(s^2 + 40s + 3600)(s^2 + 160s + 1600)}$			
X	Wind speed (m/s)	Phase Margin	Gain Margin
-1349.4	13.22	77° at 1 rad/s	10.9 dB at 4.09 rad/s
-472.5	16.00	79° at 1 rad/s	15.3 dB at 6.45 rad/s
-933.7	16.00	67° at 2 rad/s	9.4 dB at 6.45 rad/s
-576.4	20.10	69° at 2 rad/s	9.8 dB at 6.53 rad/s

Table C.11 The controllers used in Chapter 8.

Appendix D Induction generator dynamics

In this appendix a simple model of an induction generator is derived which is used in the model of the power train described in Appendix B. The description is a generalisation of previous analysis of the generator dynamics (Bossanyi and Jervis, 1988).

D.1 Dynamics

The dynamics of an induction generator is presented with respect to an orthogonal set of axes (the d - q axes) chosen to rotate at an arbitrary electrical angular velocity $\omega_e = \dot{\theta}_e$. It is assumed that the stator windings are identical and therefore have an identical number of effective turns, identical resistances, leakage inductances and self inductances. Similarly, the rotor windings are assumed identical. Factors, which influence the dynamics but are neglected, are the non-linear aspects of the magnetic circuit, the variation in resistance due to temperature and frequency changes and the harmonic content of the M.M.F. wave. Choosing the d - q reference axes to rotate at synchronous frequency ω_s , *i.e.* $\omega_e = \omega_s$, and noting that the rotor voltages are zero, since the rotor coils of a cage induction generator are shorted together, the equations of motion (Krause and Thomas, 1965) for the fluxes, ψ , of a three phase induction generator are

$$\begin{bmatrix} \dot{\psi}_{qs} \\ \dot{\psi}_{ds} \\ \dot{\psi}_{qr} \\ \dot{\psi}_{dr} \end{bmatrix} = \omega_s \begin{bmatrix} -K_1 & -1 & K_2 & 0 \\ 1 & -K_1 & 0 & K_2 \\ K_4 & 0 & -K_3 & \varepsilon \\ 0 & K_4 & -\varepsilon & -K_3 \end{bmatrix} \begin{bmatrix} \psi_{qs} \\ \psi_{ds} \\ \psi_{qr} \\ \psi_{dr} \end{bmatrix} + \omega_s \begin{bmatrix} V_{qs} \\ V_{ds} \\ 0 \\ 0 \end{bmatrix} \quad (\text{D.1})$$

(Dynamic equations, in terms of the fluxes rather than currents, is preferred since the former facilitate the required reduction in the order of the equations). The suffices q and d indicate components resolved in the direction of the q and d axes, respectively, and the suffices s and r indicate stator and rotor quantities, respectively. (The primes indicate that the rotor quantities are referred to the stator). The slip, ε , is

$$\varepsilon = (p\omega_R - \omega_s)/\omega_s \quad (\text{D.2})$$

where ω_R is the rotational speed of the rotor, p is the number of pole pairs and the stator voltages, V_{qs} and V_{ds} , are related to the supply voltage E by

$$V_{qs} = E \cos(\omega_s t - \theta_s) ; V_{ds} = -E \sin(\omega_s t - \theta_s) \quad (D.3)$$

with $(\omega_s t - \theta_s)$ constant. The dimensionless coefficients, K_i , $i=1,4$, are defined

$$\begin{aligned} K_1 &= r_s (X'_{lr} + X_m) / a ; K_2 = r_s X_m / a \\ K_3 &= r'_r (X'_{ls} + X_m) / a ; K_4 = r'_r X_m / a \end{aligned} \quad (D.4)$$

with

$$a = X_{ls} X'_{lr} + X_m X'_{lr} + X_m X_{ls} \quad (D.5)$$

where r_s is the stator resistance and r'_r is the rotor resistance. The stator leakage reactance X_{ls} , the rotor leakage reactance X'_{lr} and the magnetising reactance X_m are related to the stator leakage inductance L_{ls} , the rotor leakage inductance L'_{lr} and the magnetising inductance M , respectively by

$$X_{ls} = \omega_s L_{ls} ; X'_{lr} = \omega_s L'_{lr} ; X_m = \omega_s M \quad (D.6)$$

The generated power, P , is

$$P = \frac{3}{2} \left((K_1 \Psi_{qs} - K_2 \Psi'_{qr}) V_{qs} / r_s + (K_1 \Psi_{ds} - K_2 \Psi'_{dr}) V_{ds} / r_s \right) \quad (D.7)$$

and the generator reaction torque, T_G , is

$$T_G = \frac{3}{2} p / (\omega_s r_s) \cdot K_2 \cdot (\Psi'_{qr} \Psi_{ds} - \Psi'_{dr} \Psi_{qs}) \quad (D.8)$$

Of course, (D.1) does not represent the complete set of dynamics. Although, the turbine is assumed to be connected to a reasonably strong grid, there is a voltage drop across the local power network connecting the wind turbine and, possibly, other turbines in a wind farm to the grid. Nevertheless, the voltage drop is small and the dynamic interaction is weak, since power losses in the local power network are small. Hence, the supply voltage, E , may be considered an external input and essentially the same as the grid voltage during normal operation.

The steady state solution of (D.1) is

$$\Psi_{qso} = \frac{V_{qs} [K_1 \epsilon^2 + K_3 (K_1 K_3 - K_2 K_4)] - V_{ds} [\epsilon^2 - K_2 K_4 \epsilon + K_3^2]}{[(K_1 K_3 - K_2 K_4)^2 + K_3^2 - 2K_2 K_4 \epsilon + (1 + K_1^2) \epsilon^2]} \quad (D.9)$$

$$\Psi_{dso} = \frac{V_{qs} [\epsilon^2 - K_2 K_4 \epsilon + K_3^2] + V_{ds} [K_1 \epsilon^2 + K_3 (K_1 K_3 - K_2 K_4)]}{[(K_1 K_3 - K_2 K_4)^2 + K_3^2 - 2K_2 K_4 \epsilon + (1 + K_1^2) \epsilon^2]} \quad (D.10)$$

$$\dot{\Psi}_{qro} = \frac{V_{qs}[K_4\varepsilon + K_4(K_1K_3 - K_2K_4)] - V_{ds}[K_3K_4 - K_1K_4\varepsilon]}{[(K_1K_3 - K_2K_4)^2 + K_3^2 - 2K_2K_4\varepsilon + (1+K_1^2)\varepsilon^2]} \quad (D.11)$$

$$\dot{\Psi}_{dro} = \frac{V_{qs}[K_3K_4 - K_1K_4\varepsilon] + V_{ds}[K_4\varepsilon + K_4(K_1K_3 - K_2K_4)]}{[(K_1K_3 - K_2K_4)^2 + K_3^2 - 2K_2K_4\varepsilon + (1+K_1^2)\varepsilon^2]} \quad (D.12)$$

with generated power

$$P_o = -\frac{3}{2} / r_s \cdot \frac{[K_1^2\varepsilon^2 - K_2K_4\varepsilon + (K_1K_3 - K_2K_4)^2] E^2}{[(K_1K_3 - K_2K_4)^2 + K_3^2 - 2K_2K_4\varepsilon + (1+K_1^2)\varepsilon^2]} \quad (D.13)$$

generator reaction torque

$$T_{Go} = \frac{3}{2} p / (\omega_s r_s) \cdot \frac{K_2K_4\varepsilon E^2}{[(K_1K_3 - K_2K_4)^2 + K_3^2 - 2K_2K_4\varepsilon + (1+K_1^2)\varepsilon^2]} \quad (D.14)$$

and slope of the torque/speed curve

$$D_e = \frac{dT_G / d\varepsilon}{d\omega_r} = p T_{Go} / (\omega_s \varepsilon) \cdot \frac{[K_3^2 + (K_1K_3 - K_2K_4)^2 - (1+K_1^2)\varepsilon^2]}{[(K_1K_3 - K_2K_4)^2 + K_3^2 - 2K_2K_4\varepsilon + (1+K_1^2)\varepsilon^2]} \quad (D.15)$$

The per-unit parameter values, for a 60 Hz induction generator, are

$$X_m = 3.6665 ; X_{ls} = 0.0869 ; X'_{lr} = 0.090 ; r_s = 0.0374 ; r'_r = 0.0154$$

The generator has a rated power of 330 kW at 1.44 % slip with 2 pole pairs and a supply voltage of 480V. From (D.13), (D.14) and (D.15), the power, reaction torque and slope of torque/speed curve at rated are 330.8 kW, 1823 Nm and 679.3 Nm.s/rad, respectively, which are in very good argument with the manufacturer's data sheet. The efficiency, Eff , of the generator

$$Eff = P_o / (\omega_r T_{Go}) = 0.949.$$

D.2 Reduced order dynamics

Typically, the K_i and ε are all much less than 1, e.g. for the 60 Hz generator

$$K_1 = 0.2139 ; K_2 = 0.2087 ; K_3 = 0.08811 ; K_4 = 0.08607$$

and at rated

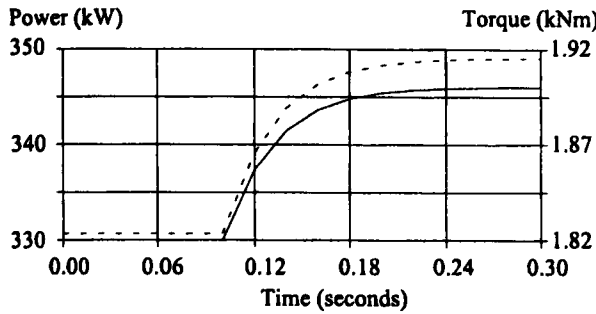
$$\varepsilon = 0.0144$$

Hence, the time scale associated with the time evolution of $\dot{\Psi}_{qr}$ and $\dot{\Psi}_{dr}$ is much slower than that for Ψ_{qs} and Ψ_{ds} . When equations (D.1) are linearised about the rated operating point, the eigenvalues of the above generator are $-33.0 \pm j 1.25$ and $-80.9 \pm j 372.7$ clearly indicating the fast and slow time scales. The dynamics can be treated as a singularly perturbed systems (Kokotovic, 1986). Retaining only the slow dynamics, the equations of motion (D.1) simplify to

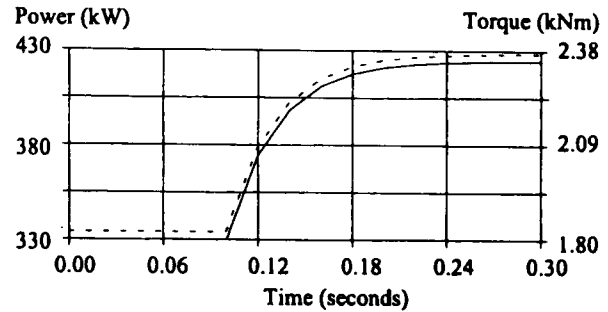
$$\begin{bmatrix} \dot{\Psi}_{qr}' \\ \dot{\Psi}_{dr}' \end{bmatrix} = \frac{\omega_s}{(1+K_I^2)} \begin{bmatrix} -[K_3 + K_I(K_I K_3 - K_2 K_4)] & [(1+K_I^2)\varepsilon - K_2 K_4] \\ -[(1+K_I^2)\varepsilon - K_2 K_4] & -[K_3 + K_I(K_I K_3 - K_2 K_4)] \end{bmatrix} \begin{bmatrix} \Psi_{qr}' \\ \Psi_{dr}' \end{bmatrix} + \frac{\omega_s K_4}{(1+K_I^2)} \begin{bmatrix} K_I V_{qs} - V_{ds} \\ V_{qs} + K_I V_{ds} \end{bmatrix} \quad (D.16)$$

with

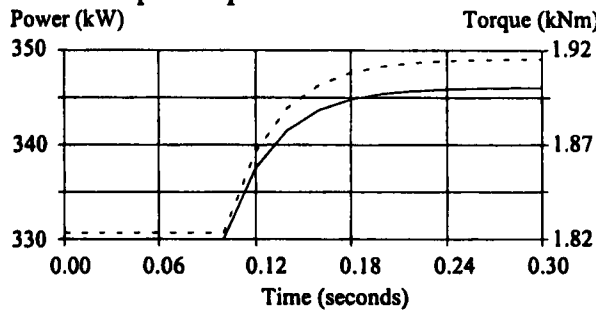
$$\begin{bmatrix} \Psi_{qs} \\ \Psi_{ds} \end{bmatrix} = \frac{K_2}{1+K_I^2} \begin{bmatrix} K_I & -1 \\ 1 & K_I \end{bmatrix} \begin{bmatrix} \Psi_{qr}' \\ \Psi_{dr}' \end{bmatrix} + \frac{1}{1+K_I^2} \begin{bmatrix} K_I V_{qs} - V_{ds} \\ V_{qs} + K_I V_{ds} \end{bmatrix} \quad (D.17)$$



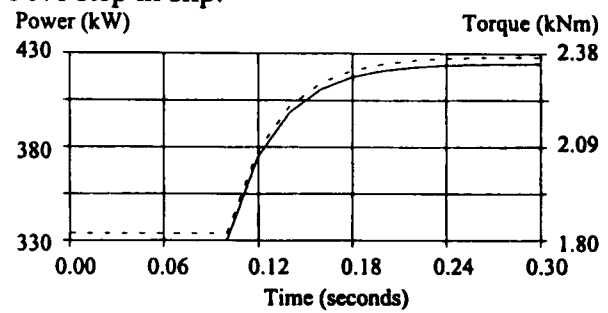
a) The open loop time response of (D.1) to a 5% step in slip.



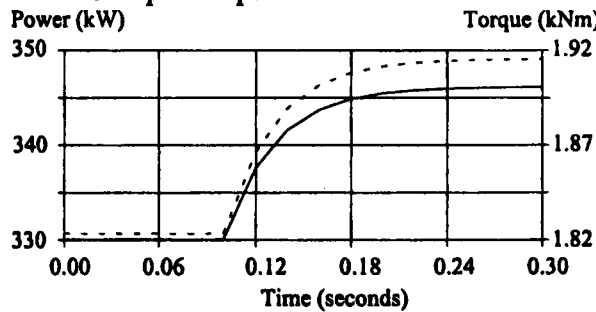
b) The open loop time response of (D.1) to a 30% step in slip.



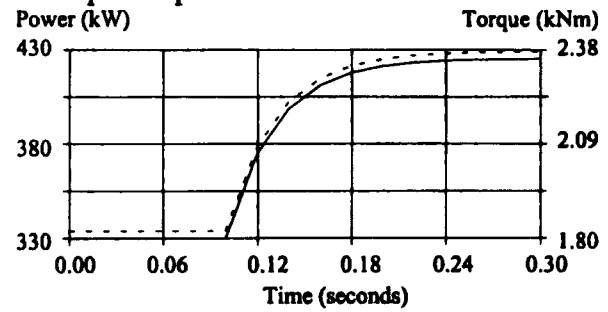
c) The open loop time response of (D.16) to a 5% step in slip.



d) The open loop time response of (D.16) to a 30% step in slip.



e) The open loop time response of (D.18) to a 5% step in slip.



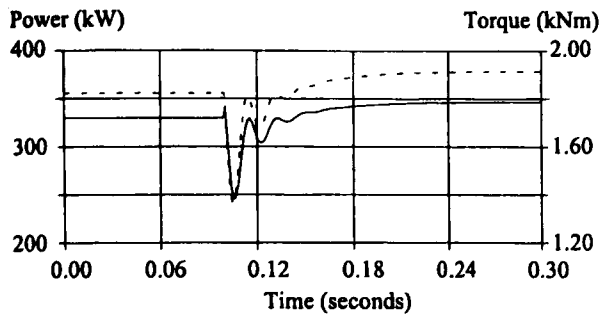
f) The open loop time response of (D.18) to a 30% step in slip.

Key : — Power - - - - Torque

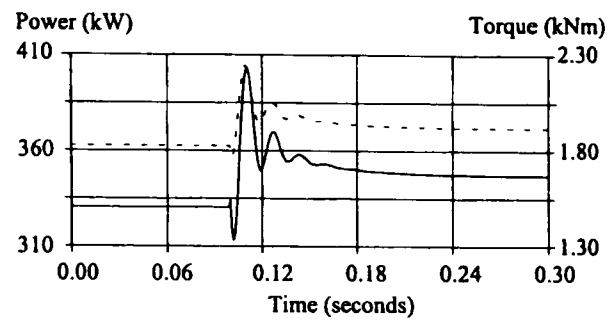
Figure D.1 Step responses of slip for the 60 Hz generator.

When equations (D.16) are linearised, the eigenvalues are $-31.8 \pm j 1.05$ in close argument, as required, with the slow eigenvalues of (D.1). The time responses of both systems (D.1) and (D.16) to 5% and 30% steps in slip for the 60 Hz generator, Figures D.1a to D.1d, and 5% steps in V_{qs} and V_{ds} , Figures D.2a to D.2d, confirm that the dynamic response of the generator is dominated by the slow dynamics and that the dynamics of the generator are well represented by (D.16). The higher frequency component is only evident in the responses to

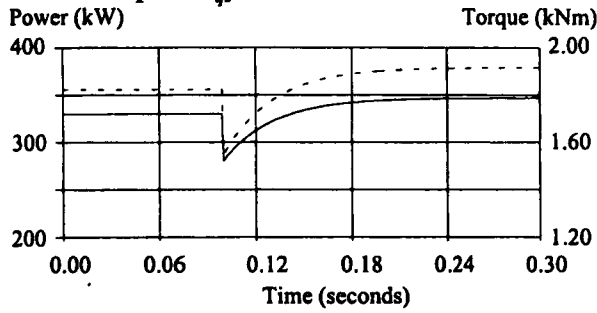
steps in V_{qs} and V_{ds} but the discrepancy is unimportant, in the context of this paper since step changes in V_{qs} and V_{ds} represent external disturbances to the power train and the higher frequency is outside the frequency range of interest.



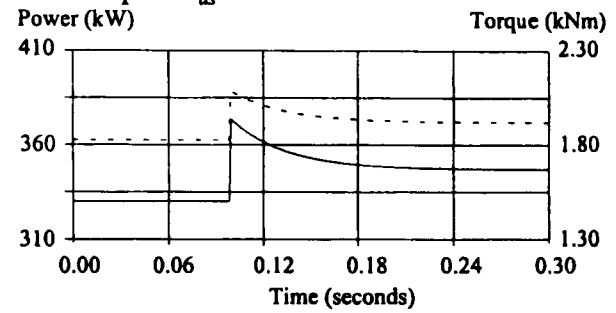
a) The open loop time response of (D.1) to a 5% step in V_{qs} .



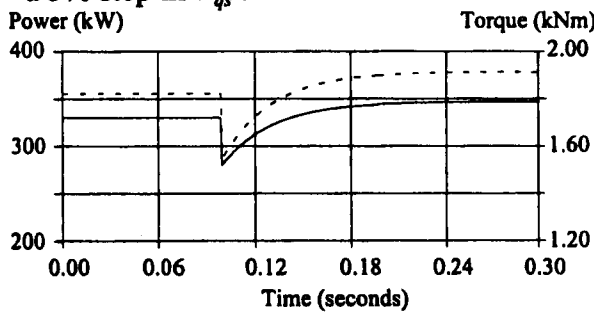
b) The open loop time response of (D.1) to a 5% step in V_{ds} .



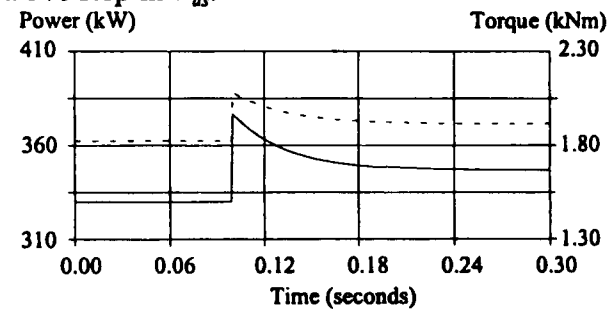
c) The open loop time response of (D.16) to a 5% step in V_{qs} .



d) The open loop time response of (D.16) to a 5% step in V_{ds} .



e) The open loop time response of (D.21) to a 5% step in V_{qs} .



f) The open loop time response of (D.21) to a 5% step in V_{ds} .

Key : ——— Power - - - - - Torque

Figure D.2 Step responses of voltage for the 60 Hz generator.

D.3 Simple linear models

When equations (D.16) are linearised about the rated operating point, the transfer function relating changes in slip, $\Delta\epsilon$, to changes in torque, ΔT_G , is

$$\Delta T_G = \frac{dT_G}{d\epsilon} \cdot H(s) \cdot \Delta\epsilon \quad (\text{D.18})$$

where

$$H(s) = \frac{[(s/\omega_s) \frac{\{K_3 + K_1(K_1K_3 - K_2K_4)\}}{\{K_3^2 + (K_1K_3 - K_2K_4)^2 - (1 + K_1^2)\epsilon^2\}} + 1]}{[(s/\omega_s)^2 \frac{(1 + K_1^2)}{\{K_3^2 + (K_1K_3 - K_2K_4)^2 - 2K_2K_4\epsilon + (1 + K_1^2)\epsilon^2\}} + (s/\omega_s) \frac{2\{K_3 + K_1(K_1K_3 - K_2K_4)\}}{\{K_3^2 + (K_1K_3 - K_2K_4)^2 - 2K_2K_4\epsilon + (1 + K_1^2)\epsilon^2\}} + 1]} \quad (D.19)$$

The change in power, ΔP , is related to the change in ΔT_G by

$$\Delta P = \Delta T_G \omega_{Ro} \text{Eff} \quad (D.20)$$

The time responses of the linear second order model, (D.18) to (D.20), to 5% and 30% steps in slip for the 60 Hz generator, Figures D.1e and D.1f, are very similar to those of the non-linear models (D.1) and (D.16).

The transfer functions relating changes in supply voltage components, ΔV_{qs} and ΔV_{ds} , to changes in torque, ΔT_G , are

$$\Delta T_G = \frac{dT_G}{d(\frac{1}{2}V_{qs}^2)} \cdot Q_1(s) \cdot \Delta V_{qs} \quad ; \quad \Delta T_G = \frac{dT_G}{d(\frac{1}{2}V_{ds}^2)} \cdot Q_2(s) \cdot \Delta V_{ds} \quad (D.21)$$

where

$$Q_1(s) = \frac{[(\frac{s}{\omega_s})^2 \frac{\{(1 + K_1^2)\epsilon - K_2K_4\} V_{qs} - (K_3 + K_1(K_1K_3 - K_2K_4)) V_{ds}}{2\epsilon\{K_3^2 + (K_1K_3 - K_2K_4)^2 - 2K_2K_4\epsilon + (1 + K_1^2)\epsilon^2\}} + (\frac{s}{\omega_s}) \frac{\{2\epsilon(K_3 + K_1(K_1K_3 - K_2K_4)) V_{qs} - (K_3^2 + (K_1K_3 - K_2K_4)^2 - (1 + K_1^2)\epsilon^2) V_{ds}\}}{2\epsilon\{K_3^2 + (K_1K_3 - K_2K_4)^2 - 2K_2K_4\epsilon + (1 + K_1^2)\epsilon^2\}} + V_{qs}]}{[(\frac{s}{\omega_s})^2 \frac{(1 + K_1^2)}{\{K_3^2 + (K_1K_3 - K_2K_4)^2 - 2K_2K_4\epsilon + (1 + K_1^2)\epsilon^2\}} + (\frac{s}{\omega_s}) \frac{2\{K_3 + K_1(K_1K_3 - K_2K_4)\}}{\{K_3^2 + (K_1K_3 - K_2K_4)^2 - 2K_2K_4\epsilon + (1 + K_1^2)\epsilon^2\}} + 1]} \quad (D.22)$$

and

$$Q_2(s) = \frac{[(s/\omega_s)^2 \frac{\{(K_3 + K_1(K_1K_3 - K_2K_4)) V_{qs} + ((1 + K_1^2)\epsilon + K_2K_4) V_{ds}\}}{2\epsilon\{K_3^2 + (K_1K_3 - K_2K_4)^2 - 2K_2K_4\epsilon + (1 + K_1^2)\epsilon^2\}} + (s/\omega_s) \frac{\{(K_3^2 + (K_1K_3 - K_2K_4)^2 - (1 + K_1^2)\epsilon^2) V_{qs} + 2\epsilon(K_3 + K_1(K_1K_3 - K_2K_4)) V_{ds}\}}{2\epsilon\{K_3^2 + (K_1K_3 - K_2K_4)^2 - 2K_2K_4\epsilon + (1 + K_1^2)\epsilon^2\}} + V_{ds}]}{[(s/\omega_s)^2 \frac{(1 + K_1^2)}{\{K_3^2 + (K_1K_3 - K_2K_4)^2 - 2K_2K_4\epsilon + (1 + K_1^2)\epsilon^2\}} + (s/\omega_s) \frac{2\{K_3 + K_1(K_1K_3 - K_2K_4)\}}{\{K_3^2 + (K_1K_3 - K_2K_4)^2 - 2K_2K_4\epsilon + (1 + K_1^2)\epsilon^2\}} + 1]} \quad (D.23)$$

The time responses of the linear second order models, (D.21) to (D.23), to 5% steps in V_{qs} and V_{ds} for the 60 Hz generator, Figures D.2e and D.2f, are again very similar to those of the non-linear models (D.1) and (D.16) in particular. Assuming

$$\Delta V_{qs} = \Delta E \cos(\omega_s t - \theta_s) \quad ; \quad \Delta V_{ds} = -\Delta E \sin(\omega_s t - \theta_s) \quad (D.24)$$

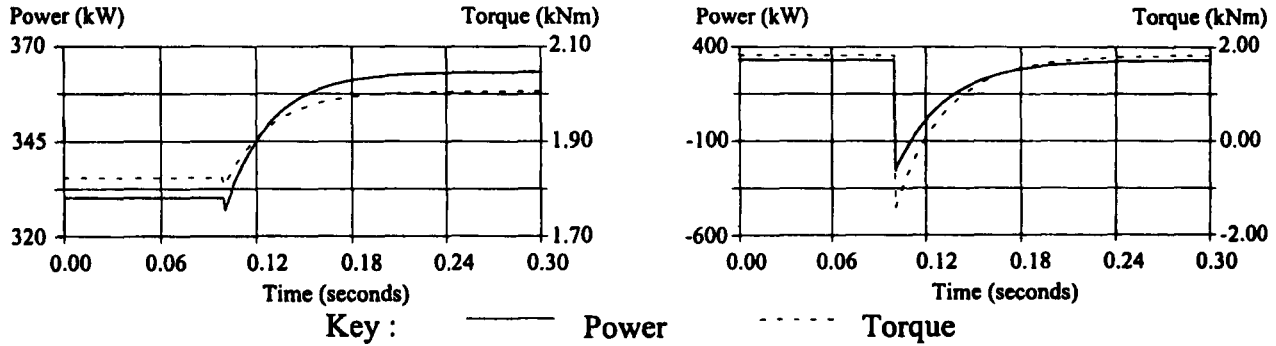
which is sufficient for investigating the dynamic response of the drive train to grid faults, the transfer function, relating changes in supply voltage, ΔE , to changes in torque, ΔT_G , is

$$\Delta T_G = \frac{dT_G}{dE} \cdot Q(s) \cdot \Delta E \quad ; \quad \frac{dT_G}{dE} = \frac{2T_{G0}}{E} \quad (\text{D.25})$$

where

$$Q(s) = \frac{[(s/\omega_s)^2 \frac{\{(1+K_1^2)\epsilon - K_2K_4\}}{2\epsilon\{K_3^2 + (K_1K_3 - K_2K_4)^2 - 2K_2K_4\epsilon + (1+K_1^2)\epsilon^2\}} + (s/\omega_s) \frac{\{K_3 + K_1(K_1K_3 - K_2K_4)\}}{\{K_3^2 + (K_1K_3 - K_2K_4)^2 - 2K_2K_4\epsilon + (1+K_1^2)\epsilon^2\}} + 1]}{[(s/\omega_s)^2 \frac{(1+K_1^2)}{\{K_3^2 + (K_1K_3 - K_2K_4)^2 - 2K_2K_4\epsilon + (1+K_1^2)\epsilon^2\}} + (s/\omega_s) \frac{2\{K_3 + K_1(K_1K_3 - K_2K_4)\}}{\{K_3^2 + (K_1K_3 - K_2K_4)^2 - 2K_2K_4\epsilon + (1+K_1^2)\epsilon^2\}} + 1]} \quad (\text{D.26})$$

The time response of the model (D.26) to a 5% step in E for the 60 Hz generator is depicted in Figure D.3.



a) The open loop time response of (D.26) to a 5% step in E . b) The open loop time response of (D.28) to a 5% step in phase in θ .

Figure D.3

Assuming

$$V_{qs} + \Delta V_{qs} = E \cos(\omega_s t - \theta_s - \Delta\theta_s) \quad ; \quad V_{ds} + \Delta V_{ds} = -E \sin(\omega_s t - \theta_s - \Delta\theta_s) \quad (\text{D.27})$$

the transfer function, relating changes in the phase of the supply voltage, $\Delta\theta_s$, to changes in torque, ΔT_G , is

$$\Delta T_G = -(\omega_s / p) D_e \cdot R(s) \cdot \Delta\theta_s \quad (\text{D.28})$$

where

$$R(s) = \frac{(s/\omega_s) \left[\left(\frac{s}{\omega_s} \right) \frac{\{K_3 + K_1(K_1K_3 - K_2K_4)\}}{\{K_3^2 + (K_1K_3 - K_2K_4)^2 - 2K_2K_4\epsilon + (1+K_1^2)\epsilon^2\}} + 1 \right]}{[(s/\omega_s)^2 \frac{(1+K_1^2)}{\{K_3^2 + (K_1K_3 - K_2K_4)^2 - 2K_2K_4\epsilon + (1+K_1^2)\epsilon^2\}} + (s/\omega_s) \frac{2\{K_3 + K_1(K_1K_3 - K_2K_4)\}}{\{K_3^2 + (K_1K_3 - K_2K_4)^2 - 2K_2K_4\epsilon + (1+K_1^2)\epsilon^2\}} + 1]} \quad (\text{D.29})$$

The time response of the model (D.29) to a 5% step in θ , for the 60 Hz generator is depicted in Figure D.3b.

The frequencies of the poles of (D.19) are close to the frequency of the zero since

$$\frac{[K_3 + K_1(K_1K_3 - K_2K_4)]}{[K_3^2 + (K_1K_3 - K_2K_4)^2 - (1+K_1^2)\epsilon^2]} \approx 1/K_3$$

and

$$\frac{(1 + K_1^2)}{[K_3^2 + (K_1K_3 - K_2K_4)^2 - 2K_2K_4\epsilon + (1+K_1^2)\epsilon^2]} \approx 1/K_3^2$$

$$\frac{[K_3 + K_1(K_1K_3 - K_2K_4)]}{[K_3^2 + (K_1K_3 - K_2K_4)^2 - 2K_2K_4\epsilon + (1+K_1^2)\epsilon^2]} \approx 1/K_3$$

Hence, the transfer function $H(s)$ may be approximated by

$$H^*(s) = \frac{1}{\frac{(s/\omega_s) \frac{[K_3 + K_1(K_1K_3 - K_2K_4)]}{[K_3^2 + (K_1K_3 - K_2K_4)^2 - (1+K_1^2)\epsilon^2]} + 1} \quad (D.30)$$

The Bode plots for $H(s)$ and $H^*(s)$ are depicted in Figure D.4 showing the close agreement.

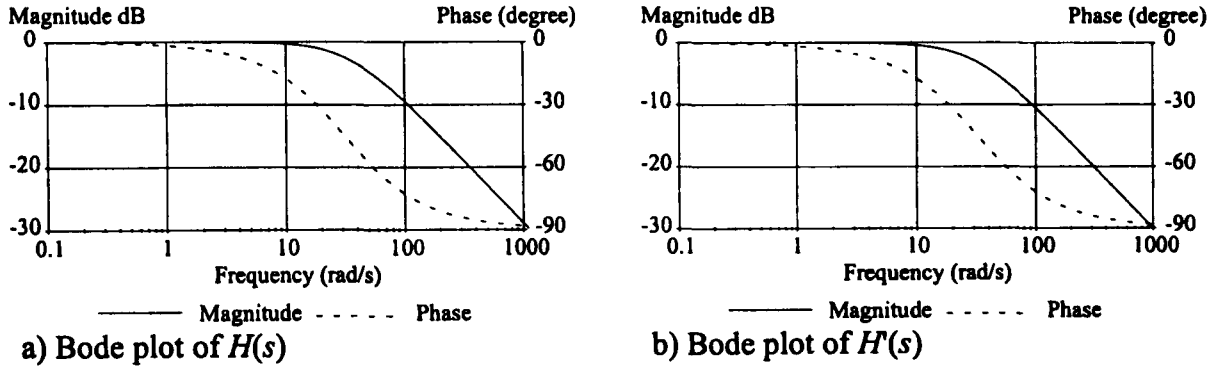


Figure D.4 Dynamic relationship of $\Delta\epsilon$ to ΔT_G .

Similarly, the transfer function $R(s)$ may be approximated by

$$R^*(s) = \frac{(s/\omega_s)}{\frac{\{K_3 + K_1(K_1K_3 - K_2K_4)\}}{[(s/\omega_s) \frac{\{K_3^2 + (K_1K_3 - K_2K_4)^2 - (1+K_1^2)\epsilon^2\}} + 1]} \quad (D.31)$$

However no corresponding simplification of $Q(s)$ is possible.

It follows from the above that a simple linear model for the generator dynamics, with the supply voltage constant, is

$$\tau \dot{T}_G + T_G = D_e(\omega_R - \omega_s/p) \quad (D.32)$$

where the time constant, τ , is

$$\tau = \frac{[K_3 + K_1(K_1K_3 - K_2K_4)]}{\omega_s [K_3^2 + (K_1K_3 - K_2K_4)^2 - (1+K_1^2)\epsilon^2]} \quad (D.33)$$

For the 60 Hz generator, the time constant is 31 msecs. The equation of motion for the mechanical aspect of the generator dynamics is

$$I \dot{\omega}_R = T_E - T_G - \gamma \omega_R \quad (\text{D.34})$$

where I is the generator rotor inertia, γ is the viscous damping coefficient and T_E is the external driving torque applied to the generator. The combined electrical and mechanical dynamics are depicted in Figure D.5. In general, the generator rotor inertia is small and D_e / I is much greater than 1. Consequently, the electrical dynamics of the generator are enclosed in a strong feedback loop and the disturbances due to ΔE and $\Delta \theta_s$ are rejected. Hence, any difference in the combined electrical and mechanical dynamics, when replacing the full non-linear description of the generator electrical dynamics (D.1) by (D.32) and the simple first order linear description (D.28), is minimised.

The simple model (D.32) is used to model the generator dynamics in Chapter 3, Appendix B and Chapter 4.

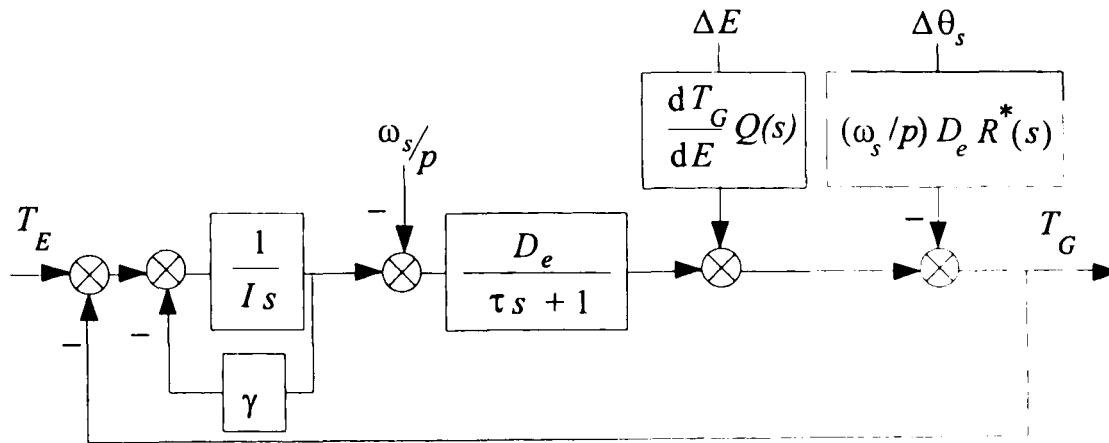


Figure D.5 The combined electrical and mechanical dynamics of the generator.

Appendix E Comparable machines

To compare the performance of wind turbines with different numbers of blades or power ratings without favouring one configuration over another, scaling of certain parameters is required. To obtain a set of comparable or 'equivalent' machines presents some difficulty as manufacturers tend to favour the characteristics they have used in the past (Armstrong, 1995). Table E.1 describes some characteristics of the wide variety of machines which have been built. This appendix describes the assumptions which have been made and the scaling which has been undertaken in an attempt to achieve a set of comparable machines. The appendix is in two parts. First it considers the scaling of comparable two- and three-bladed rotors. Secondly, it considers the effects on machine parameters of increasing rated power and varying rotor velocities. The majority of the relationships are based on simple scaling rules and are used to obtain the results described in Chapter 5 and 6.

Make	Size	No. of blades	Rotor radius	Tip speed
Nibe B	630 kW	3	20m	71 m/s
WTS 75 Nässudden	2MW	2	37.5m	98 m/s
Howden 330/33	330 kW	3	16.5m	60 m/s
Howden 1000/45	1 MW	3	27.5m	70 m/s
WEG MS3	300 kW	2	16.0m	84 m/s

Table E.1 Examples of different commercial wind turbine configurations

E.1 Equivalent rotor designs for two- and three-bladed machines

To obtain a set of unambiguously equivalent rotors to enable the comparison of two- and three-bladed wind turbines presents some difficulty (Jamieson and Brown, 1992). Harrison *et al.* (1990) and Platts (1990) both suggest that it is appropriate to compare blades of the same size for three- and two-bladed rotors. This implies a solidity ratio of $2/3$ and tip speed ratio of $3/2$ for the two-bladed rotor compared to the three-bladed rotor. If the tip speed of the three-bladed rotor is in the region of 60 to 70 m/s as is normal commercial practice, then a two-bladed machine with a tip speed in the range of 90 to 105 m/s would be unacceptable where noise is an issue. Such an increase in tip speed could also not be

accommodated without changing materials and stress limits. Commercial practice does not exhibit any general rules, see Table E.1, but three-bladed rotors usually have a lower tip speed than two-bladed rotors.

To ensure a fair comparison each rotor should be subject to similar stresses and the below rated performance should be similar. Hence a possible choice of criteria for comparable rotors is that they have

- (i) the same root stress;
- (ii) the same rated wind speed and similar performance below rated wind speed (Jamieson and Brown, 1992).

Two and three-bladed rotors are designed using aerodynamic strip theory (computer code - Anderson, 1990b) ensuring that the rotors have the same stress at the blade root and the same rotor weight (the blades being made of the same material). The following assumptions are made for each machine of the same power rating.

- (a) The radii of the rotors are the same.
- (b) The tip speeds are such that the stress at the blade root is the same for each machine; therefore the tip speeds vary.
- (c) The blade profile - the LS1 aerofoil - can be scaled to achieve criteria (i) and (ii).
- (d) The twist of the blades is the same on all rotors.

The assumption that the stress at the blade root is constant is an over-simplification as it takes no account of the design differences which will result if the two bladed machine is teetered as is usually the case.

Equivalent rotors are also required for the comparison of 300 kW and 1 MW rotors. There are intrinsic scaling rules applicable to increasing size (Frandsen *et al.*, 1984) and the assumptions made are discussed in Section E.2.

The section modulus of an aerofoil, as shown in Figure E.1, is proportional to

$$(T/c)^{1.2} (t/c)^{0.7} (x/c)^{0.9} c^3 \quad (\text{Jamieson, 1991}) \quad (\text{E.1})$$

where c is the chord

t is the thickness of the load bearing section

T is the depth of the chord

x is the width of the load bearing section

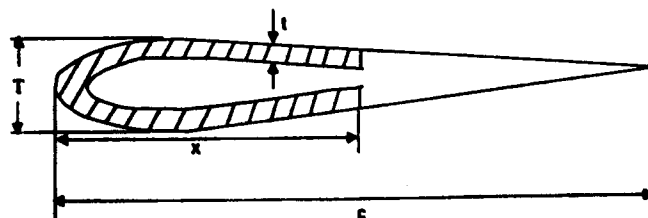


Figure E.1 An aerofoil.

On scaling the blade profile, T/c and x/c are constant so the section modulus scales as $t^{0.7} c^{2.3}$. Since, the stress on a blade, σ_n , is inversely proportional to the section modulus (Jamieson, 1991) and the number of blades, it follows that

$$s_n \propto t_n^{-0.7} c_n^{-2.3} n^{-1} \quad (\text{E.2})$$

where

t_n is the thickness of load bearing section on a n -bladed machine

c_n is the chord of a blade on a n -bladed machine

n is the number of blades

Since $n c_n$ is proportional to solidity, the optimum rotor speeds are related such that $n c_n \Omega_n$ is constant (Jamieson and Brown, 1992) where Ω_n is the rotor speed of a n -bladed machine. Therefore,

$$\Omega_n \propto (n c_n)^{-1} \quad (\text{E.3})$$

Using (E.2), two and three-bladed rotors have the same root bending stress provided

$$(t_2/t_3)^{0.7} = 3/2 (c_3/c_2)^{2.3} \quad (\text{E.4})$$

However, to obtain rotors of equal weight

$$2 c_2 t_2 = 3 c_3 t_3 \quad (\text{E.5})$$

Hence using (E.5), to eliminate t_2 and t_3 from (E.4)

$$(c_3/c_2)^{1.6} = (2/3)^{0.3}$$

and thus

$$c_3/c_2 = 0.9268$$

From (E.3), it follows that

$$\Omega_2/\Omega_3 = 3/2 c_3/c_2 = 1.39$$

The basic reference rotor is chosen to be a three-bladed rotor similar to that of the Howden HWP33/330. It has a radius of 16.5 m and a rotor speed of 3.64 rad/s which is equivalent to a tip speed of 60 m/s. The blade sections are the LS1 aerofoil. The rotors of the machines investigated in Chapters 5 and 6 are based on this Howden rotor as follows.

E.1.1 Equivalent rotors for the 300 kW machines

From the above analysis for the 300 kW machines, a two-bladed rotor with the same root bending moment as the three-bladed rotor has a tip speed of approximately 84 m/s and a chord 1.079 times that of the three-bladed machine. The radius is chosen to be the same as the three-bladed rotor and hence the rotor speed is 5.09 rad/s.

Rotor		I	II
No. of blades		2	3
Radius (m)		16.5	16.5
Tip speed (m/s)		84	60
Rotor speed (rad/s)		5.09	3.64
Rated power (kW)		300	300
Blade profile			
Radius	Twist	Chord	Chord
0.662	11.5	0.964	1.110
3.000	11.5	1.929	2.219
4.000	-	1.821	2.096
5.000	-	1.731	1.992
10.000	5.0	-	-
14.000	-	0.845	0.973
15.500	-	0.714	0.821
16.500	0.0	0.536	0.616

Table E.2 Machine parameters for 300 kW machines with equal stress at the blade root.

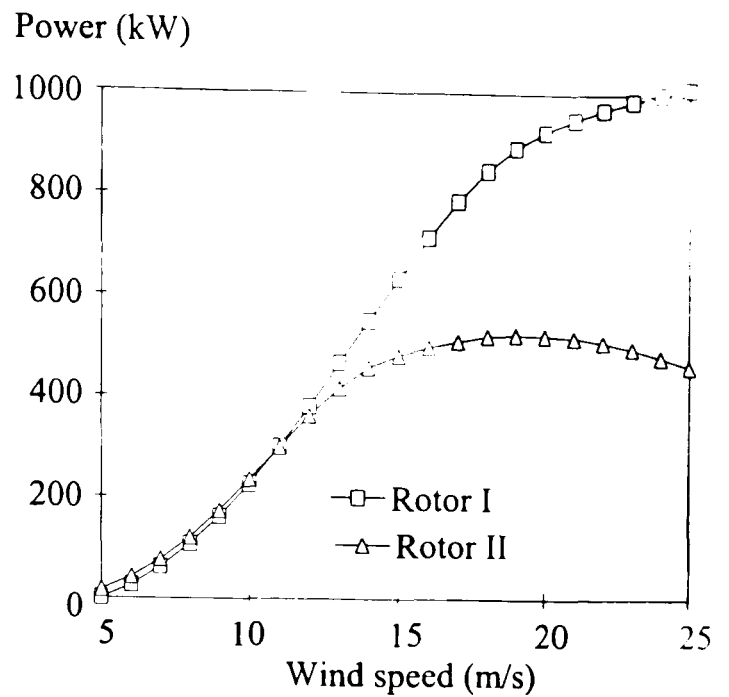


Figure E.2 Power curves for full-span regulated machines with Rotors I and II.

The details of the two rotors are summarised in Table E.2 and the corresponding power curves are shown in Figure E.2. The power curve for the two-bladed wind turbine is very similar to that of the WEG MS3. However, the two curves in Figure E.2 differ below rated power, 300 kW, and hence do not satisfy design criterion (ii). Hence a second definition of equivalent rotors is also considered.

The properties of the two-bladed rotor are satisfactory, but the three-bladed rotor must be amended for the two rotors to be considered equivalent. Criterion (i) for equivalent rotors must be relaxed. It can be replaced by the requirement that three-bladed rotors have the same tip speed as the two-bladed rotor and the same solidity, that is, $2c_2 = 3c_3$.

The blade profile of the two-bladed rotor in Table E.2 is scaled to obtain blade profiles for the three-bladed rotors, see Table E.3. The corresponding power curves are shown in Figure E.3a. The power curves are not similar for below rated wind speed. Fortunately relatively slight changes in radii and compensatory changes in blade profile reduce these differences. The properties of the three-bladed rotor, so obtained, are summarised in Table E.3 and Figure E.3b.

Rotor III Scaled from two bladed rotor Rotor radius = 16.5 m			Rotor IV Adjusted rotor radius Rotor radius = 16.15 m		
Radius	Chord	Twist	Radius	Chord	Twist
0.662	0.643	11.5	0.648	0.657	11.5
3.000	0.876	11.5	2.936	1.314	11.5
4.000	0.827	-	3.915	1.240	-
5.000	0.383	-	4.894	1.179	-
10.000	-	5.0	9.788	-	5.0
14.000	0.563	-	13.703	0.575	-
15.500	0.476	-	15.171	0.486	-
16.500	0.357	0.0	16.150	0.365	0.0

Table E.3 Blade profile for three-bladed rotors with a tip speed of 84 m/s for various radii.

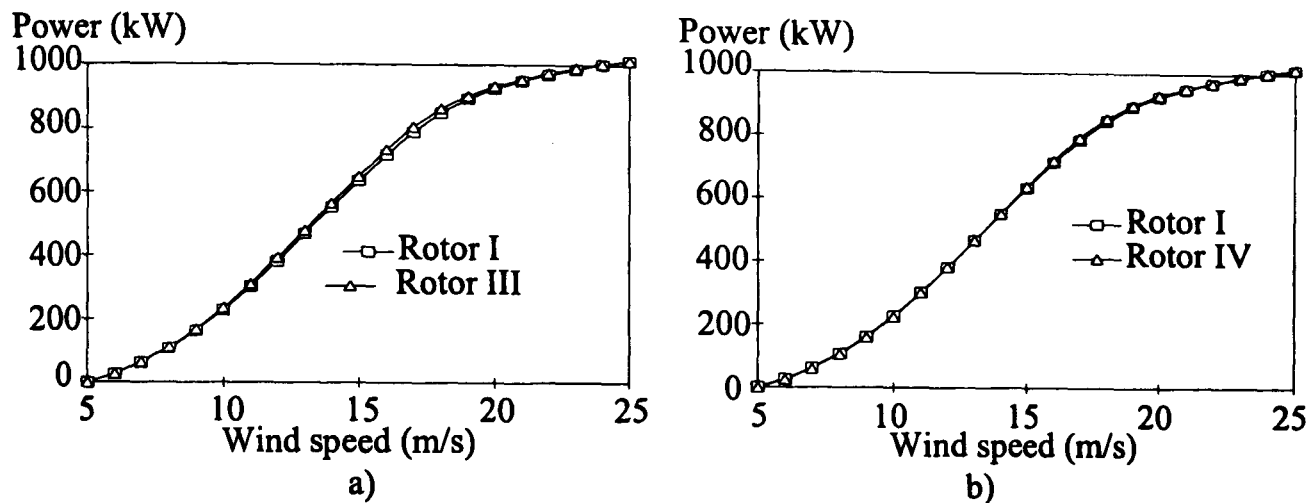


Figure E.3 Power curves for Rotors III and IV.

The performance of the two-bladed rotor is acceptable as a basis for comparison. However, as discussed earlier, the speed of the three-bladed rotor is expected to be less than that of the two-bladed one. Hence this approach is not entirely satisfactory either.

A compromise between the two approaches described probably represents the best approach to defining equivalent three-bladed rotors. The rotor speed for the three-bladed rotor is chosen to be 66 m/s. The radius of the rotor is chosen so that the below rated performance of all three rotors is similar. The properties of the three-bladed rotor, so obtained, are summarised by Tables E.4.

The set of rotors chosen for the purpose of comparing the performance of different wind turbine configurations are Rotor I of Table E.2 and the Rotor V of Table E.4. However, to investigate the sensitivity of performance to tip speed, the set of rotors is enlarged by the inclusion of Rotor IV of Table E.3. The power curves of the three rotors with no control are shown in Figure E.4. The blade pitch angle corresponding to rated power as wind speed varies is depicted in Figure 5.1 for all three 300 kW full-span regulated rotors.

The corresponding torque tables for each of the three rotors, together with the aerodynamic torque partial derivatives are given in Tables G.1 and G.2.

Rotor V - rotor radius = 16 m		
Radius	Chord	Twist
0.642	0.873	11.5
2.909	1.856	11.5
3.879	1.753	-
4.848	1.666	-
9.697	-	5.0
13.576	0.814	-
15.030	0.687	-
16.000	0.516	0.0

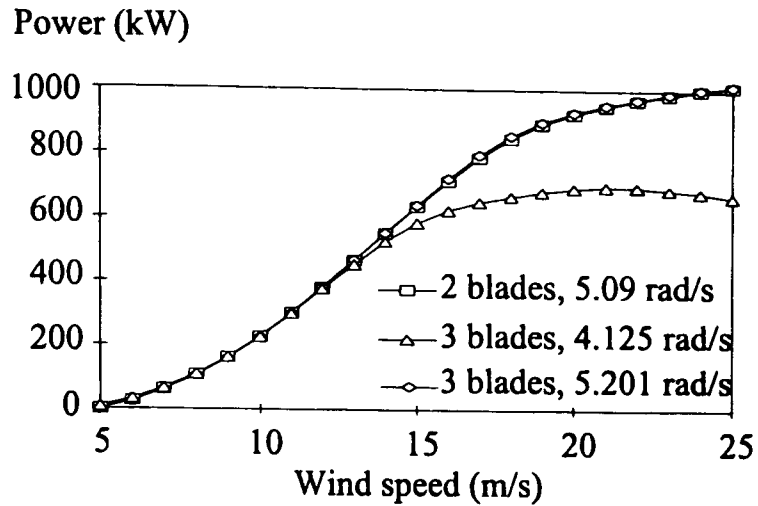


Table E.4 Blade profile for three-bladed machine with a tip speed of 66 m/s. **Figure E.4** Power curves for Rotors I, IV and V with no control.

Configurations with part-span regulation are also investigated. Suitable tip sizes for each of the three rotors are chosen on basis of the requirement that the tips would be used to shut down the machine in a 30 m/s wind speed. The tip sizes for each rotor are given in Table E.5. The tip pitch angle corresponding to rated power as wind speed varies is depicted in Figure 6.1 for all three 300 kW tip-regulated rotors. The corresponding torque tables for each of the three tip-regulated rotors, together with the aerodynamic torque partial derivatives are given in Tables G.3 and G.4.

Number of blades	2	3	3
Tip speed (m/s)	84	84	66
Radius (m)	16.50	16.15	16.00
Tip length (m)	3.5	3.5	3.0

Table E.5 Tip sizes for each of the 300 kW tip regulated machines.

E.1.2 Equivalent rotors for the 1 MW machines

For the 1 MW machines the basic reference rotor was initially chosen to be a three-bladed rotor similar to that of the Howden HWP55/1000 machine at Richborough. It has a radius of 27.5 m and a rotor speed of 2.544 rad/s (Leithead *et al.*, 1991a), which is equivalent to a tip speed of 70 m/s. The blade sections are the LS1 aerofoil. The Richborough machine is a tip-regulated machine with a tip 4 m long. However, using the aerodynamic torque coefficient program (Anderson, 1990b) the tip angle versa wind speed curve for rated power is not monotonic at high wind speeds. Hence a machine with these aerodynamic

characteristics is not controllable on high wind speed sites if the changes in the aerodynamic gain due to changes in wind speed are scheduled as described in Appendix C. It was investigated whether this problem could be avoided by increasing the length of the tip. However, due to the internal inaccuracy of the aerodynamic program, it predicted that the tip was required to be 6 m long before the tip angle versus wind speed curve was monotonic. A tip this size (relative to the rotor radius) loses the aerodynamic features of a tip-regulated machine compared with a full-span pitch machine and hence was considered unrealistic. For this reason the rotor radius was increased to 30 m and the solidity of the blade adjusted accordingly. It should be noted that this is rather large for a 1 MW wind turbine when compared with the size of 1 MW wind turbines being developed under CEC JOULE (e.g. ELKRAFT 1 MW, a full-span pitch regulated machine which has a rotor radius of 25 m). However, to ensure that the rotor behaviour for all the 1 MW machines considered is similar when in below-rated wind speeds a rotor radius of 30 m is chosen. In reality the radius of a 1 MW full-span pitch regulated machine would probably be smaller than this.

As with the 300 kW machines, three 1 MW rotors were considered. The two-bladed rotor has a tip speed of approximately 84 m/s and the tip speed for the three-bladed rotor is chosen to be either 66 m/s (which has a similar rotor bending moment to the two-bladed machine), or 84 m/s (which has a same solidity to the two-bladed machine). As previously the radii of the rotors are adjusted slightly so that the below rated performance of all three rotors is similar. The properties of the three rotors, so obtained, are summarised in Table E.6. The power curves of the three rotors with no control is shown in Figure E.5. The blade pitch angle corresponding to rated power as wind speed varies is depicted in Figure 5.1 for all three 1 MW full-span regulated rotors. The corresponding torque tables for each of the three rotors, together with the aerodynamic torque partial derivatives are given in Tables G.1 and G.2.

Suitable tip sizes for each of the tip-regulated machines are chosen on basis of the requirement that the pitch versus wind speed curve is monotonic with increasing wind speed and the machine can be braked in 30 m/s wind speed. The tip size for each tip is given in Table E.7. The tip pitch angle corresponding to rated power as wind speed varies is depicted in Figure 6.1 for all three 1 MW tip regulated rotors. The corresponding torque tables for each of the three rotors, together with the aerodynamic torque partial derivatives are given in Tables G.3 and G.4.

Rotor No. of blades	VI 2		VII 3		VIII 3	
Radius (m)	30.0		29.44		29.33	
Tip speed (m/s)	85		84		66	
Rotor speed (rad/s)	2.8		2.85		2.25	
Rated Power (kW)	1000		1000		1000	
Blade profile						
Twist	Radius	Chord	Radius	Chord	Radius	Chord
11.5	1.204	1.752	1.181	1.191	1.177	1.674
11.5	5.454	3.505	5.353	2.381	5.333	3.347
-	7.273	3.310	7.137	2.249	7.110	3.161
-	9.091	3.147	8.921	2.139	8.888	3.005
5.0	18.182	-	17.842	-	17.776	-
-	25.454	1.536	24.979	1.044	24.886	1.467
-	28.182	1.297	27.656	0.881	27.552	1.239
0.0	30.000	0.974	29.440	0.661	29.33	0.930

Table E.6 Rotor parameters for 1 MW machines.

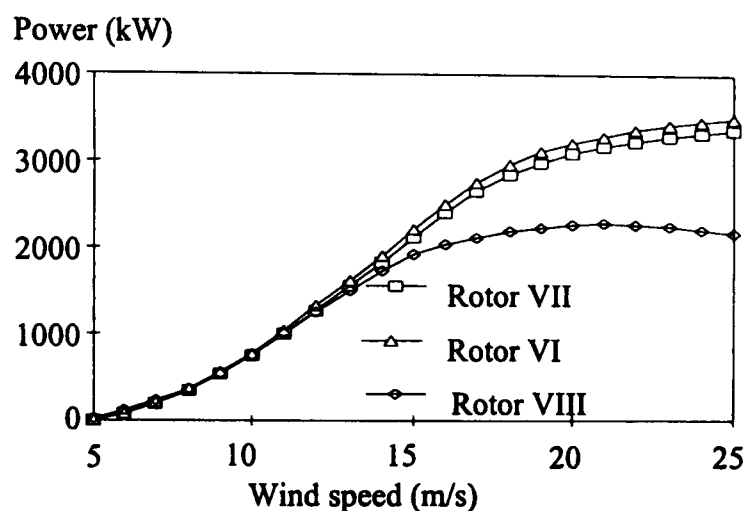


Figure E.5 Power curves for Rotors VI, VII and VIII with no control.

Number of blades	2	3	3
Tip speed (m/s)	84	84	66
Radius (m)	30	29.6	29.4
Tip length (m)	5.12	5.14	5.00

Table E.7 Tip sizes for each 1 MW configuration.

E.1.3 Discussion

Two- and three-bladed machines have been compared by, amongst others, Platts (1990) who claims that two-bladed machines are cheaper to build. However, Platt (1990) compared machines with blades of equal weight and assumed that weight is directly proportional to cost. In an attempt to be more realistic, the rotors designed here and compared in Chapters 5 and 6 are assumed (see Table 5.1) to have either similar weights, e.g. Rotors I and IV, and VI and VIII (where the weight has been maintained by adjusting the load bearing thickness of the airfoil), or similar solidities (in which case the three-bladed

rotor is approximately 50% heavier than the two-bladed one , *i.e.* Rotors I and V, and VI and VII. It could be argued that the comparisons of Rotors I and IV, and VI and VIII are not totally realistic since it has been assumed that the load-bearing thickness of the aerofoil of a two-bladed machine is greater than that on a three-bladed machine. However, to provide a valid basis for comparison it was necessary to make this assumption. In practice, however, if the aerofoils of a two-bladed machine and a three-bladed one had identical load-bearing thicknesses, the rotor of the three-bladed machine would weigh 30% more than that of the two-bladed machine and not 50% more as assumed by Platts (1990). The extra weight would require larger bearings at the hub. This additional mass, and hence increase in rotor inertia, although costing more in materials, would improve power control performance (see Chapter 3).

Unlike three-bladed machines, two-bladed machines also require a teetering mechanism at the hub to reduce the otherwise unacceptably large flap-wise blade loads.

Table E.8 gives a summary of some of the pros and cons of two- and three-bladed wind turbines.

	Two blades	Three blades
Advantage	Less material to build rotor.	No teetering required.
Disadvantages	Requires teetering	More material to build rotor.

Table E.8 Comparison of the advantages of two- and three-bladed machines.

For full-span regulated machines, the blades are normally actuated in unison at the hub where space is not too limited. On tip-regulated machines, separate actuators at the tips are required where space is very limited and some 'communication' is needed from the tips to the hubs where synchronisation is normally controlled. This communication could be, for example, by cables or hydraulics. Tip devices are lighter than full-span devices and so faster actuator accelerations and velocities can be achieved on tip-regulated machines for the same motive force. If tip devices are electromechanically driven there may be safety implications due the risk of lightning strikes (Agius *et al.*, 1993). Hence tip-regulated machine actuators tend to be hydraulically driven. The long stretch of hydraulic piping required leads to problems with tip synchronisation as seen on the Howden HWP1000/45 machine at Richborough (Leithead *et al.*, 1991a). Tip devices may also require additional structural mass to support the tip actuators and hence increase slightly the rotor inertia.

Assuming steady-state loading, the use of full-span blade pitch gives rise to higher fatigue loading at the blade root (40% on Howden HWP330/33 - Anderson, 1990a), but lower fatigue loading at the tip joint (60% on Howden HWP330/33 - Anderson, 1990a).

Table E.9 summarises the advantages and disadvantages of full-span and tip regulation.

	Full-span	Tip
Advantages	No problem with space for actuator nor synchronisation	Lighter inertia - possible actuator rates faster. Worse flap-wise tip moments (Anderson, 1990).
Disadvantages	Worse root flap-wise moments (Anderson, 1990).	May need more structure in tip to support actuator mechanism. Long hydraulic pipes or electrical wires from hub to tips Problems may arise in space to fit actuators in tip. Problems may arise with synchronisation

Table E.9 Comparison of the advantages of full-span and tip regulation.

E.2 The effects of power rating and rotor speed on machine parameters

E.2.1 Wind model

The wind model depends on the size of the rotor and hub height as explained in Appendix A. In keeping with commercial practice, a hub height of 30 m was assumed for the 300 kW machines, while 50 m was assumed for the 1 MW machines.

E.2.2 Spectral loads

The model for the spectral loads seen in the drive-train is described by (3.6) and (3.7). (3.6) has two parameters, a_{nr} and b_{nr} , which depend on the machine configuration. The width of the spectral peak at 3 dB below its maximum value is $2a_{nr}$. The standard deviation of the drive-train loads at $n\Omega$ are determined by $\sqrt{b_{nr}^2 / 2a_{nr}}$. Using this information typical intensities of the $n\Omega$ loads for below rated operation have been inferred from data monitoring programmes previously conducted on commercial two- and three-bladed machines. (WEG MS3 - Leithead and Agius, 1991, Howden HWP330/33 - Wilkie *et al.*, 1989, Howden HWP1000/45 - Leithead *et al.*, 1991a). The parameters for the three-bladed machines and the two bladed 1 MW machine are scaled from the model values obtained for the corresponding commercial machines. The scaling of model parameter a_{nr} is scaled by the rotor velocity. Unfortunately no measured data is available from a commercial two-bladed 1 MW machine. The parameter a_{nr} is scaled as follows

$$a_{nr} = \frac{a_{nr \text{ 2 bladed 300 kW}}}{\Omega_o \text{ 2 bladed 300 kW}} \cdot \frac{\Omega_o \text{ 3 bladed 300 kW}}{a_{nr \text{ 3 bladed 300 kW}}} \cdot \frac{a_{nr \text{ 3 bladed 1 MW}}}{\Omega_o \text{ 3 bladed 1 MW}} \cdot \Omega_o \text{ 2 bladed 1 MW}$$

The intensity of the peak is assumed to be that of the two-bladed 300 kW machine scaled by the square of the ratio of the power ratings. The parameter values used for each configuration are given in Table C.1.

E.2.3 Effect of size on machine parameters

The drive-train parameters used for the 300 kW and 1 MW machines investigated in Chapters 5 and 6 are based on those from commercial machines and are listed in Table E.10 and Table E.11 respectively. The stiffness and inertia of the low-speed shaft are adjusted to obtain the first drive-train frequency and damping factor as required using (3.19) and (3.21). The gearbox ratio and torque speed curve are calculated as follows:

$$N = (slip + 1)\theta_G / p \quad (E.6)$$

$$De = \frac{P_r \cdot p^2}{Effy \cdot slip(slip + 1)\theta_G^2} \quad (E.7)$$

where P_r is rated power

p is the number of generator pole pairs

$Effy$ is the efficiency of the generator and gearbox.

Machine parameter	Value	Machine parameter	Value
Inertia of high speed shaft	3.8 kgm ²	Inertia of high speed shaft	55 kgm ²
Stiffness of high speed shaft	3.01E+5 Nm/rad	Stiffness of high speed shaft	4.848E+6 Nm/rad
Generator slip	1.5%	Generator slip	1.0%
Gearbox and generator efficiency	91%	Gearbox and generator efficiency	95 %
Generator time constant	0.03 s	Generator time constant	0.05s
Power transducer time constant	0.02 s	Power transducer time constant	0.02
No. of pole pairs	2	No. of pole pairs	3
Grid frequency	50 Hz	Grid frequency	50 Hz

Table E.10 Parameters for 300 kW machines. **Table E.11** Parameters for 1 MW machines.

The actuator parameters used for the 300 kW and 1 MW machines investigated in Chapters 5 and 6 are listed in Tables E.12.

Actuator parameter	300 kW	1 MW
Pitch transducer time constant (s)	0.005	0.05
Tacho gain (V/rad/s)	0.032	0.32
Servo gain (Nm/V)	63	63
Pitch transducer gain (V/rad)	12.5	12.5
Servo inertia (Kgm ²)	0.011	1.1
Servo time constant (s)	0.0035	0.035

Table E.12 Actuator parameters.

Appendix F Modelling of novel tip devices

The modelling of two novel tip devices, the fledge and the compliant tip, is described in this appendix. The models are used in determining the power-control performance of the devices, which is described in Chapter 7.

When a wind turbine loses the grid connection or has a gearbox failure the rotor can accelerate to extremely high speeds, which may cause structural damage. Therefore braking devices are required to be fast-acting and reliable. Typically, two independent brakes are needed for emergency braking to satisfy safety requirements, such as those of Germanisher Lloyd (1993). Historically tips were considered as suitable air brakes as they are lighter than full-span pitch regulation devices and the majority of the aerodynamic lift comes from the last sixth of the blade. The design of the size of the tip is dictated by its braking ability. Hence the geometry of a fledge used for power control should also be dictated by its braking capability. In the first section of this appendix, the dynamic behaviour of the fledge is described, and an investigation into the effect of its geometry and masses on its braking ability. In the second section the modelling of the compliant tip is described.

Both these novel devices are investigated when mounted on a machine based on the Howden HWP33/330, which is a 300 kW, three-bladed, tip-regulated machine whose physical parameters are listed in Table F.1. Experimental measurements have been made on two of these machines in the Howden Altamont Pass wind farm (Anderson, 1990a, Anderson and Jamieson, 1988) which have been extensively studied (Jamieson 1993). The transfer function of the power train (the relationship between the aerodynamic torque, T_{aero} , and the electrical power at the generator, P_e) using the parameters in Table F.1 and (3.31) is

$$G(s) = \frac{89.77}{(s^2 + 3.067s + 25.78)(s^2 + 1.933s + 2322)} \quad (\text{F.1})$$

and its Bode plot is shown in Figure F.1. The first drive-train mode is at 5.08 rad/s, and the second is at 48.19 rad/s. The damping ratio of the first drive-train mode is 0.302.

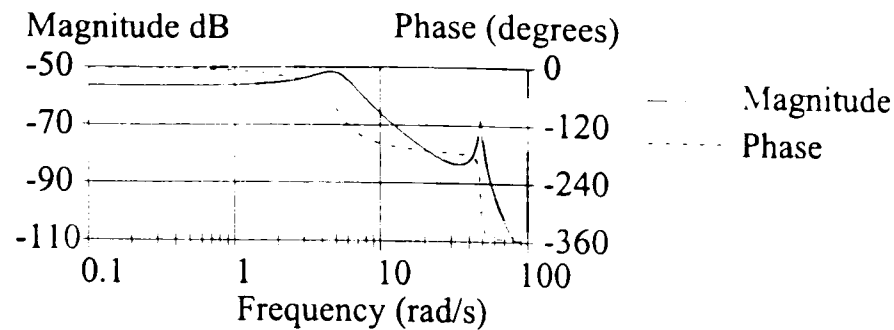


Figure F.1 Bode plot of the power-train transfer function of the Howden HWP33/330.

F.1 The ball-joint fledge

In this section, the equations of motion for three independent fledges are derived and the geometry suitable for emergency braking is described. These are used in Chapter 7 to assess power control performance

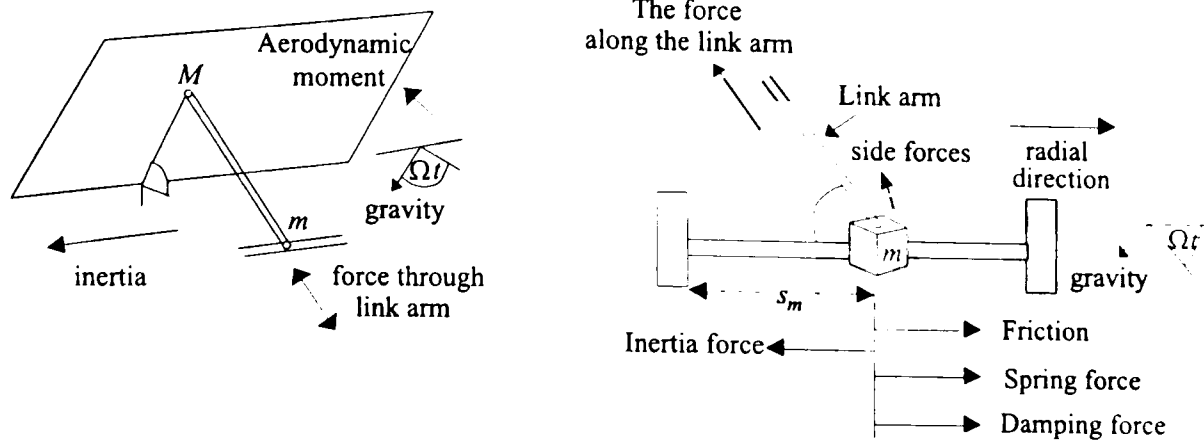
The UK Department of Energy supported two studies to investigate the feasibility of the fledge. The first, by Jamieson and Agius (1989), investigated the aerodynamic behaviour of the fledge, while the second led by the National Wind Turbine Centre (NWTC 1994) investigated the dynamics of the device as a brake and a power control device by simulation. The NWTC study also investigated the mechanical design of the fledge and tested a scale model in the laboratory. As part of that, the equations of motion below were derived by Jamieson and used here to investigate the braking and power control behaviour of the device.

F.1.1 The forces acting on the fledge plate

For the case of braking, *e.g.* when the rotor speed reaches a critical level - above 110% rated, the three fledges are allowed to move. Since the forces acting on the three fledges are different the simulation must cater for the dynamic effects caused by them moving independently.

When the fledge plate and the sliding mass are allowed to move by a release mechanism (different types of which are considered in NWTC (1994)), the plate then opens under the aerodynamic moment acting on the plate and the inertial force acting on the sliding mass. Opposing the opening is static friction along the slide which it is assumed can be ignored. When the fledge plate is fully open it acts as an efficient braking device (Jamieson and Agius, 1990). The forces acting on the fledge mechanism are shown in Figure F.2. As the plate opens, the aerodynamic lift is reduced to zero and then drag increasingly opposes the opening. When the plate reaches 90° it is stopped from opening further as the mass is at the end of the slide. Then the static friction on the slide opposes the plate closing. Once the

angle of fledge deployment is larger than a critical angle the rotor speed starts to decrease as the fledge acts as a brake.



M is the mass of the fledge plate

s_m is the displacement of the mass along the slide

g is gravity

m is the mass of the sliding mass

Ω is the rotor speed

a) The forces acting on the fledge plate

b) The forces acting on the sliding mass

Figure F.2 The forces acting on the fledge.

F.1.1.1 The aerodynamics of the fledge

The aerodynamic torque of the fledge, T_{aero} , is calculated using tables of C_q values parameterised by the tip-speed ratio, λ , and the angle of rotation of the fledge plate, θ (NWTC, 1994) and

$$T_{aero} = 0.5\pi\rho R^3 V^2 C_q(\theta, \lambda) \quad (F.2)$$

The aerodynamic moment acting on the fledge plate is calculated from

$$M_{aero}(\lambda, \theta, \dot{\theta}) = -1/2\rho(V^2 + (\Omega R + r_e \dot{\theta})^2) c_m c^2 l \quad (F.3)$$

where r_e is the effective radius to the centre of pressure of fledge plate

c is the chord of the blade

l is the length of the fledge

c_m is the pitching moment coefficient

The pitching moment, c_m , is an empirical fit to experimental data supplied by Howden, as

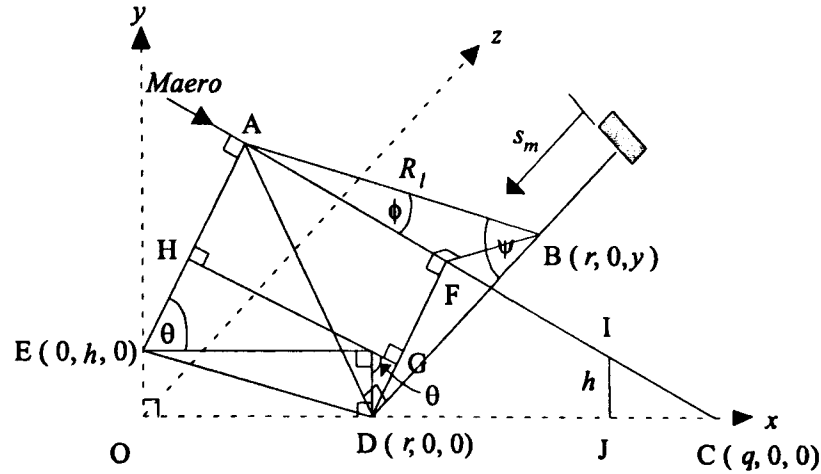
$$c_m = 0.13\theta^2 - 0.19\alpha - 0.02 \quad (F.4)$$

where α is the angle of attack, which from a simple velocity triangle is

$$\alpha = \tan^{-1}(V / \Omega R + r_e \dot{\theta}) \quad (F.5)$$

F.1.2 The geometry of the fledge

Figure F.3 shows a schematic diagram of the fledge mechanism where it is assumed that the fledge plate has a centre of mass at A and mass M ; the sliding mass has a centre of mass at B and mass m ; the points, A, C, D, O and E all lie in the x, y plane; and the hinge and the slide run parallel to the z axis. It is also assumed that the link arm is attached to A and B.



where r is the distance from the centre of mass of the fledge plate to the axis of rotation
 h is the offset normal to rotor plane of axis of rotation of the fledge plate
 R_l is the length of the link rod
 ψ is the angle between the link rod and the radial direction
 ϕ is the angle between the link arm and normal to the fledge plate

Figure F.3 The geometry of the ball-joint fledge.

The length of travel of the sliding mass, s_m , is

$$s_m = R_l (\cos \psi_o - \cos \psi) \quad (\text{F.6})$$

where $\sin \psi_o = h / R_l$

R_l is the length of the link rod

ψ_o is the value of ψ when the fledge plate is closed, *i.e.* $\theta = 0$.

From triangles AED, ABD and EOD,

$$R_l^2 \sin^2 \psi = 2r^2 + h^2 - 2r(r \cos \theta - h \sin \theta) \quad (\text{F.7})$$

The distance the mass has moved along the slide, s_m , is obtained from (F.2) and (F.3), as

$$s_m = R_l \cos \psi_o - \sqrt{(R_l^2 - 2r^2 - h^2 + 2r^2 \cos \theta - 2rh \sin \theta)} \quad (\text{F.8})$$

The acceleration and velocity of the sliding mass can be calculated by differentiating (F.8).

From triangle ABD,

$$y = BD = R_l \cos \psi \quad (\text{F.9})$$

From triangles AEI and ICJ,

$$q = OC = EI + JC = (r + h \sin \theta) / \cos \theta \quad (\text{F.10})$$

From quadrilateral AFHG and triangle ABF,

$$\cos \phi = (r \sin \theta + h \cos \theta) / R_l \quad (\text{F.11})$$

F.1.3 The equations of motion of the fledge

Projecting the co-ordinates on to the rotor plane, from Figure F.4, B has the co-ordinates $((R_o + sm) \cos \xi, (R_o + sm) \sin \xi, 0)$ and A' has the co-ordinates $(\tau \cos \xi - r(1 - \cos \theta) \sin \xi, \tau \sin \xi - r(1 - \cos \theta) \cos \xi, r \sin \theta + h)$, where $\tau = (R_o + R_l \cos \psi_o)$

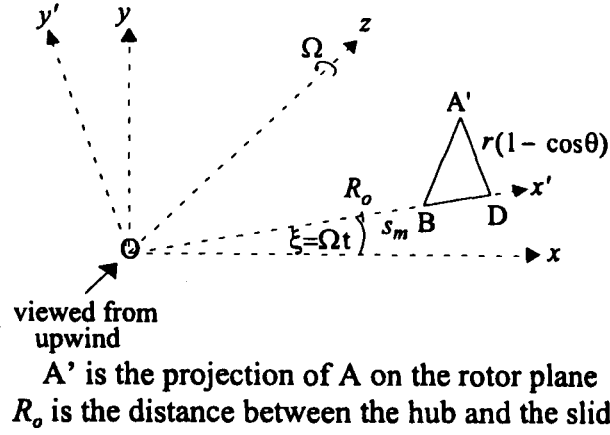


Figure F.4 The geometry of the ball-joint fledge.

The kinetic energy for three fledges and the rotor inertia is

$$\begin{aligned} T &= \frac{1}{2} \sum_{i=1}^3 \left[M(\dot{x}_{Ai}^2 + \dot{y}_{Ai}^2 + \dot{z}_{Ai}^2) + m(\dot{x}_{Bi}^2 + \dot{y}_{Bi}^2 + \dot{z}_{Bi}^2) \right] + \frac{1}{2} I_{rot} \Omega^2 \\ &= \frac{1}{2} M \sum_{i=1}^3 \left[\tau^2 \Omega^2 + r^2 (1 - \cos \theta_i)^2 \Omega^2 + r^2 \dot{\theta}_i^2 + 2\tau r \Omega \dot{\theta}_i \sin \theta_i \right] \\ &\quad + \frac{1}{2} m \sum_{i=1}^3 \left[(R_o + s_{m_i})^2 \omega^2 + \dot{s}_{m_i}^2 \right] + \frac{1}{2} I_{rot} \Omega^2 \end{aligned} \quad (\text{F.12})$$

where $i = 1, 2, 3$ and I_{rot} is the inertia of the rotor.

The potential energy for three fledges is

$$V = \sum_{i=1}^3 \left[mg(R_o + s_{m_i}) \sin \xi_i + Mg[\tau \sin \xi_i + r(1 - \cos \theta_i) \cos \xi_i] + \frac{m}{2} k_s s_{m_i}^2 + \frac{m}{2} k_d s_{m_i} \dot{s}_{m_i} \right] \quad (\text{F.13})$$

where $\xi_i = \Omega t + 2\pi(i - 1) / n$

k_s is the spring coefficient of the slide

k_d is the damping coefficient of the slide

Equations of motion for a fledge plate

The equations of motion for a fledge plate can be obtained from

$$\frac{d}{dt} \left(\frac{\partial(T+V)}{\partial \dot{\theta}_i} \right) - \frac{\partial(T+V)}{\partial \theta_i} = Maero_i - Q_i r \cos \phi_i - T_i \quad (\text{F.14})$$

where $\cos \phi_i = (r \sin \theta_i + h \cos \theta_i) / R_l$

$Maero_i$ is the fledge aerodynamic pitching moment

T_i is any external force opposing the opening of the fledge plate

Q_i is the force in the link arm

Hence,

$$\begin{aligned} Mr^2 \ddot{\theta}_i = & -Mtr\dot{\Omega} \sin \theta_i + Mr^2 (1 - \cos \theta_i) \sin \theta_i \Omega^2 - Q_i r (r \sin \theta_i + h \cos \theta_i) / R_l \\ & - T_i - Mgr \cos(\Omega t + (i-1)2\pi/n) \sin \theta_i + Maero_i \end{aligned} \quad (\text{F.15})$$

Equations of motion for the sliding mass

$$\frac{d}{dt} \left(\frac{\partial(T+V)}{\partial \dot{s}_{m_i}} \right) - \frac{\partial(T+V)}{\partial s_{m_i}} = Q_i \cos \psi_i - T_{is} - F_i$$

where F_i is the friction force opposing the mass moving along the slide

T_{is} is an external force acting on the sliding mass opposing increasing s_{m_i}

The accelerating of each actuation mass, ignoring friction which is small, is described by

$$\begin{aligned} \ddot{s}_{m_i} = & \Omega^2 (R_o + s_{m_i}) + \frac{Q_i}{mR} (R_l \cos \psi_o - s_{m_i}) - k_s s_{m_i} - k_d \dot{s}_{m_i} \\ & - g \sin(\Omega t + (i-1)2\pi/n) - \frac{T_{is}}{m} \end{aligned} \quad (\text{F.16})$$

Equations of motion for the rotor

$$\frac{d}{dt} \left(\frac{\partial(T+V)}{\partial \dot{\xi}} \right) - \frac{\partial(T+V)}{\partial \xi} = \sum_{i=1}^3 \frac{Taero_i}{3} - Torgen \quad (\text{F.17})$$

where $\dot{\xi} = \omega$ and $\partial T / \partial \xi = 0$

$Taero_i$ is the torque at the rotor due to the i^{th} fledge

$Torgen$ is the torque experienced on the rotor from the generator

The acceleration of the rotor is described by

$$\dot{\Omega} = \frac{\sum_{i=1}^3 \frac{Tor_i}{3} - Torgen - M\tau r \sum_{i=1}^3 (\ddot{\theta}_i \sin \theta_i - \dot{\theta}_i^2 \cos \theta_i) - \omega \left(2Mr^2 \sum_{i=1}^3 (1 - \cos \theta_i) \sin \theta_i \dot{\theta}_i + 2m \sum_{i=1}^3 (R_o + s_{m_i}) \dot{s}_{m_i} \right) - mg \sum_{i=1}^3 (R_o + s_{m_i}) \cos(\Omega t + (i-1)2\pi/3) - Mg \sum_{i=1}^3 (\tau \cos(\Omega t + (i-1)2\pi/3) - r \sin(\Omega t + (i-1)2\pi/3)(1 - \cos \theta_i))}{3M\tau^2 + Mr^2 \sum_{i=1}^3 (1 - \cos \theta_i)^2 + m \sum_{i=1}^3 (R_o + s_{m_i})^2 + I_{rot}} \quad (F.18)$$

F.1.4 The fledge dynamics

The motion of the fledge plate can be changed by varying the geometry of the fledge mechanism, the mass of the fledge plate and the mass of the sliding mass. The geometry of the fledge is described by the variables θ_{max} , r , R_l , h and R_o , (see Figure F.3). R_o is considered to be fixed as it depends on difference between the length of the blades and of the fledge plate. (The length of the fledge plate is taken from that used in the NWTTC study (1994).)

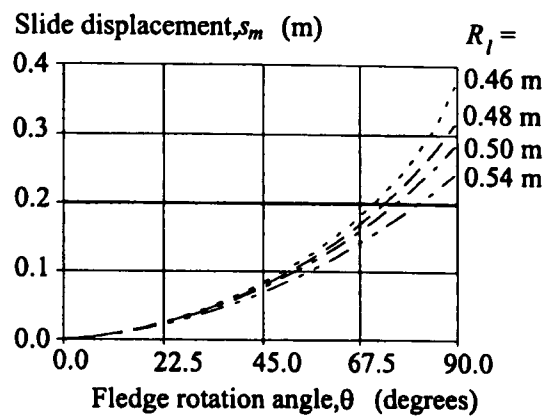
F.1.4.1 Behaviour required of the fledge to be an effective brake

The purpose of this section is to discuss the feasibility of using the fledge to slow and possibly stop a wind turbine when the rotor speed becomes higher than normal, and to investigate the size which such a fledge would have to be. Generally the length of the tip device is the minimum necessary to meet the Risø criterion for air brakes that the rotor should not idle off-load in a wind of 30 m/s at a speed greater than its normal operating speed (Jamieson *et al.*, 1992).

When a fledge is deployed to large angles it has been proved in wind-tunnel tests by Jamieson and Agius (1989) to brake the rotor speed efficiently. However, to be a useful brake the fledge also requires additional features. The fledge plates must be able to move sufficiently rapidly that they act as brakes before the rotor speed reaches a dangerously high level. The fledge plates must also be able to reach high angles of deployment and then remain open until the rotor has stopped or its velocity is small. In addition, the velocity of the actuating mass just before it reaches the end of its slide must be small so that the kinetic energy dissipated into the structure on impact is not large. The fledge must possess all the above features in all operational wind speeds.

F.1.4.2 The effect of geometry on braking

It was assumed that there are no external forces acting on the fledge plate or the sliding mass when the fledge is allowed to move. Although when R_l is increased the deployment time of the fledge plate is hardly affected, the maximum value of ψ is decreased and therefore, by (F.8), the maximum slide displacement is decreased. Therefore for large R_l , a small final rotational velocity of the fledge plate causes a large final sliding mass velocity and hence a large amount of kinetic energy to dissipate within the structure. The relationships between the fledge angle, θ , and the slide displacement, s_m , for various values of R_l are shown in Figure F.5.



The fledge geometry is chosen to be $h = 0.04$ m, $r = 0.3$ m, $R_o = 15.25$ m, $m = 5$ kg and $M = 10$ kg.

Figure F.5 The effect of the value of R_l on the relationship between θ and s_m .

F.1.4.3 The effect of the masses of the fledge plate and the sliding mass on braking

As the mass of the fledge plates is increased, the inertia of the wind turbine increases so the rotor acceleration is reduced, but the plates takes longer to deploy so braking is slower - see Figure F.6.

If the sliding mass is very light then the inertial force acting on a plate is insufficient to oppose the aerodynamic closing forces on the plate before it is fully deployed. In this case the fledge plate will never deploy, but settles at an intermediate value of θ . The geometry can be selected so that the fledge can act as a brake as in Figure F.7c. As the mass of the sliding mass is increased, higher maximum values of θ are reached until the plate will fully deploy. With this size of sliding mass the fledge plate is held open until the closing forces on the plate are large enough so that it closes slightly and settles to an intermediate value of θ - see Figure F.7b. As the sliding mass is increased further the deployment time is reduced. Therefore the plate remains fully open for longer and it closes more slowly, see Table F.1. However, the velocity of the sliding mass at the end of the slide, and hence the wear and tear

on the structure, and the amount of kinetic energy to be dissipated in the structure due to stopping the mass, all increase.

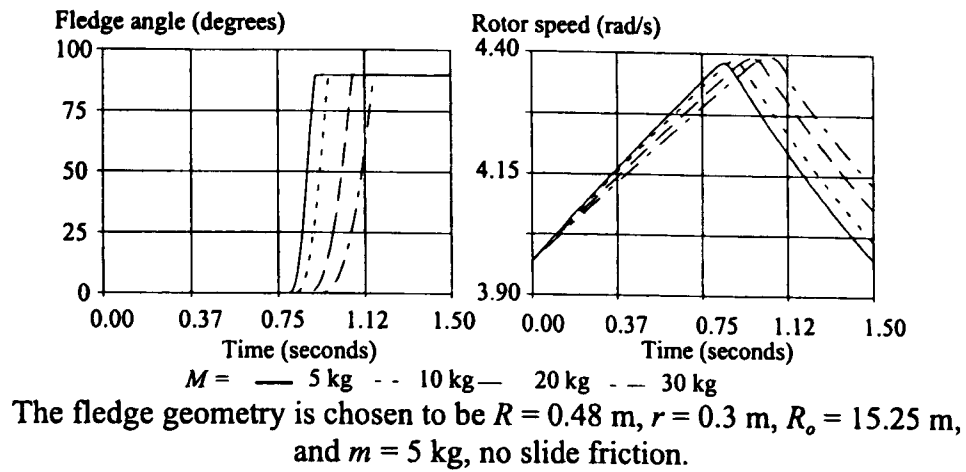
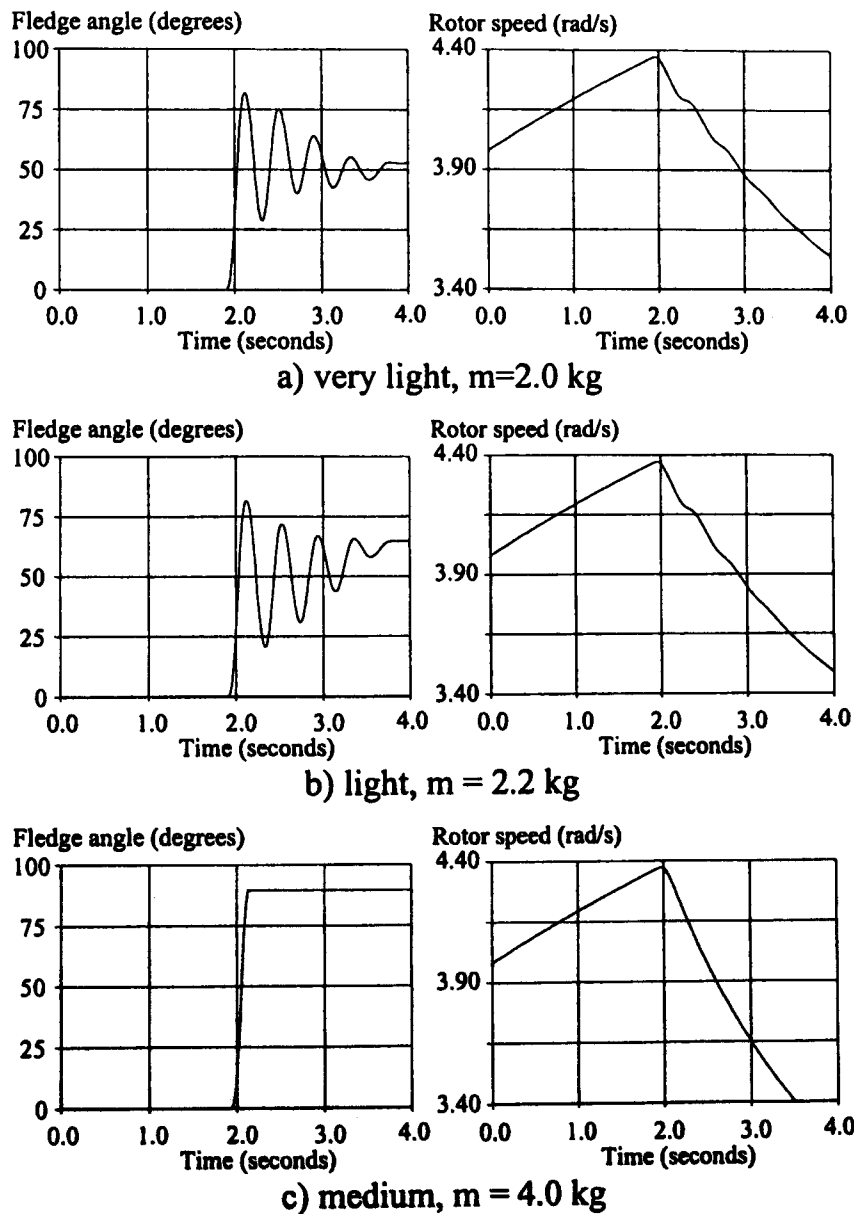


Figure F.6 The effect of the mass of the fledge plate on braking.

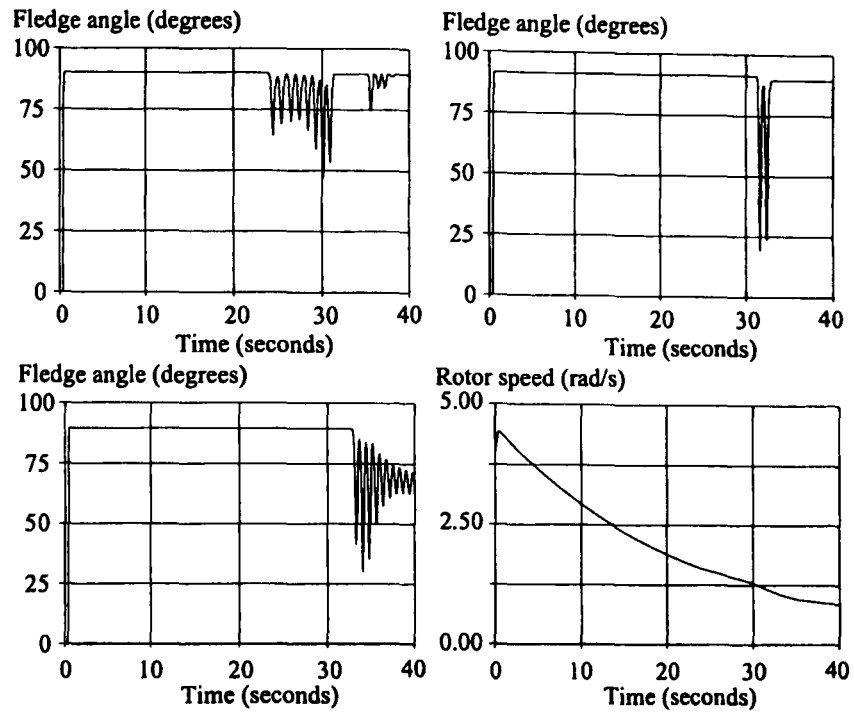


The fledge geometry is chosen to be $R = 0.48$ m, $r = 0.3$ m, $R_o = 15.25$ m, and $M = 10$ kg, slide friction coefficient = 0.05, wind = 8 m/s

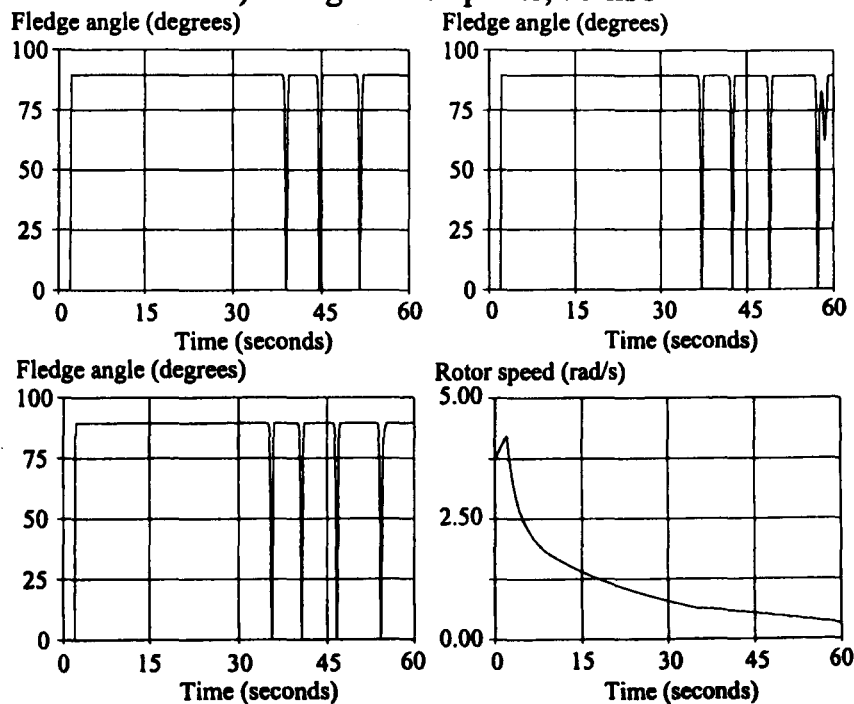
Figure F.7 The effect of the mass of the sliding mass on braking.

Actuating mass (kg)	3.0	5.0	7.0	10.0	20.0
Final velocity of actuating mass (m/s)	8.11	9.83	10.73	11.40	12.44

Table F.1 The effect of size of the actuating mass and its velocity just before the end of the slide is reached.



a) in high wind speeds, 25 m/s



b) in low wind speeds, 8 m/s

(The fledge geometry is chosen to be $R = 0.48$ m, $r = 0.3$ m, $R_o = 15.25$ m, $m = 5$ kg, $M = 10$ kg, no slide friction.)

Figure F.8 The closing behaviour of the three ball-joint fledges.

Simulation of the fledge indicates that when the rotor speed has been considerably reduced, the inertia forces acting on the mass and fledge plate and static forces acting on the actuating mass are exceeded by the closing aerodynamic moment so that the plates start to

close - see Figure F.8. This occurs when the rotor speed is approximately 1.5 rad/s. The mass will then move back along the slide and the fledge plate will close until it stops due to the reduction of the aerodynamic moment. In high winds (e.g. 25 m/s and above) a fledge closes slightly, oscillates and then reopens as the next fledge starts to close - see Figure F.8a. Fortunately the rotor speed is still decreasing as the fledges close only slightly. However, in low wind speeds (e.g. 8 m/s) the fledges flap one at a time to increasingly low angles - see Figure F.8b. In this case the rotor speed is maintained around 1.0 rad/s and the wind turbine is not fully stopped. Therefore the machine is not fully stopped until a mechanical brake is also applied or the fledge plates are stopped physically from returning. Various locking mechanisms for the latter purpose are considered by NWTC (1994).

F.1.4.4 The effect of external forces on braking

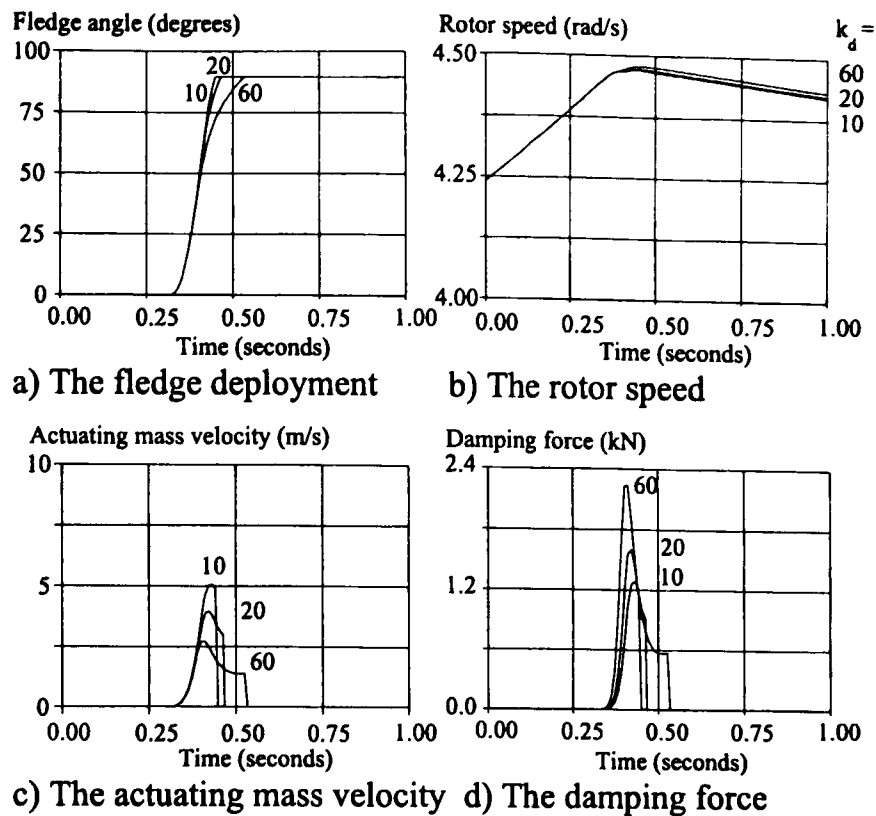
As the magnitude of the wind speed is increased the fledge plate deploys more rapidly, although the value of θ required before braking occurs remains almost unchanged. As the fledge plate deploys so quickly it is not particularly affected by wind turbulence.

The effect of increasing the damping force is to decrease the velocity of the sliding mass and so increase the fledge deployment time, see Figure F.9. The maximum damping force required to limit the final velocity of the actuating mass to a sensible value is relatively small (2.3 kN in high winds). Applying damping in this way allows the fledge to act as an effective air brake. The maximum forces acting on the fledge components are relatively small in very high winds - see Table F.2.

Similarly increasing the spring force decreases the velocity of the sliding mass and so increases the fledge deployment time (Figure F.10). However, in this case the spring force is also present when the fledge plate is fully open and so the tendency for the fledge plate to close is increased, particularly in light winds.

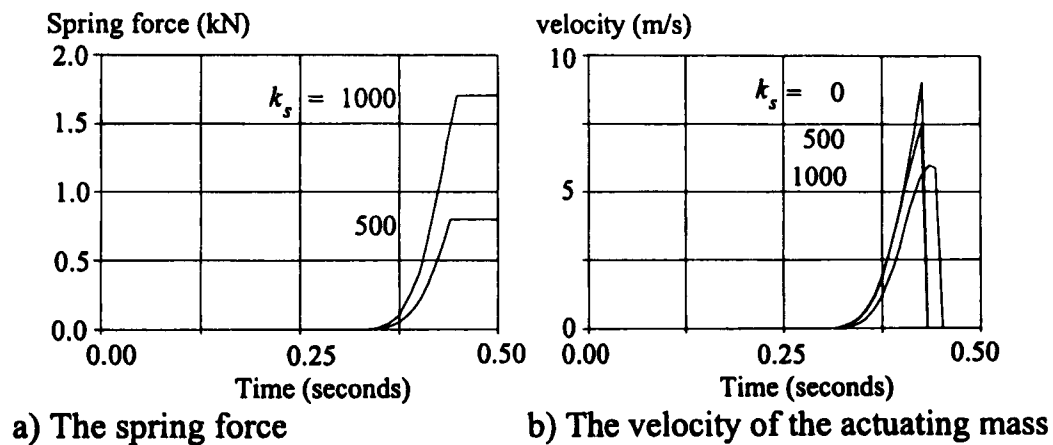
	Maximum value is below
Net force on the slide	0.36 kN
Centrifugal force	1.6 kN
Link reaction	1.25 kN
Side force	2.6 kN
Applied force	2.6 kN
Link reaction moment	0.55 kN
Rotor dynamic torques	29 Nm
Net torque on the fledge plate	290 Nm

Table F.2 The maximum loads on the components of the ball-joint fledge when damping on the slide is used to control the motion of the fledge (no slide friction).



($R_l = 0.48$ m, $r = 0.3$ m, $R_o = 15.25$ m, $m = 5$ kg, $M = 10$ kg, no slide friction, wind speed = 25 m/s).

Figure F.9 The effect of damping on the actuating mass on the fledge deployment.



($R_l = 0.48$ m, $r = 0.3$ m, $R_o = 15.25$ m, $m = 5$ kg, $M = 10$ kg, no slide friction, wind speed = 25 m/s).

Figure F.10 The effect of a spring on the actuating mass on the fledge deployment.

F.1.4.5 Cable control mechanism

All the simulations assume so far that all three plates are released simultaneously although evolve differently when the rotor speed exceeds 110% of rated speed. Various release mechanisms are considered in NWTC (1994). However, the cable system is the only one suitable for both braking and power control. For the investigation of the fledges as a control device in Chapter 7 this geometry is chosen such that $R_l = 0.48$ m, $r = 0.3$ m, $R_o = 15.25$ m, $m = 5$ kg, and $M = 10$ kg.

The moment acting on the fledge plate by the cable is

$$T_i k r \cos \theta_i / 2 \quad (\text{F.19})$$

where k is the ratio of r and the distance from the cable attachment on the plate to the pulley.

The cable control mechanism can be described as follows. Three cables are attached to a tripod at the hub, with each extending radially along a blade and around a pulley to the fledge plate below its centre of mass (see Figure F.11). The pulley and the centre of mass of the plate are chosen to be equidistant from the plate's hinge. An additional cable (B in Figure F.11) links the sliding mass to the original cable (A in Figure F.11). While θ is below a critical value, θ_{crit} , cable B is slack and cable A applies a tension to the fledge plate. When θ is greater than θ_{crit} the cable tension is applied to the sliding mass via cable B, whilst cable A becomes slack. The changeover of tension is achieved because the distance moved by the cable attached to the fledge plate when the fledge is fully deployed is smaller than that moved by the actuating mass along the slide. The advantage of this arrangement is that the tension in the cable is initially applied directly to the plate to prevent the initial deployment being too rapid, while the tension is later applied directly to the mass to greatly reduce its final velocity. In order to ensure that the plates move in unison, the three cables are attached to a tripod attached to a damper. The tripod essentially equalises the tension of the three cables and prevents the plates from flapping, when held closed by a pretension force.

The horizontal length from the apex of the tripod to the centroid of its base, L_t , is a function of the lengths of the cables from the pulley to the tripod: cable lengths L_1, L_2, L_3 as follows

$$L_t = \frac{1}{3} \cot \varphi \sqrt{9\sigma^2 \sin^2 \varphi - 4(L_1^2 + L_2^2 + L_3^2 - L_1 L_2 - L_2 L_3 - L_1 L_3)} \quad (\text{F.20})$$

where σ is the length of the sides of the tripod and φ is the distance from the apex of the tripod to the centroid of its base.

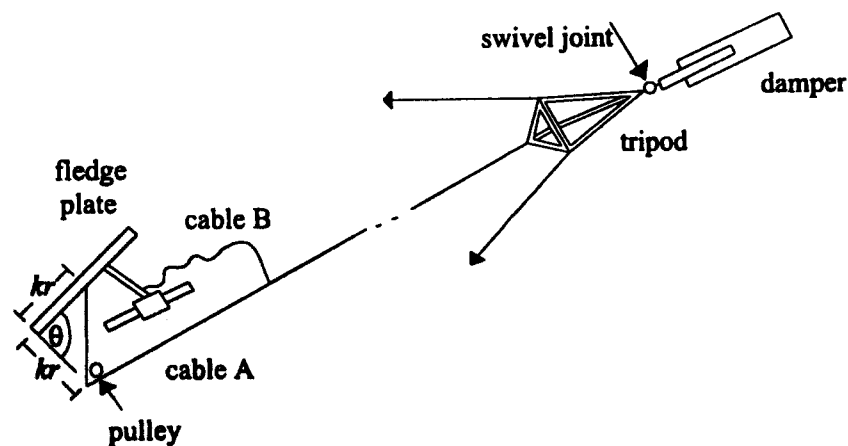


Figure F.11 The fledge actuating system.

The speed of the damper is

$$d_{vel} = -\frac{1}{3} \sum_{i=1}^3 L_i + 2Lt \sum_{i=1}^3 (2L_i^2 - \sum_{\substack{j=1, \\ j \neq i}}^3 L_i L_j) \quad (F.21)$$

The force applied by the damping device is modelled to be

$$Tens = k_{dd} d_{vel}^2 + k_{damp} \quad (F.22)$$

where $Tens$ is the cable tension force

k_{dd} is the damping coefficient

d_{vel} is the velocity of the damper mass

k_{damp} is a fixed tension

This cable tension is divided between the three attached cables as follows

$$T_i = \frac{Tens}{3} \left(\frac{(2L_i - \sum_{\substack{k=1 \\ k \neq i}}^3 L_k) 2 \cot \varphi}{\sqrt{(9s^2 \sin \varphi - 4(\sum_{k=1}^3 L_k^2 - \sum_{k=1}^3 \frac{L_1 L_2 L_3}{L_k}))}} - 1 \right) \quad (F.23)$$

Results from the simulation show that a maximum damping force of under 3 kN will restrict \dot{s}_m at the end of the slide to below 1.5 m/s, see Figures F.12a and F.12b. The fledge plates now deploy quickly and hence the maximum rotor speed is reasonable. The forces in the link rod and the side forces on the slide are reasonable, see Figure F.12e and F.12f. The discontinuities in these plots are due to the change-over of tension. The maximum velocity of the damper is not large, see Figure F.12g. The peak in the cable tension at the point of changeover is present because the velocities of the fledge plate and the sliding mass are different. Although the mass dynamics of the tripod and the cables are not included in the simple model used in the simulation, a time delay was introduced so that the change in cable velocity was smoothed to take account of the inertia effects and it had little effect on the size of the peak. The peak can be reduced if the cable attached to the actuating mass is either slightly elastic or includes a very stiff spring.

The simulation indicates that the ball-joint fledges can be used as effective air brakes in all wind speeds. Although two deployed fledges are sufficient to brake the machine this may unbalance the forces on the rotor. The ball-joint system can be easily tuned so that all three fledges deploy, the maximum rotor speed is not dangerously high and the velocity of the sliding mass at the end of deployment is small. The plates do have a tendency to close at low rotor speeds but this can be overcome by some lock-out mechanism. The fledge plate can be made relatively light (10 kg). The geometry can be chosen so that when the plate is closed, the leverage is small between it and the sliding mass so that the plate will open when

released; the leverage is high at the end of deployment, helping to keep the fledge open; and the actuating mass can be light and hence small (5 kg). The advantages of the tripod cable system are that (a) a small damping force is required to obtain good fledge deployment, with low side forces; (b) the system is cheap; (c) the fledges move nearly in unison; and (d) the system does not require a high initial closing force. The forces on all the components appear to be low and hence the fledge can easily be engineered.

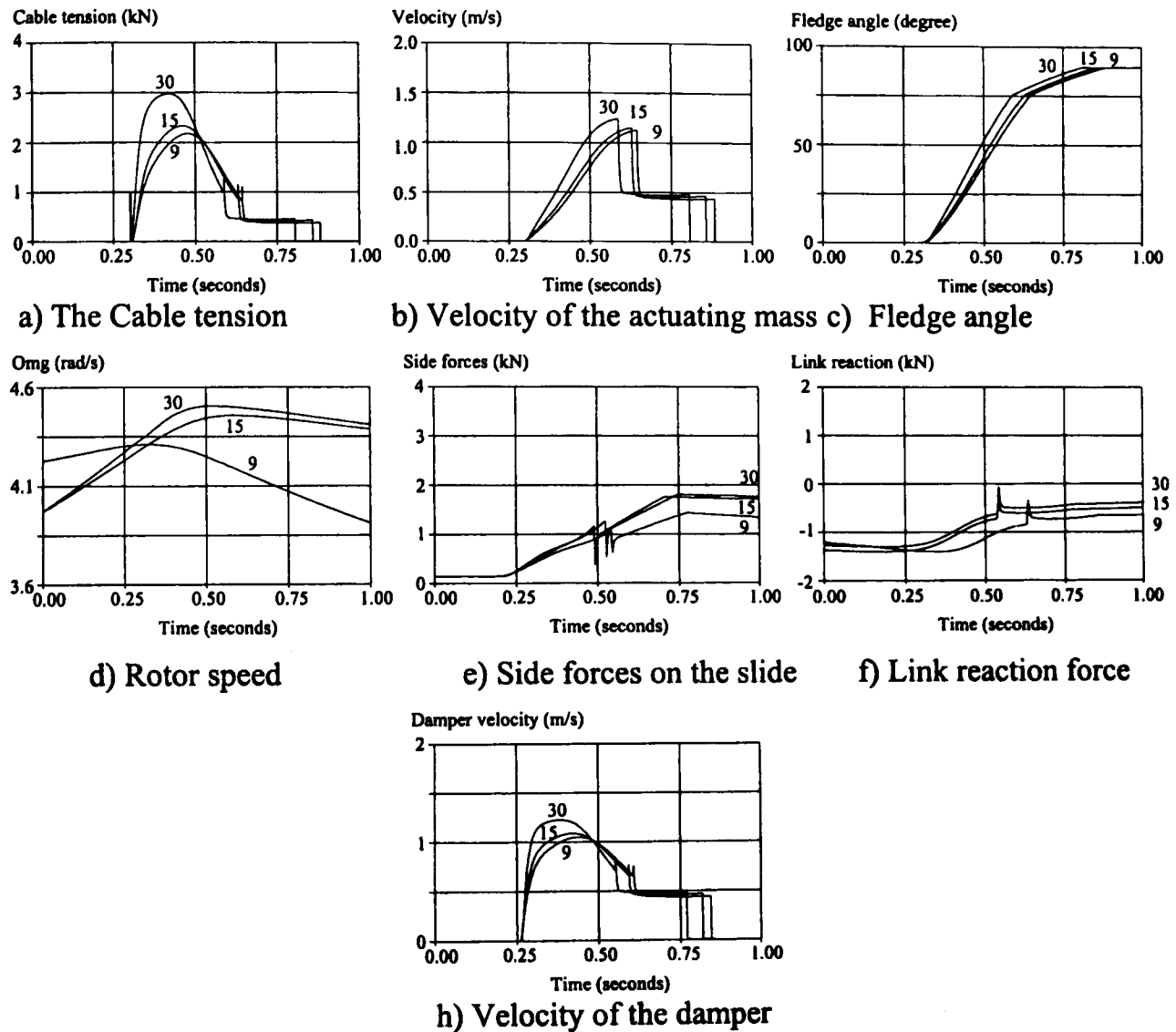


Figure F.12 The fledge deployment and forces required when damping is applied linearly in wind speeds of 8 m/s, 15 m/s and 30 m/s.

F.1.5 The dynamics of the ball-joint fledge power-control device

With the tripod and cable mechanism, the fledges can be considered as acting in unison and the equations of motion can be simplified as follows

$$\ddot{\theta} = -\tau \frac{\dot{\Omega}}{r} \sin \theta + (1 - \cos \theta) \sin \theta \Omega^2 - \frac{Q}{MrR} (r \sin \theta + h \cos \theta) - \frac{T}{Mr} k \cos(\theta / 2) + \frac{Maero}{Mr^2} \quad (F.24)$$

where T is the tension applied to the fledge plate via a cable

Q is the force in the link arm

The accelerating of each actuation mass is described by

$$\ddot{s}_m = \Omega^2 (R_o + s_m) + \frac{Q}{MR} (R \cos \psi_o - s_m) - k_s s_m - k_d \dot{s}_m^2 - \frac{T_o}{m} - \frac{F}{m} \quad (\text{F.25})$$

where F is the friction force opposing the mass moving along the slide

T_o is the tension applied to the actuating mass via a cable

The acceleration of the rotor is described by

$$\ddot{\Omega} = \frac{Taero / 3 - Torgen / 3 - M\tau r \ddot{\theta} \sin \theta - M\tau r \dot{\theta}^2 \cos \theta - \Omega \left(2Mr^2 \dot{\theta} (1 - \cos \theta) \sin \theta + 2m(R_o + s_m) \dot{s}_m \right)}{M\tau^2 + Mr^2 (1 - \cos \theta)^2 + m(R_o + s_m)^2 + Irot / 3} \quad (\text{F.26})$$

The distance the mass has moved along the slide, s_m , is obtained from geometry as

$$s_m = R \cos \psi_o - \sqrt{(R^2 - 2r^2 - h^2 + 2r^2 \cos \theta - 2rh \sin \theta)} \quad (\text{F.27})$$

F.2 Modelling issues for the compliant tip

The ACSL (ACSL 1987) model for the Howden 33/330 wind turbine (Wilkie and Leithead, 1989) is modified to be suitable for investigating the feasibility of the compliant tip to enhance power control. The main modifications are the inclusion of aerodynamic tables for the compliant tip (Anderson, 1990), actuator dynamics (Campbell, 1990), a PI controller¹ and the compliant tip controller (Anderson *et al.*, 1990). Other minor additions made to the simulation are models of wind speed sensed by the tip and the remaining part of the blade (Leithead, 1992), a dummy tip and actuator to enable the effects of high frequency spectral peaks on the internal operation of the actuator to be investigated, modelling of noise on any signals which are measured, namely the aerodynamic moment, the tip acceleration and position, and the spectral disturbances sensed in the wind speed seen only by the tip and not in the rotor torque (which are described in Appendix A).

¹ PI controller for 16 m/s is $6.47 \times 10^{-6} (1 + 10/s)$

F.2.1 The aerodynamics of the compliant tip

The aerodynamic torque coefficients, the aerodynamic moment, the angle of attack and the root bending moment are all found from look-up tables supplied by Anderson *et al.* (1990). They are all parameterised by the current tip angle and the tip speed ratio. There were two look-up tables for the aerodynamic torque coefficients, one for the area swept by the tip and the other for the remainder of the rotor. The aerodynamic torque is calculated as follows.

$$T_a = \frac{1}{2} \rho \pi R^3 (V_r^2 C_{qr} + V_o^2 C_{qo}) \quad (\text{F.28})$$

where V_o is the wind speed seen by the tip

V_r is the wind speed sensed by the remainder of the rotor

C_{qo} is the torque coefficient for the tip

C_{qr} is the torque coefficient for the remainder of the rotor

F.2.2 The compliant tip actuator

The actuator model is described in detail by Campbell (1990) and its dynamics are described below.

The transfer function relating the tip demand to the spool position is

$$\begin{aligned} \frac{x_v}{\beta_d} &= \text{filter} \times \text{gain of the spool} \times \text{spool dynamics} \\ &= \frac{55^2}{(s + 55)^2} \cdot 0.15 \cdot \frac{600^2}{s^2 + 432000s + 600^2} \end{aligned} \quad (\text{F.29})$$

The filter is to reduce the sensitivity of the spool dynamics to high-frequency noise. The load flow in the actuator, Ql , is

$$Ql = Cdw \times x_v \times \sqrt{Ps - \text{sign}(x_v) \times Pl} - Kce \times Pl \quad (\text{F.30})$$

where Cdw is $Cd w \sqrt{2} / \sqrt{\rho}$ (Merit, 1967) = $45 \times 10^{-9} \text{ m}^4/\text{kg}$

C_d is the discharge coefficient

w is the area gradient for each orifice

ρ is the fluid density

Ps is the supply pressure = 14106 N/m^2

Pl is the load pressure

Kce is the coefficient of fluid leakage = $2.34 \times 10^{-12} \text{ m}^3\text{Pa/s}$

The rate of change of load pressure with respect to time is

$$\frac{dPl}{dt} = \int \frac{4\beta_e}{V_t} (Ql - A \times r \times vel) dt \quad (F.31)$$

where A is the area of the piston = 0.002 m³

r is the crank radius = 0.04 m

β_e is the effective bulk radius = 700×10⁶

V_t is the trapped volume of fluid in the actuator = 150×10⁻⁶ m³

vel is the tip velocity (rad/s)

The tip acceleration, acc in rad/s² is

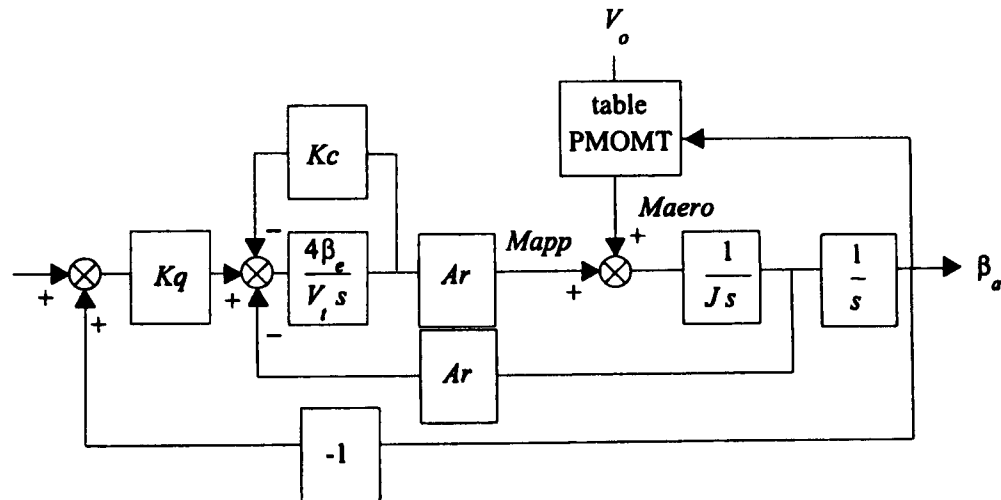
$$acc = (A \times Pl - Maero \times r) / (M_p r + I_a / r) \quad (F.32)$$

where $Maero$ is the aerodynamic moment acting on the tip and is calculated using a coefficient from a two-dimensional look-up table parameterised by the current tip angle and the wind speed sensed by the tip.

M_p is the mass of the piston = 2 kg

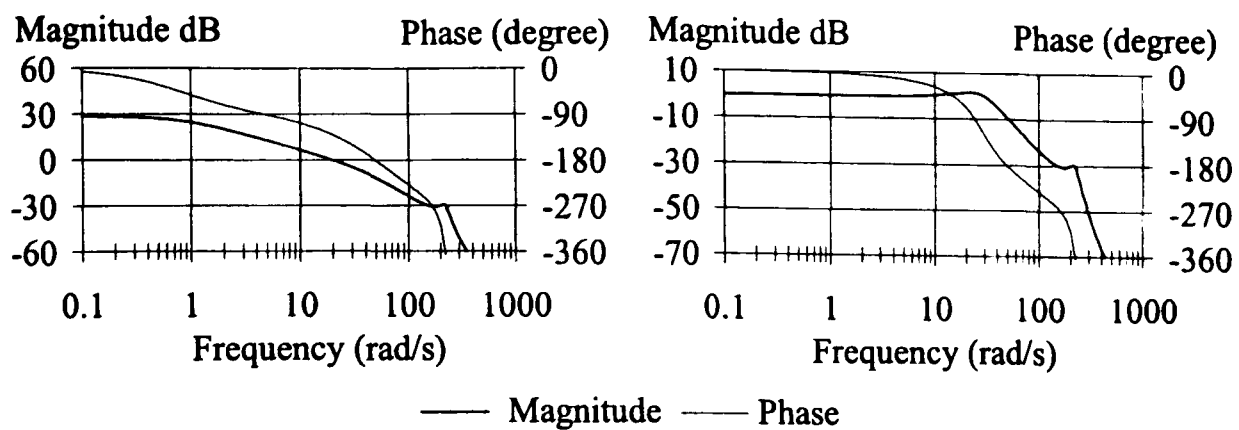
I_a is the tip inertia = 2.54 kg m²

Equation (F.30) is linearised and the block diagram of the linear actuator is shown in Figure F.13. Bode plots of the open and closed-loop transfer functions are shown in Figure F.14. The actuator dynamics were further simplified for control design purposes to the first-order approximation 23/(s+23).



where Kq is 15. 55²/(s+55)², J is the tip inertia, $Mapp$ is the applied moment acting on the tip, table PMOMT is aerodynamic moment table, and β_a is the tip position.

Figure F.13 The block diagram of the linearised actuator.



a) Bode plot of the open-loop transfer function b) Bode plot of the closed-loop transfer function

Figure F.14 Bode plots of the linearised actuator dynamics.

Parameter	Value
Rated Power	300 kW
Number of blades	3
Rotor radius	16.5 m
Length of tip	2.5 m
Tip chord	0.65 m
Hub height	30 m
Distance from rotor plane to tower	3.5 m
Tower radius	0.9 m
Grid frequency	60 Hz
No. of generator pole pairs	2
Generator slip	1.44 %
Generator and gearbox efficiency	91 %
Power transducer time constant	0.02 s
Gradient of torque to speed curve	698.7 Nms/rad
Synchronous speed	191.2 rad/s
Rated low-speed shaft speed	3.92 rad/s
Generator electrical time constant ²	0.2 s
Inertia of the low-speed shaft	1.9012×10 ⁵ Kgm ²
Inertia of the high-speed shaft	3.8 Kgm ²
Stiffness of the low-speed shaft	12.6×10 ⁶ Nm/rad
Stiffness of the high-speed shaft	3.01×10 ⁵ Nm/rad
Gearbox ratio	48.8

Table F.3 The machine parameters for the Howden 330 kW wind turbine.

² This figure is too large, it has been left unchanged in studies made by Wilkie and Leithead (1988) and Leithead *et al.*, (1991a), a value of 0.03 would be more realistic.

Appendix G Aerodynamic torque tables

As described in Chapter 2 the aerodynamics are defined in terms of torque coefficients, C_q , which are dependent on the rotor design of each machine. This appendix lists these torque coefficients and the corresponding partial derivatives of aerodynamic torque with respect to wind speed and pitch angle for rated power for each of the machine configurations studied.

G.1 Full-span regulated machines

Table G.1 gives the torque coefficients for Configurations A to F of Chapter 5. Table G.2 gives the corresponding partial derivatives of aerodynamic torque with respect to wind speed and pitch angle for rated power.

G.2 Tip-regulated machines

Table G.3 gives the torque coefficients for Configurations G to L of Chapter 6. Table G.4 gives the corresponding partial derivatives of aerodynamic torque with respect to wind speed and pitch angle for rated power.

G.3 Fledge

The torque coefficient tables for the fledge investigated in Appendix F and Chapter 7 are listed in Table G.5.

G.4 Compliant tip

The torque coefficient tables associated for the compliant tip and the remaining part of the blade investigated in Chapter 7 are listed in Table G.6. The aerodynamic torque partial derivatives with respect to pitch angle are listed in Table G.7.

G.5 Full-span regulated machine

Table G.8 gives the torque coefficients for the full-span regulated machine investigated in Chapter 8. Table G.9 gives the corresponding partial derivatives of aerodynamic torque with respect to pitch angle for rated power.

		Tip speed ratio (rad)												
P		2.80	3.00	3.23	3.36	3.50	3.65	3.82	4.00	4.20	4.42	4.67	4.94	5.25
i	0	0.02505	0.02933	0.03422	0.03683	0.03954	0.04243	0.04557	0.04901	0.05265	0.05627	0.05953	0.06200	0.06351
t	2	0.03003	0.03433	0.03903	0.04163	0.04444	0.04745	0.05055	0.05356	0.05623	0.05838	0.05989	0.06081	0.06115
c	4	0.03435	0.03856	0.04339	0.04598	0.04855	0.05097	0.05308	0.05481	0.05612	0.05702	0.05745	0.05743	0.05692
h	6	0.03815	0.04239	0.04665	0.04855	0.05019	0.05153	0.05257	0.05328	0.05366	0.05363	0.05319	0.05231	0.05087
	8	0.04143	0.04484	0.04754	0.04855	0.04933	0.04983	0.05006	0.04996	0.04948	0.04862	0.04730	0.04550	0.04324
a	10	0.04311	0.04512	0.04639	0.04670	0.04675	0.04651	0.04594	0.04504	0.04380	0.04212	0.03995	0.03734	0.03408
n	12	0.04292	0.04372	0.04370	0.04335	0.04271	0.04176	0.04050	0.03885	0.03678	0.03434	0.03144	0.02796	0.02386
g	14	0.04129	0.04095	0.03972	0.03870	0.03738	0.03578	0.03384	0.03152	0.02884	0.02565	0.02190	0.01755	0.01255
l	16	0.03839	0.03693	0.03453	0.03295	0.03108	0.02888	0.02631	0.02338	0.01993	0.01599	0.01148	0.00636	0.00042
e	18	0.03436	0.03190	0.02851	0.02638	0.02393	0.02118	0.01801	0.01438	0.01030	0.00567	0.00043	-0.00562	-0.01268
(d	20	0.02943	0.02608	0.02168	0.01907	0.01612	0.01278	0.00904	0.00482	0.00008	-0.00529	-0.01148	-0.01854	-0.02672
e	22	0.02377	0.01954	0.01428	0.01117	0.00770	0.00384	-0.00049	-0.00534	-0.01081	-0.01700	-0.02397	-0.03191	-0.04102
g	24	0.01748	0.01249	0.00631	0.00273	-0.00124	-0.00564	-0.01054	-0.01600	-0.02207	-0.02885	-0.03656	-0.04523	-0.05502
r	26	0.01071	0.00489	-0.00214	-0.00615	-0.01056	-0.01541	-0.02075	-0.02666	-0.03322	-0.04044	-0.04823	-0.05678	-0.06700
e	28	0.00341	-0.00311	-0.01079	-0.01514	-0.01990	-0.02507	-0.03067	-0.03664	-0.04299	-0.05025	-0.05928	-0.07055	-0.08295
e	30	-0.00417	-0.01118	-0.01938	-0.02388	-0.02862	-0.03360	-0.03916	-0.04583	-0.05396	-0.06285	-0.06488	-0.06252	-0.06942
s)	35	-0.02195	-0.02984	-0.03843	-0.03665	-0.03791	-0.04066	-0.04421	-0.04891	-0.05474	-0.06203	-0.07102	-0.08275	-0.09622

		Tip speed ratio (rad)											
P		5.60	6.00	6.46	7.00	7.43	7.64	8.40	9.33	10.50	12.00	14.00	16.80
i	0	0.06408	0.06386	0.06278	0.06020	0.05787	0.05675	0.05173	0.04558	0.03806	0.02858	0.01633	-0.00052
t	2	0.06090	0.05995	0.05829	0.05580	0.05351	0.05248	0.04816	0.04238	0.03533	0.02632	0.01508	-0.00072
c	4	0.05580	0.05412	0.05171	0.04852	0.04586	0.04456	0.03958	0.03346	0.02600	0.01646	0.00354	-0.01565
h	6	0.04893	0.04628	0.04293	0.03887	0.03544	0.03384	0.02779	0.02041	0.01103	-0.00134	-0.01880	-0.04721
	8	0.04027	0.03667	0.03240	0.02719	0.02293	0.02093	0.01329	0.00378	-0.00856	-0.02520	-0.04924	-0.09016
a	10	0.03024	0.02571	0.02026	0.01376	0.00838	0.00586	-0.00378	-0.01603	-0.03210	-0.05439	-0.08727	-0.14010
n	12	0.01904	0.01337	0.00667	-0.00136	-0.00796	-0.01105	-0.02321	-0.03885	-0.05981	-0.08925	-0.13310	-0.20280
g	14	0.00674	-0.00009	-0.00820	-0.01797	-0.02610	-0.03002	-0.04527	-0.06503	-0.09166	-0.12910	-0.18540	-0.27650
l	16	-0.00651	-0.01471	-0.02454	-0.03640	-0.04637	-0.05111	-0.06965	-0.09374	-0.12640	-0.16470	-0.24370	-0.35670
e	18	-0.02093	-0.03067	-0.04222	-0.05620	-0.06788	-0.07345	-0.09545	-0.12430	-0.16310	-0.21680	-0.29760	-0.43870
(d	20	-0.03619	-0.04724	-0.06050	-0.07662	-0.09007	-0.09645	-0.12100	-0.15220	-0.19610	-0.26390	-0.37580	-0.50740
e	22	-0.05160	-0.06403	-0.07854	-0.09543	-0.10950	-0.11640	-0.14520	-0.18700	-0.24450	-0.26930	-0.35040	-0.50280
g	24	-0.06595	-0.07848	-0.09434	-0.11590	-0.13520	-0.14430	-0.17200	-0.16990	-0.21310	-0.28350	-0.40330	-0.60980
r	26	-0.08018	-0.09707	-0.11560	-0.11000	-0.11790	-0.12070	-0.14910	-0.19070	-0.25110	-0.34360	-0.48870	-0.73280
e	28	-0.08209	-0.08311	-0.09586	-0.11330	-0.13200	-0.14030	-0.17710	-0.22810	-0.30080	-0.40850	-0.57680	-0.85950
e	30	-0.07862	-0.09205	-0.11060	-0.13470	-0.15550	-0.16660	-0.20930	-0.26800	-0.35180	-0.47490	-0.66770	-0.98990
s)	35	-0.11310	-0.13360	-0.16030	-0.19360	-0.22290	-0.23650	-0.29460	-0.37310	-0.48430	-0.64750	-0.90140	-1.32600

Table G.1a) 300 kW, 2 blades, tip speed 84 m/s full-span regulated - Configuration A.

		Tip speed ratio (rad)										
P		2.80	3.00	3.23	3.50	3.82	4.20	4.42	4.67	4.94	5.25	5.60
i	0	0.02606	0.03056	0.03575	0.04139	0.04771	0.05524	0.05919	0.06276	0.06541	0.06690	0.06734
t	2	0.03130	0.03587	0.04083	0.04651	0.05306	0.05930	0.06163	0.06321	0.06409	0.06436	0.06398
c	4	0.03589	0.04030	0.04541	0.05099	0.05598	0.05924	0.06016	0.06056	0.06049	0.05986	0.05859
h	6	0.03986	0.04438	0.04902	0.05292	0.05549	0.05660	0.05653	0.05604	0.05503	0.05346	0.05133
	8	0.04341	0.04715	0.05010	0.05204	0.05281	0.05215	0.05123	0.04977	0.04783	0.04538	0.04221
a	10	0.04534	0.04753	0.04892	0.04931	0.04845	0.04611	0.04429	0.04199	0.03918	0.03573	0.03163
n	12	0.04520	0.04610	0.04609	0.04502	0.04265	0.03868	0.03607	0.03296	0.02927	0.02491	0.01985
g	14	0.04350	0.04317	0.04186	0.03938	0.03558	0.03026	0.02686	0.02289	0.01830	0.01303	0.00690
l	16	0.04046	0.03893	0.03636	0.03267	0.02762	0.02084	0.01667	0.01190	0.00652	0.00026	-0.00702
e	18	0.03619	0.03357	0.02996	0.02511	0.01884	0.01068	0.00580	0.00028	-0.00610	-0.01349	-0.02214
(d	20	0.03096	0.02741	0.02274	0.01686	0.00936	-0.00008	-0.00573	-0.01224	-0.01964	-0.02820	-0.03809
e	22	0.02498	0.02049	0.01493	0.00796	-0.00067	-0.01153	-0.01802	-0.02533	-0.03361	-0.04314	-0.05418
g	24	0.01832	0.01304	0.00652	-0.00145	-0.01123	-0.02331	-0.03041	-0.03846	-0.04748	-0.05762	-0.06891
r	26	0.01116	0.00502	-0.00238	-0.01124	-0.02191	-0.03494	-0.04242	-0.05045	-0.05939	-0.07025	-0.08434
e	28	0.00347	-0.00340	-0.01147	-0.02101	-0.03221	-0.04501	-0.05272	-0.06239	-0.07418	-0.08615	-0.08238
e	30	-0.00450	-0.01187	-0.02043	-0.03001	-0.04111	-0.05679	-0.06546	-0.06383	-0.06505	-0.07261	-0.08232
s)	35	-0.02308	-0.03146	-0.03898	-0.03942	-0.04617	-0.05734	-0.06500	-0.07441	-0.08671	-0.10080	-0.11840

		Tip speed ratio (rad)									
P		6.00	6.46	7.00	7.64	8.40	9.33	10.50	12.00	14.00	16.80
i	0	0.06691	0.06558	0.06296	0.05875	0.05337	0.04681	0.03865	0.02849	0.01551	-0.00202
t	2	0.06286	0.06091	0.05813	0.05451	0.04982	0.04395	0.03625	0.02688	0.01508	-0.00148
c	4	0.05671	0.05409	0.05064	0.04639	0.04111	0.03467	0.02686	0.01693	0.00350	-0.01642
h	6	0.04848	0.04490	0.04058	0.03528	0.02891	0.02119	0.01141	-0.00145	-0.01956	-0.05016
	8	0.03836	0.03386	0.02834	0.02176	0.01378	0.00386	-0.00898	-0.02631	-0.05130	-0.09452
a	10	0.02684	0.02109	0.01427	0.00600	-0.00409	-0.01686	-0.03358	-0.05679	-0.09100	-0.14600
n	12	0.01387	0.00683	-0.00158	-0.01171	-0.02441	-0.04071	-0.06255	-0.09320	-0.13890	-0.21270
g	14	-0.00027	-0.00878	-0.01898	-0.03158	-0.04747	-0.06809	-0.09584	-0.13490	-0.19360	-0.28860
l	16	-0.01561	-0.02589	-0.03829	-0.05365	-0.07296	-0.09807	-0.13220	-0.17220	-0.25330	-0.37200
e	18	-0.03232	-0.04438	-0.05896	-0.07696	-0.09990	-0.13000	-0.17030	-0.22630	-0.31040	-0.45590
(d	20	-0.04962	-0.06347	-0.08026	-0.10090	-0.12640	-0.15890	-0.20480	-0.27590	-0.38930	-0.54360
e	22	-0.06710	-0.08211	-0.09961	-0.12160	-0.15210	-0.19610	-0.25560	-0.27930	-0.35830	-0.52360
g	24	-0.08203	-0.09889	-0.12180	-0.15120	-0.17190	-0.17650	-0.21770	-0.29640	-0.42150	-0.63710
r	26	-0.10190	-0.11930	-0.11250	-0.12650	-0.15620	-0.19960	-0.26270	-0.35940	-0.51080	-0.76580
e	28	-0.08695	-0.10040	-0.12000	-0.14680	-0.18540	-0.23870	-0.31470	-0.42720	-0.60300	-0.89910
e	30	-0.09644	-0.11590	-0.14110	-0.17440	-0.21900	-0.28090	-0.36790	-0.49660	-0.69800	-1.03500
s)	35	-0.13980	-0.16780	-0.20260	-0.24820	-0.30810	-0.39020	-0.50640	-0.67700	-0.94220	-1.38500

Table G.1b) 300 kW, 3 blades, tip speed 84 m/s full-span regulated - Configuration B.

		Tip speed ratio (rad)												
P		2.200	2.357	2.538	2.640	2.750	2.870	3.000	3.143	3.300	3.474	3.667	3.882	4.125
i	0	0.02010	0.02387	0.02953	0.03285	0.03638	0.04019	0.04432	0.04875	0.05336	0.05817	0.06338	0.06906	0.07490
t	2	0.02548	0.03062	0.03662	0.03998	0.04359	0.04743	0.05141	0.05562	0.06017	0.06515	0.07030	0.07507	0.07874
c	4	0.03161	0.03693	0.04302	0.04635	0.04983	0.05353	0.05750	0.06180	0.06624	0.07047	0.07399	0.07650	0.07787
h	6	0.03727	0.04263	0.04855	0.05181	0.05531	0.05903	0.06281	0.06642	0.06954	0.07195	0.07359	0.07437	0.07433
	8	0.04237	0.04760	0.05352	0.05674	0.05997	0.06301	0.06564	0.06777	0.06932	0.07025	0.07051	0.07003	0.06875
a	10	0.04688	0.05211	0.05758	0.06012	0.06231	0.06410	0.06543	0.06631	0.06663	0.06636	0.06533	0.06368	0.06118
n	12	0.05099	0.05561	0.05946	0.06093	0.06204	0.06275	0.06301	0.06278	0.06199	0.06053	0.05842	0.05551	0.05188
g	14	0.05393	0.05703	0.05905	0.05959	0.05977	0.05950	0.05875	0.05743	0.05552	0.05304	0.04987	0.04599	0.04112
l	16	0.05492	0.05646	0.05685	0.05650	0.05571	0.05449	0.05277	0.05054	0.04773	0.04421	0.04007	0.03499	0.02905
e	18	0.05417	0.05422	0.05297	0.05177	0.05016	0.04807	0.04552	0.04239	0.03862	0.03423	0.02900	0.02297	0.01597
(d	20	0.05186	0.05045	0.04771	0.04572	0.04334	0.04047	0.03707	0.03312	0.02853	0.02319	0.01707	0.01009	0.00196
e	22	0.04812	0.04538	0.04123	0.03856	0.03543	0.03180	0.02771	0.02294	0.01753	0.01136	0.00438	-0.00374	-0.01320
g	24	0.04317	0.03917	0.03375	0.03040	0.02666	0.02233	0.01750	0.01200	0.00582	-0.00121	-0.00930	-0.01849	-0.02909
r	26	0.03716	0.03202	0.02545	0.02149	0.01709	0.01211	0.00660	0.00040	-0.00664	-0.01456	-0.02346	-0.03353	-0.04506
e	28	0.03026	0.02408	0.01640	0.01187	0.00686	0.00130	-0.00490	-0.01182	-0.01945	-0.02802	-0.03762	-0.04824	-0.05992
e	30	0.02260	0.01544	0.00675	0.00169	-0.00387	-0.01000	-0.01666	-0.02404	-0.03218	-0.04101	-0.05041	-0.06090	-0.07401
s)	35	0.00086	-0.00817	-0.01851	-0.02415	-0.02997	-0.03633	-0.04377	-0.05258	-0.06072	-0.05722	-0.06175	-0.06896	-0.07836

		Tip speed ratio (rad)											
P		4.400	4.714	5.077	5.500	5.841	6.000	6.600	7.333	8.25	9.429	11.000	13.200
i	0	0.07982	0.08247	0.08256	0.08026	0.07735	0.07604	0.06891	0.06140	0.05228	0.04112	0.02719	0.00907
t	2	0.08072	0.08114	0.08023	0.07776	0.07523	0.07388	0.06813	0.06127	0.05251	0.04218	0.02963	0.01334
c	4	0.07819	0.07745	0.07547	0.07245	0.06956	0.06809	0.06257	0.05551	0.04701	0.03670	0.02352	0.00517
h	6	0.07343	0.07146	0.06859	0.06446	0.06082	0.05909	0.05257	0.04457	0.03475	0.02245	0.00580	-0.01888
	8	0.06653	0.06350	0.05924	0.05388	0.04955	0.04745	0.03941	0.02967	0.01752	0.00139	-0.02109	-0.06508
a	10	0.05780	0.05336	0.04793	0.04135	0.03584	0.03324	0.02343	0.01125	-0.00439	-0.02540	-0.05572	-0.10990
n	12	0.04729	0.04168	0.03484	0.02674	0.02004	0.01692	0.00481	-0.01036	-0.03025	-0.05761	-0.09789	-0.16250
g	14	0.03531	0.02837	0.02027	0.01044	0.00234	-0.00149	-0.01620	-0.03507	-0.06022	-0.09542	-0.14760	-0.23310
l	16	0.02206	0.01396	0.00417	-0.00753	-0.01726	-0.02186	-0.03984	-0.06313	-0.09428	-0.13790	-0.18850	-0.30830
e	18	0.00784	-0.00182	-0.01333	-0.02728	-0.03881	-0.04435	-0.06592	-0.09366	-0.13090	-0.16290	-0.26260	-0.38960
(d	20	-0.00762	-0.01890	-0.03240	-0.04853	-0.06197	-0.06836	-0.09324	-0.12560	-0.16900	-0.22870	-0.31680	-0.46690
e	22	-0.02420	-0.03708	-0.05220	-0.07048	-0.08572	-0.09297	-0.12100	-0.15600	-0.20270	-0.27420	-0.39080	-0.52560
g	24	-0.04128	-0.05542	-0.07228	-0.09209	-0.10800	-0.11540	-0.14490	-0.18750	-0.24980	-0.29000	-0.35780	-0.50830
r	26	-0.05821	-0.07313	-0.08995	-0.11090	-0.13020	-0.13990	-0.17850	-0.18680	-0.21390	-0.28630	-0.40600	-0.61740
e	28	-0.07289	-0.08894	-0.11050	-0.13600	-0.13090	-0.13020	-0.15070	-0.18840	-0.24760	-0.33930	-0.48320	-0.73160
e	30	-0.09067	-0.10700	-0.09925	-0.11510	-0.12870	-0.13730	-0.17100	-0.22040	-0.29240	-0.39770	-0.56700	-0.84760
s)	35	-0.09112	-0.10840	-0.13050	-0.15890	-0.18390	-0.19610	-0.24660	-0.31490	-0.41190	-0.55640	-0.77960	-1.15500

Table G.1c) 300 kW, 3 blades, tip speed 66 m/s, full-span regulated - Configuration C.

		Tip speed ratio (rad)										
		2.80	3.00	3.23	3.50	3.82	4.20	4.42	4.67	4.94	5.25	5.60
P	0	0.02505	0.02933	0.03422	0.03954	0.04556	0.05264	0.05626	0.05952	0.06199	0.06350	0.06407
i	2	0.03002	0.03432	0.03903	0.04443	0.05054	0.05623	0.05837	0.05988	0.06080	0.06115	0.06089
t	4	0.03434	0.03855	0.04338	0.04854	0.05307	0.05611	0.05701	0.05744	0.05743	0.05691	0.05579
c	6	0.03814	0.04238	0.04664	0.05018	0.05257	0.05365	0.05362	0.05318	0.05230	0.05086	0.04892
h	8	0.04142	0.04483	0.04753	0.04932	0.05005	0.04947	0.04861	0.04729	0.04550	0.04323	0.04026
a	10	0.04310	0.04511	0.04638	0.04674	0.04593	0.04379	0.04211	0.03995	0.03733	0.03408	0.03024
n	12	0.04291	0.04371	0.04370	0.04271	0.04049	0.03678	0.03433	0.03143	0.02796	0.02386	0.01904
g	14	0.04128	0.04095	0.03971	0.03737	0.03383	0.02883	0.02564	0.02189	0.01755	0.01255	0.00674
l	16	0.03839	0.03693	0.03453	0.03107	0.02631	0.01993	0.01599	0.01148	0.00636	0.00042	-0.00651
e	18	0.03436	0.03189	0.02850	0.02393	0.01801	0.01030	0.00567	0.00043	-0.00562	-0.01267	-0.02092
(d	20	0.02943	0.02607	0.02168	0.01612	0.00903	0.00008	-0.00529	-0.01147	-0.01853	-0.02671	-0.03618
e	22	0.02377	0.01954	0.01428	0.00770	-0.00049	-0.01081	-0.01700	-0.02397	-0.03190	-0.04101	-0.05159
g	24	0.01748	0.01249	0.00631	-0.00124	-0.01054	-0.02206	-0.02884	-0.03655	-0.04522	-0.05501	-0.06593
r	26	0.01070	0.00489	-0.00213	-0.01056	-0.02074	-0.03322	-0.04043	-0.04822	-0.05676	-0.06698	-0.08017
e	28	0.00341	-0.00311	-0.01078	-0.01989	-0.03066	-0.04298	-0.05024	-0.05927	-0.07053	-0.08293	-0.08206
e	30	-0.00416	-0.01118	-0.01937	-0.02861	-0.03916	-0.05395	-0.06284	-0.06485	-0.06251	-0.06941	-0.07860
s)	32	-0.01173	-0.01903	-0.02697	-0.03666	-0.04953	-0.04956	-0.05349	-0.05944	-0.06670	-0.07720	-0.09058

		Tip speed ratio (rad)									
		6.00	6.46	7.00	7.64	8.40	9.33	10.50	12.00	14.00	16.80
P	0	0.06385	0.06277	0.06020	0.05675	0.05173	0.04558	0.03807	0.02858	0.01634	-0.00050
i	2	0.05994	0.05829	0.05579	0.05247	0.04815	0.04237	0.03533	0.02632	0.01509	-0.00072
t	4	0.05411	0.05170	0.04851	0.04456	0.03958	0.03345	0.02600	0.01646	0.00354	-0.01564
c	6	0.04627	0.04293	0.03887	0.03384	0.02779	0.02041	0.01102	-0.00134	-0.01880	-0.04720
h	8	0.03666	0.03240	0.02719	0.02093	0.01329	0.00378	-0.00856	-0.02519	-0.04924	-0.09014
a	10	0.02571	0.02026	0.01376	0.00586	-0.00378	-0.01602	-0.03209	-0.05439	-0.08725	-0.14010
n	12	0.01337	0.00667	-0.00136	-0.01105	-0.02321	-0.03884	-0.05980	-0.08923	-0.13310	-0.20280
g	14	-0.00009	-0.00820	-0.01796	-0.03001	-0.04526	-0.06502	-0.09165	-0.12910	-0.18540	-0.27640
l	16	-0.01471	-0.02454	-0.03639	-0.05110	-0.06964	-0.09372	-0.12640	-0.16470	-0.24370	-0.35670
e	18	-0.03067	-0.04221	-0.05619	-0.07344	-0.09543	-0.12430	-0.16300	-0.21680	-0.29750	-0.43860
(d	20	-0.04723	-0.06049	-0.07660	-0.09644	-0.12100	-0.15220	-0.19610	-0.26390	-0.37570	-0.50730
e	22	-0.06402	-0.07853	-0.09540	-0.11630	-0.14520	-0.18700	-0.24440	-0.26930	-0.35030	-0.50260
g	24	-0.07846	-0.09432	-0.11590	-0.14430	-0.17190	-0.16980	-0.21310	-0.28350	-0.40330	-0.60970
r	26	-0.09706	-0.11550	-0.11000	-0.12070	-0.14900	-0.19070	-0.25100	-0.34360	-0.48860	-0.73270
e	28	-0.08309	-0.09584	-0.11320	-0.14020	-0.17710	-0.22810	-0.30080	-0.40840	-0.57660	-0.85930
e	30	-0.09203	-0.11060	-0.13470	-0.16650	-0.20930	-0.26790	-0.35170	-0.47480	-0.66760	-0.98970
s)	32	-0.10760	-0.12920	-0.15690	-0.19430	-0.24280	-0.30960	-0.40450	-0.54320	0.75960	-1.12200

Table G.1d) 1 MW, 2 blades, tip speed 84 m/s, full-span regulated - Configuration D.

		Tip speed ratio (rad)										
		2.80	3.00	3.23	3.50	3.82	4.20	4.42	4.67	4.94	5.25	5.60
P	0	0.02592	0.03039	0.03554	0.04118	0.04751	0.05497	0.05889	0.06252	0.06514	0.06665	0.06712
i	2	0.03113	0.03568	0.04060	0.04627	0.05283	0.05903	0.06136	0.06297	0.06385	0.06413	0.06376
t	4	0.03570	0.04009	0.04515	0.05074	0.05574	0.05899	0.05991	0.06032	0.06026	0.05965	0.05839
c	6	0.03965	0.04416	0.04876	0.05267	0.05525	0.05636	0.05630	0.05581	0.05482	0.05326	0.05116
h	8	0.04319	0.04691	0.04986	0.05180	0.05258	0.05194	0.05103	0.04956	0.04766	0.04522	0.04205
a	10	0.04512	0.04731	0.04869	0.04909	0.04824	0.04592	0.04412	0.04180	0.03904	0.03559	0.03152
n	12	0.04498	0.04588	0.04588	0.04482	0.04245	0.03852	0.03593	0.03279	0.02916	0.02482	0.01978
g	14	0.04329	0.04297	0.04168	0.03921	0.03540	0.03013	0.02676	0.02275	0.01825	0.01298	0.00688
l	16	0.04027	0.03875	0.03621	0.03253	0.02746	0.02076	0.01663	0.01180	0.00651	0.00027	-0.00698
e	18	0.03602	0.03342	0.02984	0.02500	0.01872	0.01064	0.00580	0.00021	-0.00604	-0.01342	-0.02203
(d	20	0.03082	0.02728	0.02266	0.01679	0.00927	-0.00007	-0.00568	-0.01226	-0.01952	-0.02807	-0.03791
e	22	0.02486	0.02039	0.01489	0.00793	-0.00072	-0.01147	-0.01790	-0.02529	-0.03342	-0.04293	-0.05392
g	24	0.01823	0.01298	0.00652	-0.00144	-0.01124	-0.02320	-0.03023	-0.03837	-0.04721	-0.05734	-0.06856
r	26	0.01111	0.00500	-0.00234	-0.01118	-0.02187	-0.03477	-0.04218	-0.05030	-0.05906	-0.06991	-0.08395
e	28	0.00345	-0.00338	-0.01137	-0.02090	-0.03212	-0.04478	-0.05242	-0.06222	-0.07378	-0.08568	-0.08181
e	30	-0.00447	-0.01181	-0.02030	-0.02986	-0.04098	-0.05652	-0.06507	-0.06330	-0.06467	-0.07223	-0.08191
s)	32	-0.01237	-0.01993	-0.02812	-0.03845	-0.05144	-0.05116	-0.05550	-0.06187	-0.06948	-0.08050	-0.09449

		Tip speed ratio (rad)									
		6.00	6.46	7.00	7.64	8.40	9.33	10.50	12.00	14.00	16.80
P	0	0.06671	0.06542	0.06284	0.05865	0.05343	0.04685	0.03870	0.02859	0.01569	-0.00184
i	2	0.06267	0.06077	0.05799	0.05438	0.04973	0.04392	0.03625	0.02692	0.01516	-0.00132
t	4	0.05653	0.05394	0.05050	0.04625	0.04102	0.03464	0.02683	0.01692	0.00355	-0.01628
c	6	0.04832	0.04477	0.04046	0.03515	0.02884	0.02117	0.01140	-0.00141	-0.01945	-0.04993
h	8	0.03823	0.03376	0.02826	0.02166	0.01374	0.00389	-0.00892	-0.02617	-0.05106	-0.09408
a	10	0.02675	0.02105	0.01423	0.00594	-0.00405	-0.01673	-0.03343	-0.05652	-0.09060	-0.14530
n	12	0.01382	0.00685	-0.00157	-0.01172	-0.02430	-0.04046	-0.06227	-0.09278	-0.13830	-0.21170
g	14	-0.00026	-0.00870	-0.01889	-0.03152	-0.04725	-0.06771	-0.09541	-0.13430	-0.19270	-0.28720
l	16	-0.01554	-0.02573	-0.03811	-0.05350	-0.07262	-0.09753	-0.13150	-0.17140	-0.25210	-0.37020
e	18	-0.03217	-0.04412	-0.05869	-0.07672	-0.09943	-0.12920	-0.16950	-0.22510	-0.30880	-0.45370
(d	20	-0.04939	-0.06311	-0.07988	-0.10050	-0.12580	-0.15800	-0.20380	-0.27460	-0.38750	-0.54050
e	22	-0.06677	-0.08164	-0.09911	-0.12110	-0.15140	-0.19500	-0.25430	-0.27760	-0.35660	-0.52100
g	24	-0.08162	-0.09834	-0.12120	-0.15060	-0.17030	-0.17530	-0.21670	-0.29500	-0.41950	-0.63410
r	26	-0.10140	-0.11850	-0.11180	-0.12600	-0.15540	-0.19850	-0.26140	-0.35770	-0.50840	-0.76230
e	28	-0.08648	-0.09980	-0.11930	-0.14640	-0.18450	-0.23740	-0.31320	-0.42510	-0.60010	-0.89490
e	30	-0.09597	-0.11520	-0.14040	-0.17380	-0.21800	-0.27930	-0.36620	-0.49420	-0.69470	-1.03000
s)	32	-0.11220	-0.13460	-0.16350	-0.20260	-0.25280	-0.32210	-0.42100	-0.56530	-0.79040	-1.16800

Table G.1e) 1 MW, 3 blades, tip speed 84 m/s, full-span regulated- Configuration E.

		Tip speed ratio (rad)										
		2.20	2.36	2.54	2.75	3.00	3.30	3.47	3.67	3.88	4.13	4.40
P	0	0.01980	0.02358	0.02914	0.03583	0.04366	0.05260	0.05725	0.06258	0.06808	0.07406	0.07894
i	2	0.02508	0.03026	0.03614	0.04294	0.05068	0.05933	0.06414	0.06945	0.07411	0.07793	0.07994
t	4	0.03113	0.03648	0.04245	0.04912	0.05668	0.06534	0.06947	0.07314	0.07562	0.07708	0.07745
c	6	0.03672	0.04211	0.04792	0.05452	0.06196	0.06867	0.07105	0.07277	0.07358	0.07357	0.07273
h	8	0.04176	0.04701	0.05283	0.05915	0.06480	0.06849	0.06943	0.06973	0.06930	0.06803	0.06590
a	10	0.04621	0.05147	0.05685	0.06150	0.06463	0.06586	0.06563	0.06460	0.06303	0.06051	0.05723
n	12	0.05027	0.05492	0.05871	0.06125	0.06226	0.06128	0.05990	0.05776	0.05497	0.05127	0.04684
g	14	0.05319	0.05632	0.05831	0.05903	0.05805	0.05490	0.05253	0.04929	0.04554	0.04062	0.03497
l	16	0.05420	0.05575	0.05614	0.05504	0.05216	0.04720	0.04382	0.03960	0.03469	0.02865	0.02187
e	18	0.05347	0.05353	0.05230	0.04956	0.04500	0.03821	0.03397	0.02862	0.02281	0.01569	0.00781
(d	20	0.05120	0.04979	0.04710	0.04283	0.03666	0.02822	0.02307	0.01681	0.01008	0.00181	-0.00748
e	22	0.04752	0.04476	0.04069	0.03503	0.02740	0.01736	0.01140	0.00425	-0.00358	-0.01319	-0.02385
g	24	0.04263	0.03861	0.03330	0.02635	0.01732	0.00579	-0.00100	-0.00927	-0.01813	-0.02890	-0.04072
r	26	0.03670	0.03154	0.02508	0.01690	0.00655	-0.00652	-0.01416	-0.02326	-0.03297	-0.04467	-0.05741
e	28	0.02989	0.02368	0.01614	0.00680	-0.00481	-0.01917	-0.02743	-0.03724	-0.04746	-0.05930	-0.07187
e	30	0.02234	0.01514	0.00660	-0.00379	-0.01641	-0.03172	-0.04022	-0.04983	-0.05995	-0.07331	-0.08948
s)	32	0.01411	0.00604	-0.00340	-0.01454	-0.02779	-0.04279	-0.05141	-0.06278	-0.07535	-0.07709	-0.07899

		Tip speed ratio (rad)									
		4.71	5.08	5.50	6.00	6.60	7.33	8.25	9.43	11.00	13.20
P	0	0.08171	0.08199	0.07987	0.07586	0.06895	0.06153	0.05251	0.04143	0.02761	0.00963
i	2	0.08045	0.07964	0.07730	0.07353	0.06793	0.06124	0.05258	0.04233	0.02991	0.01369
t	4	0.07679	0.07489	0.07196	0.06772	0.06227	0.05534	0.04689	0.03667	0.02359	0.00541
c	6	0.07087	0.06801	0.06398	0.05870	0.05226	0.04438	0.03461	0.02240	0.00590	-0.01854
h	8	0.06296	0.05870	0.05347	0.04711	0.03916	0.02955	0.01747	0.00148	-0.02079	-0.06337
a	10	0.05293	0.04748	0.04102	0.03301	0.02330	0.01128	-0.00425	-0.02507	-0.05504	-0.10860
n	12	0.04138	0.03449	0.02654	0.01682	0.00484	-0.01012	-0.02986	-0.05693	-0.09672	-0.16060
g	14	0.02821	0.02005	0.01040	-0.00140	-0.01597	-0.03453	-0.05947	-0.09430	-0.14580	-0.23020
l	16	0.01397	0.00411	-0.00739	-0.02154	-0.03931	-0.06223	-0.09310	-0.13620	-0.18240	-0.30440
e	18	-0.00162	-0.01321	-0.02690	-0.04377	-0.06507	-0.09236	-0.12930	-0.16090	-0.25920	-0.38260
(d	20	-0.01847	-0.03207	-0.04789	-0.06748	-0.09204	-0.12380	-0.16680	-0.22580	-0.31240	-0.46100
e	22	-0.03641	-0.05163	-0.06956	-0.09175	-0.11940	-0.15370	-0.20000	-0.27080	-0.38600	-0.51520
g	24	-0.05450	-0.07145	-0.09084	-0.11380	-0.14300	-0.18500	-0.24670	-0.28530	-0.34930	-0.50200
r	26	-0.07193	-0.08884	-0.10940	-0.13820	-0.17610	-0.17960	-0.21110	-0.28280	-0.40090	-0.60960
e	28	-0.08754	-0.10920	-0.13400	-0.12820	-0.14870	-0.18580	-0.24440	-0.33510	-0.47910	-0.72040
e	30	-0.10500	-0.09790	-0.11350	-0.13550	-0.16880	-0.21730	-0.28860	-0.39260	-0.55970	-0.83670
s)	32	-0.08950	-0.10400	-0.12580	-0.15640	-0.19760	-0.25410	-0.33520	-0.45520	-0.64210	-0.95650

Table G.1f) 1 MW, 3 blades, tip speed 66 m/s, full-span regulated- Configuration F.

Wind speed	Tip angle (°)	$\partial T/\partial \beta$ (kNm/°)	$\partial T/\partial V$ (kNm/m/s)
11.3	0.00	-1.458	15.000
12	3.12	-4.479	14.292
13	5.70	-6.563	14.646
14	7.70	-8.333	15.188
15	9.41	-9.792	15.708
16	10.97	-10.938	16.229
17	12.40	-12.083	16.875
18	13.80	-13.438	17.500
19	15.03	-14.583	18.271
20	16.25	-15.833	18.917
21	17.40	-16.875	19.563
22.0	18.53	-17.813	20.167
23	19.64	-18.958	20.750
24	20.75	-20.208	21.167
25	21.80	-21.250	22.000

Configuration A.

Wind speed	Tip angle (°)	$\partial T/\partial \beta$ (kNm/°)	$\partial T/\partial V$ (kNm/m/s)
11.3	0.00	-1.538	14.228
12	3.10	-4.038	13.324
13	5.70	-6.153	13.651
14	7.72	-7.883	14.151
15	9.44	-9.037	14.689
16	11.00	-10.190	15.132
17	12.42	-11.344	15.728
18	13.86	-12.690	16.305
19	15.04	-13.555	17.016
20	16.27	-14.709	17.612
21	17.44	-15.766	18.227
22	18.59	-16.728	18.804
23	19.68	-17.881	19.362
24	20.76	-18.785	19.785
25	21.80	-19.804	20.515

Configuration B.

Wind speed	Tip angle (°)	$\partial T/\partial \beta$ (kNm/°)	$\partial T/\partial V$ (kNm/m/s)
11.3	0.00	-0.242	16.848
12	4.57	-3.879	16.218
13	7.85	-6.182	16.824
14	10.30	-7.879	17.479
15	12.40	-9.212	18.303
16	14.26	-10.667	19.152
17	15.98	-12.000	19.952
18	17.60	-13.212	20.655
19	19.13	-14.424	21.479
20	20.59	-15.515	22.182
21	21.99	-16.727	23.006
22	23.33	-17.818	23.806
23	24.63	-19.152	24.267
24	25.89	-20.364	25.261
25	27.11	-21.576	26.061

Configuration C.

Table G.2a) Partial derivatives for the 300 kW full-span regulated rotors

Wind speed	Tip angle (°)	$\partial T/\partial \beta$ (kNm/°)	$\partial T/\partial V$ (kNm/m/s)
11.2	0.00	-10.133	93.619
12	3.55	-29.186	87.742
13	6.00	-42.524	89.747
14	7.95	-51.221	93.218
15	9.65	-60.272	97.473
16	11.15	-67.990	100.978
17	12.55	-78.084	104.215
18	13.90	-80.142	107.677
19	15.15	-90.544	114.017
20	16.40	-100.206	117.653
22	18.65	-112.683	123.734
23	19.80	-115.436	126.621
24	20.85	-126.060	133.413
26	22.90	-139.468	137.013
28	24.85	-154.759	146.858
30	26.70	-169.918	156.730

Configuration D.

Wind speed	Tip angle (°)	$\partial T/\partial \beta$ (kNm/°)	$\partial T/\partial V$ (kNm/m/s)
11.2	0.00	-9.569	92.354
12	3.82	-27.858	87.549
13	6.22	-44.966	90.063
14	8.11	-54.739	93.159
15	9.75	-61.025	96.769
16	11.23	-69.068	100.623
17	12.62	-79.232	104.621
18	13.94	-81.715	108.525
19	15.17	-92.293	112.710
20	16.37	-102.038	116.107
22	18.63	-115.192	123.783
23	19.7	-117.795	128.426
24	20.76	-128.759	132.220
26	22.78	-142.925	140.312
28	24.71	-158.118	147.511
30	26.56	-174.301	158.199

Configuration E.

Wind speed	Tip angle (°)	$\partial T/\partial \beta$ (kNm/°)	$\partial T/\partial V$ (kNm/m/s)
11.22	0.00	-4.814	109.068
12	5.25	-29.769	106.607
13	8.30	-43.727	111.082
14	10.65	-54.767	116.159
15	12.65	-64.511	120.736
16	14.50	-73.890	125.427
17	16.20	-83.026	132.207
18	17.80	-85.761	136.121
19	19.30	-95.214	142.136
20	20.75	-104.933	144.814
22	23.50	-117.844	155.270
23	24.75	-128.871	162.507
24	26.05	-140.520	165.471
26	28.40	-155.731	173.886
28	30.65	-172.011	182.927
30	32.85	-178.957	199.399

Configuration F.

Table G.2b) Partial derivatives for the 1 MW full-span regulated rotors

		Tip speed ratio (rad)												
P		2.8	3	3.231	3.36	3.5	3.652	3.818	4	4.2	4.421	4.667	4.941	5.25
i	0	0.02505	0.02933	0.03422	0.03683	0.03954	0.04243	0.04557	0.04901	0.05265	0.05627	0.05953	0.06200	0.06351
t	2	0.02650	0.03079	0.03546	0.03818	0.04111	0.04410	0.04708	0.05003	0.05295	0.05583	0.05855	0.06076	0.06215
c	4	0.02762	0.03188	0.03686	0.03952	0.04212	0.04454	0.04682	0.04915	0.05170	0.05440	0.05699	0.05906	0.06027
h	6	0.02867	0.03304	0.03734	0.03940	0.04141	0.04339	0.04543	0.04764	0.05005	0.05257	0.05497	0.05682	0.05782
	8	0.02950	0.03300	0.03631	0.03809	0.03995	0.04181	0.04372	0.04575	0.04796	0.05027	0.05247	0.05410	0.05485
a	10	0.02899	0.03177	0.03482	0.03649	0.03819	0.03988	0.04158	0.04341	0.04542	0.04756	0.04955	0.05095	0.05146
n	12	0.02767	0.03026	0.03301	0.03452	0.03605	0.03756	0.03910	0.04076	0.04258	0.04450	0.04628	0.04747	0.04775
g	14	0.02613	0.02844	0.03088	0.03222	0.03359	0.03495	0.03633	0.03783	0.03949	0.04122	0.04278	0.04370	0.04368
l	16	0.02427	0.02629	0.02848	0.02969	0.03094	0.03216	0.03339	0.03471	0.03617	0.03769	0.03902	0.03968	0.03936
e	18	0.02215	0.02397	0.02592	0.02701	0.02812	0.02919	0.03025	0.03140	0.03268	0.03398	0.03505	0.03540	0.03467
(d	20	0.01989	0.02150	0.02322	0.02418	0.02516	0.02609	0.02700	0.02796	0.02901	0.03003	0.03078	0.03076	0.02964
e	22	0.01750	0.01891	0.02042	0.02126	0.02209	0.02286	0.02356	0.02429	0.02509	0.02586	0.02635	0.02607	0.02461
g	24	0.01502	0.01625	0.01752	0.01821	0.01887	0.01944	0.01997	0.02054	0.02118	0.02177	0.02201	0.02143	0.01976
r	26	0.01248	0.01348	0.01447	0.01503	0.01559	0.01608	0.01651	0.01694	0.01741	0.01791	0.01827	0.01787	0.01584
e	28	0.00983	0.01063	0.01150	0.01202	0.01249	0.01289	0.01330	0.01388	0.01461	0.01497	0.01427	0.01212	0.00938
e	30	0.00719	0.00795	0.00874	0.00927	0.00992	0.01059	0.01097	0.01079	0.01012	0.00983	0.01642	0.02168	0.01876
s)	35	0.00212	0.00228	0.00320	0.01032	0.01279	0.01287	0.01301	0.01286	0.01250	0.01184	0.01054	0.00802	0.00377

		Tip speed ratio (rad)											
P		5.60	6.00	6.46	7.00	7.43	7.64	8.40	9.33	10.50	12.00	14.00	16.80
i	0	0.06408	0.06386	0.06278	0.06020	0.05787	0.05675	0.05173	0.04558	0.03806	0.02858	0.01633	-0.00052
t	2	0.06261	0.06226	0.06108	0.05889	0.05677	0.05568	0.05142	0.04542	0.03807	0.02887	0.01767	0.00267
c	4	0.06055	0.06004	0.05871	0.05637	0.05414	0.05300	0.04857	0.04277	0.03563	0.02691	0.01591	0.00100
h	6	0.05789	0.05715	0.05557	0.05295	0.05053	0.04929	0.04458	0.03844	0.03084	0.02142	0.00930	-0.00751
	8	0.05467	0.05367	0.05180	0.04885	0.04616	0.04481	0.03961	0.03281	0.02425	0.01350	-0.00065	-0.02078
a	10	0.05101	0.04972	0.04752	0.04416	0.04109	0.03956	0.03364	0.02593	0.01615	0.00354	-0.01348	-0.03849
n	12	0.04701	0.04534	0.04270	0.03881	0.03533	0.03359	0.02682	0.01793	0.00645	-0.00866	-0.02954	-0.05980
g	14	0.04261	0.04056	0.03744	0.03293	0.02888	0.02686	0.01897	0.00857	-0.00500	-0.02312	-0.04867	-0.08704
l	16	0.03790	0.03536	0.03160	0.02629	0.02158	0.01925	0.01011	-0.00195	-0.01787	-0.03954	-0.07112	-0.11970
e	18	0.03273	0.02962	0.02521	0.01914	0.01376	0.01110	0.00058	-0.01341	-0.03194	-0.05704	-0.09300	-0.15320
(d	20	0.02728	0.02368	0.01862	0.01166	0.00555	0.00255	-0.00904	-0.02422	-0.04488	-0.07445	-0.12310	-0.19690
e	22	0.02179	0.01765	0.01212	0.00487	-0.00154	-0.00477	-0.01822	-0.03743	-0.06372	-0.09373	-0.12550	-0.18940
g	24	0.01696	0.01280	0.00645	-0.00312	-0.01183	-0.01604	-0.03025	-0.03236	-0.05528	-0.08611	-0.13990	-0.22790
r	26	0.01149	0.00506	-0.00203	0.00243	-0.00279	-0.00402	-0.01971	-0.04085	-0.07035	-0.11260	-0.17640	-0.28040
e	28	0.01616	0.01574	0.00818	-0.00165	-0.01066	-0.01516	-0.03330	-0.05795	-0.09194	-0.14060	-0.21410	-0.33430
e	30	0.01464	0.00843	-0.00018	-0.01178	-0.02209	-0.02718	-0.04767	-0.07548	-0.11390	-0.16910	-0.25270	-0.38960
a)	35	-0.00253	-0.01112	-0.02253	-0.03769	-0.05109	-0.05769	-0.08427	-0.12030	-0.17040	-0.24250	-0.35240	-0.53300

Table G.3a) 300 kW, 2 blades, tip speed 84 m/s, tip regulated - Configuration G.

		Tip speed ratio (rad)										
P		2.80	3.00	3.23	3.50	3.82	4.20	4.42	4.67	4.94	5.25	5.60
i	0	0.02606	0.03056	0.03575	0.04139	0.04771	0.05524	0.05919	0.06276	0.06541	0.06690	0.06734
t	2	0.02779	0.03241	0.03730	0.04321	0.04975	0.05598	0.05891	0.06165	0.06386	0.06517	0.06549
c	4	0.02926	0.03371	0.03898	0.04471	0.04978	0.05450	0.05712	0.05968	0.06172	0.06281	0.06288
h	6	0.03046	0.03519	0.03988	0.04413	0.04808	0.05243	0.05483	0.05715	0.05891	0.05972	0.05953
	8	0.03163	0.03549	0.03883	0.04233	0.04596	0.04984	0.05197	0.05402	0.05549	0.05601	0.05548
a	10	0.03133	0.03409	0.03698	0.04017	0.04333	0.04668	0.04856	0.05036	0.05155	0.05176	0.05092
n	12	0.02976	0.03224	0.03477	0.03751	0.04023	0.04314	0.04476	0.04628	0.04721	0.04713	0.04594
g	14	0.02787	0.03000	0.03214	0.03448	0.03678	0.03927	0.04067	0.04193	0.04254	0.04209	0.04049
l	16	0.02561	0.02736	0.02915	0.03117	0.03312	0.03517	0.03631	0.03728	0.03757	0.03675	0.03470
e	18	0.02299	0.02447	0.02598	0.02767	0.02925	0.03085	0.03173	0.03239	0.03230	0.03101	0.02836
(d	20	0.02019	0.02141	0.02264	0.02402	0.02522	0.02634	0.02688	0.02715	0.02663	0.02489	0.02176
e	22	0.01723	0.01821	0.01918	0.02024	0.02101	0.02154	0.02179	0.02178	0.02096	0.01880	0.01513
g	24	0.01417	0.01493	0.01562	0.01628	0.01662	0.01680	0.01684	0.01653	0.01539	0.01307	0.00954
r	26	0.01104	0.01153	0.01189	0.01228	0.01242	0.01227	0.01226	0.01217	0.01121	0.00822	0.00245
e	28	0.00779	0.00804	0.00826	0.00853	0.00859	0.00896	0.00865	0.00704	0.00400	0.00123	0.01146
e	30	0.00455	0.00476	0.00492	0.00548	0.00571	0.00337	0.00292	0.01312	0.01580	0.01195	0.00674
s)	35	-0.00165	-0.00214	-0.00054	0.00883	0.00833	0.00650	0.00506	0.00292	-0.00057	-0.00606	-0.01388

		Tip speed ratio (rad)									
P		6.00	6.46	7.00	7.64	8.40	9.33	10.50	12.00	14.00	16.80
i	0	0.06691	0.06558	0.06296	0.05875	0.05337	0.04681	0.03865	0.02849	0.01551	-0.00202
t	2	0.06490	0.06342	0.06085	0.05723	0.05256	0.04654	0.03858	0.02911	0.01747	0.00197
c	4	0.06208	0.06044	0.05769	0.05388	0.04903	0.04295	0.03547	0.02644	0.01509	-0.00027
h	6	0.05844	0.05648	0.05340	0.04925	0.04405	0.03755	0.02951	0.01963	0.00689	-0.01085
	8	0.05406	0.05175	0.04827	0.04365	0.03785	0.03054	0.02135	0.00982	-0.00543	-0.02730
a	10	0.04913	0.04641	0.04242	0.03712	0.03046	0.02204	0.01134	-0.00246	-0.02122	-0.04905
n	12	0.04371	0.04044	0.03582	0.02975	0.02207	0.01220	-0.00056	-0.01739	-0.04085	-0.07644
g	14	0.03779	0.03396	0.02858	0.02148	0.01245	0.00077	-0.01451	-0.03496	-0.06404	-0.10830
l	16	0.03141	0.02680	0.02047	0.01221	0.00169	-0.01197	-0.03007	-0.05480	-0.09055	-0.14660
e	18	0.02441	0.01904	0.01180	0.00237	-0.00981	-0.02576	-0.04686	-0.07539	-0.11670	-0.18530
(d	20	0.01722	0.01107	0.00280	-0.00784	-0.02119	-0.03843	-0.06223	-0.09715	-0.15070	-0.23580
e	22	0.01001	0.00343	-0.00505	-0.01648	-0.03262	-0.05541	-0.08567	-0.10920	-0.14600	-0.22890
g	24	0.00431	-0.00365	-0.01545	-0.03055	-0.04066	-0.04602	-0.06917	-0.11100	-0.17430	-0.27850
r	26	-0.00540	-0.01216	-0.00506	-0.01576	-0.03404	-0.05870	-0.09332	-0.14300	-0.21820	-0.34160
e	28	0.00776	-0.00127	-0.01304	-0.02911	-0.05048	-0.07932	-0.11920	-0.17650	-0.26350	-0.40630
e	30	-0.00096	-0.01138	-0.02526	-0.04353	-0.06772	-0.10030	-0.14550	-0.21060	-0.30960	-0.47250
s)	35	-0.02438	-0.03814	-0.05626	-0.08004	-0.11150	-0.15400	-0.21310	-0.29850	-0.42900	-0.64410

Table G.3b) 300 kW, 3 blades, tip speed 84 m/s, tip regulated - Configuration H.

		Tip speed ratio (rad)											
P		2.2	2.357	2.538	2.64	2.75	2.87	3	3.143	3.3	3.474	3.667	3.882
i	0	0.02010	0.02387	0.02953	0.03285	0.03638	0.04019	0.04432	0.04875	0.05336	0.05817	0.06338	0.06906
t	2	0.02329	0.02708	0.03151	0.03465	0.03831	0.04215	0.04605	0.05036	0.05522	0.06030	0.06528	0.07011
c	4	0.02596	0.02872	0.03319	0.03628	0.03974	0.04353	0.04766	0.05218	0.05679	0.06111	0.06503	0.06901
h	6	0.02734	0.03016	0.03437	0.03748	0.04117	0.04508	0.04893	0.05271	0.05638	0.05991	0.06344	0.06723
	8	0.02857	0.03117	0.03566	0.03880	0.04214	0.04534	0.04833	0.05142	0.05473	0.05809	0.06143	0.06500
a	10	0.02947	0.03233	0.03633	0.03877	0.04135	0.04396	0.04666	0.04960	0.05274	0.05586	0.05892	0.06221
n	12	0.03049	0.03268	0.03535	0.03733	0.03968	0.04215	0.04468	0.04740	0.05028	0.05315	0.05597	0.05898
g	14	0.03051	0.03154	0.03369	0.03555	0.03773	0.04000	0.04228	0.04475	0.04740	0.05003	0.05263	0.05541
l	16	0.02923	0.02990	0.03176	0.03340	0.03536	0.03741	0.03951	0.04179	0.04424	0.04666	0.04900	0.05151
e	18	0.02760	0.02796	0.02944	0.03090	0.03270	0.03458	0.03650	0.03859	0.04082	0.04301	0.04512	0.04737
(d	20	0.02567	0.02569	0.02687	0.02818	0.02981	0.03152	0.03326	0.03516	0.03721	0.03918	0.04105	0.04301
e	22	0.02343	0.02319	0.02409	0.02526	0.02674	0.02830	0.02987	0.03160	0.03344	0.03519	0.03676	0.03835
g	24	0.02100	0.02052	0.02116	0.02220	0.02354	0.02495	0.02636	0.02790	0.02950	0.03094	0.03218	0.03344
r	26	0.01841	0.01771	0.01814	0.01905	0.02025	0.02149	0.02270	0.02398	0.02534	0.02656	0.02760	0.02866
e	28	0.01572	0.01483	0.01503	0.01579	0.01681	0.01786	0.01888	0.02003	0.02127	0.02236	0.02321	0.02416
e	30	0.01297	0.01188	0.01178	0.01239	0.01330	0.01427	0.01524	0.01630	0.01745	0.01859	0.01985	0.02089
s)	35	0.00580	0.00441	0.00418	0.00492	0.00617	0.00732	0.00774	0.00772	0.00963	0.02263	0.02301	0.02350

		Tip speed ratio (rad)											
P		4.4	4.714	5.077	5.5	5.841	6	6.6	7.333	8.25	9.429	11	13.2
i	0	0.07982	0.08247	0.08256	0.08026	0.07735	0.07604	0.06891	0.06140	0.05228	0.04112	0.02719	0.00907
t	2	0.07891	0.08126	0.08124	0.07940	0.07678	0.07554	0.06911	0.06172	0.05255	0.04184	0.02892	0.01265
c	4	0.07729	0.07947	0.07929	0.07731	0.07464	0.07337	0.06729	0.06012	0.05144	0.04109	0.02854	0.01272
h	6	0.07508	0.07702	0.07662	0.07439	0.07155	0.07020	0.06385	0.05640	0.04749	0.03677	0.02360	0.00650
	8	0.07229	0.07395	0.07322	0.07067	0.06759	0.06612	0.05935	0.05142	0.04181	0.03002	0.01519	-0.00469
a	10	0.06895	0.07029	0.06921	0.06630	0.06292	0.06131	0.05396	0.04524	0.03454	0.02123	0.00401	-0.01987
n	12	0.06515	0.06617	0.06474	0.06133	0.05755	0.05575	0.04768	0.03799	0.02593	0.01057	-0.00988	-0.03918
g	14	0.06096	0.06161	0.05974	0.05583	0.05159	0.04957	0.04061	0.02968	0.01584	-0.00214	-0.02662	-0.06255
l	16	0.05644	0.05670	0.05434	0.04979	0.04499	0.04271	0.03260	0.02015	0.00423	-0.01671	-0.04574	-0.08941
e	18	0.05162	0.05141	0.04844	0.04311	0.03765	0.03504	0.02373	0.00971	-0.00841	-0.03269	-0.06693	-0.11870
(d	20	0.04643	0.04564	0.04201	0.03592	0.02984	0.02694	0.01442	-0.00125	-0.02170	-0.04873	-0.08686	-0.14680
e	22	0.04086	0.03959	0.03541	0.02859	0.02184	0.01862	0.00497	-0.01168	-0.03349	-0.06497	-0.11310	-0.18710
g	24	0.03532	0.03358	0.02880	0.02152	0.01471	0.01148	-0.00290	-0.02305	-0.05114	-0.07623	-0.10740	-0.16790
r	26	0.02990	0.02812	0.02360	0.01556	0.00677	0.00233	-0.01587	-0.02051	-0.03426	-0.07037	-0.12430	-0.21140
e	28	0.02591	0.02312	0.01569	0.00613	0.01380	0.01216	-0.00078	-0.02216	-0.05187	-0.09390	-0.15650	-0.25740
e	30	0.01891	0.01771	0.02854	0.01922	0.01053	0.00619	-0.01259	-0.03726	-0.07082	-0.11830	-0.18940	-0.30430
a)	35	0.02181	0.01740	0.00907	-0.00322	-0.01487	-0.02053	-0.04441	-0.07596	-0.11920	-0.18100	-0.27410	-0.42580

Table G.3c) 300 kW, 3 blades, tip speed 66 m/s, tip regulated - Configuration I.

		Tip speed ratio (rad)										
		2.80	3.00	3.23	3.50	3.82	4.20	4.42	4.67	4.94	5.25	5.60
P	0	0.02505	0.02933	0.03422	0.03954	0.04556	0.05264	0.05626	0.05952	0.06199	0.06350	0.06407
t	2	0.02639	0.03065	0.03535	0.04100	0.04693	0.05287	0.05583	0.05862	0.06086	0.06226	0.06273
h	4	0.02740	0.03167	0.03665	0.04188	0.04664	0.05172	0.05453	0.05720	0.05931	0.06055	0.06085
a	6	0.02838	0.03273	0.03703	0.04119	0.04537	0.05021	0.05285	0.05534	0.05726	0.05830	0.05842
g	8	0.02912	0.03263	0.03605	0.03985	0.04380	0.04829	0.05074	0.05305	0.05477	0.05560	0.05547
e	10	0.02859	0.03148	0.03469	0.03824	0.04183	0.04597	0.04826	0.05038	0.05189	0.05248	0.05213
(d	12	0.02737	0.03009	0.03302	0.03626	0.03956	0.04336	0.04545	0.04738	0.04870	0.04908	0.04846
e	14	0.02595	0.02841	0.03106	0.03401	0.03702	0.04053	0.04245	0.04417	0.04524	0.04536	0.04443
g	16	0.02424	0.02644	0.02886	0.03158	0.03432	0.03749	0.03921	0.04072	0.04155	0.04139	0.04011
r	18	0.02229	0.02430	0.02652	0.02899	0.03144	0.03429	0.03581	0.03708	0.03762	0.03708	0.03535
e	20	0.02022	0.02204	0.02404	0.02627	0.02846	0.03092	0.03218	0.03316	0.03336	0.03246	0.03034
e	22	0.01802	0.01966	0.02146	0.02346	0.02530	0.02731	0.02835	0.02909	0.02904	0.02783	0.02528
s)	24	0.01575	0.01722	0.01880	0.02050	0.02200	0.02373	0.02459	0.02509	0.02477	0.02336	0.02082
	26	0.01342	0.01468	0.01601	0.01749	0.01882	0.02026	0.02104	0.02165	0.02148	0.01974	0.01580
	28	0.01099	0.01207	0.01329	0.01465	0.01588	0.01768	0.01832	0.01795	0.01619	0.01378	0.01980
	30	0.00857	0.00961	0.01075	0.01230	0.01372	0.01533	0.01359	0.02015	0.02493	0.02237	0.01862
	32	0.00634	0.00742	0.00897	0.00993	0.00985	0.02128	0.02141	0.02133	0.02004	0.01708	0.01234

		Tip speed ratio (rad)									
		6.00	6.46	7.00	7.64	8.40	9.33	10.50	12.00	14.00	16.80
P	0	0.06385	0.06277	0.06020	0.05675	0.05173	0.04558	0.03807	0.02858	0.01634	-0.00050
t	2	0.06239	0.06122	0.05904	0.05583	0.05155	0.04549	0.03812	0.02887	0.01759	0.00253
h	4	0.06037	0.05906	0.05674	0.05339	0.04896	0.04311	0.03594	0.02718	0.01611	0.00118
a	6	0.05773	0.05620	0.05362	0.05000	0.04531	0.03916	0.03158	0.02218	0.01012	-0.00651
g	8	0.05454	0.05275	0.04988	0.04591	0.04077	0.03402	0.02557	0.01496	0.00104	-0.01862
e	10	0.05093	0.04883	0.04558	0.04110	0.03531	0.02772	0.01815	0.00584	-0.01070	-0.03480
(d	12	0.04692	0.04441	0.04068	0.03563	0.02906	0.02038	0.00926	-0.00533	-0.02541	-0.05425
e	14	0.04253	0.03959	0.03528	0.02945	0.02185	0.01180	-0.00125	-0.01862	-0.04299	-0.07930
g	16	0.03776	0.03422	0.02918	0.02246	0.01371	0.00212	-0.01310	-0.03373	-0.06370	-0.10950
r	18	0.03248	0.02835	0.02260	0.01495	0.00493	-0.00844	-0.02608	-0.04994	-0.08397	-0.14070
e	20	0.02702	0.02228	0.01571	0.00706	-0.00397	-0.01847	-0.03805	-0.06586	-0.11160	-0.18080
e	22	0.02146	0.01627	0.00942	0.00029	-0.01239	-0.03050	-0.05531	-0.08622	-0.11540	-0.17460
s)	24	0.01697	0.01105	0.00211	-0.01004	-0.02393	-0.02659	-0.04804	-0.07679	-0.12720	-0.20930
	26	0.00986	0.00315	0.00670	0.00094	-0.01389	-0.03386	-0.06159	-0.10130	-0.16090	-0.25780
	28	0.01963	0.01257	0.00333	-0.00936	-0.02643	-0.04965	-0.08155	-0.12710	-0.19570	-0.30770
	30	0.01288	0.00485	-0.00601	-0.02047	-0.03972	-0.06585	-0.10190	-0.15340	-0.23140	-0.35880
	32	0.00565	-0.00334	-0.01556	-0.03169	-0.05314	-0.08228	-0.12250	-0.18030	-0.26780	-0.41110

Table G.3d) 1 MW, 2 blades, tip speed 84 m/s, tip regulated - Configuration J.

		Tip speed ratio (rad)										
		2.80	3.00	3.23	3.50	3.82	4.20	4.42	4.67	4.94	5.25	5.60
P	0	0.02592	0.03039	0.03554	0.04118	0.04751	0.05497	0.05889	0.06252	0.06514	0.06665	0.06712
t	2	0.02731	0.03185	0.03673	0.04268	0.04908	0.05546	0.05861	0.06163	0.06393	0.06531	0.06567
h	4	0.02842	0.03287	0.03810	0.04379	0.04897	0.05426	0.05720	0.06008	0.06226	0.06346	0.06363
a	6	0.02940	0.03405	0.03870	0.04319	0.04761	0.05263	0.05540	0.05808	0.06004	0.06104	0.06100
g	8	0.03029	0.03413	0.03774	0.04176	0.04594	0.05059	0.05314	0.05561	0.05736	0.05812	0.05782
e	10	0.02987	0.03293	0.03628	0.04005	0.04385	0.04809	0.05046	0.05273	0.05426	0.05479	0.05423
(d	12	0.02858	0.03147	0.03452	0.03794	0.04140	0.04531	0.04747	0.04952	0.05084	0.05114	0.05032
e	14	0.02708	0.02968	0.03243	0.03554	0.03868	0.04226	0.04426	0.04610	0.04718	0.04717	0.04603
g	16	0.02527	0.02759	0.03008	0.03293	0.03580	0.03904	0.04082	0.04243	0.04326	0.04296	0.04145
r	18	0.02319	0.02531	0.02758	0.03018	0.03275	0.03563	0.03721	0.03858	0.03910	0.03842	0.03645
e	20	0.02098	0.02290	0.02495	0.02731	0.02958	0.03207	0.03339	0.03443	0.03462	0.03359	0.03122
e	22	0.01866	0.02038	0.02223	0.02433	0.02625	0.02828	0.02937	0.03018	0.03013	0.02876	0.02596
s)	24	0.01625	0.01780	0.01942	0.02120	0.02278	0.02454	0.02545	0.02602	0.02572	0.02421	0.02149
	26	0.01379	0.01512	0.01648	0.01806	0.01947	0.02096	0.02184	0.02259	0.02238	0.02030	0.01583
	28	0.01122	0.01237	0.01364	0.01510	0.01647	0.01836	0.01892	0.01838	0.01661	0.01482	0.02268
	30	0.00869	0.00981	0.01102	0.01276	0.01415	0.01380	0.01449	0.02455	0.02582	0.02309	0.01902
	32	0.00638	0.00759	0.00923	0.01006	0.01054	0.02211	0.02217	0.02213	0.02076	0.01755	0.01243

		Tip speed ratio (rad)									
		6.00	6.46	7.00	7.64	8.40	9.33	10.50	12.00	14.00	16.80
P	0	0.06671	0.06542	0.06284	0.05865	0.05343	0.04685	0.03870	0.02859	0.01569	-0.00184
t	2	0.06514	0.06374	0.06119	0.05755	0.05288	0.04678	0.03872	0.02913	0.01734	0.00168
h	4	0.06294	0.06140	0.05872	0.05493	0.05013	0.04399	0.03640	0.02724	0.01577	0.00042
a	6	0.06008	0.05830	0.05536	0.05130	0.04623	0.03977	0.03177	0.02198	0.00950	-0.00761
g	8	0.05665	0.05459	0.05133	0.04690	0.04137	0.03429	0.02539	0.01433	-0.00009	-0.02034
e	10	0.05277	0.05039	0.04673	0.04177	0.03557	0.02761	0.01754	0.00473	-0.01243	-0.03730
(d	12	0.04851	0.04569	0.04153	0.03597	0.02896	0.01989	0.00819	-0.00700	-0.02783	-0.05880
e	14	0.04385	0.04058	0.03583	0.02945	0.02138	0.01087	-0.00281	-0.02088	-0.04616	-0.08384
g	16	0.03881	0.03494	0.02942	0.02211	0.01286	0.00079	-0.01516	-0.03662	-0.06723	-0.11460
r	18	0.03327	0.02880	0.02255	0.01428	0.00372	-0.01019	-0.02859	-0.05324	-0.08836	-0.14580
e	20	0.02757	0.02247	0.01538	0.00613	-0.00544	-0.02044	-0.04088	-0.07019	-0.11470	-0.18550
e	22	0.02183	0.01636	0.00906	-0.00081	-0.01442	-0.03365	-0.05956	-0.08556	-0.11410	-0.18220
s)	24	0.01726	0.01073	0.00088	-0.01200	-0.02353	-0.02770	-0.04670	-0.08190	-0.13460	-0.22040
	26	0.00953	0.00373	0.00820	-0.00047	-0.01599	-0.03687	-0.06608	-0.10760	-0.16990	-0.27110
	28	0.01980	0.01236	0.00243	-0.01122	-0.02916	-0.05341	-0.08690	-0.13450	-0.20630	-0.32320
	30	0.01279	0.00425	-0.00738	-0.02282	-0.04302	-0.07028	-0.10810	-0.16200	-0.24350	-0.37660
	32	0.00526	-0.00434	-0.01732	-0.03452	-0.05701	-0.08740	-0.12960	-0.19000	-0.28140	-0.43100

Table G.3e) 1 MW, 3 blades, tip speed 84 m/s, tip regulated - Configuration K.

		Tip speed ratio (rad)									
		2.20	2.36	2.54	2.75	3.00	3.30	3.47	3.67	3.88	4.13
P	0	0.01980	0.02358	0.02914	0.03583	0.04366	0.05260	0.05725	0.06258	0.06808	0.07406
t	2	0.02293	0.02675	0.03110	0.03773	0.04538	0.05442	0.05935	0.06448	0.06917	0.07399
h	4	0.02559	0.02836	0.03275	0.03915	0.04696	0.05600	0.06021	0.06426	0.06811	0.07251
a	6	0.02696	0.02979	0.03392	0.04055	0.04824	0.05563	0.05905	0.06268	0.06636	0.07056
g	8	0.02817	0.03079	0.03519	0.04154	0.04767	0.05400	0.05725	0.06069	0.06414	0.06807
e	10	0.02906	0.03193	0.03587	0.04077	0.04602	0.05203	0.05506	0.05820	0.06137	0.06504
(d	12	0.03007	0.03228	0.03490	0.03912	0.04406	0.04960	0.05237	0.05527	0.05818	0.06155
e	14	0.03011	0.03115	0.03326	0.03720	0.04170	0.04674	0.04930	0.05196	0.05465	0.05774
g	16	0.02885	0.02953	0.03135	0.03486	0.03895	0.04362	0.04596	0.04837	0.05079	0.05358
r	18	0.02724	0.02761	0.02906	0.03222	0.03597	0.04024	0.04236	0.04453	0.04670	0.04918
e	20	0.02534	0.02536	0.02651	0.02937	0.03277	0.03667	0.03858	0.04050	0.04240	0.04450
e	22	0.02313	0.02288	0.02376	0.02633	0.02942	0.03295	0.03464	0.03626	0.03780	0.03946
a)	24	0.02072	0.02023	0.02086	0.02318	0.02596	0.02905	0.03045	0.03173	0.03296	0.03431
	26	0.01817	0.01746	0.01787	0.01992	0.02233	0.02494	0.02613	0.02721	0.02824	0.02928
	28	0.01551	0.01461	0.01480	0.01653	0.01857	0.02093	0.02200	0.02289	0.02381	0.02511
	30	0.01279	0.01169	0.01159	0.01306	0.01498	0.01716	0.01829	0.01959	0.02060	0.02046
	32	0.00999	0.00865	0.00839	0.00981	0.01169	0.01451	0.01543	0.01506	0.01463	0.02693

		Tip speed ratio									
		4.71	5.08	5.50	6.00	6.60	7.33	8.25	9.43	11.00	13.20
P	0	0.08171	0.08199	0.07987	0.07586	0.06895	0.06153	0.05251	0.04143	0.02761	0.00963
t	2	0.08050	0.08067	0.07898	0.07530	0.06908	0.06180	0.05274	0.04213	0.02928	0.01311
h	4	0.07871	0.07872	0.07688	0.07313	0.06724	0.06014	0.05155	0.04129	0.02881	0.01311
a	6	0.07629	0.07605	0.07397	0.06996	0.06380	0.05643	0.04759	0.03695	0.02387	0.00689
g	8	0.07324	0.07267	0.07027	0.06590	0.05932	0.05147	0.04195	0.03025	0.01552	-0.00418
e	10	0.06962	0.06870	0.06592	0.06113	0.05398	0.04535	0.03474	0.02155	0.00447	-0.01919
(d	12	0.06554	0.06426	0.06101	0.05563	0.04776	0.03818	0.02622	0.01102	-0.00924	-0.03824
e	14	0.06103	0.05931	0.05557	0.04952	0.04076	0.02998	0.01627	-0.00154	-0.02576	-0.06130
g	16	0.05618	0.05396	0.04960	0.04273	0.03287	0.02059	0.00481	-0.01590	-0.04461	-0.08778
r	18	0.05096	0.04814	0.04301	0.03517	0.02411	0.01029	-0.00765	-0.03166	-0.06549	-0.11660
e	20	0.04527	0.04178	0.03591	0.02718	0.01493	-0.00051	-0.02073	-0.04758	-0.08507	-0.14430
e	22	0.03931	0.03527	0.02868	0.01897	0.00563	-0.01074	-0.03233	-0.06354	-0.11110	-0.17450
s)	24	0.03338	0.02875	0.02174	0.01198	-0.00213	-0.02205	-0.04984	-0.07407	-0.10160	-0.16540
	26	0.02803	0.02365	0.01584	0.00286	-0.01491	-0.01528	-0.03316	-0.06887	-0.12220	-0.20830
	28	0.02307	0.01576	0.00667	0.01269	-0.00007	-0.02112	-0.05054	-0.09211	-0.15400	-0.25360
	30	0.01807	0.02846	0.01945	0.00671	-0.01172	-0.03600	-0.06925	-0.11620	-0.18640	-0.29990
	32	0.02764	0.02108	0.01088	-0.00380	-0.02423	-0.05117	-0.08816	-0.14070	-0.21940	-0.34710

Table G.3f) 1 MW, 3 blades, tip speed 66 m/s, tip-regulated - Configuration L.

Wind speed	Tip angle (°)	$\partial T/\partial \beta$ (kNm/°)	$\partial T/\partial V$ (kNm/m/s)
11.3	0.00	0.609	14.047
12	6.47	2.220	13.418
13	11.33	3.242	13.065
14	14.90	3.929	12.770
15	17.77	4.715	12.141
16	20.14	5.108	10.904
17	22.05	5.305	8.821
18	23.49	5.599	6.660
19	24.50	5.796	5.049
20	25.38	5.894	4.283
21	25.97	6.189	4.047
22	26.60	6.385	3.949
23	27.19	6.680	3.615
24	27.64	7.073	2.849
25	28.00	7.269	2.240

Configuration G.

Wind speed	Tip angle (°)	$\partial T/\partial \beta$ (kNm/°)	$\partial T/\partial V$ (kNm/m/s)
11.3	0.00	-0.846	14.132
12	5.60	-2.307	13.324
13	10.40	-3.461	12.940
14	13.30	-4.326	12.767
15	15.98	-4.999	12.036
16	18.15	-5.672	10.998
17	19.85	-6.153	9.017
18	21.11	-6.441	6.960
19	22.05	-6.729	5.653
20	22.83	-7.018	5.191
21	23.53	-7.402	5.134
22	24.22	-7.691	4.999
23	24.83	-8.075	4.576
24	25.33	-8.460	3.980
25	25.77	-8.844	3.576

Configuration H.

Wind speed	Tip angle (°)	$\partial T/\partial \beta$ (kNm/°)	$\partial T/\partial V$ (kNm/m/s)
11.2	0.00	-0.242	16.848
12	9.22	-1.818	16.024
13	15.80	-2.788	14.642
14	20.26	-3.514	12.509
15	23.25	-3.636	8.824
16	25.12	-3.879	5.794
17	26.39	-4.000	4.533
18	27.40	-4.121	4.121
19	28.34	-4.364	3.442
20	28.98	-4.606	2.473
21	29.33	-4.848	1.236
22	29.53	-4.970	0.945
23	29.70	-5.455	0.655
24	29.76	-5.818	0.373
25	29.77	-6.303	0.291

Configuration I.

Table G.4a) Partial derivatives for the 300 kW tip-regulated rotors

Wind speed	Tip angle (°)	$\partial T/\partial \beta$ (kNm/°)	$\partial T/\partial V$ (kNm/m/s)
11.2	0.00	-0.4786	93.619
12	7.75	-14.559	87.543
13	12.65	-21.231	83.513
14	16.30	-26.883	83.918
15	19.25	-29.294	83.211
16	21.70	-30.924	72725
17	23.80	-31.952	53680
18	25.55	-28.792	32.034
19	26.70	-25.853	35.623
20	27.65	-27.435	22.237
22	28.85	-28.229	17.025
23	29.45	-29.087	18.850
24	29.75	-35.087	8.183
26	30.10	-32.308	6.404
28	30.35	-44.519	3.660
30	30.45	-51.742	2.010

Configuration J.

Wind speed	Tip angle (°)	$\partial T/\partial \beta$ (kNm/°)	$\partial T/\partial V$ (kNm/m/s)
11.2	0.00	-2.007	92.359
12	7.5	-16.315	87.970
13	11.98	-22.610	87.236
14	15.35	-27.687	85.355
15	18.12	-33.277	81.977
16	20.44	-35.132	72.673
17	22.36	-36.382	60.543
18	23.74	-38.290	43.397
19	24.78	-37.485	32.779
20	25.51	-40.865	27.550
22	26.82	-41.758	22.985
23	27.34	-44.993	21.833
24	27.79	-48.335	18.082
26	28.41	-50.449	13.102
28	28.87	-56.799	11.047
30	29.19	-64.242	8.947

Configuration K.

Wind speed	Tip angle (°)	$\partial T/\partial \beta$ (kNm/°)	$\partial T/\partial V$ (kNm/m/s)
11.2	0.00	-1.280	109.068
12	9.48	-15.663	101.832
13	14.80	-21.832	92.312
14	18.55	-26.980	80.207
15	21.05	-29.848	56.200
16	22.65	-31.831	39.778
17	23.80	-33.829	36.483
18	24.80	-35.382	33.134
19	25.70	-37.738	28.848
20	26.35	-38.788	21.027
22	27.25	-43.981	15.106
23	27.55	-45.603	13.608
24	27.85	-47.188	12.341
26	28.30	-52.397	32.341
28	29.55	-55.270	54.605
30	31.50	-60.813	56.743

Configuration L.

Table G.4b) Partial derivatives for the 1 MW tip-regulated rotors

		Tip angle (degrees)							
		0	3	7	14	23	41	71	90
T	-12	0.0008	0.0008	0.0008	0.0008	0.0008	0.0008	0.0028	0.0018
i	0.1	0.0009	0.0009	0.0009	0.0009	0.0009	0.0009	0.0038	0.0019
p	0.2	0.001	0.001	0.001	0.001	0.001	0.001	0.0041	0.0012
	0.3	0.0012	0.0013	0.0013	0.0013	0.0013	0.0013	0.0035	0.0004
s	0.4	0.0015	0.0015	0.0015	0.0015	0.0015	0.0015	0.0029	-0.0004
p	0.5	0.0018	0.0019	0.0019	0.0019	0.0019	0.0019	0.0023	-0.0012
e	0.6	0.0022	0.0023	0.0023	0.0023	0.0023	0.0023	0.0017	-0.0018
e	0.7	0.0027	0.0028	0.0028	0.0028	0.0028	0.0028	0.0011	-0.0023
d	0.8	0.0032	0.0033	0.0033	0.0033	0.0033	0.0033	0.0005	-0.0029
	0.9	0.004	0.0033	0.0033	0.0033	0.0033	0.0033	0.0004	-0.0013
r	1	0.004	0.0033	0.0033	0.0033	0.0033	0.0033	0.0004	-0.0013
a	2	0.0131	0.0103	0.0107	0.0156	0.0188	0.0084	-0.002	-0.0028
t	3	0.0285	0.0281	0.0279	0.0259	0.022	0.0129	-0.0004	-0.004
i	4	0.0491	0.0447	0.0438	0.0396	0.035	0.0197	-0.0014	-0.0071
o	5	0.0693	0.0628	0.0612	0.0551	0.0478	0.0263	-0.0061	-0.0127
	6	0.0702	0.0634	0.0607	0.0527	0.0429	0.0134	-0.0329	-0.0406
(r	7	0.0605	0.0522	0.0489	0.0383	0.0258	-0.0134	-0.0759	-0.0851
a	8	0.0476	0.0379	0.0339	0.0201	0.0044	-0.0461	-0.127	-0.1379
d)	9	0.0353	0.0237	0.019	0.0017	-0.0177	-0.081	-0.1827	-0.1956
	10	0.0232	0.0098	0.0038	-0.0172	-0.0409	-0.1185	-0.2432	-0.2585
	11	0.0115	-0.0038	-0.011	-0.0363	-0.0648	-0.1653	-0.3082	-0.3262
	12	-0.0003	-0.0176	-0.0262	-0.056	-0.0899	-0.209	-0.3783	-0.3992

Table G.5 The aerodynamic torque coefficients, C_q for the fledge.

Tip speed ratio												
1.50	1.75	2.00	2.25	2.50	2.75	3.00	3.25	3.50	3.75	4.00	4.25	
0.01802	0.02184	0.02566	0.03426	0.04621	0.05741	0.06801	0.07736	0.08669	0.09495	0.10000	0.10160	
Tip speed ratio												
4.50	4.75	5.00	5.50	6.00	6.50	7.00	7.50	8.00	9.00	10.00	12.00	15.00
0.10110	0.09965	0.09713	0.09061	0.08288	0.07555	0.06853	0.06202	0.05559	0.04370	0.03301	0.01390	-0.01315

Table G.6a) Main blade aerodynamic torque coefficient for compliant tip investigation

		Tip speed ratio												
		2.40	2.60	2.80	3.00	3.20	3.40	3.60	3.80	4.00	4.20	4.40	4.60	4.80
T	-4	0.00284	0.00373	0.00582	0.00798	0.00937	0.01039	0.01150	0.01261	0.01351	0.01428	0.01495	0.01574	0.01641
i	-2	0.00444	0.00689	0.00897	0.01021	0.01141	0.01266	0.01368	0.01460	0.01559	0.01662	0.01735	0.01800	0.01829
p	0	0.00740	0.00942	0.01068	0.01204	0.01324	0.01427	0.01541	0.01659	0.01757	0.01823	0.01855	0.01844	0.01837
	2	0.00952	0.01086	0.01227	0.01342	0.01462	0.01593	0.01700	0.01766	0.01792	0.01794	0.01785	0.01772	0.01756
a	4	0.01075	0.01218	0.01338	0.01475	0.01601	0.01676	0.01701	0.01697	0.01684	0.01670	0.01653	0.01630	0.01608
n	6	0.01186	0.01314	0.01459	0.01564	0.01602	0.01597	0.01579	0.01560	0.01535	0.01507	0.01476	0.01442	0.01406
g	8	0.01271	0.01418	0.01499	0.01504	0.01482	0.01455	0.01424	0.01386	0.01344	0.01299	0.01251	0.01203	0.01153
l	10	0.01359	0.01421	0.01403	0.01369	0.01331	0.01284	0.01229	0.01169	0.01108	0.01047	0.00983	0.00918	0.00851
e	12	0.01341	0.01309	0.01263	0.01208	0.01144	0.01073	0.00997	0.00918	0.00838	0.00757	0.00676	0.00595	0.00513
(d	14	0.01226	0.01169	0.01098	0.01014	0.00923	0.00830	0.00734	0.00638	0.00540	0.00440	0.00340	0.00239	0.00137
e	16	0.01089	0.01001	0.00899	0.00790	0.00679	0.00566	0.00450	0.00333	0.00214	0.00095	-0.00025	-0.00146	-0.00268
g	18	0.00923	0.00804	0.00678	0.00548	0.00415	0.00280	0.00144	0.00007	-0.00131	-0.00271	-0.00413	-0.00558	-0.00706
r	20	0.00732	0.00588	0.00440	0.00288	0.00134	-0.00021	-0.00177	-0.00335	-0.00497	-0.00662	-0.00832	-0.01007	-0.01185
e	21	0.00630	0.00475	0.00315	0.00153	-0.00011	-0.00176	-0.00343	-0.00514	-0.00690	-0.00871	-0.01055	-0.01243	-0.01435
e	22	0.00525	0.00358	0.00187	0.00015	-0.00159	-0.00335	-0.00515	-0.00700	-0.00891	-0.01085	-0.01282	-0.01482	-0.01685
s)	23	0.00417	0.00238	0.00057	-0.00125	-0.00309	-0.00498	-0.00693	-0.00893	-0.01096	-0.01301	-0.01508	-0.01719	-0.01934
	24	0.00305	0.00116	-0.00074	-0.00267	-0.00464	-0.00668	-0.00876	-0.01087	-0.01300	-0.01514	-0.01732	-0.01956	-0.02185
	25	0.00191	-0.00008	-0.00208	-0.00413	-0.00625	-0.00841	-0.01060	-0.01279	-0.01500	-0.01725	-0.01956	-0.02191	-0.02426
	26	0.00075	-0.00133	-0.00345	-0.00564	-0.00788	-0.01014	-0.01240	-0.01466	-0.01699	-0.01935	-0.02171	-0.02401	-0.02624
	27	-0.00042	-0.00261	-0.00486	-0.00718	-0.00951	-0.01183	-0.01415	-0.01653	-0.01892	-0.02125	-0.02346	-0.02565	-0.02805
	28	-0.00160	-0.00391	-0.00630	-0.00871	-0.01109	-0.01347	-0.01589	-0.01829	-0.02056	-0.02270	-0.02500	-0.02771	-0.03091
	29	-0.00280	-0.00525	-0.00774	-0.01020	-0.01263	-0.01509	-0.01748	-0.01968	-0.02183	-0.02435	-0.02746	-0.03100	-0.03449
	30	-0.00404	-0.00660	-0.00914	-0.01163	-0.01413	-0.01654	-0.01868	-0.02089	-0.02369	-0.02714	-0.03068	-0.03332	-0.02638
	31	-0.00530	-0.00794	-0.01049	-0.01303	-0.01547	-0.01760	-0.01987	-0.02293	-0.02654	-0.02963	-0.02457	-0.02273	-0.02459
	32	-0.00656	-0.00921	-0.01180	-0.01430	-0.01643	-0.01874	-0.02199	-0.02558	-0.02728	-0.01943	-0.02129	-0.02423	-0.02719

Table G.6b) The aerodynamic torque coefficient due to the compliant tip, C_q .

		Tip speed ratio											
		5.00	5.20	5.40	5.60	5.80	6.00	6.20	6.40	6.60	6.80	7.00	7.20
T	-4	0.01683	0.01692	0.01658	0.01610	0.01575	0.01534	0.01487	0.01436	0.01379	0.01322	0.01262	0.01199
i	-2	0.01820	0.01800	0.01760	0.01706	0.01643	0.01581	0.01538	0.01491	0.01440	0.01388	0.01336	0.01281
p	0	0.01822	0.01803	0.01770	0.01743	0.01689	0.01628	0.01583	0.01522	0.01457	0.01407	0.01364	0.01320
	2	0.01738	0.01698	0.01673	0.01646	0.01616	0.01587	0.01555	0.01514	0.01481	0.01430	0.01394	0.01350
a	4	0.01581	0.01553	0.01523	0.01492	0.01459	0.01427	0.01394	0.01360	0.01325	0.01291	0.01255	0.01219
n	6	0.01369	0.01331	0.01291	0.01251	0.01210	0.01169	0.01128	0.01086	0.01045	0.01003	0.00961	0.00919
g	8	0.01101	0.01048	0.00996	0.00944	0.00892	0.00840	0.00787	0.00734	0.00681	0.00628	0.00574	0.00522
l	10	0.00784	0.00717	0.00650	0.00584	0.00519	0.00452	0.00385	0.00317	0.00248	0.00178	0.00108	0.00038
e	12	0.00430	0.00346	0.00261	0.00176	0.00091	0.00005	-0.00082	-0.00170	-0.00259	-0.00348	-0.00440	-0.00531
(d	14	0.00035	-0.00069	-0.00173	-0.00278	-0.00385	-0.00493	-0.00603	-0.00715	-0.00828	-0.00943	-0.01060	-0.01180
e	16	-0.00392	-0.00518	-0.00647	-0.00777	-0.00911	-0.01047	-0.01186	-0.01328	-0.01473	-0.01621	-0.01771	-0.01925
g	18	-0.00857	-0.01012	-0.01171	-0.01332	-0.01498	-0.01666	-0.01838	-0.02013	-0.02191	-0.02373	-0.02558	-0.02747
r	20	-0.01366	-0.01550	-0.01738	-0.01930	-0.02124	-0.02323	-0.02527	-0.02735	-0.02948	-0.03167	-0.03391	-0.03620
e	21	-0.01629	-0.01826	-0.02027	-0.02233	-0.02444	-0.02660	-0.02881	-0.03108	-0.03346	-0.03588	-0.03835	-0.04087
e	22	-0.01891	-0.02102	-0.02317	-0.02539	-0.02767	-0.02999	-0.03236	-0.03475	-0.03718	-0.03965	-0.04212	-0.04461
s)	23	-0.02155	-0.02382	-0.02613	-0.02848	-0.03085	-0.03324	-0.03562	-0.03802	-0.04045	-0.04296	-0.04556	-0.04827
	24	-0.02419	-0.02654	-0.02889	-0.03122	-0.03355	-0.03591	-0.03838	-0.04099	-0.04376	-0.04672	-0.04987	-0.05321
	25	-0.02658	-0.02885	-0.03113	-0.03352	-0.03608	-0.03886	-0.04188	-0.04515	-0.04862	-0.05223	-0.05594	-0.05967
	26	-0.02848	-0.03089	-0.03357	-0.03654	-0.03983	-0.04333	-0.04696	-0.05059	-0.05408	-0.05716	-0.05965	-0.06203
	27	-0.03079	-0.03393	-0.03738	-0.04097	-0.04450	-0.04769	-0.04928	-0.04342	-0.04328	-0.04547	-0.04701	-0.04949
	28	-0.03443	-0.03798	-0.04117	-0.04254	-0.03651	-0.03667	-0.03827	-0.04079	-0.04222	-0.04561	-0.04910	-0.05272
	29	-0.03724	-0.03193	-0.02947	-0.03184	-0.03341	-0.03662	-0.03988	-0.04329	-0.04686	-0.05061	-0.05451	-0.05855
	30	-0.02587	-0.02758	-0.03070	-0.03380	-0.03707	-0.04054	-0.04420	-0.04801	-0.05196	-0.05606	-0.06027	-0.06463
	31	-0.02759	-0.03063	-0.03390	-0.03740	-0.04107	-0.04489	-0.04885	-0.05294	-0.05718	-0.06157	-0.06609	-0.07075
	32	-0.03043	-0.03390	-0.03753	-0.04130	-0.04522	-0.04930	-0.05352	-0.05790	-0.06242	-0.06709	-0.07193	-0.07691

Table G.6c) The aerodynamic torque coefficient due to the compliant tip, C_q (continued).

Wind speed (m/s)	11.6	12	13	14	15	16	17	18	19	20	21	22	23	24
Tip (degrees)	0.0	5.9	13.5	18.1	20.8	22.5	23.8	24.9	25.8	26.4	26.9	27.2	27.5	27.6
$dT/d\beta$ (Nm/degree)	0.4	1.7	2.9	3.7	4.2	4.6	4.9	5.1	5.4	5.7	6	6.3	6.6	6.8

Table G.7 The aerodynamic torque partial derivatives with respect to tip angle for the compliant tip.

P		Tip speed ratio (rad)											
		2	3	4	5	6	7	8	9	10	11	12	13
i	-3	0.0137	0.0312	0.0608	0.0799	0.0755	0.0662	0.0560	0.0455	0.0352	0.0251	0.0149	0.0062
t	0	0.0189	0.0436	0.0729	0.0799	0.0758	0.0682	0.0597	0.0518	0.0445	0.1728	0.0299	0.0229
c	3	0.0247	0.0552	0.0745	0.0752	0.0703	0.0635	0.0569	0.0506	0.0446	0.3855	0.0321	0.0260
h	6	0.0310	0.0622	0.0706	0.0664	0.0592	0.0515	0.0439	0.0366	0.0296	0.0224	0.0150	0.0080
	9	0.0379	0.0629	0.0525	0.0540	0.0436	0.0333	0.0229	0.0124	0.0016	-0.0092	-0.0197	-0.0295
a	12	0.0447	0.0594	0.0515	0.0388	0.0248	0.0103	-0.0046	-0.0201	-0.0365	-0.0531	-0.0685	-0.0825
n	15	0.0492	0.0525	0.0336	0.0212	0.0026	-0.0171	-0.0378	-0.0599	-0.0833	-0.1071	-0.1286	-0.1479
g	18	0.0504	0.0433	0.0239	0.0014	-0.0227	-0.4840	-0.0760	-0.1052	-0.1357	-0.1670	-0.1962	-0.2226
l	20	0.0493	0.0362	0.0132	-0.0129	-0.0410	-0.0708	-0.1025	-0.1385	-0.1803	-0.2248	-0.2646	-0.2997
e	25	0.0422	0.0164	-0.0162	-0.0519	-0.0934	-0.1364	-0.1817	-0.2322	-0.2896	-0.3504	-0.4047	-0.4541
(°)	30	0.0301	-0.0064	-0.0488	-0.0874	-0.1299	-0.1853	-0.2508	-0.3245	-0.4072	-0.4932	-0.5701	-0.6386

Table G.8 The torque tables, C_q coefficients.

Wind speed (m/s)	Pitch angle (°)	$\partial T/\partial \beta$ (kNm/°)
12.83	0	-4.129
12.995	1.43	-8.903
13.22	3	-11.513
13.895	6	-18.361
14.811	9	-25.440
15.955	12	-32.674
16.244	12.65	-35.830
17.39	15	-38.950
18.97	18	-45.810
20.1	20	-52.980
21.66	22.485	-59.143
23.445	25	-64.460
27.245	30	-79.600

Table G.9 Partial derivative of aerodynamic torque with respect to pitch angle.

Appendix H Machine performance

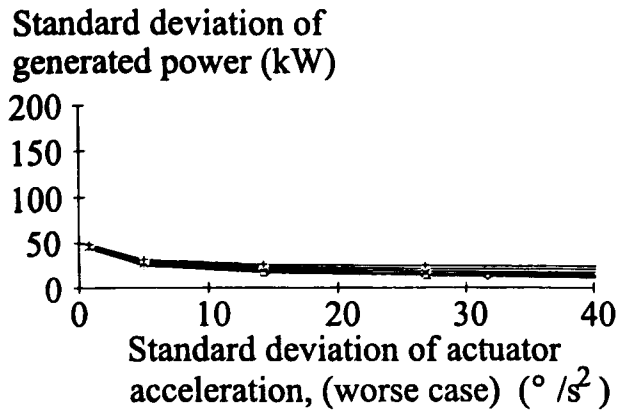
This appendix contains figures showing the performance for each of the conventional full-span and tip-regulated machines considered in Chapters 4 and 5.

Figures H.1a to H.5a show, for each of the full-span regulated wind turbine configurations investigated, the standard deviations of generated power for each wind speed against the standard deviations of the actuator acceleration for the worse case¹; that is, the standard deviation of the actuator acceleration induced at 12 m/s by the controller cross-over frequency as it varies. Similarly, Figures H.1b to H.5b show for each of the full-span regulated wind turbine configurations investigated the standard deviations of generated power for each wind speed plotted against the standard deviations of the actuator velocity for 12 m/s.

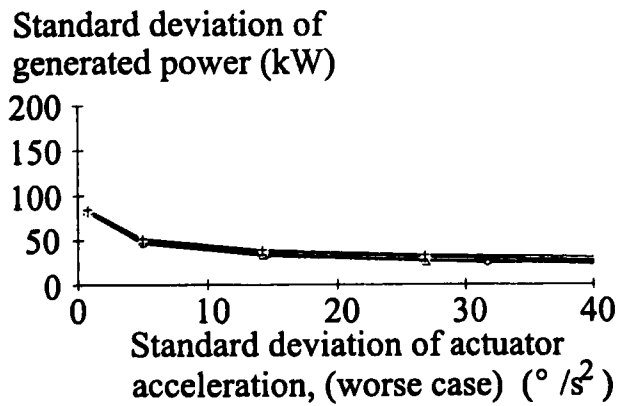
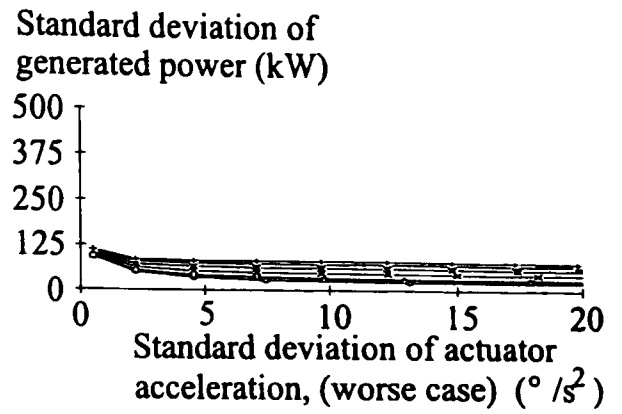
Figures H.6a to H.10a show, for each of the full-span regulated wind turbine configurations investigated, the standard deviation of generated power against the standard deviation of the actuator acceleration as it varies with cross-over frequency for each wind speed. Similarly, Figures H.6b to H.10b show the standard deviation of generated power against the standard deviation of the actuator velocity for each wind speed

Similarly Figures H.11a to H.20b show the performance of the tip-regulated machines.

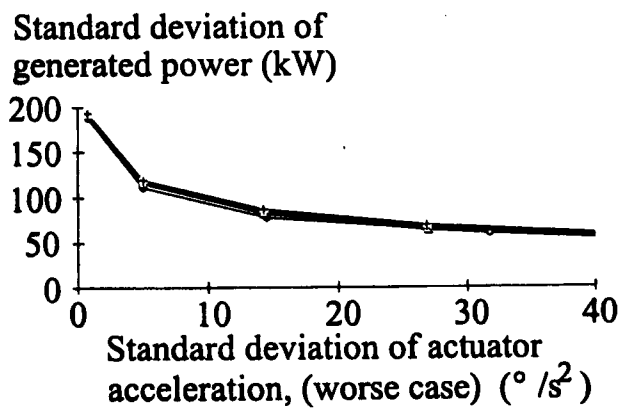
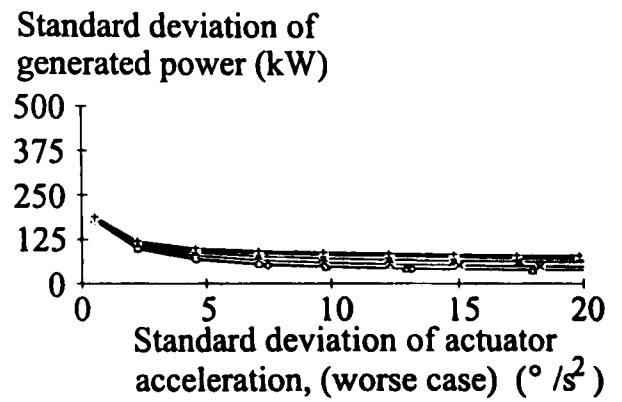
¹ For any of the mean wind speeds considered the wind speed may momentarily reach 12 m/s and the actuator activity is more sensitive to this instantaneous wind speed than long term wind speeds.



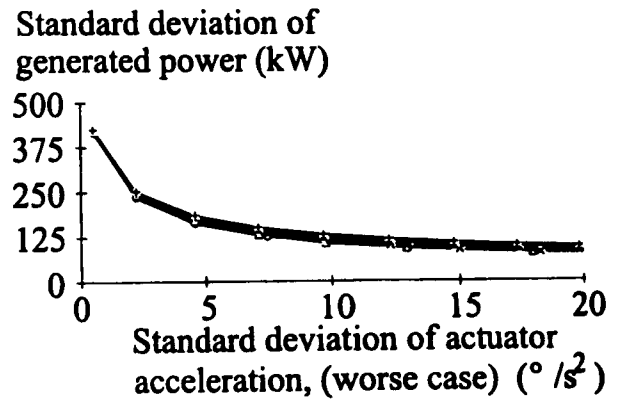
Wind speed 12 m/s



Wind speed 16 m/s



Wind speed 23 m/s



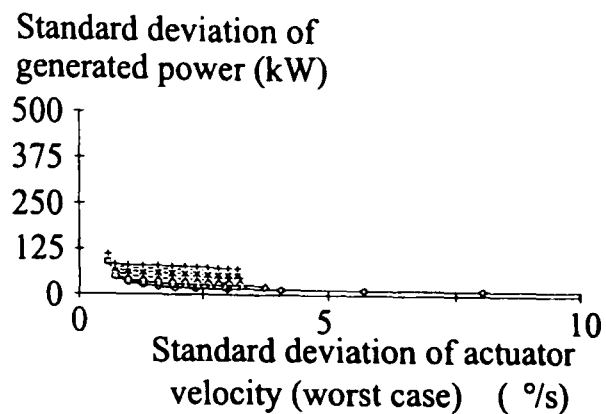
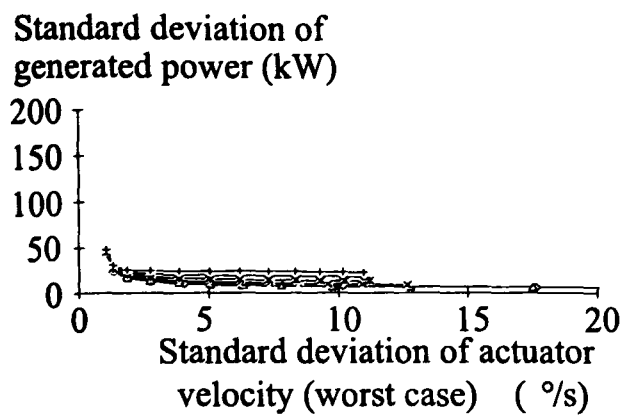
300 kW

1 MW

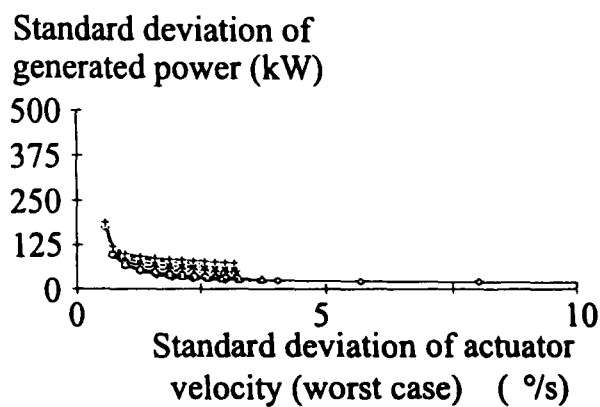
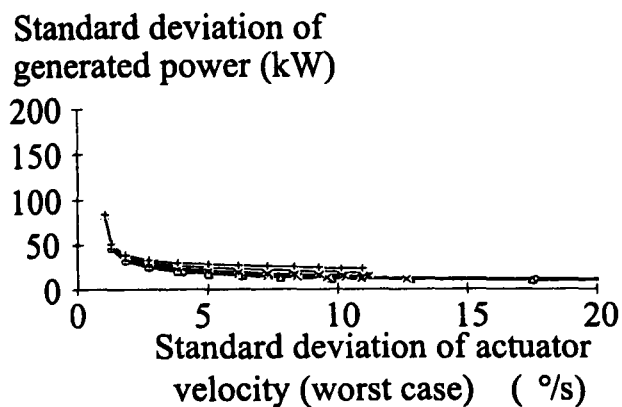
First drive-train mode

→ 2.0 rad/s → 3.0 rad/s → 4.0 rad/s → 5.0 rad/s → 6.0 rad/s → 7.0 rad/s

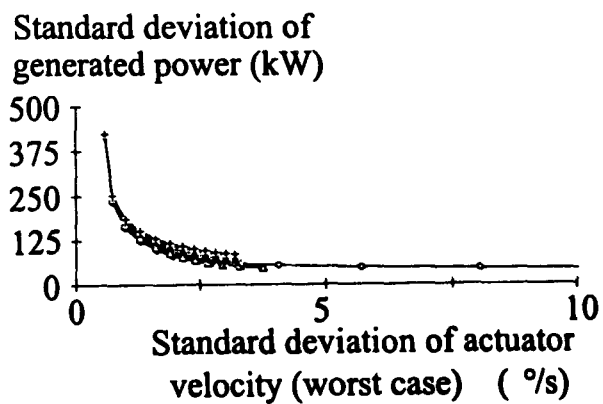
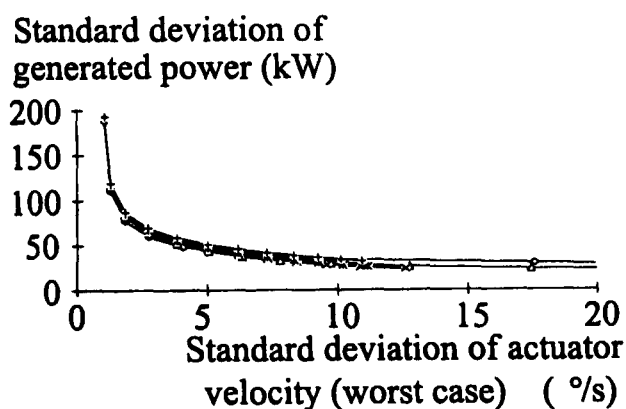
Figure H.1a Worst case performance (actuator acceleration) of two-bladed ($1/2$ nominal $2\Omega_0$) machines Aa and Da.



Wind speed 12 m/s



Wind speed 16 m/s



Wind speed 23 m/s

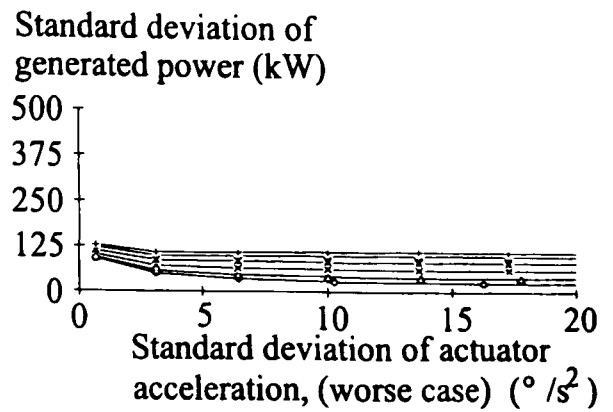
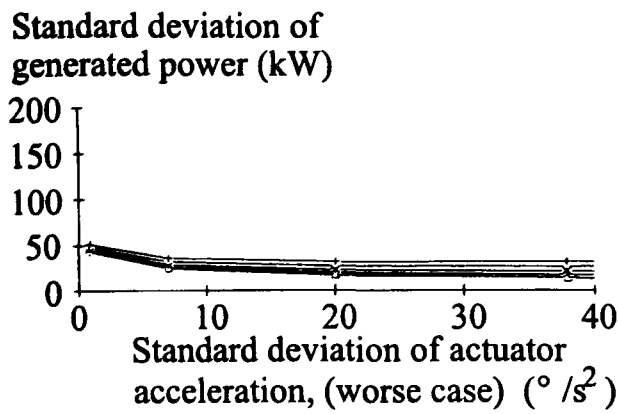
300 kW

1 MW

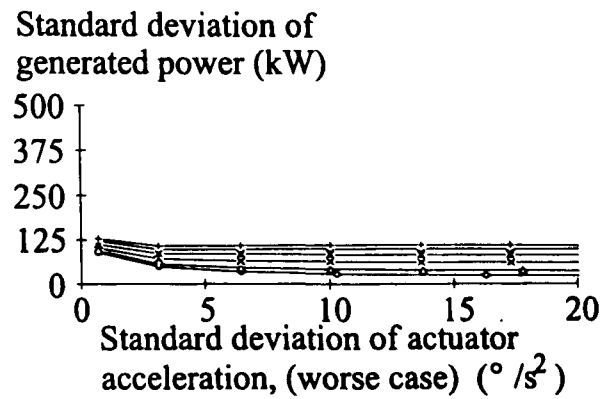
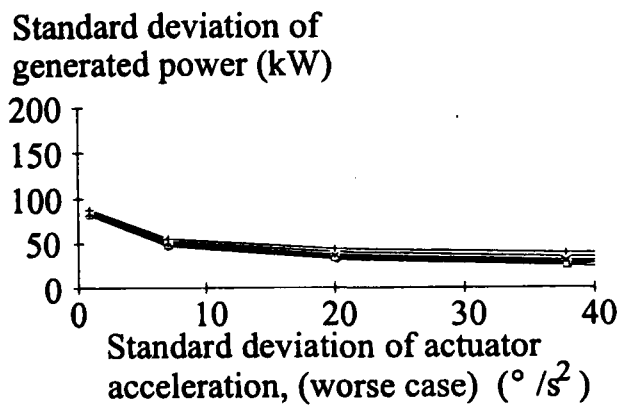
First drive-train mode

○ 2.0 rad/s □ 3.0 rad/s × 4.0 rad/s * 5.0 rad/s ◊ 6.0 rad/s + 7.0 rad/s

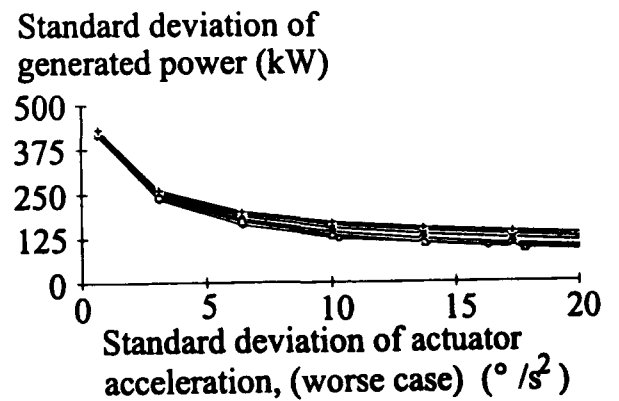
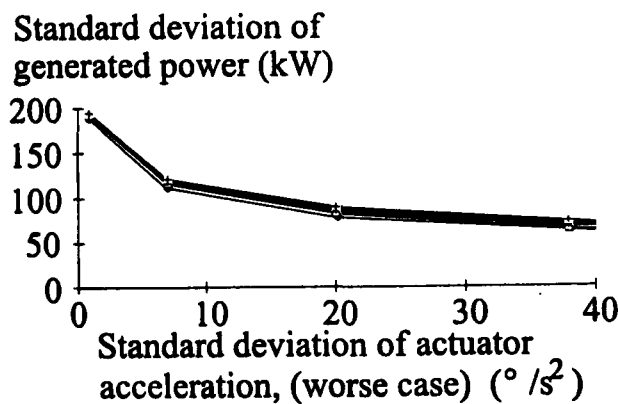
Figure H.1b Worst case performance (actuator velocity) of two-bladed ($1/2$ nominal $2\Omega_0$) machines Aa and Da.



Wind speed 12 m/s



Wind speed 16 m/s



Wind speed 23 m/s

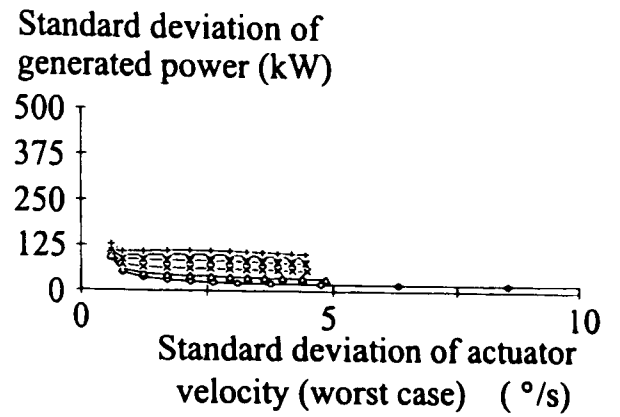
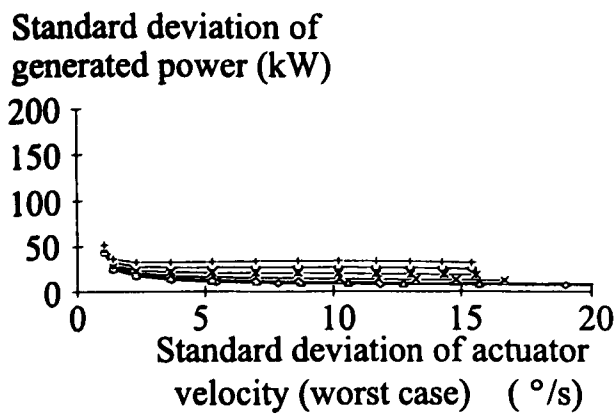
300 kW

1 MW

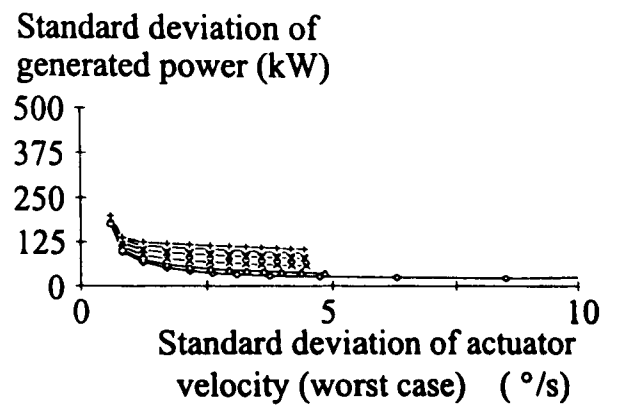
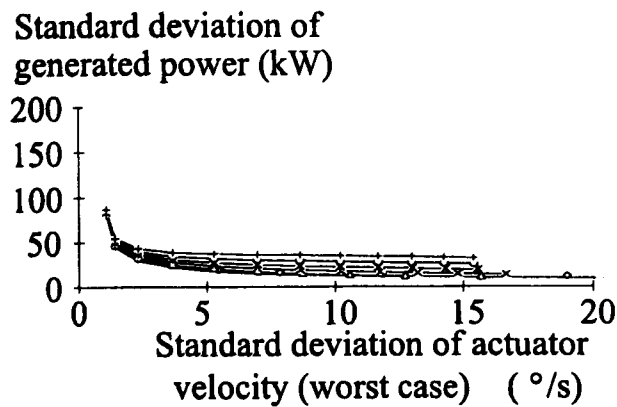
First drive-train mode

→ 2.0 rad/s → 3.0 rad/s → 4.0 rad/s → 5.0 rad/s → 6.0 rad/s → 7.0 rad/s

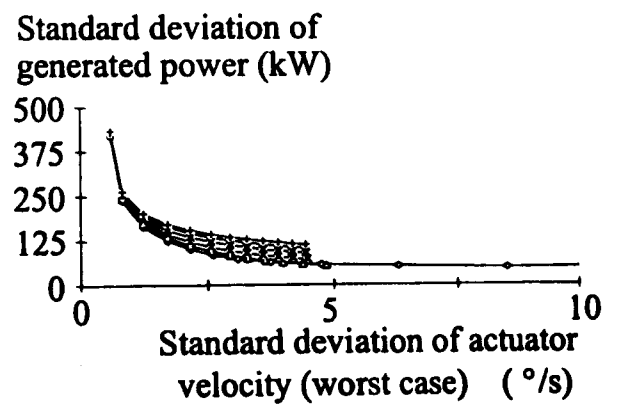
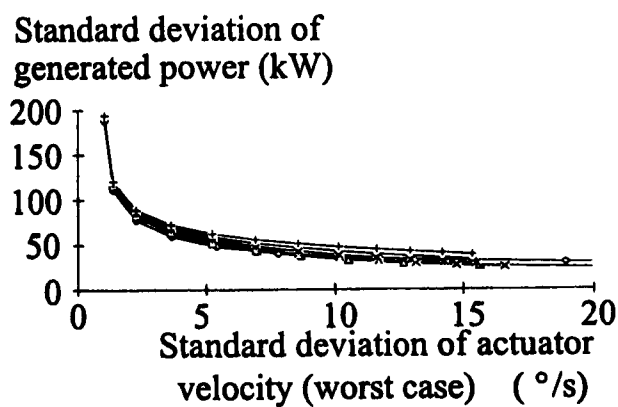
Figure H.2a Worst case performance (actuator acceleration) of two-bladed (nominal $2\Omega_0$) machines Ab and Db.



Wind speed 12 m/s



Wind speed 16 m/s



Wind speed 23 m/s

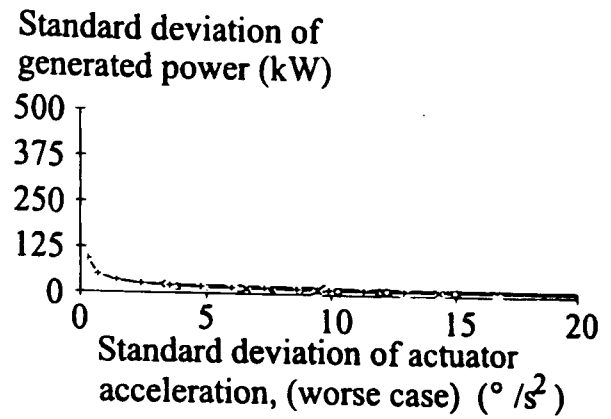
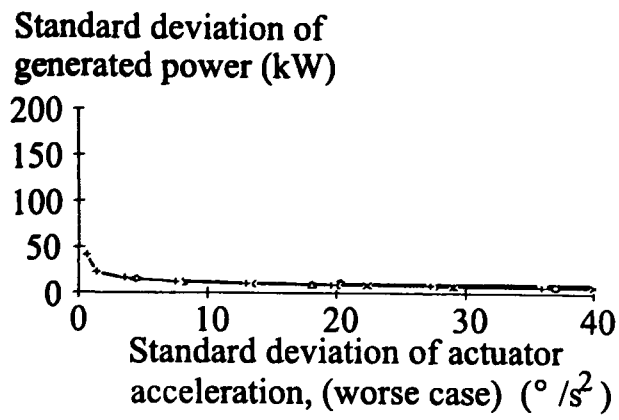
300 kW

1 MW

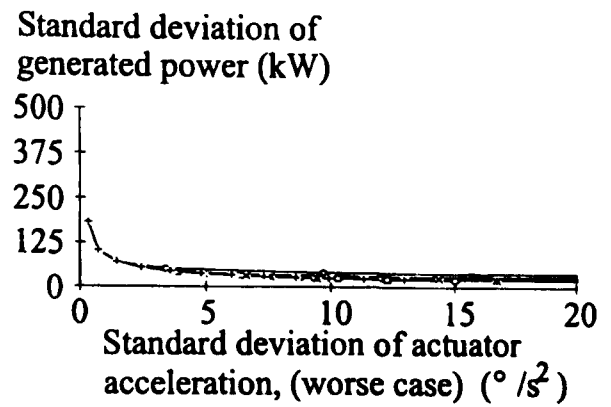
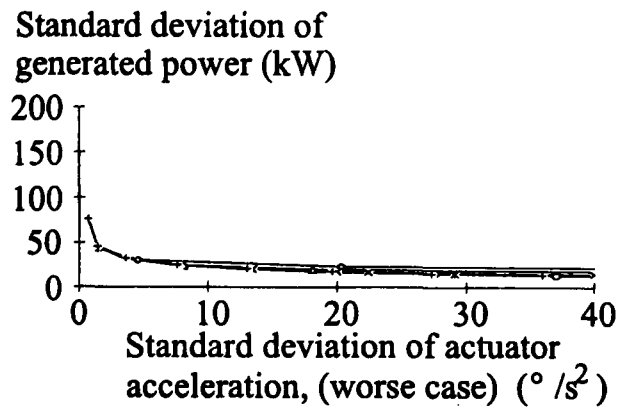
First drive-train mode

\diamond 2.0 rad/s
 \circ 3.0 rad/s
 \times 4.0 rad/s
 \cdot 5.0 rad/s
 \square 6.0 rad/s
 \star 7.0 rad/s

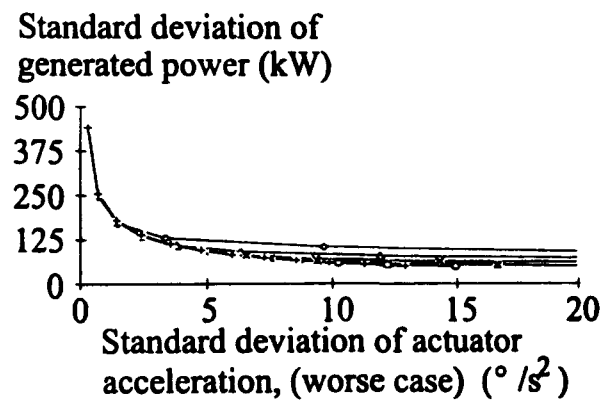
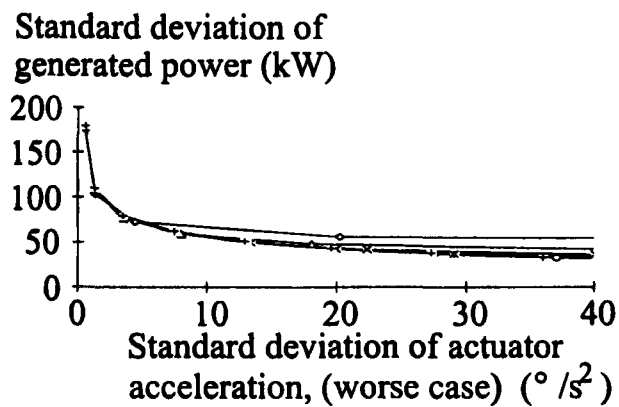
Figure H.2b Worst case performance (actuator velocity) of two-bladed (nominal $2\Omega_0$) machines Ab and Db.



Wind speed 12 m/s



Wind speed 16 m/s



Wind speed 23 m/s

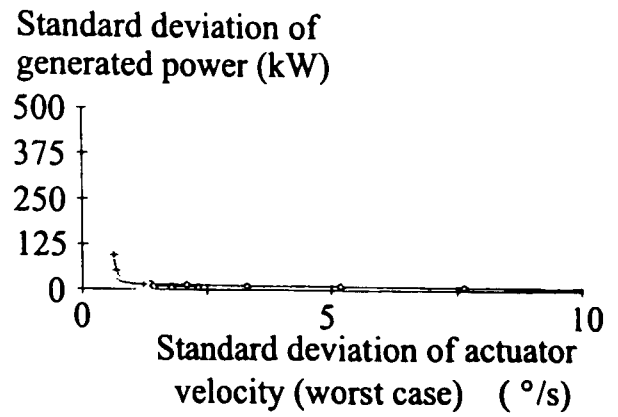
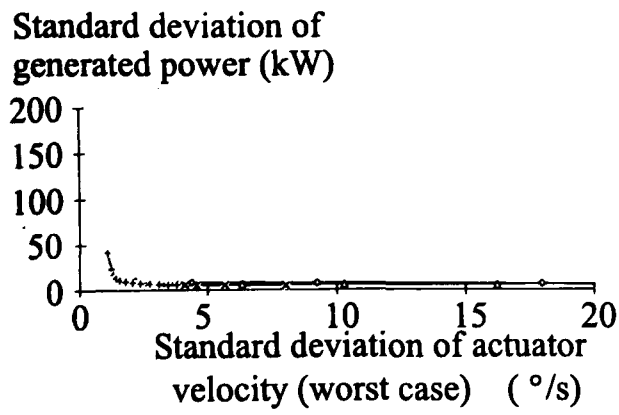
300 kW

1 MW

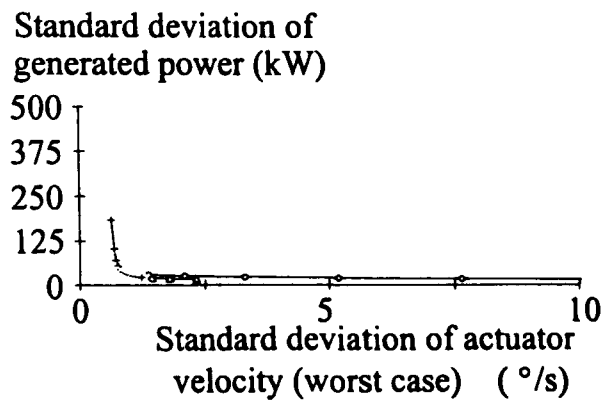
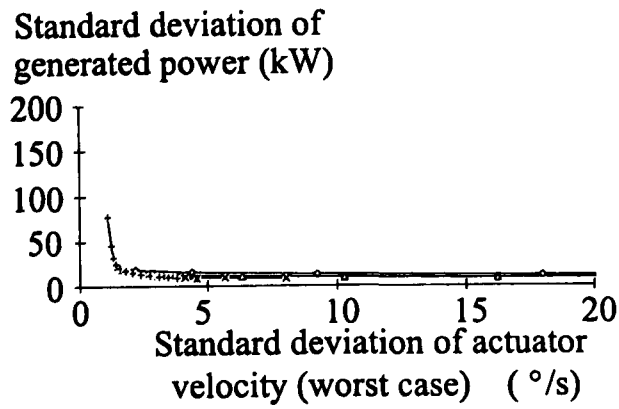
First drive-train mode

○ 2.0 rad/s ◐ 3.0 rad/s × 4.0 rad/s ◑ 5.0 rad/s ◒ 6.0 rad/s ◓ 7.0 rad/s

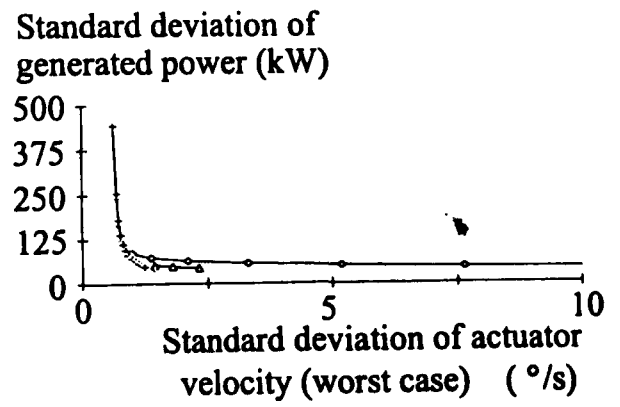
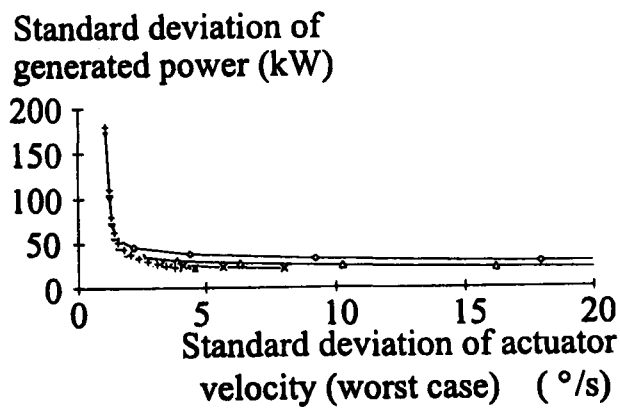
Figure H.3a Worst case performance (actuator acceleration) of three-bladed (faster rotor speed) machines B and E.



Wind speed 12 m/s



Wind speed 16 m/s



Wind speed 23 m/s

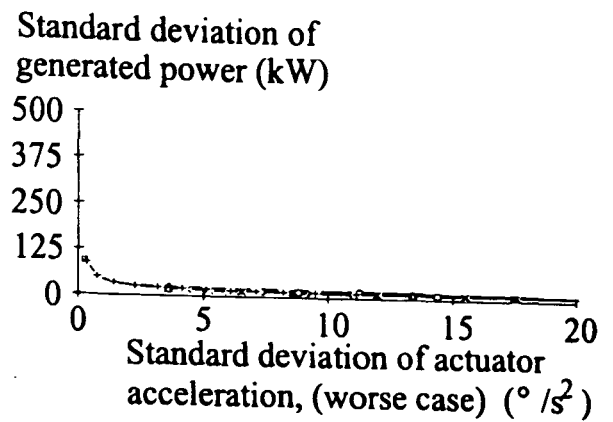
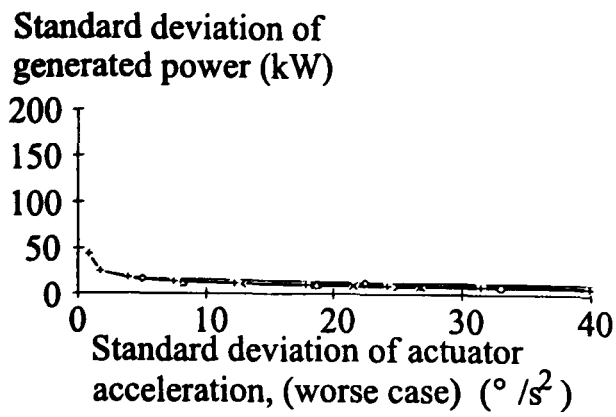
300 kW

1 MW

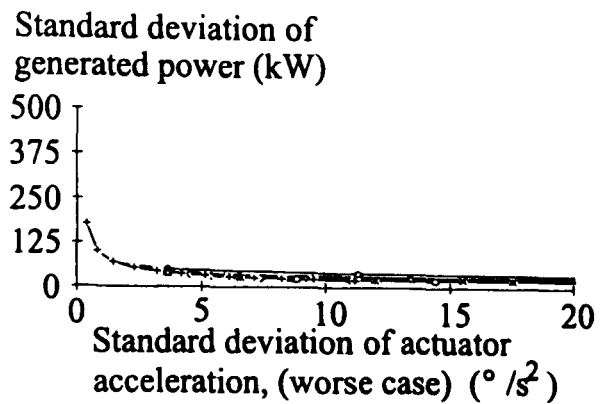
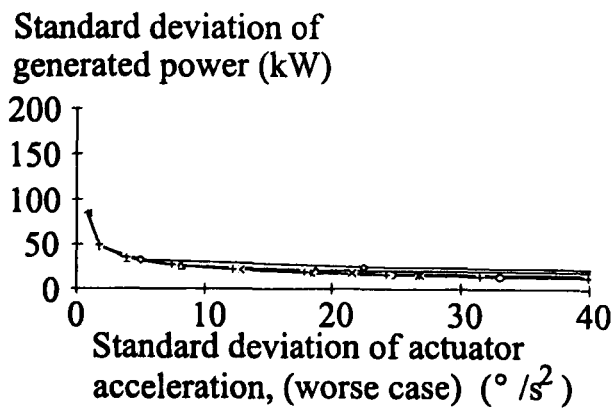
First drive-train mode

→ 2.0 rad/s → 3.0 rad/s → 4.0 rad/s → 5.0 rad/s → 6.0 rad/s → 7.0 rad/s

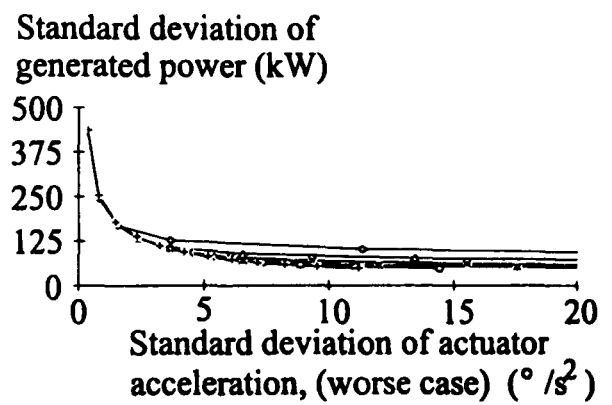
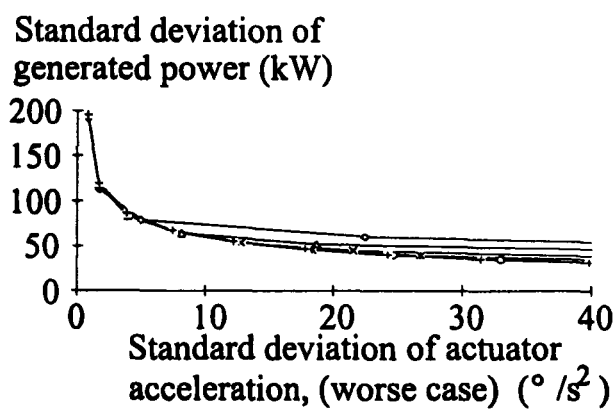
Figure H.3b Worst case performance (actuator velocity)
of three-bladed (fast velocity) machines B and E.



Wind speed 12 m/s



Wind speed 16 m/s



Wind speed 23 m/s

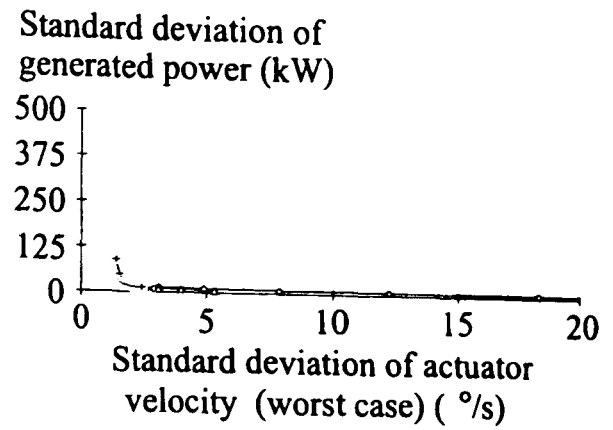
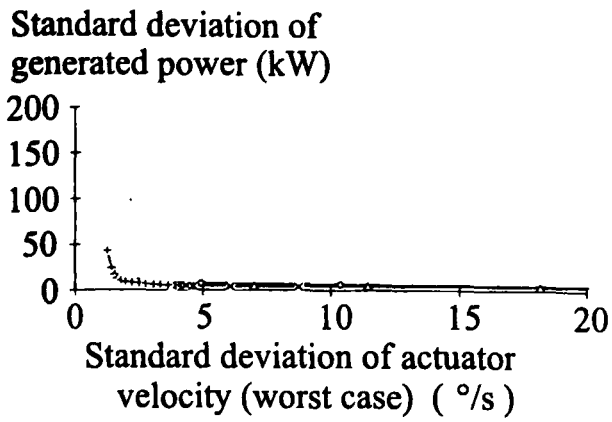
300 kW

1 MW

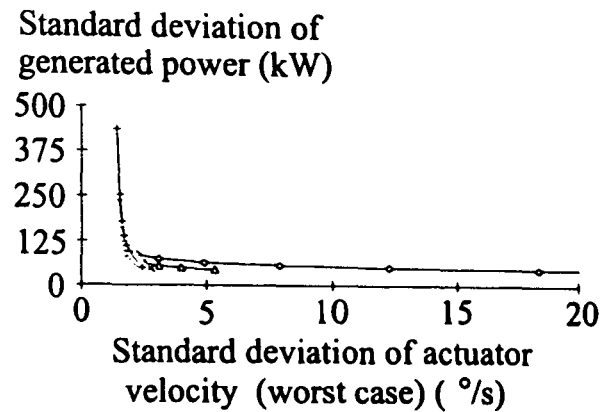
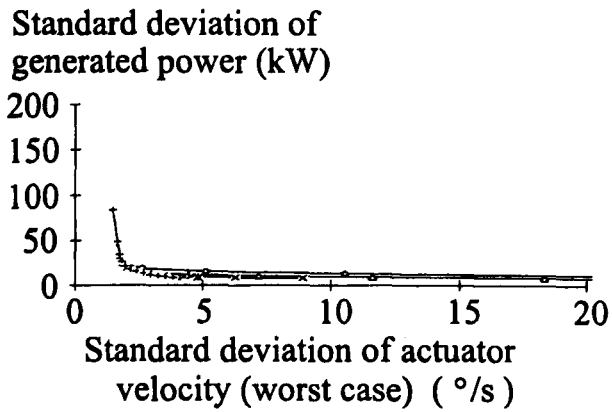
First drive-train mode

→ 2.0 rad/s → 3.0 rad/s → 4.0 rad/s → 5.0 rad/s → 6.0 rad/s → 7.0 rad/s

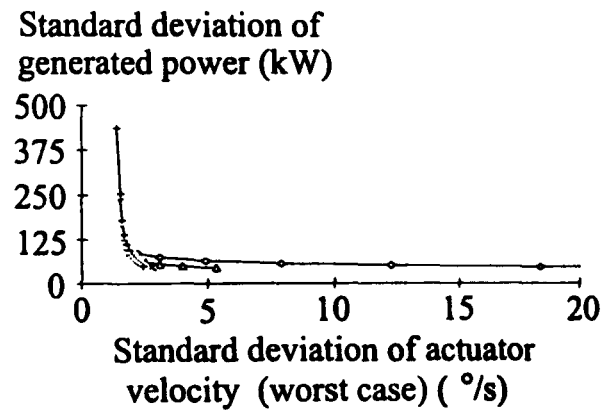
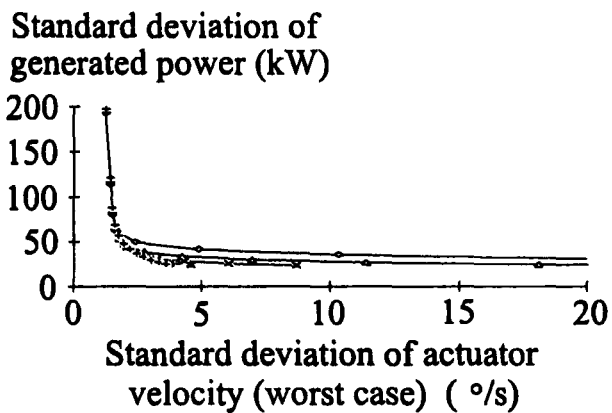
Figure H.4a Worst case performance (actuator acceleration) of three-bladed (nominal $3\Omega_0$) machines Ca and Fa.



Wind speed 12 m/s



Wind speed 16 m/s



Wind speed 23 m/s

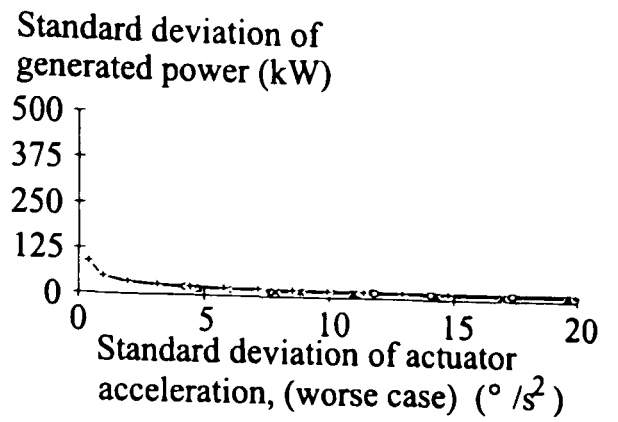
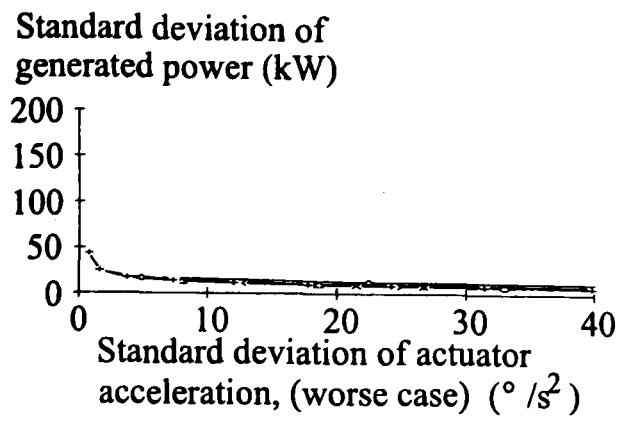
300 kW

1 MW

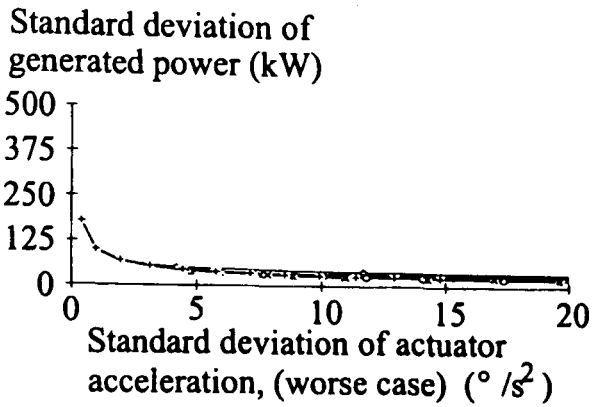
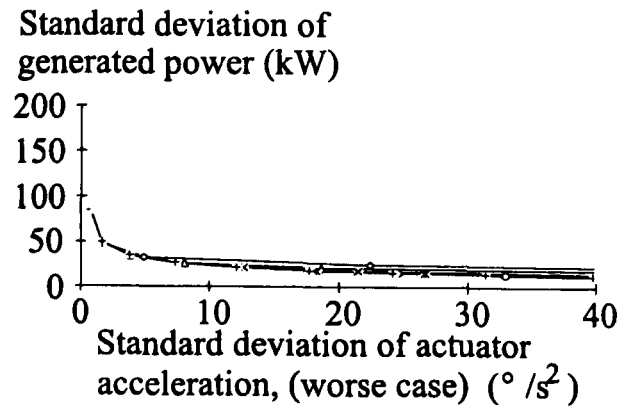
First drive-train mode

→ 2.0 rad/s → 3.0 rad/s → 4.0 rad/s → 5.0 rad/s → 6.0 rad/s → 7.0 rad/s

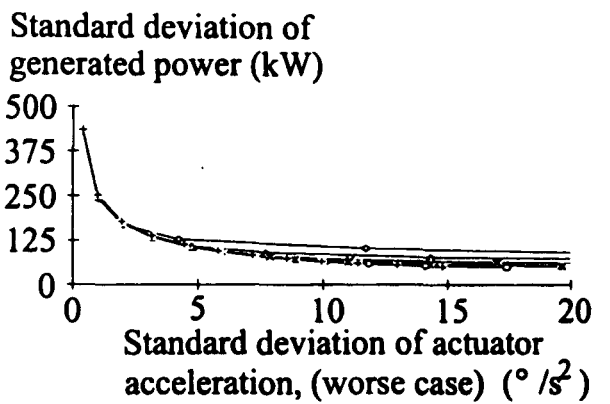
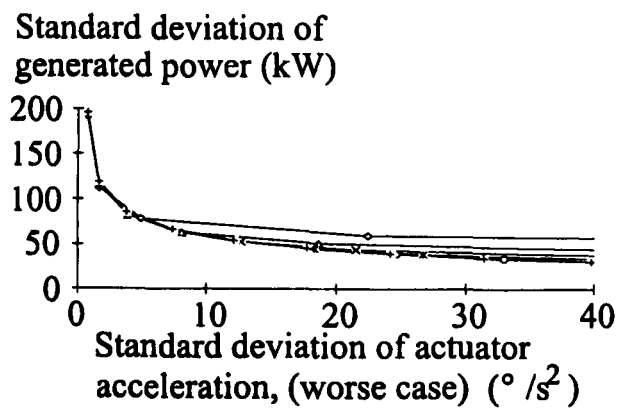
Figure H.4b Worst case performance (actuator velocity) of three-bladed (nominal $3\Omega_0$) machines Ca and Fa.



Wind speed 12 m/s



Wind speed 16 m/s



Wind speed 23 m/s

300 kW

1 MW

First drive-train mode

→ 2.0 rad/s → 3.0 rad/s → 4.0 rad/s → 5.0 rad/s → 6.0 rad/s → 7.0 rad/s

Figure H.5a Worst case performance (actuator acceleration)
of three-bladed ($2 \times$ nominal $3\Omega_n$) machines Cb and Fb.

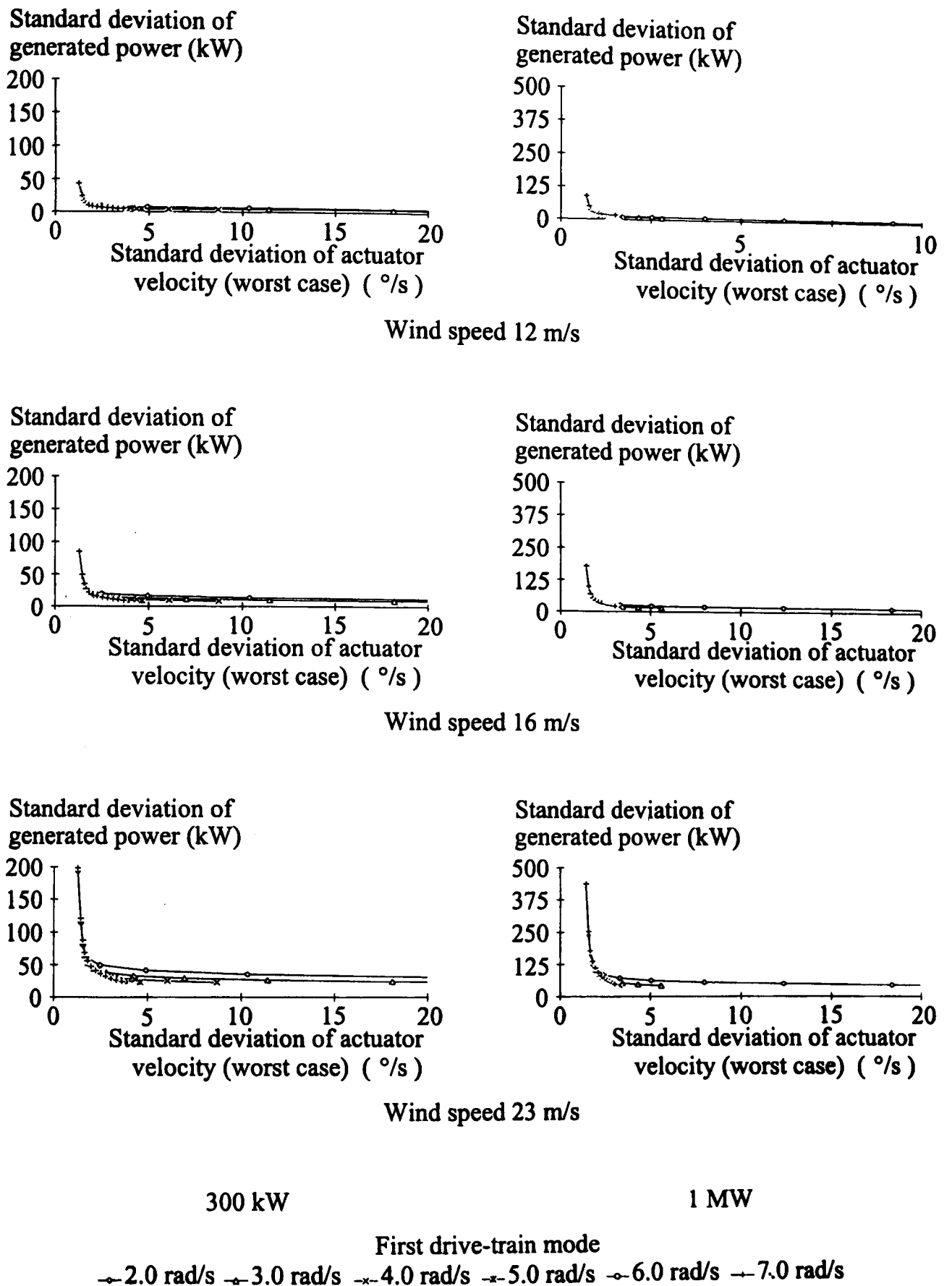
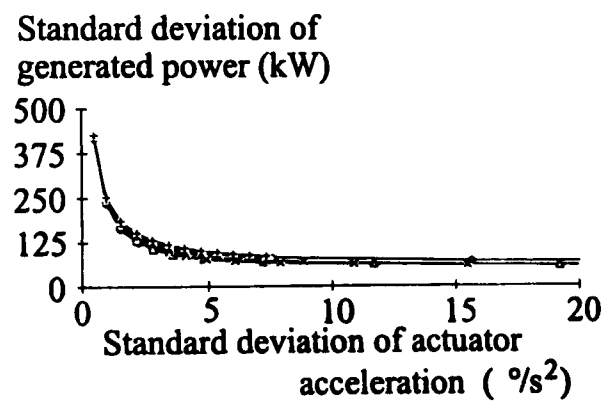
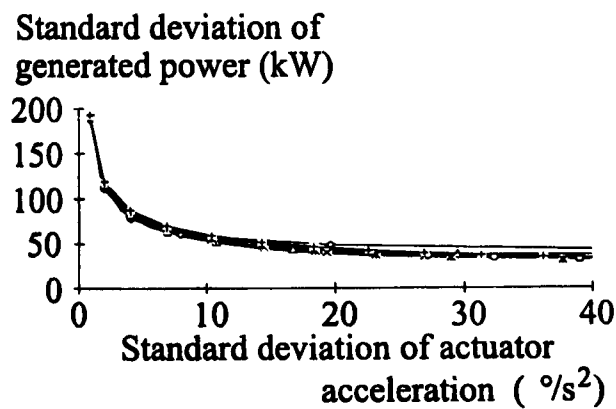
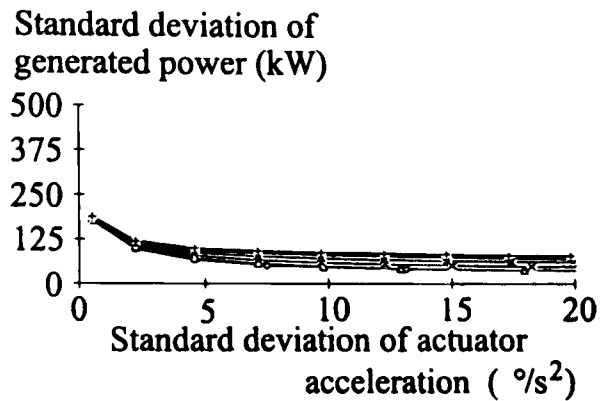
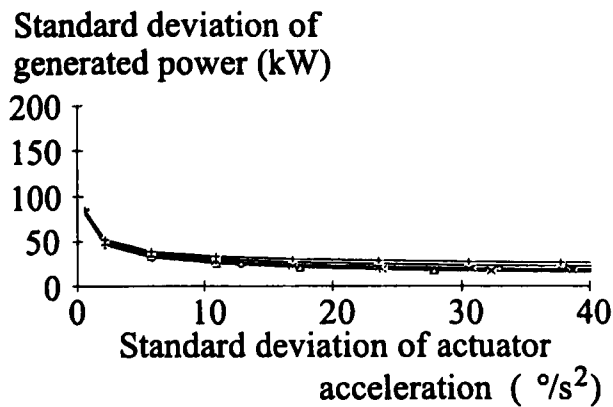
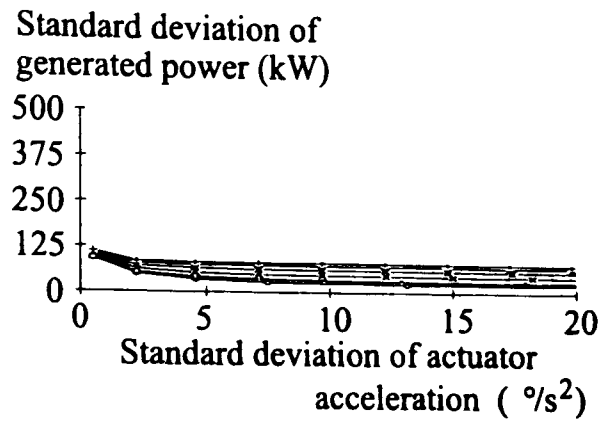
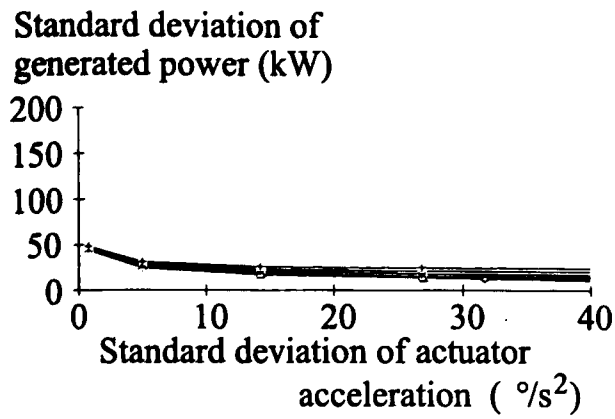


Figure H.5b Worst case performance (actuator velocity) of three-bladed ($2 \times$ nominal $3\Omega_0$) machines Cb and Fb.



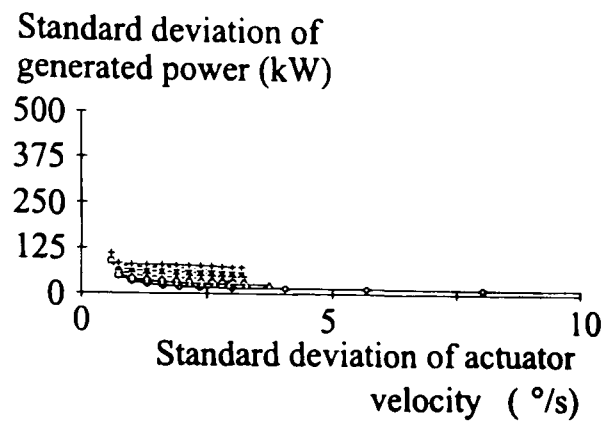
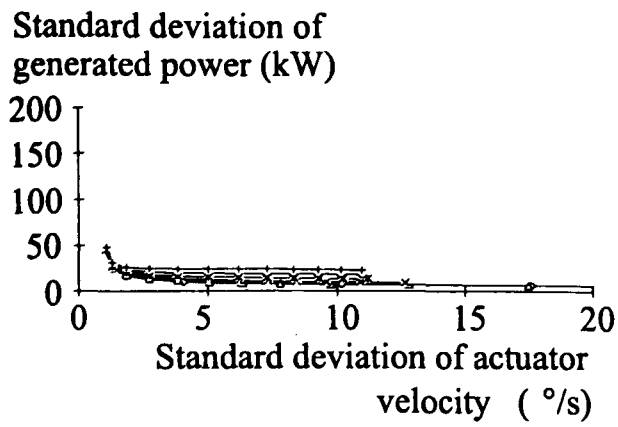
300 kW

1 MW

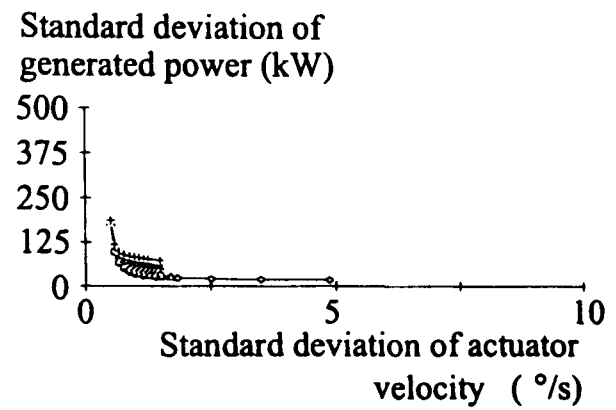
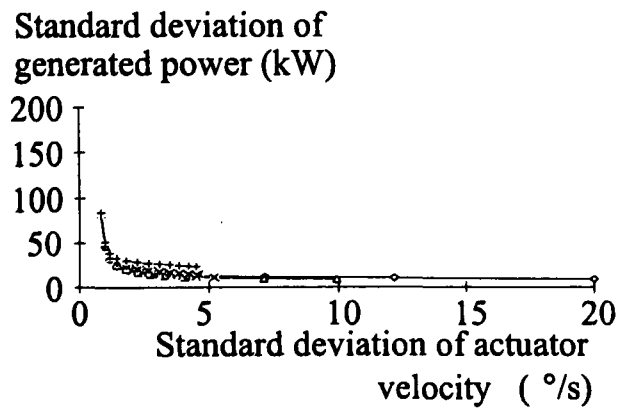
First drive-train mode

→ 2.0 rad/s → 3.0 rad/s → 4.0 rad/s → 5.0 rad/s → 6.0 rad/s → 7.0 rad/s

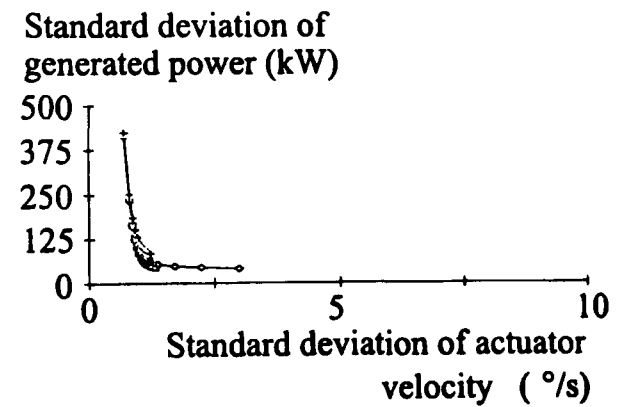
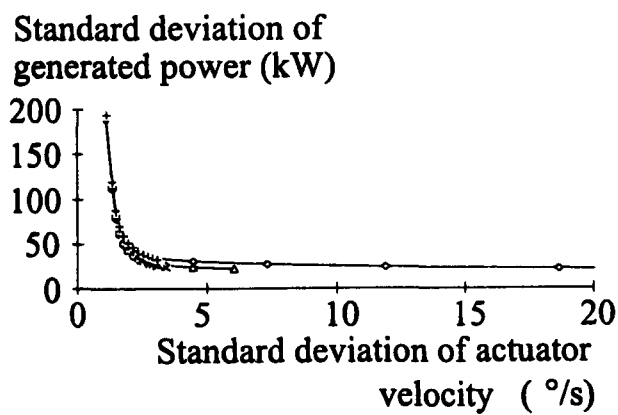
Figure H.6a Performance (actuator acceleration) of two-bladed ($1/2 \times$ nominal $2\Omega_o$) machines Aa and Da.



Wind speed 12 m/s



Wind speed 16 m/s



Wind speed 23 m/s

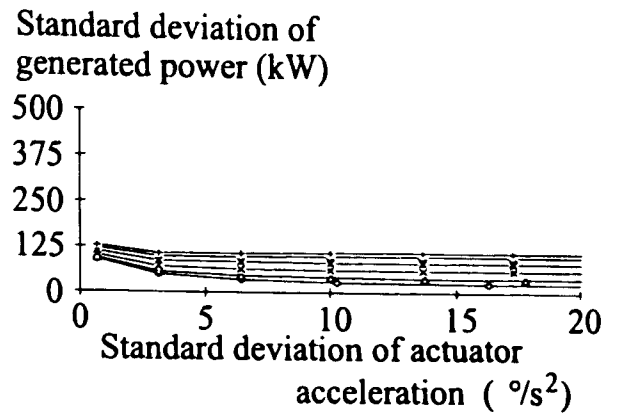
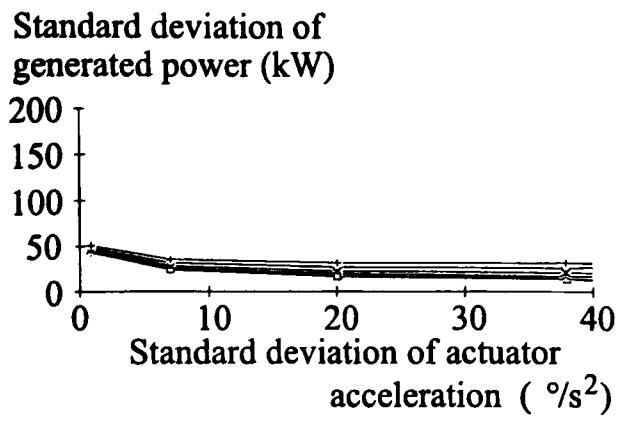
300 kW

1 MW

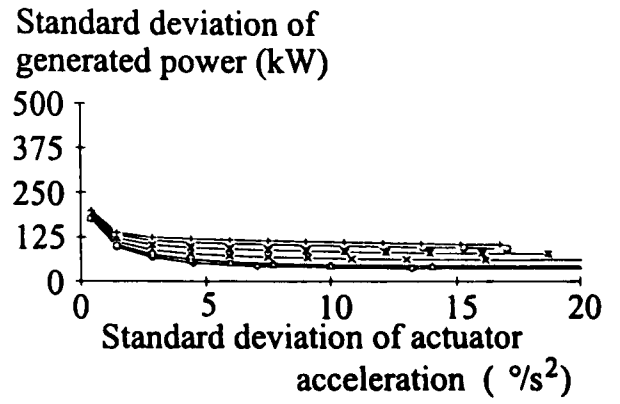
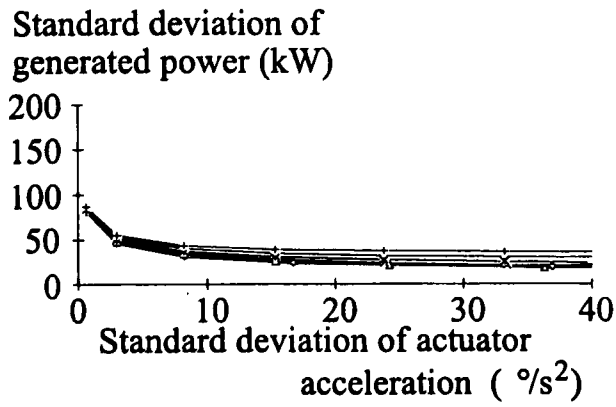
First drive-train mode

→ 2.0 rad/s → 3.0 rad/s → 4.0 rad/s → 5.0 rad/s → 6.0 rad/s → 7.0 rad/s

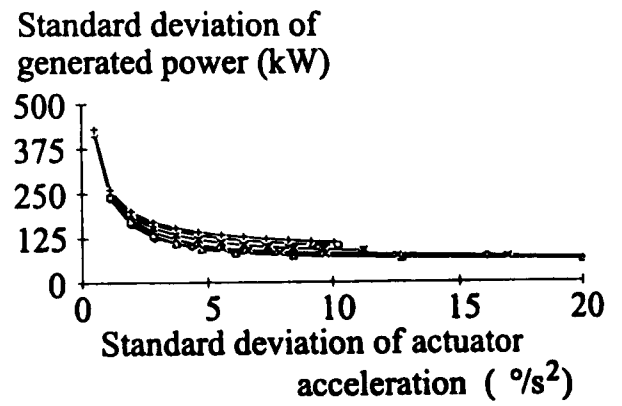
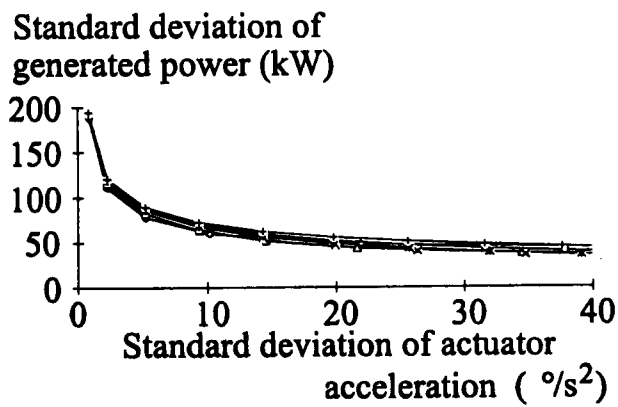
Figure H.6b Performance (actuator velocity)
of two-bladed ($1/2 \times$ nominal $2\Omega_0$) machines Aa and Da.



Wind speed 12 m/s



Wind speed 16 m/s



Wind speed 23 m/s

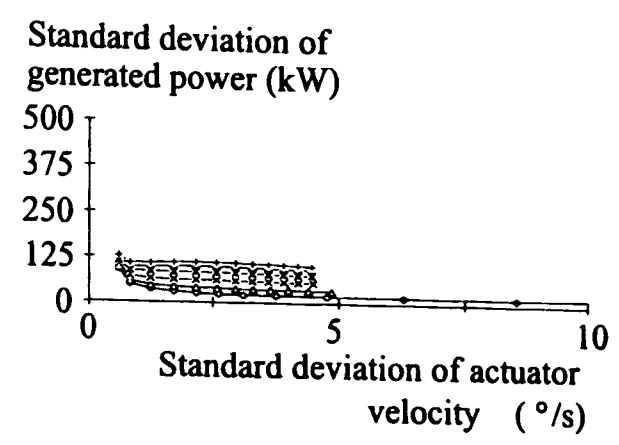
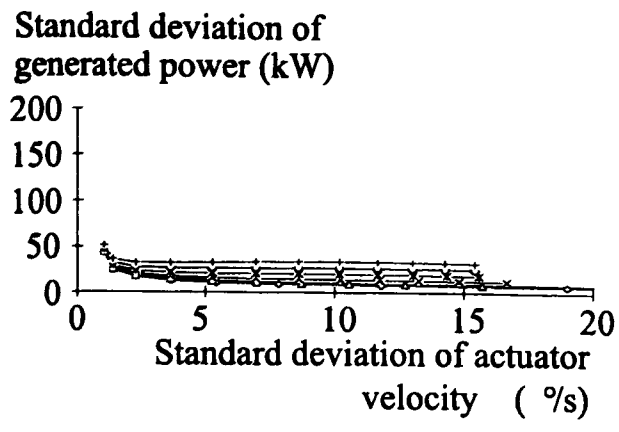
300 kW

1 MW

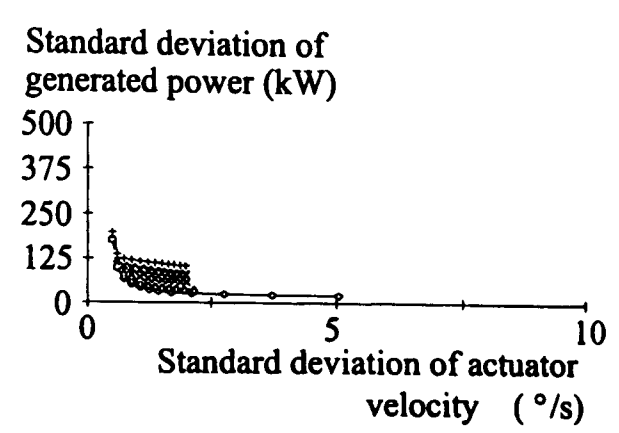
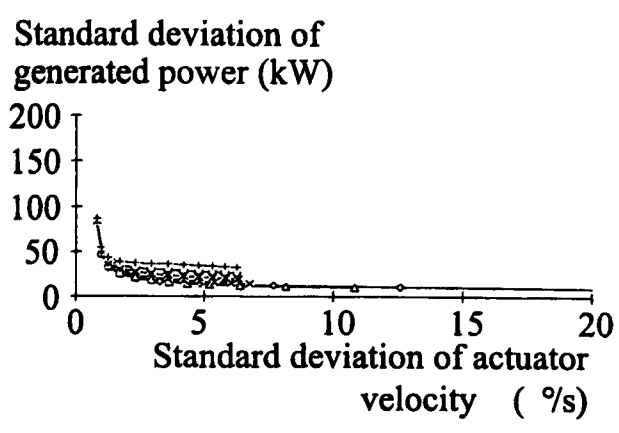
First drive-train mode

→ 2.0 rad/s → 3.0 rad/s → 4.0 rad/s → 5.0 rad/s → 6.0 rad/s → 7.0 rad/s

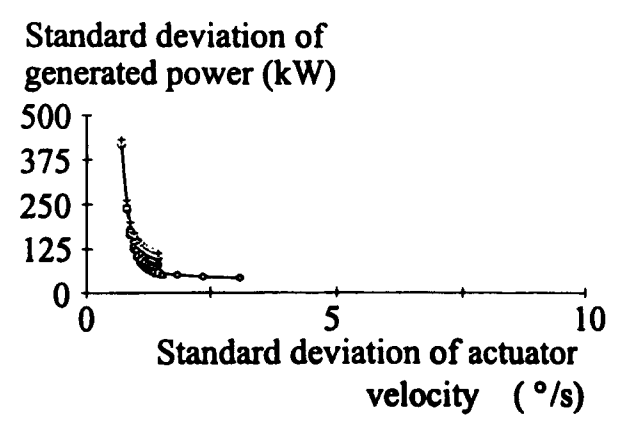
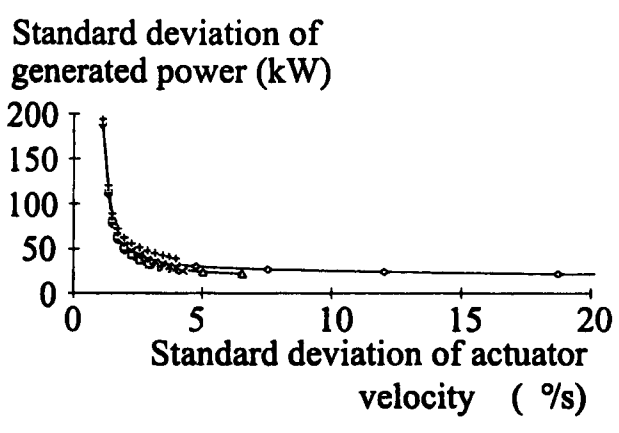
Figure H.7a Performance (actuator acceleration) of two-bladed (nominal $2\Omega_0$) machines Ab and Db.



Wind speed 12 m/s



Wind speed 16 m/s



Wind speed 23 m/s

300 kW

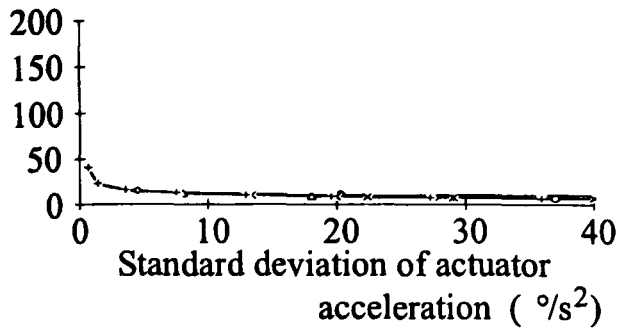
1 MW

First drive-train mode

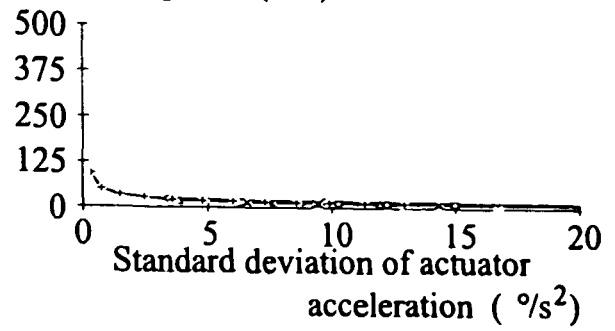
→ 2.0 rad/s → 3.0 rad/s → 4.0 rad/s → 5.0 rad/s → 6.0 rad/s → 7.0 rad/s

Figure H.7b Performance (actuator velocity) of two-bladed ($2\Omega_o$) machines Ab and Db.

Standard deviation of generated power (kW)

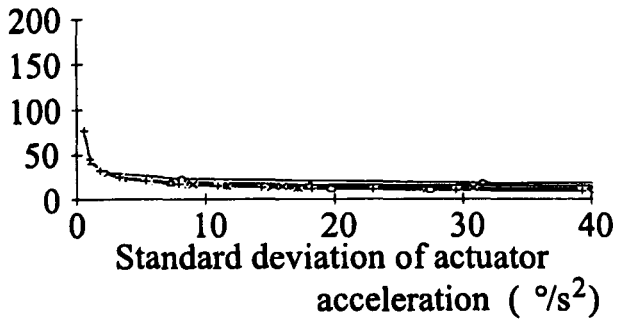


Standard deviation of generated power (kW)

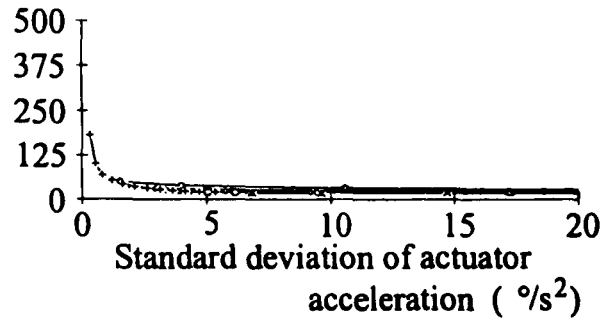


Wind speed 12 m/s

Standard deviation of generated power (kW)

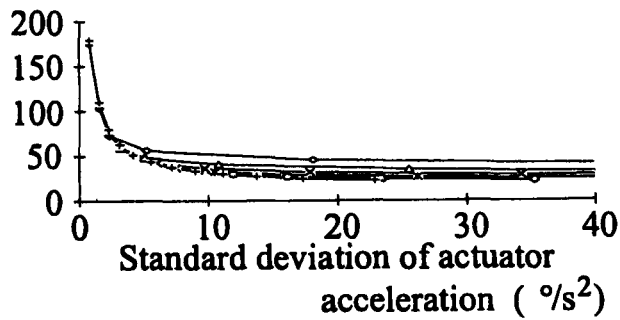


Standard deviation of generated power (kW)

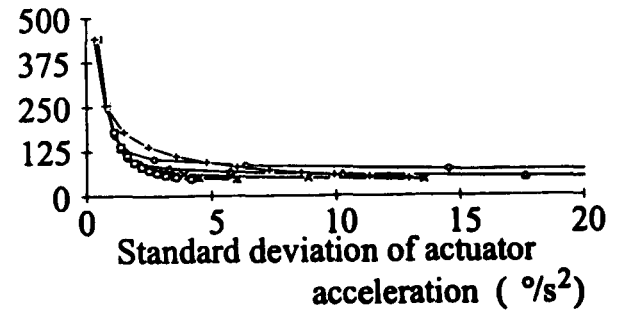


Wind speed 16 m/s

Standard deviation of generated power (kW)



Standard deviation of generated power (kW)



Wind speed 23 m/s

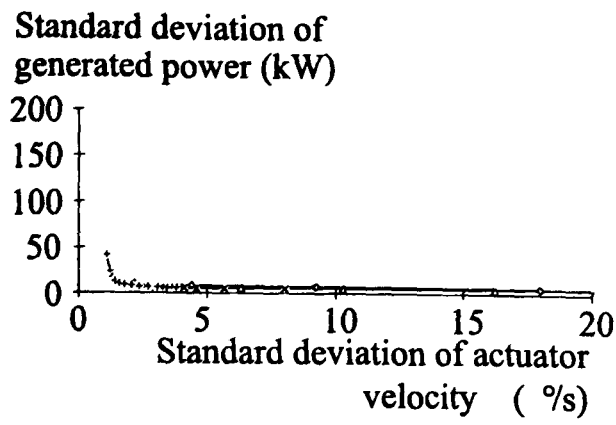
300 kW

1 MW

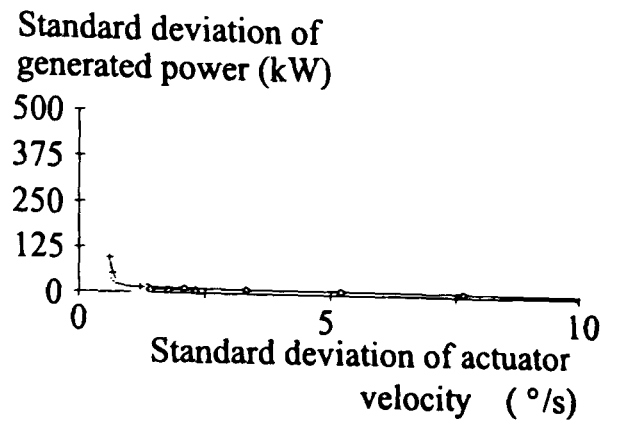
First drive-train mode

→ 2.0 rad/s → 3.0 rad/s → 4.0 rad/s → 5.0 rad/s → 6.0 rad/s → 7.0 rad/s

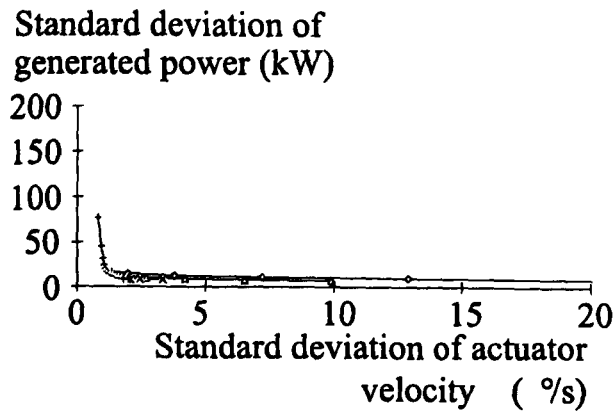
Figure H.8a Performance (actuator acceleration) of three-bladed (fast velocity) machines B and E.



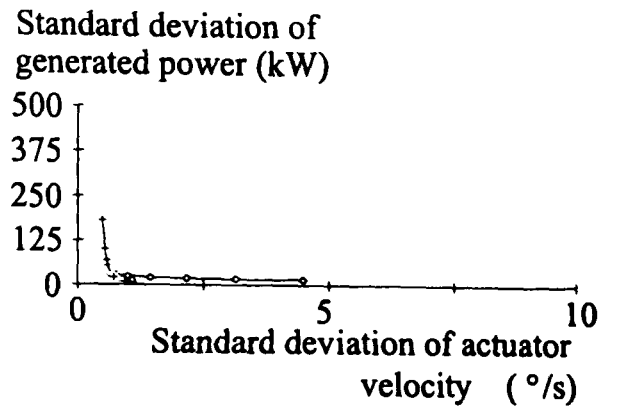
Wind speed 12 m/s



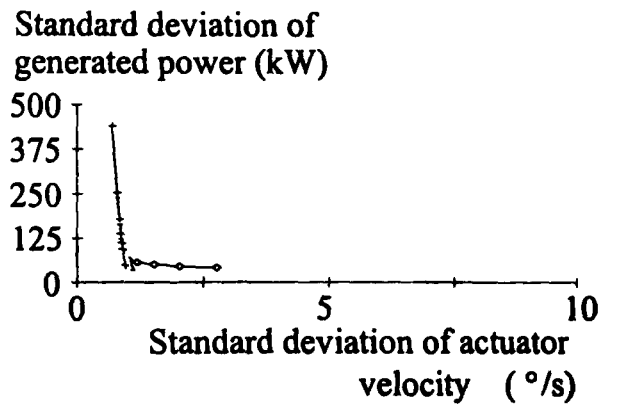
Wind speed 16 m/s



Wind speed 23 m/s



300 kW

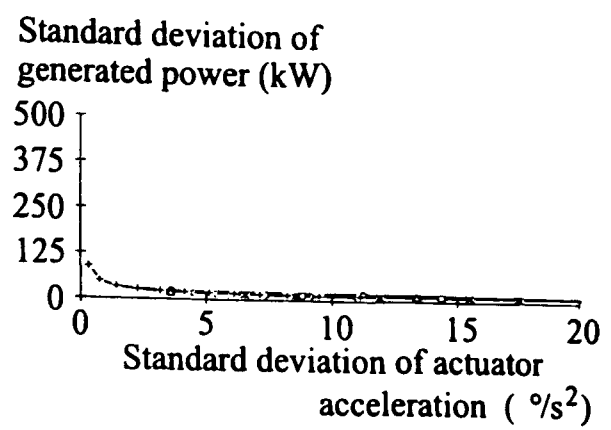
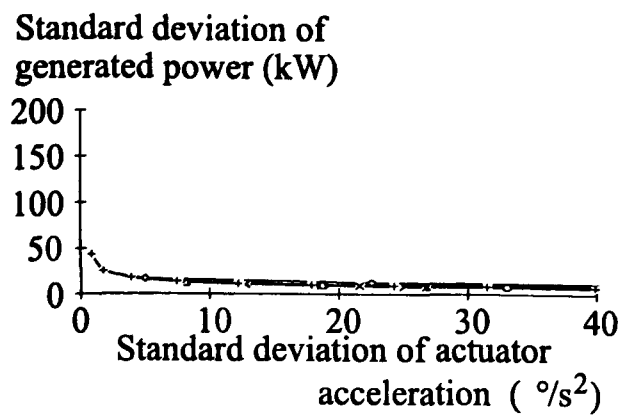


1 MW

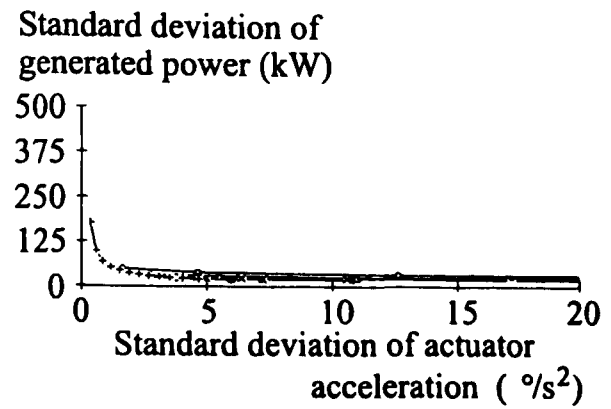
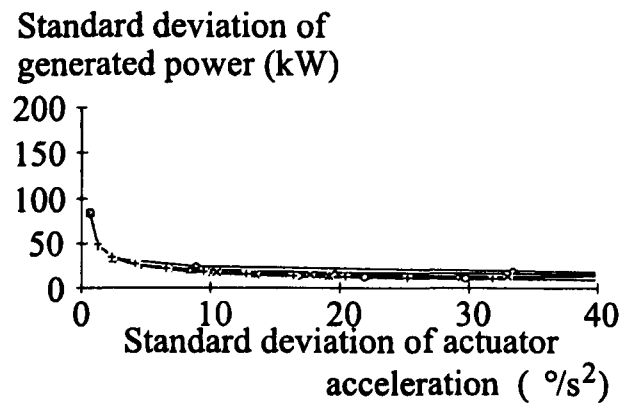
First drive-train mode

→ 2.0 rad/s → 3.0 rad/s → 4.0 rad/s → 5.0 rad/s → 6.0 rad/s → 7.0 rad/s

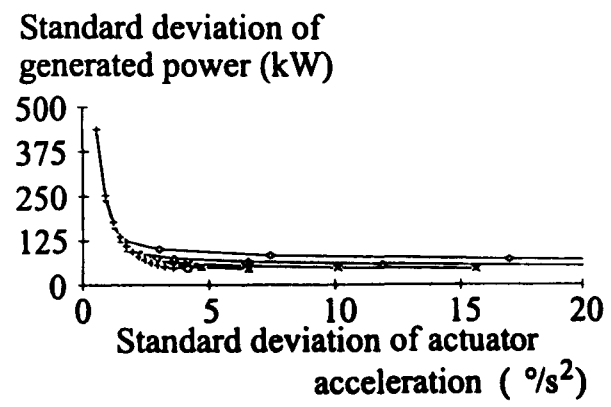
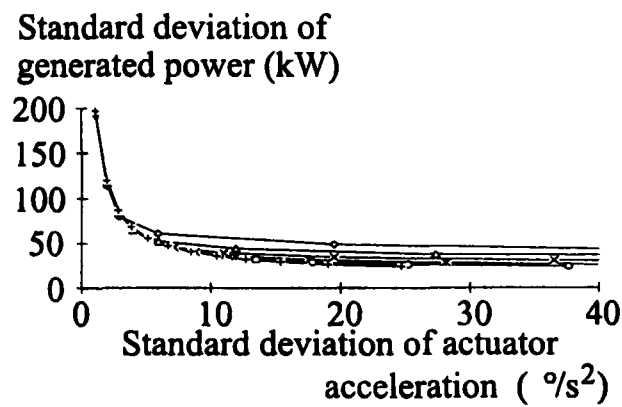
Figure H.8b Performance (actuator velocity) of three-bladed (fast velocity) machines B and E.



Wind speed 12 m/s



Wind speed 16 m/s



Wind speed 23 m/s

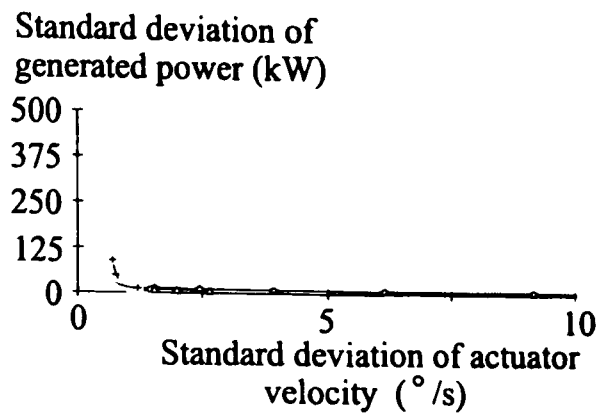
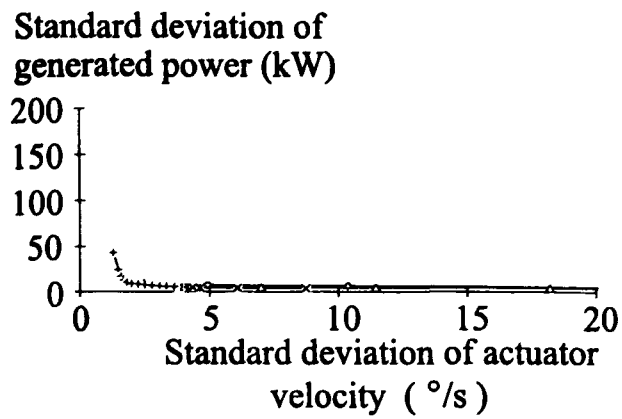
300 kW

1 MW

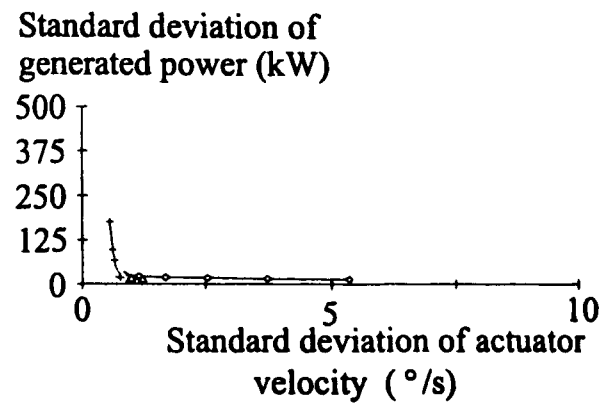
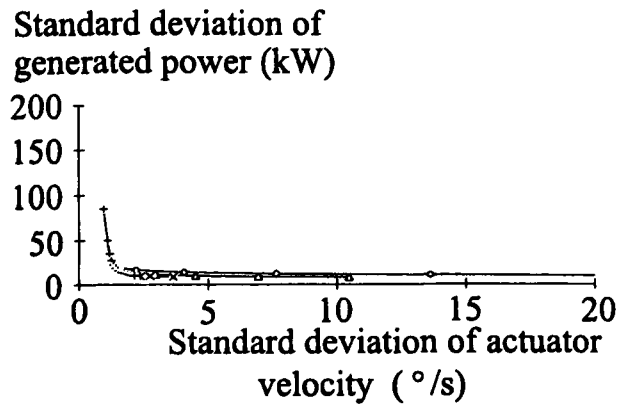
First drive-train mode

→ 2.0 rad/s → 3.0 rad/s → 4.0 rad/s → 5.0 rad/s → 6.0 rad/s → 7.0 rad/s

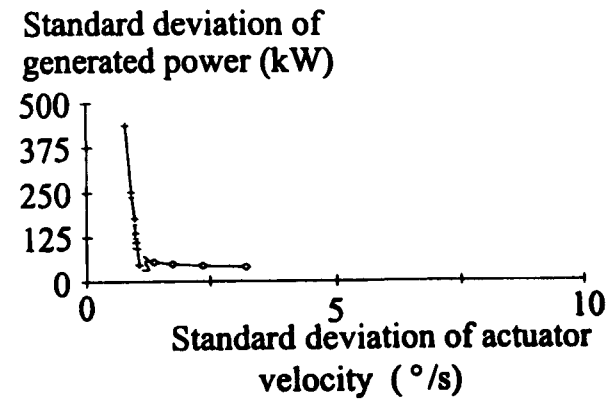
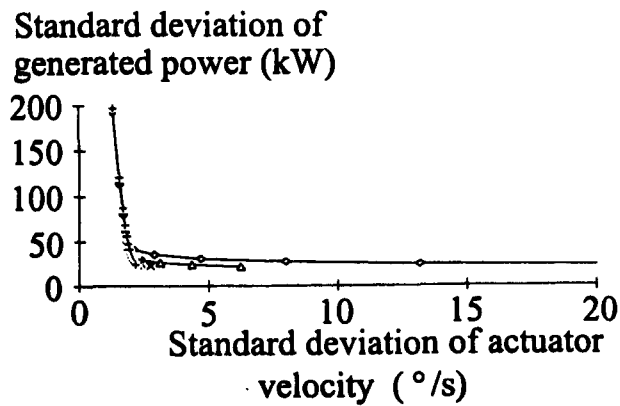
Figure H.9a Performance (actuator acceleration)
of three-bladed (nominal $3\Omega_p$) machines Ca and Fa.



Wind speed 12 m/s



Wind speed 16 m/s



Wind speed 23 m/s

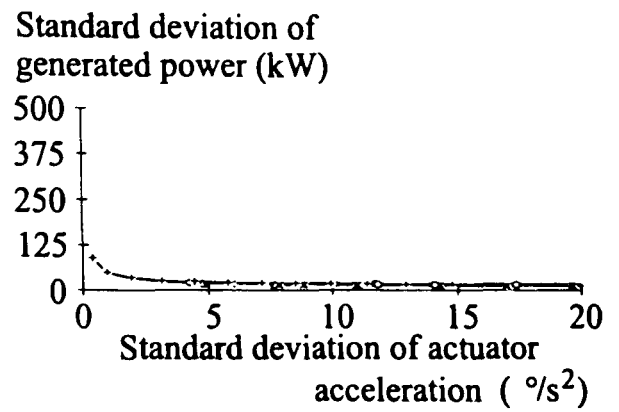
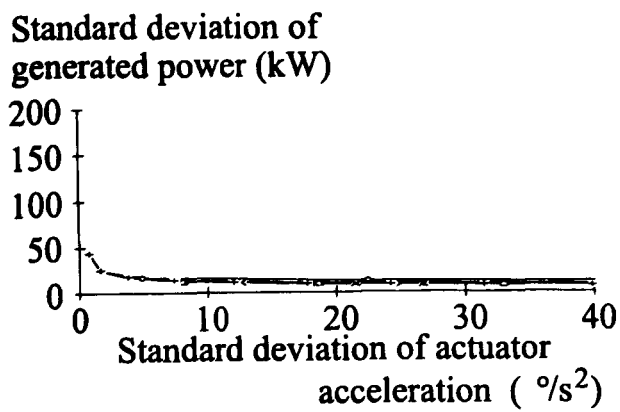
300 kW

1 MW

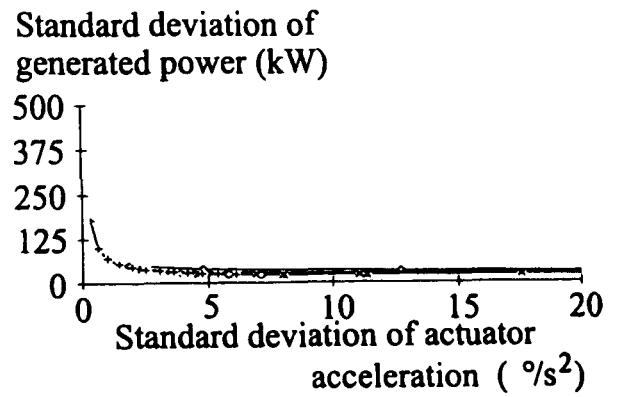
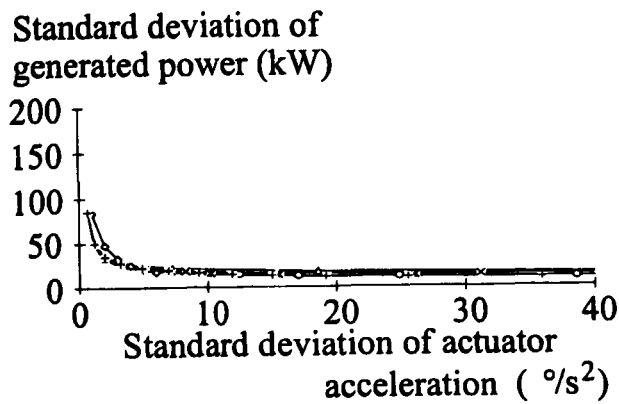
First drive-train mode

○ 2.0 rad/s ○ 3.0 rad/s × 4.0 rad/s × 5.0 rad/s ○ 6.0 rad/s → 7.0 rad/s

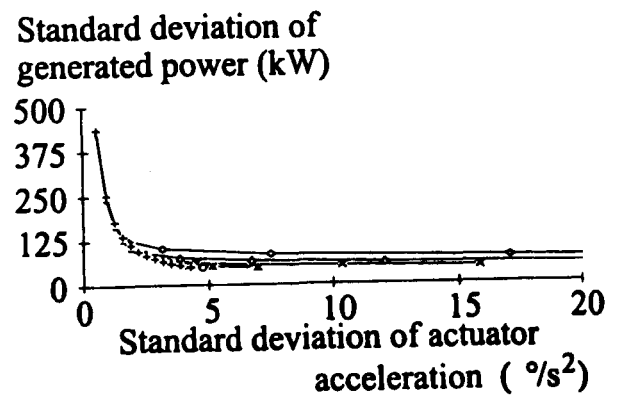
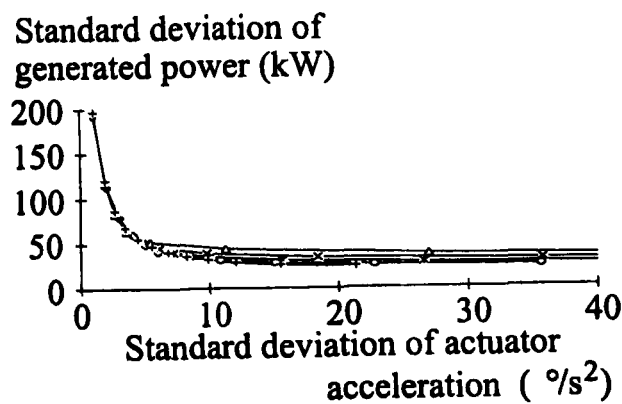
Figure H.9b Performance (actuator velocity)
of three-bladed (nominal $3\Omega_o$) machines Ca and Fa.



Wind speed 12 m/s



Wind speed 16 m/s



Wind speed 23 m/s

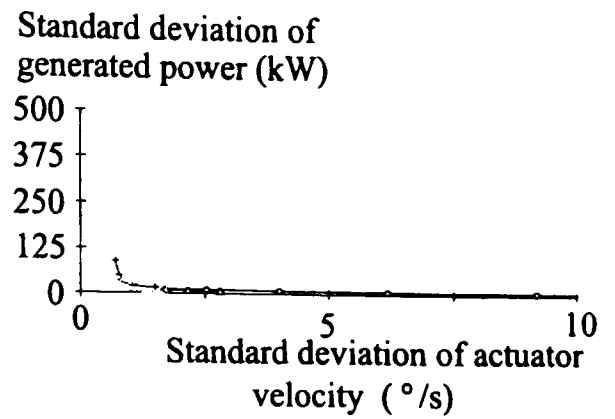
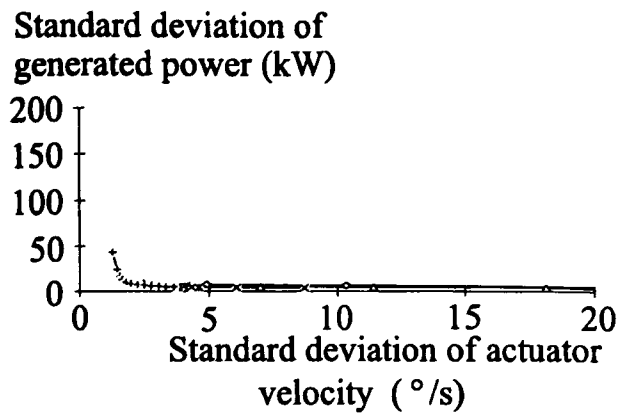
300 kW

1 MW

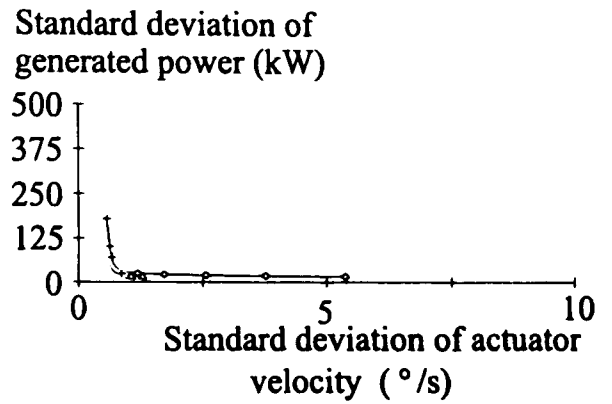
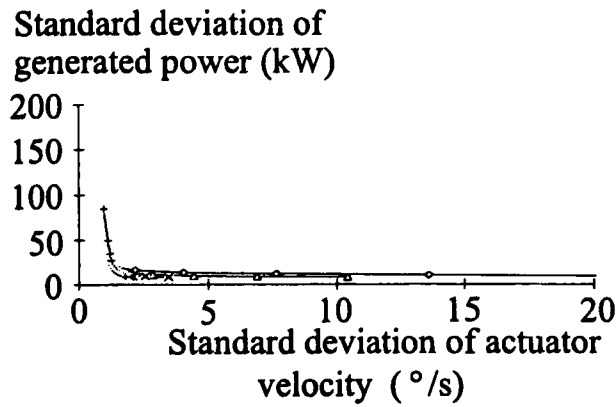
First drive-train mode

—○— 2.0 rad/s —□— 3.0 rad/s —×— 4.0 rad/s —*— 5.0 rad/s —◇— 6.0 rad/s —+— 7.0 rad/s

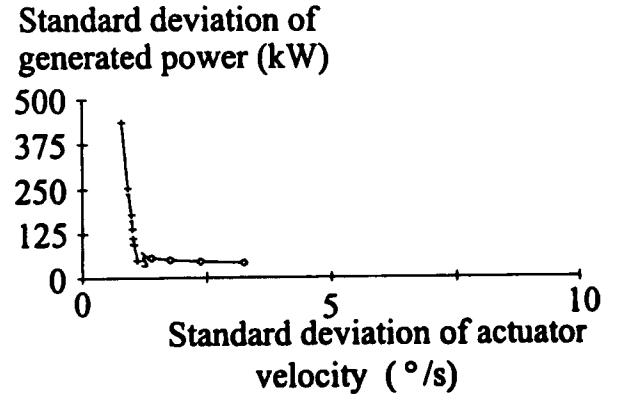
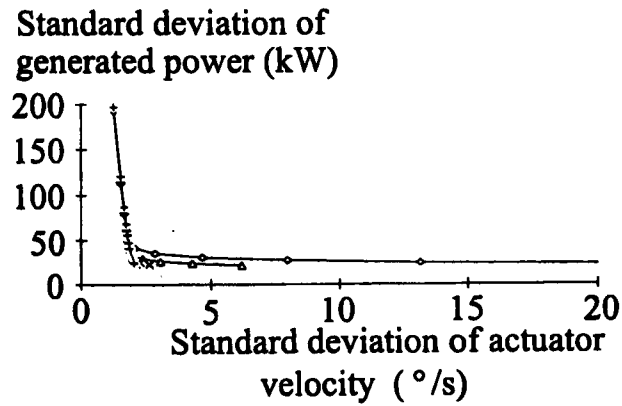
Figure H.10a Performance (actuator acceleration) of three-bladed ($2 \times$ nominal $3\Omega_n$) machines Cb and Fb.



Wind speed 12 m/s



Wind speed 16 m/s



Wind speed 23 m/s

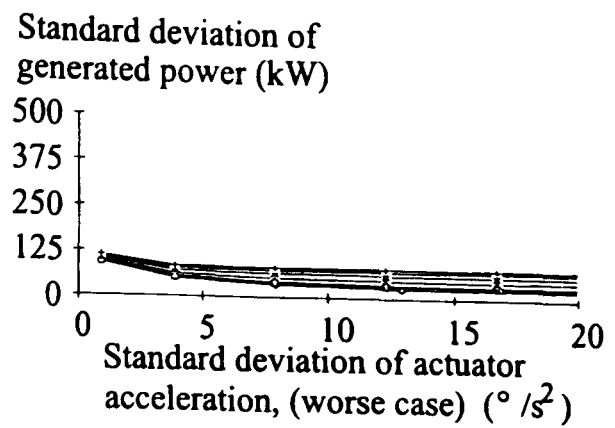
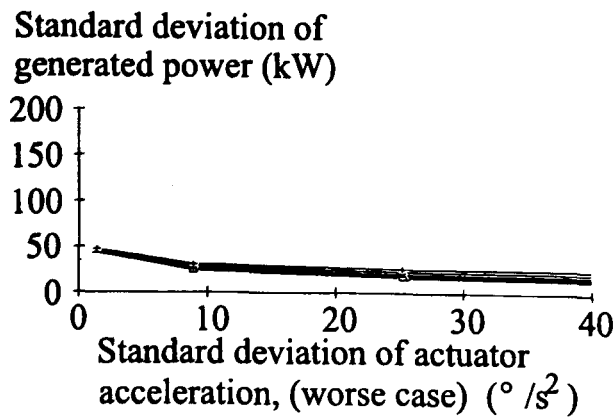
300 kW

1 MW

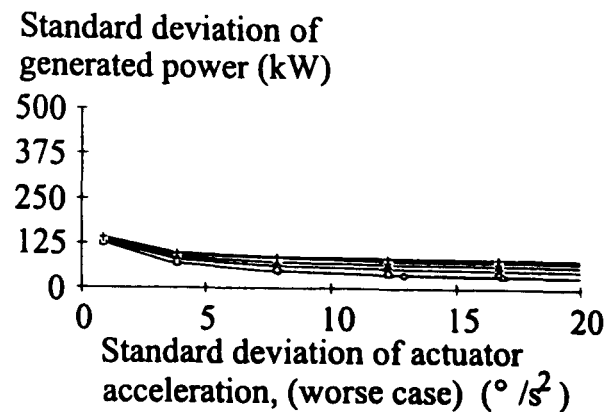
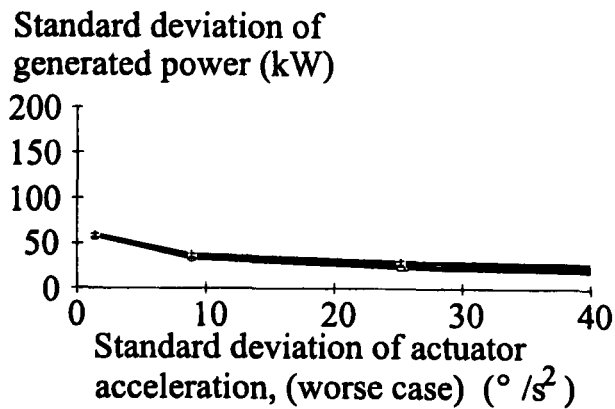
First drive-train mode

→ 2.0 rad/s → 3.0 rad/s → 4.0 rad/s → 5.0 rad/s → 6.0 rad/s → 7.0 rad/s

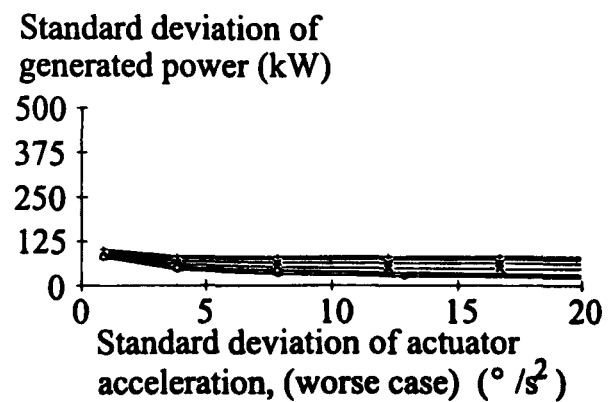
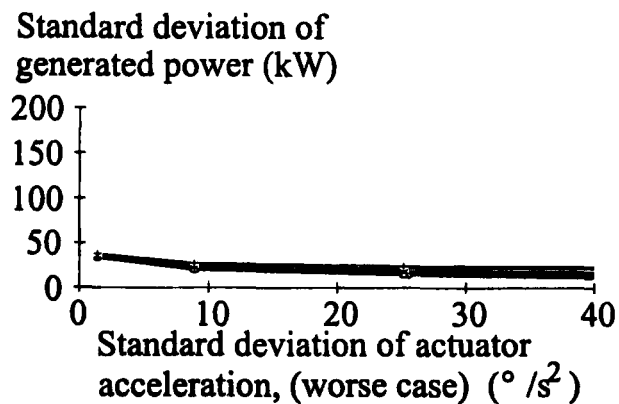
Figure H.10b Performance (actuator velocity)
of three-bladed ($2 \times$ nominal $3\Omega_o$) machines Cb and Fb.



Wind speed 12 m/s



Wind speed 16 m/s



Wind speed 23 m/s

300 kW

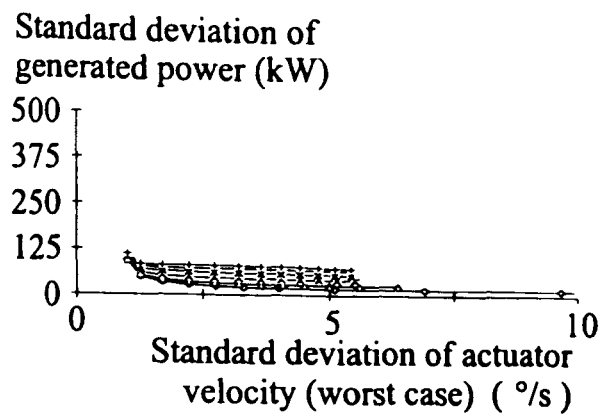
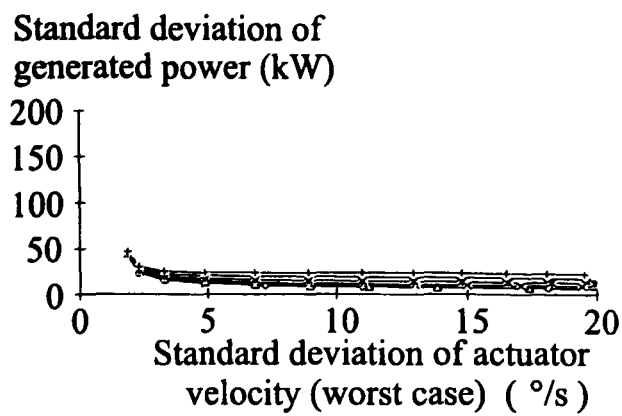
1 MW

First drive-train mode

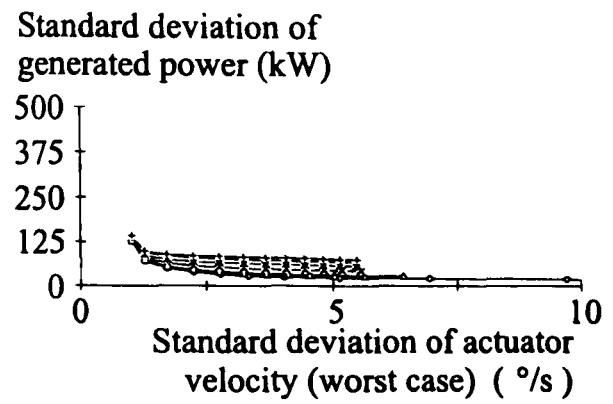
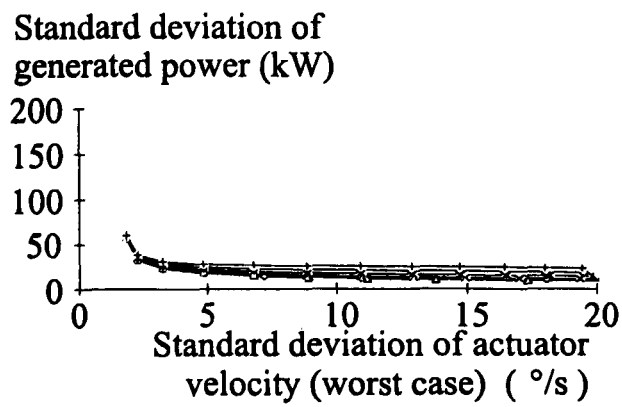
→ 2.0 rad/s → 3.0 rad/s → 4.0 rad/s → 5.0 rad/s → 6.0 rad/s → 7.0 rad/s

Figure H.11a Worst case performance (actuator acceleration)

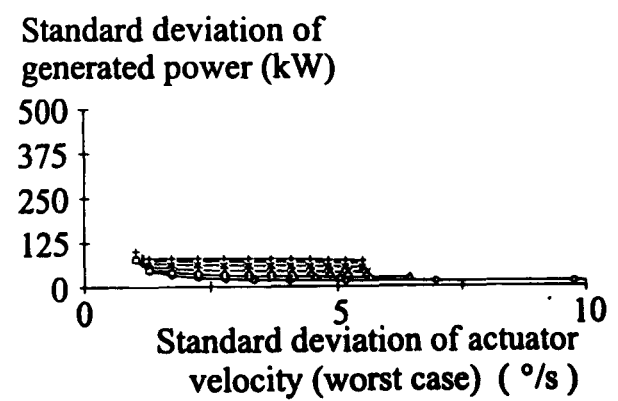
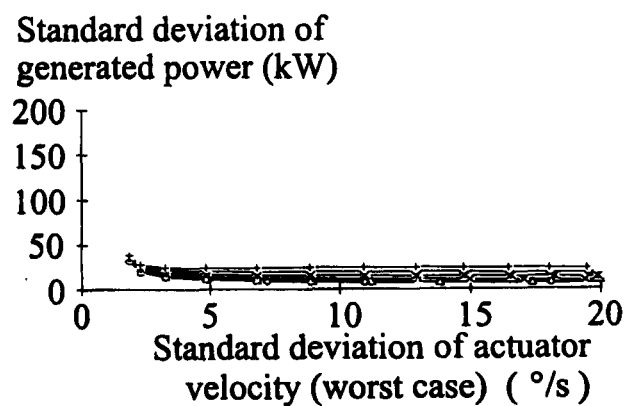
of two-bladed ($1/2$ nominal $2\Omega_0$) machines Ga and Ja.



Wind speed 12 m/s



Wind speed 16 m/s



Wind speed 23 m/s

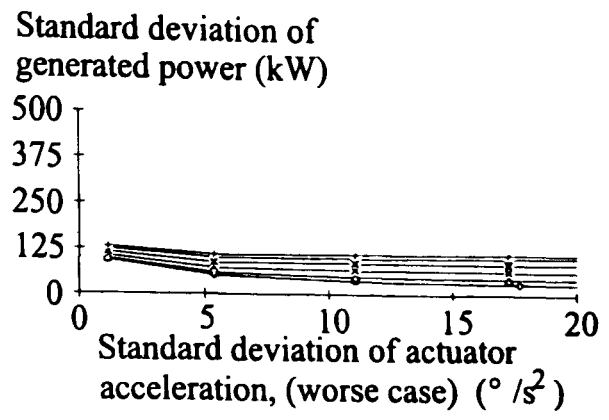
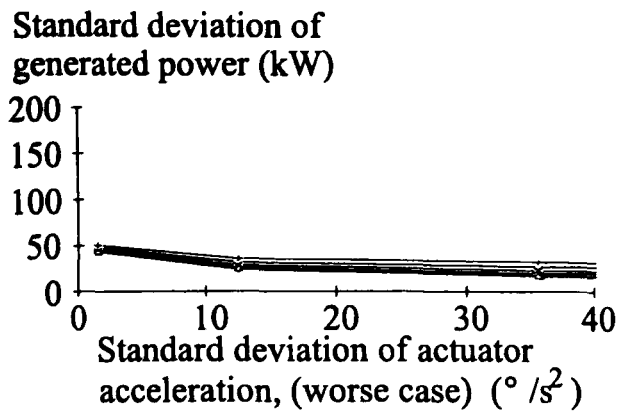
300 kW

1 MW

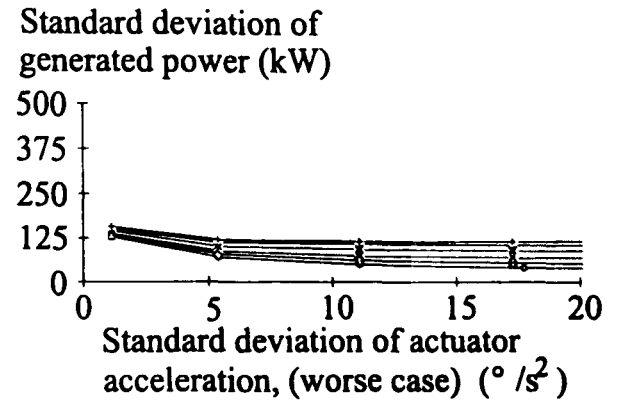
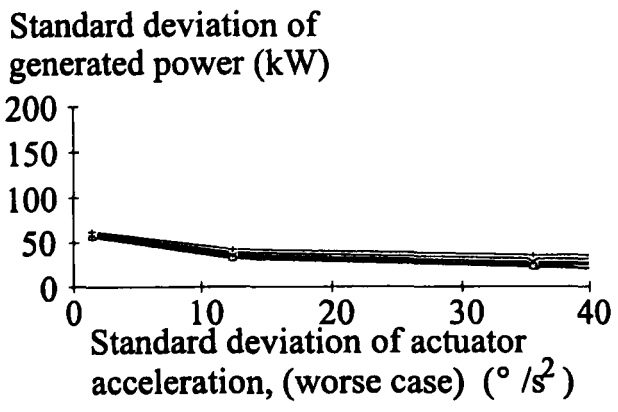
First drive-train mode

\circ -2.0 rad/s \square -3.0 rad/s \times -4.0 rad/s \star -5.0 rad/s \diamond -6.0 rad/s \rightarrow -7.0 rad/s

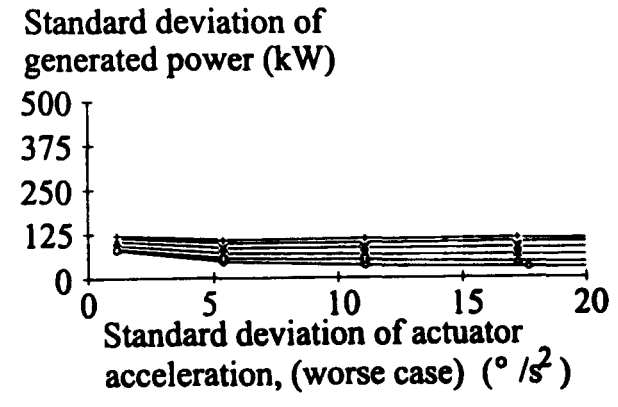
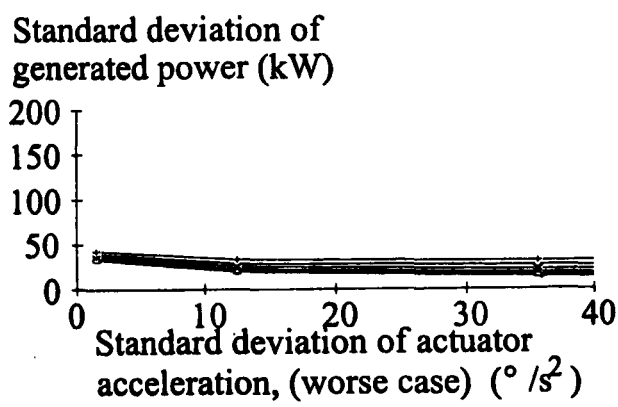
Figure H.11b Worst case performance (actuator velocity) of two-bladed ($1/2$ nominal $2\Omega_o$) machines Ga and Ja.



Wind speed 12 m/s



Wind speed 16 m/s



Wind speed 23 m/s

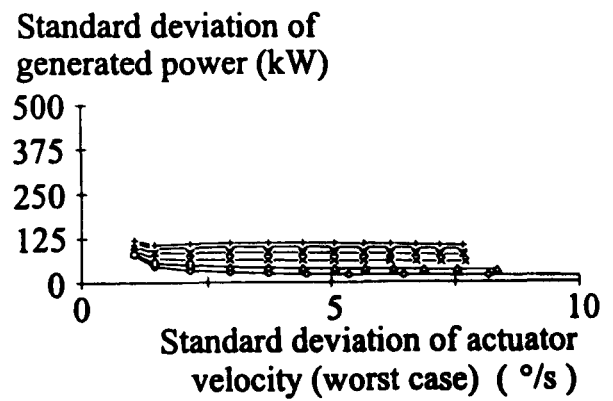
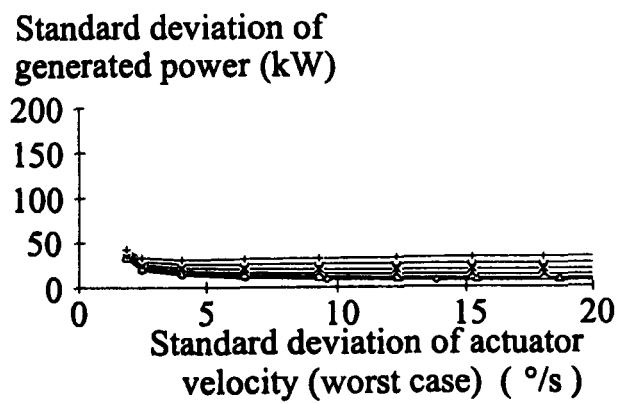
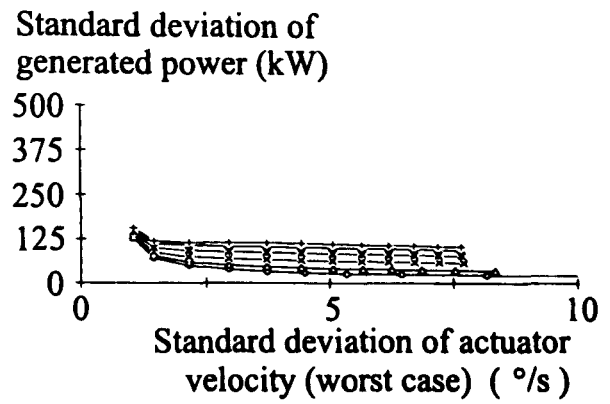
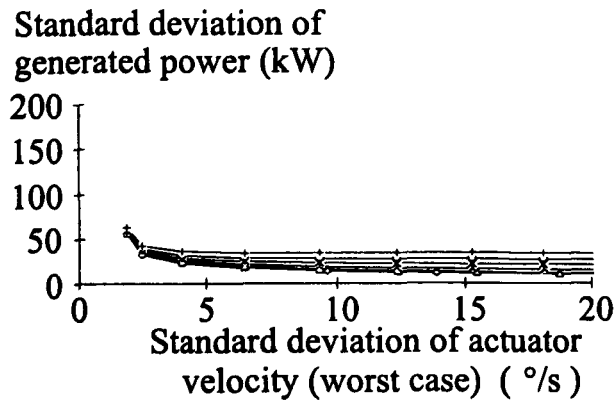
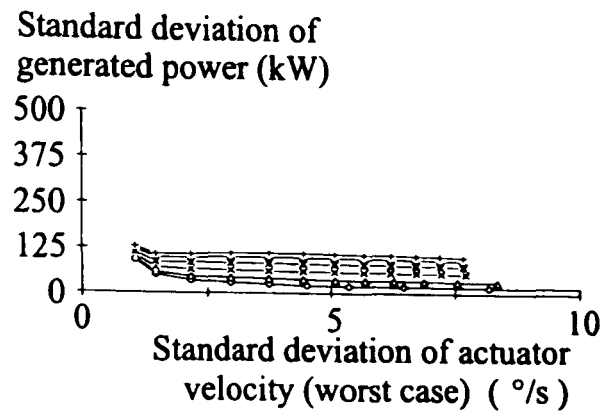
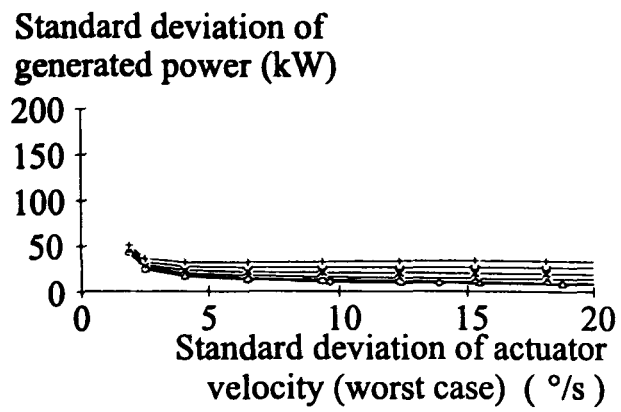
300 kW

1 MW

First drive-train mode

○ 2.0 rad/s ◓ 3.0 rad/s × 4.0 rad/s × 5.0 rad/s ◓ 6.0 rad/s ◓ 7.0 rad/s

Figure H.12a Worst case performance (actuator acceleration) of two-bladed (nominal $2\Omega_0$) machines Gb and Jb.



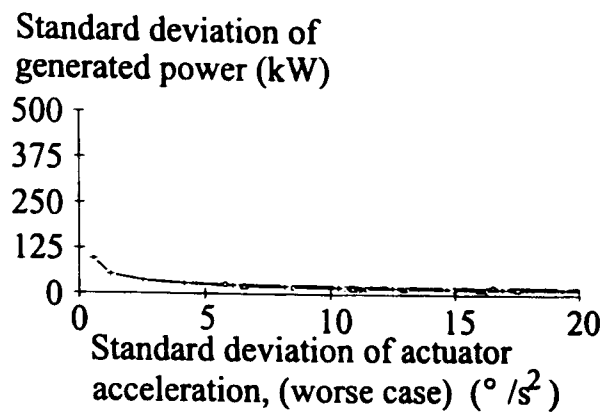
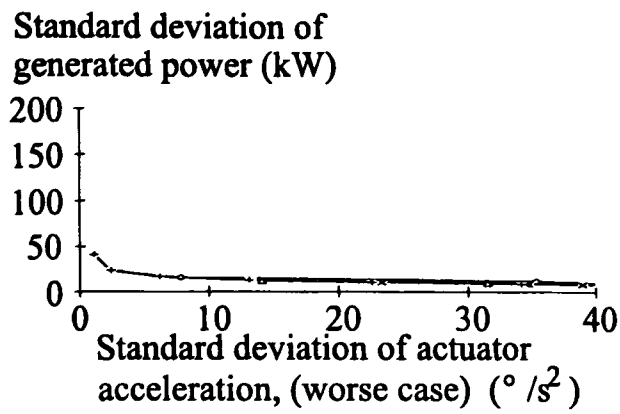
300 kW

1 MW

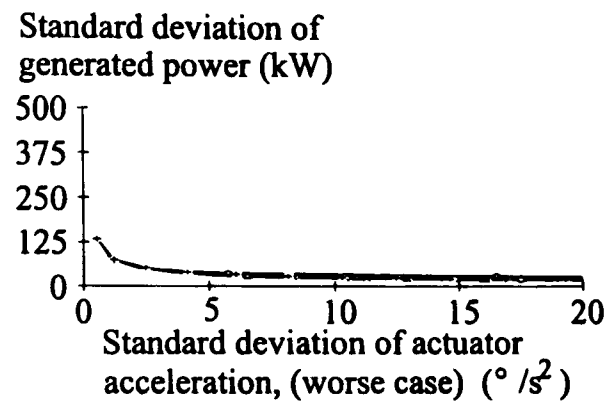
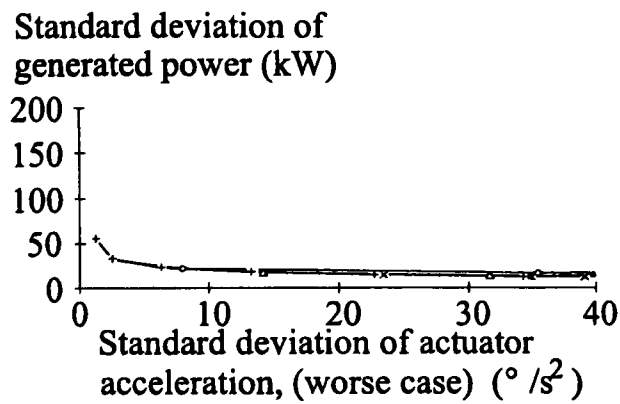
First drive-train mode

→ 2.0 rad/s → 3.0 rad/s → 4.0 rad/s → 5.0 rad/s → 6.0 rad/s → 7.0 rad/s

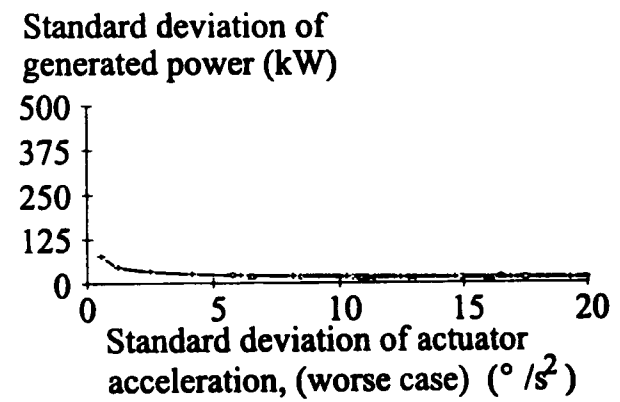
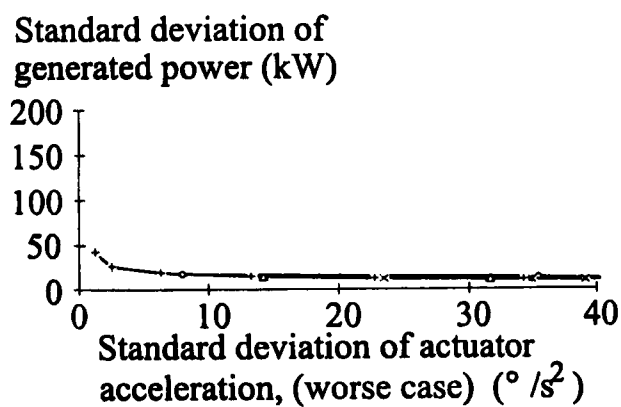
Figure H.12b Worst case performance (actuator velocity) of two-bladed (nominal $2\Omega_0$) machines Gb and Jb.



Wind speed 12 m/s



Wind speed 16 m/s



Wind speed 23 m/s

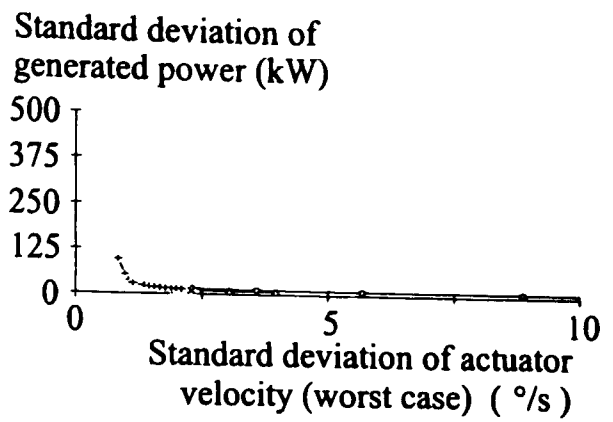
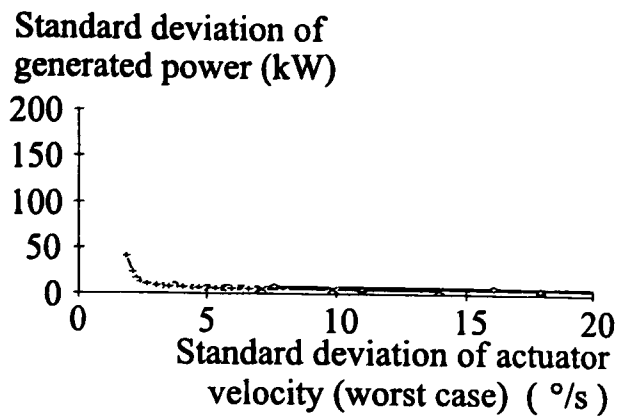
300 kW

1 MW

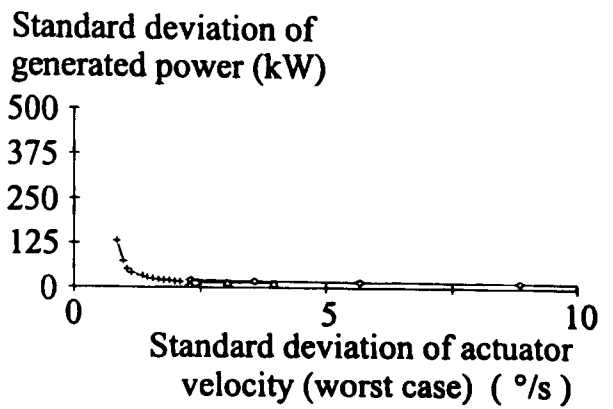
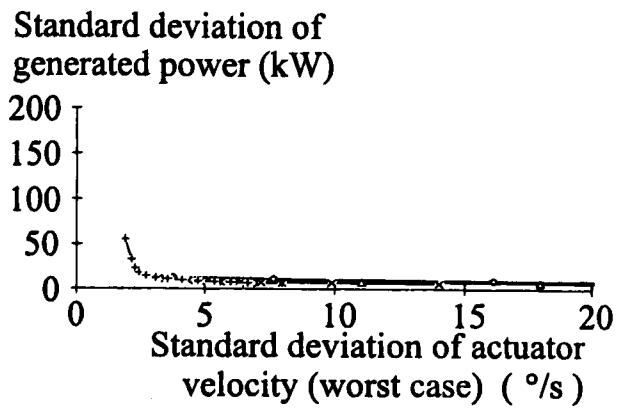
First drive-train mode

—○— 2.0 rad/s —+— 3.0 rad/s —x— 4.0 rad/s —-— 5.0 rad/s —○— 6.0 rad/s —-— 7.0 rad/s

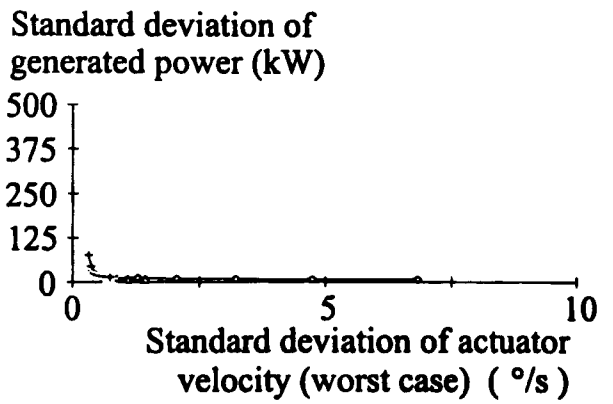
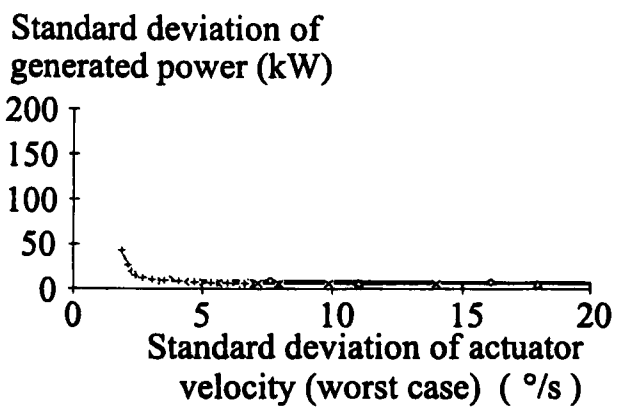
Figure H.13a Worst case performance (actuator acceleration) of three-bladed (faster rotor speed) machines H and K.



Wind speed 12 m/s



Wind speed 16 m/s



Wind speed 23 m/s

300 kW

1 MW

First drive-train mode

○ 2.0 rad/s ◐ 3.0 rad/s × 4.0 rad/s × 5.0 rad/s ◑ 6.0 rad/s → 7.0 rad/s

Figure H.13b Worst case performance (actuator velocity)
of three-bladed (fast velocity) machines H and K.

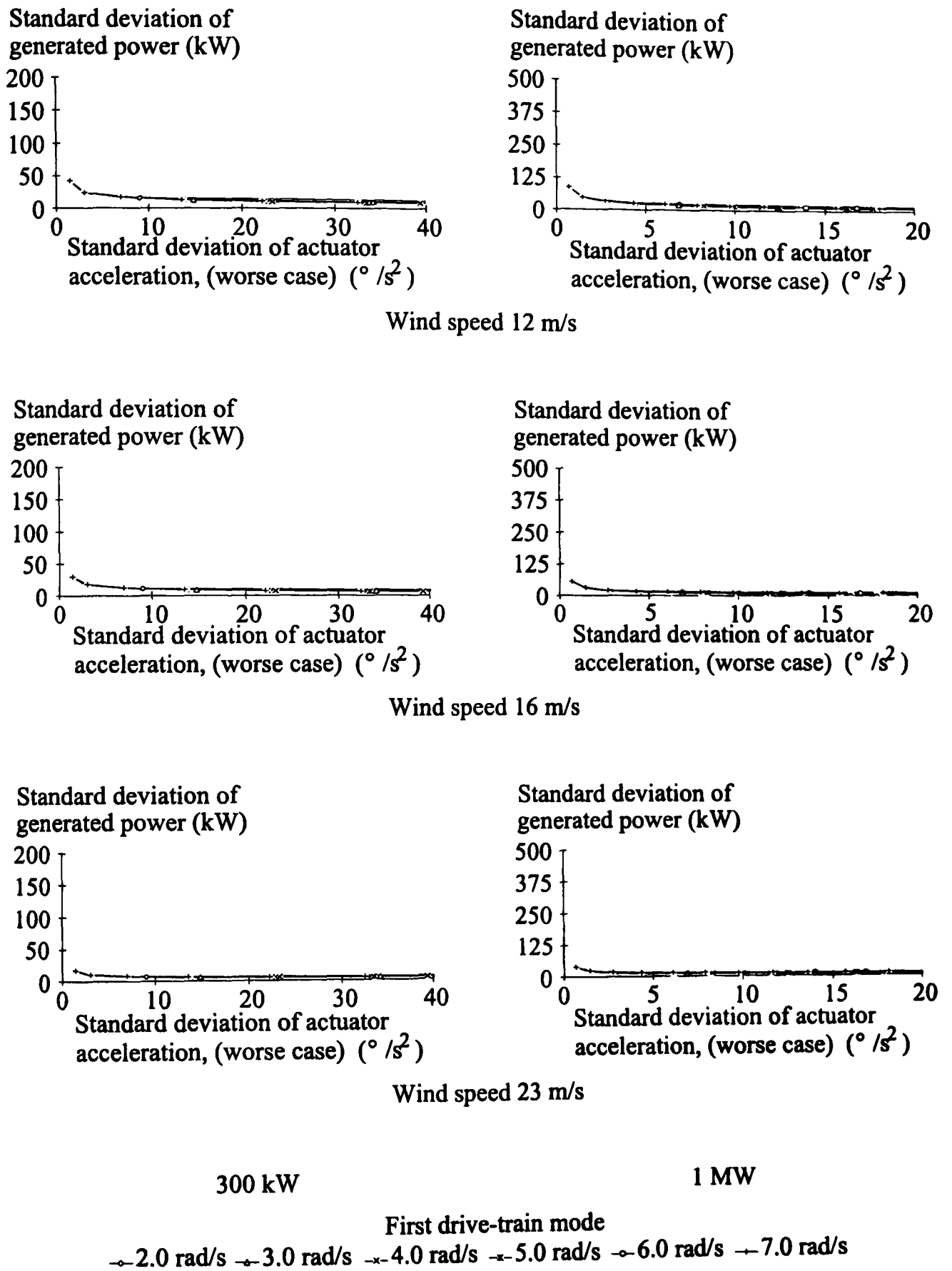
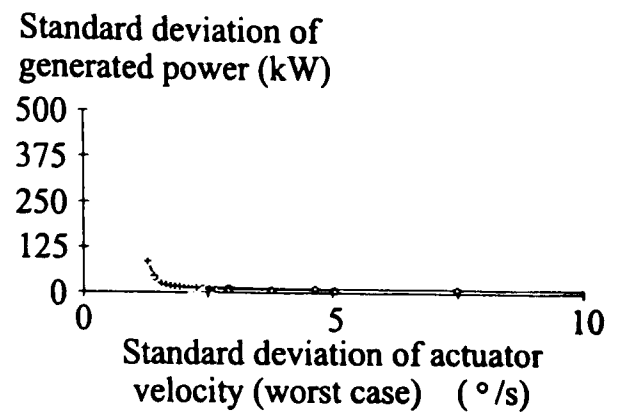
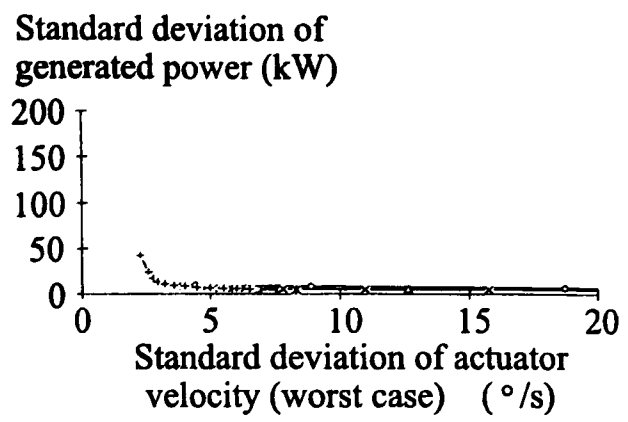
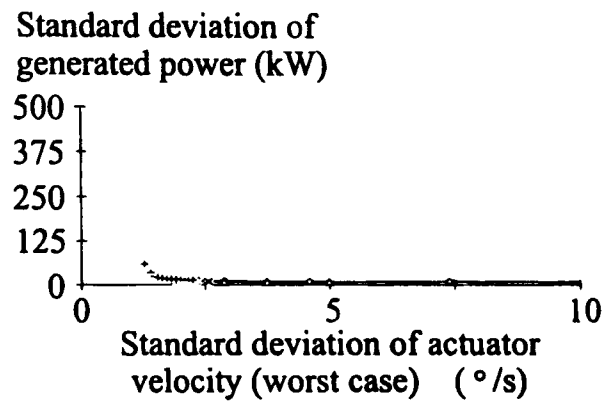
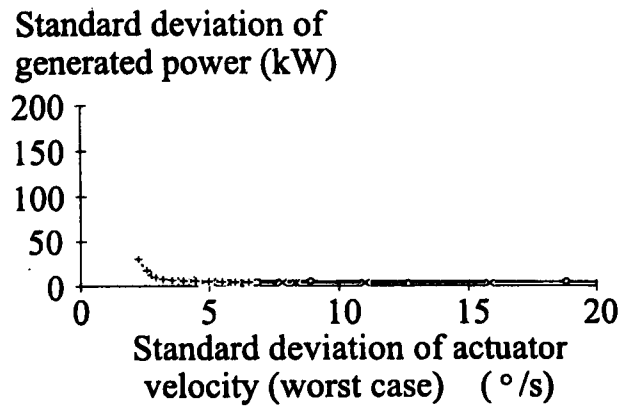


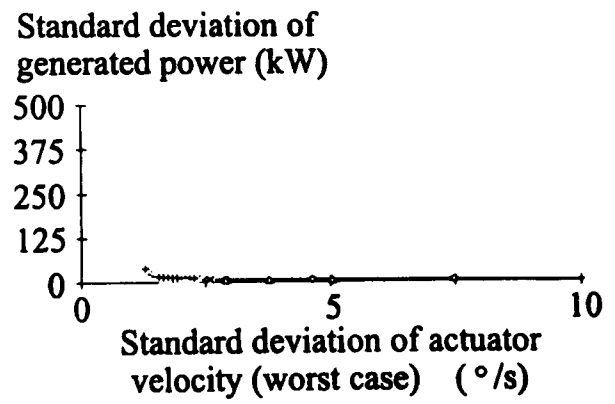
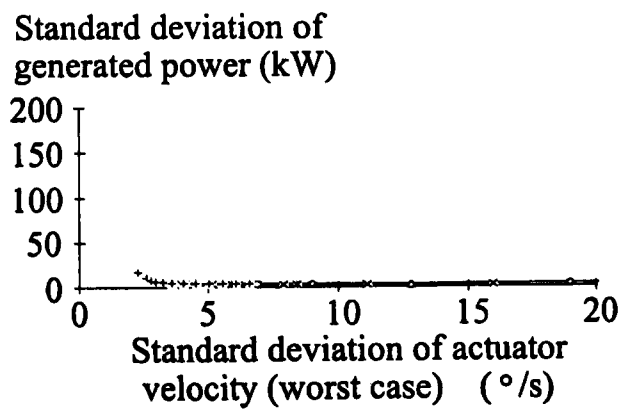
Figure H.14a Worst case performance (actuator acceleration) of three-bladed (nominal $3\Omega_0$) machines Ia and La.



Wind speed 12 m/s



Wind speed 16 m/s



Wind speed 23 m/s

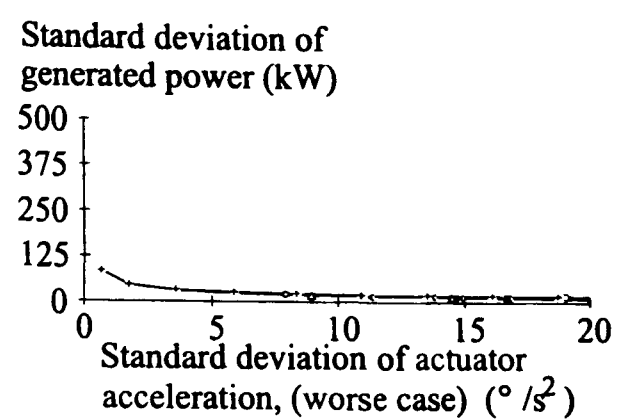
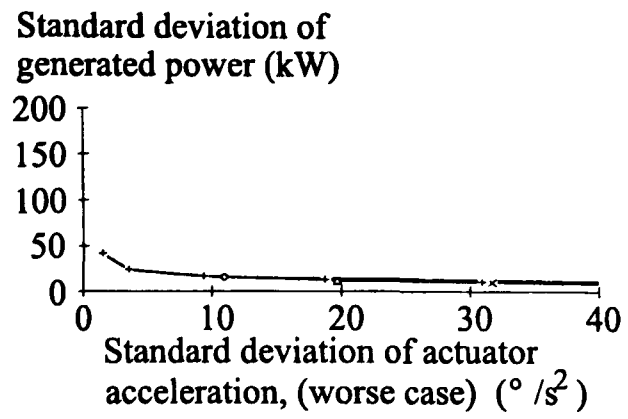
300 kW

1 MW

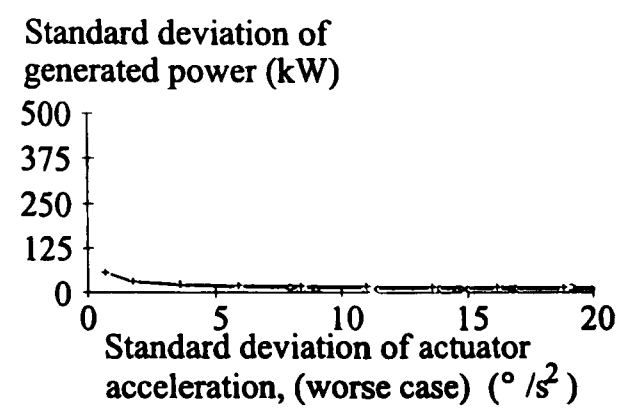
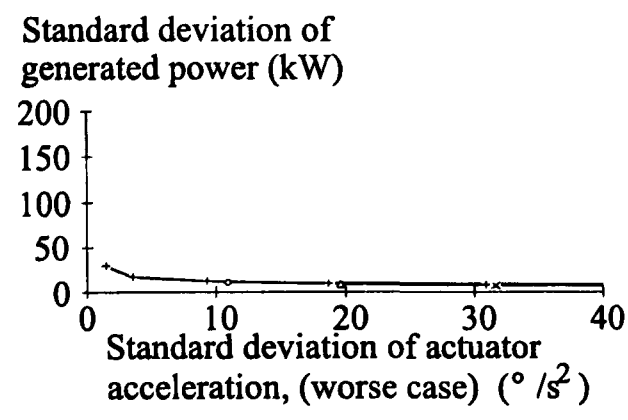
First drive-train mode

○ 2.0 rad/s ◓ 3.0 rad/s × 4.0 rad/s ⊖ 5.0 rad/s ◐ 6.0 rad/s ⊕ 7.0 rad/s

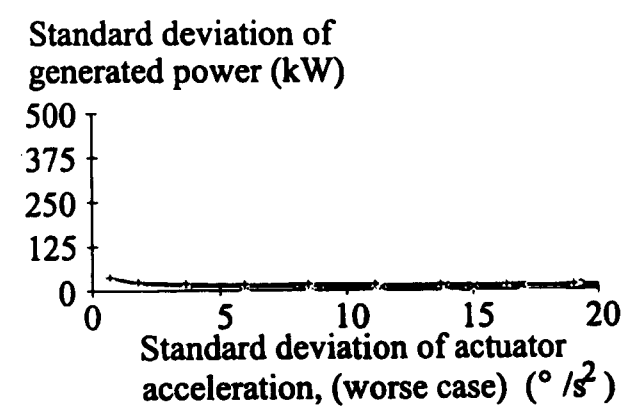
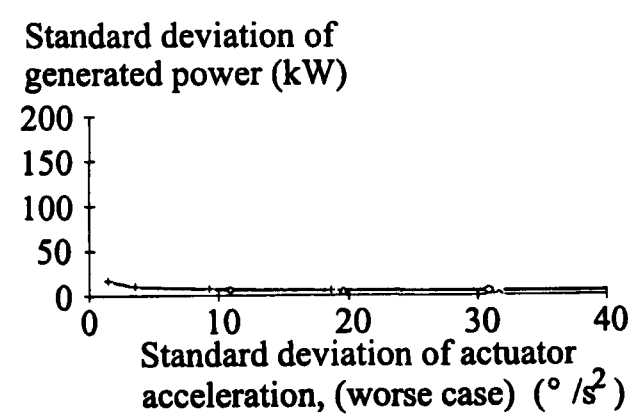
Figure H.14b Worst case performance (actuator velocity)
of three-bladed (nominal $3\Omega_0$) machines Ia and La.



Wind speed 12 m/s



Wind speed 16 m/s



Wind speed 23 m/s

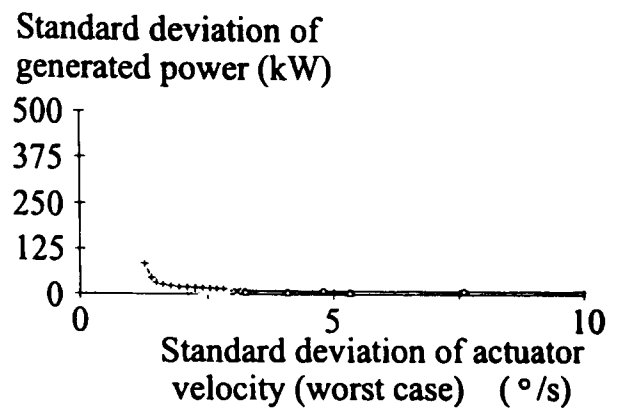
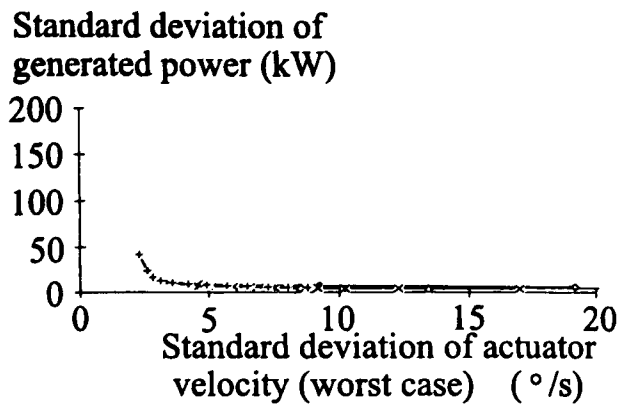
300 kW

1 MW

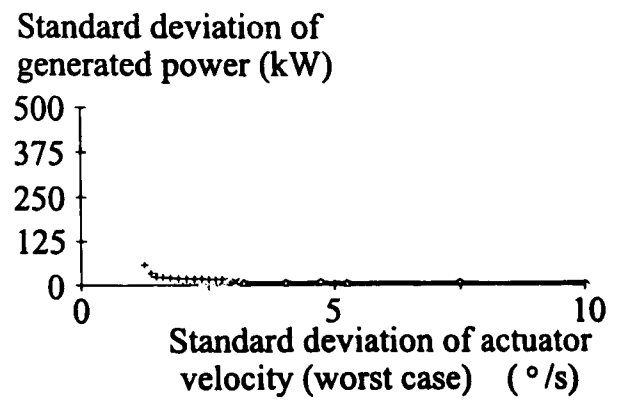
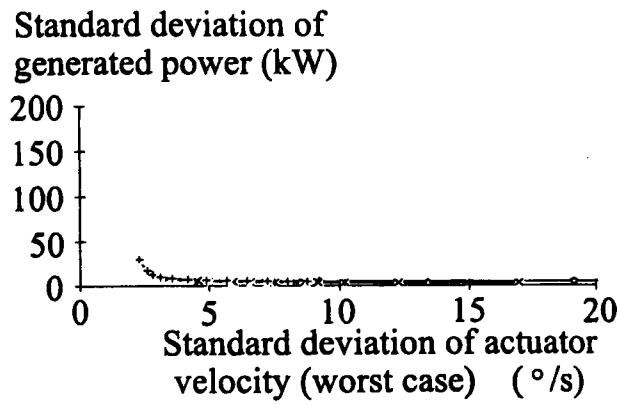
First drive-train mode

→ 2.0 rad/s → 3.0 rad/s → 4.0 rad/s → 5.0 rad/s → 6.0 rad/s → 7.0 rad/s

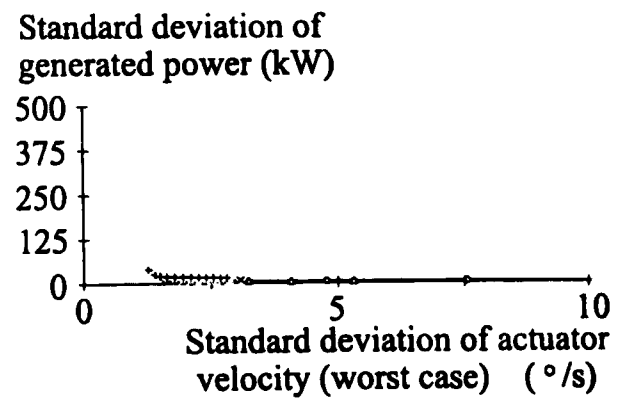
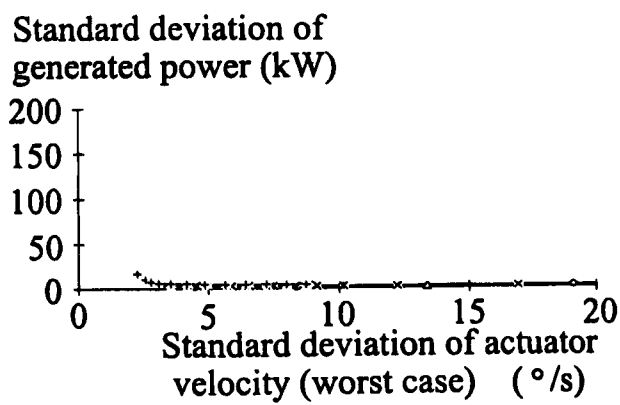
Figure H.15a Worst case performance (actuator acceleration) of three-bladed ($2 \times$ nominal $3\Omega_0$) machines Ib and Lb.



Wind speed 12 m/s



Wind speed 16 m/s



Wind speed 23 m/s

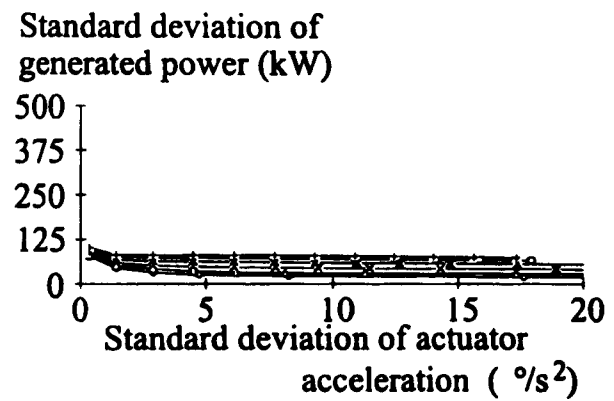
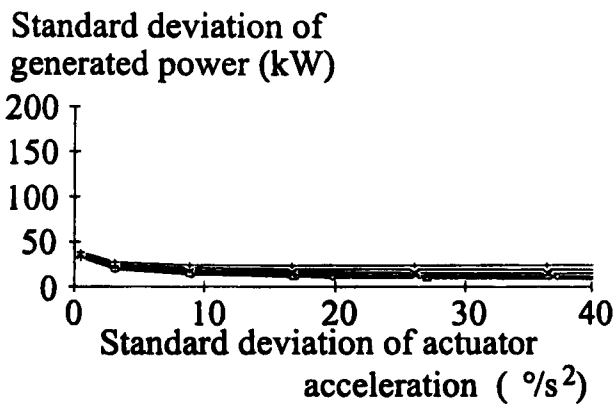
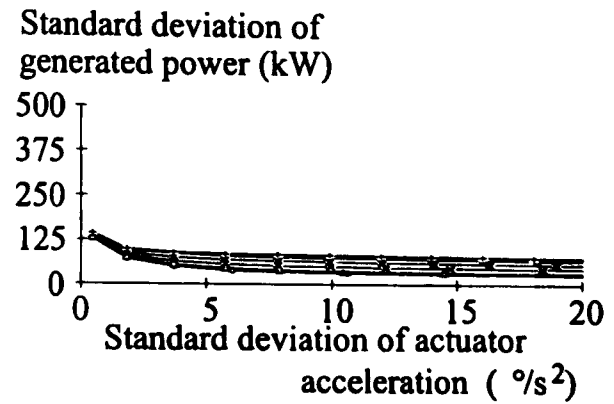
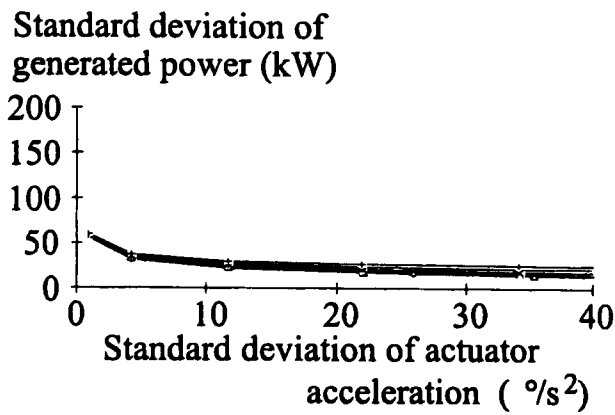
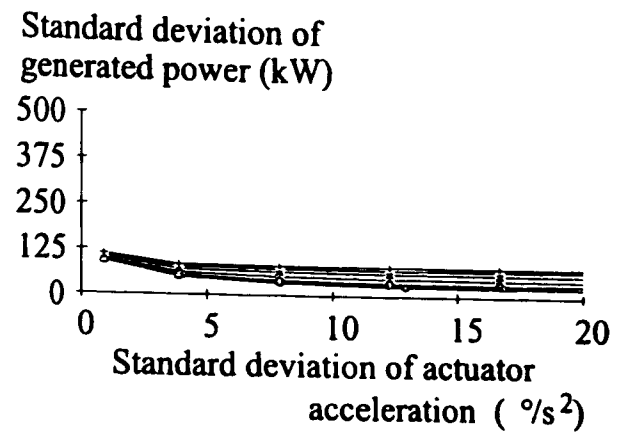
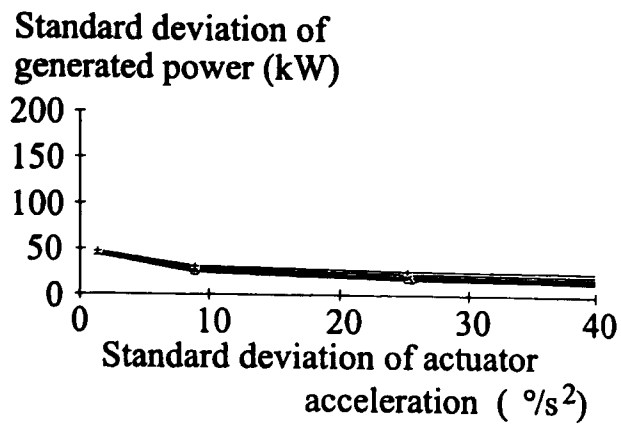
300 kW

1 MW

First drive-train mode

○ 2.0 rad/s ◐ 3.0 rad/s × 4.0 rad/s -x- 5.0 rad/s ◑ 6.0 rad/s → 7.0 rad/s

Figure H.15b Worst case performance (actuator velocity) of three-bladed ($2 \times$ nominal $3\Omega_n$) machines Ib and Lb.



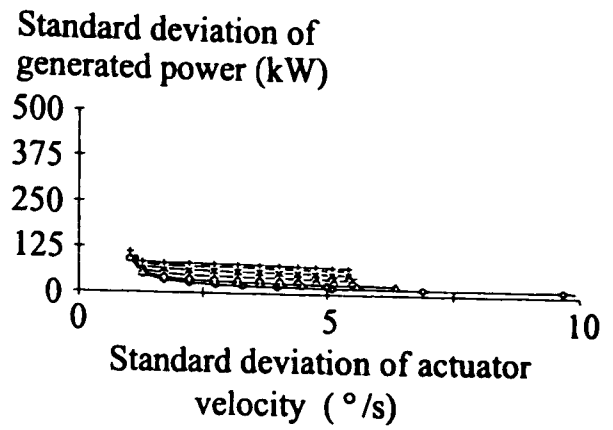
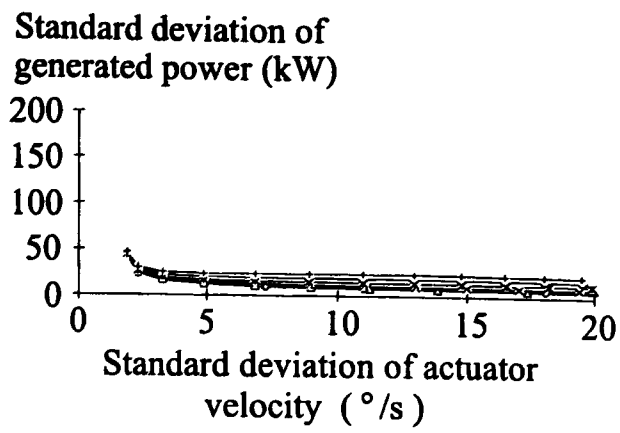
300 kW

1 MW

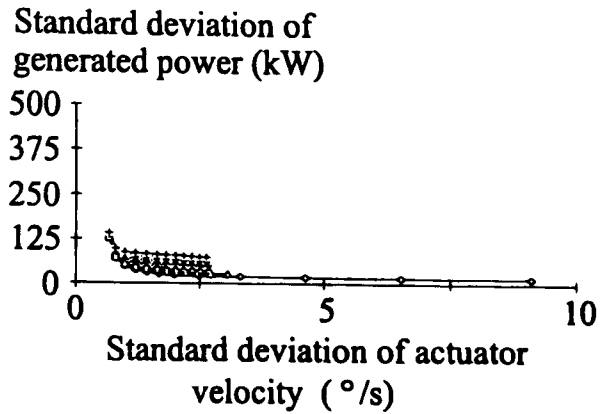
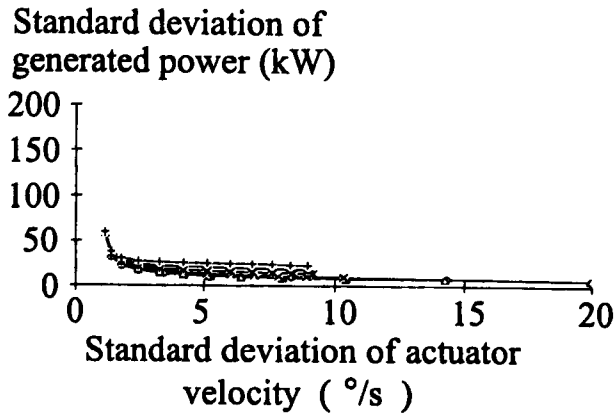
First drive-train mode

\circ 2.0 rad/s
 \square 3.0 rad/s
 \times 4.0 rad/s
 \star 5.0 rad/s
 \diamond 6.0 rad/s
 \triangle 7.0 rad/s

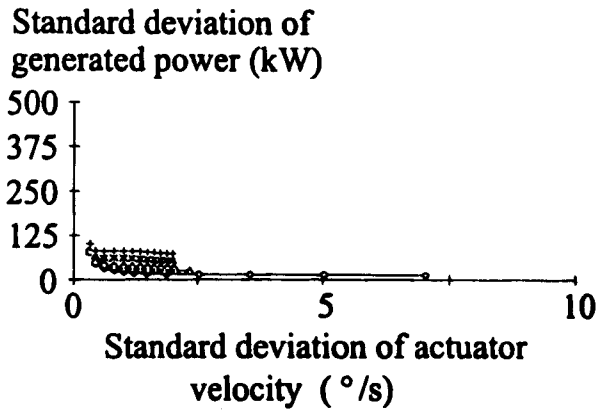
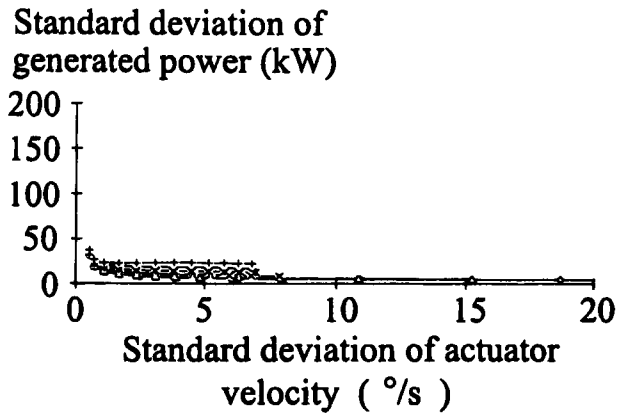
Figure H.16a Performance (actuator acceleration)
of two-bladed ($1/2 \times \text{nominal } 2\Omega_0$) machines Ga and Ja.



Wind speed 12 m/s



Wind speed 16 m/s



Wind speed 23 m/s

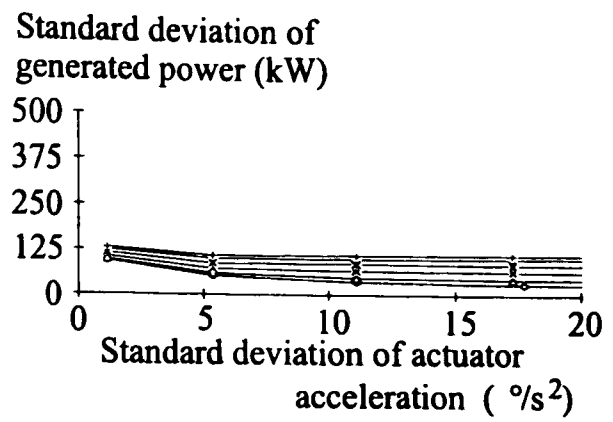
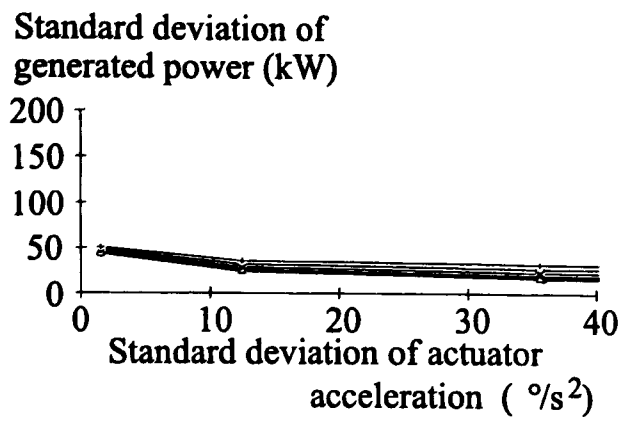
300 kW

1 MW

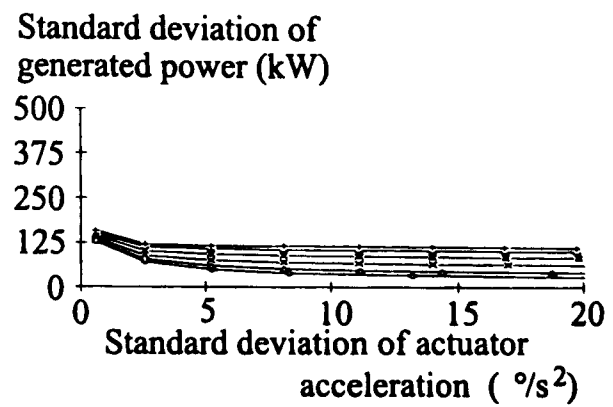
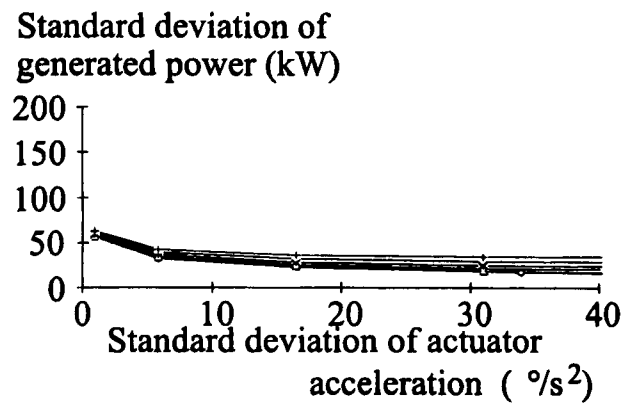
First drive-train mode

—○— 2.0 rad/s —□— 3.0 rad/s —×— 4.0 rad/s —*— 5.0 rad/s —◇— 6.0 rad/s —△— 7.0 rad/s

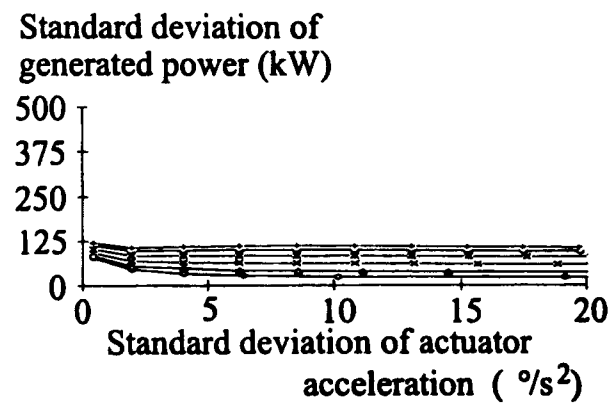
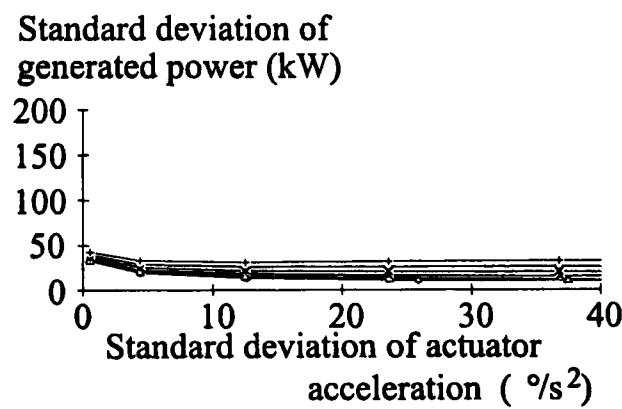
Figure H.16b Performance (actuator velocity)
of two-bladed ($1/2 \times \text{nominal } 2\Omega_0$) machines Ga and Ja.



Wind speed 12 m/s



Wind speed 16 m/s



Wind speed 23 m/s

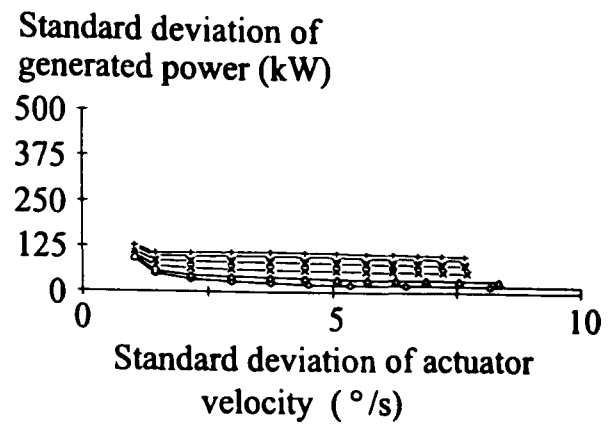
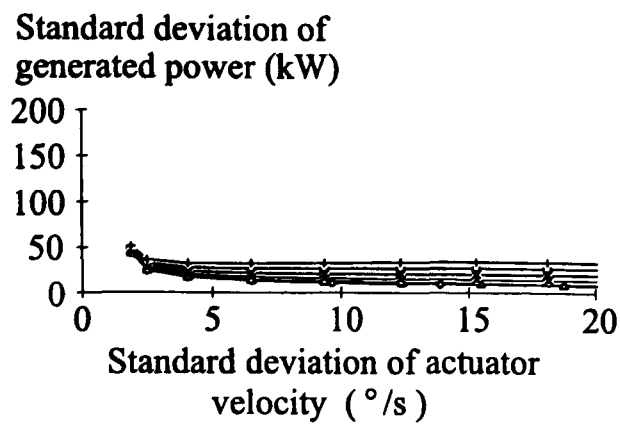
300 kW

1 MW

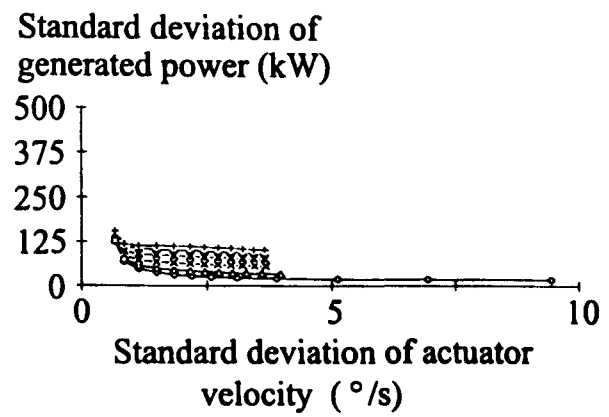
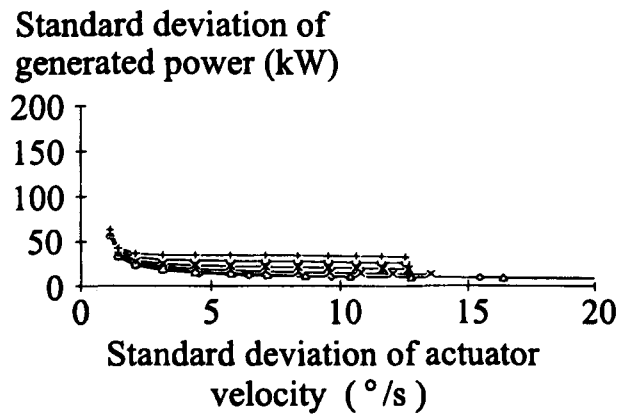
First drive-train mode

→ 2.0 rad/s → 3.0 rad/s → 4.0 rad/s → 5.0 rad/s → 6.0 rad/s → 7.0 rad/s

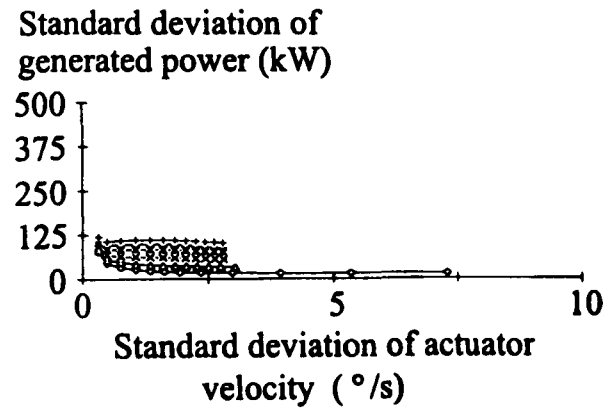
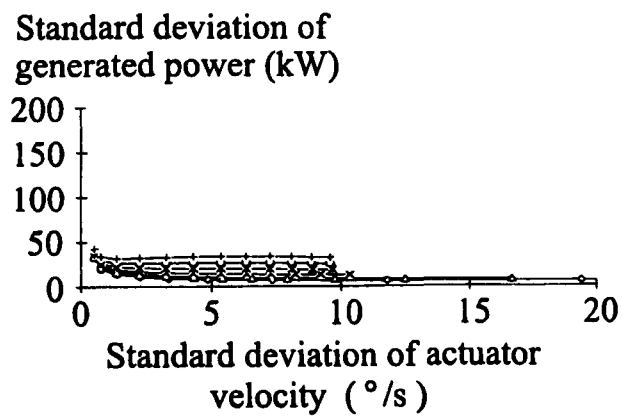
Figure H.17a Performance (actuator acceleration) of two-bladed (nominal $2\Omega_0$) machines Gb and Jb.



Wind speed 12 m/s



Wind speed 16 m/s



Wind speed 23 m/s

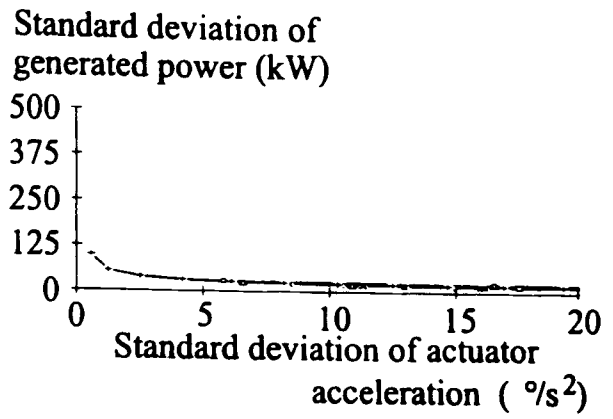
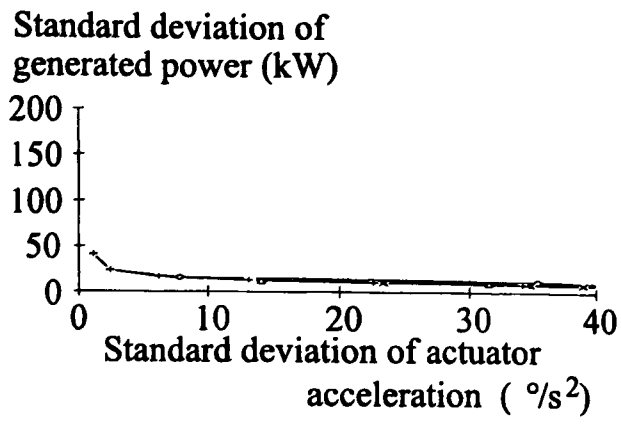
300 kW

1 MW

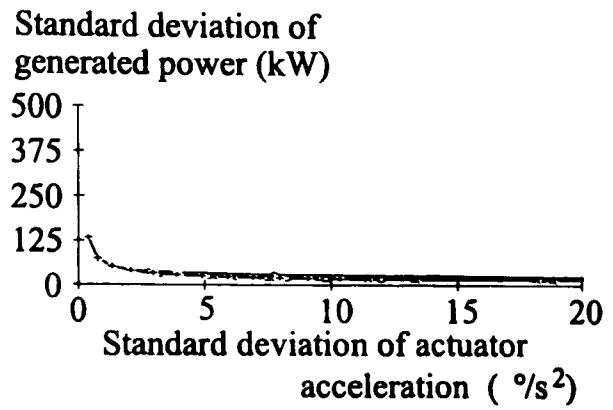
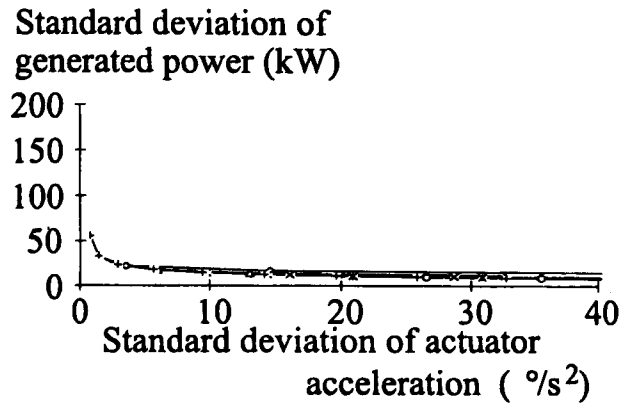
First drive-train mode

\circ -2.0 rad/s
 \triangle -3.0 rad/s
 \times -4.0 rad/s
 \square -5.0 rad/s
 \diamond -6.0 rad/s
 \rightarrow -7.0 rad/s

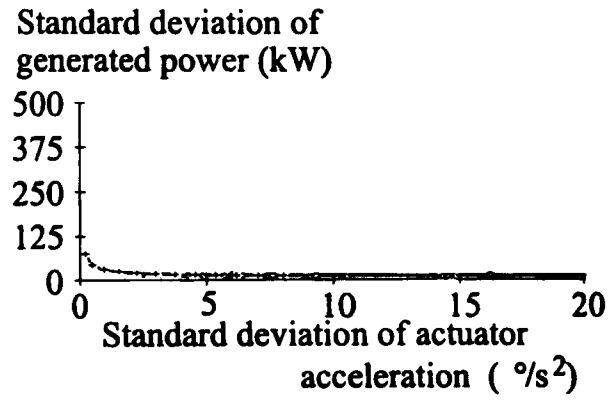
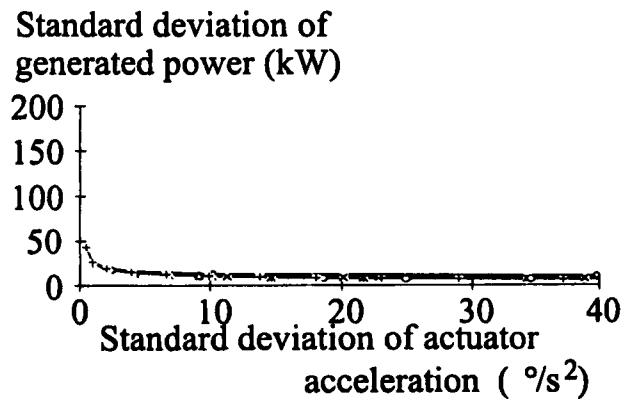
Figure H.17b Performance (actuator velocity)
of two-bladed (nominal $2\Omega_0$) machines Gb and Jb.



Wind speed 12 m/s



Wind speed 16 m/s



Wind speed 23 m/s

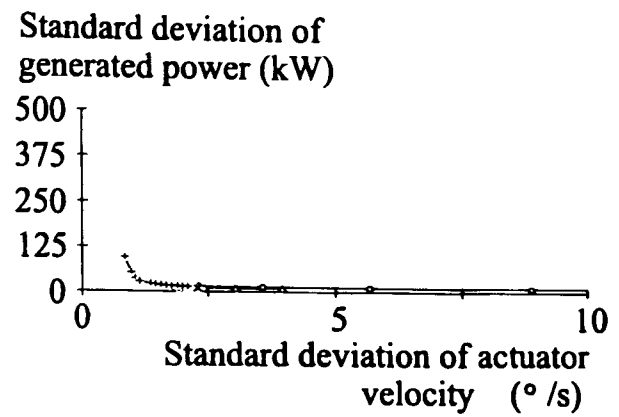
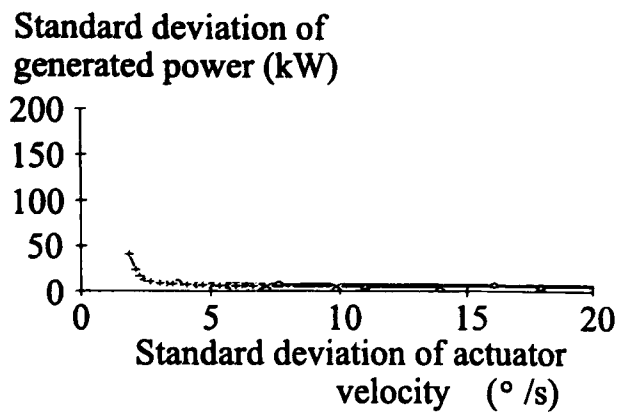
300 kW

1 MW

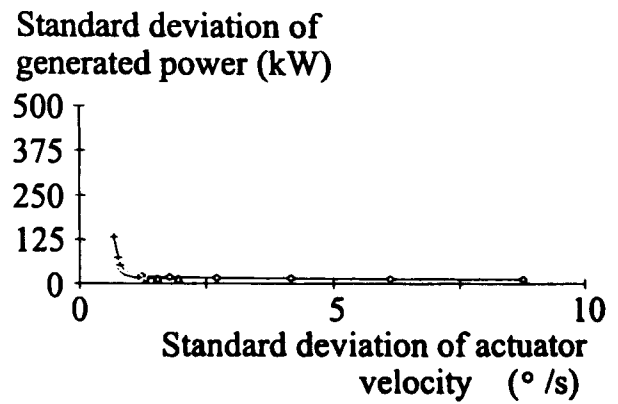
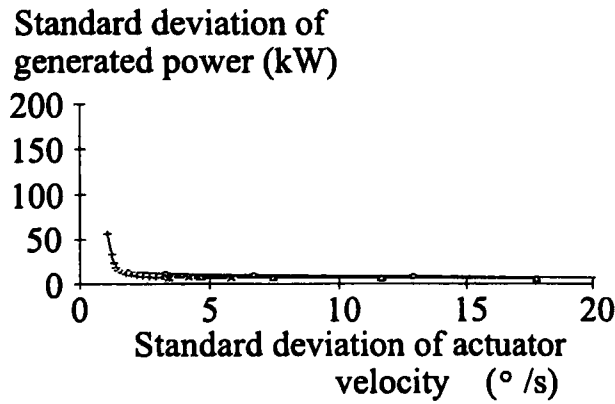
First drive-train mode

→ 2.0 rad/s → 3.0 rad/s → 4.0 rad/s → 5.0 rad/s → 6.0 rad/s → 7.0 rad/s

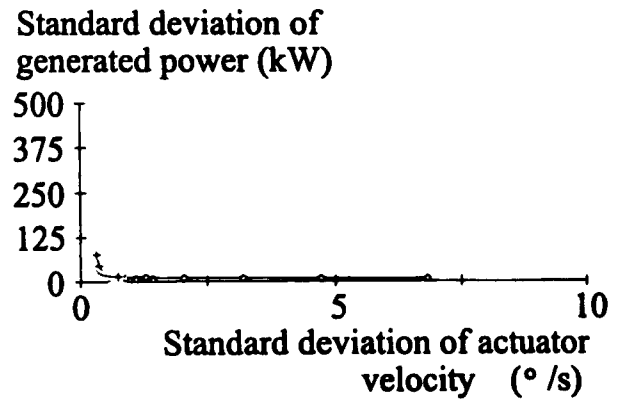
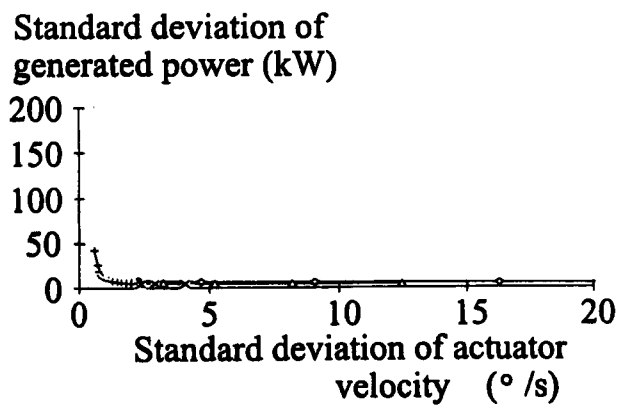
Figure H.18a Performance (actuator acceleration) of three-bladed (fast velocity) machines H and K.



Wind speed 12 m/s



Wind speed 16 m/s



Wind speed 23 m/s

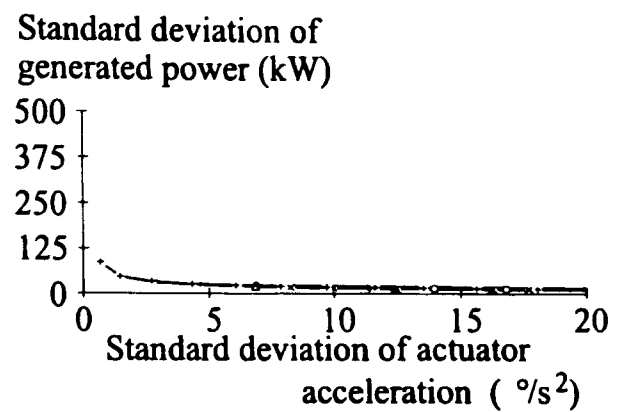
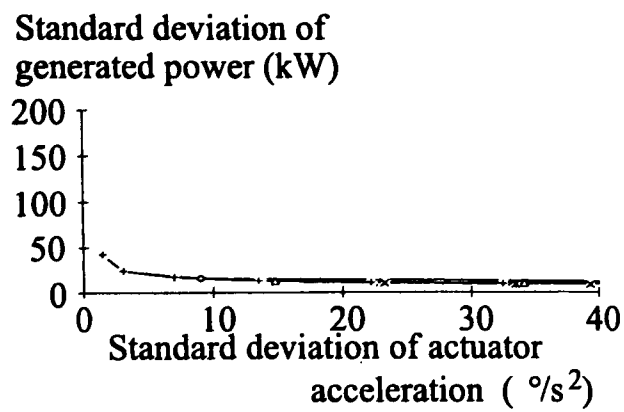
300 kW

1 MW

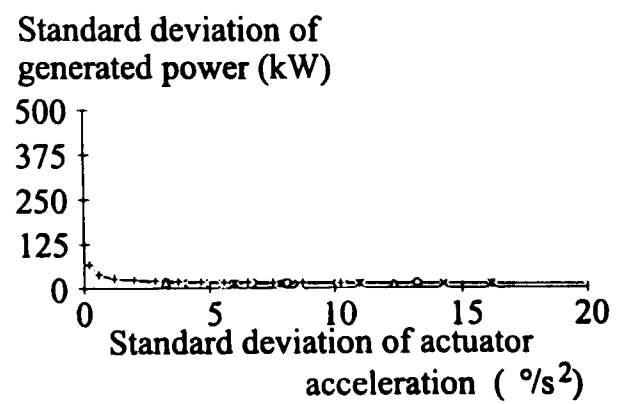
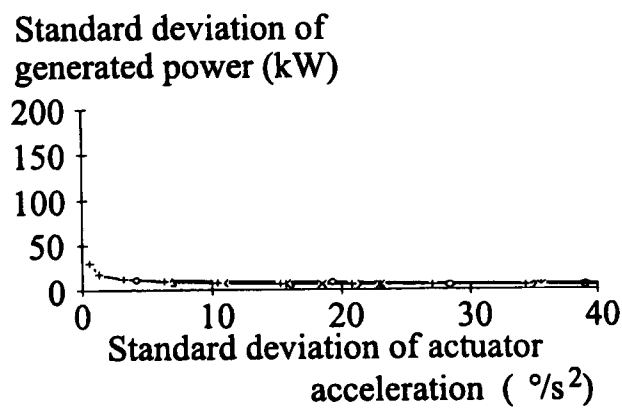
First drive-train mode

—○— 2.0 rad/s —●— 3.0 rad/s —×— 4.0 rad/s —+— 5.0 rad/s —◊— 6.0 rad/s —*— 7.0 rad/s

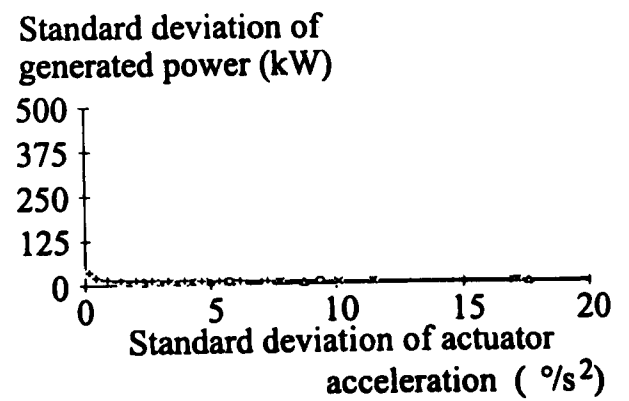
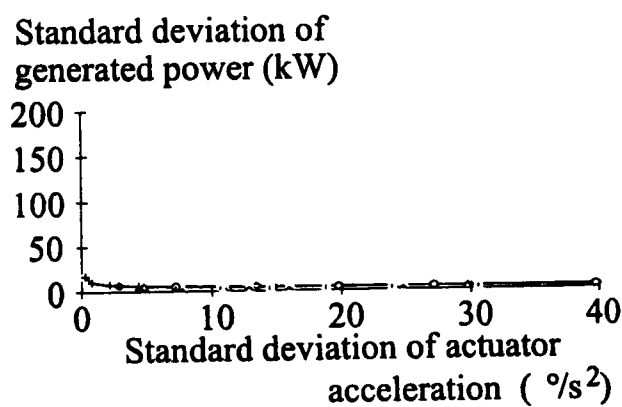
Figure H.18b Performance (actuator velocity) of three-bladed (fast velocity) machines H and K.



Wind speed 12 m/s



Wind speed 16 m/s



Wind speed 23 m/s

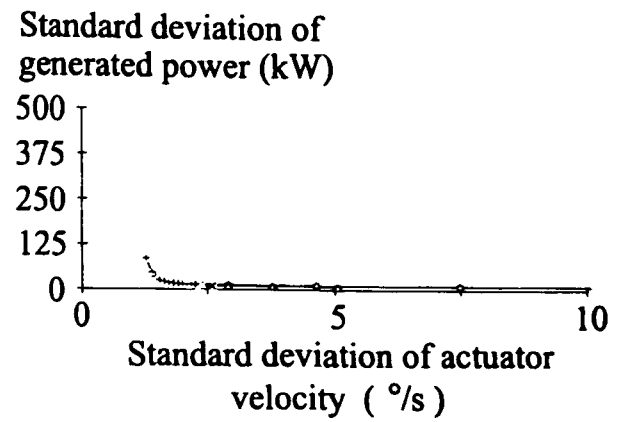
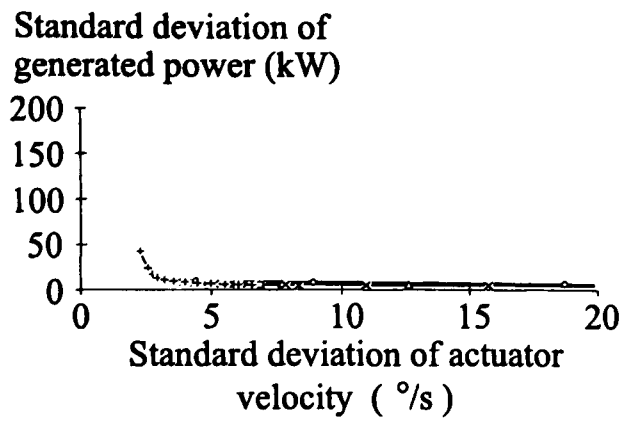
300 kW

1 MW

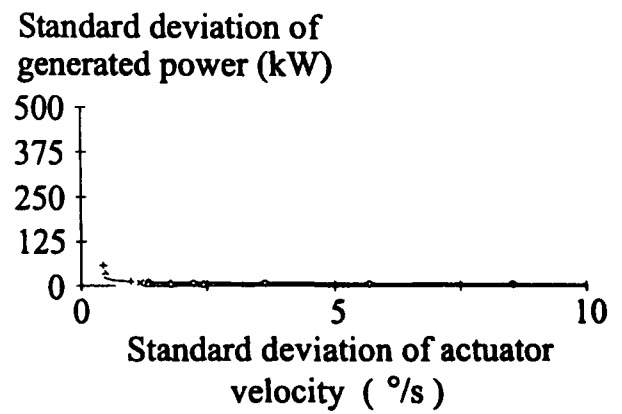
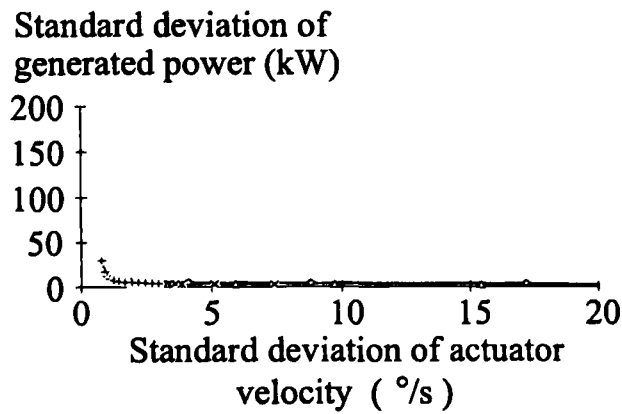
First drive-train mode

—○— 2.0 rad/s —△— 3.0 rad/s —×— 4.0 rad/s —□— 5.0 rad/s —◇— 6.0 rad/s —◇— 7.0 rad/s

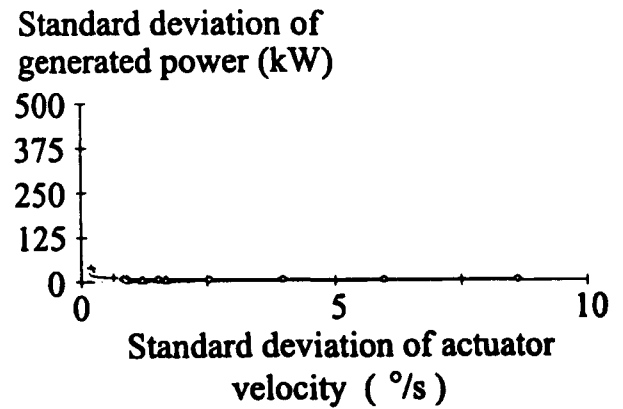
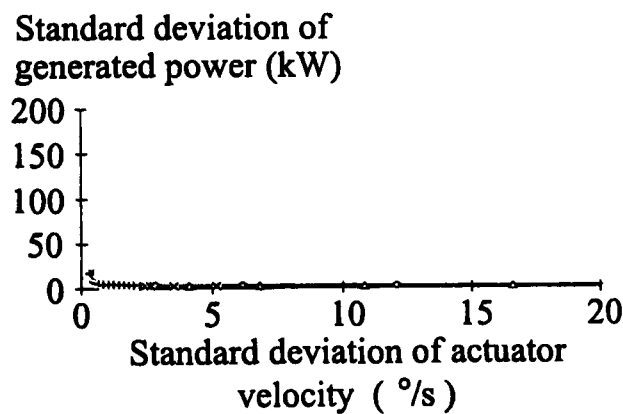
Figure 6.19a Performance (actuator acceleration) of three-bladed (nominal $3\Omega_0$) machines 1a and 1a.



Wind speed 12 m/s



Wind speed 16 m/s



Wind speed 23 m/s

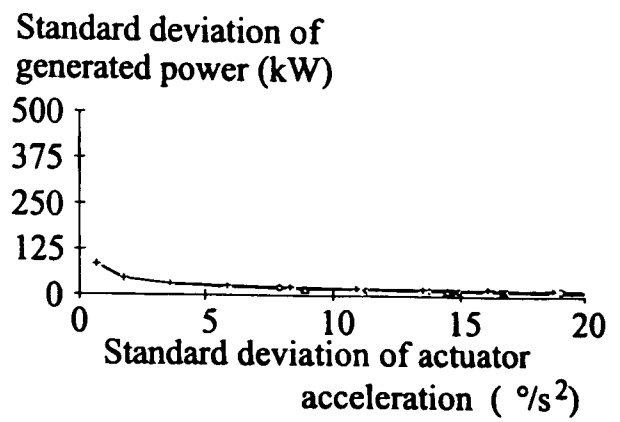
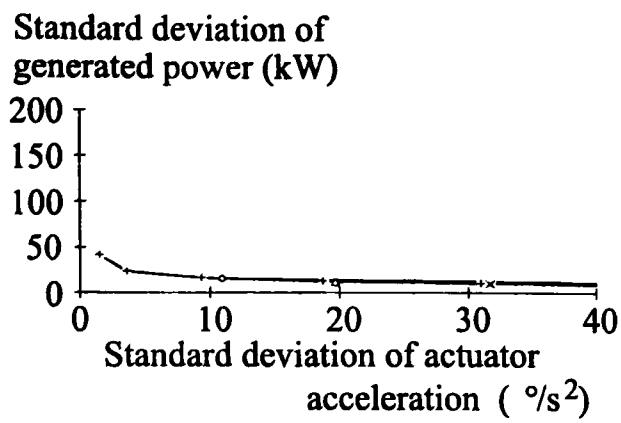
300 kW

1 MW

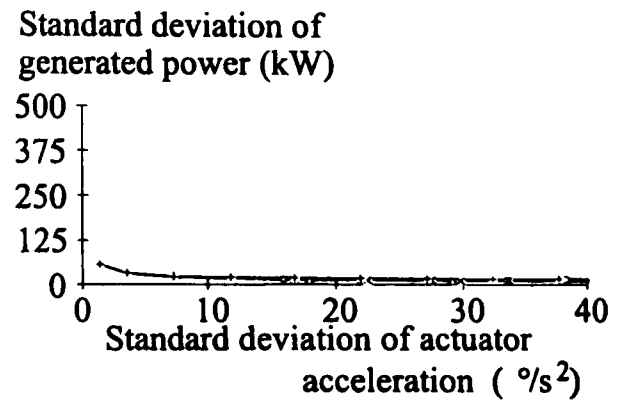
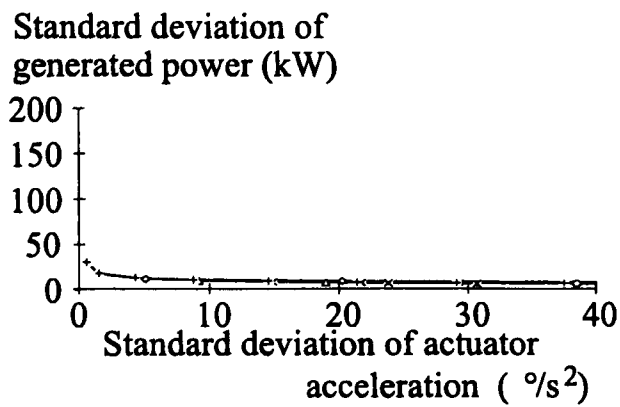
First drive-train mode

○ 2.0 rad/s ○ 3.0 rad/s × 4.0 rad/s × 5.0 rad/s ○ 6.0 rad/s × 7.0 rad/s

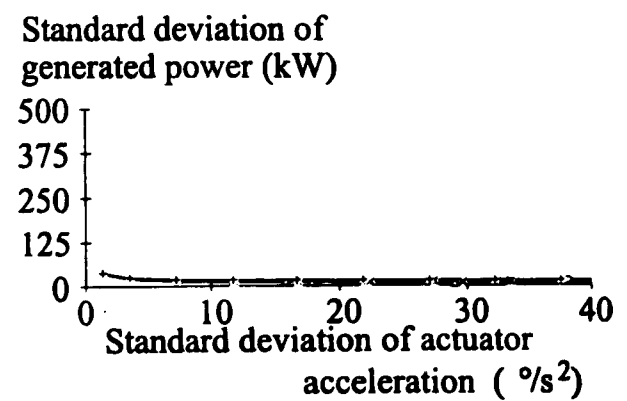
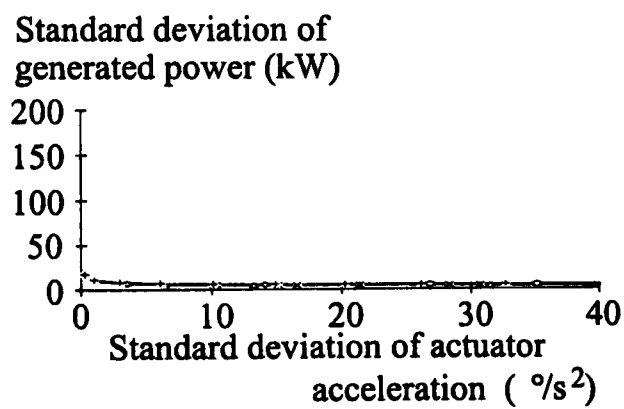
Figure H.19b Performance (actuator velocity)
of three-bladed (nominal $3\Omega_o$) machines Ia and La.



Wind speed 12 m/s



Wind speed 16 m/s



Wind speed 23 m/s

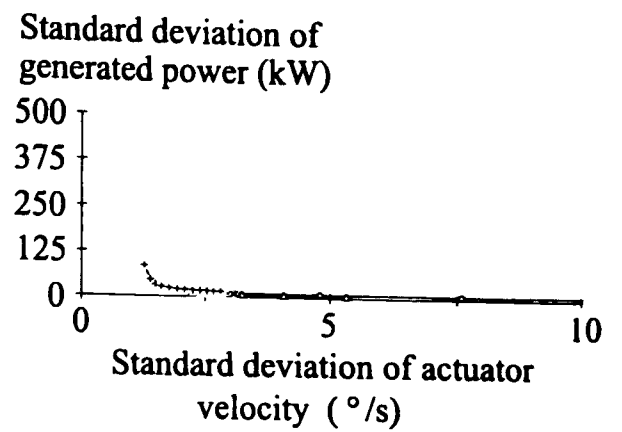
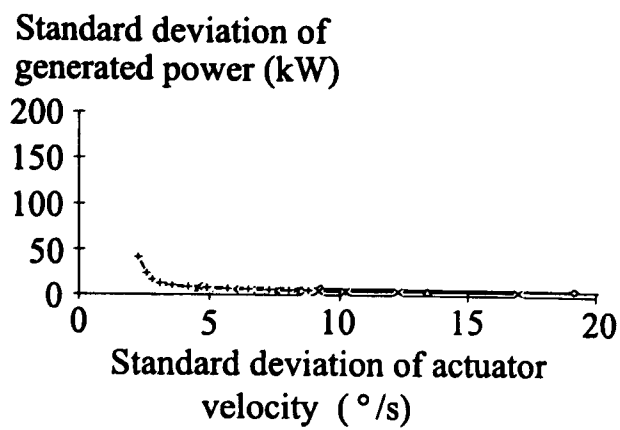
300 kW

1 MW

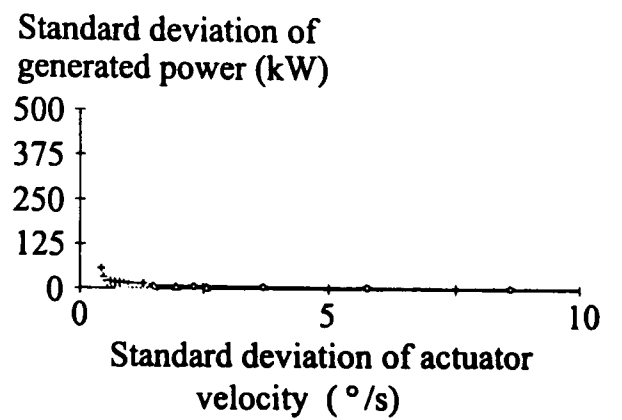
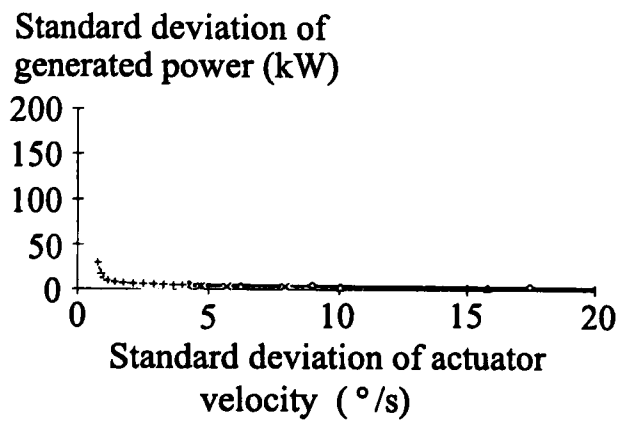
First drive-train mode

○ 2.0 rad/s ◐ 3.0 rad/s × 4.0 rad/s -x- 5.0 rad/s ◑ 6.0 rad/s -+ 7.0 rad/s

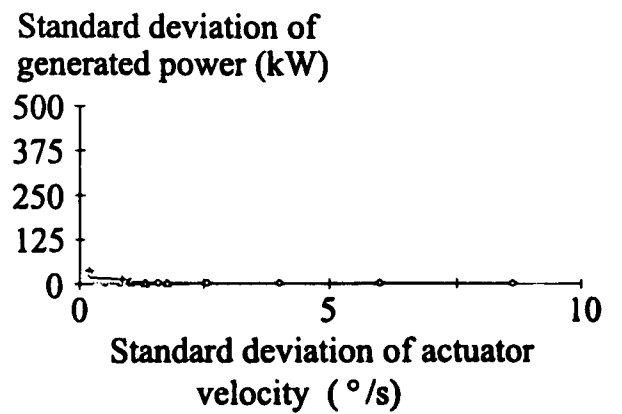
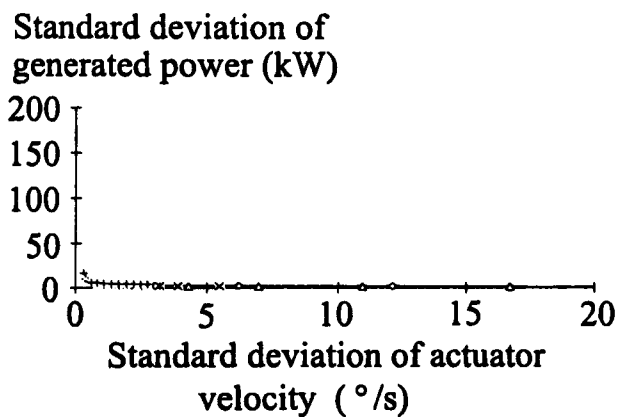
Figure H.20a Performance (actuator acceleration) of three-bladed ($2 \times$ nominal $3\Omega_o$) machines Ib and Lb.



Wind speed 12 m/s



Wind speed 16 m/s



Wind speed 23 m/s

300 kW

1 MW

First drive-train mode

—○— 2.0 rad/s —□— 3.0 rad/s —×— 4.0 rad/s —◇— 5.0 rad/s —△— 6.0 rad/s —▽— 7.0 rad/s

Figure H.20b Performance (actuator velocity)
of three-bladed ($2 \times$ nominal $3\Omega_0$) machines Ib and Lb.